NOVEL NEUTRON DETECTORS

A Dissertation
Presented to
The Academic Faculty

by

Eric Anthony Burgett

In Partial Fulfillment
of the Requirements for the Degree
of Doctorate in Philosophy in the
School of Mechanical Engineering, Nuclear Engineering

Georgia Institute of Technology
May, 2010

NOVEL NEUTRON DETECTORS

Approved by:

Dr. Nolan E. Hertel, Advisor
School of Mechanical Engineering,
Nuclear Engineering Program
Georgia Institute of Technology

Dr. Benjamin Klein
School of Electrical and Computer Engineering
Georgia Institute of Technology

Dr. Chris C-K Wang
School of Mechanical Engineering,
Nuclear Engineering Program
Georgia Institute of Technology

Dr. Ian Ferguson
School of Electrical and Computer Engineering
University of North Carolina, Charlotte

Dr. Christopher Summers
School of Materials Science and Engineering
Georgia Institute of Technology

Dr. Tony Hill
Idaho National Laboratory
U.S. Department of Energy

Dr. Chatyanya Deo
School of Mechanical Engineering,
Nuclear Engineering Program
Georgia Institute of Technology

Dr. Mike Heffner
Lawrence Livermore National Laboratory
U.S. Department of Energy

Date Approved: April 5th, 2010

To my family

ACKNOWLEDGEMENTS

One of the first principles I was taught is that with God, and a bit of hard work, you can do anything. He has guided me every step of my life and will continue to guide me, wherever life takes me. I must thank my loving and understanding wife, Angel. Without her support and tolerance of the long hours and numerous bad attitudes, none of this would have been possible. I must thank my parents, Louis and Joyce Burgett. As a child, they provided guidance and instilled a strong work ethic and the notion that only your best is good enough. I am positive that this has made me the person I am today.

I must thank my advisor, Dr. Nolan E. Hertel, a man who saw some potential in a wide eyed undergraduate almost ten years ago. Guiding and nurturing my academic and lifelong growth like a second father, I owe him an immense debt of gratitude I don't know if I can ever repay. I would like to thank Dr. Ian Ferguson for his support in the endeavor of me learning the MOCVD growth process. His views on life, love, family and scholarly research have had a large impact on my life. I would like to thank Dr. Hertel and Dr. Ferguson for their foresight to create the interdisciplinary group Pioneering Research In Nuclear Detection (PRIND). This program was the start to this whole project. I would like to thank Dr. Christopher Summers for the numerous wonderful afternoon brain storming sessions and for the continuous motivation to think outside the box. Without his help and motivation, none of the photonic crystal scintillator work would have been realized. I would like to thank Drs. Chris Wang, Chatyanya Deo, Benjamin Klein, Mike Heffner, and Tony Hill for taking time out of their busy schedules to be a part of my dissertation reading committee and give their advice on this research.

I would like to thank all of the members of the Ferguson research group particularly, Mohammad Jamil, Andrew Melton, and Tahir Zaidi. Over the last two years, their knowledge of MOCVD and the ECE field inspired me to learn the growth processes and accomplish this research. Without their expertise and coaching, a sign of a good advisor, none of the MOCVD work would have been completed. They were the ones there at 2 AM helping finish proposals, or tearing vacuum pumps apart when they would go down. For this, I am grateful. I would like to thank John Blair, who spent countless hours in the cleanroom patterning and etching the photonic crystal structures. I would like to thank Dwayne Blaylock his friendship and support, helping with all of the projects over the years. Lastly, I would like to thank all of the members past and present of "Team Hertel", in particular Randi Palmer for helping run some of the data collection. From the former members of Team Hertel, I learned a lot from everyone who are now spread across the country. Thanks to everyone who has helped over the years. It has been great and I can't have imagined it any other way.

TABLE OF CONTENTS

Page

Contents

LIST OF TABLES

LIST OF FIGURES

Page

LIST OF EQUATIONS

LIST OF SYMBOLS AND ABBREVIATIONS

ADC	Analog to Digital Converter
AFM	Atomic Force Microscopy
ALD	Atomic Layer Deposition
Å	Angstrom
APD	Avalanche Photodiode
ATM	Atmospheres (Pressure)
AZO	Aluminum Doped Zinc Oxide
BL	Blue Luminescence
BSS	Bonner Sphere Spectrometer
BUMS	Bonner sphere Unfolding Made Simple
CAD	Computer Aided Design
CCD	Charge Coupled Detector
CHM	Condensed History Method
Ci	Curie (Activity)
Cm	centimeter
CSDA	Continuous Slowing Down Approximation

CVT	Chemical Vapor Transport
DBR	Distributed Bragg Reflector
DC	Direct Current
DEB	Diethylboron
DEZ	Diethylzinc
D-T	Deuterium-Tritium reaction
FDTD	Finite Difference Time Domain
FTIR	Fourier Transform Infrared
FWHM	Full Width Half Maximum
GHz	Gigahertz (Frequency)
GL	Green Luminescence
GSDS	Graphite Slowing Down Spectrometer
HPGe	High Purity Germanium Detector
HCP	Heavy Charged Particle
keV	Kiloelectron Volt
LANL	Los Alamos National Laboratory
LANSCE	Los Alamos Neutron Science Center
LED	Light Emitting Diodes

LET	Linear Energy Transfer
eV	Electron Volt
LSDS	Lead Slowing Down Spectrometer
MCA	Multichannel Analyzer
MCM	Monte Carlo Method
MCP-PMT	Microchannel Plate Photomultiplier Tube
MCS	Multichannel Scalar
MeV	Megaelectron Volt
MHz	Megahertz (Frequency)
MIT	Massachusetts Institute of Technology
mm	millimeter
MOCVD	Metallorganic Chemical Vapor Deposition
mr/hr	Dose Rate of millirotegens/hour
MRI	Magnetic Resonance Imaging
NCIA	Neutron Capture Isotope Algorithm
NIM	Nuclear Instrumentation Module
Nm	nanometer
NORM	Naturally Occurring Radioactive Material

Ns	nanosecond
PBG	Photonic Band Gap
PC	Photonic Crystal
PL	Photoluminescence
PMT	Photomultiplier Tube
Ps	Picosecond
RF	Radio Frequency
RPM	Rotation per Minute
S(α,β)	Thermal Upscattering Treatment
SCA	Single Channel Analyzer
SCA-In	Single Channel Analyzer Input
SCVD	Seeded Chrystal Chemical Vapor Deposition
SEM	Scanning Electron Microscope
SNM	Special Nuclear Material
THz	Terahertz (Frequency)
TM	Transverse Magnetic
TE	Transverse Electric
TMG	Trimethylgallium

Torr	Pressure
µm	micrometer
UV	Ultraviolet
XRD	X-Ray Diffraction
ZnO	Zinc Oxide

SUMMARY

A new set of thermal neutron detectors has been developed as a near term ^{3}He tube replacement. The zinc oxide scintillator is an ultrafast scintillator which can be doped to have performance equal to or superior to ^{3}He tubes. Originally investigated in the early 1950s, this room temperature semiconductor has been evaluated as a thermal neutron scintillator. Zinc oxide can be doped with different nuclei to tune the band gap, improve optical clarity, and improve the thermal neutron detection efficiency. The effects of various dopant effects on the scintillation properties, materials properties, and crystal growth parameters have been analyzed. Two different growth modalities were investigated: bulk melt grown materials as well as thin film scintillators grown by metalorganic chemical vapor deposition (MOCVD). MOCVD has shown significant advantages including precise thickness control, high dopant incorporation, and epitaxial coatings of neutron target nuclei.

Detector designs were modeled and simulated to design an improved thermal neutron detector using doped ZnO layers, conformal coatings and light collection improvements including Bragg reflectors and photonic crystal structures. The detectors have been tested for crystalline quality by XRD and FTIR spectroscopy, for scintillation efficiency by photo-luminescence spectroscopy, and for neutron detection efficiency by alpha and neutron radiation tests. Lastly, a novel method for improving light collection efficiency has been investigated, the creation of a photonic crystal scintillator. Here, the flow of optical light photons is controlled through an engineered structure created with the scintillator materials. This work has resulted in a novel radiation detection material

for the near term replacement of ^{3}He tubes with performance characteristics equal to or superior to that of ^{3}He.

CHAPTER I

INTRODUCTION

Current state-of-the-art detectors in widespread use are still utilizing materials and methods originally developed before or during the height of the cold war. Developments in novel neutron detection methods have been slow over the years (1). New and novel detection materials and mechanisms for neutron detection have been minimal over the last 50 years with only incremental improvements in designs, new experimental and calculated response matricies, and better pulse processing electronics. The relatively slow growth in neutron detection technology has been in part because there has not been a large need for better radiation detector materials or methods.

The main goal of this dissertation is to solve two main problems in neutron detection utilizing one novel neutron detection material, zinc oxide. The first main goal is driven by homeland security needs for improved neutron detection materials in a near term replacement for ^{3}He tubes, a thermal neutron detector in widespread use (2). The second need is driven by the nuclear physics community and their need for a neutron detector which is "optically" thin, having a low areal density, very fast, and highly efficient (3). Both applications demand a new neutron detecting material with excellent neutron versus gamma discrimination capabilities, very high efficiencies, and is cost effective. The solution that has been developed comes from ZnO that has been doped to improve its neutron detection performance.

Current Need for Neutron Detection

There are two main needs outlined in this dissertation for new neutron detection materials and methods. The first centers on the acute need for ^{3}He tube replacement technologies. This need is being driven by the large usage of ^{3}He tubes in portal monitors which are now being deployed worldwide (4). The second need is a need from the nuclear physics community (3). The physics community uses ^{3}He as a cryogenic liquid with temperatures colder than standard liquid helium. Competing against an already dwindiling supply of ^{3}He, the material is becoming scarce. Its uses include cooling samples to cooling MRI magnets, and cooling superconducting magnets at the world's largest accelerators. ^{4}He has a boiling point of 4.2K at 1 atm, while ^{3}He has a boiling point of 3.2K at 1 atm (1). The lower boiling point has added benefits for superconducting magnets.

The second physics need is for the creation of new neutron detectors. As the Department of Energy entertains closing the fuel cycle domestically, and introducing Generation IV (Gen-IV) reactors, an increased need is placed on precision nuclear data files for the transuranics (5). Not only are cross section measurements important in this campaign, but also the need for improved data on the fission neutron distribution and multiplicities of the transuranics. Ideally, one would measure the neutron multiplicity, angular dependence, energy dependence, and time dependence of all of the transuarnic isotopes in support of this need. To do this, a number of detection systems have been proposed, but are limited in the data in which they can collect due to one drawback or another. Often, one can make a neutron sensitive detector, but cannot make it discriminate gamma rays. The balance between scintillation speed, neutron versus gamma discrimination, neutron detection efficiency, fabrication cost, and detector volume is traditionally a lopsided balance favoring a few of the parameters, but not all.

The second driving motivator for this work is the near term replacement thermal neutron detector for the ^{3}He tube. After the attacks of September 11th, there became a much larger demand on protecting the nation and abroad from the use of nuclear weapons. During the cold war, the nuclear threat was always well known. Only the superpower nations had nuclear weapons. Following the fall of the Soviet Union, the threat of a terrorist's usage of nuclear weapons became the primary concern. Unlike the traditional cold war scenario in which nuclear weapons would be deployed using an intercontinental ballistic missile, a terrorist detonated nuclear weapon would be smuggled into the country in which it would be deployed. Detecting the special nuclear material inside a nuclear weapon became a very high priority for national security.

Detecting special nuclear material or SNM is a difficult proposition. SNM includes any fissionable isotope such as ^{235}U, ^{239}Pu. Also controlled by the federal government, materials that can be used in increasing the yield of a nuclear weapon such as ^{3}H or ^{6}Li are regulated. The difficulty in detecting SNM is that it does not emit radiation which is very penetrating. Fissionable SNM emits primarily low energy photons, beta particles, and alpha particles. These radiations are easily shielded with a small amount of lead or other high Z material. If a terrorist were to try to smuggle SNM into the country, they would have considered the potential passive countermeasures and prepared by shielding it from the primary detection modality, gamma spectroscopy.

A representative gamma spectrum from bare ^{235}U can be seen in Figure 1. Of the probable photons that are emitted, they are primarily low energy photons with energies less than 200 keV. This energy region of gamma rays is easily shielded with a minimal amount of lead. If the uranium or plutonium is assembled into a solid mass, due to its high Z number and high density, it's self shielding prohibits most of the gamma rays from exiting the volume. A more penetrating radiation inspection tool is needed to locate SNM. One such penetrating radiation is neutron radiation. Unlike gamma ray radiation shielding tendencies to make more efficient shielding materials from high Z number, high

density materials, neutron radiation is not easily shielded. Since neutrons can be created in a controlled fashion using pulsed accelerator sources, from cosmic sources, or from radiochemical or radioisotope sources, it is the penetrating radiation of choice for active interrogation or detection. (6) SNM, mainly ^{238}Pu, ^{240}Pu ^{242}Pu, produces neutrons as a result of its decay by means of spontaneous fission, albeit with a low frequency (7). SNM also has a high cross section for photon induced neutron production known as photonuclear production or fission induced by gamma rays known as photofission (8). Lastly, neutrons can induce fission in the SNM. These neutrons caused by either induced fission or spontaneous fission are very penetrating in many materials and can be detected at long distances. These neutrons can be significantly more difficult to shield then their gamma ray counterparts.

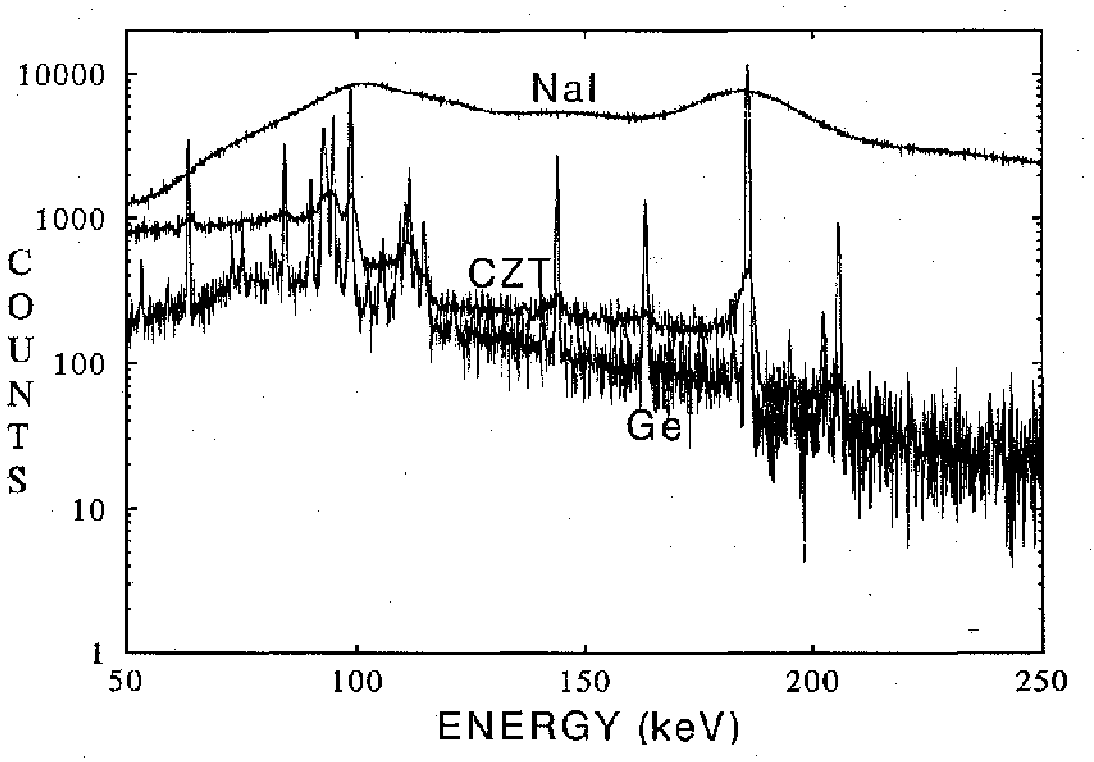

Figure 1 Reference ^{235}U spectrum taken from a HPGe, CZT and NaI(Tl) detector. (9; 10)

Due to their penetrating nature, a number of passive and active neutron detection systems have been proposed. A passive neutron detection system is merely an array of

gamma and neutron detectors that can have sophisticated software to interpret the data collected by the array of detectors. An active system is more sophisticated in which an active source of radiation, either electron accelerator produced bremsstrahlung spectra at high energies, or neutrons generated from a D-T, D-D or photoneutron source are used to actively induce fission. These active interrogation systems are either one or two sided detector systems. A one sided system relies only on a bank of neutron and/or gamma ray detectors co-located with the accelerator, having the entirety of the system on one side of the object to be scanned (11). A two sided active interrogation system uses detectors on both sides of the object. This two sided active interrogation system has the added advantage of twice the detection efficiency but is not well suited for deployment in a hostile theater such as a battle field (12). The two sided approach is mostly utilized in the cargo container inspection systems.

Currently both the active and passive neutron detection systems utilize a moderate and capture detection scheme based on ^{3}He tubes (13). The increased deployment of portal monitors having ^{3}He tubes in them is causing a national shortage of ^{3}He. By way of congressional act (10) it was mandated that all ports of entry into the United States be monitored by portal monitors and all cargo containers get screened. ^{3}He is found in a relatively small abundance in nature in the natural distribution of helium at 0.000137% (14). ^{3}He, however, is primarily collected during the production of tritium. As tritium decays, it produces a beta particle and transitions to ^{3}He. The main source of ^{3}He production was the Department of Energy stockpile stewardship program in the maintenance and construction of nuclear weapons. Since we as a nation have not been reprocessing tritium, the stockpiles of ^{3}He have dwindled.

History of Neutron Detection

Tightening supplies of ^{3}He have forced researchers to go back and reevaluate previous neutron detection technologies. Neutrons, being a neutral particle are more difficult to detect than electrons or alphas because they are neutral particles. To detect them, one must harness a material with a large cross section for charged particle production. The lighter atomic numbered materials tend to center around a handful of nuclei whose inner spin-orbit coupling is near to either one or a pair of magic numbers. The nuclei traditionally used as a neutron target are ^{1}H, ^{3}He , ^{10}B , ^{6}Li, ^{157}Gd, ^{235}U, In, and Ag. Previous neutron detection technologies focused around one of five main categories; gas filled tubes, solid foil based detectors, liquid scintillators, inorganic scintillators and solid state detectors.

The gas filled tubes relied on initially ^{10}B containing compounds using $^{10}B(n,\alpha)^{7}Li$ reaction. One such system is a $^{10}BF_3$ gas-filled tube. Here, boron trifloride (a caustic and toxic gas) is filled into a cylindrical or spherical chamber. High voltages upwards of 2000V are needed to achieve good gas amplification which is hindered by high gas fill pressures. These tubes are easy to use, fairly rugged, but are filled with a toxic gas and pose a shipping problem. A solution to this today is the gas filled ^{10}B lined cylindrical tube. This removes the toxic boron trifloride gas and replaced it with a safer P-10 or pure argon mixture. These tubes too required relatively high voltages. ^{10}B filled tubes however suffer from what is known as the "wall effect", particularly in the ^{10}B lined tubes. Due to the center of mass balance in the $^{10}B(n,\alpha)$ reaction, at thermal energies, it is likely that one of the two heavy charged particles will strike the wall. Since no ionization events occur in the fill gas of the tube, that energy is lost. The "wall effect" makes a stair step pulse height distribution which can be seen in Figure 2. Due to the low mass number, gamma discrimination is still possible with the ^{10}B gas filled detectors.

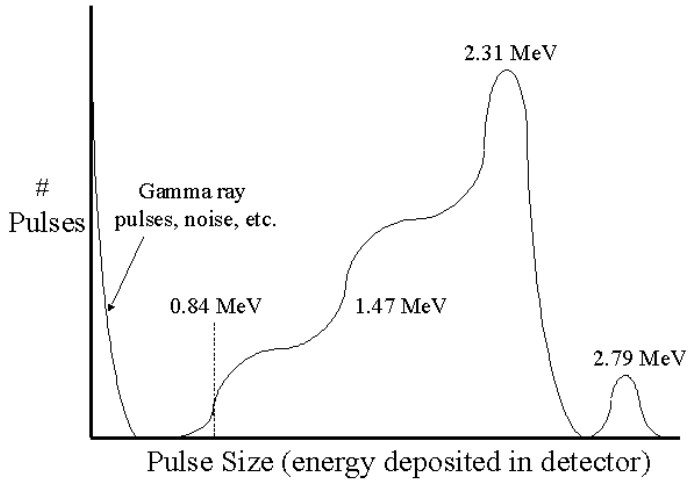

Figure 2. Wall effect in ^{10}B detectors.

^{3}He is used as an invaluable thermal neutron detector. It's low Z number makes it ideal for gamma discrimination. The Q value for the reaction of $^{3}He(n,p)$ is quite large (764 keV) (15) depositing a significant amount of energy into the gas cavity. Large gas amplifications can be achieved with the dry fill gas. However, operating voltages in excess of 3000V are not uncommon for larger filled tubes. To raise the detection efficiencies, fill gas pressures between 2 and 10 ATM are routinely used. To increase the detection efficiencies at higher energies, ^{3}He tubes are often surrounded by a hydrogenous neutron thermalizing material (moderator material) such as polyethylene. The polyethylene is used to slow fast neutrons down to thermal energies where the cross section for ^{3}He is large. Neutron spectrometers such as the Bonner Sphere Spectrometer (16) (17) (18) have been created around the ^{3}He tube. By varying the moderator thickness the energy response of the ^{3}He tube can be varied producing unique energy responses. These unique energy responses can be deconvolved through a mathematical unfolding process. The versatility and neutron versus gamma discrimination of the ^{3}He tube is one of the primary reasons for its popularity, and thusly, its high demand. The high demand for these tubes has caused the shortage which needs to be addressed. (19)

Another thermal neutron detector system is based on activation reactions in foils. Some of the first neutron detectors called "Moon detectors" were Geiger Muller tubes with a silver foil placed over the window of the detector (20). The silver was activated by thermal neutrons and the activation products rapidly decays with a 3 second and 15 second half lives (21). These tubes were good, but due to the activation and subsequent decay of the activation products, the tubes were slow to activate and produce usable signals. An extension of this idea was to incorporate a fissionable material into a gas filled detector, and thus the fission chamber was created. Here, a gas filled proportional detector has fissionable material deposited on the inside. Neutrons induce fission and one of the two fission fragments enter the fill gas of the detector. This was actually the first neutron detector developed in which the fission process was observed. (22) This reaction method is favorable due to the large energy and consequently large pulse produced by these events. The fission process releases approximately 180 MeV to the two fission fragments. By combining various fissionable and fertile isotopes, such as ^{235}U, ^{238}U, ^{237}Np, and utilizing the threshold for fission of the fertile isotopes, one can develop a crude idea of the neutron energy profile. By taking the ratio of counts from several threshold fissioning isotopes and a thermal fissioning isotope, an idea of thermal and fast fluence rates can be discerned (23). These detectors, however, require the use of fissionable material.

Another neutron detection method which has been investigated over the last 40 years is the solid state neutron detection method. Solid state neutron detectors based on silicon diodes were originally coated with a neutron detector material such as ^{6}Li, ^{10}B, or ^{235}U. With the increase in microelectronics fabrication methods, recent developments have included making pillar, monolithic, and trench etched silicon diode structures. Here, holes, rods, or long trenches are etched in a silicon diode wafer. Using a thermal evaporation process, ^{6}LiF or ^{10}B is infiltrated into the void spaces. By infiltrating more material into the structure, higher detection efficiencies are possible. A second reason for

infiltrating the material into the diode structure itself is to collect both charged particles produced in the (n,α) reaction. By collecting both fragments, the neutron versus gamma discrimination capability increases. Examples of the trench and pillar silicon structures are shown below in Figure 3 and Figure 4 (24) (25).

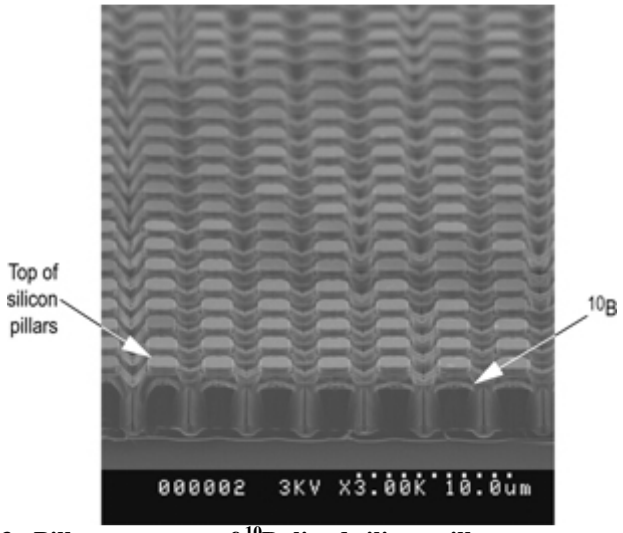

Figure 3. Pillar structure of ^{10}B lined silicon pillars grown at LLNL.

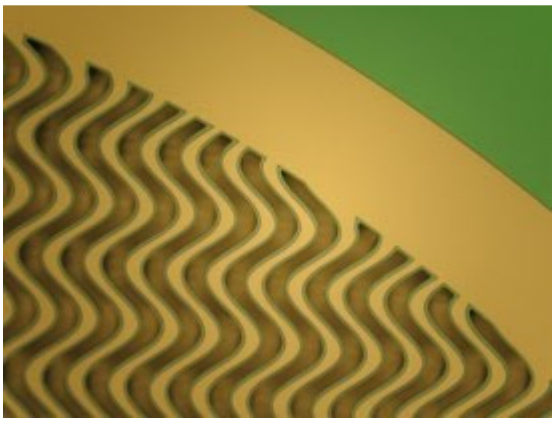

Figure 4 Silicon trench detector filled with ^{10}B designed at Kansas State University. (26)

The silicon trench detectors are a promising detection method but often suffer from breakdown of the silicon structures, problems infiltrating the ^{10}B into the structure, and difficulties fabricating the devices. Authors of these detectors have claimed intrinsic detection efficiencies upwards of 50% for thermal neutrons. One of the drawbacks of

these systems is the rate of charge collection, particularly after infiltration with neutron detector materials. ^{6}Li is the scourge of the semiconductor world and passivates the P-i-N structure of the semiconductor rendering it useless. The infiltration process is difficult to ensure no lithium diffusion into the semiconductor itself.

Another method for detecting neutrons is through the scintillation process. Several detector designs around the scintillation process have been conceived over the years including organic and inorganic solutions. Inorganic detectors such as ^{6}LiI are attractive because they readily absorb thermal neutrons. The ^{6}LiI scintillator however has a high Z number making it also sensitive to gamma ray radiation. In a large format, it is difficult to discriminate gamma ray radiation from neutron radiation if the crystal is made very large. Crystals made from boron and gadolinium has also been proposed. Any material containing gadolinium has the difficulty of high Z number and large gamma ray responses.

A non-crystalline scintillator which is inorganic comes from scintillating glasses. Lithiated glass scintillators are a decent neutron detector material with high lithium content. However, these scintillators are also suffer from poor neutron versus gamma discrimination. For fast neutron detection, the organic scintillator is a good tool. Organic scintillators are made from an aromatic hydrocarbons, one in particular favored historically is anthracene (27). These can be either solid single crystals, or dissolved in a solvent to form liquid scintillators. Today the more common scintillators are the organic scintillators with POPOP dyes such as BC501a (28), EJ301 (29) and the original NE213 (30). These materials utilize the (n,p) scattering cross section of hydrogen as the detection modality for fast neutrons. Utilizing pulse shape discrimination, gamma and neutron radiation can be detected and separated simultaneously (31). Numerous detection devices have been designed using this system. Improvements on this system over the years have included capture gated neutron detection and spectroscopy. Here, pulse heights are recorded for all of the proton scatters that lead up to the capture of a

thermalized neutron by dissolved ^{10}B or ^{6}Li in the scintillator matrix (32). The capture pulse, due to its significantly higher energy release, is larger than all of the proton scatter pulses. The proton scatter pulses are then summed from approximately 500 keV to the original incident neutron energy (33). This summation can be used to ascertain the incident neutron energy. This method however is slow and computationally intensive. Energies below 500 keV cannot be ascertained because the energy imparted to the hydrogen nucleus at these energies is too low to be detected in the scintillator. Lastly, all organic scintillators are flammable to some extent (34). Liquid scintillators are particularly flammable being dissolved in Toluene, Xylene or Naphthalene.

Hypothesis

To date, there is no unified solution to the neutron detection problem produced by the niche that ^{3}He tubes currently fill. ^{3}He tubes are the mainstream thermal neutron detector in widespread use. Gas filled detectors based on ^{10}B gasses either have a low neutron versus gamma discrimination, have poor detection efficiencies and/or are made from a toxic gas. Solid foil based neutron detection materials have low detection efficiencies, and are slow to respond. Fission chambers rely on radioactive material and are relatively small in size. Inorganic scintillators and glasses suffer from slow speeds and poor neutron versus gamma discrimination capabilities in large crystalline structures. Organic scintillators while fast, are made from flammable liquids or if cast into a solid, cannot discriminate neutrons from gammas. A new detector with properties that meets or exceeds the performance of ^{3}He tubes is needed. It is hypothesized that zinc oxide (ZnO) scintillators, doped with neutron detector materials and wavelength shifting materials, improved through the aid of a photonic crystal structure, can serve as the thermal neutron detector to replace ^{3}He. To evaluate the novel ZnO scintillator as a neutron detector, a matrix of six points will be used. The six points are neutron detection efficiency, neutron

versus gamma discrimination, scintillation wavelength, scintillation speed, optical clarity, and ease of growth/size of the detector. The six main characteristics of the novel ZnO scintillators will be tested against current industry standard detectors. Important parameters such as detection efficiencies and gamma discrimination capabilities in particular will be tested against standard neutron detectors such as ^{3}He tubes and lithiated glass scintillators.

CHAPTER II

SCINTILLATION AND DETECTOR THEORY

Scintillation detectors date back to the 1930s during the peak of the research on radium and the beginnings of nuclear physics research. Radiation detection focuses on detecting, quantifying using and understanding energetic charged and neutral subatomic particles and heavy charged particles. The starting point for all radiation detection is the quantification of the ionization in a material. For charged particles, the ionization events are a direct result from the energetic particle traveling through the detector material. The challenge is in the detection of neutral particles. To detect neutral particles or indirectly ionizing particles, a conversion reaction must occur in which the particle decays, has an interaction producing a charged particle, or scatters off of a charged particle producing a recoiling charged particle. In the early 1930s, researchers found that if heavy charged particles such as alpha particles strike special screens, such as zinc sulphide, they produced flashes of light. These flashes of light were actually scintillation events. Under slow count rates, the human eye could visibly quantify the number of light flashes. The need for field deployable light, reliable detectors fueled research on scintillation detection.

Scintillation radiation detection has not changed significantly in the last 80 years, with the exception of digitization of the signals. Ionization events still occur producing electrons and holes, these electrons are collected either directly or indirectly and digitized. The physics behind radiation detection are the same. Ionizing radiation of some form or another is brought incident on a radiation detection material. The ionizing radiation looses its energy to the material. For a semiconductor or gas filled detector, the charge is directly collected. For a scintillator a portion of the energy is converted to

luminescent or phosphorescent light. The light is then collected by way of the eye, a photomultiplier tube or avalanche photodiode, and is then digitized.

Radiation Interaction Mechanisms

In an effort to better describe the design of the ZnO scintillator that will be described in subsequent chapters, a brief description of radiation interactions and detection principles will be described here. The primary engineering goal of this dissertation is to create a neutron detector which can discriminate gamma ray radiation from neutron radiation. The radiation fields where one would want to measure neutrons are always contaminated with gamma ray backgrounds. These can arise from a number of reasons including naturally occurring radioactive material (NORM), terrestrial background radiation, cosmic radiation, as well as intentional gamma emitting sources from the benign (a nuclear medicine patient) to intense accelerator sources for active interrogation and neutron induced gammas. For both homeland security and nuclear physics applications, one needs a detection material and system that is capable of detecting neutrons in gamma ray fields and do so with accuracy.

From a radiation physics standpoint, an accelerator source generates a large background of contamination gamma rays as well as the neutron interactions producing more gamma rays in the surrounding materials. From the homeland security application passive monitoring system, one is trying to detect one to ten neutrons in a short amount of time over a background of 10^5 gamma rays (35). The SNM, particularly plutonium, emitting primarily alphas and low energy x-rays which are easily shielded, also has a probability, albeit very small, to spontaneously fission releasing a number of neutrons. From an active interrogation system point of view, a large burst of photons or neutrons are produced, and the detector must not be blinded by this pulse. It then needs to detect the few neutrons that make it back to the detector array. If the detector array is slow with slow pulse rise and decay times, pulses can bleed together. The time to resolve the pulse

height is determined by the physics of the detector such as charge collection and mean migration time. The simplest form of neutron versus gamma discrimination is in the use of a low level discriminator, as used in ^{3}He tubes. Gamma rays imparting little energy into the active volume of the detector produce small pulse heights. Neutrons however produce charged particles which impart a larger amount of energy. If the resolving time between pulses is too long, the electronics may add two or more pulses together. Then the electronics system cannot discriminate one pulse from another, or the pulses sum to produce a pulse that looks like a neutron. If the detector system is to sensitive to gamma rays, it will be "blinded" by the gamma flash and continue to saturate the PMT for a long period of time. The time the detector is blinded by the gamma flash limits the effective time the detector can measure neutrons. To understand neutron detection and what is required of a newly developed system for detecting neutrons and having good gamma discrimination, a brief description of gamma ray interactions and detection methods is needed. Once one has an understanding of gamma detection, then a neutron detection system can be designed to minimize its efficiency for detecting gamma rays.

Gamma Ray Interactions

For a radiation detector to be sensitive to gamma rays, it must be able to detect electrons. Gamma rays, being a neutral electromagnetic wave/particle interact by three main mechanisms: Compton scattering, pair production, or photoelectric absorption. A representative photon cross section is shown in Figure 5.

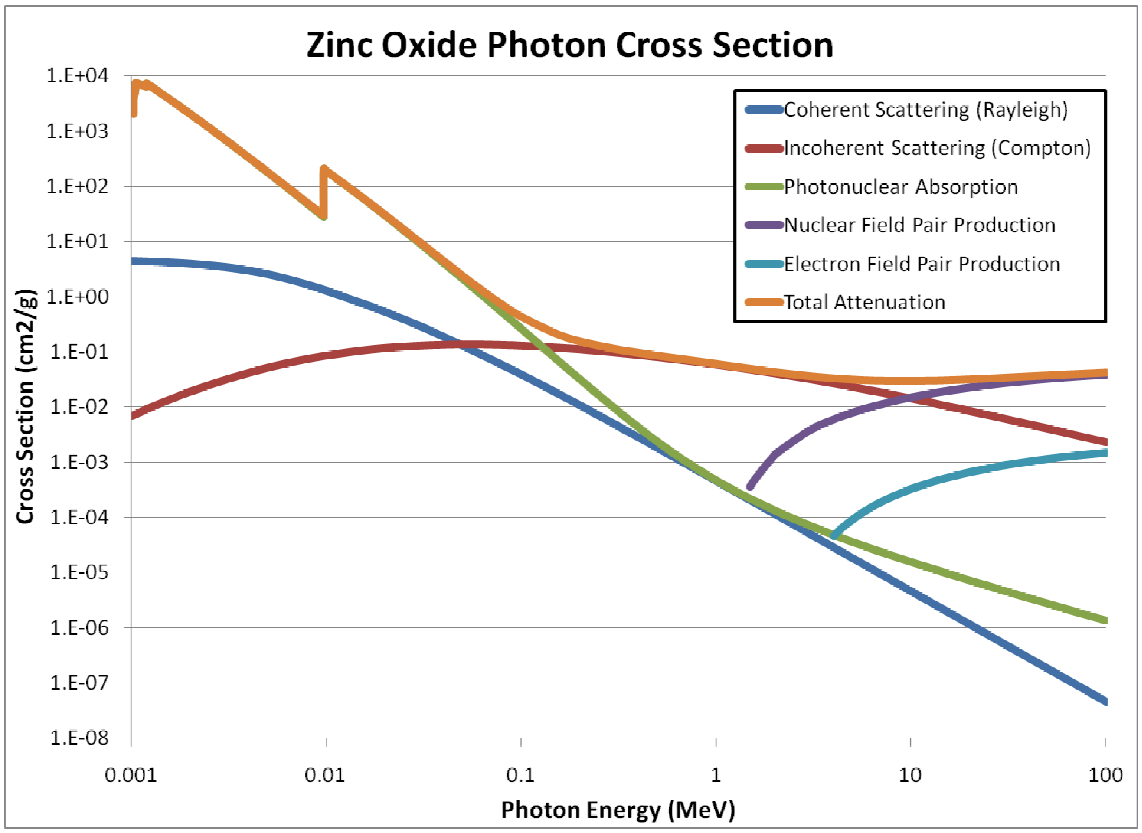

Figure 5 Photon cross section for the ZnO scintillator. Included are the total cross section, coherent and incoherent scattering (Compton scattering), photoelectric absorption, and pair production.

At low energies, photoelectric absorption dominates, while at high energies, pair production is dominant. At higher energies pair production (down to 1.022 MeV) dominates. In the intermediate energies between the pair production and the photoelectric absorption, Compton scattering dominates. In photoelectric absorption, the full energy of the photon is absorbed. An inner K-shell electron in this process is struck by the incident gamma ray and is ejected. This electron carries away the amount of

energy of the incident photon less the binding energy of that electron. This full energy capture in one single interaction from the gamma rays is desirable for gamma ray detection. When observing the cross section, one can note large saw tooth step discontinuities. These arise from the electron orbital energy states. K, L and S shell electron lines can be seen for high Z materials. In low Z materials, such as ZnO, only K shell step discontinuities can be seen.

Compton scattering is a scattering of the incident gamma ray by a free or loosely bound electron. The gamma ray exits the scattering event with a lower energy. The maximum energy lost in the Compton scattering event is given by Equation 1. Here the incident energy (energy denoted by hν) of the photon is scattered to the new energy hν'. m_oc^2 is the rest masss of an electron (0.511 MeV). Equation 2 shows the Compton electron's maximum energy after the scattering reaction.

$$h\nu'|_{\theta=\pi} = \frac{h\nu}{1 + {2h\nu}/{m_oc^2}}$$

Equation 1 Equation for the photon's minimum energy exiting a Compton scattering event for a 180 degree scattering

$$E_{e-}|_{\theta=\pi} = \frac{{2h\nu}/{m_oc^2}}{1 + {2h\nu}/{m_oc^2}}$$

Equation 2 Equation for the recoiling Compton electron's energy after exiting the maximum energy loss reaction from a gamma ray.

Pair production is where a gamma ray interacts in the field of an electron or a nucleus. The photon disappears in this reaction and an electron-positron pair is created. The electron-positron pair recoil with a substantial kinetic energy. The positron eventually annihilates into two 511 keV photons.

In the photoelectric absorption reaction, the electron leaves the orbitals of the original reaction nucleus but due to a low energy does not travel very far. The energy range of this reaction is minimal but dominant for high Z materials. The photoelectric

absorption reaction dominates most materials to 100 to a few hundred keV. Above this energy region, the photon's wavelength is to small to directly excite the electron. Instead it interacts ballistically to produce recoil electrons in a scattering reaction. The primary sources of gamma rays, particularly in the accelerator regime fall in the Compton scattering region. Background radiation from NORM is also dominated with sources of radiation from ~300 keV(radon progeny) to around 1.4 MeV (^{40}K). The electrons produced in this reaction follow the formula shown in Equation 3.

$$E_{e-} = h\nu - h\nu' = h\nu\left(\frac{\left({}^{h\nu}/_{m_o c^2}\right)(1-\cos\theta)}{1+\left({}^{h\nu}/_{m_o c^2}\right)(1-\cos\theta)}\right)$$

Equation 3 The Compton scatter equation which can be solved for depending on the scattering angle theta.

For active interrogation systems where energies of 20 to 50 MeV are used, photons are produced by electrons interacting in a target to produce a bremsstrahlung spectrum. The bremsstrahlung spectrum usually has an average energy of 1/3 the incident electron energy. (36) Using a 6 or 10 MV accelerator to produce the photon source term, this corresponds to an average photon energy of 2 to 3 MeV. A typical bremstralung photon spectrum from an active interrogation system can be seen in Figure 6. Other active interrogation systems use particle accelerators to create neutron sources. Reactions such as D-T or p-n reactions are just a few suggested neutron sources for active interrogation. Most all active interrogation systems, however, still produce gamma ray or x-ray background radiation terms.

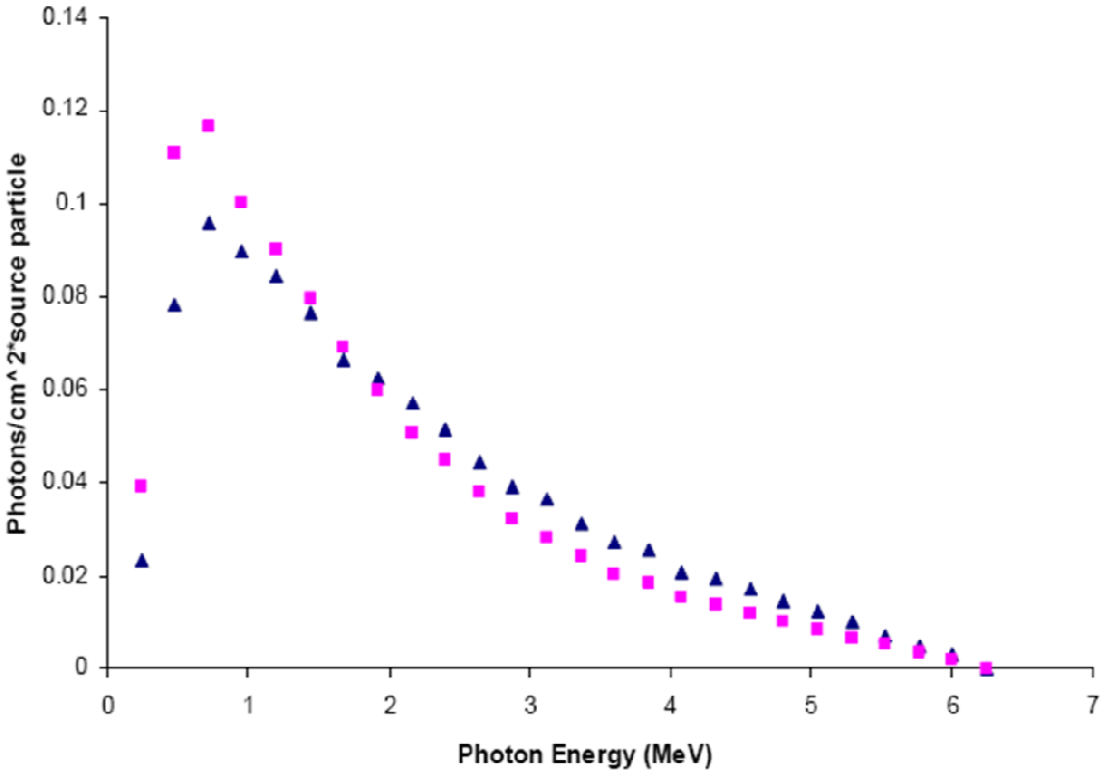

Figure 6 Sample x-ray spectra calculated for a Varian 6 MV accelerator using a tungsten target.

While the minimum energy required for the pair production reaction to occur is 1.022 MeV, it is slow to increase in cross section until approximately 10 MeV. For this region, the primary photon interaction mechanism is through Compton scattering for most background gamma ray and accelerator produced photon sources. These Compton electrons are responsible for most of the energy that is deposited in photon interactions. These Compton electrons have a significant range, from mm to cm before they fully deposit all of their energy. The range of electrons of various energies in zinc is shown in Figure 7.

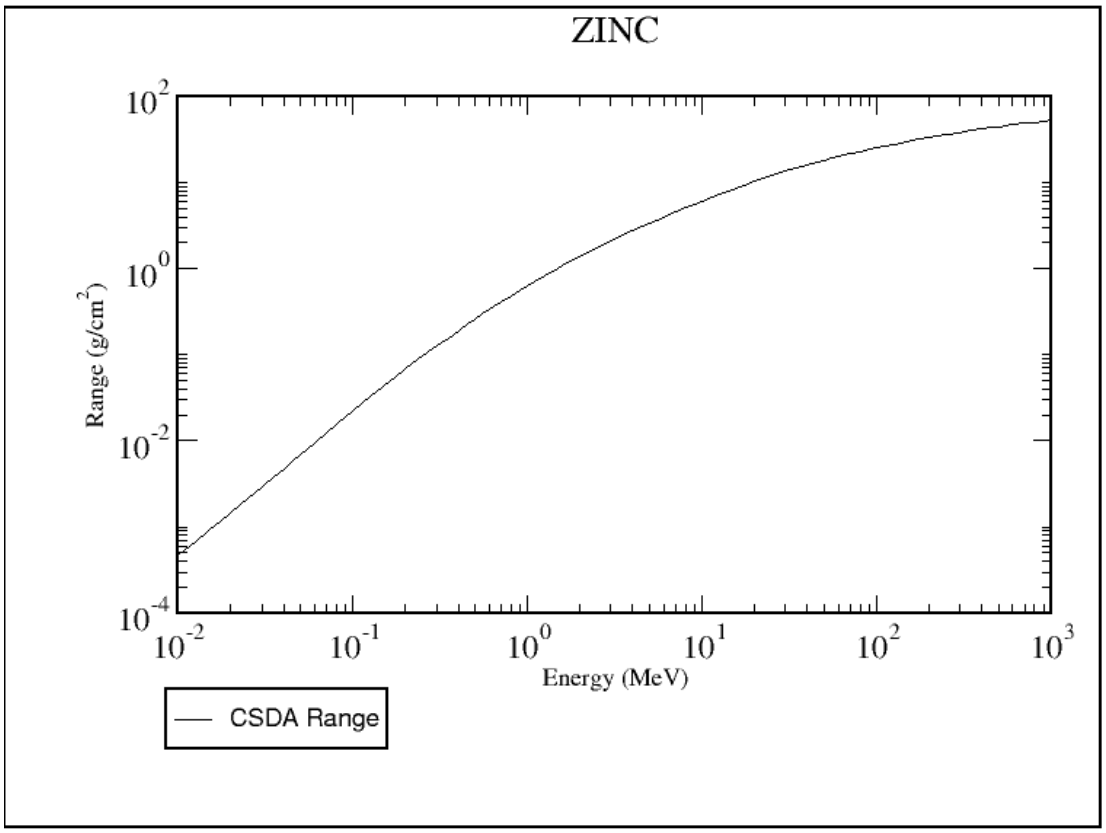

Figure 7 Continuous slowing down approximation to electrons in zinc. At low energies the electrons have a range of a few mm while at higher energies, 1 MeV and above, the range is cm.

Energetic electrons (energies greater than 100 eV) travel through material in a very unique fashion. There are two primary reactions electrons can undergo to loose energy. They can have a reaction with an atomic electron or they can be deflected and trajectory bent by the positive nuclear charge. Due to the small size of the two particles, and strong electronic repulsion, the direct interaction with atomic electrons is relatively unlikely, and occurs primarily only at higher energies where the electrons can overcome the Coulomb repulsive force. Since an electron is a very light subatomic particle with a negative charge, and it is passing through a sea of atomic electrons, each with a negative charge and being bound to an atom, a very large mass, these energetic electrons can be deflected on their path. The larger the number of atomic electrons per unit volume, the

more efficient a material is at absorbing the energy of the scattered electrons. This is the primary reason high Z and high density materials are such efficient shields and detectors. As the energetic electron moves, it experiences the repulsive force of all of the atomic electrons in its vicinity. This produces billions of micro reactions per mm. This causes a very small amount of energy to be lost to the surrounding electrons. When simulating the transport of electrons through a medium, a method known as the Condensed History Method (CHM) is used. Depending on the energetic particles energy, there is an expected value of a distance between large energy loss reactions from electron-electron scattering. The CHM method is used to estimate the distance between these large reactions and save on computation time. Each micro reaction causes an infinitesimal loss in energy and angle. The CHM method assumes a straight line trajectory of the electron between a macroscopic angle and energy loss position. This saves enormous computational resources by carrying out this approximation. The efficiency of this CHM range can be tuned in radiation transport codes by manually tuning the step size which forces more reactions to occur per unit length with an appropriate loss of energy which ensures the problem simulations are conducted in a physically correct fashion.

For gamma spectroscopy detection it is desirable to determine the energy of the incident gamma ray. To do this, the spectroscopist makes use of detectors which can fully absorb the gamma ray and all of its recoil electrons energies. A combination of high Z materials and large cross sectional areas/volumes are used to ensure the full energy is deposited in the active detector volume. The primary goal of the spectroscopist is to obtain a full energy peak, corresponding to the incident gamma energy. The gamma ray may undergo numerous Compton scattering events before it is finally absorbed by photoelectric absorption. By collecting all of the information available from these events and summing them, the full energy peak or photopeak can be measured and observed. This however assumes the “large detector” paradigm in which all of the corresponding energy is fully absorbed in the detector. In practice, a smaller detector is used, in which it

is probable that some portion of the gamma rays will scatter in the detector volume and still have enough energy to leave the detector volume without being absorbed. In this case, a unique gamma spectrum feature arises knonw as the Compton continuum. Since Compton scattered electrons are scattered into a continuum of energies based on the scattering angle which can range from 0 to 2π in the center of mass, it produces a continuum of energy deposited. The electron is typically stopped in the active detector material while the gamma ray escapes. If the gamma ray were to be stopped, the energy deposited in the photoelectric absorption would sum with the scattered energy and sum to the energy of the incident gamma ray. In very thin scintillators, this effect is even more pronounced resulting in almost no photopeak whatsoever and just a Compton continuum appears. As one creates a scintillator in which the size is is smaller than the CSDA range of the Compton scattered electrons, another extreme appears. In these thin scintillators a portion of the Compton electron energies gets deposited. This mishapened continuum is due to the fact it is not probable for the electron to deposit much energy in the scintillator matrix. This physical trait can be exploited as will be described in the following chapter.

Gamma Ray Detection

In semiconductor gamma ray detectors such as a High Purity Germanium (HPGe), Cadmium Zinc Telluride (CZT), Germanium drifted with Lithium (GeLi), or Silicon drifted with Lithium (SiLi), these electrons and corresponding holes or ions are directly collected by a bias applied across the semiconductor's intrinsic region. The reverse biased junction prevents ambient electrons from jumping across the band gap. These detectors are almost always cooled to some extent, with some of them cooled to liquid nitrogen temperatures or below. When the full energy is collected, the number of electron-hole pairs that are produced directly corresponds to the incident gamma ray energy. For scintillation detectors, electron hole pairs are not directly collected. The electrons are allowed to recombine in the scintillator structure. Often this results in a

non-radiative de-excitation. Occasionally, depending on the scintillation efficiency of the scintillator material, the ionized electrons will de-excite radiatively, releasing an optical photon quanta of energy directly corresponding to the energy it lost. Even though it is not a direct collection of ionization events, it is however a reasonably linear proportion between the energy imparted and the number of optical photons produced. The non-linearity of a scintillator becomes a problem at low energies and has been the focus of a significant amount of study in significant detail with specialized testing facilities such as SLYNCI at Lawrence Livermore National Laboratory (37).

Neutron Interactions and Detection

Now that an understanding of gamma ray detection is laid out, neutron detection theory can be built on this base. Neutrons are only similar to gamma ray radiation in that they are both neutral particles. Neutrons do not interact with electrons, rather they interact with atomic nuclei. Being a neutral particle, they are not affected by the strong electrostatic repulsion of the nucleus as protons would be or the electron cloud as electrons would be. Neutrons can interact by one of two main modalities, scatter events and absorption events. Scatter events can either be elastic (where momentum and energy are conserved) or ineleastic (where energy is conserved, but momentum is not). In a special case of absorption for high energy neutrons, multiple neutrons can be ejected such as the (n,2n), (n,3n) or (n,xn) reactions. Absorption events can be broken into radiative capture resulting in gamma ray production, a fission reaction where the compound nucleus is so unstable it splits into two or more fragments, or charged particle production producing alpha, proton or other exotic combinations of them.

All of the above reactions can be utilized to make an active neutron detector in one way or another. Preference in creating thermal neutron detectors is given to reactions with large Q values producing highly ionizing particles. Elastic scattering has been used in fast neutron detection, namely, in such detectors as organic scintillators which have a

high hydrogen content. Neutron elastic scattering with the hydrogen nucleus results in the nucleus (a proton) recoiling with kinetic energy. This elastic scattering reaction is the reaction that is being measured and the difference in pulse rise and fall times between gamma ray and neutron radiation gives rise to the neutron versus gamma discriminating capabilities seen in liquid and solid scintillators. Inelastic scattering can be used in conjunction with a gamma ray detector to detect neutrons (38). The inelastic scattering neutron detector is not a practical solution for the two proposed applications, homeland security and nuclear physics, because they rely solely on gamma ray detection equipment to detect the neutron reaction. For each of these applications, the gamma ray signal resulting from neutron inelastic scattering is small in comparison to the gamma ray backgrounds. This method however has been used with Prompt Neutron Gamma Activation Analysis to determine trace quantities of materials in a sample. The inelastic cross section interactions and radiative capture cross sections result in gamma ray spectra which are unique to the isotope being investigated. An important reaction that is commonly used is the radiative capture reaction on a few specific isotopes which result in their immediate de-excitation by electron capture which is followed by internal conversion. Following internal conversion, auger-electron emission electron production ensues. This reaction produces numerous characteristic x-rays and auger-electrons which can be collected for neutron detection. High Z, high A nuclei such as Gd and Hf posess this reaction. In this reaction, over 7 MeV of energy total can be released between gamma rays and electrons (39). Since this reaction modality results in electron and photon production large detector volumes are needed to detect these particles. In addition the signals produced by auger-electron/internal conversion reactions appear almost identically in a pulse height distribution to those produced by gamma rays. If full energy collection is possible, requiring a large detector volume, then neutron versus gamma discrimination is still possible. This however is not typically the case and only partial energy is collected. This makes the signal almost indistinguishable from gamma ray

radiation. Novel detection systems such as the capture gated neutron spectrometer have been built on this system, combining an organic scintillator such as NE213 or BC501a with a gadolinium solution. This method requires the entire pulse history to be digitized and the user analyze the pulse history backwards in time from the neutron capture reaction. They can then sum the proton recoil events to get an idea of the original neutron energy. This system however is plagued by the gamma contamination problem discussed earlier as well as the requirement that it be used in a low count rate field. Otherwise, one cannot accurately separate the pulse histories.

The primary mode for detecting neutrons, however, is through the creation of heavy charged particle such as alphas, protons, or fission fragments. The (n,p), (n,α) and (n,fission) reactions for the vast majority of isotopes are threshold reactions. Nuclei such as ^{3}He, ^{6}Li and ^{10}B are one neutron away from doubly closed pack low energy states. Upon capturing a neutron, at least one distinct closed packed state promptly forms inside the nucleus. These two nuclei, usually consisting of an alpha particle and something, either a triton or a lithium nucleus, instantly repel each other in an exothermic reaction in the center of mass. Converting to the lab system, the momentum from the incident neutron dictates the direction of the exiting channels. The positive Q value for the reaction is of paramount importance in neutron detection. This exothermic reaction releases energy to the two charged particles which can be easily detected. Most thermal neutron detectors today utilize one of the three target nuclei above. A table of common neutron target nuclei reactions, their relative cross section, and their energies can be found in Table 1.

Table 1 Cross sections, Q values and reaction products from selected neutron target nuclei.

reaction	*Q*-value (MeV)	cross section (in barns) for thermal (0.025 eV) neutrons
$^{10}B + n \rightarrow ^{7}Li + \alpha$	2.31	3,840
$^{6}Li + n \rightarrow ^{3}H + \alpha$	4.78	940
$^{3}He + n \rightarrow ^{3}H + p$	0.764	5,330
$^{235}U + n \rightarrow X + Y$ (fission fragments)	~200	575

Heavy Charged Particle Interactions and Transport

Heavy charged particles (HCPs) are high Linear Energy Transfer (LET) radiation. High LET radiation, while experiencing the Coulombic forces of the surrounding atoms, have enough mass and momentum that they tend to travel in a straight line, and are rarely deflected. High LET radiation looses energy in a linear fashion with energy which follows the Bethe-Block stopping power formula. The Bethe-Bloch stopping power equation can be seen in Equation 4.

$$S = -\frac{\partial E}{\partial x}$$

$$-\frac{\partial E}{\partial x} = \frac{4\pi e^4 z^2}{m_o v^2} NB$$

$$B = Z\left[\ln\frac{2m_o v^2}{I}\right] - \ln\left(1 - \frac{v^2}{c^2}\right) - \frac{v^2}{c^2}$$

$$R = \int dx = \int \frac{dE}{S} \int_E^0 \frac{dE}{(dE/dx)}$$

Equation 4. Beta-Bloch stopping power formula and the range formula

Above, *S* is the stopping power which is the energy loss per unit length. Above, *e* is the charge on an electron, *z* is the charge of the particle. When one integrates the inverse of the Bethe-Bloch equation from the incident particle energy down to zero, one can determine the range of the high LET radiation described as *R* above. The Bethe-

Bloch range equation can be seen in Equation 4. The Bethe-Block and range equations are directly proportional to the square of the charge on the ionizing particle and it's mass. This makes heavier and higher charged particles such as alpha particles, have less range then protons, if the two particles have equal initial energies. Unlike electrons whose range is mm to cm, alphas and protons of similar energies will only travel a few microns in the same material. One can simulate the transport of these charged particles either by direct numerical solution and the Monte Carlo Method (MCM) (40) or through modified slowing down approximations such as the Vavilov model (41). Two simulation software packages have been used herein, SRIM2005 (42) and MCNPX (43). SRIM, the Shielding of Radiation Interactions in Matter is a numberical solution of the Bete-Block stopping power solution using the MCM. MCNPX is a full MCM code which can track neutrons, and produce charged secondary particles. An example of the range and deflection of a heavy charged particle versus an electron can be seen in Figure 8. One can see the range of the electron is orders of magnitude longer than that of the HCP. Shown in Figure 9 is a logarithmic axis also showing 500 keV electrons. Electrons take orders of magnitude more material to deposit their energy.

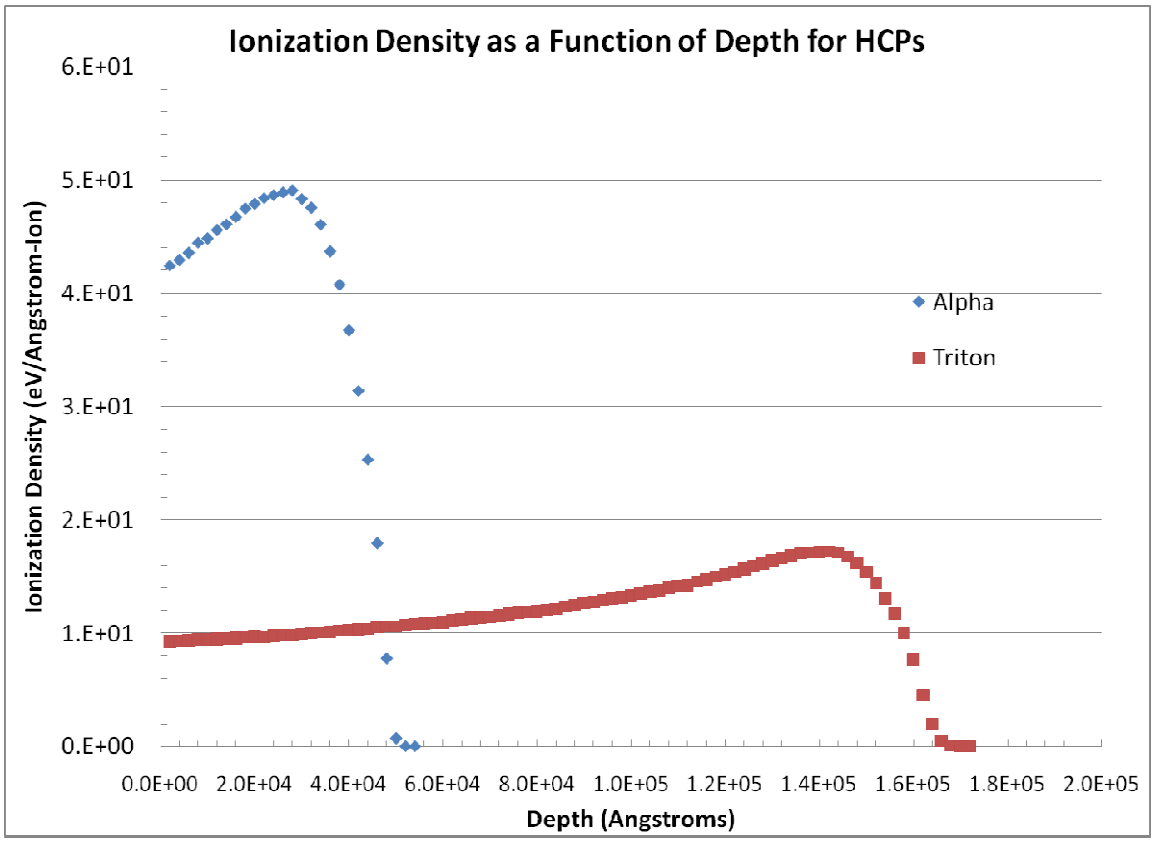

Figure 8 Energy loss profile for alpha particles in ZnO calculated by SRIM.

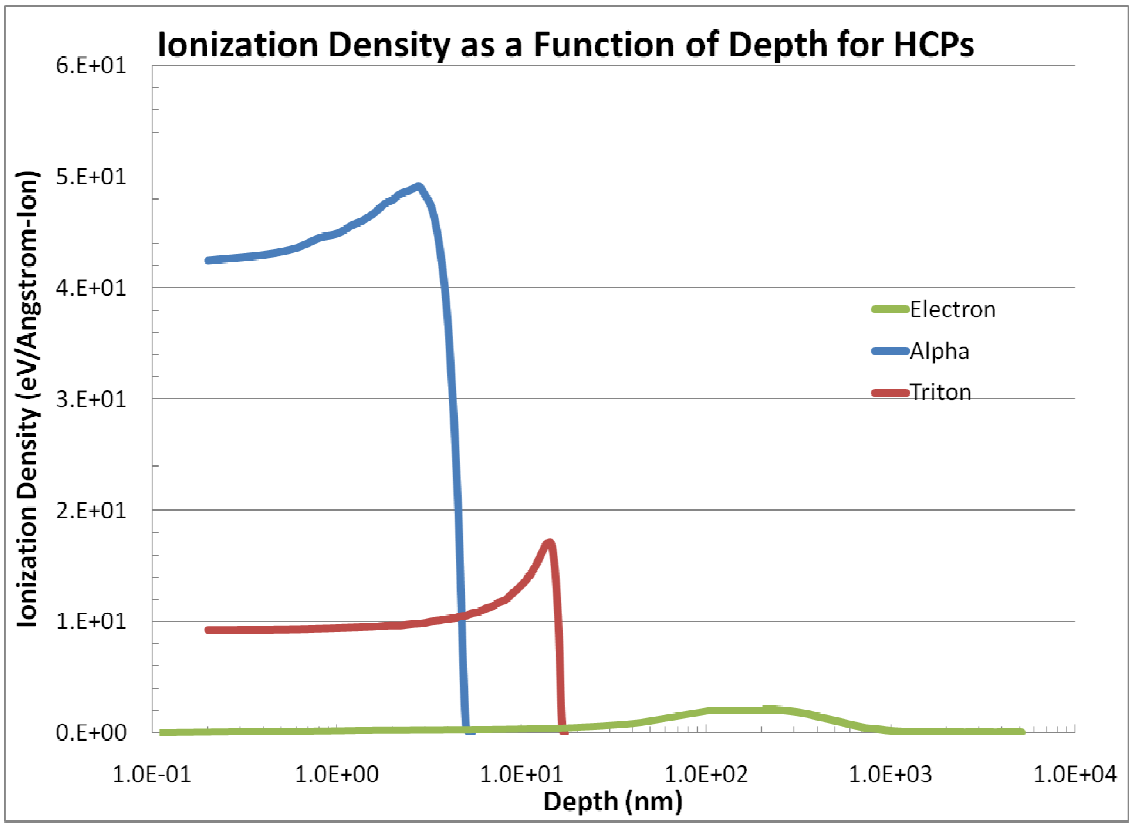

Figure 9 Range and ionization density for HCPs as well as electrons.

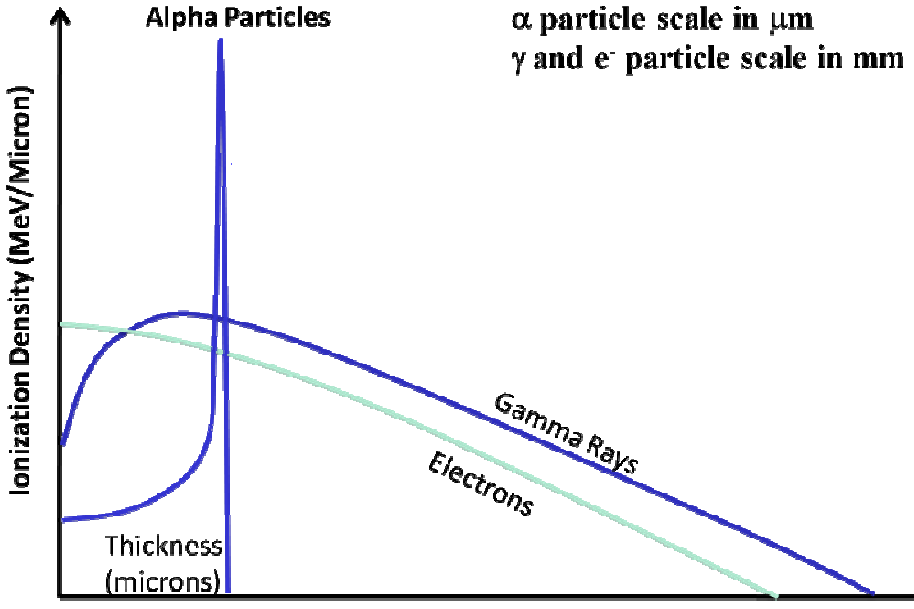

Figure 10 range and energy loss profile for electrons, gamma rays and alpha particles. (44)

Also it should be noted the energy loss profile of the HCP versus the electron produces a higher ionization density at the end of the HCP track whereas the electron produces a higher ionization density in the beginning. The energy loss profile of the HCP has what is known as the Bragg peak, or a region at the end of the particle's track which has a very high ionization density. If one integrates the amount of energy deposited as a function of thickness, particularly towards the end of the Bragg peak, one can see the energy imparted per micron is significantly lower for electrons than HCPs. This physical difference will be exploited and demonstrated in subsequent chapters to produce efficient neutron detectors with low gamma ray sensitivities.

Radiation Detector Theory

Now that an understanding of the ionization processes of both gamma rays and heavy charged particles has been described, one can now collect that energy by way of a scintillation radiation detector. The following radiation detection theory section is taken from Knoll (45). For a much deeper, in depth discussion of the radiation detection discussion, the reader is encouraged to read his book. In gas filled detectors such as ^{3}He, $^{10}BF_3$ and ^{10}B lined tubes, the heavy charged particles travel through the fill gas producing ionization events. These ionization events are directly collected by applying a bias voltage between the tube wall (cathode) and the central anode wire. By increasing this voltage, charge collection moves from a linear collection with no amplification (ionization chamber region), to an amplification region known as the proportional region. Gas amplification occurs when the ionized electrons are accelerated with such force that they too cause more ionization events. Finally, above the proportional region, is the Geiger discharge region. In this region, the voltage and accelerating force on the electron is so strong it produces a Townsend cascade and a Geiger avalanche forms. The avalanche completely ionizes the gas along the length of the wire producing a large pulse. However, in the linear ion chamber region and the linear proportional voltage region, the

detector is considered to be non-paralyzable. This means that if two pulses were to arrive nearly simultaneously, the second one before the first one could be cleared and quenched, that the second pulse would add to the first pulse and "ride on top". Sophisticated electronics can correct for this problem. The decrease in count rate can be equated to Equation 5. In the following equation for the non-paralyzable model, n equals the true interaction rate, m equals the recorded or measured count rate and tau is the system dead time, or time to recover from the pulse.

$$n = \frac{m}{1 - m\tau}$$

Equation 5. The non-paralyzable model for radiation detection systems.

Once one operates a tube into the Geiger discharge region, the detector becomes paralyzable. If two pulses show nearly simultaneously, the detector can no longer resolve both pulses and the second pulse to arrive are ignored. Due to the long charge collection times of these detectors, they can easily become paralyzable. Detectors can become paralyzable also if the physics of the detector charge collection is slow and the pulse rise time and decay time are slow and the rate of radiation interactions is high. In the following equation for the non-paralyzable model, n equals the true interaction rate, m equals the recorded or measured count rate and tau is the system dead time, or time to recover from the pulse.

$$m = n * e^{-n\tau}$$

Equation 6 The paralyzable detector model for radiation detectors.

When designing detector systems, particularly for high count rate applications, it is important to design them in a non-paralyzable fashion. A paralyzable detector will begin to actually decrease in count rate as the count rate increases past its maximum count rate response. One never knows which side of the saturation peak you are

functioning. The correlation between count rates and observed responses for the paralyzable and non-paralyzaable detector models can be seen in Figure 11.

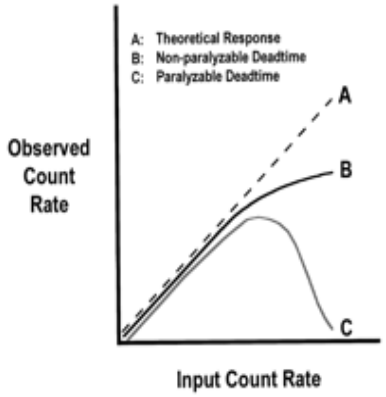

Figure 11 Paralyzable versus non-paralyzable detector models.

Scintillation Detector Theory

The scintillation process however is significantly more complicated. As radiation passes through matter, it loses energy through ionization events. The amount of energy required to produce an ion-electron pair is known as the work function. Once ionized, the atoms or molecules need to de-excite. Unlike gas filled tubes and semiconductor detectors which directly collect the charge by means of a high voltage field sweeping the charge, scintillation detectors allow the atoms or molecules of the scintillator to de-excite in the detector material. Materials that are classified as insulators or semiconductors have electron energy bands where electrons can exist. There are two primary bands, the lower band being the valence band and the upper band being the conduction band. The valence band are electrons bound at lattice sites of the crystalline structure, while the conduction bands are electrons who have enough energy that they are free to migrate through the crystalline structure. Between the valence band and the conduction band lays the forbidden zone. Electrons cannot occupy this zone between the conduction and valance bands in a standard scintillator crystal. Accompanying the valence and conduction bands, doped scintillators possesses activator sites which consist of acceptor and donor bands.

This is due to the fact that when a scintillator relies on the energy difference between the conduction and valence bands, the recombination efficiency is typically low and results in a optical photon far outside the visible range into the far UV spectrum. A standard band diagram for a semiconducting scintillator can be seen in Figure 12. Excited nuclei also exhibit a multitude of energy states in the immediate vicinity to the conduction and valence bands. This is due to the thermal energy in the system. The vibrational states add a small variation in the gap energy, albeit extremely small. This contributes to the broadening of the scintillation fluorescence peak.

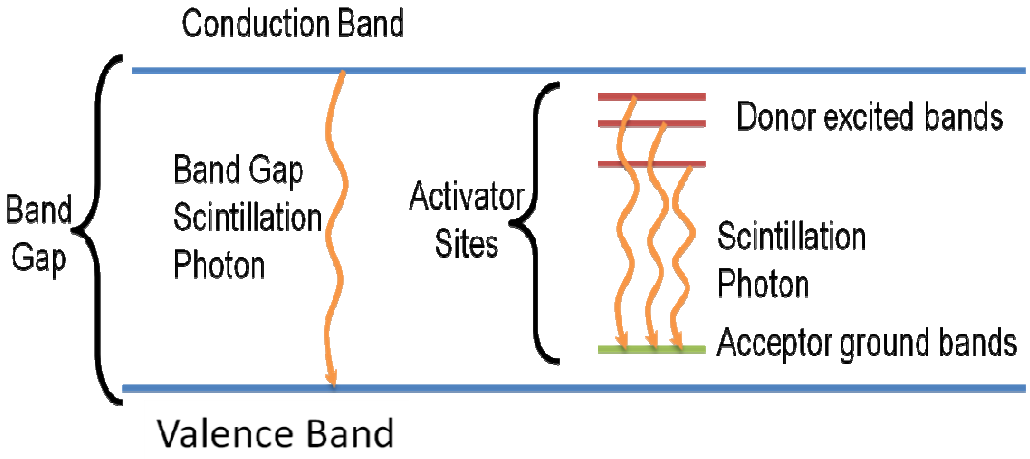

Figure 12 Band structure of standard semiconductor material scintillator such as CsI(Tl), NaI(Tl), or doped ZnO. Donor bands in red provide a lower energy excitation level in the scintillator band structure for electrons to exist in. Acceptor bands lie above the valence band further narrowing the energy difference an electron needs to jump across. This is important in insulating materials in particular.

In a traditional inorganic doped scintillator such as NaI(Tl), LiI(Eu), or CsI(Tl), electrons can drift through the lattice until they encounter an acceptor location. A small fraction of the ionized electrons can de-excite by dropping into the acceptor band and release excess energy in a quanta of light, which is lower in energy than the band gap between the valence and conduction bands. This process can be relatively slow due to the long migration times between ionization and de-excitation. Most electrons, however,

deposit their energy into the crystalline lattice non-radiatively as phonons of heat. Radiations (gammas, betas, scattered electrons, alphas, protons and fission fragments) which are of concern for detection have tens of keV of energy up to tens of MeV. Using the approximation of a 3 electron volt work function, a 1 MeV particle will produce ~3.3 x 10^5 ionization events (46). If the de-excitation time is a Poisson distribution, very long decay times on the order of tens to hundreds of microseconds are possible (47). Not all of the excitation events form optical light pulses. Some electrons fall into traps originating from a number of different origins including crystalline defects, contaminates to the crystal and just phonon de-excitation. In undoped inorganic scintillators, such as ZnO, BaF, CsI, the electron preferentially de-excite locally since there are no activator sites. This can result in a very fast scintillation pulse, but at a photon energy which can be centered in the UV range (48). The band gap in these structures undoped structures preferentially allows electrons to directly de-excite across the band gap.

Organic scintillators can have their electrons de-excite anywhere along the molecular chain and as a result are usually faster than inorganic scintillators (27). Organic scintillators usually utilize molecular chains containing the benzene ring structure for its singlet and triplet decay modes. Due to the number of different singlet and triplet bands, and the ability for intercrossing between the bands, the scintillation spectrum is significantly broader than for an inorganic scintillator. However, the number of available de-excitation bands is higher, resulting in higher luminosities than inorganic scintillators. A representative scintillation band diagram can be seen in Figure 13 for an organic scintillator.

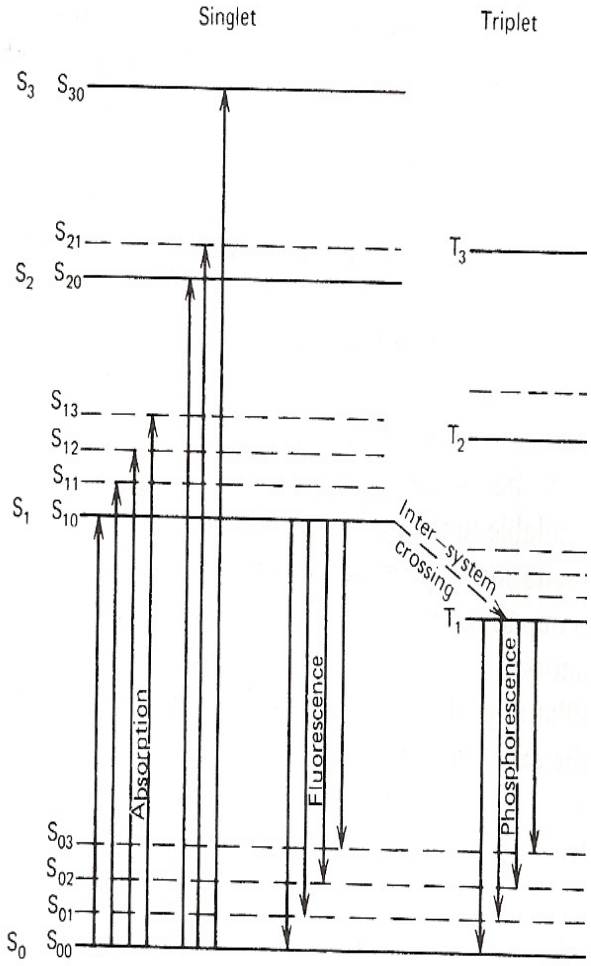

Figure 13 Organic scintillator band diagram showing the numerous excitation and fluorescence modes.

The scintillation wavelength of light depends directly on the bandgap schema of the material. Very large band gaps generate short ultraviolet scintillation pulses. Very small band gaps make very long wavelength scintillation pulses closer to the green wavelengths. Most scintillators de-exitation fluorescence wavelengths are in the near ultra-violet to blue (45). Longer wavelengths usually result in longer pulse decay times as exhibited in NaI(Tl) and $LaBr_3$. This is due to the mean lifetime of the electron being longer, usually due to elevated temperatures of the scintillator material, and that electron's ability to reach shallower acceptor locations. Without donors or acceptors, a

scintillator produces light at the band gap wavelength. Near the band gap transition, the transmission of light is negligible, and the index of refraction is very high. This is why to produce large volume scintillators such as those used in gamma radiation detection, acceptor and donor dopants are added to produce scintillation light in a longer wavelength so it is not absorbed by the scintillator immediately (49).

When evaluating new scintillation materials one must be mindful of the scintillation spectrum as well as the efficiency of the light collection system being used. Having a bright scintillator is important, but if one cannot convert the signal to a usable electronic signal, it is useless. Scintillation light is collected through one or many light conversion tools. Currently photomultiplier tubes (PMTs) are the staple of scintillation light collection. Other systems such as avalanche photodiodes (APDs) show promise at replacing the PMT. Traditionally APDs have low gains and are slow. This over recent years has changed and improved dramatically.

The purpose of the light collection device is to focus the optical light pulses onto an electron conversion material. This device, the photocathode, converts light over a given frequency domain into free electrons. The photocathode material is selected to have a very low work function. When considering ones choices for PMT or APD structures, care must be given to the vacuum envelope that surrounds the device. Low cost, standard photon counting photomultiplier tubes are encased in borosilicate glass. Borosilicate glass has a wavelength cutoff of approximately 380 nm (50). The direct band gap scintillation mechanism produces most of its scintillation light below this cutoff at higher energies. Effectively with an inappropriate PMT envelope, no light can reach the photocathode.

When light strikes the photocathode, electrons are produced. A large operating voltage (hundreds of volts) focuses the electrons onto the first dynode. The electrons then cascade down the multiplier tube dynodes (anywhere between 2 and 14) amplifying the number of electrons at each stage. The number of stages and operating voltage

directly correspond to the pulse amplification in the PMT. A diagram of the PMT can be seen in Figure 14. (51)

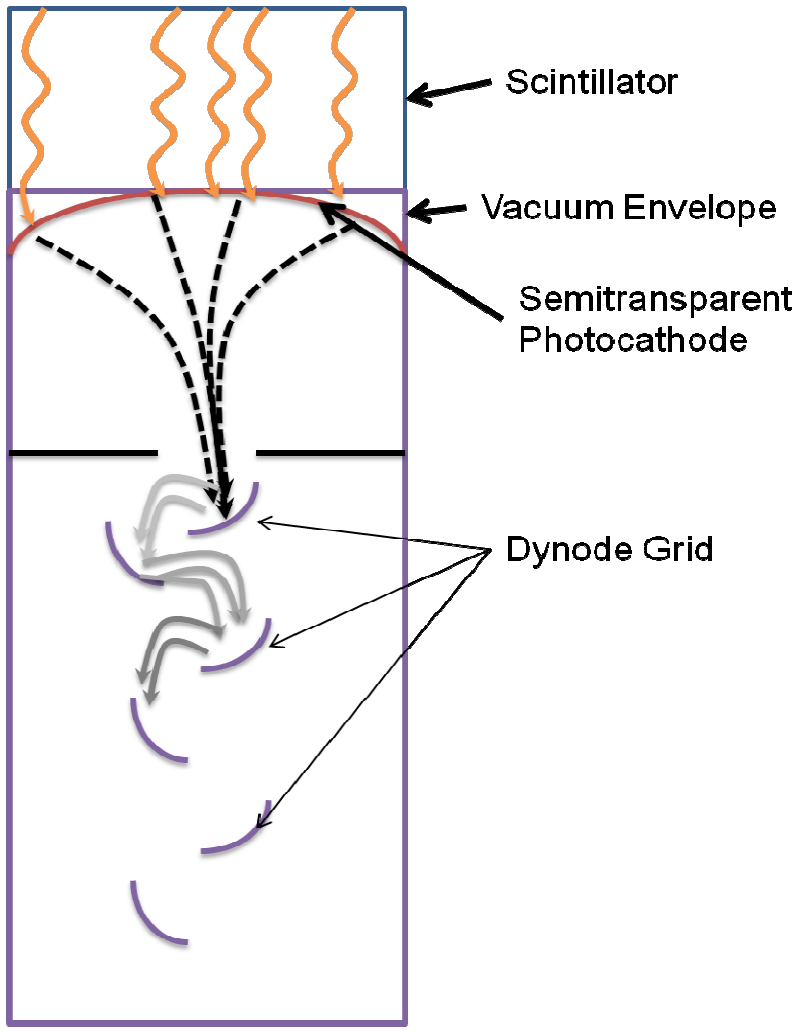

Figure 14 Standard PMT configuration

At the end of the dynode chain, the anode collects the signal using a typical resistor/capacitor bridge shown in Figure 15. An APD works in a similar fashion. Here the reverse bias voltage causes amplification not by striking dynodes, but by electrons accelerating in a reverse bias junction until it strikes a multiplication region. A typical design of an APD structure can be seen in Figure 16 (52). The simplicity of the APD

structure, rugged design, low voltage operation and small mass of the APD make it a promising road for light collection research. Due to it's smaller mass, it is less sensitive to gamma ray radiation than to the glass envelope of the PMT.

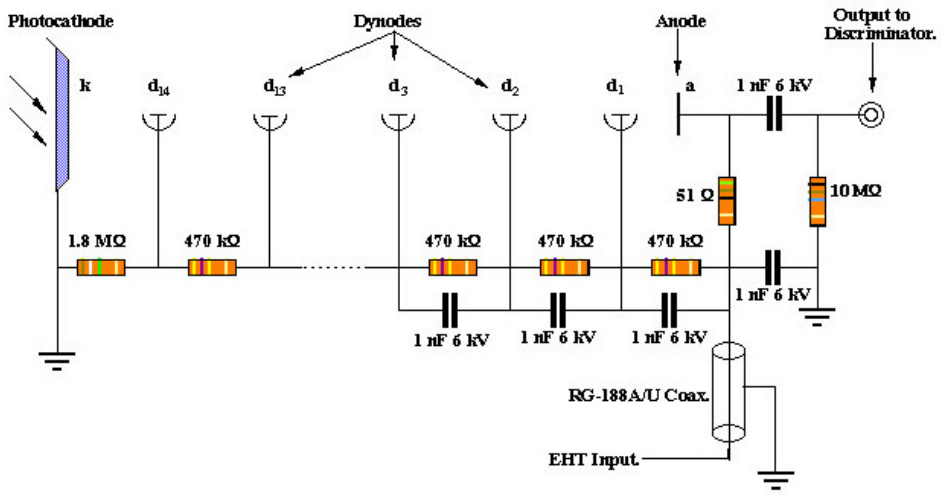

Figure 15 Typical resistor bridge network for a 14 dynode PMT.

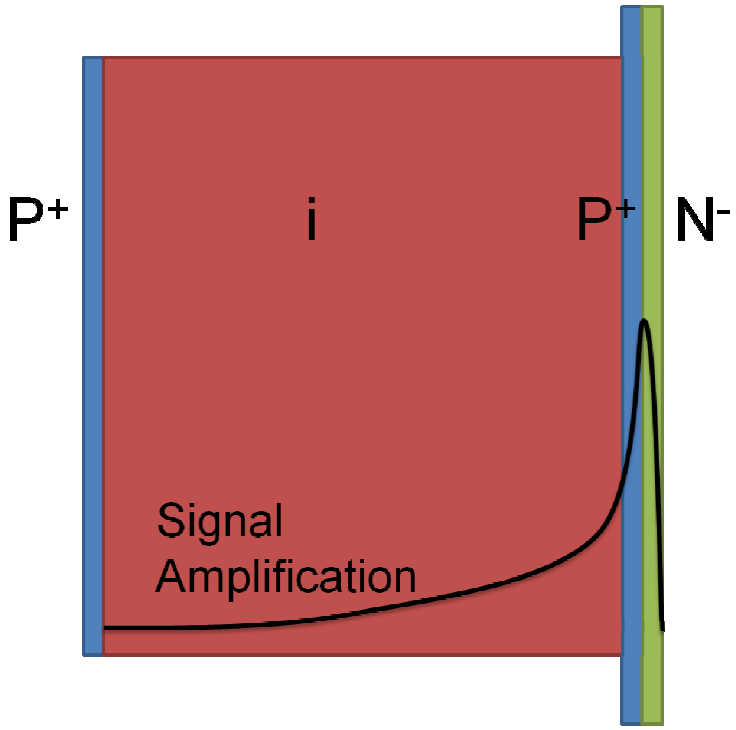

Figure 16 Typical APD configuration showing signal amplification in the PN region after light collection in the intrinsic region. The entire device is only ~10 µm thick.

CHAPTER III

THE ZINC OXIDE SCINTILLATOR

ZnO is a promising radiation scintillating inorganic crystal for thermal neutron detection. ZnO crystals have several significant advantages over current neutron detector materials. Originally investigated in the 1950s and 1960s, ZnO was investigated with ZnS (53). In the 1960s, Will Lehmann explored the use of donor impurities in semiconducting ZnO (54). Lehmann prepared Ga-doped ZnO powder. At the time, only powdered forms were available. Large crystal growth had not been achieved yet for these materials such as ZnO. In the early 1990s, renewed interest in zinc oxide returned as researchers began searching for more efficient ultraviolet LEDs. A significant amount of research was conducted on n-type doped ZnO. Researchers were searching for P-type doped ZnO. The research into n-type and for P-type ZnO laid the groundwork for developing efficient scintillators proposed herein.

For scintillation applications; today, many different dopants such as Gd, B and Li are possible in ZnO crystals (55). It was proposed by Lehmann that the substitution of Zn atoms with Ga introduced a degenerate donor band overlapping the bottom of the conduction band in addition to creating more electrons by ionization caused by high energy radiation. The donor band electrons recombined with ionization holes in the valence band, resulting in near band edge emission and a decay time of <1ns. The luminosities were comparatively low, since the scintillation properties were measured in powder material; however, ZnO scintillation properties can be drastically improved by producing single crystals. With recent advances in crystal growth technology, this is

possible. By doping or coating the ZnO crystal with neutron target nuclei, an ultrafast scintillator capable of detecting neutrons with high efficiencies can be realized[1]. It is important to distinguish "dopant" versus "alloy" quantities of nuclei in the following discussion. Semiconductor dopant levels are up to traditionally 0.1% atom fractions (56). Above this, alloying occurs. In this work, dopant quantities will refer to atomic compositions up to 10% atom fraction. This is a drastic increase in "doping" from traditional semiconductor work.

Zinc oxide has a room temperature bandgap of 3.37 eV (375 nm) and an exciton binding energy of 60 meV (57). This II-VI semiconductor has been heavily researched for many optoelectric applications from LEDs to solar cells to laser diodes. Pure ZnO has optical transparency ranging between 380 and 2500nm (58). Interest in ZnO has grown recently due to its large photo-response and tunable bandgap. Alloying ZnO films with MgO and CdO potentially permits the bandgap to be controlled between 2.8 and 6.1eV, which facilitates bandgap engineering (59). The exciton binding energy of ZnO is twice that of GaN (28meV) (60). In ZnO the excitation remains dominant in optical processes even above room temperature, giving an advantage over other inorganic scintillators for excitation–related device applications. This very same characteristic is what prevents the ZnO scintillator from having a significant temperature coefficient in its response. The higher excitation binding energy of ZnO at room temperature enables fast electron-hole recombination during scintillation, and the chances of electron trapping are reduced compared to other scintillator materials due to a higher excitation binding

---

[1] Cermet, Inc. is a commercial vendor of ZnO bulk crystals and has successfully grown up to 10 weight percent Li doped ZnO single crystals for scintillator applications.

energy. The band diagram showing the impact of vacancies on the scintillation properties of ZnO can be found in Figure 17. (61)

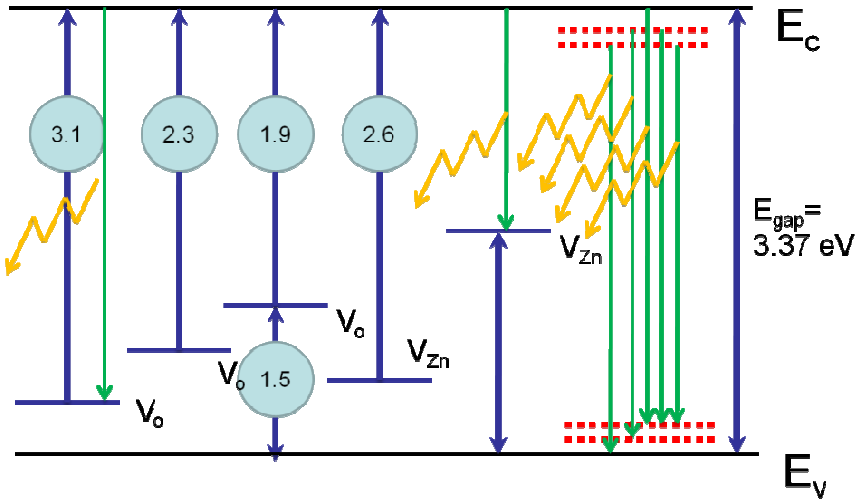

Figure 17 Band diagram for room temperature undoped ZnO. Red dashed lines are donor and acceptor lines created by thermal exitaiton of the material, blue lines indicate an energy state created by a vacancy in either oxygen or zinc. Green lines indicate possible de-exitation routes which result in yellow scintillation wavelengths.

These ultrafast rise and fall times will allow this scintillator to perform well in a high count rate environments. Rise times of 35 ps and a decay time of 0.65ns have been reported. (62) Digitized pulses from a fast MCP-PMT from Ref. (62) can be seen in Figure 18. These response times are faster than all other organic or inorganic scintillators currently available commercially. (45) Part of the reason for ZnO's ultra fast response is the fact it is a room temperature semiconductor. Similar to other undoped scintillators such as CsI, BaF, etc. these scintillators can be quite bright, and have very short decay times.

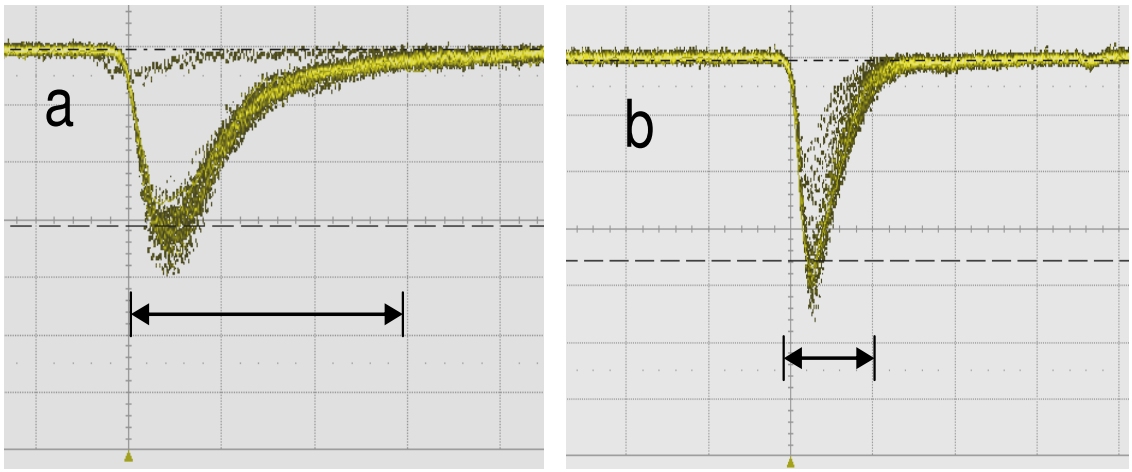

Figure 18 High Speed of response of Cermet's Li doped ZnO scintillator compared to that of a plastic scintillator (BC400 fast plastic). Figures A and B are 1 mV per division vertical, 1 ns per division horizontal. (63)

Zinc oxide can exist in three crystalline forms, a hexagonal wurzite structure, a cubic zincblende, a rare zinc rocksalt and an amorphous form. It is not until one begins to alloy ZnO or increase the growth pressure that the rocksalt phase forms. It is preferable to use wurzite ZnO over zincblende phase for many reasons. Wurzite structures are stable at room temperatures. Growth conditions for ZnO favor the wurzite structure. (64)Zincblende structured ZnO can be grown over a suitable substrate. For wurzite ZnO, growth on sapphire substrates is common. ZnO wurzite phase has lattice constants of A=3.25 Å and C=5.2 Å which gives a C/A ratio of ~1.6 which is nearly a perfect lattice for a hexagonal structured material which would have a C/A ratio of 1.6333. (65) Zinc oxide however is tolerant to growth on a variety of different materials. Depending on the orientation of the substrate or seed crystal, or lack thereof, different ZnO orientations can be achieved.

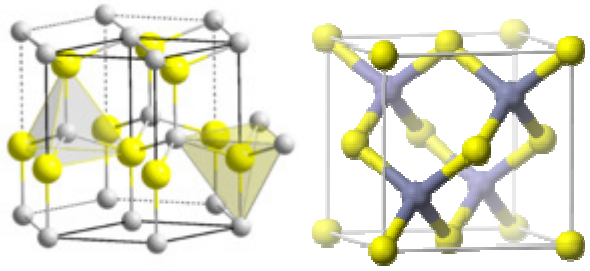

Figure 19 Wurzite and Zincblende structures of ZnO.

Zinc oxide however is a relatively soft material with a Mohs hardness scale value of only 4.5 (66). It is durable to most solvents and water, but can be etched by strong bases and acids. It is stable to 1975 C where it will begin to decompose. Above 800 C in an atmosphere with oxygen, it will accept oxygens and fill zinc vacancies. The wurzite and zincblend structures do not contain an inversion symmetry. At no point in the crystal structure does the reflection of the structures become the structure. Because of this, these structures posses a high piezoelectricity. To further help its piezoelectricity, the wurzite structure is largely ionicly bonded (67). The piezoelectric effect in future work could be utilized for other novel radiation detection methods such as piezoelectric nanorod arrays or thin films.

Zinc oxide is a transparent crystal with a relatively low index of refraction in the visible region. Due to its band gap, the index of refraction near the band edge rises in excess of 3. In the optical wavelengths however, its index of refraction is ~1.9. The index of refraction as a function of wavelength follows the equation seen below. Graphically, the index of refraction can be seen in Figure 20. (68)

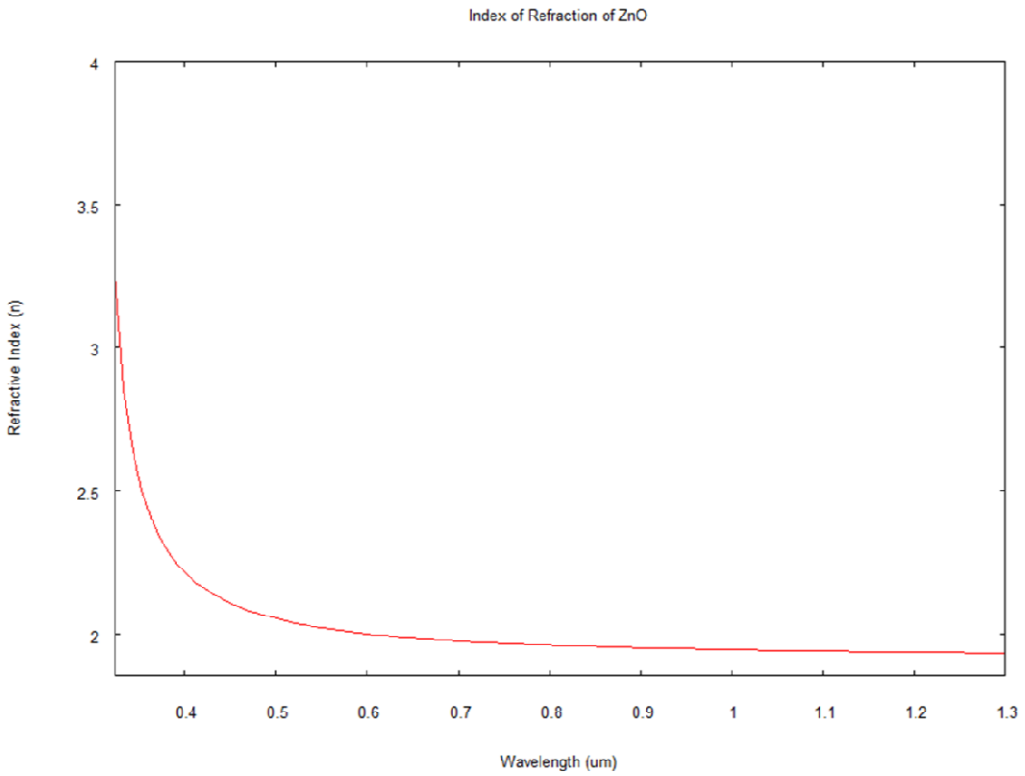

Figure 20 Index of refraction for ZnO. Data taken from (69).

Zinc oxide crystals can be doped with a number of different nuclei. Most of the work currently has been in search of P-type dopants. P-type material, or semiconductor material which is rich in acceptor locations, is difficult to achieve in ZnO. Several N-type dopants exist and focus on Group V elements such as Ga and Al. P type dopants focus on Group I nuclei such as Li, Na, K, and N (70). More interesting to detecting neutrons, ZnO can be doped with neutron detecting target nuclei such as boron and lithium. This provides the unique opportunity to produce new neutron detectors.

ZnO Crystal Growth

There are a number of different crystal growth methods for ZnO scintillators. They are broken into two distinct groups, bulk growth and thin film/nanoparticle growth. Bulk growth can be divided into melt growth, hydrothermal growth, Seeded Chemical

Vapor Deposition (SCVT) and Chemical Vapor Deposition (CVT) growth. Each growth method is pioneered by a primary commercial company.

SCVT growth is primarily done by Eagle Pitcher and have reported growth rates of 40 μm per hour in a horizontal tube furnace at 1000 – 12000 C (71). They use a zinc source, hydrogen as a carrier gas with an overpressure of water vapor to maintain stoichometry. In this process, the entire crystal is seeded by an initial ZnO crystal. 5.08 cm crystals are routinely grown by this method (72). The growth rate for this method however bottlenecks and asymptotically approaches a steady state value lower than the 40 μm per hour. Doping is difficult for this method, as a suitable source must be available and be able to be sublimate to the gas phase.

Chemical Vapor Transport is similar to SCVT, but there is no seed crystal present to nucleate growth. This method usually has a lower crystalline quality due to the random nature of the initial growth. This method however is a low cost initial growth option for bulk materials. Using a standard horizontal tube furnace, the growth is conducted by submlimation of zinc under a hydrogen carrier gas. Oxygen or water are used as the other reagent, monitoring the partial pressure of carrier gas and reactant gasses (73).

Melt grown materials are primarily the domain of Cermet Inc, the leader in bulk melt growth materials. Cermet utilizes a patented crystal growth technology of high pressure, cold wall bulk melt growth to produce doped and undoped ZnO single crystals. Cermet's crystal growth technology is a high-pressure induction melting apparatus, wherein the melt is contained in a water-cooled crucible. An RF heat source is used during the melting operation. Induced fields in the charge material produce eddy currents, which produce joule heating in the material until a molten phase is achieved. The highly refractory melt produced is contained in a cold wall crucible, by a solid thermal barrier that forms between the molten material composed of the same composition. The cooled material prevents the molten material from directly contacting

the crucible cooling surface. This entire melting process is carried out in a controlled gas atmosphere ranging from 1atm to over 100atm. This prevents the loss of volatile components, as well as the decomposition of compounds into atomic species (74). Cermet has melted ZnO in 6 inch diameter crucibles, producing kilogram-sized boules from which inch-sized single crystals were cut. A schematic of the ZnO crystal growth furnace can be seen in Figure 21. Due to the bulk melt, high dopant levels can be achieved using this method.

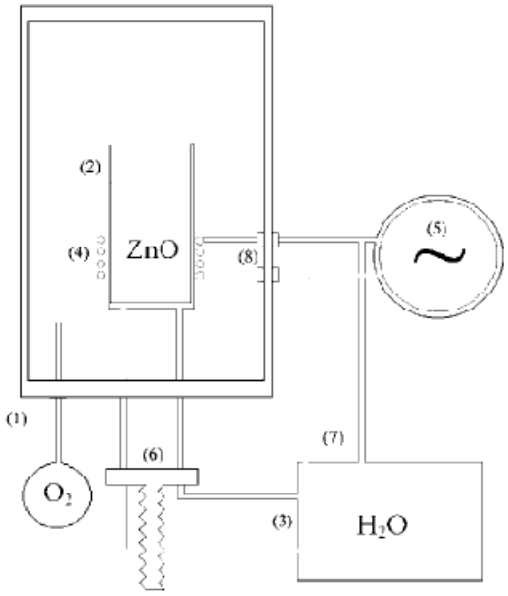

Figure 21 Schematic of the Cermet high pressure ZnO growth furnace (74). 1 is the oxygen overpressure supply. 2 is the water cooled cold wall growth chamber. Three is the special inlet and outlet piping to the high pressure chamber for the water circulation supply. 4 are the RF induction heating coils. 5 is the RF drive power for the heating coils. Six through eight are special penetrations into the patented growth chamber.

Hydrothermal growth of ZnO consists of a solution of a solvent such as LiOH, NaOH or KOH are used at very high pressures (150 ATM+) and a temperature less than 400 C. Zinc oxide is dissolved under extreme conditions, and then allowed to precipitate slowly out of solution as the pressure/temperature is brought down (75). This growth rate is exceptionally slow (mm per day) and contain high concentrations of contaminant

nuclei from the solvent (76). Recent advances under some speculation have quoted exceptional crystalline quality of 8 arc seconds (77).

Each method described above has been researched for nearly twenty years. While hydrothermal growth has produced the best reported crystalline quality, it has the drawback of incorporation of contaminants that are unwanted for scintillation applications. Melt growth shows the best promise, and highest speed, largest boules of usable material for scintillation materials. Melt growth also shows the most promise for doping with neutron target materials. Cermet's growth process allows for *in situ* doping of almost any practical dopant with relative ease. CVT and SCVT, while able to grow at high growth rates, the cost of fabrication of materials by these methods is cost prohibitive as well as inability to dope the materials results in these methods not being compatible with scintillation detector needs.

ZnO Metalorganic Chemical Vapor Deposition

One growth mechanism used herin for ZnO is through the use of Metalorganic Chemical Vapor Deposition, or MOCVD. MOCVD is an epitaxial growth method of chemical vapor deposition system in which the alkyl precursors are attached to an organic molecule. Metalorganics are usually volatile pyrophoric liquid materials which aids in the growth process. Special growth reactors are required for MOCVD crystal growth. These water cooled reactors can grow various materials from GaN to GaAs, InP, to ZnO (78). Subtle changes are needed to the internal components of these reactors to make them suitable for use with the different precursors. The change between growth materials however is a costly and time consuming one to disassemble and rebuild the tool. MOCVD allows the user very fine control of the grown structure, dopant levels, and can produce a very uniform epitaxial layer. A schematic of the specially designed reactor chamber can be seen in Figure 22 (78).

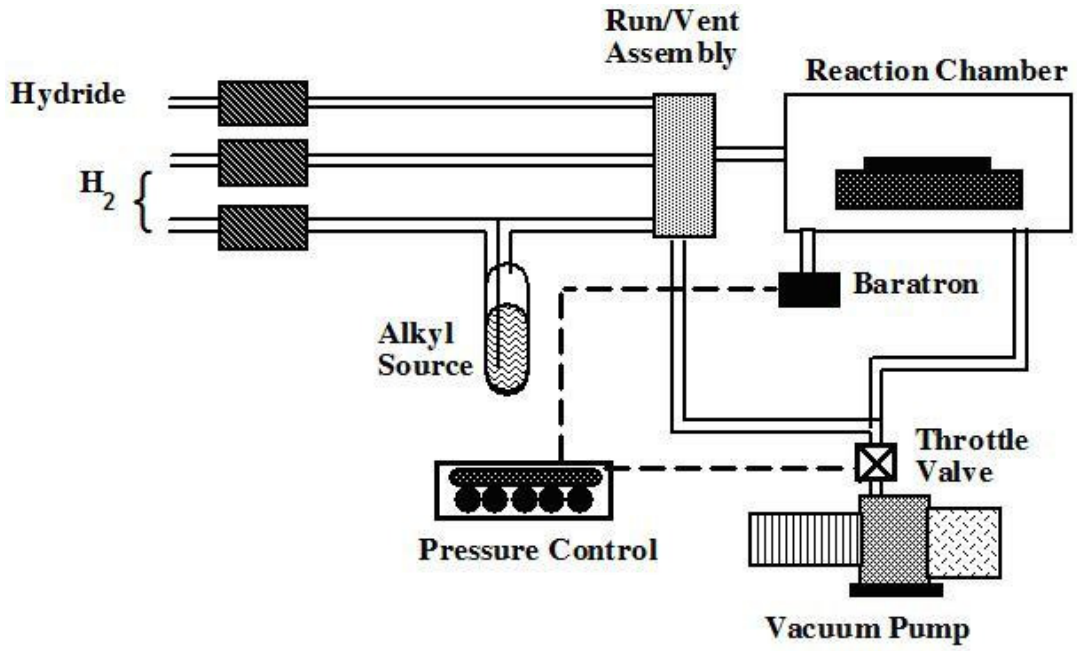

Figure 22 Schematic of a standard MOCVD growth chamber.

The substrate is heated using a special heater which is capable of rapid changes in temperature and can operate in vacuum as well as extreme environments such as oxidizing or reducing atmospheres. Different designs of reactors have been proposed over the years however the most common one in mass production is the rotating platter model (79). The rotating platter spins under a shower head which emits the metalorganic precursor (80). For ZnO growth, low pressure growth is preferable. The growth chamber is kept between 0.1 and 100 torr. The design relies on a "stable" reactor condition in which laminar flow is maintained over the wafers (81). Significant effort is put into designing the vessel head which regulates the laminar flow. This complex fluid dynamics problem has been the effort of mechanical engineers and material scientists for years. As the metalorganic precursor is heated, it is cracked, breaking the hydrogen and carbon nuclei and leaving the free metal ion in the gas phase flow. A reactant gas is then flowed simultaneously or in pulsed mode over the reactor chamber. The reactant gas completes the other half of the compound semiconductor. In multicomponent

semiconductors, multiple alkyl sources and reactant gasses can be pulsed or flowed into the chamber. For ZnO growth, diethylzinc is the metalorganic of choice. In MOCVD growth, either oxygen (O_2), nitrous oxide, or nitrogen monoxide can be used as the reactant gas (82). Ideally, oxygen or nitrous oxide are the best choices. These two gas molecules crack to form free oxygen. Nitrous oxide also produces N_2, however N_2 is quite stable and does not incorporate into the matrix. N_2 is the common carrier gas that is flowed to maintain laminar flow over the reactor chamber for this very reason. Nitrogen monoxide however when cracked leaves free nitrogen. This free nitrogen readily gets absorbed into the matrix resulting in nitrogen doped samples (83). The reaction for ZnO MOCVD growth using Oxygen as the gas can be seen in Equation 7. MOCVD growth of ZnO is one of the only completely green reactions producing safe, non-toxic byproduct offgasses.

$$(C_2H_5)_2Zn + 7\,O_2 \rightarrow ZnO + 5\,H_2O + 4\,CO_2$$

Equation 7 Stoichometry balance of the ZnO reaction.

Dopant gasses can be added during the growth conditions in a pulsed or continuous fashion. Dopant gasses are ideally metalorganic liquds similar to diethylzinc. Trimethylgallium is used frequently for gallium doping, while diethylboron is used for boron doping. Trimethylindium is used for indium doping. These metalorganics are sometimes too efficient at doping in comparison to the zinc oxide growth. The rate at which a metalorganic is picked up and flowed through the reactor is based on partial pressures through a bubbler. The metalorganic source is contained in a sealed stainless steel bubbler. A carrier gas, particularly nitrogen in the ZnO MOCVD growth process, is flowed over through the liquid. The bubbler is put in a recirculating bath filled with antifreeze. The metalorganic source is so volatile, many of them have boiling points below 10 C. Based on the flow rate and pressure inside the bubbler, the percentage of metalorganic molecules in the gas phase is directly related to the partial pressure of the

source. Precise control over the source pressure must be maintained for uniform doping. By increasing the temperature of the source, increasing the carrier gas flow, or decreasing the pressure, the amount of metalorganic molecules can be precisely controlled. To minimize the pressure differential in the bubbler, bypass lines are often installed. This allows rapid switching at pressure and a constant flow rate between the metaloranic source and just carrier gas to minimize spiking in the doping profile.

A complicated series of mass flow controllers, solenoid valves and pressure controllers/transducers regulates the gas flow of the carrier gas, reactant gas and the metalorganic sources. Vacuum is maintained by a high volume, high vacuum pump setup. These usually include two stage vacuum/blower configurations. The internal chamber pressure is regulated on the exhaust side through an exhaust butterfly valve. The butterfly valve is controlled digitally on a feedback loop from the main chamber pressure transducer. Temperature is controlled by way of a substrate controller which has a feedback loop with an resistive thermal detector, RTD, and a pyrometer for operation above 700 C. The rotation of the wafer is controlled by this controller as well. A DC motor is supplied a specific current which has a feedback loop to an optical RPM meter. The off gas is filtered through a roughing filter, a fine particulate filter and then into the vacuum/blower configuration. The blower moves the off gas to a scrubber and decomposition chamber. The scrubber removes the volatile gasses that may still be present and decomposes the remaining organic molecules. The off gas is washed and then ejected to the outside world. Precision control over the growth conditions is controlled by way of computer interfaces driving the solenoids, mass flow controllers, pressure controllers, temperature controllers, wafer controllers and exhaust valve controller.

Characterization and growth health tools can be integrated into the MOCVD chamber. Items such as surface reflectance and ellipsometry can be used to determine the thin film growth conditions (84). Surface reflectance is measured using a fiber optic

wide band light source to direct light into the growth chamber. The same fiber optic measures the reflected light from the surface of the rotating wafer. The measurements are gated on the rotational speed of the wafer so as to only measure the reflectance of the wafer and not the spinning platter which makes up the majority of the area (85). A figure depicting the reflectance measurement system can be seen in Figure 23.

Figure 23 An example reflectance measurement system.

As the thin crystalline film begins to grow, there become interference patterns between the background reflectance and the observed reflectance. These interference patterns oscillate as the crystal becomes thicker. These oscillations, if looking at a monochromatic light source produce a damped sinusoidal oscillation. The damped nature of the pattern is indicative of light absorbance in the thin film. For ZnO, one full oscillation at 730 nm light corresponds to ~250 nm of growth. A sample surface reflectance measurement for growth of ZnO can be seen in Figure 35.

This inline characterization technique was crucial for optimizing inline growth parameters such as chamber pressure effects on growth, growth rates, dopant levels and optical quality. The health of the crystal growth process can be easily monitored without having to stop the reaction, cool the chamber, and bring the chamber back to atmospheric conditions. Growth is carried out in near clean room conditions. Every opportunity for

contaminants to be introduced to the material must be avoided. It was also of a paramount asset in achieving two dimensional thin film growth over three dimensional thin film growth.

In the MOCVD growth of ZnO and other materials such as GaN, it is desirable to achieve two dimensional crystalline growth. In two dimensional growth, the thin film is growing along the surface of the substrate producing a highly uniform thin film. This growth condition is an extremely fine balance of temperature, pressure, precursor control and luck. It is usually a high growth rate regime where very few defects exist and good growth controlled by diffusion mass transport. When any of the conditions vary, particularly pressure, three dimensional growth becomes the primary growth modality. Here, individual seeds growth vertically, forming nanorod like structures. This produced polycrystalline materials. For scintillation detectors, polycrystalline materials are highly undesirable. The crystalline defects and abundance of grain boundaries produces trapping locations, and longer scintillation decay times as well as scintillation outside the band gap. ZnO growth in the MOCVD process has a very narrow window in which 2D growth can occur. Pressure sensitivities are extreme and have been found to be mandatorally regulated around 10 to 50 torr. Outside this region, the metalorganic after cracking preferentially sticks to the surface and does not diffuse into a smooth 2D growth. Above 50 torr, the metalorganic, after cracking, cannot reach the surface before combining with an oxygen nuclei and produces a powdery surface which is highly undesirable. The knife edge growth conditions also require growth between 475 and 550 C. Above 550 C, growth is hindered and slowed to rates below 100 nm per hour. Below 475, a sufficient quantity of oxygen cannot be cracked. Switching oxygen precursor gasses may improve this requirement. Zinc oxide growth observed during this work has been found to be a hybrid of 2D and 3D growth, alternating between vertical 3D growth nucleation, which then coalleceses and diffuses into 2D uniform thin film growth (86). For work presented here, growth was preferentially better above 525 C.

The crystallinity of the MOCVD grown ZnO samples is heavily dependent on the substrate it is grown on. The lattice mismatch between the substrate and the ZnO structure should be minimized. ZnO however is a phenomenal material with a very high tolerance to strain in the first layers. ZnO has a wide set of lattice constants at A=3.25 Å and C=5.2 Å. Sapphire is the preferred substrate to grow on with a lattice mismatch parameter of approximately 30%. Even with such a large mismatch of lattice constants, ZnO can recover within the first 100 angstroms and result in high quality 2D growth (87). ZnO has been grown on everything from sapphire to silicon to silicon oxide and glass. During the course of this work, ZnO growth on silicon, silicon oxide, sapphire and glass have all been demonstrated. By utilizing techniques described in the following section, high quality films can be grown on just about any material including non wurzite structures or amorphous materials.

ZnO Hybrid MOCVD Atomic Layer Deposition Growth

Lastly, for very precise thin films, it is possible to hybridize the growth conditions to produce a growth process which is surface limiting, known as atomic layer deposition. In atomic layer deposition, one precursor at a time is pulsed during the growth process (88). Following the growth pulse of the first precursor, a purge pulse of carrier gas is used to clear the chamber. Following this purging pulse, a cracking gas is introduced cracking the dangling molecule. A purge gas pulse clears this cracking gas. Next, the second precursor is pulsed. Again, a carrier gas purge is introduced, and lastly, a new cracking gas is used to break the dangling molecule attached to the other half of the second precursor. Unlike before in the MOCVD growth conditions where both gasses are flowed simultaneously, only one gas is in the chamber at a time. To further ensure uniform thin films are formed, the growth conditions are self limiting. Leaving a dangling chain exposed on one surface limits the reaction to nucleate atoms one atom thick across the surface. This one atomic thick layer then cracks the limiting molecule

off exposing the bond for the next reactant gas. The second reactant gas then is introduced. The diethylzinc source is still used, but the oxygen source is replaced with a water vapor source. Water vapor functionalizes the atomic surface with a hydroxide molecule on the surface. The stoichometric balance equations can be seen in Equation 8 and Equation 9.

$$ZnOH^* + Zn(CH_2CH_3)_2{}^* \rightarrow ZnOZn(CH_2CH_3)\ {}^* + (CH_3CH_3)$$

Equation 8 First chemical balance of the ZnO ALD reaction using diethylzinc and water.

$$Zn(CH_2CH_3)\ {}^* + H_2O \rightarrow ZnOH^* + (CH_3CH_3)$$

Equation 9 Second phase to the chemical balance of the ZnO ALD reaction using diethylzinc and water.

The pulsed growth cycle alternated between diethylzinc, and water vapor. Water vapor was produced by using a fillable stainless steel bubbler and heating the feed line leading up to the reactor chamber. Growth rates were found to be approximately 2 Å per pulse cycle which is in agreement with other ALD of ZnO work. This was determined both by inline reflectance measurements as well as post growth filmetrics reflectance measurements. An animation of the ALD growth process for ZnO can be seen in Figure 24. The blue spheres represent the zinc nuclei, the white spheres are oxygen grey spheres are carbon and the light blue spheres are hydrogen.

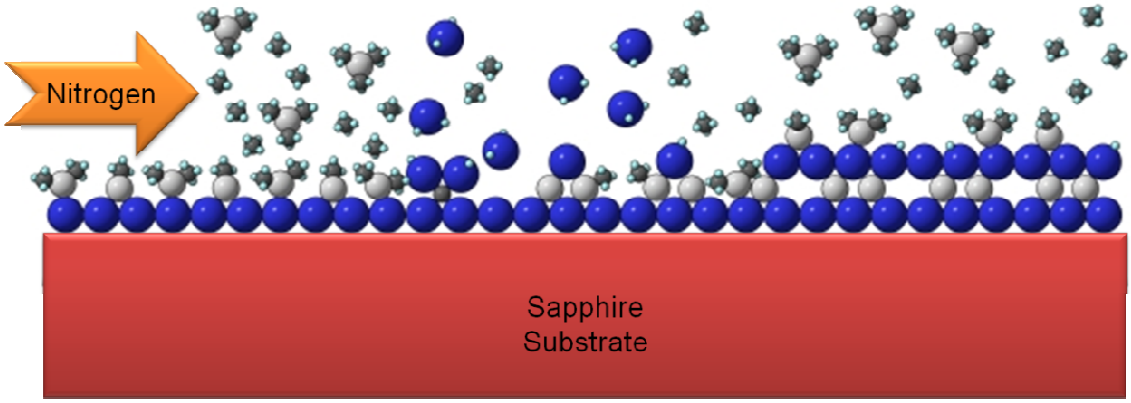

Figure 24 ALD of ZnO using water molecules and diethylzinc.

The benefit to ALD growth for initial growth over a substrate or patterned structure because ALD can achieve very high conformal coatings at extreme aspect ratios of 10,000 to 1. This is only possible due to the surface limiting reaction. Otherwise, using the MOCVD growth process, the small features of a patterens structures would be meshed over by the rapid growth process. ALD by its very nature is a slow growth process, but a growth process which has its place in this future work. It is noted that due to the self limiting reaction, amorphous material is the primary result of ALD growth. Amorphous material is almost always guaranteed if growing via the ALD method over a strong lattice mismatch material.

Example ZnO Scintillators

Several representative samples of ZnO materials are shown in this section. Both bulk and MOCVD grown materials are shown as they are the focus of this work. Bulk grown materials from large cubes to large cylindrical boules, to thin wafers are possible. Ten micron thick layered scintillators are also shown. Shown in Figure 25 is a large bulk melt growth sample which has been polished by Cermet. Shown in Figure 26 is an SEM image of the low pit etch density of the single crystal ZnO scintillators grown by Cermet. Shown in Figure 27 are several Cermet grown wafers of ZnO showing undoped and

doped ZnO. Shown in Figure 28 are several large crystal cubes of ZnO next to a 5.12 cm diameter PMT. Shown in Figure 29 is a comparison between MOCVD grown and bulk grown materials. The samples are of high quality, optically clear and will prove to be good, high efficiency neutron detectors.

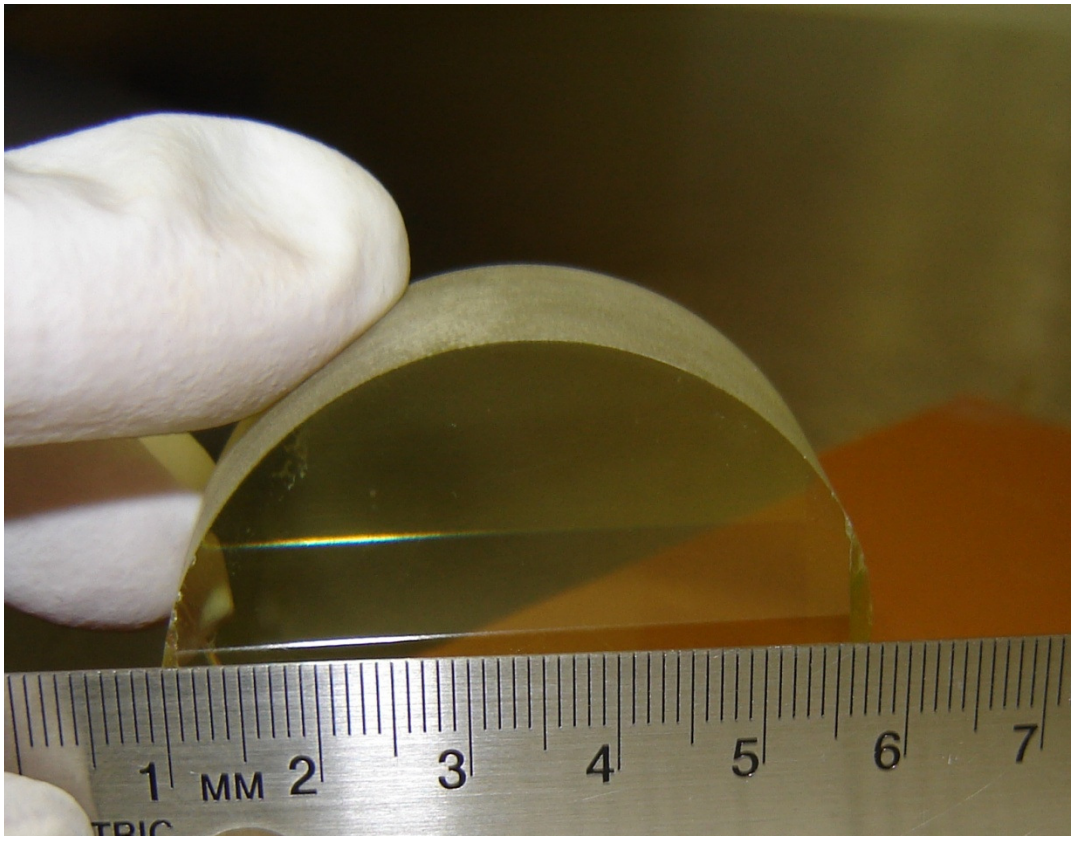

Figure 25 Large boule of single crystal ZnO grown by Cermet Inc. Photo courtesy of Jeff Nause, Cermet Inc.

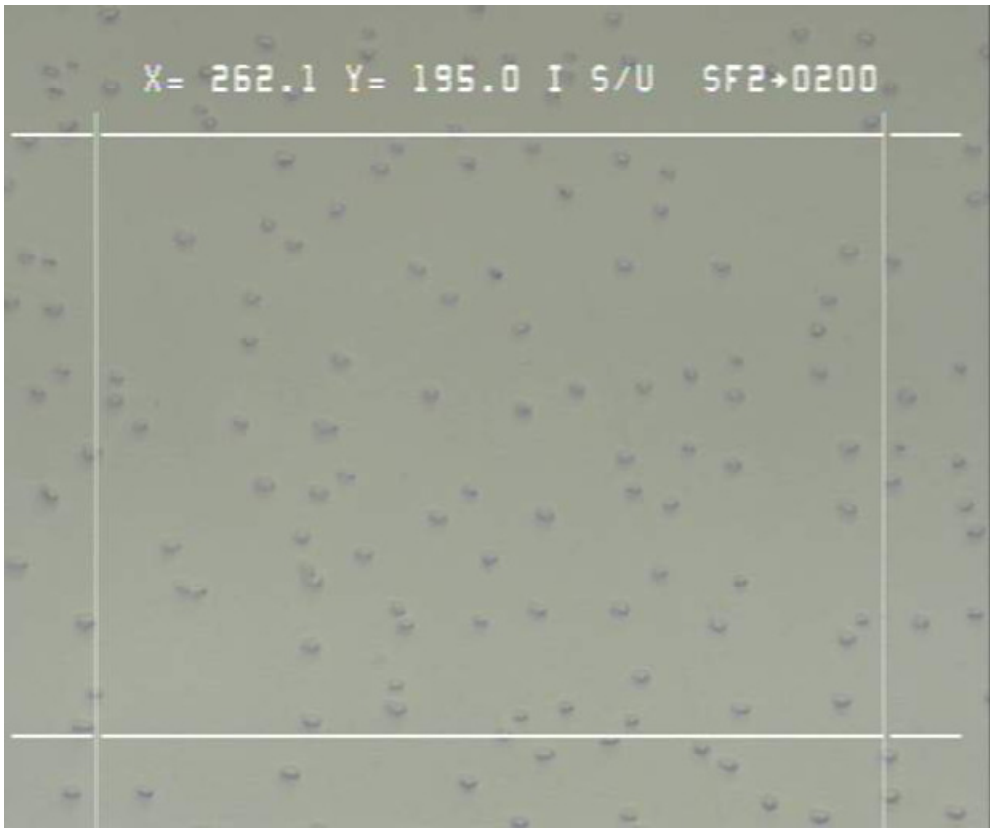

Figure 26 SEM image of Cermet grown bulk ZnO crystal showing low pit etch density. Photo courtesy of Jeff Nause, Cermet Inc.

A 2" ZnO boule accompanied by an optical micrograph indicating low etch pit density is shown in Figure 25. Figure 26 shows various undoped and doped ZnO boules and wafers. Because of the band gap enhancement in addition to the high thermal neutron cross section, lithium and gadolinium dopants are the principal dopants investigated. The proposed work hopes to achieve levels up to 10 weight percent dopant in the crystal. In addition coating the surface of the scintillators with Li and Gd through evaporation and diffusion techniques were investigated as possible pathways to producing a thermal neutron sensitive detector.

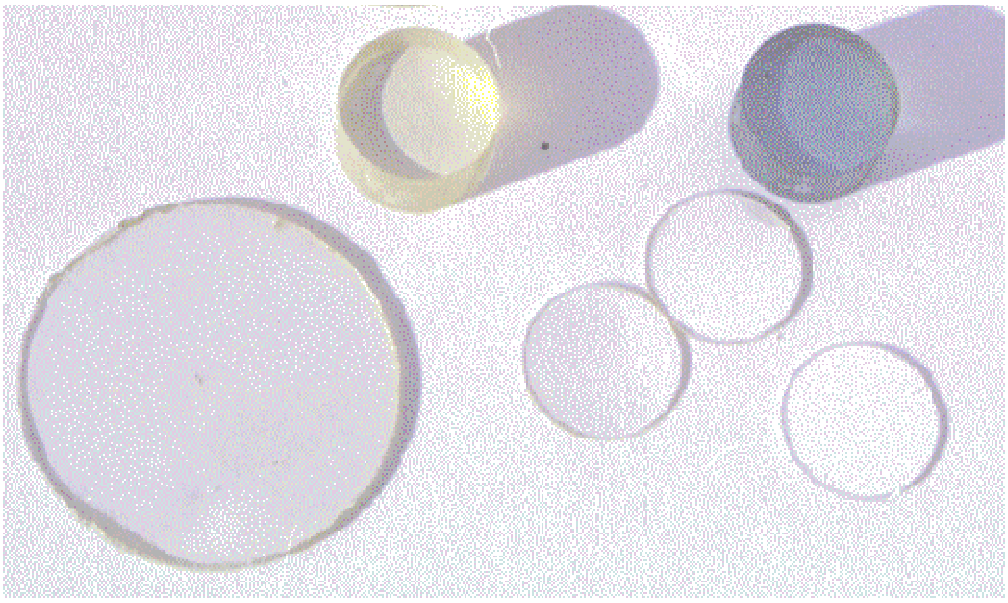

Figure 27 Wafers of doped and undoped ZnO from the bulk melt growth process.

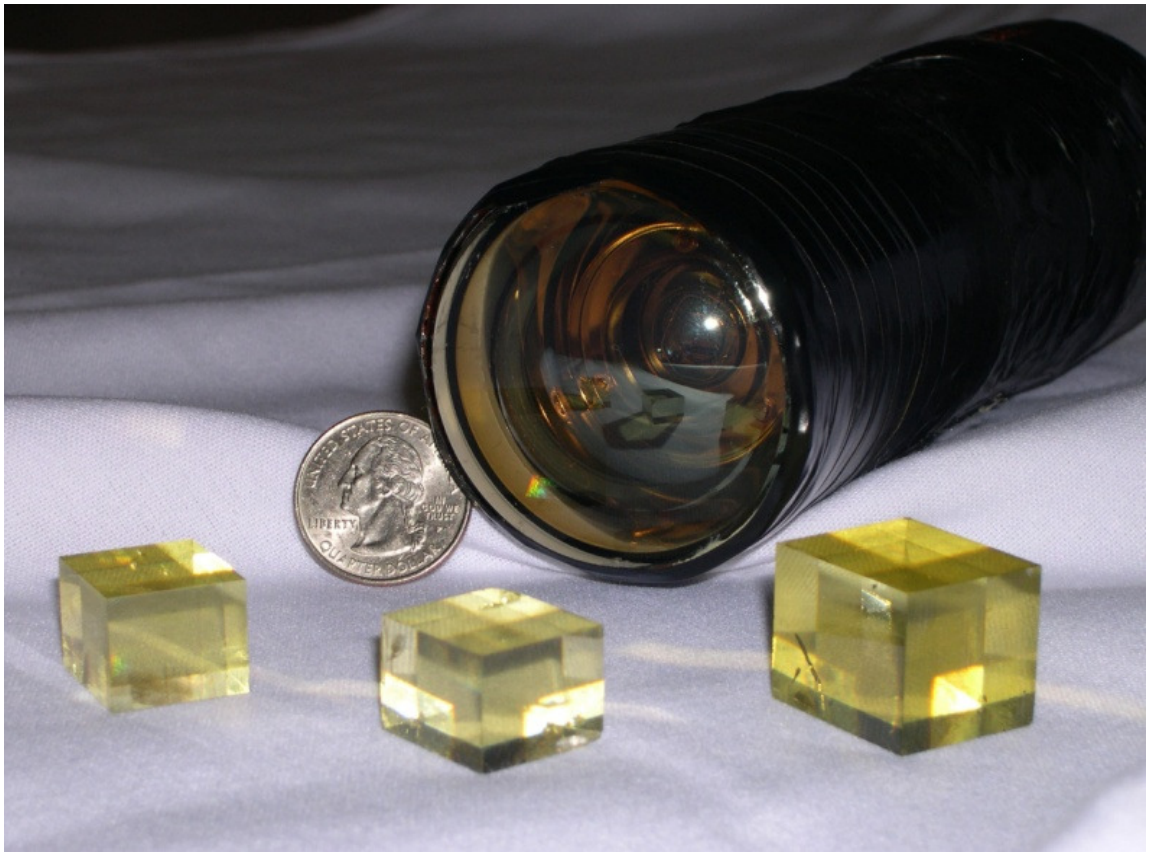

Figure 28 Large cubes of polished ZnO. The left and right cubes are undoped ZnO while the center cube is lithium doped ZnO.

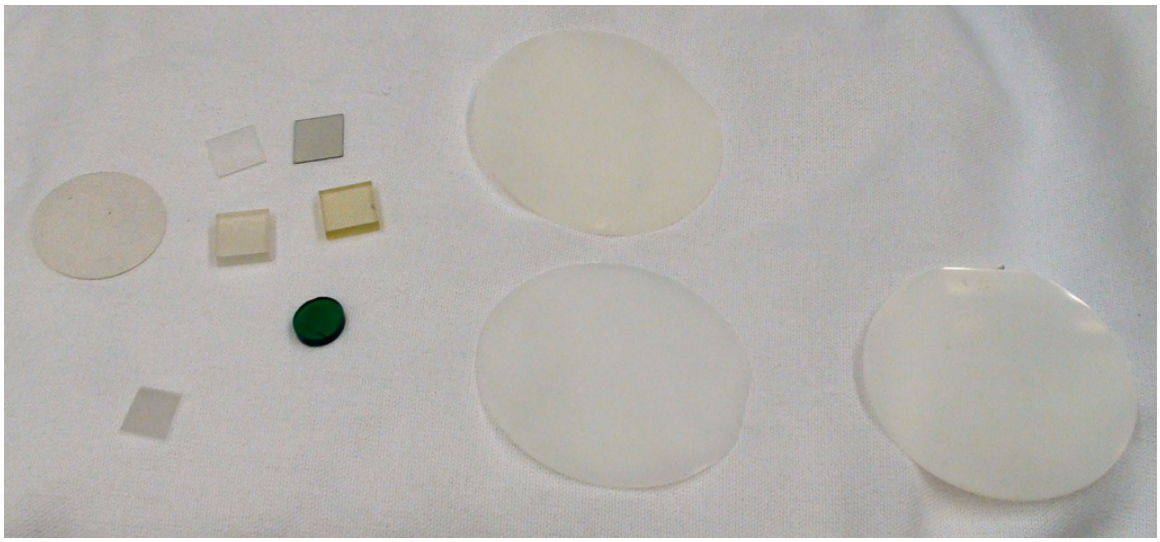

Figure 29. Shown on the left, small bulk grown ZnO samples including indium, lithium, cobalt and undoped ZnO. On the right, the two inch wafers showing MOCVD grown ZnO.

CHAPTER IV

CRYSTAL CHARACTERIZATION TECHNIQUES

To determine the crystalline quality and initial performance testing of the ZnO scintillators as neutron detectors, several characterization techniques were employed. These techniques included testing for crystalline quality, photoluminescence spectroscopy, scanning electron microscope interrogation, optical microscope interrogation, chemical bevel interrogation, ex-situ surface reflectance and Fourier transform infrared spectroscopy. Most of these techniques were adopted from the semiconductor research arena to shed light on the scintillation detector performance. These techniques were employed to rapidly screen the samples to determine the impact on various growth conditions and dopant concentrations on the ZnO scintillator performance. Three main parameters in particular are investigated using these methods. The scintillation wavelength, dopant concentrations and crystalline quality are measured using these crystal characterization techniques. Crystalline quality was tested using three main methods, optical microscopy, scanning electron microscope (SEM) microscopy, and x-ray diffraction analysis. The effect of dopant concentrations on scintillation wavelength were investigated with photoluminescence spectroscopy. The dopant levels were qualitatively measured using Fourier Transform Infrared Spectroscopy (FTIR). Physical parameters such as the scintillator thickness was measured using surface reflectance measurements and chemical bevel interrogation using Atomic Force Microscopy (AFM).

Photoluminescence Spectroscopy Analysis Method

One of the analysis methods used in this work to determine the scintillator's performance was to use a photoluminescence spectrometer. The photoluminescence spectroscopy method is a non-destructive method of probing the electron states, band gaps, and scintillation behavior of a material without exposing it to radiation. This rapid scanning solution is taken from the materials science and semiconductor world for investigating band gap transitions. There it aids in band-gap engineering. For the ZnO scintillator, there are two primary scintillation modes which dominate the photoluminescence spectrum. The first is the direct band gap de-exitation. This radiative transition between the conduction and valence electron bands is useful in determining the effect of alloying on the ZnO scintillator. The second mode of scintillation which can be found in the ZnO scintillator are defect driven emissions. These defect driven decay modes consist in ZnO of oxygen vacancies or excess oxygen centers, carbon trapping interstitially as well as oxygen replacement, zinc vacancies, and dopant centers. In addition, crystalline defects can result in longer wavelength de-excitations. All of these defects result in scintillation wavelengths outside the band gap at longer wavelengths. These defect centers result in longer decay times.

A laser, either pulsed or continuous wave, is brought incident on the scintillator to be tested. The lasers used in these experiments were a using a 325nm Melles-Griot HeCd laser and a 248nm NeCu pulsed laser system. The laser is first reflected by a high quality mirror. It is then filtered to remove all but the primary photon signature of 235nm. It is then focused through a set of optics making the beam a very intense spot. The laser beam is then refracted with a small right triangular prism. This steers the beam at an angle of approximately 45 degrees onto the sample. The laser has an energy significantly above the band gap energy of the scintillators. This laser beam excites the electrons in a similar fashion to that of ionizing radiation, albeit with a lower incident energy. The scintillation

light is focused through two lenses and sent through one final filter which protects the monochrometer. The continuous wave system is coupled to a Acton Spectra Pro 2300i monochromater and PIXIS 100 1600 channel single row CCD camera which produces in a single measurement a large portion of the scintillation spectrum. The pulsed monochrometer however has a single CVI monochromator and Hamamatsu PMT to convert light to a usable signal.

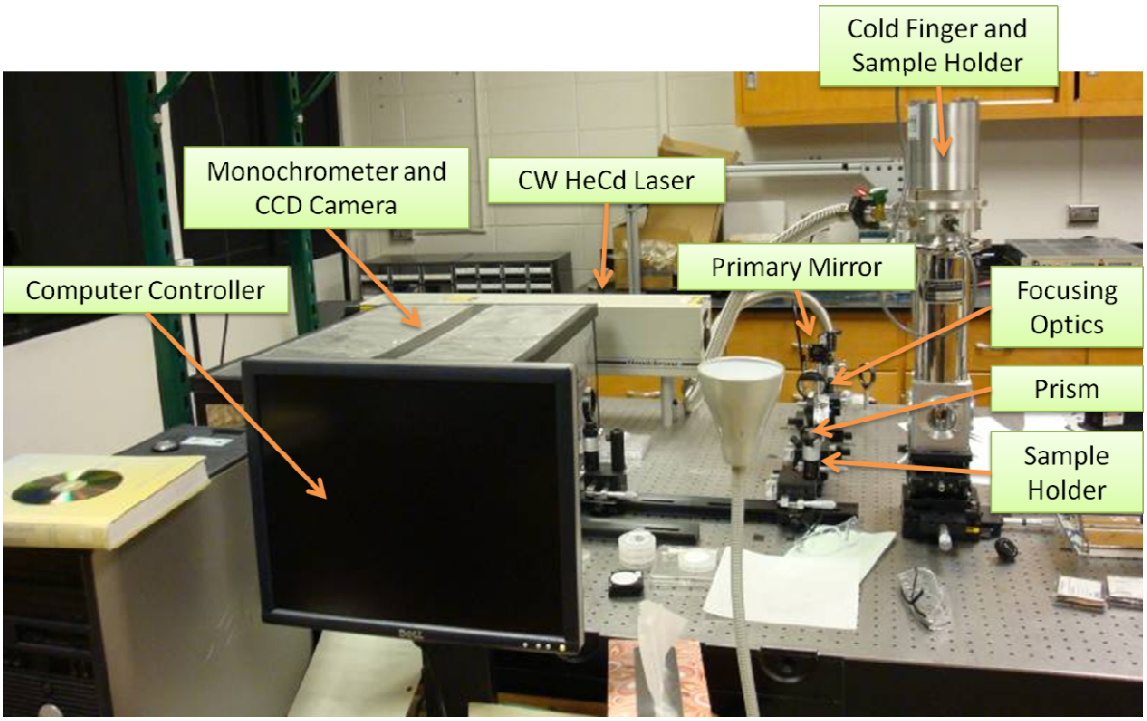

Figure 30 The continuous wave laser PL measurement system. Also shown is the cold finger cryostat for liquid helium measurements. The monochrometer is housed under the aluminum box.

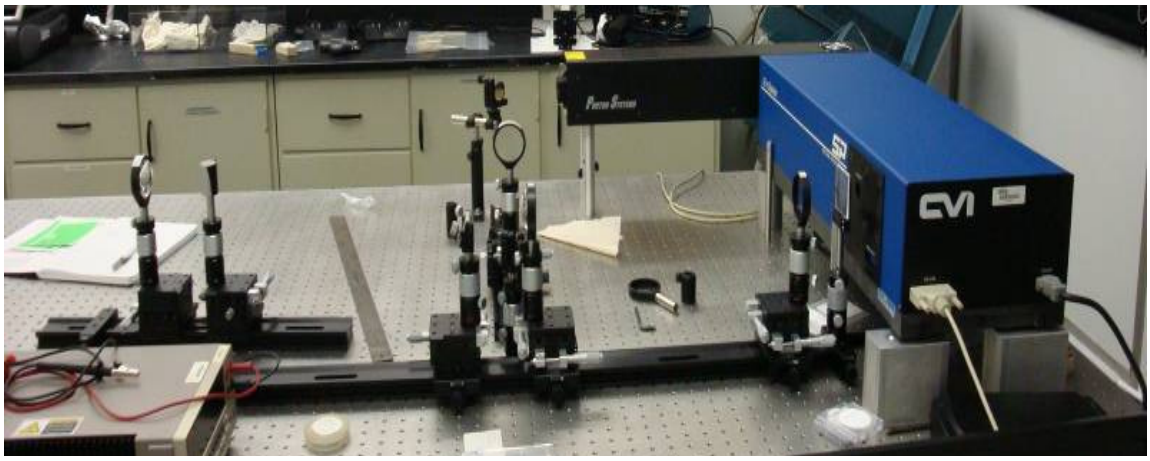

Figure 31 Pulsed PL measurement system with single channel monochrometer and Hamamatsu PMT.

Photo-excitation causes electrons within the material to move into permissible excited states. When these electrons return to their equilibrium states, the excess energy is released and may include the emission of light (a radiative process) or may not (a nonradiative process). The energy of the emitted light (photoluminescence) relates to the difference in energy levels between the two electron states involved in the transition between the excited state and the equilibrium state. The quantity of the emitted light is related to the relative contribution of the radiative process.

By studying the de-excitation process one can study the band gap structure and the introduction of activator locations, resulting in acceptor and donor bands. Once an electron is excited it wants to return to equilibrium, also known as "recombination," can involve both radiative and nonradiative processes. The amount of photoluminescence and its dependence on the level of photo-excitation and temperature are directly related to the dominant recombination process. Analysis of photoluminescence helps to understand the underlying physics of the recombination mechanism. Radiative transitions in semiconductors also involve localized defect levels. The photoluminescence energy associated with these levels can be used to identify specific defects, and the amount of photoluminescence can be used to determine their concentration. Another specific

transition to monitor is the nonradiative processes which are associated with localized defect levels, whose presence is detrimental to material quality and subsequent device performance. Thus, material quality can be measured by quantifying the amount of radiative recombination. In ZnO these are hypothesized to result in the green luminescence (GL) spectra. The hypothesized defect levels can arise from oxygen or zinc vacancies primarily, but to a lesser extent, those produced through excessive doping.

The systems used here also have the capability to measure the photoluminescence spectra at various temperatures down to 3 K, or liquid helium temperatures. By attaching the sample to a cold finger which has been evacuated of all air by a turbo-molecular pump, the sample can be cooled. The sample is housed inside a vacuum vessel with quartz glass windows. This allows one to measure phonon states and defect donor bands to very high resolutions. However, the direct study of band gap, acceptor bands, and donor bands falls outside the scope of this work. The important item to take away from PL measurements is the wavelength shift at room temperature. At liquid helium temperatures, the wavelength shift is dramatic, at room temperature the shift is blurred by the Gaussian distribution in the wavelengths based on the thermal excitation of the material.

Due to the small beam spot size of the laser system, high spatial resolutions on the grown samples was able to be measured using the PL system. This allowed for uniformity studies to be performed. In early samples grown by the MOCVD method, nonuniform samples and excess carbon trapping in samples was common. Quantification on oxygen vacancies, carbon trapping and crystalline quality were able to be made using the CW PL system.

Fourier Transform Infrared Spectroscopy

One method used to ascertain lithium loading of the ZnO samples was to run Fourier Transform Infrared Spectroscopy, or FTIR spectroscopy. FTIR spectroscopy is

designed to detect different bond patterns in a material. The most common form of FTIR is transmittance FTIR. In transmittance FTIR, a broad spectrum infrared light source is pulsed against a sample. The wavelength of infrared light, on the order of 15,000 to 20,000 nm passes through the sample. A series of detectors tuned to in this case the mid infrared and far infrared collects data in the phase space of distance. The wavelength of light used in FTIR corresponds to the length of molecular bonds of the material and gives a unique fingerprint of what is in the sample. Using a set of mirrors and a beam splitter, one infrared beam is split and while moving one mirror and holding the other mirror constant, a set of interference patterns are produced. These patterns pass through the sample and are collected simultaneously by the optical sensors. This device, known as an interferometer, measures the interference patterns of the absorbed infrared light. To ascertain the actual absorption spectrum in a frequency domain, a Fourier Transform is applied to the raw data. This results in a frequency domain spectrum from the sample. Due to the thin film nature of the ZnO doped scintillators that were produced, the absorbance spectra was dominated by the thick sapphire substrate the scintillators were grown on. To overcome this, a second method known as diffuse reflectivity was employed to determine the loading of lithium and other dopants into the samples. The samples were measured at Los Alamos National Laboratory Materials Science and Technology division using a Bruker Virtex 80v FTIR with coverage from UV to THz. The Bruker Virtex 80v can be seen in Figure 32.

Figure 32 The FTIR Bruker Virtex 80. The LANL version has the addition of the MIR, FIR and now the NIR.

This benchtop unit utilizes a vacuum system to minimize the impact of water vapor on the sample analysis. It also had an active mirror alignment system which aided in measuring the samples particularly for the diffuse reflectance measurements. Points of interest are shown below for the Li peak and nitrogen interstitals found in the ZnO achieved in Li doping and N doping using NH_3. While the FTIR yields definitive results on whether a sample contains a dopant or not, it does not have the ability to quantify the results without a set of known calibration points. It can yield qualitative results, and quantitative results relative to one another. Absolute measurements however are not possible using the diffuse reflectivity FTIR system which was needed because of the sample substrates.

Optical Reflectance Measurement Characterization

The optical characterization method utilized in this work was a surface reflectance measurement system. The system was a Filmetrics FT10. This system uses a wide spectrum high intensity lamp to produce an initial spectrum. This spectrum is focused onto a fiber optic and then into the sample holder. In the sample holder, a lens focuses the beam on a predescribed height on the sample stage. Light is reflected from the sample and collected by another fiber and routed back to the controller box. The light is

then passed through a monochrometer and read out by a single line CCD. This spectrum of reflectance will vary as the thickness of the material increases.

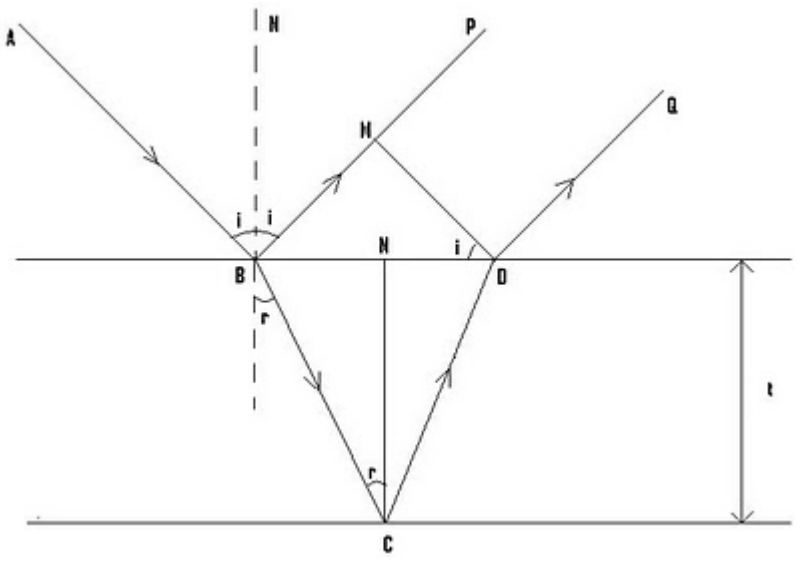

Figure 33 Physical representation of the surface reflectance measurement system used for determining material thickness.

Shown in Figure 33 is a physical representation of what is occurring in the surface reflectance measurement. Light coming in from location A strikes the film surface. Due to the higher index of refraction in the scintillator it is bent down. A portion of the beam is reflected towards N while the part that enters the surface is pointed at C. The angle r is determined by the ratio of the two indicies of refraction and the entering angle i. The reflected light is always reflected like a mirror with angle i. The light that enters the material reflects off the bottom surface with the same angle r. It then strikes the top surface again. Here the light is bent back at a shallower angle, i again. This light is nearly parallel to the reflected light from the incident light beam. This puts the two light waves slightly out of phase producing the interference patterns one sees in the analysis.

A reference standard such as a plain sapphire substrate was used as the thickness of record. The dark current is subtracted from the reflectance signal. The dark current is taken by holding the reference sample at a 10-80 degree angle to the fiber optic light source. When measuring a thin film coating over sapphire, the thin film will produce

interference patterns based on its difference in index of refraction. These interference patterns are analyzed in the computer software to determine the thickness. A picture of the Filmetrics system can be seen in Figure 34. When the software analyzes the reflectance spectra it can fit the reflectance pattern with a sinusoidal function which is damped at lower wavelengths to correspond to the increase in index of refraction for the material.

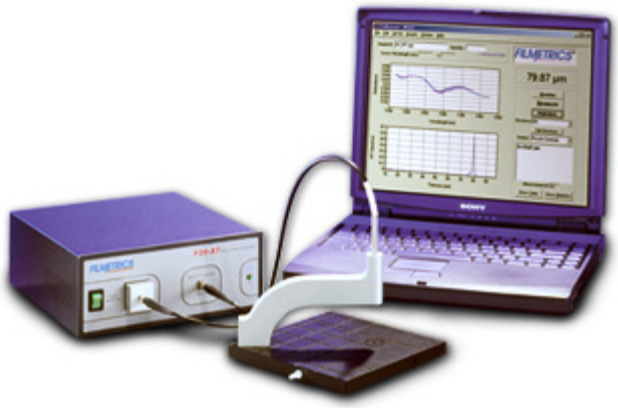

Figure 34 An example Filmetrics system with wide band light source, and CCD monocrometer.

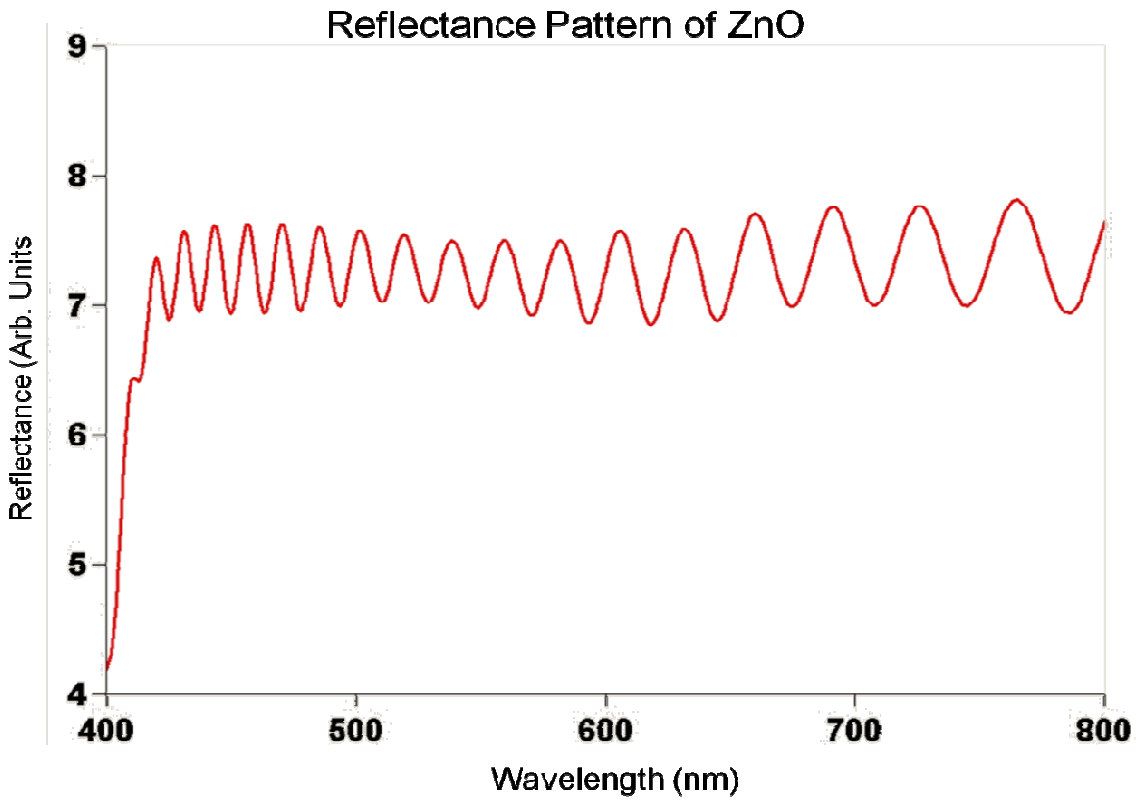

Figure 35 Reflectance pattern from a thin film ZnO scintillator.

Chemical Etch AFM Characterization

Chemical etching was also used to ensure the surface reflectance measurements were correct. In the chemical etching process, a line is etched into the surface with an acid solution. This produces a sharp line in the surface of the thin film. HCl was used for ZnO as it has an excellent selectivity between etching ZnO and leaving the sapphire substrate intact. Surface morphology was then studied using a PSIA XE-100 atomic force microscopy (AFM). The AFM unit is mounted on a vibration limiting table to minimize noise in the system. A picture of the AFM can be seen in Figure 36. Here a nanorod tip was tapped across the surface of the scintillator before and after where the step etch was made. The AFM gave several line profiles of the surface height of the sample. In all instances the AFM measurements agreed quite well with the surface reflectance measurements. Since this chemical etching process is a destructive test, it

was only used in the early stages of proof of concept. After that, only surface reflectance was used.

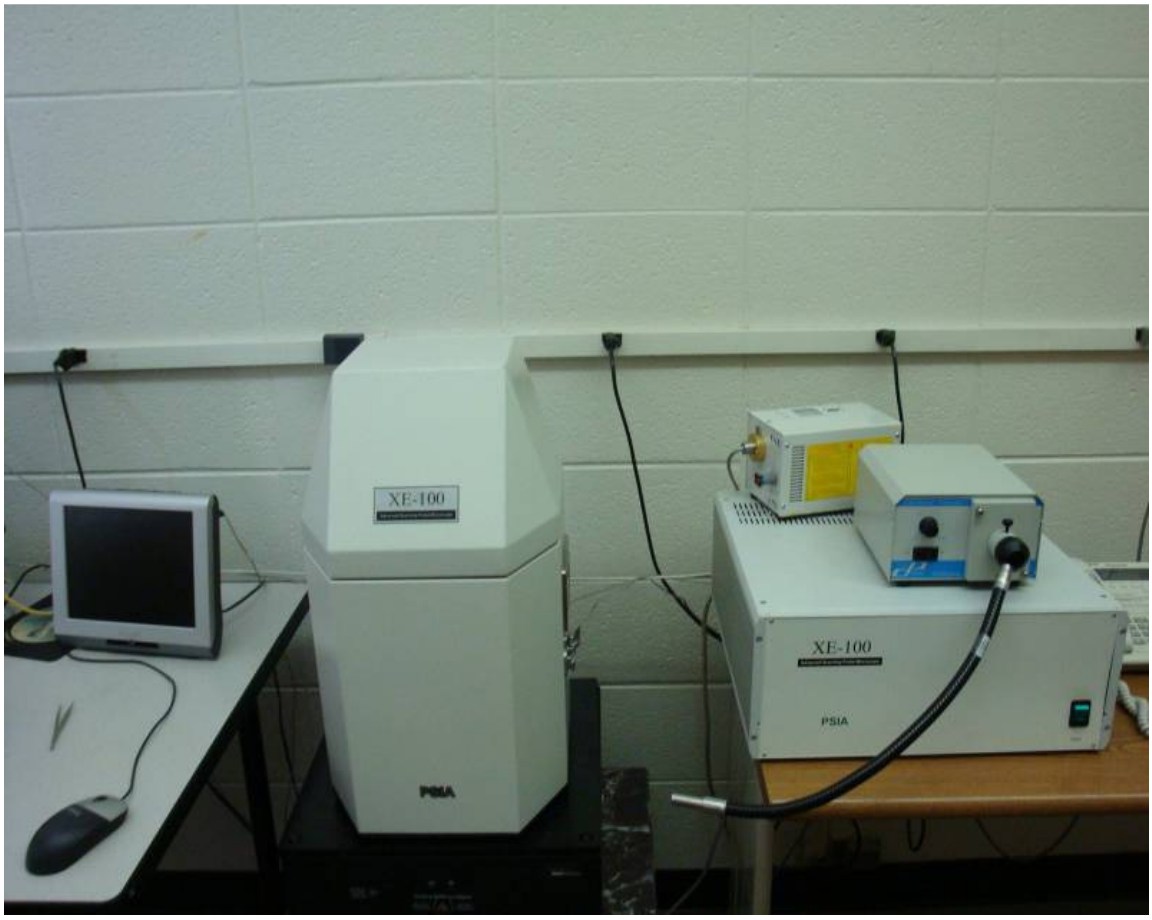

Figure 36 AFM system used for chemical etch surface profiling.

Optical and Scanning Electron Microscope Characterization

An optical microscope with digital camera interface was also used to determine the crystalline quality of the grown scintillators. This simplistic system was one of the fastest characterization tools and is often overlooked. Optical zoom rates of 10,000 were possible with the benchtop unit. Using a surface born light, even the most opaque samples could be observed. This system was crucial for determining the origins of surface defects on the MOCVD grown crystals. Nucleation points, defects, and other

inclusions could easily be found and analyzed using this system. A sample stereo microscope used in this work can be seen in Figure 37.

Figure 37 Example stereo microscope with digital camera interface used in this work.

The scanning electron microscope (SEM) was used for imaging the surface of the scintillator at resolutions and magnifications far outside the optical range of the human eye. Magnifications of 100,000 are possible with very fine resolutions. Feature diameters on the order of 10s of nm are possible. Two main modes were used in SEM characterization of the samples. Side on and top down views were used to analyze the growth of select samples of scintillators. The side on view was used to demonstrate the thickness of the material was solid, and that it was single crystal. Side on views were

added after studying the top down images obtained with the SEM. The growth conditions of ZnO growth in the current reactor were a 2D-3D growth combination. The surface morphology shows nanorod nucleation while the side on view from the SEM showed that the nanorods coalesced into one single crystal. A top down view of one of the grown ZnO samples can be seen in Figure 38. The inclusion rate on this sample is extremely small showing almost no inclusions or defects. The slight coloration of the surface is indicative of the surface nanorod nucleation. In Figure 39 is shown the side on view of a ZnO sample grown on silicon. This sample which was measured to be 250 nm shows no independent nanorod growth, rather a smooth cleaved surface. This is indicative of good 2D growth which is nucleated in the 3D regime. There is roughly a 1 μm thickness of SiO_2 that appears on the surface of the structure. The SiO_2 that appears is from the silicon oxidizing in the atmospheric air. Silicon, when exposed to atmospheric oxygen, immediately starts to oxidize. This layer can be removed by dipping the sample into HF acid solution. However, ZnO's tolerance to growth on large lattice mismatch materials makes it acceptable to have this oxide layer present.

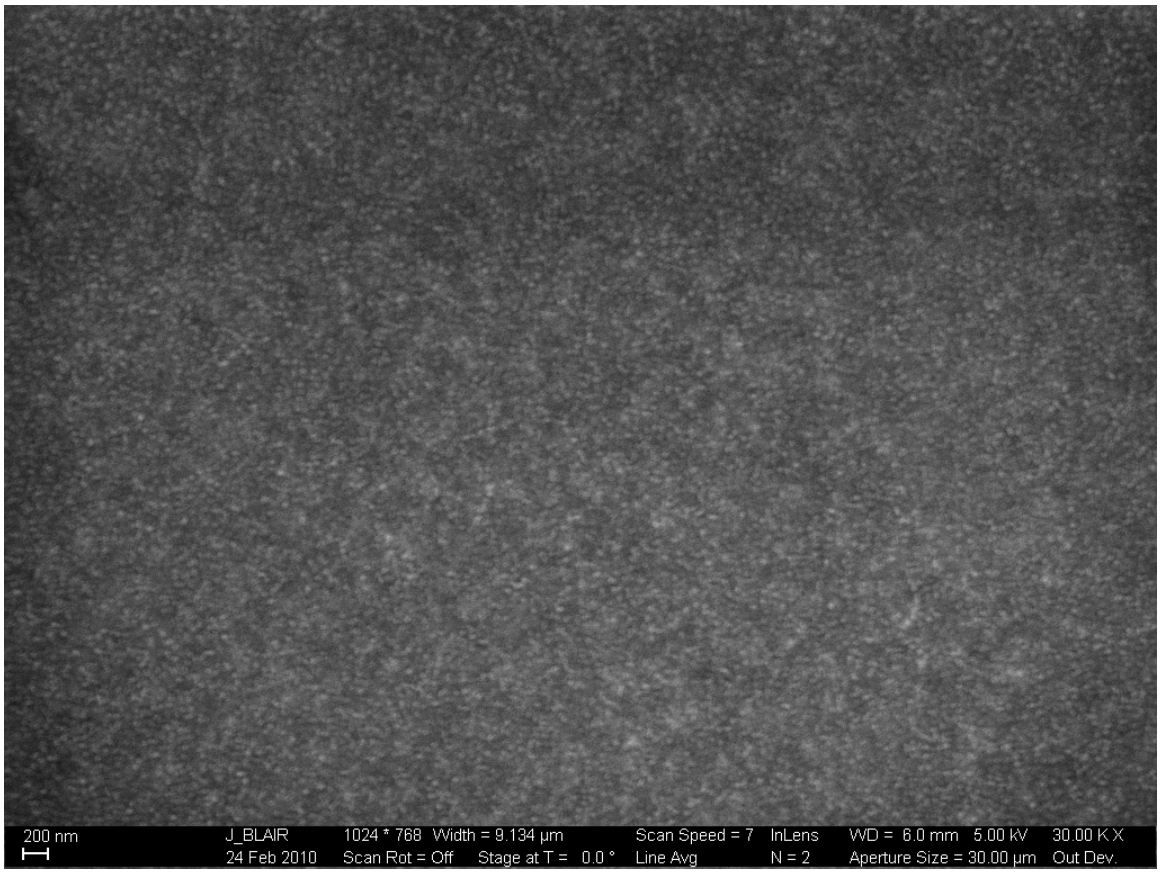

Figure 38 Top down SEM image at 30,000 optical zoom. The electron source was at 5 kV.

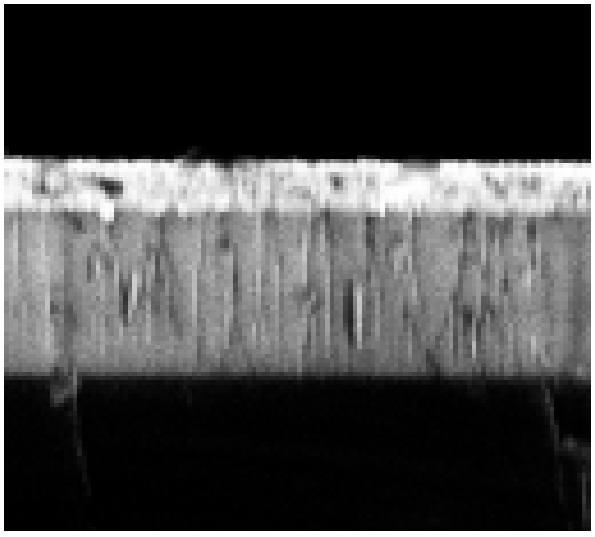

Figure 39 Side on SEM image of ZnO grown on silicon. The black region at the bottom is silicon, the light grey region above it is silicon oxide, and the top layer is ZnO. Optical zoom is 100,000x.

X-Ray Diffraction Characterization

The last method of crystalline characterization is the x-ray diffraction method. The tool that was used in this work was a Philips X'Pert Pro diffractometer for XRD measurements. XRD provides an atomistic analysis of the crystalline quality of the sample. The crystal has fixed bond lengths and a fixed orientation when grown properly. Two primary scans, the double crystal ω scan and the 2Θ- ω double crystal scans. These two scans showed relatively high crystalline quality, comparable or superior to those sited in the literature. A high quality XRD measurement indicates that uniform crystal orientation is taking place. Very thick production quality scintillators were used for this experiment. Traditionally, thin samples of 100 – 300 nm are used. In this research, 10μm samples were used. This corresponds to the larger full width at half max values that were achieved. A typical omega rocking curve sample analysis can be seen in Figure 40.

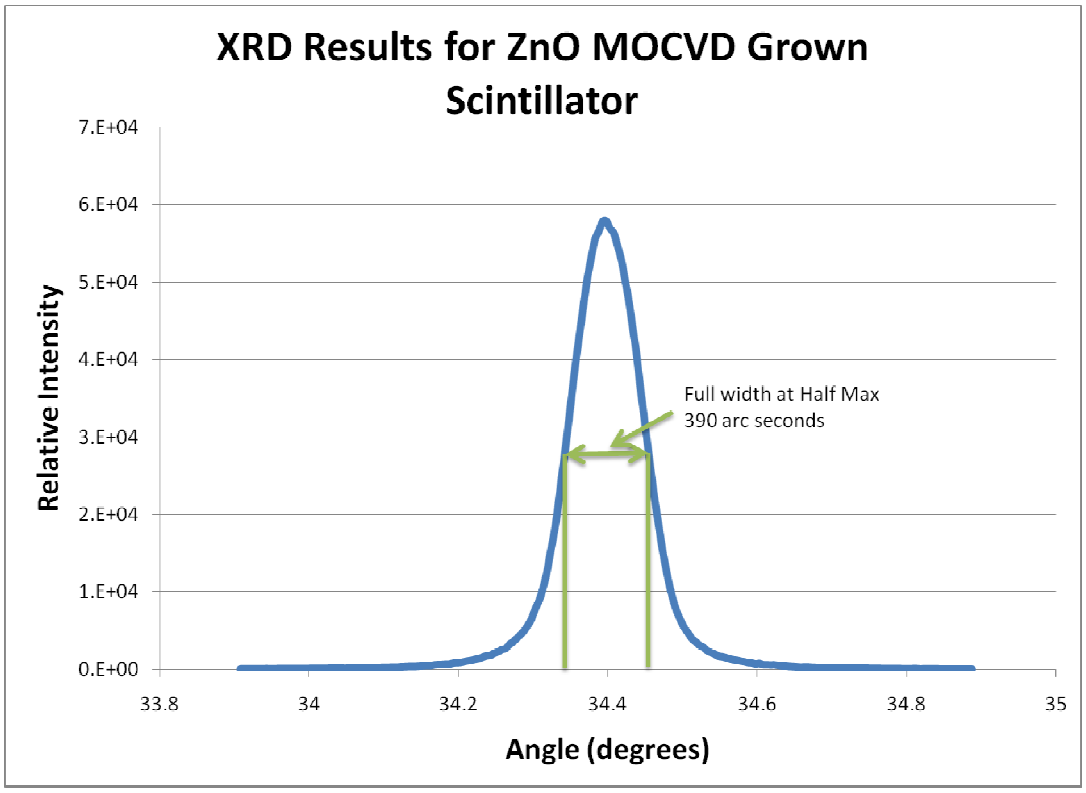

Figure 40 XRD results for a typical scintillator with a 10 µm thickness grown by the MOCVD growth method. The FWHM is 390 arc seconds.

CHAPTER V

RADIATION DETECTION CHARACTERIZATION TECHNIQUES

Three primary radiation detection tests were conducted to investigate the quality and performance of the scintillators. Up to this point, all of the characterization techniques were materials science based to ascertain the crystalline quality, the photoluminescence spectra and the thickness of the materials. These tests provide invaluable insights to the performance of a scintillator and the incremental improvements dopants will provide to the end product scintillators. Nothing can duplicate though the performance of a scintillator to various radiation fields than that of radiation testing.

Three primary radiation tests were conducted on each of the prospect scintillators to ascertain the impact of growth conditions and dopant concentrations on the scintillator performance. The first test conducted was a general alpha and gamma spectroscopy test. The second test was a neutron steady state quasi-thermal neutron source test. Lastly, a pulsed, time dependent graphite slowing down spectrometer system was used to measure the scintillator performance to a wider energy spectral range. With a combination of alpha and gamma tests to determine the base scintillator performance, a significant amount of information can be ascertained before making a neutron detection measurement. The alpha test is indicative of the relative light yield and efficiency for the scintillator. The gamma test is to measure the detector's gamma ray response in a large background gamma ray field. This gamma ray test ensures measured data will provide good neutron versus gamma discrimination. Once a suitable combination of parameters is found, neutron tests are initially carried out using the steady state neutron source. This first cut provides an excellent metric for understanding the radiation detector's performance.

Once the steady state measurement is conducted, a more sophisticated and complicated measurement using the graphite slowing down spectrometer developed for this thesis is conducted to determine the ability of the scintillator to detect neutrons above the thermal energy spectra as well as determine their relative efficiencies.

Alpha Spectroscopy and Gamma Characterization Method

Alpha spectroscopy was conducted on each of the scintillators prior to neutron testing. Alpha sources were selected based on their particle emission rates and energies. Energies were selected which were near the energies of the alpha particles produced in the (n,α) reaction on ^{6}Li and ^{10}B. These results are indicative of how a scintillator would respond if it were doped with ^{6}Li or ^{10}B containing compounds. Sources used were ^{239}Pu, ^{230}Th, ^{232}Th, and ^{241}Am. The alpha spectra for each of these nuclei are found in the figures and tables below.

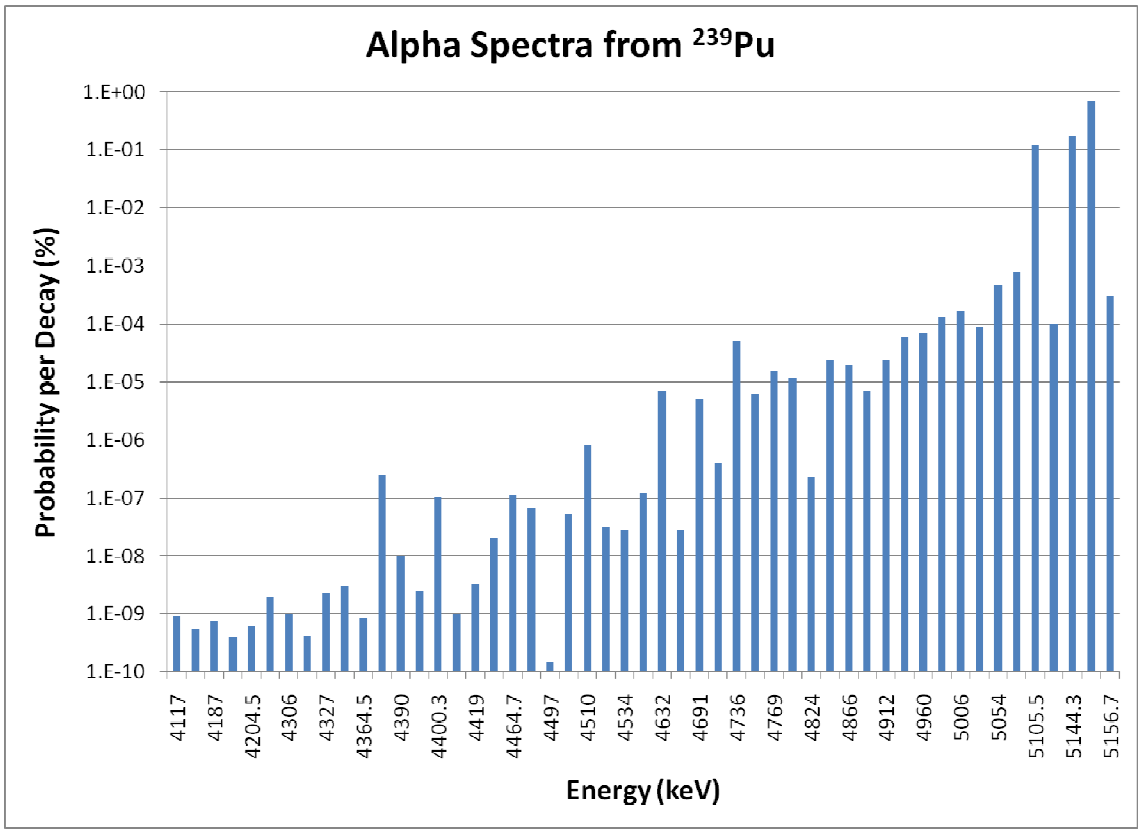

Figure 41 ^{239}Pu alpha spectra.

Table 2 Table of alpha particle energies and corresponding probabilities for ^{239}Pu.

Energy (keV)	Probability (%)	Energy (keV)	Probability (%)	Energy (keV)	Probability (%)	Energy (keV)	Probability (%)
4117	9.30E-10	4392	2.46E-09	4392	2.46E-09	4934	6.00E-05
4181	5.60E-10	4400.3	1.03E-07	4400.3	1.03E-07	4960	7.00E-05
4187	7.40E-10	4408	1.00E-09	4408	1.00E-09	4987	1.30E-04
4202	4.00E-10	4419	3.30E-09	4419	3.30E-09	5006	1.70E-04
4204.5	6.10E-10	4448.5	2.00E-08	4448.5	2.00E-08	5028	9.00E-05
4280	1.90E-09	4464.7	1.15E-07	4464.7	1.15E-07	5054	4.70E-04
4306	1.00E-09	4467.4	6.90E-08	4467.4	6.90E-08	5076	7.80E-04
4326	4.20E-10	4497	1.50E-10	4497	1.50E-10	5105.5	1.19E-01
4327	2.30E-09	4503	5.38E-08	4503	5.38E-08	5111	1.00E-04
4349	3.00E-09	4510	8.00E-07	4510	8.00E-07	5144.3	1.71E-01
4364.5	8.40E-10	4529.6	3.19E-08	4529.6	3.19E-08	5156.59	7.08E-01
4380	2.50E-07	4534	2.84E-08	4534	2.84E-08	5156.7	3.00E-04
4390	1.00E-08	4559	1.20E-07	4559	1.20E-07		

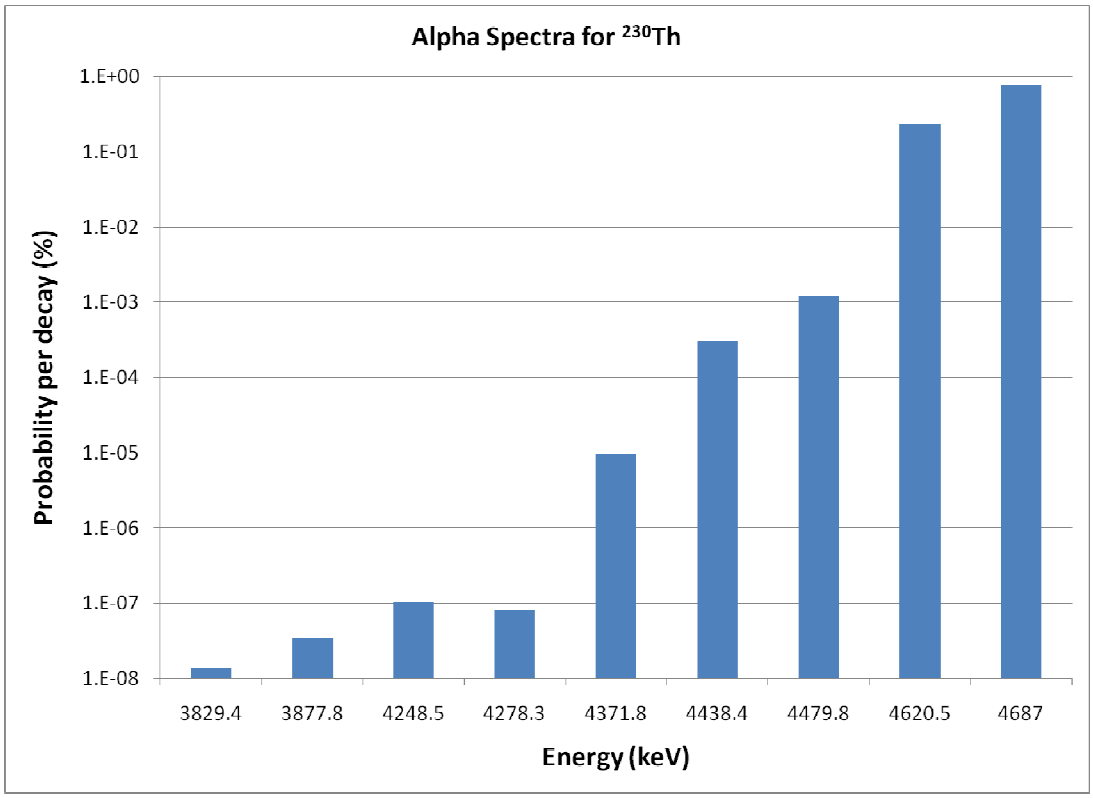

Figure 42 ^{230}Th alpha spectra.

Table 3 Table of alpha particle energies and corresponding probabilities for ^{230}Th.

Energy (keV)	Probability (%)	Energy (keV)	Probability (%)
3829.4	1.40E-06	4438.4	3.00E-02
3877.8	3.40E-06	4479.8	1.20E-01
4248.5	1.03E-05	4620.5	2.34E+01
4278.3	8.00E-06	4687	7.63E+01
4371.8	9.70E-04		

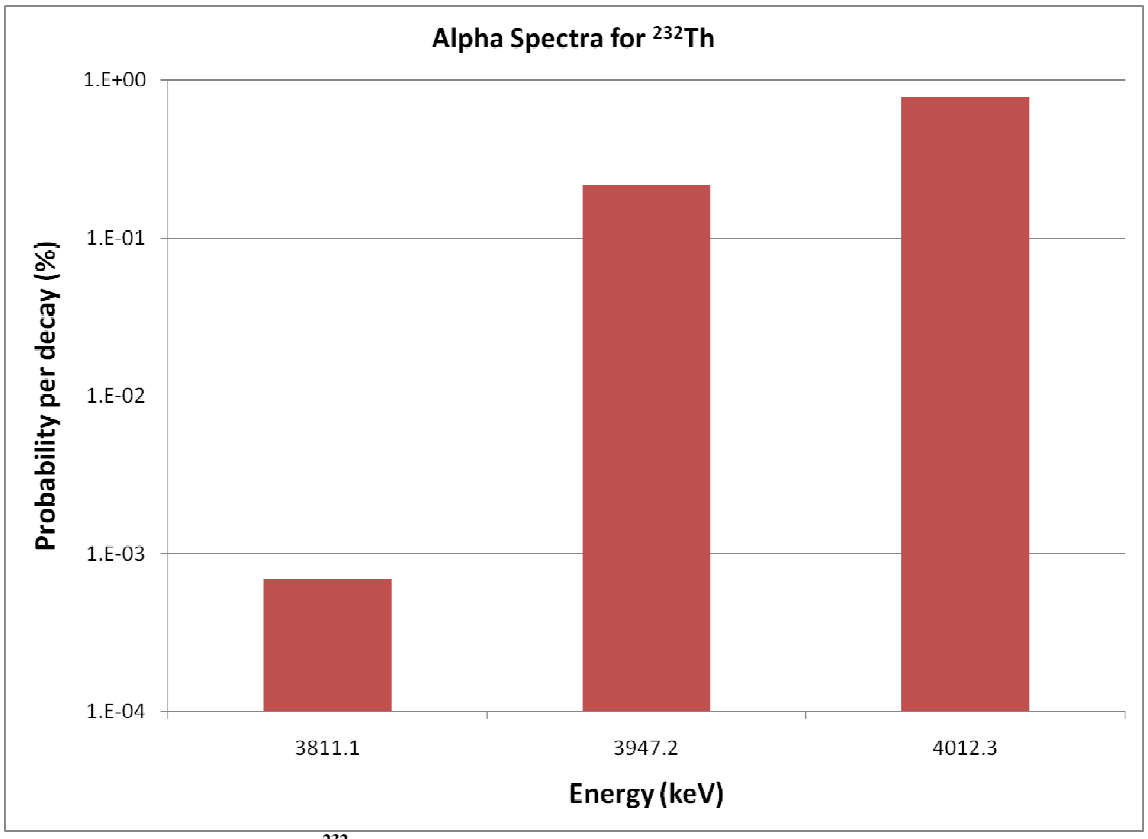

Figure 43 Alpha spectra for ^{232}Th.

Table 4 Table of alpha particle energies and corresponding probabilities for ^{232}Th.

Energy (keV)	Probability (%)
3811.1	6.90E-02
3947.2	2.17E+01
4012.3	7.82E+01

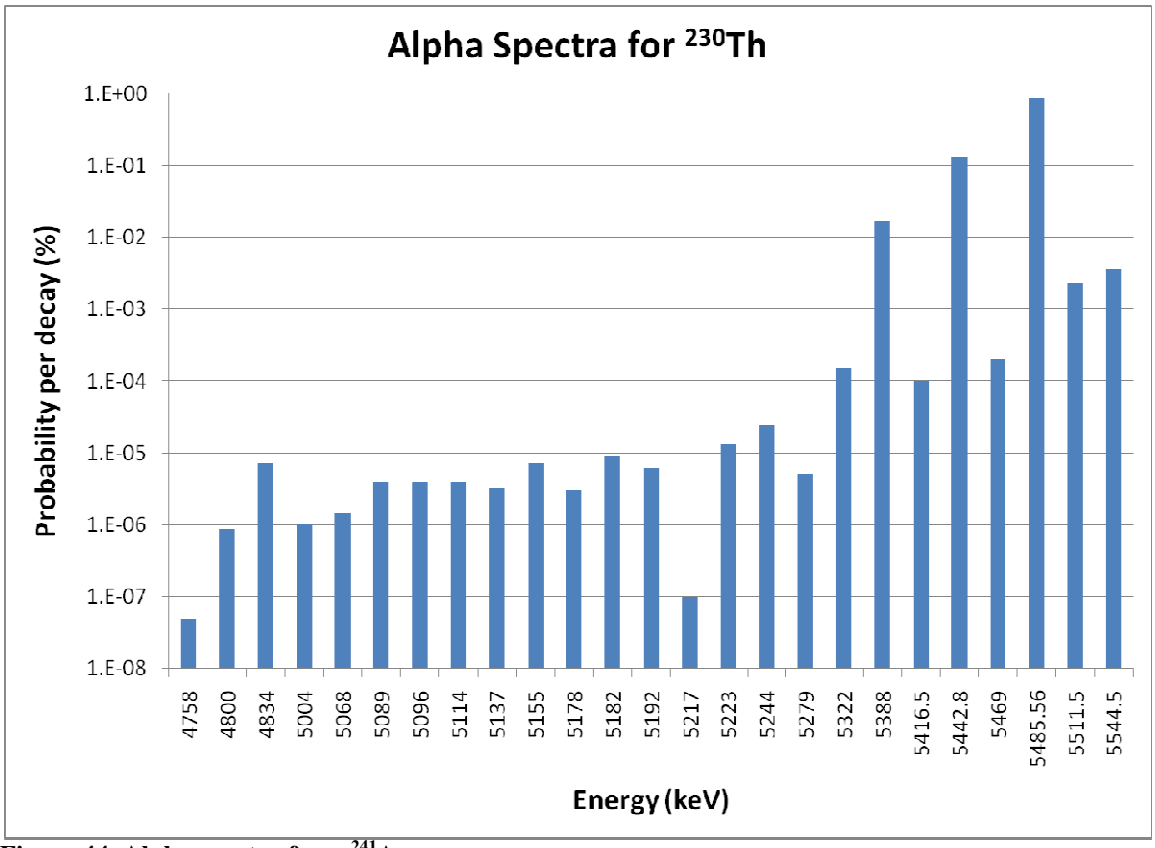

Figure 44 Alpha spectra from ^{241}Am.

Table 5 Table of alpha particle energies and corresponding probabilities for ^{241}Am.

Energy (keV)	Probability (%)	Energy (keV)	Probability (%)	Energy (keV)	Probability (%)	Energy (keV)	Probability (%)
4758	5.00E-08	5114	4.00E-06	5223	1.30E-05	5469	2.00E-04
4800	8.60E-07	5137	3.20E-06	5244	2.40E-05	5485.56	8.48E-01
4834	7.00E-06	5155	7.00E-06	5279	5.00E-06	5511.5	2.25E-03
5004	1.00E-06	5178	3.00E-06	5322	1.50E-04	5544.5	3.70E-03
5068	1.40E-06	5182	9.00E-06	5388	1.66E-02		
5089	4.00E-06	5192	6.00E-06	5416.5	1.00E-04		
5096	4.00E-06	5217	1.00E-07	5442.8	1.31E-01		

Gamma ray measurements were made using a ^{226}Ra source. A ~10 mCi source was utilized to induce a 100 mR/hr radiation field in the scintillation detector. The ^{226}Ra source was selected over other sources such as ^{60}Co or ^{137}Cs because of its softer x-ray and gamma ray spectra. The softer spectra is more likely to produce photoelectric absorption as opposed to Compton scattering. The photoelectric absorption reaction, imparting the highest amount of energy in the scintillator, is a worst case scenario.

The alpha and gamma tests were conducted in a specially designed light tight scintillation testing box. The box was made from southern yellow pine and was painted inside and out in flat black paint. Six bulkhead passthrough adapters were installed to allow two separate high voltage lines, two anode signals and two dynode signals to be removed from the light tight scintillation testing box. The lid to the box was sealed with stair stepped weather stripping to seal light leaks. The lid is held in place by six gate hasps. Two movable stands with 2 inch diameter notches to hold the PMTs and the radioactive sources. The light tight scintillation detector test box was utilized to facilitate the rapid testing of different scintillators with different alpha sources. The light box eliminates the need to wrap and package each scintillator.

The scintillator crystals were mounted directly to the PMT envelope by using optical coupling grease. For bulk samples, this provided a nice smooth interface. The optical coupling grease also allowed for MOCVD grown samples on one side polished sapphires to be used. The coupling grease cleared the interface between the crystal and removed the cloudy interface. An aluminum foil was cover was used to protect the scintillator, PMT, and hold the source in place. The PMT used in this work was a Hamamatsu with a borosilicate glass envelope. The minimum rise and fall times for this PMT were 2 nS. The fast anode signal was used for routing into the preamplifier and amplifier system. The pulse height was digitized using a 2048 channel ADC. While conducting the alpha spectra measurement, several pulses were digitized using a 100 MHz digital oscilloscope to determine the pulse rise and decay times.

Steady State Neutron Characterization Method

Steady state neutron measurements were made using the collimated thermal neutron beam. This beam is produced by using a 51 Ci ^{241}AmBe neutron source and the graphite pile. Originally designed for testing neutron containing materials such as Boral, the collimated thermal neutron beam line utilizes a neutron shielding box to remove the

background room return neutrons. A picture of the box can be seen in Figure 45. Shown in Figure 45, annotation A is the calibrated lithiated glass scintillator. B and C are the rotating platform for holding and testing boral samples, C is the boral box for shielding the room return neutrons, D is the graphite pile and E is boral shielding sandwiched between two sheets of ¾" plywood.

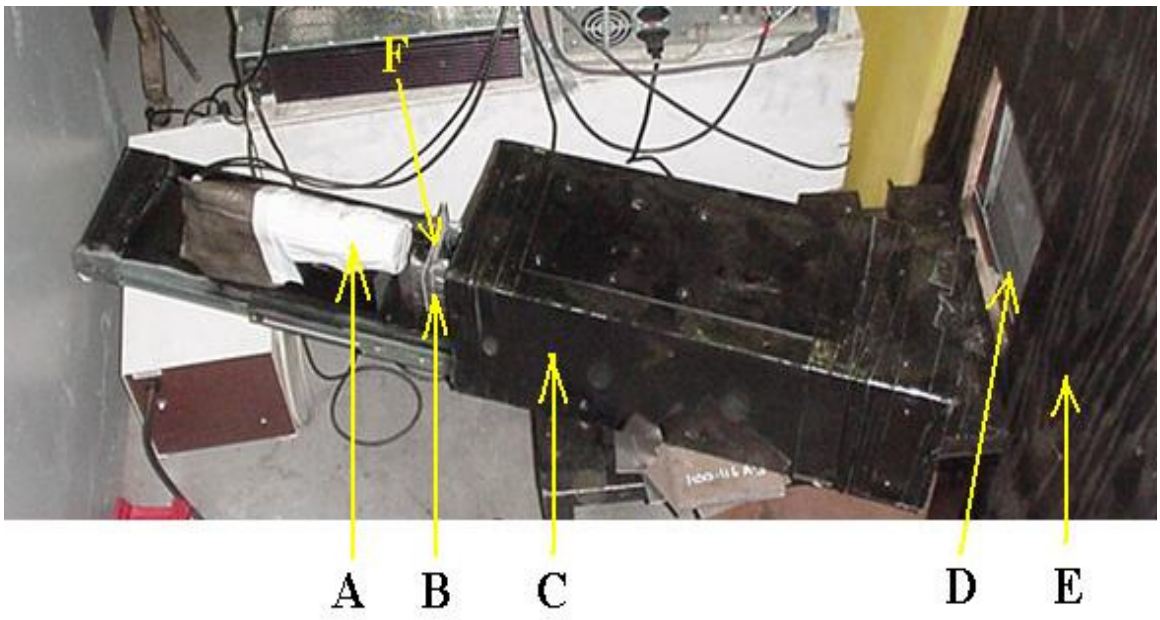

Figure 45. Collimated thermal neutron beam line and neutron testing box.

The AmBe source is a two part hemispherical ceramic matrix of ^{241}Am and Be metal. A drawing of the source, made by General Electric can be seen in Figure 46. Using the (α,n) reaction from ^{241}Am alpha particles and the beryllium metal, neutrons are born at approximately from 1-11 MeV. MCNP5 was used to calculate the neutron spectrum in the collimated thermal neutron beam line (89). Graphite was selected as the neutron thermalizer due to it's highly efficient thermalization rate and very low neutron capture cross section. The graphite pile is constructed of nuclear grade graphite, which has a lower density than normal graphite and has been purified through either a chemical or thermal purification process. The modeled density which has been verified by volume and mass measurements of several blocks that make the pile, was found to be 1.7 g/cc.

This value is in agreement with those listed in common nuclear material libraries such as the SCALE library (90). In MCNP5, the ENDF-VI cross sections were used including the graphite S(α,β) thermal upscattering cross section. The S(α,β) is required to correctly simulate the thermal upscattering which occurs in neutron transport through light media. The neutron lethargy flux profile at the test location can be seen in Figure 47. The MCNP5 model of the pile can be seen in Figure 48.

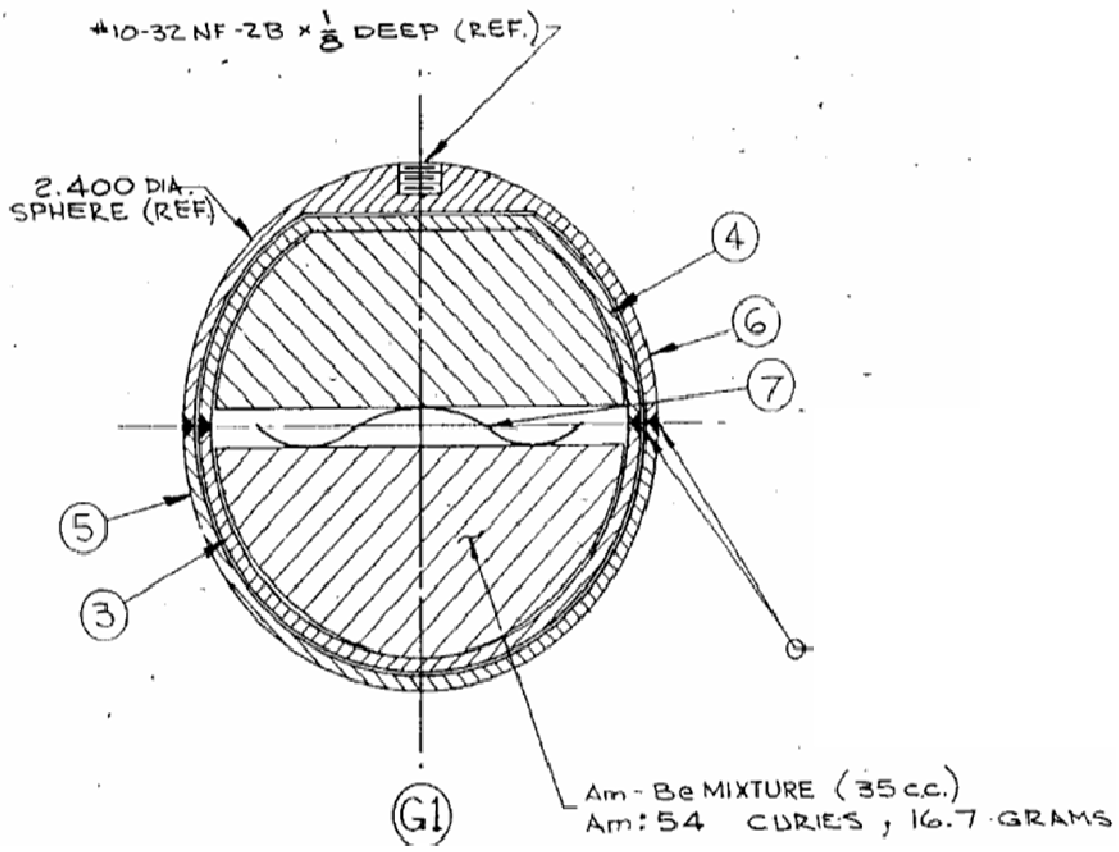

Figure 46 As built drawing of the AmBe neutron source used in the steady state neutron testing.

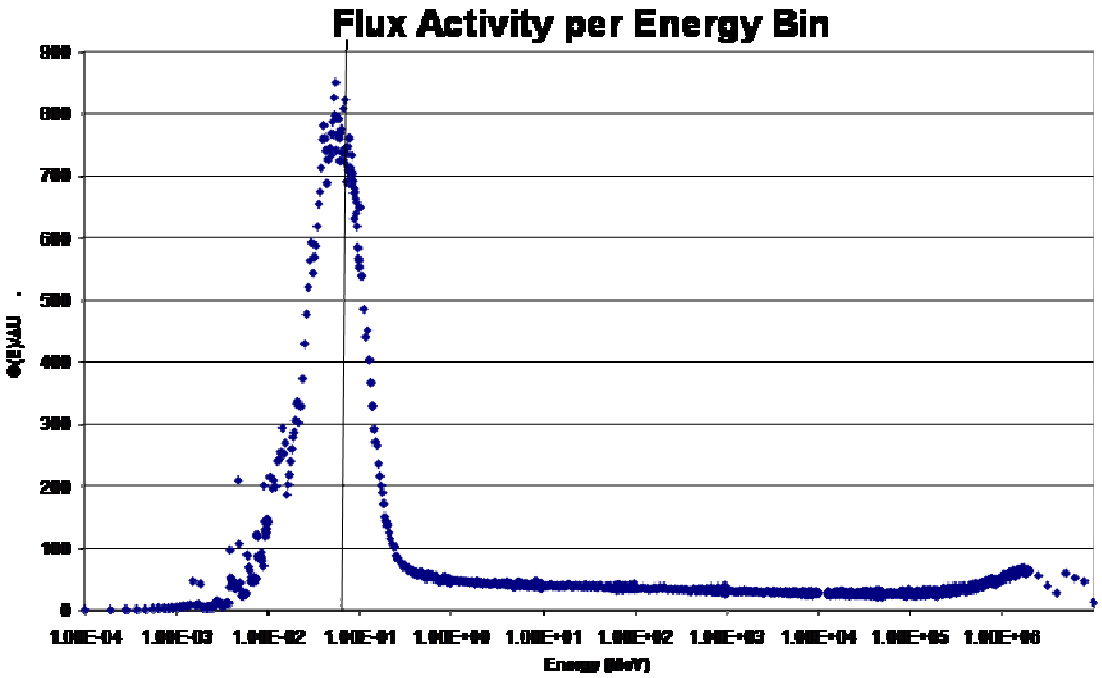

Figure 47. MCNP5 calculated neutron lethargy flux per energy bin at the test location, inside the collimated thermal neutron beam line.

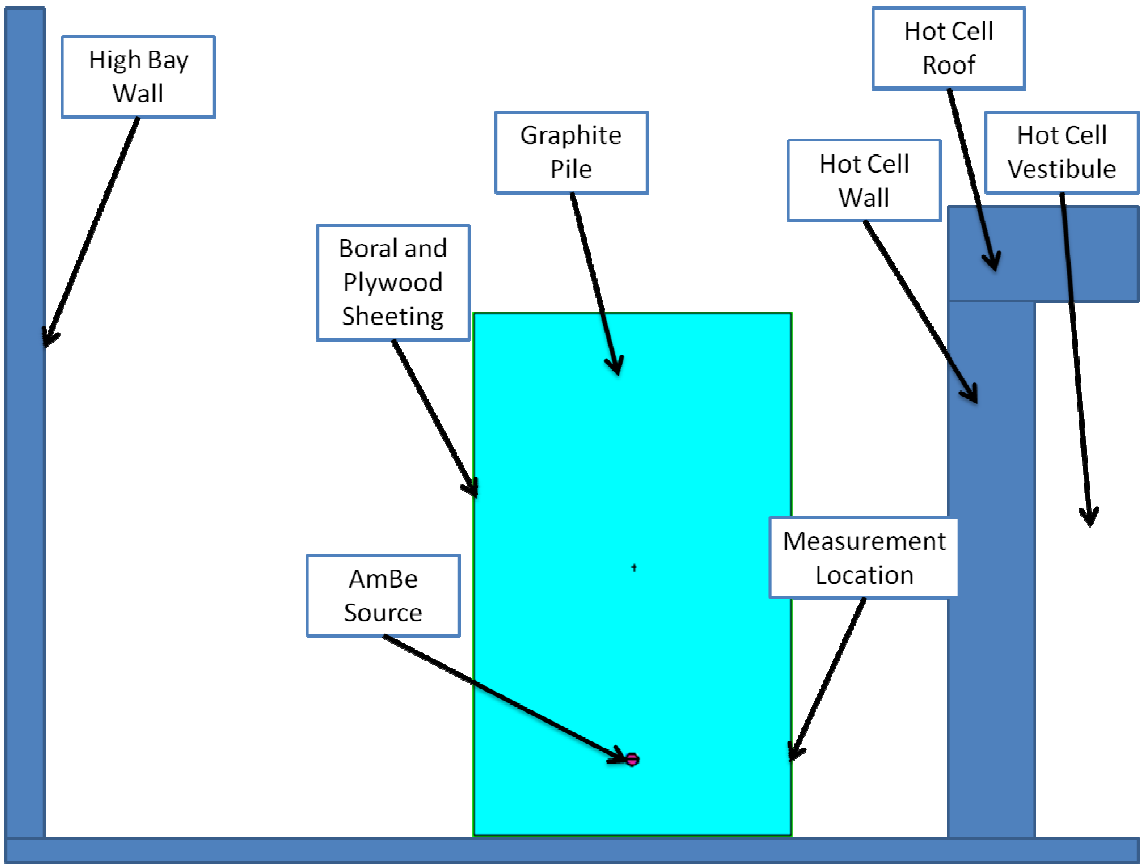

Figure 48 MCNP5 model of the steady state graphite pile driven by the AmBe source.

From the MCNP calculation, one can see that the majority of neutrons are thermalized with a small fraction (less than 1%) in the intermediate (1 eV to 100 keV) and less than 1% in the fast (1 MeV to 10 MeV) regions. To validate the neutron energy spectra that was used, a Bonner Sphere Spectrometer (BSS) was used to measure the neutron spectra (91). The spheres were centered 15 cm from the face of the pile, approximately the location of the neutron detector tests. BSS spheres of 2", 3", 5", 8", 10" and 12" were used in addition to a bare and cadmium covered scintillator. The BSS system used in this test had recently been calibrated by the author at the PTB neutron accelerator facility in Braunschweig, Germany (92). The neutron spectra was unfolded using the Maxed MXD-FC33 unfolding code. This code uses a set of experimental or calculated neutron response functions to deconvolve the detector's response from each individual sphere. The response matricies used in this work were created from

experimental data measured at PTB (93). To compare these results using the Burgett and Howell response matricies and the MXD-FC33 unfolding code (94), a second set of response matricies and unfolding codes was used. The second unfolding code used was the BUMS (Bonner Sphere Unfolding Made Simple) (95) code which is a web page based unfolding package and the Hertel and Davidson 171 group or less response matrix (96). The unfolded neutron spectra can be seen in Figure 49 and Figure 50. The differences between the two unfolded spectra are minimal. The BUMS/Hertel and Davidson response matrix configuration unfolds only one thermal neutron bin. The Burgett and Howell/MXD-FC33 package was modified using a Bayesian Estimator as the starting spectrum estimator. This allows a Gaussian to be fit over the thermal neutron bins and unfolding into 500 energy bins at 30 bins per decade allows for a more physical shape to be fit to the thermal neutron source. The "Best Spectrum" search function was used in the BUMS package to search for a suitable starting spectrum for iteration. A PWR spectrum was found to be the best initial starting spectrum. This logically is a good selection since it consists of a thermal neutron peak, a fission neutron peak and a continuum. The BUMS method is as correct as the MXD-FC33 method since there is only 2 unique responses in the thermal neutron bin region. The important thing to take away is they are approximately the same order of magnitude.

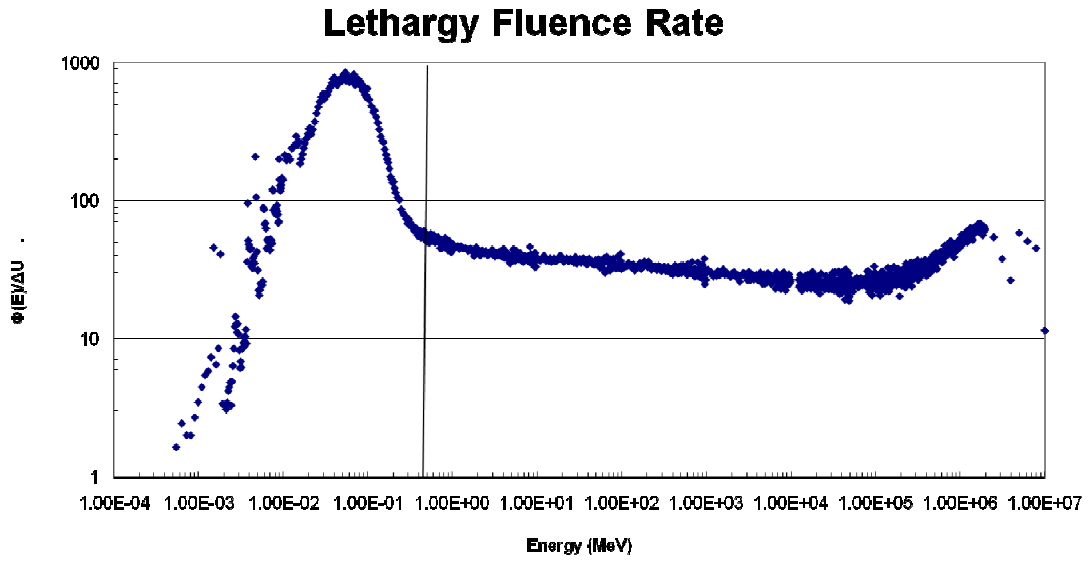

Figure 49. Bonner Sphere Spectrometer results unfolded using MXD-FC33 and the Burgett and Howell response matricies.

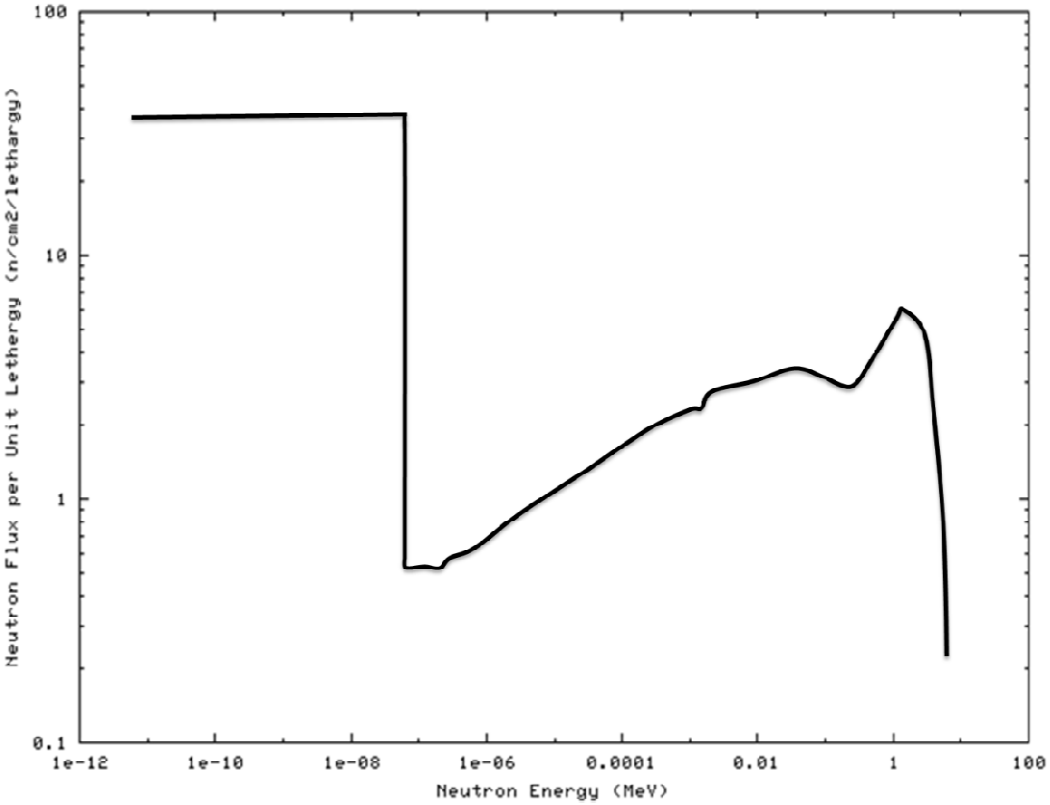

Figure 50 Neutron spectra unfolded using BUMS and the Hertel and Davidson response matricies.

Absolute thermal neutron fluxes also were measured using a foil activation analysis method. Indium foils were used as activation foils with and without cadmium covers. This measurement provides the standard metrics for a thermal beam including cadmium ratio and cadmium cutoff. Four foils were exposed to the neutron source for over eight hours. This allowed the activities of the indium foils to reach saturated activity. A table of masses and activities can be found below in Table 1.

	Type	Mass (g)	Activity A_o (Bq)
Foil A	Bare	0.119	2.67E+05
Foil B	Bare	0.1156	2.18E+05
Foil C	Cd Covered	0.1182	1.28E+04
Foil D	Cd Covered	0.1197	9.57E+03

6 Masses and activities of the foils used in the absolute neutron calculation.

The results of this test yielded a cadmium fraction of 0.954, a cadmium ratio of 21.71 and a cadmium difference of 2.31 x 10^5. The results of these tests show slight contamination of the thermal neutron beam with (α,n) neutrons and neutrons which were not fully moderated. The foil activation results yielded a thermal neutron fluence rate of 1634 +/- 124 n/cm^2/s. The neutron flux is more than adequate for neutron detector testing. Since all of the neutron detectors to be tested are not the same size, if one simply multiplies the surface area of the detector by the fluence rate, one can determine a predicted count rate and determine efficiencies for this energy profile.

Graphite Slowing Down Spectrometer Characterization Method

The steady state neutron characterization method only provides one single neutron spectrum to test with. Subtle variations in the source and detector locations can produce slight modifications in the neutron spectrum. No significant changes can be made to this steady state solution without drastically decreasing the neutron flux at the detector.

Monochromatic or Gaussian shaped distributions of neutrons as a function of time are not possible using this system. Using this system though, there is a method for producing a neutron energy fluence distribution which is Gaussian shaped in time. This method is being called the graphite slowing down spectrometer (GSDS) method (97). This system is designed after other slowing down spectrometer facilities, namely the Lead Slowing Down Spectrometer (LSDS) at the Los Alamos Neutron Science Center (LANSCE) at LANL. Here, they use an 800 MeV proton beam incident on a tungsten target to produce a large pulse of spallation neutrons. The neutron "thermalizing" material in the LSDS is made from 36 blocks of high purity lead measuring 30 cm x 30 cm x 40 cm. Spallation neutrons have a "white" neutron spectrum from 1MeV to 800 MeV. These Spallation neutrons are born in one sharp neutron pulse in time. The neutrons slow down as a function of time more or less as a "slug" of neutrons. The lighter mass of the graphite moderator in relation to the lead version causes the neutrons to loose more energy per collision. In addition, graphite has a lower 1/v absorption cross section than lead. This causes the fast neutrons to slow down faster in graphite. Due to the low capture cross section in lead, the neutrons bounce around in the lead cube for a long period of time before capture. To further aid this system, the high energy neutrons can produce spallation, (n,2n), (n,3n), and (n,n') reactions in the lead further multiplying the neutron source. Initially, the physics of the problem slow the very high neutrons down through multiplication reactions to produce a Gaussian energy shaped pulse of neutrons in time. This pulse then uniformly slows down as a function of time, bouncing around in the spectrometer. This system is used to make ratio measurements of fission cross sections on rare isotopes where large quantities of the samples are not available. The time dependent neutron spectrum can be seen in Figure 51. This spectra was calculated using MCNPX 2.5.0 by Rochmand et.al (98). At times after ~1 μs, a significant "focusing" of neutrons can be seen. This is the result of faster neutrons slowing down and loosing energy more rapidly than the slower neutrons which loose energy at a slower rate. This

focusing of neutrons can occur in any material which has a low capture cross section and a low moderating ratio. One does not want to use a material with a low A number because too much energy can be lost in a single reaction. Ideally, one wants an inefficient neutron thermalization material but still a small thermal neutron cross section.

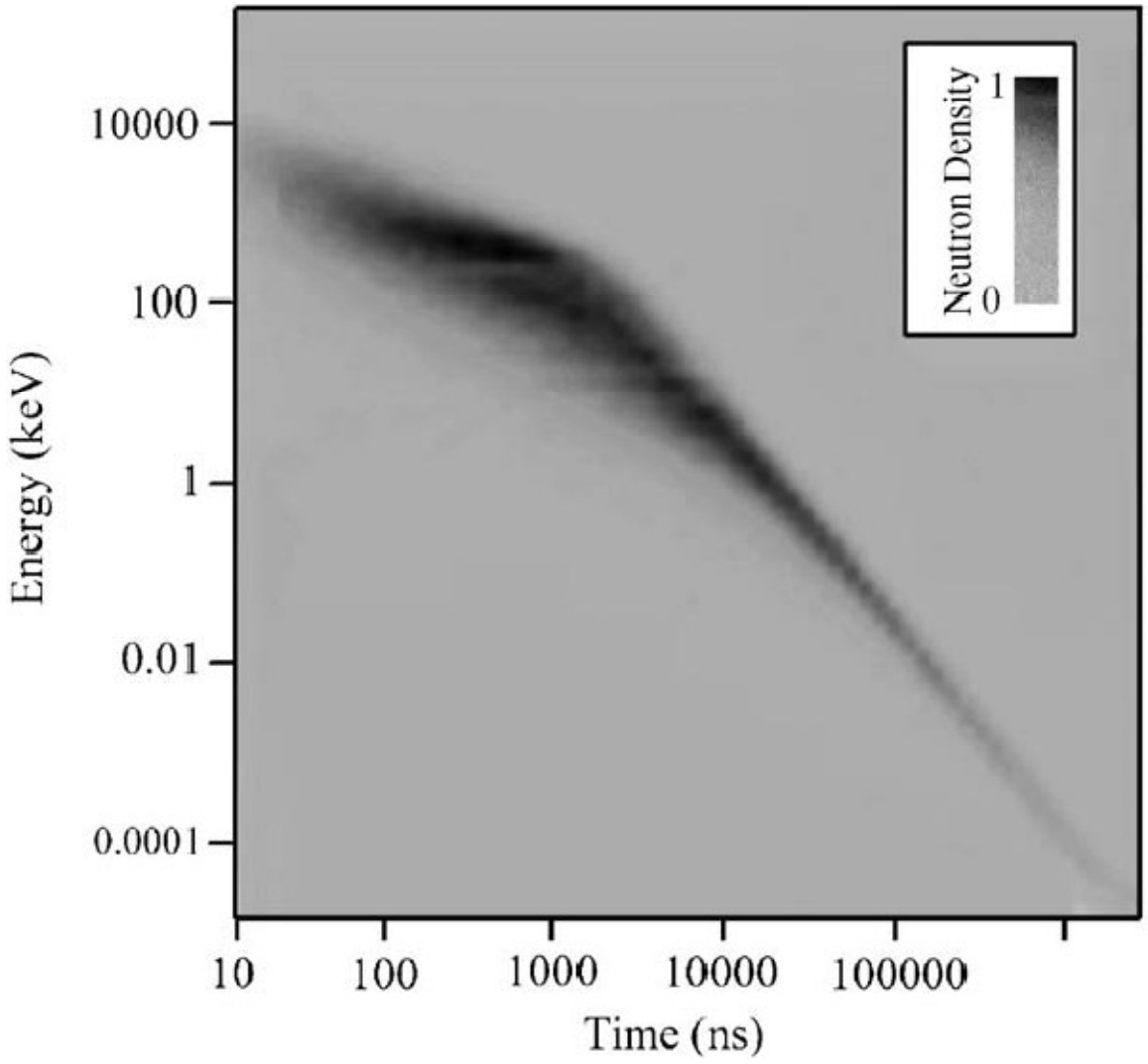

Figure 51 Time dependent energy spectra in the LANSCE LSDS.

The GSDS uses a pulsed source of neutrons from a D-T 14 MeV neutron generator available at Georgia Tech. The D-T generator at Georgia Tech is a Thermo Fisher Scientific sealed tube pulsed neutron generator model P211. The P211 is capable of producing 1 x 10^8 n/pulse. The system however is a head pulsing neutron generator

only. This means the ion source is pulsed producing a pulse of deuterium ions. This pulse is accelerated down a 150 kV accelerating bias and strikes a tritium-titania target. This produces a pulse of ~14 MeV neutrons. These neutrons have an energy and angular dependence on the center of mass and lab system for the D-T reaction. The D-T generator can be externally controlled to produce custom pulse rates between 10 and 100 Hz. The generator also produces a pulsed signal which can be used to trigger other electronics of the start of a pulse. A picture of the generator can be seen in Figure 52.

Figure 52 The Thermo Fisher Scientific P211 sealed tube neutron generator and associated electronics.

The graphite block used in the steady state problem is once again used for the GSDS. The pulse of 14 MeV neutrons is approximately 10 μS wide. This pulse width is due to the fact the generator is only a head pulsing unit. If a tail pulsing unit were available, finer resolutions could be achieved with the GSDS. However, unlike the LSDS, the pulse is nearly monochromatic during generation. Each system currently has its limitations. If a sharper DT pulse could be created, significant improvements in resolution could be realized on the GSDS. The LSDS could be improved by using a

monochromatic source of neutrons, so as to improve the timing resolution for times less than 1 μS. In the GSDS, the ~14 MeV neutrons slow down as one "slug" of neutrons as a function of time. The neutrons do experience an energy dependence based on the angle in the center of mass from the D-T reaction. The angle and energy each also have an associated probability per D-T reaction. The corresponding energy versus angular dependence of the reaction is based on the isotropic distribution of the reaction in the center of mass system, converted to the lab system. This energy versus angular dependence and its probability distribution function (PDF) can be found in Figure 53. This PDF was taken from (99) and compares nicely to data found in (100) and (101).

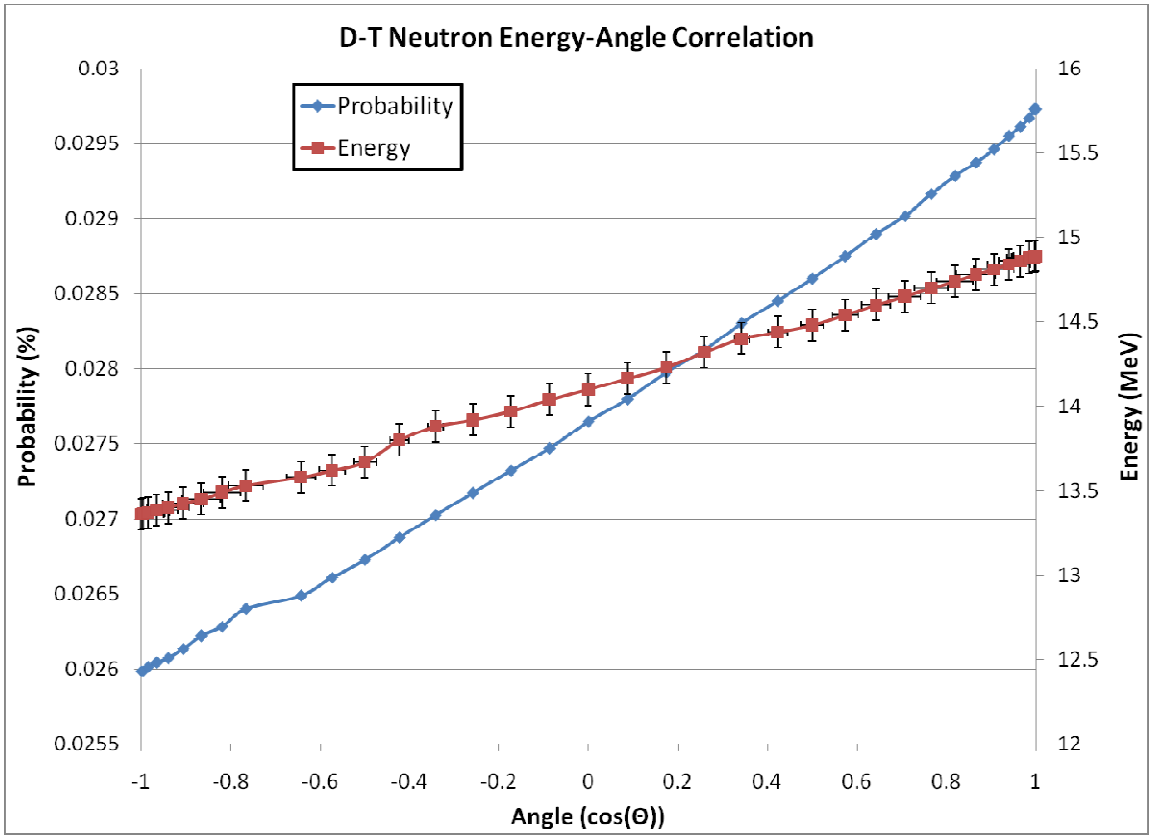

Figure 53 PDF of the energy and angular dependence of the D-T reaction in the sealed tube P211 neutron generator.

Graphite is a more efficient neutron thermalizing material able to downscatter a neutron in far fewer scattering events than lead. The GSDS time dependent neutron

spectra was calculated as a function of time in the experimental testing location. The calculation was performed using the time dependent transport capabilities of MCNP5. A number of different neutron detector locations were envisioned. There are more optimal detector locations than currently being used for the collimated thermal neutron beam line, but required significant modification to the structure. The results at the current detector location are acceptable for this current work and therefore used. The additional neutron detector locations were modeled and are presented in Appendix A. The time dependent neutron spectra were simulated with MCNP5. The graphite was modeled as nuclear grade graphite with S(α,β) cross section at 1.7 g/cc. The time dependent neutron spectrum was created by digitizing the current waveform off of the neutron generator target. This time dependence was converted to a probability distribution function and input into MCNP5 as the starting neutron time dependent spectra. A representative target waveform from the P211 can be seen in Figure 54.

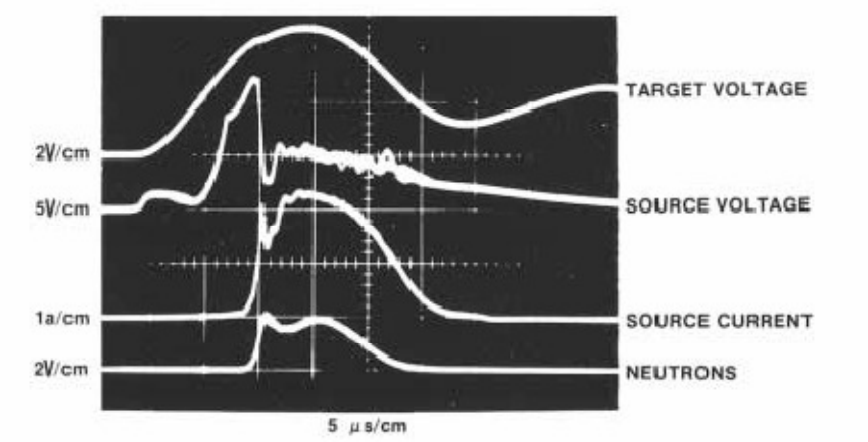

Figure 54 Target voltage, source voltage, source current and neutron production rate as a function of time for the P211 neutron generator.

The slow decaying tail of the head pulsed P211 is one of the less desirable features of the system. This produces a wide pulse which blurs the neutron spectrum as a

function of time. The time dependent neutron spectra at the collimated thermal neutron beam line can be seen in Figure 55.

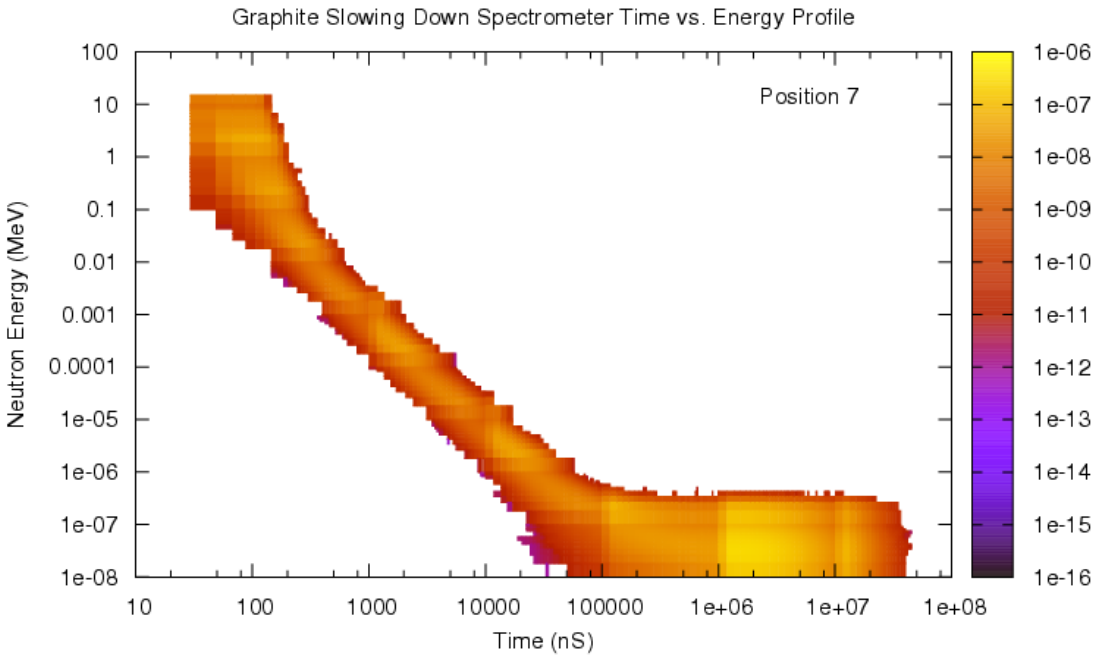

Figure 55 Time dependent neutron spectrum as a function of time after the neutron pulse.

On the x-axis is the neutron slowing down time from the start of the neutron pulse. On the y-axis is the neutron energy. The color map shows the neutron fluence rate. The "hotter" the color on the 2D contour map, the higher the neutron fluence rate. The color band is logarithmic in nature, and is shown in the key on the right. Position 7 corresponds to the location which is the face of the detector in the collimated thermal neutron beam line. One can see that due to the $S(\alpha,\beta)$ thermal upscattering and lack of a strong thermal neutron absorber, the graphite thermal neutron pulse migrates around inside the graphite cube for a long period of time. This long migration time results in the steady state thermal neutron peak which does not decrease after 10^5 nS.

The associated electronics associated with the GSDS used to calculate neutron detector efficiencies is described below. Two different data acquisition systems are run

simultaneously. The entire system is driven from an internal clock circuit inside the neutron generator. Due to a very inflexible design of the ThermoFisher Scientific P211 neutron generator driver chassis and weak signal driver boards, the system cannot be driven efficiently outside of a 50 to 100 Hz system. Outside this range, the tube cannot regulate its internal pressure well and has a tendency to blow internal components including driver boards. To alleviate this, the detector system is driven from the primary clock in the P211. Using the internal 10 Hz clock pulse, the generator fires pulses of neutrons 100 times per second. Looking at the slowing down time of the neutron spectra above, this pulse rate is acceptable and pulse wrap around does not occur. The start pulse signal, a 5 V positively thrown NIM signal is used to trigger a gate and delay generator. This produces pulses that are usable by the remainder of the detection systems. This signal is fanned out using a fast fan in – fan out module. The fan out signal is routed to the start sequence signal on an Ortec 100 MHz multichannel scalar. The MCS is a modified analog to digital converter which records count rates as a function of time. The other fan out pulse is routed to function generator. The function generator is used to produce a negative thrown DC signal which is routed to a linear gate. The linear gate is used to gate signals in the DC inhibit mode to a standard Ortec 2048 channel MCA. The MCA signal can now be gated on various portions of the neutron spectra. The custom function generator creates a "window" in a negative DC pulse that can be used to select a given time window after the neutron pulse.

The neutron signal detected through the same photomultiplier tube, preamplifier, amplifier system with the exception that the amplified pulse is now routed through a delay generator. The delay generator slows the analog pulses down in time to correspond to the time it takes the gate and delay generator to fan out the trigger signals. This system was calibrated using the "gamma flash" on the lithiated glass scintillator. This is due to the fact that the ZnO scintillators are so thin, and have such a small sensitivity to gamma rays, that no gamma flash was recorded. The signal after delay is teed and one branch

routed through the DC inhibit linear gate the other signal is routed to the single channel analyzer input on the multichannel scalar. During the initial timing calibration setup, the SCA window on the MCS was left completely open for the lithiated glass scintillator. This allowed for digitization of the gamma flash. After collecting numerous gamma flash pulses, the MCS was set to window on just the (n,α) region of the scintillators. The MCS was windowed with the assistance of the SCA Sweep feature. The MCS is actually a 512 channel multichannel analyzer. In SCA Sweep mode, each channel is swept across and a MCA looking spectrum is acquired over a long period of time. This mode looks at the count rate in each of the 512 channels which cover the range of 0 to +10V. The (n,α) peak reveals itself easily in this mode. The voltage windows can then easily be set. Once the windows are set, the MCS will only record counts in that voltage window. A schematic of the wiring diagram can be seen in Figure 56. In this, the P211 start sequence signal is used to gate the gate and delay generator as well as the analog HP Pulse Generator. The detector is running continuously with a high voltage bias supplied by an Ortec 561 high voltage power supply. The signal is routed through a preamplifier such as the Ortec 142AH or 113. The signal is then taken through a long wire bundle to the amplifier. For the multichannel scalar system, the amplified signal is directly passed into the SCA IN line on the MCS card. The scalar is set through a SCA sweep mode where all 512 channels of the MCS are cycled in sequence and a coarse ADC like signal is collected. An energy window is set in the software and the unit then functions as a standard scalar. The start sequence signal for the MCS is obtained by using a gate signal that is generated from the gate and delay generator which was started with the start sequence pulse from the P211. This standard NIM logic pulse is delayed by hand until the gamma flash on a suitable detector is seen near channel 5 of the MCS.

The ADC system is slightly different. One of the goals of the ADC system is to obtain signals as a function of time after the pulse. This was done by using the start sequence signal from the P211 and routing it back to a HP custom analog pulse

waveform generator. This allows the user to generate a negatively thrown or positively thrown signal of an arbitrary amplitude and time duration. Using the DC offset, the system was set to a baseline voltage of 0 V. The system was set to create a negative 10 V signal for a user defined length varying between 10 and 2500 µs. This waveform was routed into the DC-Inhibit signal on an Ortec linear gate. This allowed the system to be "blinded" for an arbitrary amount of time following the DT pulse. The analog detector signal was slowed down in time through an analog delay to ensure the linear gate pulse always arrives before the detector pulse. This pulse time and delay was adjusted by hand using an oscilloscope and a suitable detector with a decent gamma ray response to visualize the gamma flash.

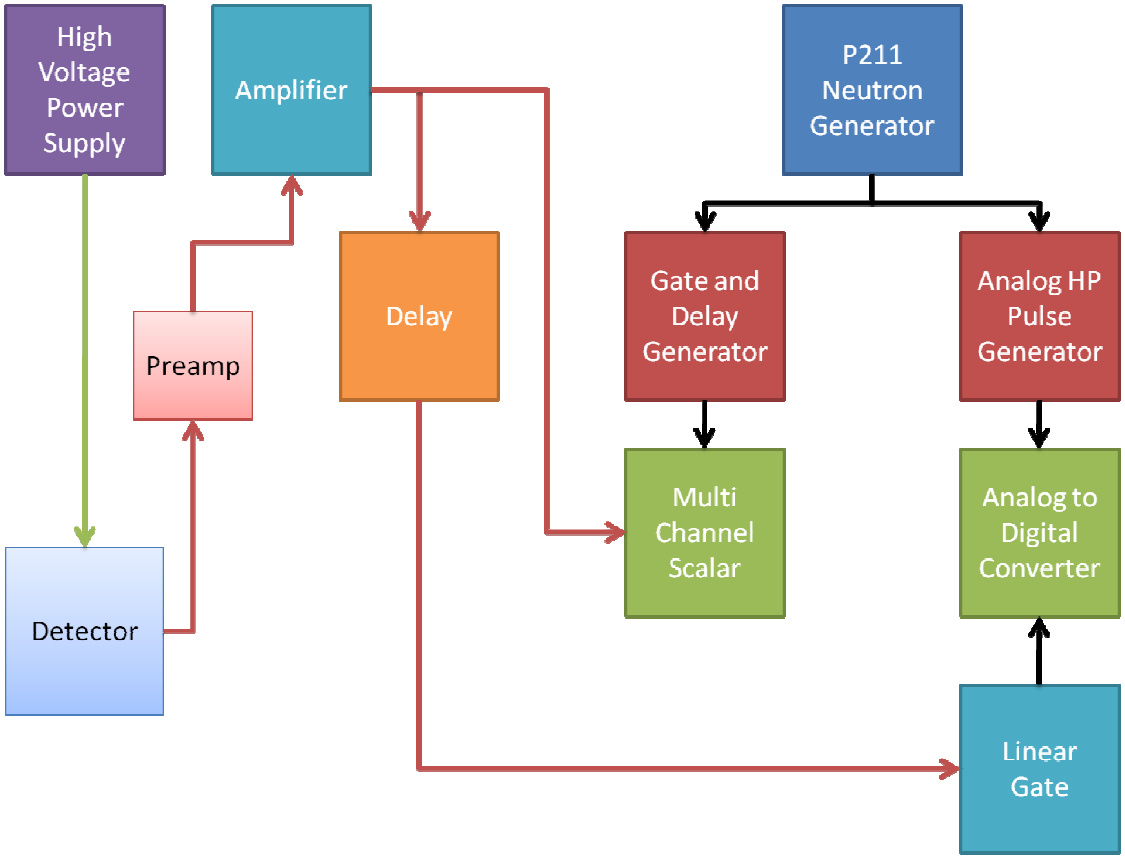

Figure 56 Simplified schematic of the pulsed DT generator timed neutron signal system.

CHAPTER VI

GROWTH AND DOPANT STUDIES

The focus of this work was on the impact of various dopants and growth methods/conditions on the scintillation detectors created from zinc oxide. Two particular types of ZnO scintillators were tested, bulk melt grown ZnO, and MOCVD grown ZnO. Due to the large overhead associated with the growth, cutting, polishing, and preparation of the ZnO melt growth scintillators, the MOCVD growth method is preferred over the melt growth process. Three classes of dopants were investigated. The first class is obviously neutron detector dopant materials. The second dopant class studied were dopants to improve the scintillation wavelength providing acceptor and donor bands. The last class of dopants studied were to improve crystalline clarity and scintillator transparency. These dopants are not mutually exclusive to one class. Often, the incorporation of dopants impacts two or more of the parameters. Six dopants were studied in particular. The dopants which were studied as the focus of this work were lithium, boron, gadolinium, aluminum, gallium and nitrogen.

Cursory investigations of bulk grown samples of cobalt, indium and magnesium doped scintillators were also undertaken. These investigations rapidly eliminated these materials from contention. Lithium and gadolinium were studied in both the bulk growth and MOCVD grown samples. Aluminum, boron, gallium, and nitrogen were only studied in MOCVD grown samples. Undoped samples were also compared to determine the impact of growth conditions on the samples grown under MOCVD.

Impact of Growth Conditions on Scintillator Performance

Three main parameters were investigated to determine the optimal MOCVD growth conditions for ZnO scintillators. The impact of the II-VI ratio is the first

parameter studied. The ratio between oxygen and zinc flow rates has a large impact on the quality of the scintillator. On either side of the optimal growth ratio are either black scintillators which have excess Zn ions and carbon trapping, or white powdery samples which have excess oxygen and are optically opaque and have poor light yields. The second parameter studied was the impact of growth temperature on the crystalline quality of the samples. If the growth temperature is too high, the growth slows and sticking/nucleartion does not occur. In this case the metalorganic sources crack too far above the platter and combine outside the laminar flow growth region over the platter. At temperatures below optimal, crystalline quality suffers and 2D growth is not possible. Samples often come out oxygen deficient due to a lower oxygen cracking fraction and are optically opaque. Lastly, growth pressures were investigated. Growth below the optimal pressure causes sticking and non-laminar flow to be achieved. The velocity of the gasses is too high in a low pressure condition. As the metalorganic source approaches the platter, it adheres directly below where it enters. The laminar flow layer is too thin, leading to sticking and 3D nucleation. If the chamber pressure is too high, the metalorganic molecules do not efficiently reach the platter. If the pressure is too high, the material quality does not decrease as rapidly as it does if it is too low. If the pressure is too high though, the growth rate immediately drops resulting in growth rates of less than 100 nm / hr which are not practical for this work.

Effect of II-VI Ratio on ZnO Samples

The effect of the II-VI ratio on growth results is drastic. Plotted below are the relative photoluminescence or PL spectra after varying the ratio between diethylzinc flow and oxygen flow. Oxygen flow rate was held constant to maintain identical flow patterns in the chamber. Pressure was held at a constant 3 torr during growth. The pressure on the DEZ source was kept at 610 torr and the temperature is held constant at 5 C. The

impact of the ratio between zinc and oxygen is shown below in Figure 57. While increasing the zinc to oxygen ratio does improve the PL intensity, the samples became visibly opaque due to excess zinc. A slight excess of zinc was found to be optimal for PL measurements and resulted in a nearly transparent thin film. When excess zinc is present, there is usually excess carbon trapping due to lack of the ability to form carbon dioxide. The carbon trapping can be seen as defect luminosities in the blue band (BL shift). In addition to the scintillator being opaque, it also slows the response by introducing a longer tail in the decay pulse heights. Excess oxygen samples became white and did not scintillate nearly as efficiently as their counterparts which were oxygen depleted. An optimal ratio of 150-200 diethylzinc flow rate to 900 oxygen flow rate was determined to be optimal for the reactor under these conditions. The flows shown below are in sccm with a zinc bubbler pressure of 600 torr.

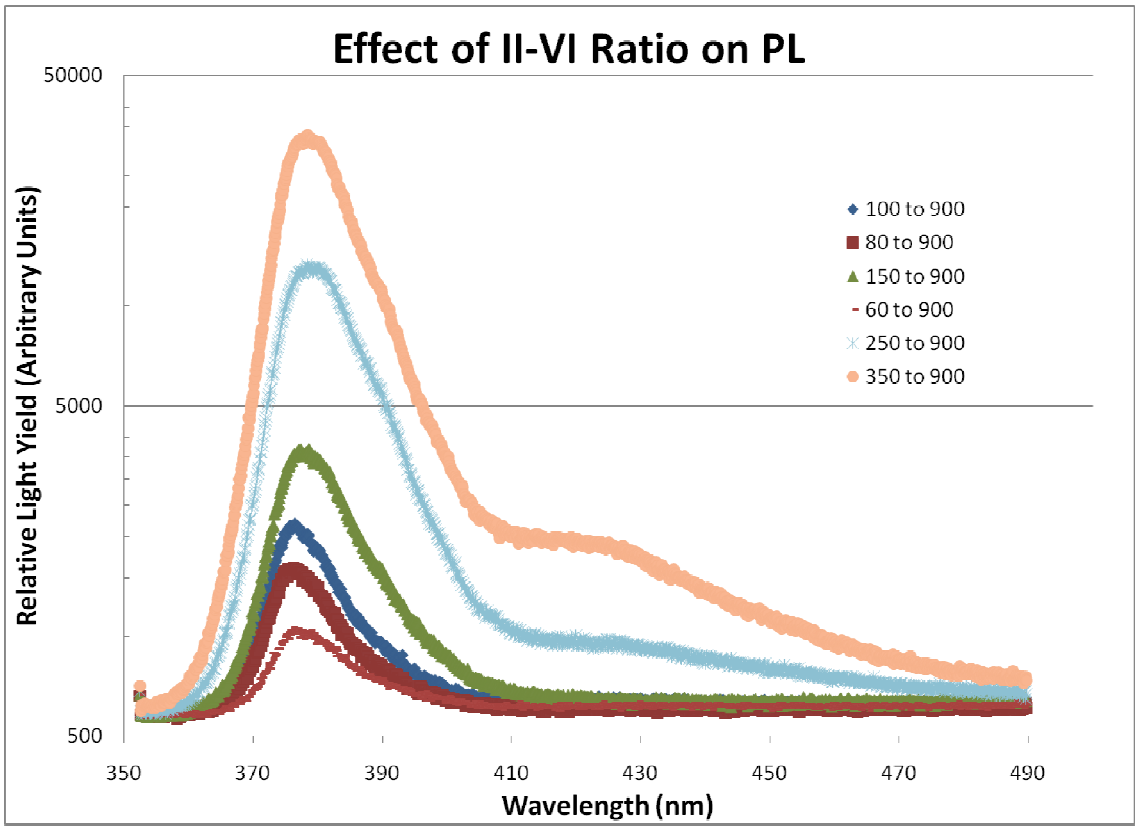

Figure 57 Effect of growth ratio between zinc flow rates and oxygen flow rates in the MOCVD growth chamber.

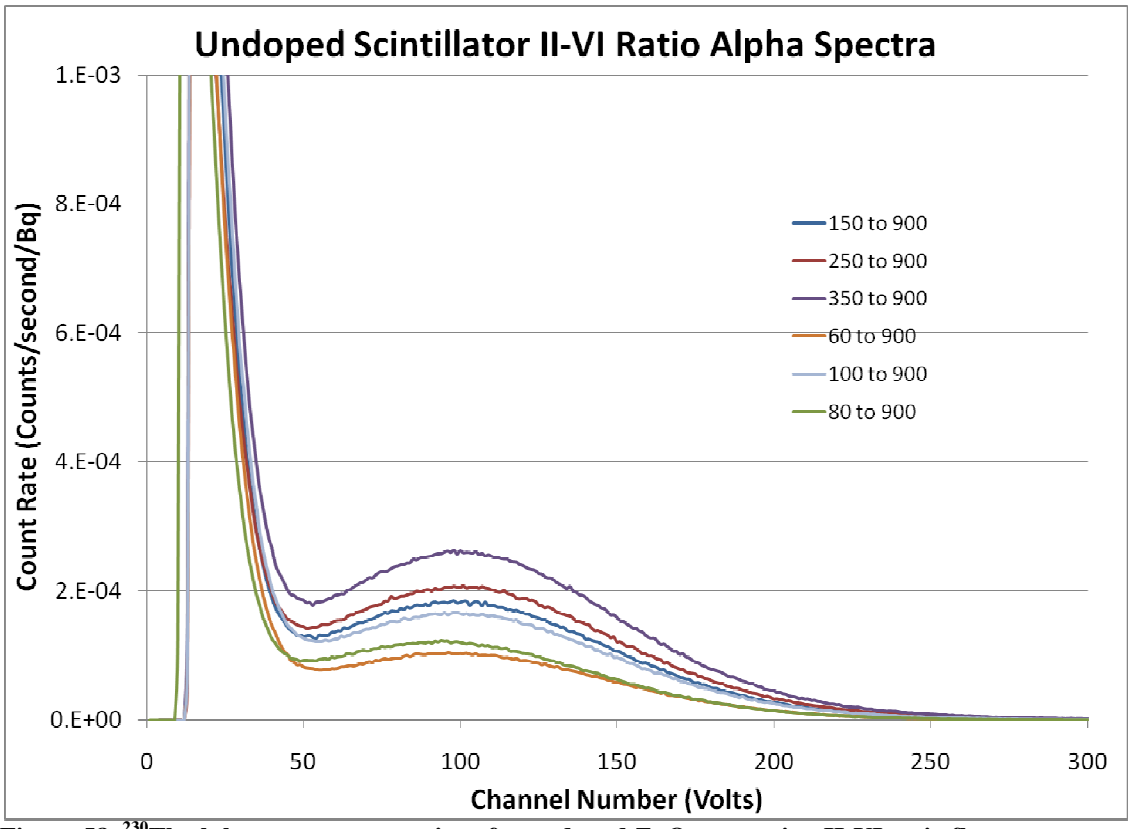

Figure 58 ^{230}Th alpha spectra comparison for undoped ZnO comparing II-VI ratio flow rates.

The ^{230}Th measured alpha spectra using the crystals grown in the II-VI study of growth conditions are shown in Figure 58. A larger alpha peak for the 350 to 900 ratio is observed indicating a higher efficiency. However, this sample has a very low transparency. In larger samples, the higher zinc to oxygen ratios do not yield practical devices. At thicknesses greater than 4 µm, these structures would be unusable. A balance between efficiency and optical clarity was reached in the 150 to 900 ratio.

Effect of Growth Temperature on ZnO Samples

Temperature regulation was studied between 400 and 600 C for growth rates. Growth rates were found to increase up to 550 C and then noticeably decrease above that temperature. Shown in Figure 59 is the impact of the temperature on the PL spectra of

the scintillators. This is further shown in Figure 60 with a logarithmic vertical axis. When the temperature is not high enough, an insufficient amount of oxygen is cracked and the scintillators come out dark with carbon trapped interstitially. Carbon trapping again can be seen in the blue luminescence peak that begins to form around 425 nm. Crystalline quality is also noticeably lower in quality with 3D growth dominating. Good quality samples at reasonable growth rates were able to be maintained at 550 C. Above 575 C, part of the PL band gap peak begins to shift and deform to lower wavelengths. At 600 C the growth is compromised and slowed considerably. The resulting alpha spectra pulse height distributions can be seen in Figure 61.

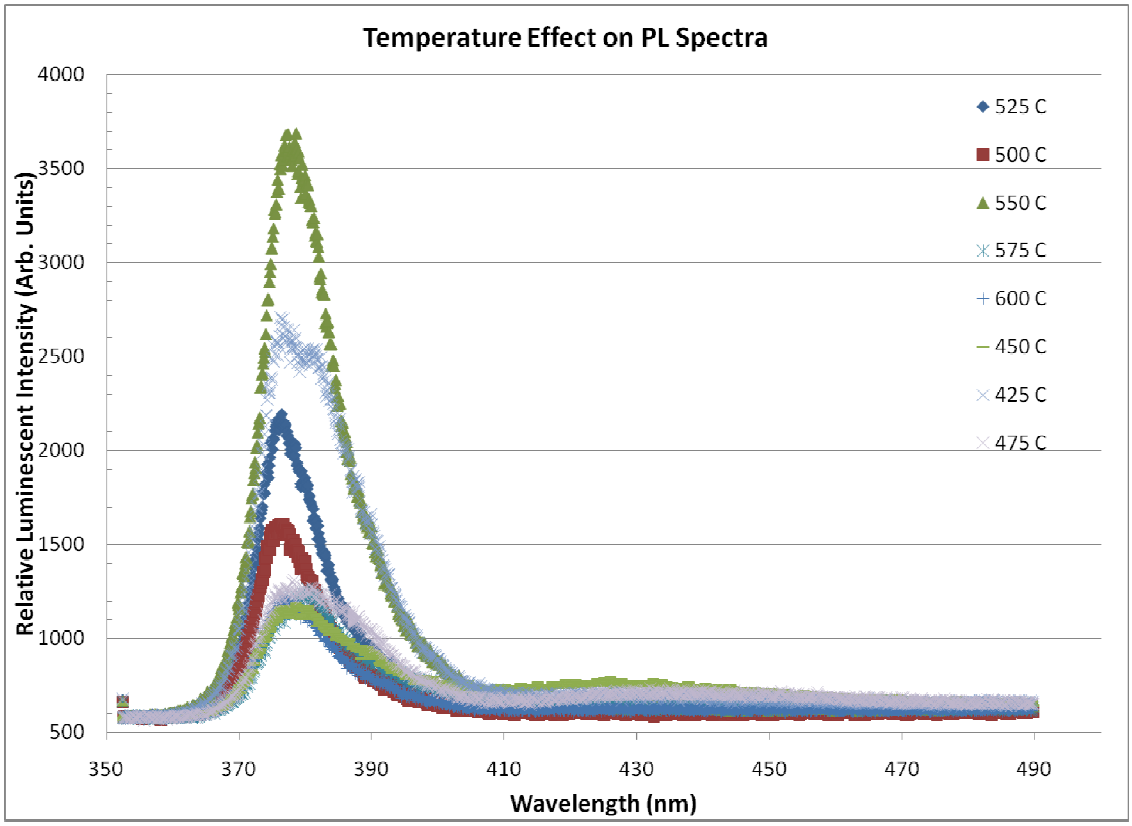

Figure 59 Effect of temperature on PL data.

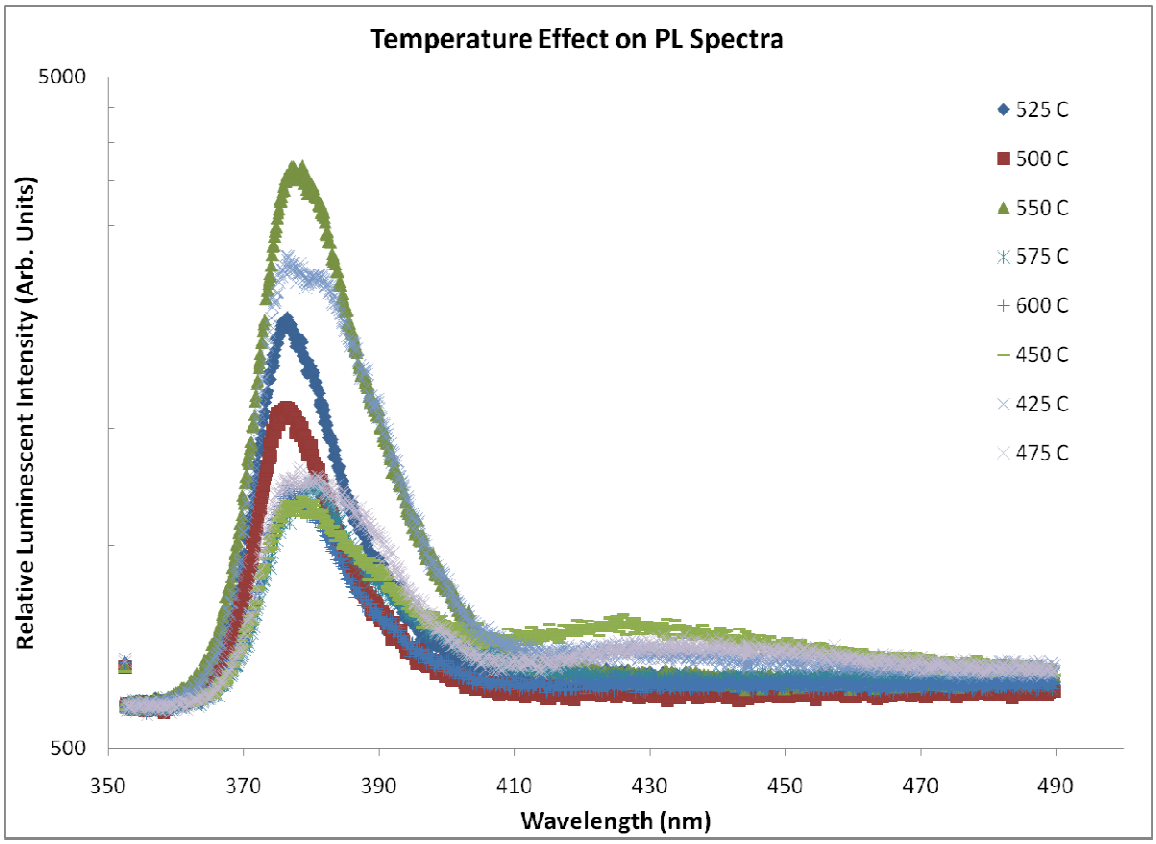

Figure 60 Effect of temperature on PL data plotted with a logarithmic vertical axis to emphasize the blue luminescence of the carbon trapping.

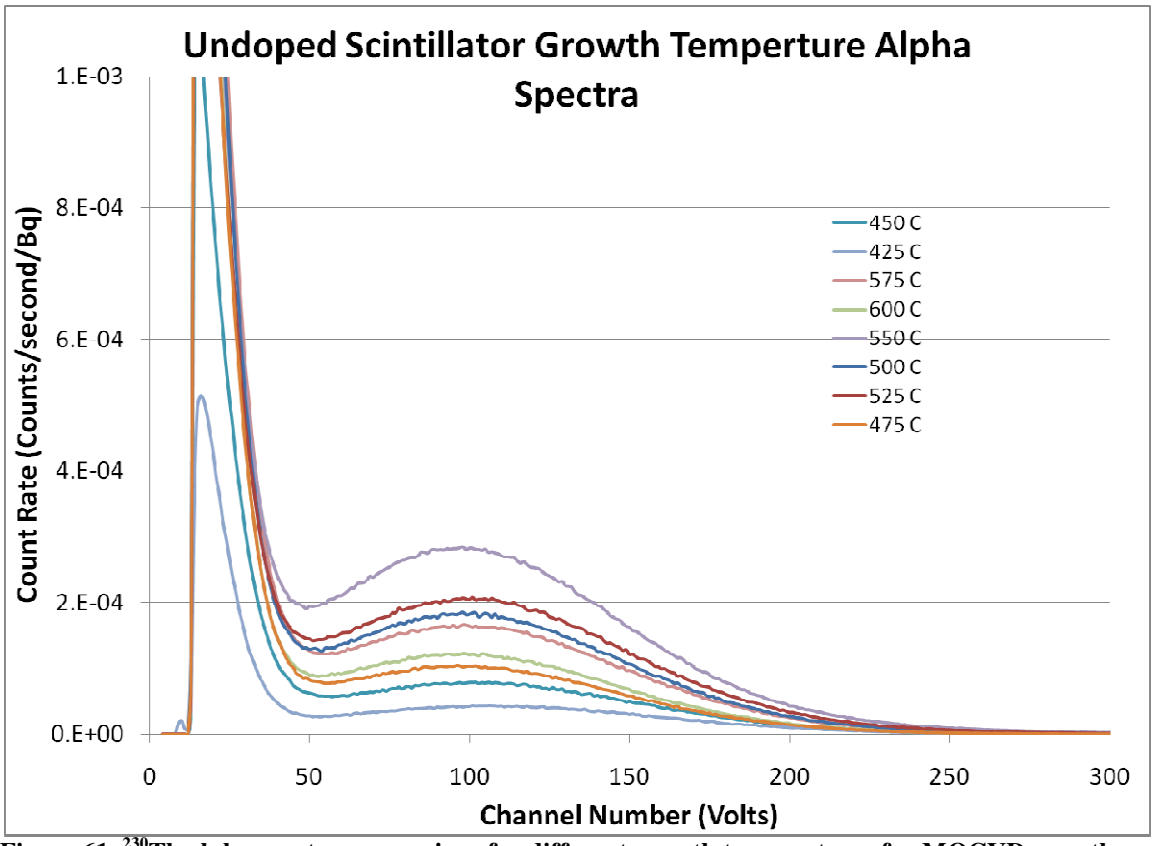

Figure 61 ^{230}Th alpha spectra comparison for different growth temperatures for MOCVD growth.

Effect of Growth Pressure on ZnO Samples

The growth pressure doesn't have as much impact on the PL spectra as does temperature or the II-VI ratio. What it does impact is the maximum growth rate and crystalline quality. Several pressures were tested. Ideally, one would grow between 50 and 10 torr. This became impossible during the course of this project. The main exhaust throttling gate valve stepper gear system stripped out. Due to the age of the tool, replacement was not an easy proposition. Pressure was regulated by a manual throttling butterfly valve which was set to approximately 5 torr. All of the growths during this project were then subsequently performed at 5 torr. At lower pressures, 2D growth became nearly impossible to achieve. Higher temperatures are the counterpart to achieving 2D growth. The limit of temperature was achieved above in Figure 59 at 575

C and a balance of temperature versus pressure was used. The XRD results shown in Figure 62 are for 10 µm thick scintillators. Narrow XRD on axis peaks indicate quality, uniform, single crystal growth of a material. Even with the pressure not being able to be regulated efficiently, good crystalline quality can still be achieved. For ten micron thick devices, the XRD results indicate a ZnO crystalline FWHM value of 395 arc seconds. While this is not a world record crystalline quality, for ten micron epitaxial layers, this is very high in quality.

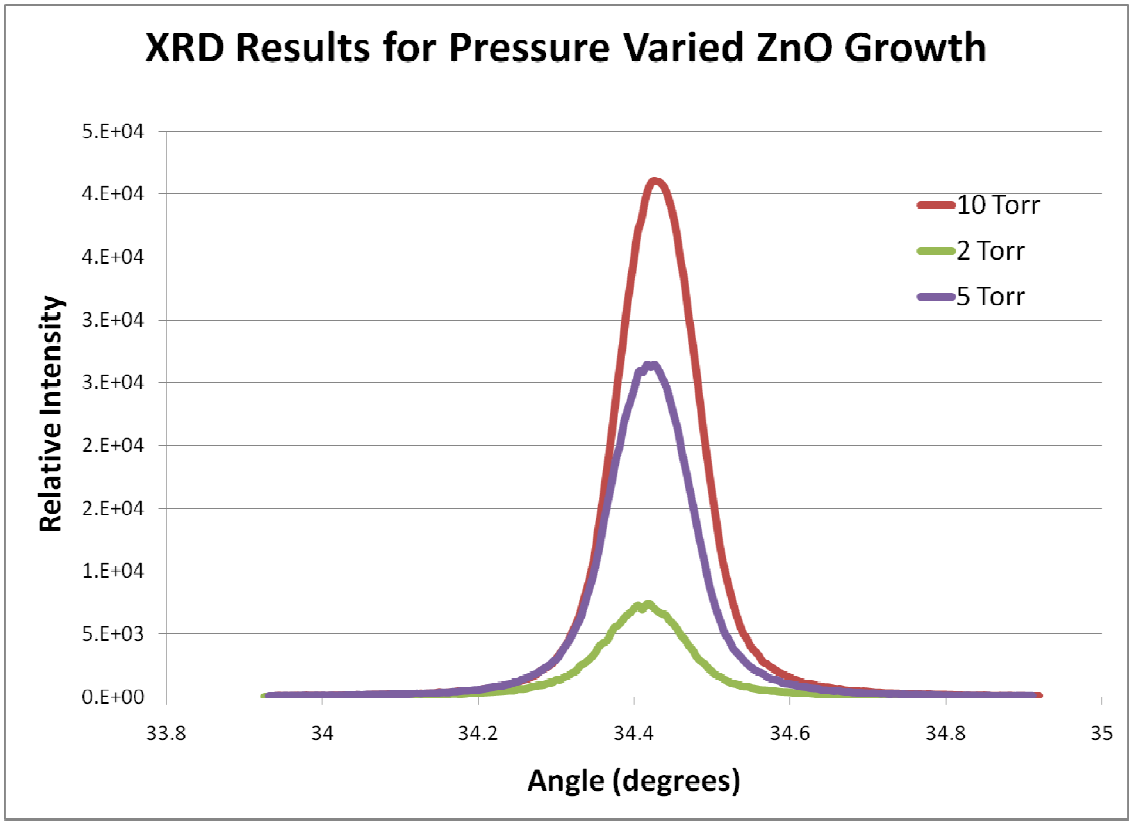

Figure 62 Effect of pressure in the growth chamber on XRD crystalline quality.

Impact of Nitrogen Doping on Scintillator Performance

Nitrogen doping was performed inline during the growth of ZnO in the MOCVD system. The nitrogen dopant that was used was ammonia, NH_3. Ammonia, when cracked, provides 1 nitrogen atom, and three hydrogen atoms. When performing nitrogen doping with ammonia, the oxygen flow rate must be increased to compensate for the

excess hydrogen present. Nitrogen doping was found to have several improvements on the growth of ZnO. Nitrogen doped samples were able to be grown at very high growth rates. Growth rates in excess of 4 µm per hour were possible. Crystalline transparency also drastically improved. Samples in excess of 15 µm were still extremely clear. All nitrogen doped samples grown had a slight peach color to them. The ammonia was found to act as a surfactant and clean the surface of excess carbon during growth. The structures usually exhibited 3D growth with nanorod structures being present to a larger degree than undoped scintillators. There was one large drawback with just plain nitrogen doping. When using ammonia, the three excess hydrogens had a tendency to become trapped in the crystalline structure. This is the first time free hydrogen atoms were released into the chamber without being attached to a carbon nuclei. The free hydrogen would become interstitially trapped in the crystalline lattice. Hydrogen functions as a deep acceptor in the scintillator and passivates the PL centers by trapping the excited electrons. The non-existant PL data can be seen in Figure 63. Based on growth filmetrics and optical clarity, an optimal growth condition was found to be a 1 sccm flow of ammonia in a pulsed growth condition, pulsing the ammonia source at a 1 to 30 ratio.

There effectively is no luminescence to the nitrogen doped scintillators and therefore no scintillation peak at all. There is a saving grace to the destroyed PL response however. A rapid thermal anneal of the scintillator under an oxygen overpressure was found to restore to a limited extent the original PL spectra. The oxygen overpressure and higher temperatures liberates the trapped hydrogen atoms and combines it to form water vapor. Overpressures of greater than 1.05 atmospheres produced oxygen rich scintillators. Rapid thermal annealing (RTA) was accomplished using a multi-zone tube furnace. One of the ends of the tube furnace was sealed with an aluminum ring held in place with a band clamp. The other end was routed through an offgass trap of water and vented through a fume hood. Annealing was accomplished at 800C and the amount of time of the anneal was varied. Oxygen flow rates of 30 sccm to 80 sccm were

maintained. The samples were loaded into a fused silica boat and moved in and out of the heated zone by way of an aluminum hook. The samples were allowed to cool outside the zone furnace inside the oxygen atmosphere. A two wafer growth run was conducted under the "optimal" pulsed ammonia growth conditions to prepare samples for the ammonia doped scintillator tests. The wafers were quartered and then annealed under different conditions. The results of these tests can be seen in Figure 64. The annealed samples slowly returned the PL spectra and the peak returned. The wavelength of scintillation had blue shifted by approximately 10 nm. As the sample annealing time was increased, the peak continued to increase but never reaches the undoped level. A maximum value was found to be approximately 5 minutes of anneal under an oxygen overpressure at 800C. After this, the samples became oxygen saturated and clouded up due to excess interstitial oxygen.

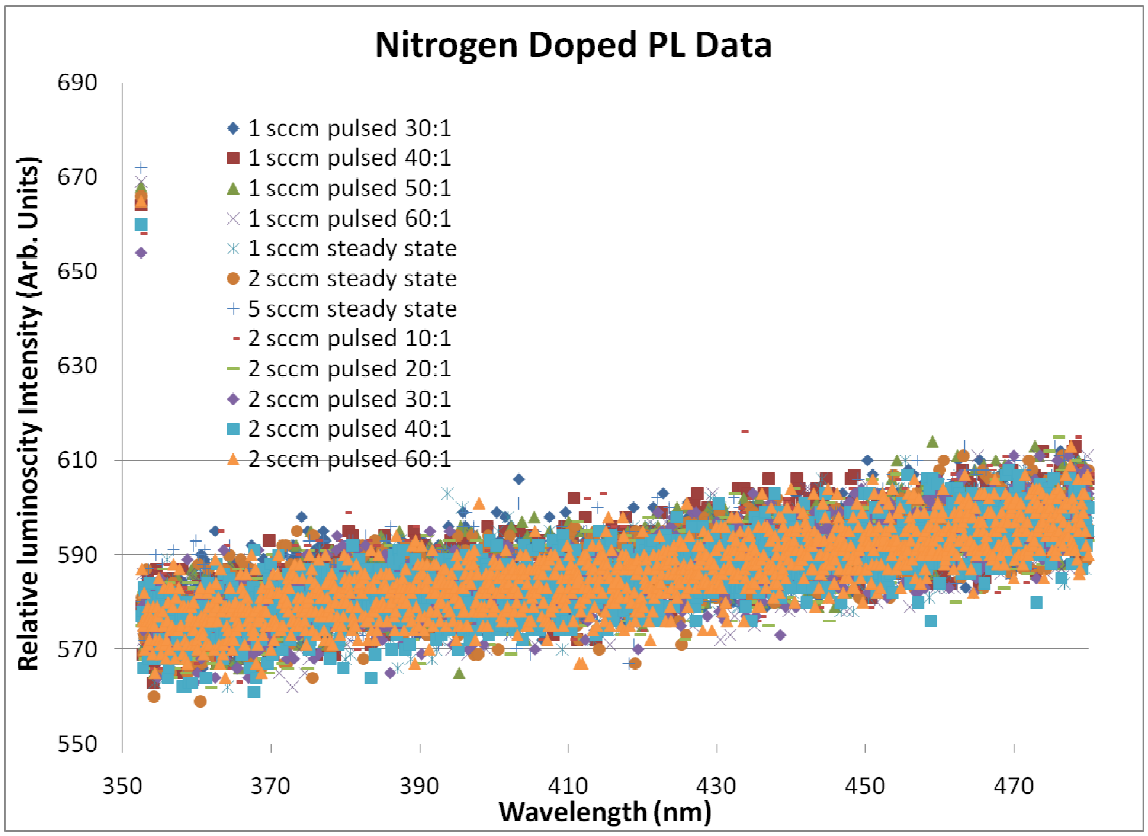

Figure 63 PL data for the Nitrogen doped studies.

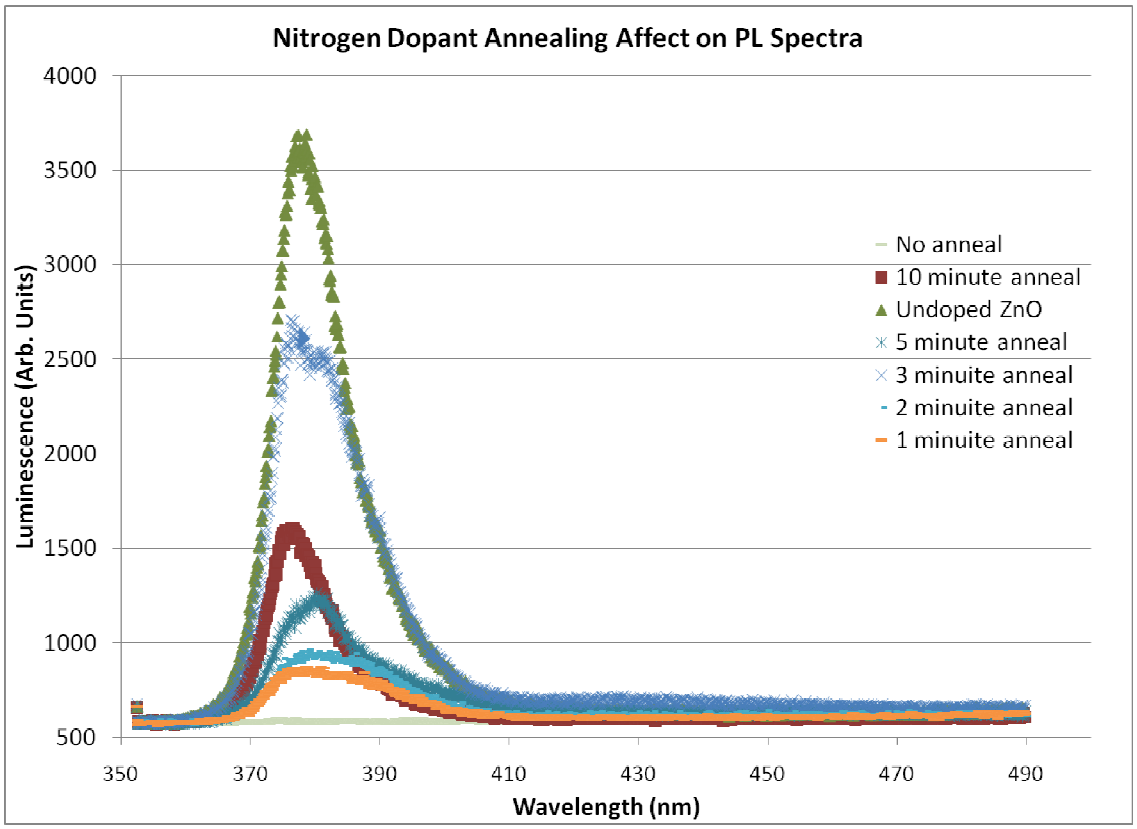

Figure 64. Nitrogen doped samples after annealing under oxygen.

Prior to annealing the nitrogen doped scintillators, these scintillators exhibited no alpha peak and no real spectrum. This was an obvious conclusion from the lack of PL data resulting from the hydrogen trapping. To reconcile this, using the annealing studies shown in Figure 64, a five minute anneal under oxygen at 800 C was performed on all of the nitrogen doped scintillators. This resulted in the return of the alpha peak. The resulting alpha peak can be seen in Figure 65. The peak position has shifted to the right indicating a slight increase in light collection.

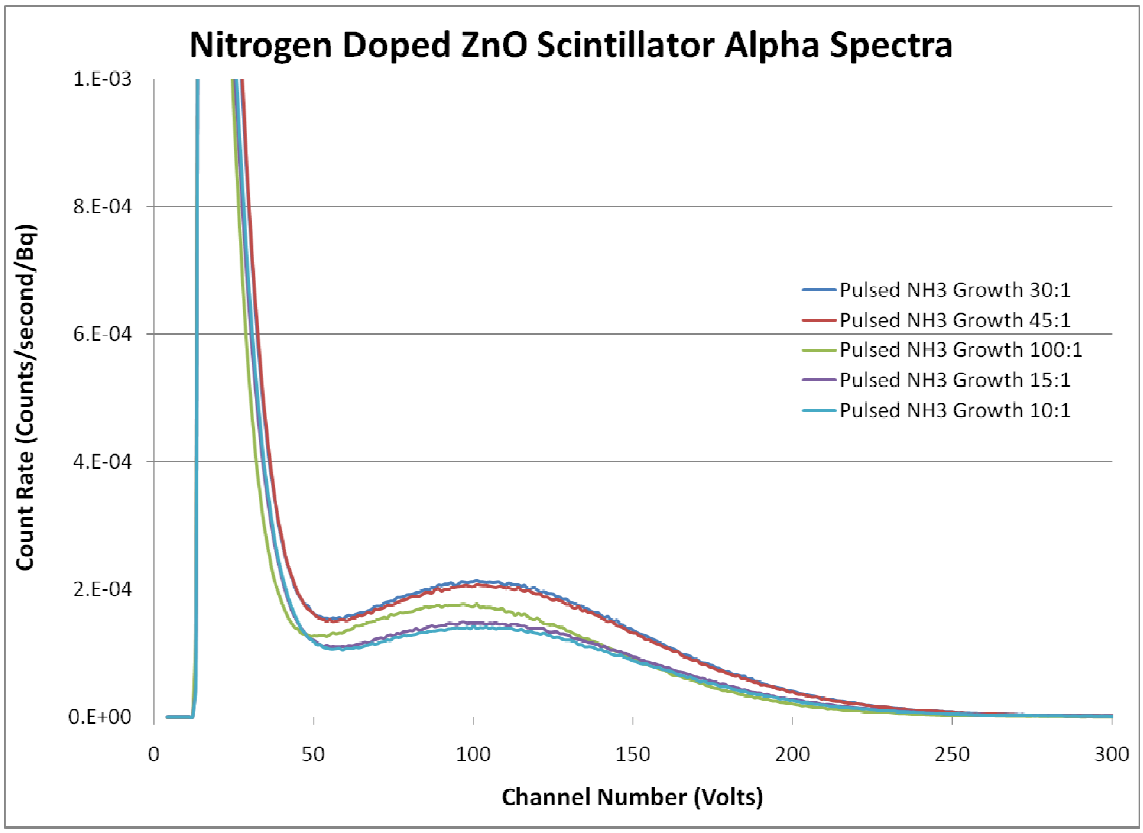

Figure 65 ^{230}Th alpha spectra comparison for nitrogen doped ZnO after 5 minute anneal under oxygen at 800 C.

Impact of Gallium Doping on Scintillator Performance

Gallium was investigated in an attempt to wavelength shift the scintillator spectrum. Gallium is intended to introduce excess activation levels for the scintillator. Gallium is far more reactive of a metalorganic source than zinc is. Trimethylgallium (TMG) was used as the dopant precursor. The sample was cooled to -1 C. An overpressure of 1000 torr was used to further lower the vapor pressure of the TMG source. Continuous flow rates had detrimental effects on the PL spectra. Samples often came out black or brown due to excess gallium. Samples were only carried forward to PL spectral measurements if they were optically clear. Gallium oxide however had a tendency to form which isn't as optically clear as ZnO is. Samples as thick as 10 µm were able to be grown, but at a lower optical clarity. The PL spectra show a wavelength

shift of roughly 7 nm on average. The PL peaks with gallium are forwardly skewed indicative of the gallium alloying in the ZnO matrix. The PL responses for the gallium doped samples can be seen in Figure 66. With as reactive as gallium is, only pulsed growth was capable of incorporating gallium into the matrix. The alpha spectroscopy results shown in Figure 67 increased detection efficiency as the gallium concentration increased to a peak value and then decreased again which confirms the PL results.

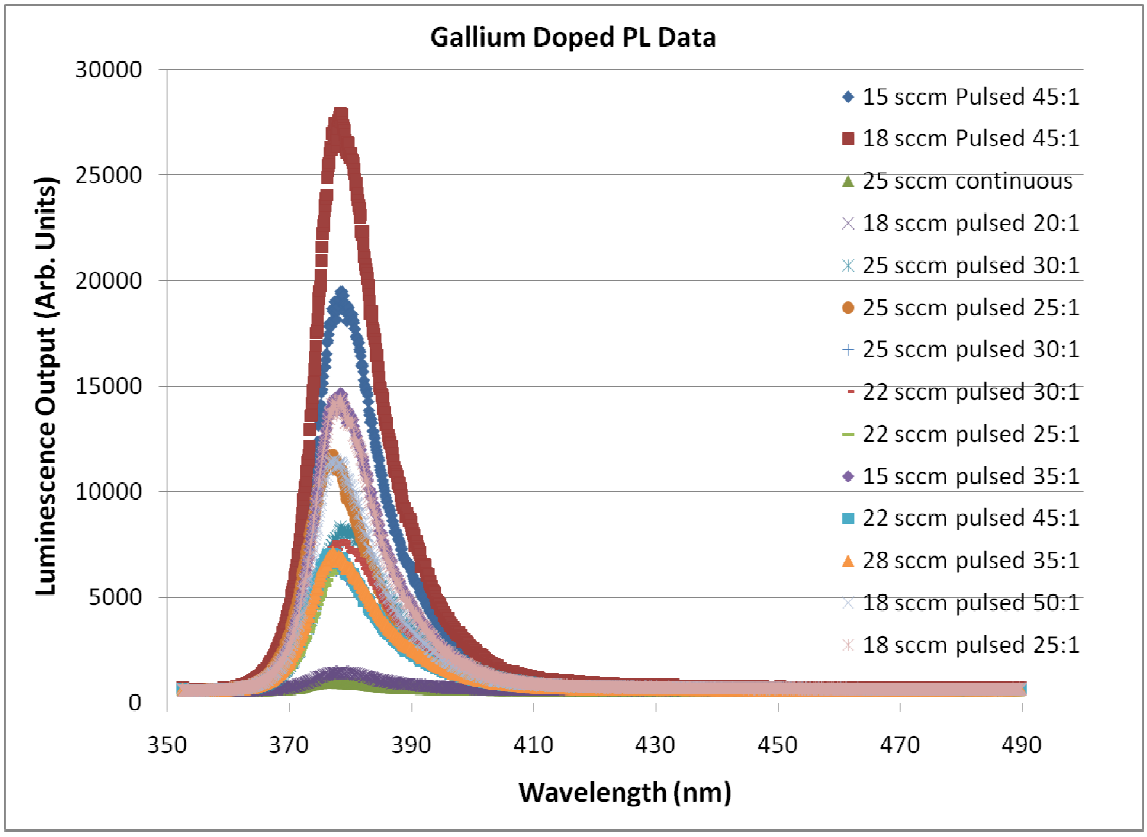

Figure 66 Gallium doped PL data.

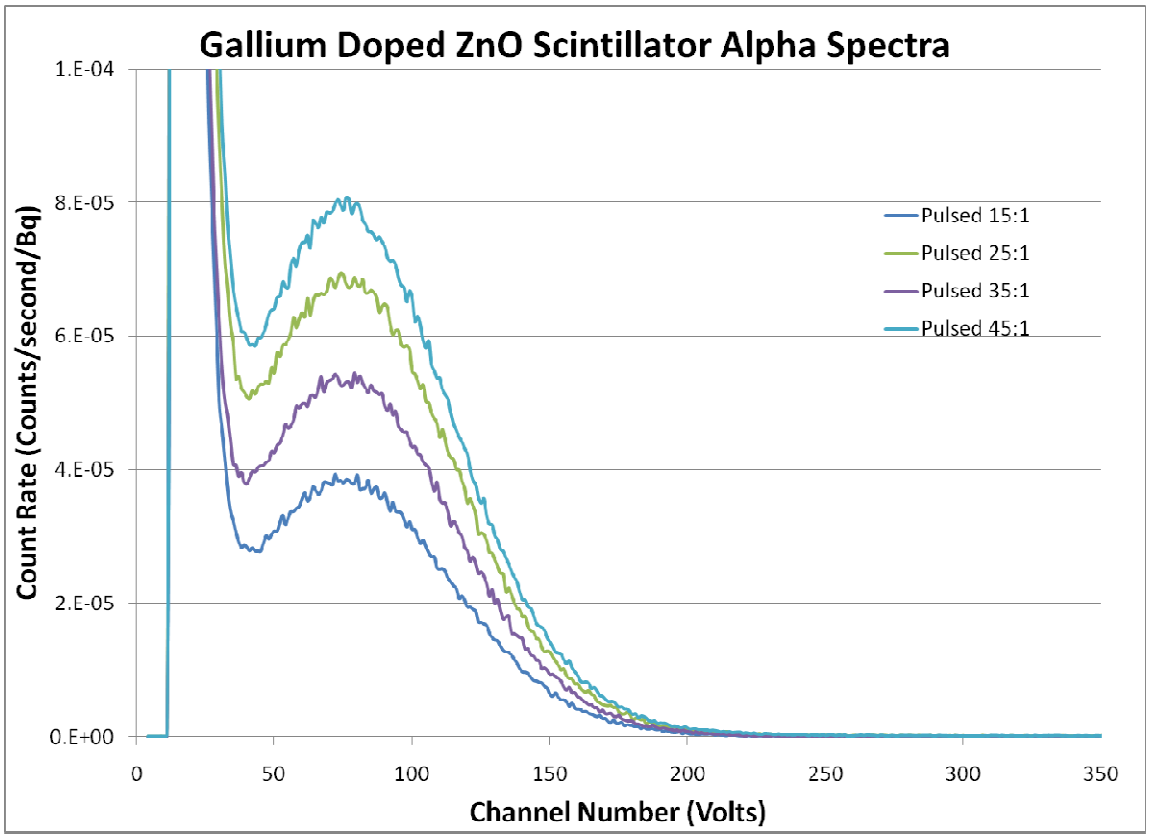

Figure 67 ^{230}Th alpha spectra comparison for gallium doped ZnO. Flow across gallium source was 18 sccm at 800 torr.

Impact of Aluminum Doping on Scintillator Performance

Aluminum doping to ZnO is a fairly common practice. Aluminum doped zinc oxide, often referred to as AZO is a highly transparent, highly conductive material that is commonly used as an ohmic contact for solar cell work. AZO forms a nice crystalline material which is very clear. AZO grows very well since the lattice structure is similar to that of sapphire, Al_2O_3. Both exhibit wurzite structures. AZO however has a tendency to shift the wavelength further to the UV region than the blue region. This opposite effect must be balanced with other materials. Since the AZO material UV shifts the scintillation light by creating deeper conduction bands than in ZnO, the luminoscity drops. AZO scintillates below its band gap edge and preferentially reabsorbs its scintillation light.

The resulting PL spectra for AZO can be seen in Figure 68. AZO does produce excellent crystalline quality materials. The crystals come out clear and can sustain MOCVD growth for over 20 μm. Dopant levels as high as 20 percent can be achieved and still maintain a PL spectral peak. The ZnO peak is still dominant as can be seen in Figure 68, but it is skewed to the left slightly with a peak wavelength of 376.3 nm. This is indicative of the scintillation spectrum being truncated by the band edge of the material. Aluminum, like gallium, is a significantly more reactive precursor material than the zinc source is. It is also an oxygen scavenger, requiring 3 times as much oxygen as ZnO does. Initial growths using continuous doping, even at low flow rates and high pressures lead to completely passivated samples. The continuous flow doped samples which were passivated however ranged from 50 to 80 percent aluminum oxide and a small fraction of zinc interstitials. Using pulsed growth, high quality AZO samples were able to be grown. When the aluminum flow was too high, the alpha spectroscopy results showed poor detection efficiencies. This can be seen in Figure 69.

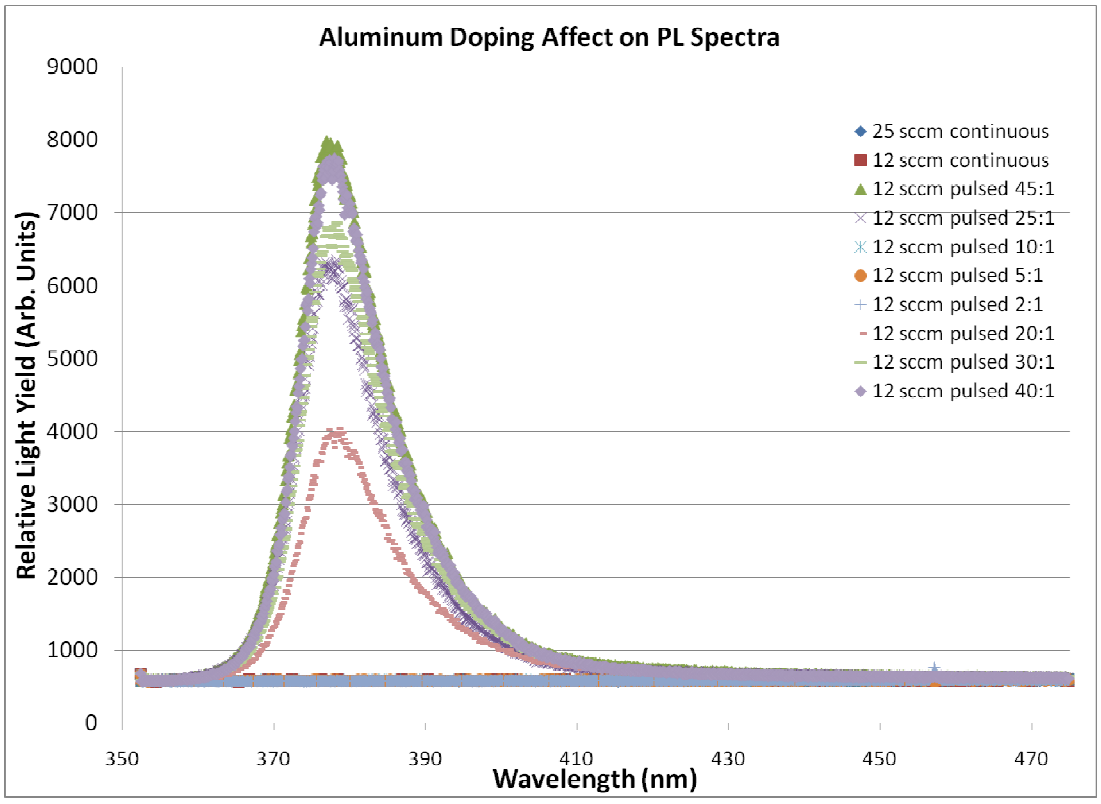

Figure 68 Aluminum doping impact on PL spectra.

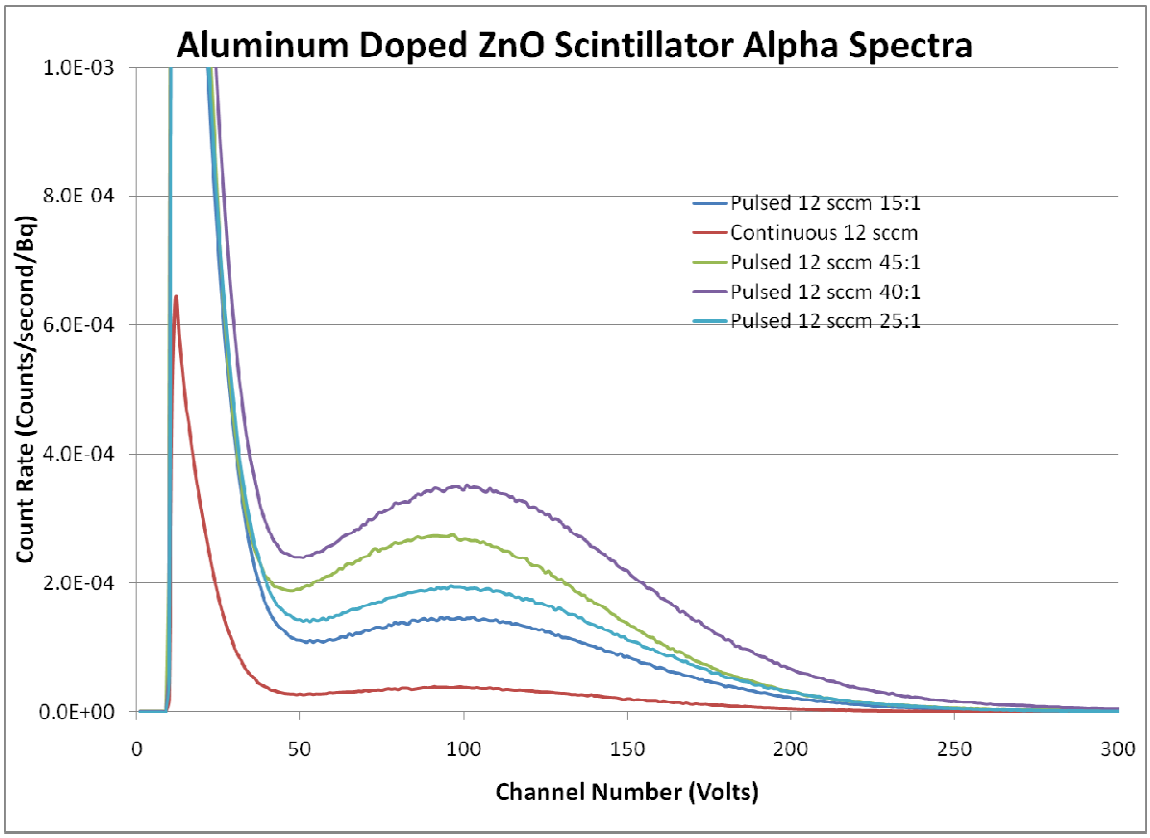

Figure 69 ^{230}Th alpha spectra comparison for aluminum doped ZnO.

Impact of Boron Doping on Scintillator Performance

Boron, a neutron target material can be directly doped into the scintillator with good results. While boron has a tendency to form boron oxide, boron doped ZnO demonstrated good photoluminescence spectrometry results. Boron added several acceptor activation levels which increased the scintillation wavelength by approximately 10 nm. Extensive studies on boron were conducted because it is a dual purpose dopant, adding neutron detection functionality as well as for improving the light yield. Diethylboron was used (DEB) as the boron precursor. This precursor is required to be kept at extremely low temperatures otherwise it remains in the gas phase and can be used rapidly. The source was kept at -20C and a pressure of 800 torr. The resulting PL

spectra for B:ZnO can be seen in Figure 70 while the alpha results can be seen in Figure 71.

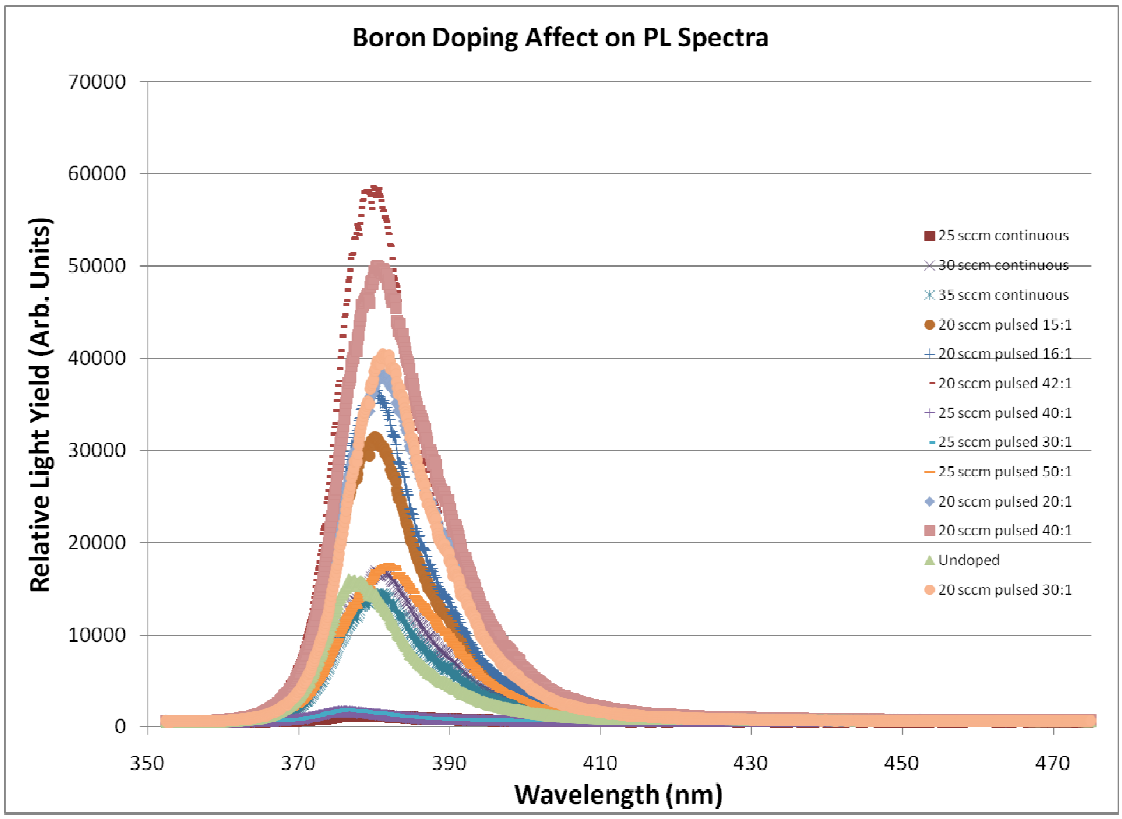

Figure 70 Impact of Boron doping on ZnO PL spectra.

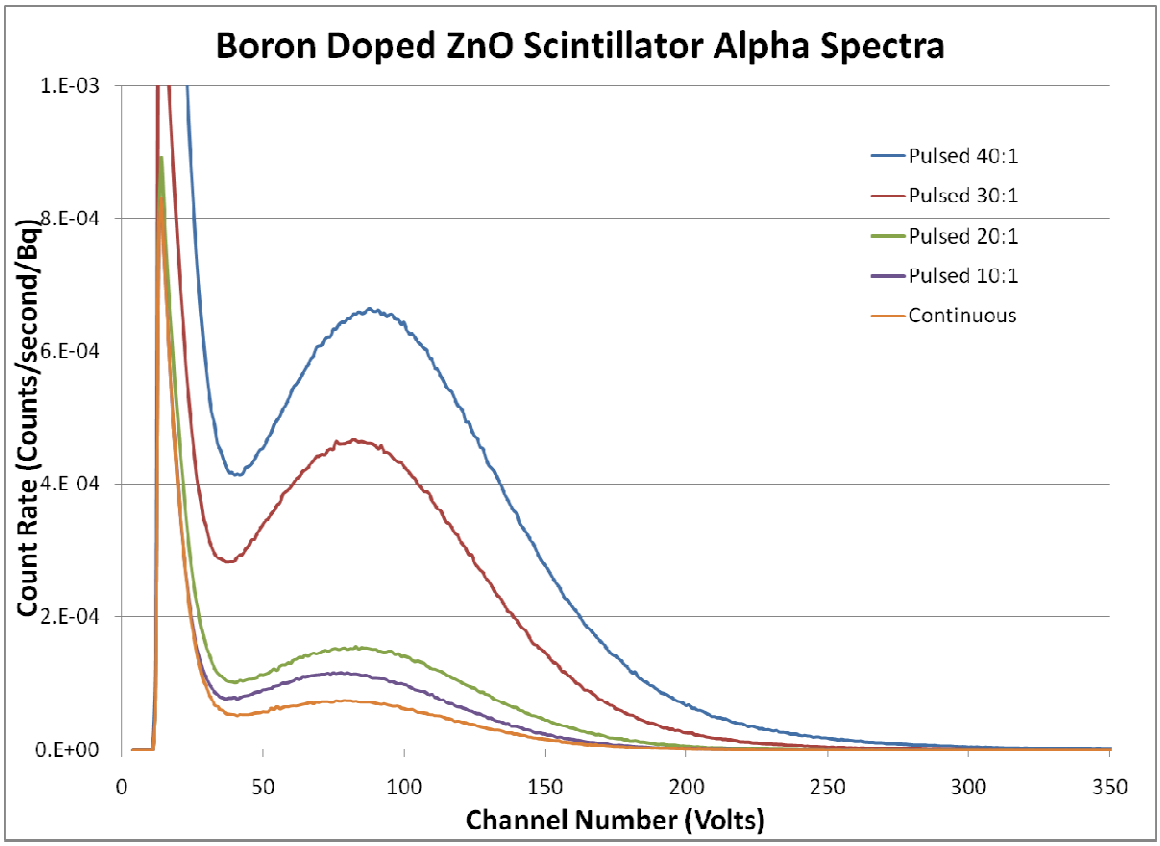

Figure 71 ^{230}Th alpha spectra comparison for boron doped ZnO. Flow across the boron bubbler was 20 sccm at 800 torr.

Impact of Lithium Doping on Scintillator Performance

Lithium also was investigated heavily as a potential dopant. Lithium samples are difficult to grow due to the lack of a good, standard lithium precursor. There are no diethyl lithium or dimethyl lithium sources. Materials which are close to these sources are lithium β-diketyonates and lithium TMHD sources. To use these sources, either liquid injection or heated precursor lines are needed. In this work lithium cyclopentadienide, lithium TMHD, t-butyllithium, and lithium acetylacetonate were all investigated as potential sources for the MOCVD process. Lithium cyclopentadienide was eliminated quickly due to the very low vapor pressure. When pulling the sample down to vacuum, most of the sample sublimated. When exposing the source to the

vacuum of the growth chamber, the source rapidly decomposed and destroyed the growth.

Lithium TMHD showed good promise. This source however required the lines to be heated. If the TMHD chemical comes in contact with a cold wall source, it will immediately plate out and clog the injection lines. A heater jacket and heater tape were used with a temperature controller to heat the injection line which was installed directly into the growth chamber. T-butyllithium dissolved in pentane was investigated as a liquid injection source. This source worked well when continuously agitated by being placed on the vacuum pump. When left still, the t-butyllithum fell out of solution and collected at the bottom of the bubbler. A separate liquid injection line was installed for this source. When using this source, the amount of material injected into the chamber was a large volume. It was considerably more difficult to control this and maintain a clear crystal. Lastly, the lithium acetylacetonate provided a good solution in a heated vapor phase. After a few days, however, this source solidified from its original fluffy powder form and turned into a rock. The sample was also then liquefied by dissolving it with acetone and attempted to be used as a liquid injection source. The samples grown by MOCVD were comparable to the bulk growth samples prepared by Cermet Inc. but with considerable more effort required to get the samples to work. A significant trial and error process was required to get clear lithium doped samples from MOCVD. The resulting PL light yield can be seen in Figure 72 and in Figure 73 can be seen the alpha spectroscopy results for lithium doped ZnO samples.

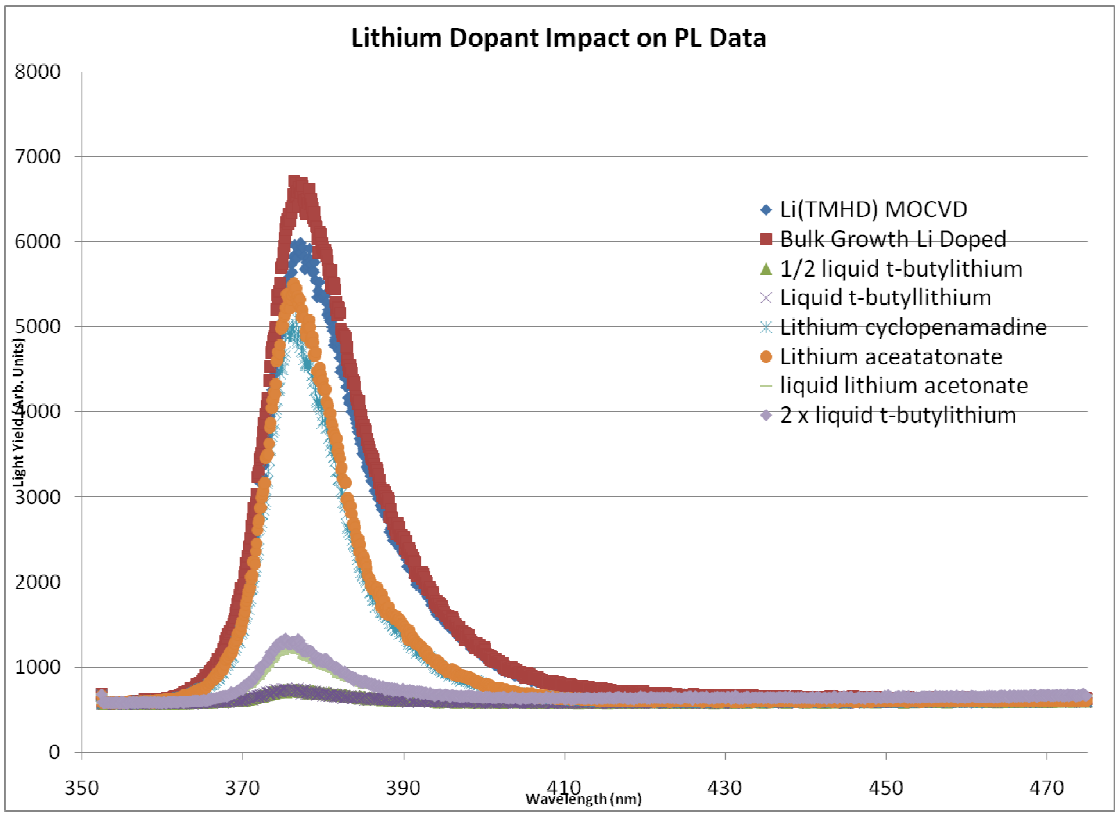

Figure 72 Lithium dopant impact on PL light yield.

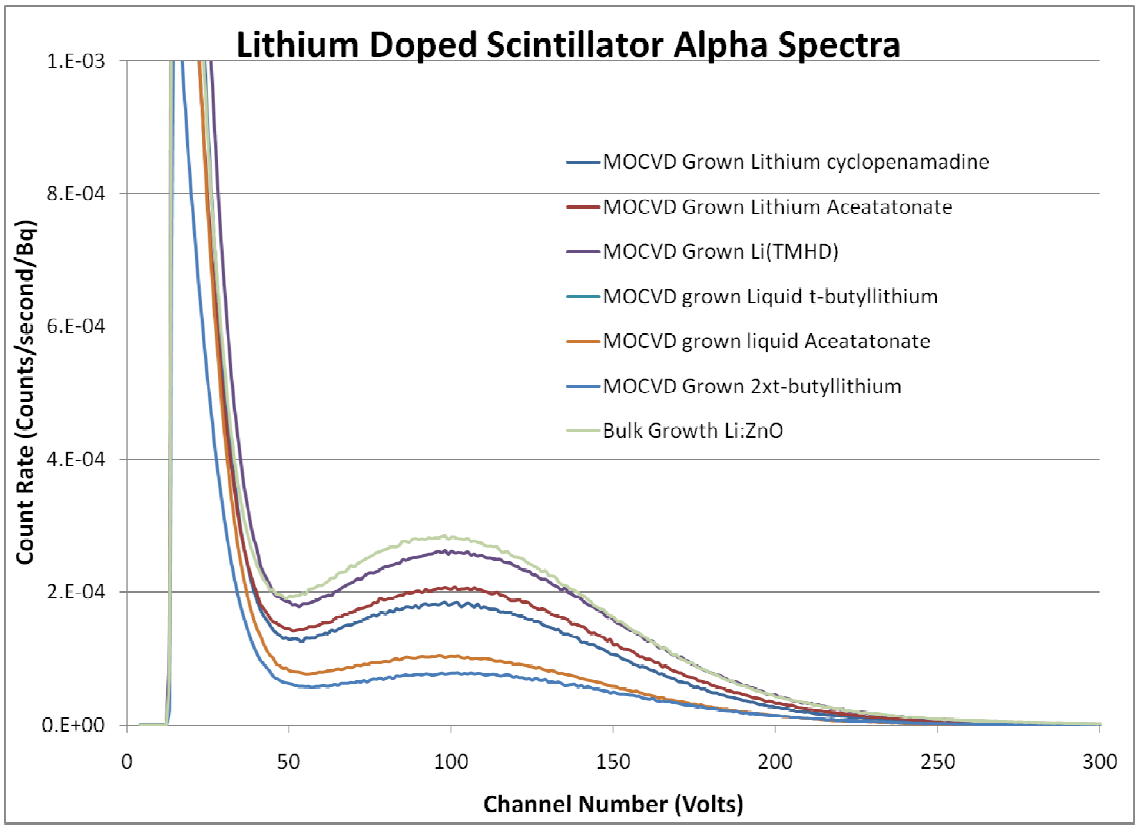

Figure 73 ^{230}Th alpha spectra comparison for lithium doped ZnO.

Impact of Gadolinium Dopants on Scintillator Performance

Gadolinium was the last major dopant to be investigated. Gadolinium in both bulk and MOCVD grown samples were prepared. A Gd(TMHD) source was used as the MOCVD precursor. This source was left over from another project and tested on the MOCVD system. The bulk growth samples are also compared against the MOCVD grown samples. The samples all compare well with one another. The gadolinium with its extensive electron structure does provide extra acceptor energy states for excited electrons. It drastically raises the effective Z number of the material. The PL spectra can be seen in Figure 74. The alpha spectra results can be seen in Figure 75. Studies on 3+ state and bound Gd were investigated. The single MOCVD Gd source limited the study from the MOCVD standpoint to flow rates over the sample. Good light yield was found

with these samples though. The gadolinium doping work was not intended to be conclusive.

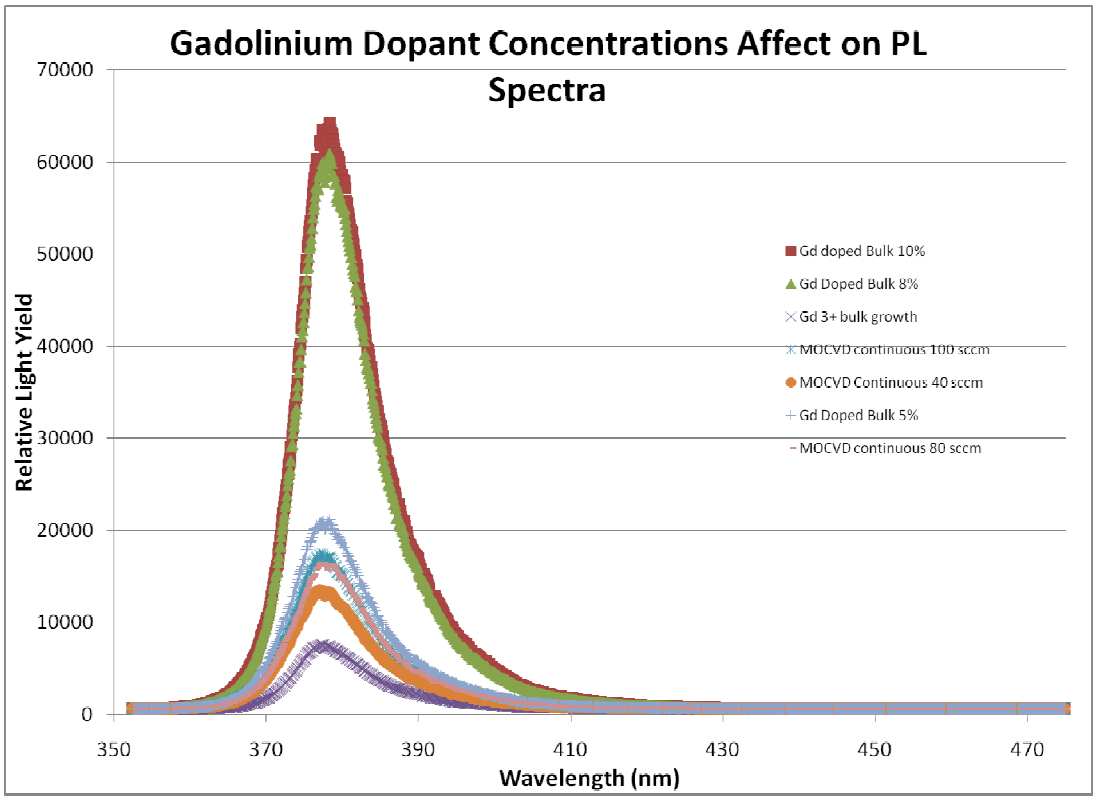

Figure 74. Impact of Gd dopants on ZnO PL data.

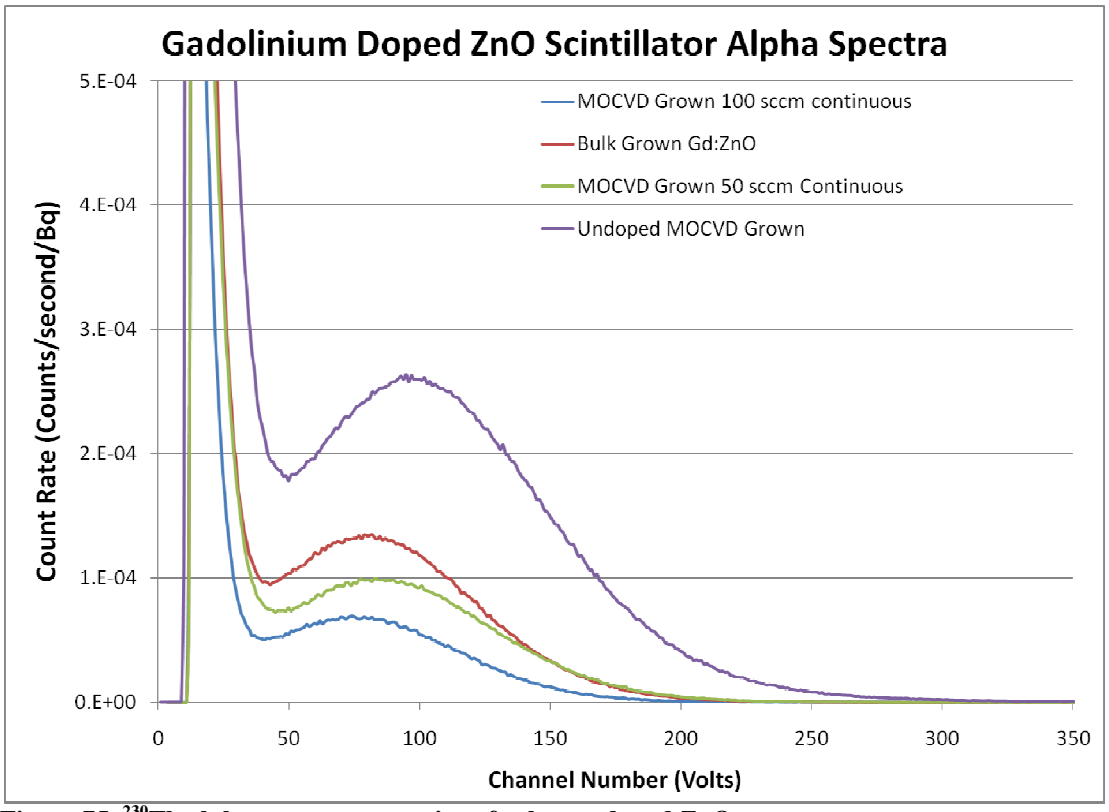

Figure 75 ^{230}Th alpha spectra comparison for boron doped ZnO.

Impact of Doping on Scintillator Speed

Pulse height time distributions for all of the samples were run for all of the scintillators tested. An example of this is shown in Figure 76. The pulses were digitized using a 1 GHz sampling oscilloscope. Rise and decay times were measured for all of the samples tested above. Selected results are presented in Figure 77. The remainder of the data can be found in Appendix D.

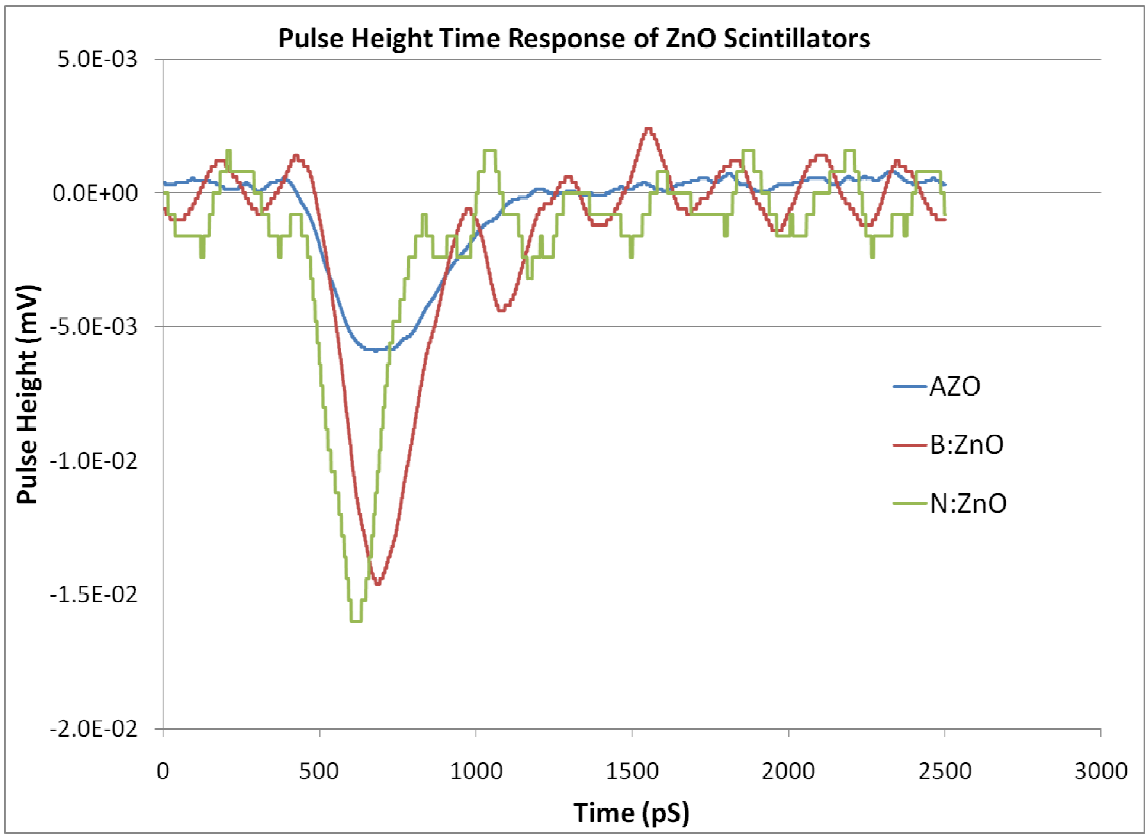

Figure 76 Pulse height rise and fall times for three scintillators.

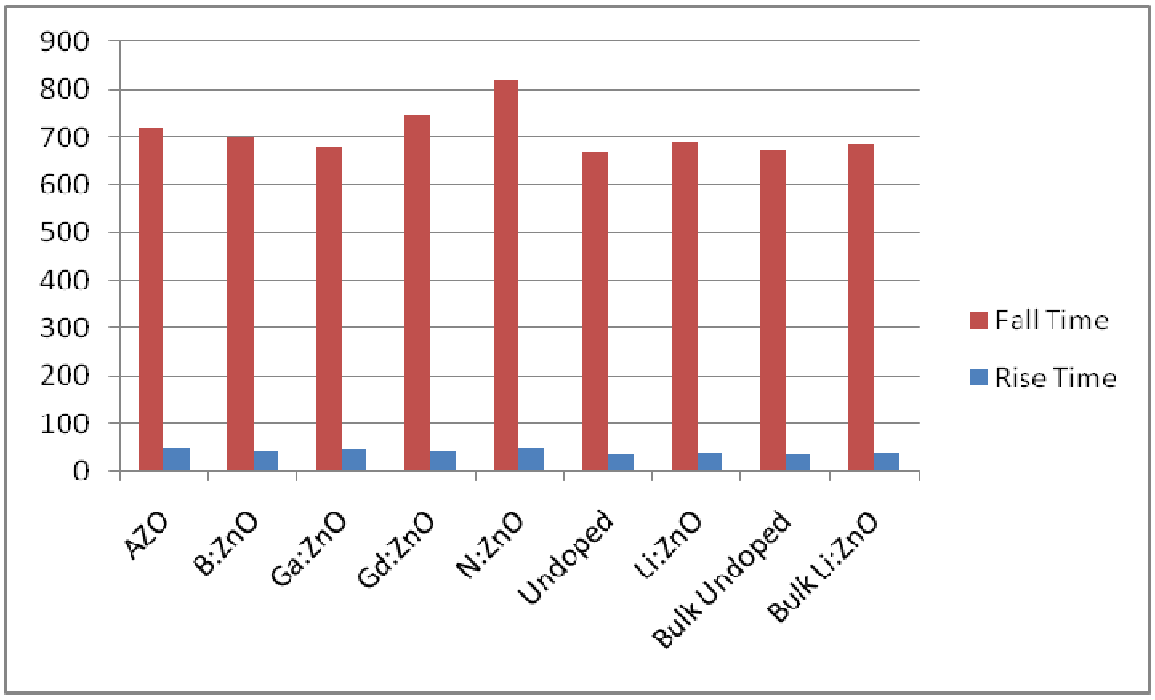

Figure 77 Rise and fall times of the best production quality scintillators.

Validation of Doping Levels Using FTIR

Selected samples were analyzed on the FTIR system at Los Alamos National Lab. The FTIR system ensures dopant levels have been incorporated into the ZnO matrix. Two different modes, diffuse reflectivity and specular absorption were used to ascertain the dopant effects and incorporation into the scintillator. In Figure 78, specular absorption is shown for all of the production samples. The spectra are dominated by the absorbance of the sapphire substrate on which the samples are grown. The lithium containing sample has a slight blurring around 1120 nm^{-1} indicative of the small amount of lithium in comparison to the sapphire. The sample has slightly less absorbance due to the improvement in optical clarity of the lithium doped ZnO. Nitrogen doped ZnO can be seen to have a small ripple around 1920 nm^{-1} indicative of a small amount of nitrogen bonding taking place. The units on the plots shown below are in wavenumber (inverse length), and either transmittance or reflectance depending on the measurement.

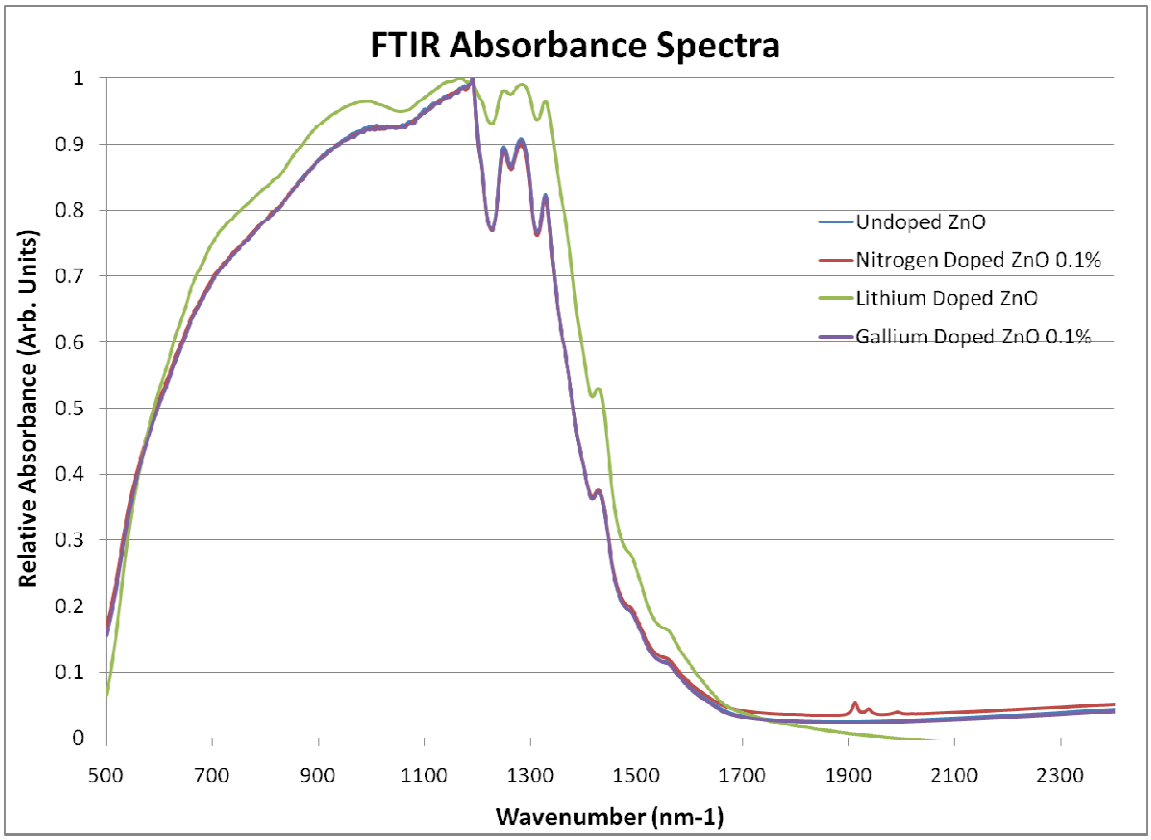

Figure 78 Specular absorption by FTIR. Spectra are dominated by the sapphire substrate.

Since the absorbance spectra are dominated by the sapphire substrate, little information can be gathered from this measurement. More detailed information can arise from the diffuse reflectivity measurement since it observes the impact of only the first few hundred nanometers on the reflection. Gallium and nitrogen are compared to undoped ZnO in Figure 79. These production scintillators were 10 µm thick samples. One can notice the large depression around 628 nm^{-1}. This is the characteristic ZnO line. The incorporation of hydrogen passivates the shorter inverse wavelengths, and depresses the 600-628 region of the reflectance spectra. Using the FTIR diffuse reflectance measurements in addition to the PL characterization measurements, doping is in fact occurring.

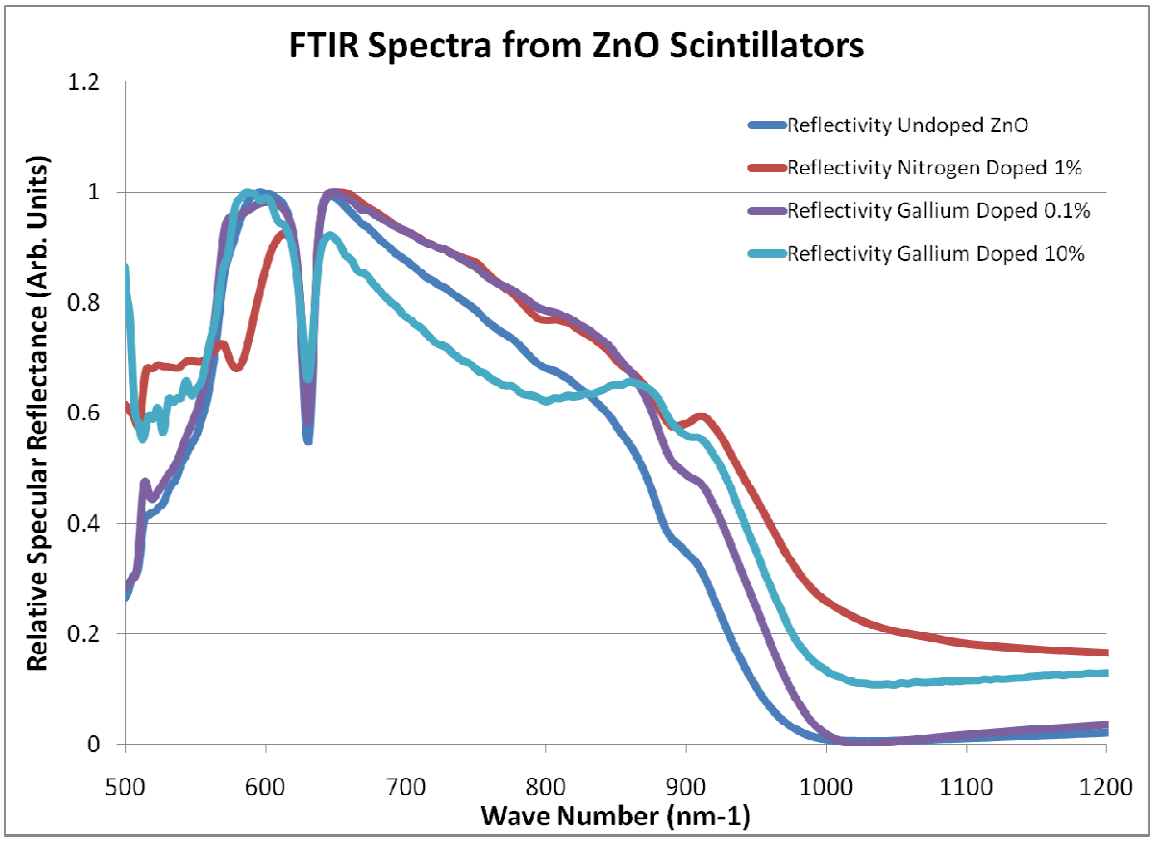

Figure 79 FTIR diffuse reflectivity spectrometry results for the ZnO Scintillators doped with gallium and nitrogen.

CHAPTER VII

THE PHOTONIC CRYSTAL SCINTILLATOR

To further improve the performance of the ZnO scintillator a new concept was introduced, that of the creation of a photonic crystal scintillator. The photonic crystal scintillator is a realization and integration between cutting edge materials science, photonics and nuclear detection research. The discussion of the photonic crystal scintillator must start with its definition. A photonic crystal is a structure with alternating layers of dielectric materials with different indicies of refraction. These structures can be manmade or occur naturally.

One of the simplest, self-organized, naturally occurring photonic crystals is an opal. The iridescent color produced by the opal is caused by a lattice of nanoscale silica spheres producing a regular periodic face centered crystal lattice. Photonic crystals (PC) have been used in optical devices for many years. A photonic crystal is an aligned periodic array of dielectric or metallo-dielectric nanostructures that affect the flow of optical photons.

Another example in nature is the wing structure of swallowtail (*Palinurus nirus*) butterflies. These butterflies have dark wings with bright blue or blue-green dorsal wing bands or patches. As discovered by Vukusic and Hooper (102), they exhibit extraordinary directional emissive properties. The wing scales comprise a pigment-infused 2D photonic crystal (PC) that provides intense directed fluorescence, which is further directionally enhanced by a distributed Bragg reflector (DBR) placed behind the PC. In Figure 80, the *Palinurus nirus* butterfly wing is scanned with an SEM. Picture A shows the top view of the wing scale structure with the repeating periodic array of air holes. Picture B below it shows the side-on view of the Distributed Bragg Reflector (DBR) structure of the wing.

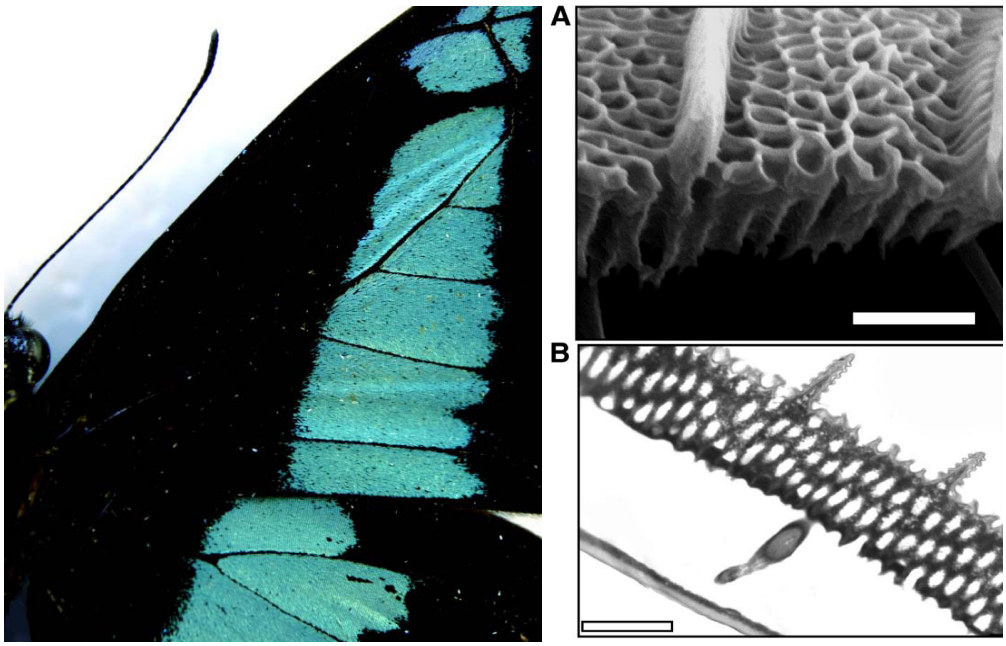

Figure 80 Wing of the *Palinurus nirus* butterfly. The blue-green color is created by a pigment that impregnates a periodic array produced in the scales of the wing of holes and scale material. Photo courtesy of (102).

In recent years, 1D, 2D and 3D photonic crystals have been realized and complex mathematical models created for modeling the flow of light. Photonic band gap (PBG) PC structures can be created to reject a range of disallowed wavelengths and/or allow only certain wavelengths to propagate. Additionally, 3D PCs can be used not only to control the wavelength of propagation while rejecting other wavelengths, but also to direct photons in a desired direction. All of these properties can be harnessed to improve the performance of scintillators in use today.

The optical properties of the butterfly wing suggest many applications for controlling light and extending the capabilities of scintillation detectors. If one considers using a relatively low dielectric constant scintillator material (doped ZnO with $n \approx 2$) in combination with a high dielectric material (silicon with $n>5$), one can design the PC slab to inhibit the lateral flow of photons within the scintillator. As a result of controlling the flow of light, one can produce slab or bulk scintillator structures which would be nearly

single-mode scintillators and improve light collection by preventing the lateral flow of light. With further enhancements, one can localize light emission to one or a few positions within each period of the repeating pattern using a defect mode to enhance light collection. Light from the scintillation process would no longer be emitted isotropically, but longitudinally focused in one direction, towards the light collection device. Thus, light intensity losses would no longer follow a $1/r^2$ term or be absorbed during multiple scatterings, but would exhibit closer to a 1/r light loss. By increasing light collection efficiencies it follows that scintillator efficiencies as well as the scintillator energy and spatial resolutions will be greatly enhanced. Using Finite Difference Time Domain (FDTD) analysis and Fourier modal analysis, structures can be designed to guide the flow of light in specified directions.

A second application is to investigate the use of a Distributed Bragg Reflector (DBR) in improving scintillator detectors. A DBR is a 1D photonic crystal structure that strongly reflects certain wavelengths of light over a wide range of incident angles. By coating the face opposite the light collection device 2D photonic crystal structure with a DBR, light would be reflected back to the collector. By using these strategies, the large photon gain from photomultiplier tubes are no longer needed and these fragile devices can be replaced by more compact, stable and robust light detection devices such as an avalanche photodiode (APD) or silicon photodiode, integrated with the photonic crystal structure.

The PC scintillator is the ideal candidate for neutron and heavy charged particle (HCP) scintillators. The photonic crystal structure based on the 2D array of repeating rods or holes in a material is ideally suited for large 2D planar arrays of thin neutron scintillating materials. Further improving its suitability for neutron detection, the structure can be grown on the same scale as the Bragg peak of the HCP track. In this Bragg peak, the most intense light yields are being produced at the end of the track,

where one can design a PC structure to guide the light produced. The dramatization of this can be seen in Figure 8.

Photonic Crystal Scintillator Theory

A photonic crystal is created by engineering alternating layers of different dielectric/index of refraction materials. The larger the difference in indicies of refraction, the better the photonic crystal's performance. The goal of the photonic crystal scintillator is to create a photonic band gap of wavelengths that cannot propagate in the plane of the photonic crystal. Inhibiting the lateral flow of light can improve the light collection by forcing more of the light to be collected by the APD or PMT.

A brief synopsis of the theory behind photonic crystals is presented herein. For a more exhaustive explanation of the process, the reader is encouraged to read *Photonic Crystals, Modeling the Flow of Light* by Joannopoulos (103). The following explanation is a summary of the process described in the book above.

In 1987 Yablonovitch and John (104)proposed that by spatially varying different dielectric materials, one could control the flow of light through light matter interactions. Optical light propagation in a material is dominated by the Maxwell's equations. In SI units the Maxwell Equations are shown in Equation 10.

$$\nabla \cdot B = 0 \qquad \nabla \times E + \frac{\partial B}{\partial t} = 0$$

$$\nabla \cdot D = \rho \qquad \nabla \times H + \frac{\partial D}{\partial t} = J$$

Equation 10 Maxwell's equations in SI units.

Here E and H represent the electric field and magnetic field respectively, D and B are the displacement and magnetic induction fields and ρ and J are the free charge and current densities. Since the composition of the materials do not change with time, ρ and J can be set to 0. In these materials, light can propagate but there is no source. If one

equates *D* to *E* and *B* to *H*, then it becomes possible to solve the equations in a similar fashion to other radiation transport problems posed in nuclear engineering. If D and E are broken into a series expansion (a Power series works well here as described by Bloembergen (105)) then:

$$\frac{D_i}{\epsilon_o} = \sum_j \epsilon_{ij} E_j + \sum_{j,k} \chi_{ijk} E_j E_k + O(E^3)$$

Equation 11 equating *D* to *E*

ε_o~8.854x10^{-12} F/m is the permissivity of vacuum. If one assumes the fields are small and linear, all the χ terms can be neglected. To simplify things further, one can assume the material is macroscopic (not atomistic) and isotropic. That relates *E(r,ω)* and *D(r,ω)* to ε_o multiplied by a scalar. This scalar dielectric function becomes $\varepsilon(r,\omega)$, which is traditionally called relative permittivity. Next, one ignores the explicit frequency dependence of the dielectric constant. Lastly, if we focus on only transparent materials, $\varepsilon(r)$ can only be positive and real. The Maxwell equations now can become

$$\nabla \cdot H(r,t) = 0 \qquad \nabla \times E(r,t) + \mu_o \frac{\partial H(r,t)}{\partial t} = 0$$

$$\nabla \cdot [\epsilon(r) E(r,t)] = 0 \qquad \nabla \times H(r,t) + \epsilon_o \epsilon(r) \frac{\partial E(r,t)}{\partial t} = 0$$

Equation 12 Maxwell's equations for transparent materials.

Similar to the neutron transport problem, these equations can be solved by separating the time and spatial dependencies. The limitation of this system of equations is that everything is assumed to be linear and lossless. Using pertebational analysis, one can solve for nonlinearities and different losses. In the current context though, this exploration is the domain for future work. To solve the above equations, we expand the separated solution in time and space into a series of harmonic modes which can be

calculated as a function of time. The harmonic modes separate the spatial profile into a complex exponential.

$$H(r,t) = H(r)e^{-ti\omega}$$

$$E(r,t) = E(r)e^{-ti\omega}$$

Equation 13 Complex exponential form of the electric and magnetic fields.

By substituting Equation 13 into Equation 11 leads to the two divergence conditions where H and E are found to be zero. To equate *H(r)* to *E(r)* one can use the curl equations.

$$\nabla \times E(r) - i\omega\mu_o H(r) = 0$$

$$\nabla \times H(r) - i\varepsilon_o \varepsilon(r) E(r) = 0$$

Equation 14. Curl equations to equate E(r) to H(r).

If one divides the bottom equation by $\varepsilon(r)$ and takes the curl, the equation decouples. Using the first equation one can eliminate *E(r).* By combining ε_o and μ_o into the speed of light in a vacuum, the result is an equation one can solve mathematically using simplistic computer codes. This combination results in the overall equation that must be solved:

$$\nabla \times \left(\frac{1}{\varepsilon(r)} \nabla \times H(r)\right) = \left(\frac{\omega}{c}\right)^2 H(r)$$

Equation 15 Master equation to solve for computing photonic crystal structures.

For the photonic crystal designer, solving these equations through this process has been grossly simplified by the creation of several computer codes which calculate these functions for us. Free computer codes such as MPB and MEEP are available to solve these equations for given structural parameters incorporated into $\varepsilon(r)$.

Photonic Crystal Scintillator Designs

There are three primary photonic crystal structural designs that are proposed herein. The photonic crystal structures proposed focus on ZnO scintillators grown over silicon rod or hole based structures. One consideration that must be understood is that while the photonic crystal structure improves light collection, it in turn lowers the amount of scintillator material at the projected end of the HCP tracks. A balance must be reached between the materials to make the photonic crystal scintillator and the scintillator material. The three designs proposed herein for the photonic crystal scintillator focus on silicon and doped ZnO scintillators. The first design is a period array of silicon rods and doped ZnO scintillator in a square array which can be seen in Figure 81. The second design is a periodic array of silicon rods and doped ZnO scintillator in a triangular array shown in Figure 82. The last design proposed is a modified honeycomb lattice of silicon rods and doped ZnO scintillators shown in Figure 83.

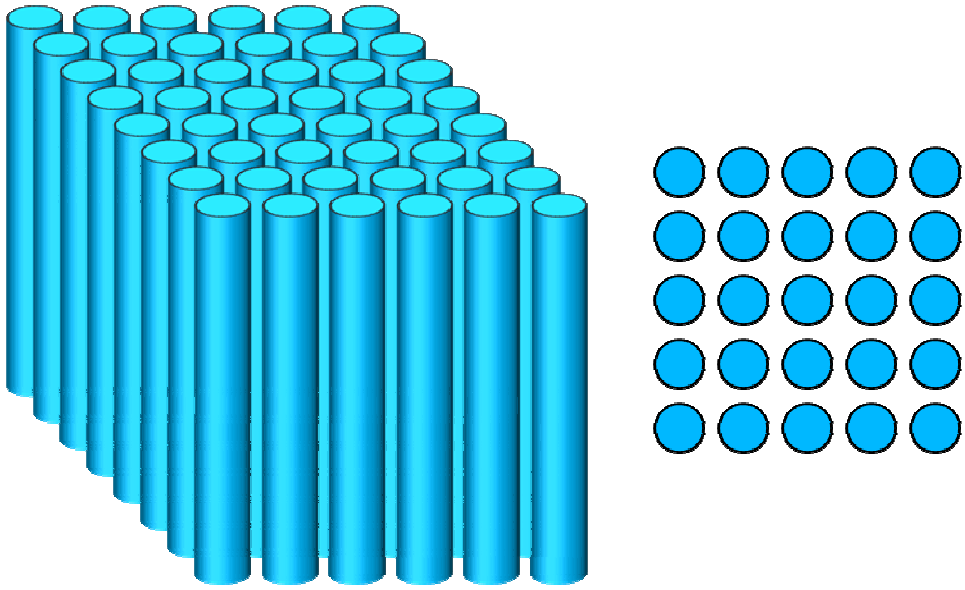

Figure 81 Square array of rods where the rods in blue are a dielectric material and the void space is filled with scintillator material. On the left is a three dimensional representation. On the right is the two dimensional representation of the same array.

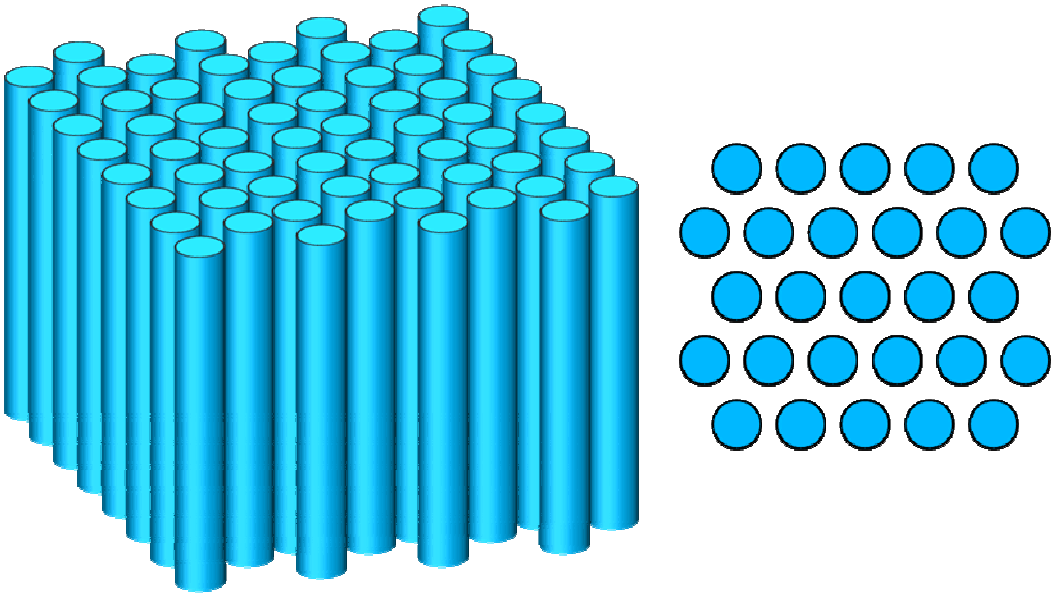

Figure 82 Triangular array of rods where the rods in blue are a dielectric material and the void space is filled with scintillator material. On the left is a three dimensional representation. On the right is the two dimensional representation of the same array.

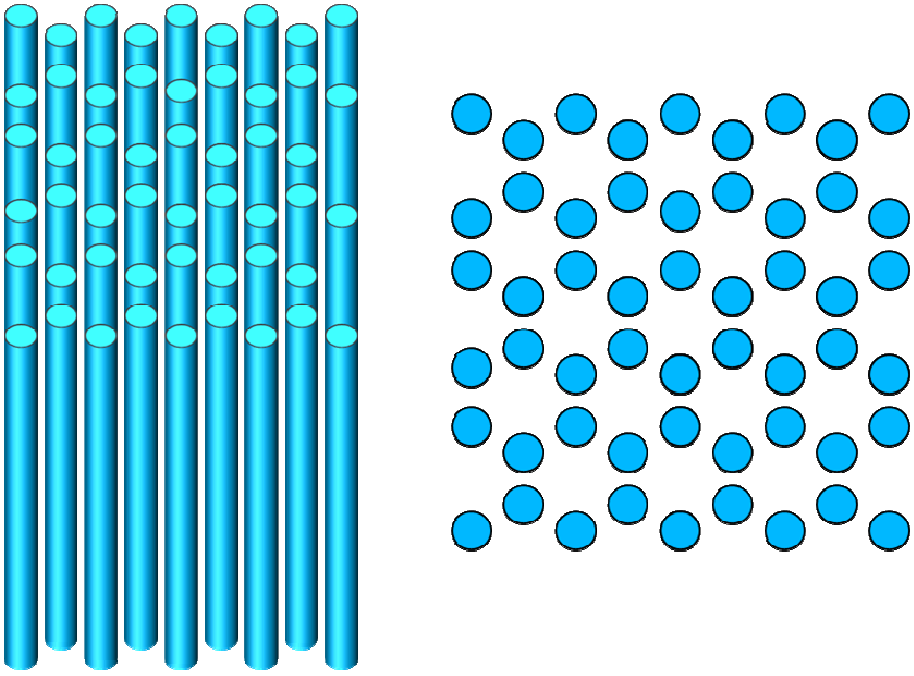

Figure 83 Honeycomb array of rods where the rods in blue are a dielectric material and the void space is filled with scintillator material. On the left is a three dimensional representation. On the right is the two dimensional representation of the same array.

When creating these designs, knowledge of the fabrication process is crucial. More exotic structures can be designed with very thin veins and small subtle features. The tolerance of these structures is highly dependent on the quality and uniformity of these features to maintain a full photonic band gap. The photonic structures that are needed to be created push the current technology of fabrication. Two dimensional slab photonic crystals, at the time of writing this dissertation, are usually fabricated in the red and infrared wavelengths. These wavelengths, 0.85μm and 1.5 μm are currently being used in optical communications such as fiber optic networking for computers. To conceptualize the photonic crystal scintillator requires working at wavelength scales down to 370-380 nm as opposed to 850-1550 nm. The feature sizes that are routinely used at the optical and infrared wavelengths are more than 2 to 4 times of those needed sizes for near UV scintillation light control. Also, current photonic crystal structures are grown on a relative thin substrate material such as silicon or silicon oxide. Thicknesses of 300 nm are common.

This size structure fits the needs of the optical communication world and proof of concept; however, to make a useful scintillator structure, significantly thicker structures are needed. Aspect ratios of 1000:1 or more are needed. The selectivity of the etching processes has improved in recent years, but still is limited and cannot produce perfectly etched structures. Vertical feature profiles must be maintained otherwise the light guiding mode of the structure will be destroyed. The feature size needed in a photonic crystal scintillator is too small for standard optical lithography. Electron beam or focused ion beam lithography is needed. The feature sizes described below even push the fabrication limits of the most advanced e-beam lithography and Bosch etching systems of today. Lastly, large index contrasts are employed by our counterparts in the optical communications relm by using silicon and air as the two dielectric materials. Bandgap differences of 5 to 6 are not uncommon. Using doped ZnO and silicon as the two dielectric materials, the bandgap creation is significantly more difficult.

The Square Lattice Photonic Crystal

The square lattice photonic crystal produces good quality transverse magnetic TM band gap structures. This is from the large electromagnetic wave concentration factor in the dielectric rods. TM band gaps were calculated for ZnO and silicon using MPB, or MIT Photonic Bands, a photonic crystal simulation computer code. This code can be programmed to iteratively search for the optimal rod thickness. The TM bandgap has been plotted against rod radius of the silicon rods. This can be seen in Figure 84. The wave modes can be seen in Figure 85.

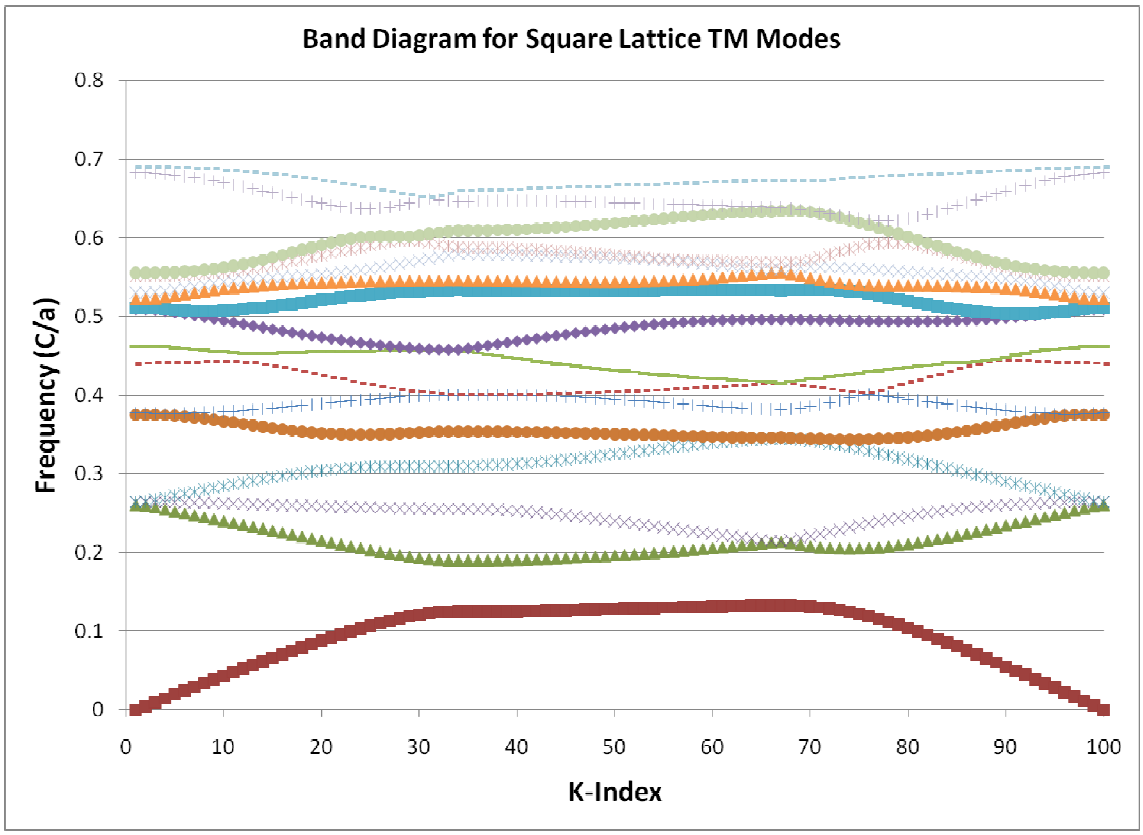

Figure 84 TM band gap calculation for a 800 nm silicon structure on a sapphire substrate with a zinc oxide interface above. The structure is for silicon rods in ZnO.

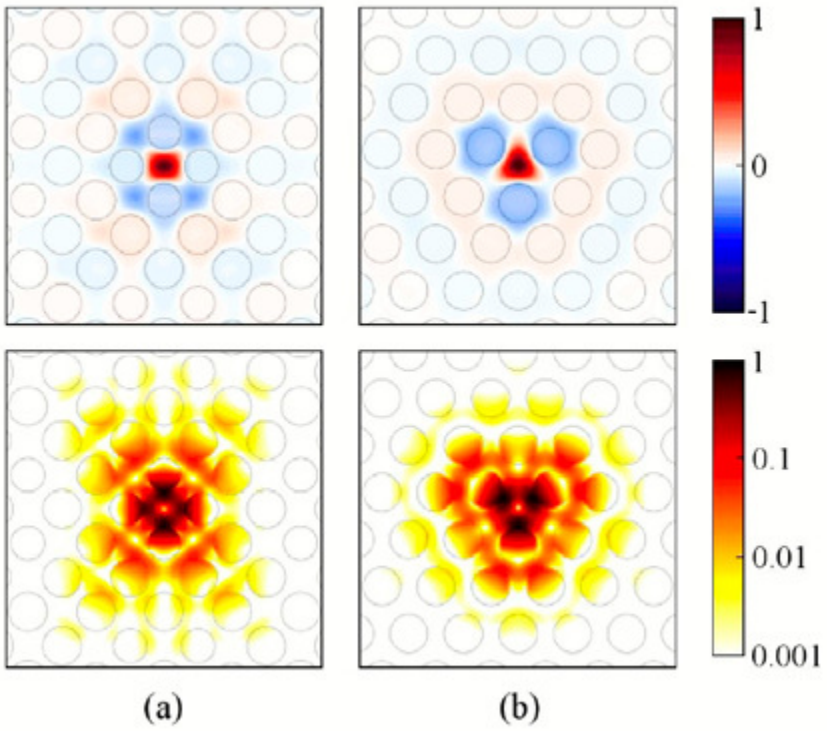

Figure 85 TM band calculations showing the first four band localizations. I need to re-generate this figure. It has been mangled.

The square band structure can be taken to the next extreme by patterning the shapes into long thin veins. The long thin veins in a square pattern allow the magnetic field to concentrate in the dielectric material. This concentration allows a large TM band gap to form. The more vein like materials in a slab photonic crystal, the more likely it is that one can produce a TM band gap by regulating the rod or vein thickness. Since the electric field cannot concentrate preferentially in the dielectric material as does the magnetic field components, no transverse electric TE gap is possible. A plot of the relative rod diameter for a square pitch structure and the corresponding maximum band gap percentage can be seen in Figure 86.

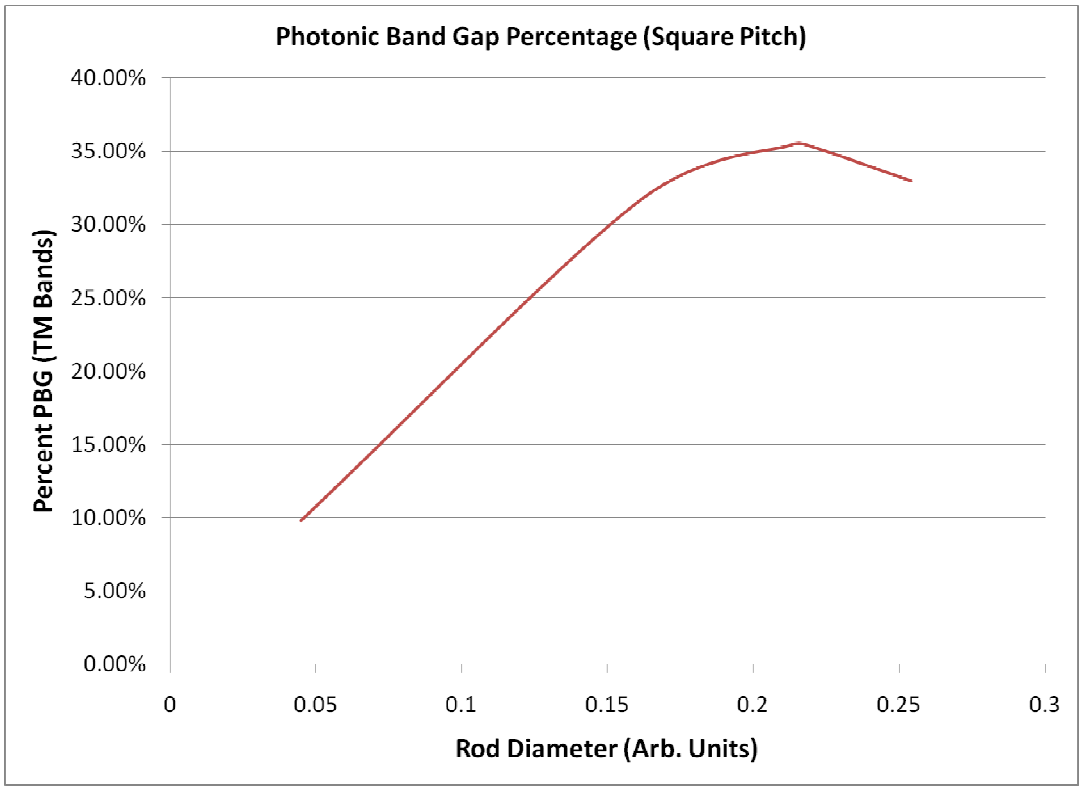

Figure 86 Photonic crystal band gap as a function of rod diameter for the square pitch of silicon rods.

The Triangular Lattice Photonic Crystal

The triangular lattice photonic crystal produces good quality overlapping TE and TM band gap structures because it combines the best of both the square lattice rods for TM modes and vein structures for TE modes. This is shown in Figure 87.

By introducing rod-like structures, and vein-like structures, both the TE and TM modes have regions in which they can concentrate. The electric component of the wave equation concentrates in the vein-like structure, while the magnetic component can concentrate in the rod-like component. The goal is to obtain a region where these two features overlap producing a full PBG. Once again, MPB was used to optimize the band gap structure. The band gap size versus rod diameter for the triangular pitch is plotted in Figure 88. The wave functions are plotted in Figure 89.

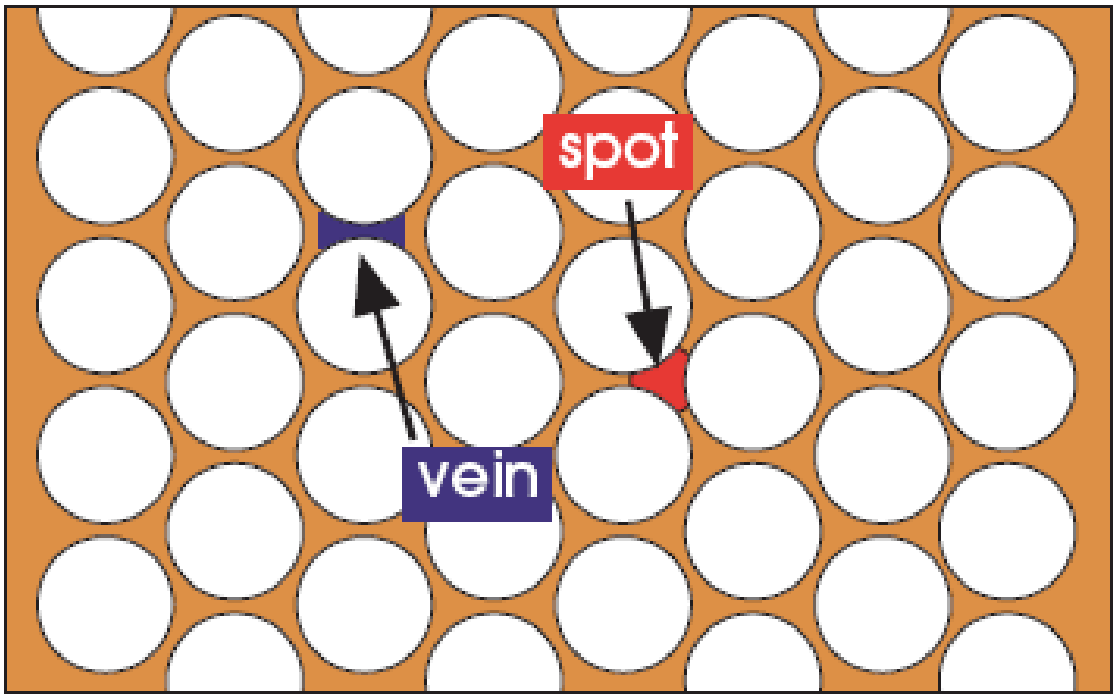

Figure 87 Triangular pitch photonic crystal showing the rod like and vein like components of the structure.

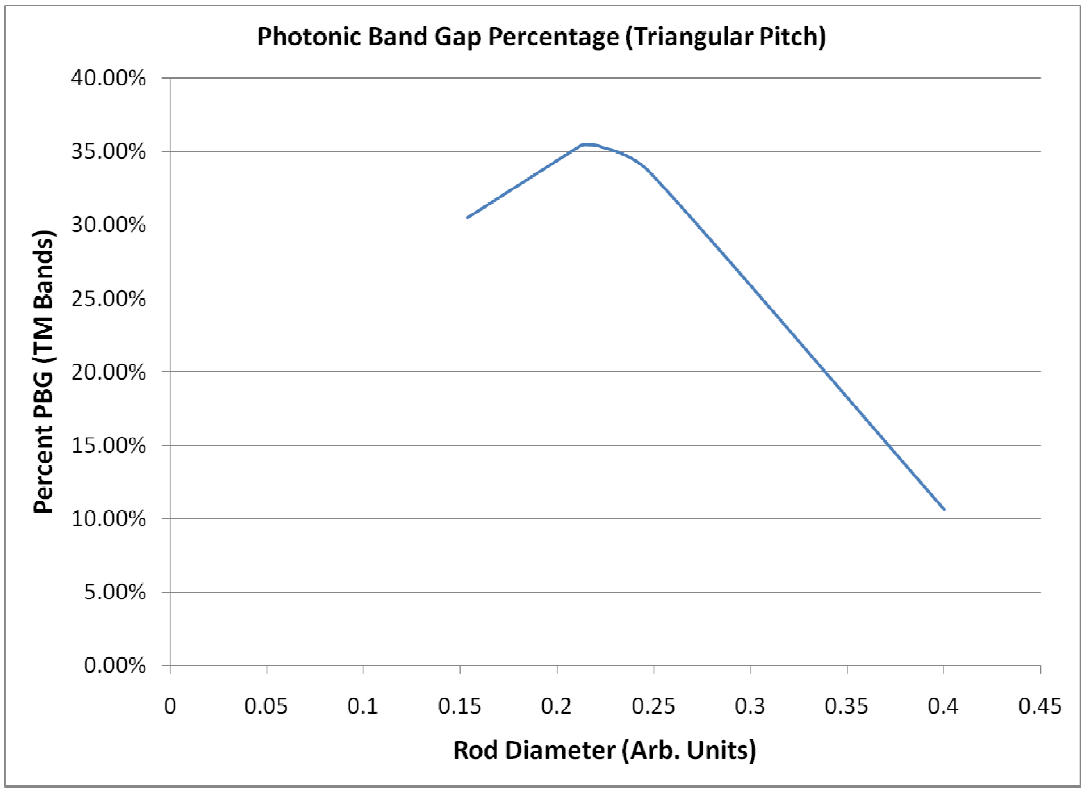

Figure 88 Triangular pitch photonic band gap calculations showing the rod diameter versus photonic band gap percentage.

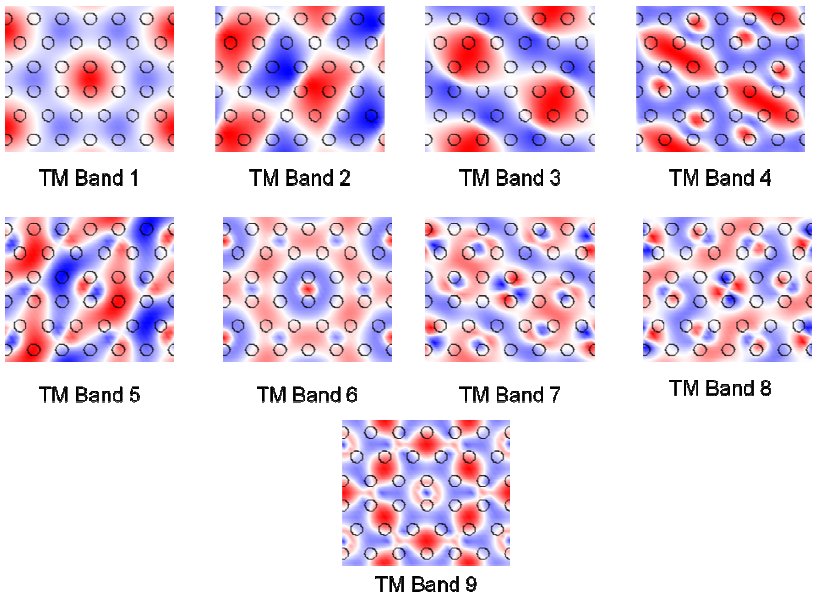

Figure 89 TM Band gap for triangular lattice.

If one considers an infinite slab of material with infinite thickness, with a very large difference in the indicies of refraction, such as silicon and air, a full PBG can be realized with this triangular lattice structure. However, when theory meets practical application for the photonic crystal scintillator, no full photonic crystal band gap is possible. When the delectric contrast is significantly smaller and the structure has finite thickness, only a TE or TM band gap can be achieved within a given frequency range. The results can be seen in Figure 90 below.

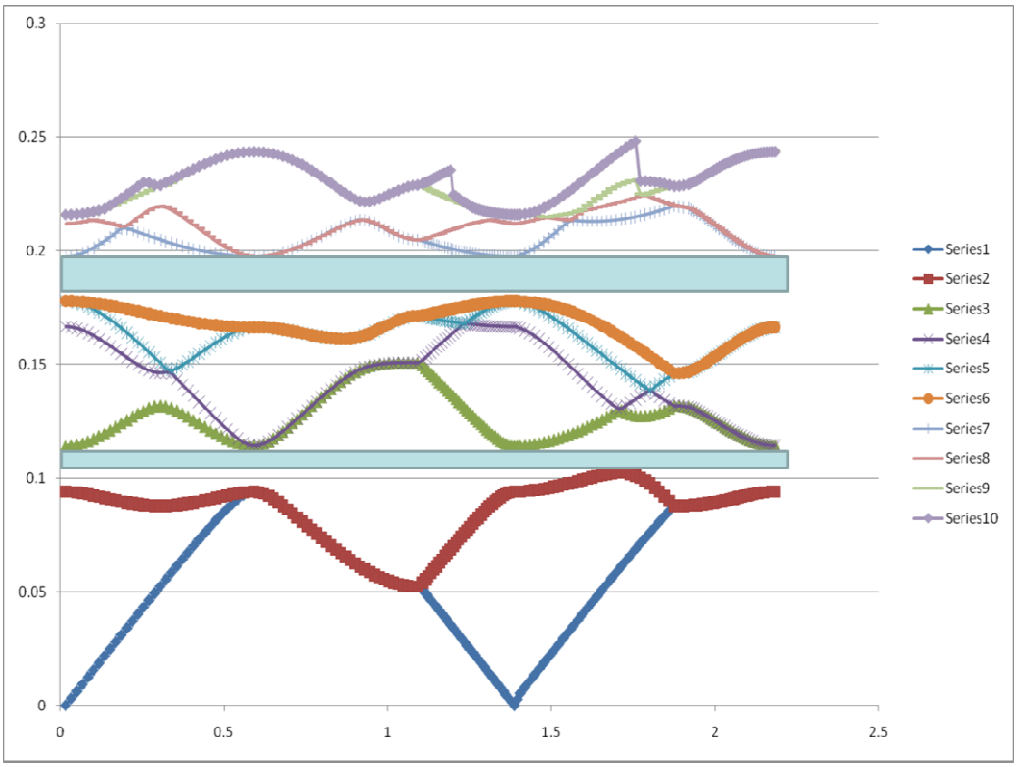

Figure 90 Triangular pitch PC structure with two small band gaps highlighted in blue.

The Honey Comb Lattice Photonic Crystal

The honeycomb lattice photonic crystal brings about circular symmetry and introduces a defect mode at every lattice constant. This can produce larger complete photonic band gaps, but in higher modes. Even under the limitations of current fabrication design and technology, this structure is feasible with the photonic crystal

scintillator. The band gap size versus rod diameter is plotted in Figure 91. The wave functions are plotted in Figure 92.

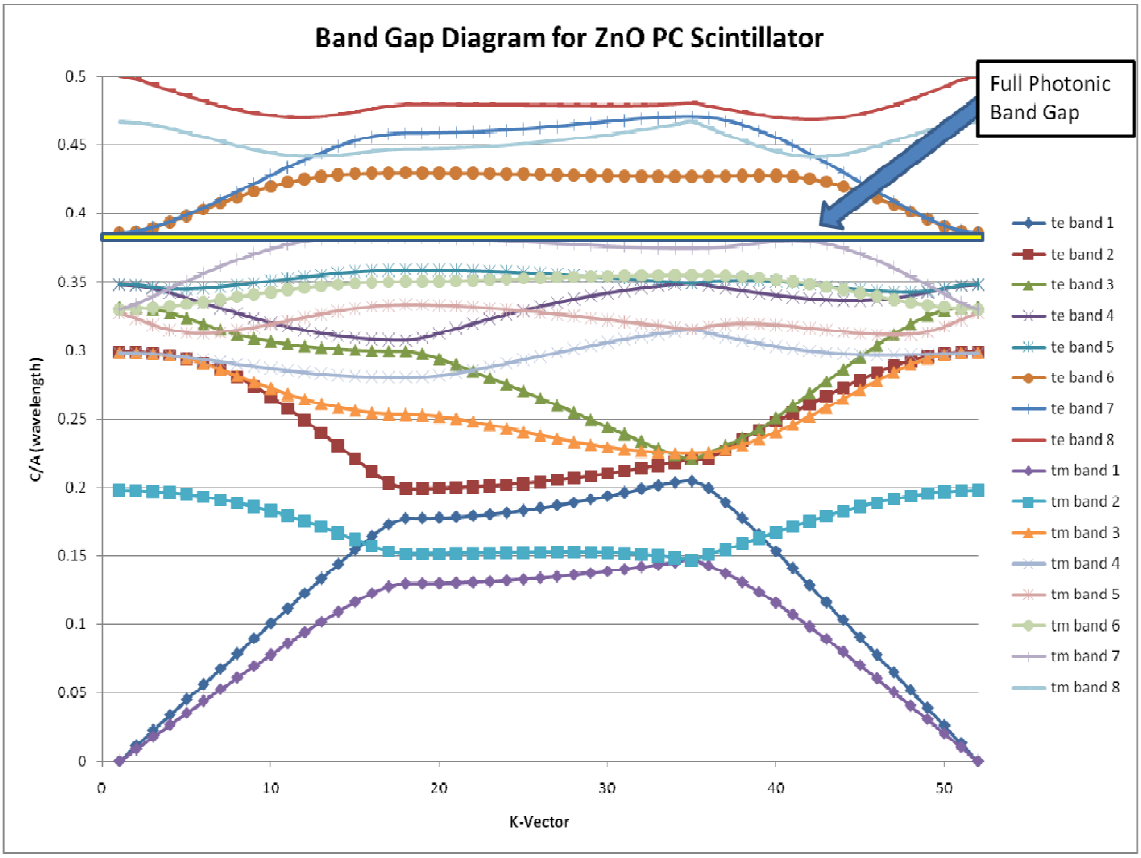

Figure 91 Full photonic band gap resulting from honeycomb lattice structure.

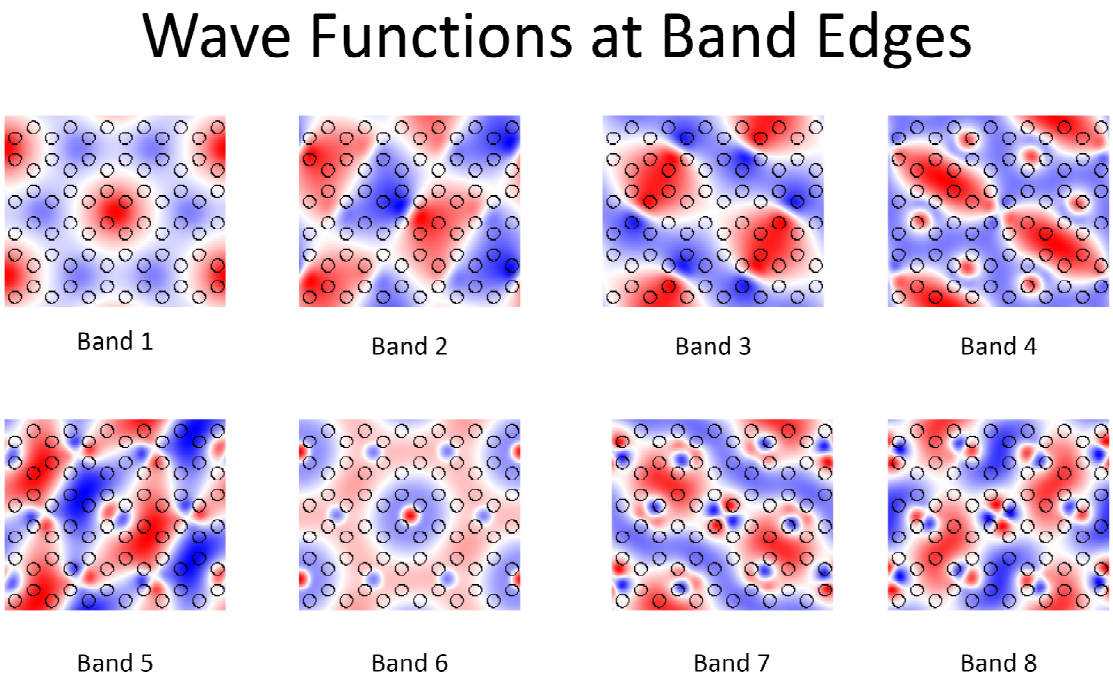

Figure 92 Wave diagrams for honeycomb photonic crystal lattice.

Lastly, one final structure is proposed which does not use the silicon rod structure. All that is used is the doped ZnO scintillator and air. In this process, the growth of the structure is inverted, and the conformal ^{6}LiF layer is applied first. ZnO is then grown over the ^{6}LiF structure. At the surface of the ZnO scintillator, an array of holes is etched into the surface. A triangular pitch was used to maximize the results. This method is advantageous since the ZnO is a more easily etched material than silicon and very high aspect ratio structures can be grown. The TE and TM band diagrams for these materials can be seen in Figure 91.

The first attempt at the of the photonic crystal scintillator was patterned from the triangular array of silicon rods and doped ZnO scintillator. The fabrication of this structure is quite complicated. First, silicon was evaporated onto the surface of a sapphire substrate using electron beam evaporation. Second, the photonic crystal structure was patterned on the silicon layer using a positive photoresist. The photoresist was developed using an electron beam photolithography technique. Positive photoresist

will resist the etching process and remain where the electron beam lithography system exposes the film. The electron beam lithography system is guided by a precise computer aided design (CAD) file created in Autocad or other suitable program. The silicon is etched off leaving behind an array of silicon nanorods.

The structures were patterned as an array of 25 µm x 25 µm square arrays of nanorods due to the limitations of the e-beam system. The e-beam system has an automatic proximity correction package installed to correct for astigmatism that is produced at the outside edges of a structure. Each small square must have it's own proximity correction, limiting the single array size that can be exposed during the e-beam lithography step. The photoresist that was not exposed to the electron beam is etched away with the silicon underneath using a newly patented Bosch etching process at Georgia Tech, whose details are not available for publication at this time.

Upon completion of the silicon etching, all that remains is a large array of silicon nanorods over a sapphire substrate. ZnO can now be grown on the surface of the structure using the pulsed ALD like growth recipes described above. The ZnO growth recipe was modified to use the ALD growth process initially for the first 100 nm. At which time the ZnO infiltrates the holes left behind by the silicon structures and it becomes a smooth surface again. A high temperature coalescence period was then cycled to improve the crystalline quality of the surface layer. The recipe was then converted over to a standard recipe and 2D growth was then resumed. This allowed for good infiltration into the pore structures. An SEM image of the square photonic crystal structure can be seen in Figure 93. While this structure is not designed for the near UV wavelengths of the PC scintillator, it is a good demonstration of the growth process. While the surface does exhibit nanorod like features, this is common of the nucleation and growth of the modified 3D-2D growth achievable with the current ZnO reactor.

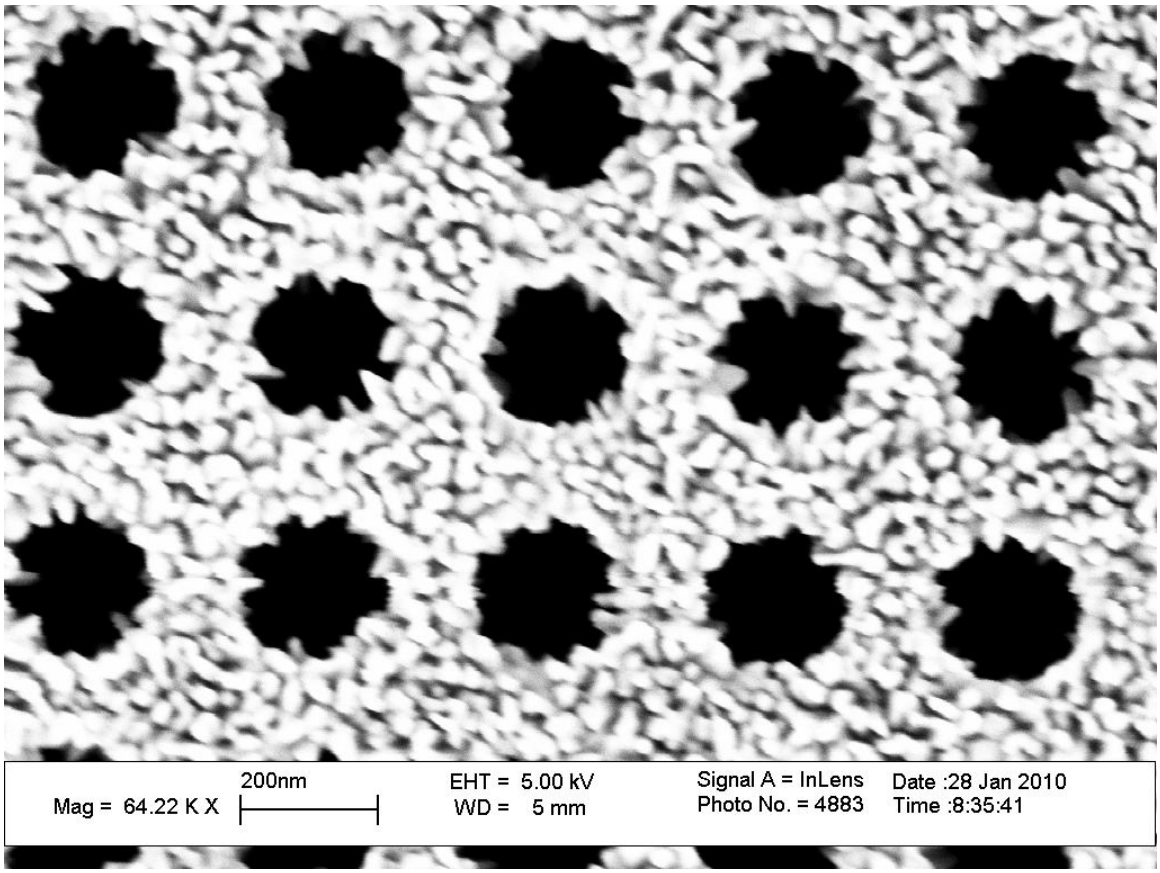

Figure 93 SEM of ZnO growth over PC square lattice structure. Nucleation is visible on the surface which is typical of the ZnO growth.

Using square lattice array photonic crystal structures designed for the green luminescence region, several initial tests were completed using PL spectra. Zinc oxide can create green luminescence due to defects described above starting on page 45. These oxygen vacancy defects can be used to test the photonic crystal scintillator design. Silicon on insulator samples was prepared by etching a square array into the silicon surface. An example of one of these grown PC scintillator structures can be seen in the SEM image above Figure 93. Since the sample was grown on silicon, alpha spectra collection, or neutron data collection is not possible. PL spectroscopy can be used however to ascertain the effectiveness of the system. The PL system was altered slightly to allow the activation laser to strike the PC structure directly. The PC structure was aligned directly with the aperture for the CCD monocrhrometer. The results are shown below for the green band luminescence. The tested results were for silicon rods

surrounded by zinc oxide as opposed to holes in silicon filled with zinc oxide which is shown in the SEM image above. The structures that were used were not optimized for the zinc oxide, silicon combination that was introduced, but still function with nearly a full TM band gap in the green. The increased light collection in the green is due to the photonic crystal enhancement. Shown in Figure 94 is the increased PL response of the PC scintillators. Two PC scintillator designs were tested, namely the silicon rods with zinc oxide infiltrated around the rod structures and silicon slab with holes infiltrated with zinc oxide scintillator. The zinc oxide recipe was slightly oxygen deficient to induce the green luminescence. Two samples grown on silicon and a standard recipe zinc oxide scintillator were included for comparison. The standard recipe on sapphire does not exhibit any GL. The two samples grown on plain silicon should be considered the baseline result for this test. The thickness of all of the samples tested was ~400 nm as indicated by surface reflectance measurements made by the Filmetrics tool. The rod structure does induce increased light outcoupling from 500 to 600 nm. The structure of silicon with holes filled with zinc oxide does show an increased response above 550 nm, but to a lesser extent than the rod structure.

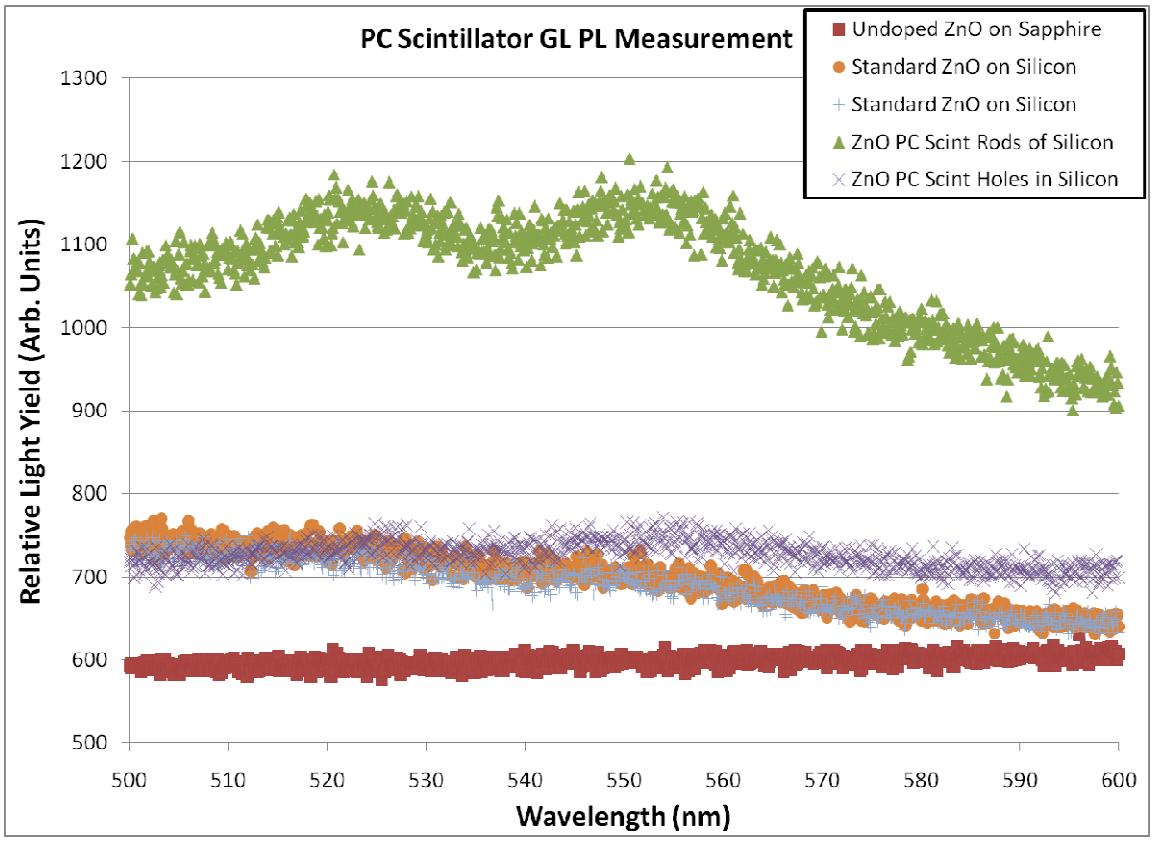

Figure 94 PC scintillator PL spectroscopy results showing improved GL for the silicon rods PC scintillator.

The GL band tests show strong promise for pursuing the UV band structures. The luminescence intensity is significantly higher for the UV band, and increased light outcoupling would be more intense. The final design should have 8 nm rods with 20 nm spacing between rods. With a vertical thickness of nearly 600 nm, this is a fabrication challenge. The initial fabrication tests yielded structures with many defects. Due to time limitations, a functional device in the UV was not able to be created before the submission of this work. However, using the designs described above, the groundwork is laid for the photonic crystal scintillator to be created in the coming months.

CHAPTER VIII

NEUTRON DETECTION PERFORMANCE

Several neutron detector tests were made using the doped ZnO neutron scintillators. The first was to measure the response of the ZnO neutron scintillators to high energy neutrons such as those directly from an (α,n) source. A ^{239}PuBe source of (α,n) neutrons was used. This free in air measurement for fast neutrons was recorded by a multichannel MCA and can be seen in Figure 95. This test was one of the first neutron tests done on this material. Undoped ZnO showed promise that a neutron versus gamma discriminating detector could be built. The next step was to design several MCNP models to test the ability of the system to detect neutrons.

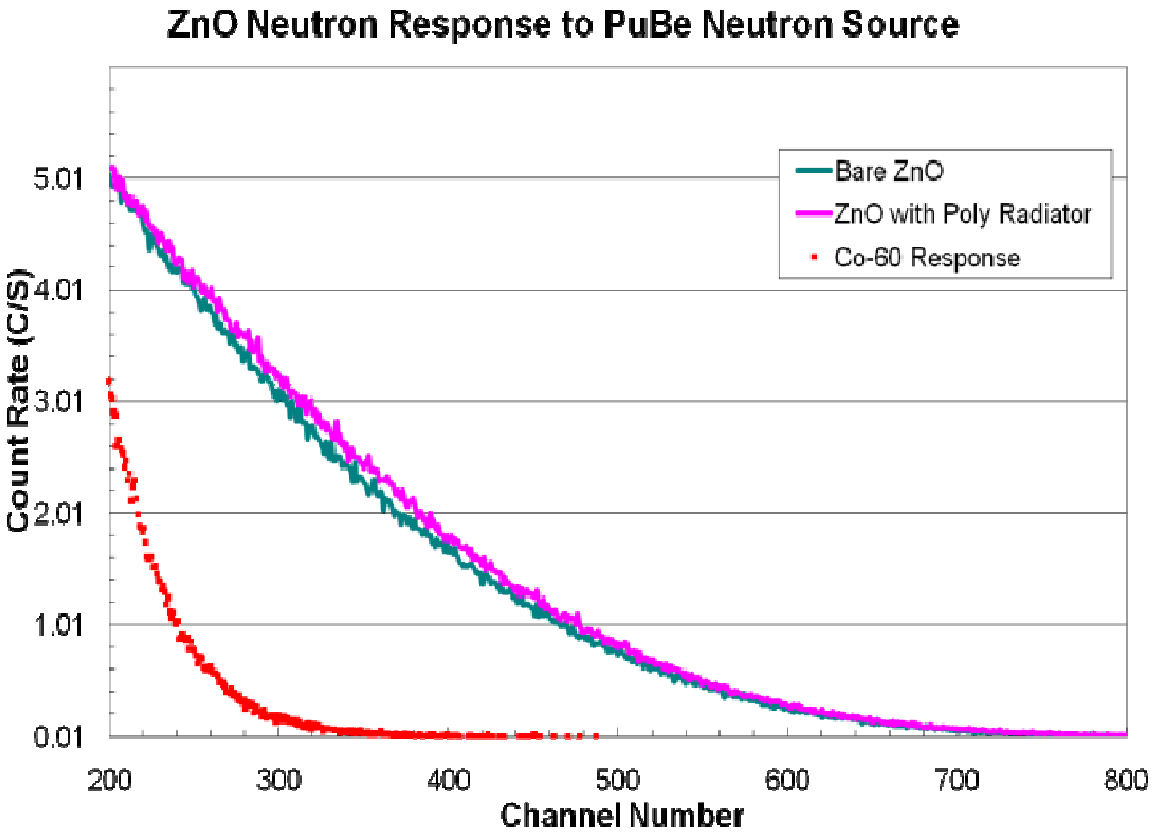

Figure 95 ZnO neutron detector response to fast neutrons.

MCNPX v2.7d was used to simulate the response of various scintillator configurations to both neutron and gamma ray fields. The energy deposition tally (F8) was used to correctly calculate the energy imparted to the scintillator. For neutron reactions, the neutron capture isotope algorithm (NCIA) was used to correctly produce the heavy charged particles resulting from the neutron capture reaction. This was done analog with neutron transport also analog in this energy region. F8 tallies were specified for photon/electrons, alphas, tritons, and protons separately. These were then summed outside the code and plotted via a 3D contour mapping package in GNUPlot (106). Configurations of just uniformly doped scintillators, stacks of 1 sided and stacks of 2 sided scintillators for a variety of thicknesses were run. For brevity, only the 1 mm samples are shown below in Figure 96 and Figure 97. The remainder of the configurations is shown in Appendix B. It was found that samples thicker than approximately 15 μm started to demonstrate compromised neutron versus gamma discrimination. At 0.5 mm, the signal from the gamma ray field emitted from a standard fission gamma spectrum is comparable to the signal from the (n,α) reactions in the scintillator. Above 1 mm the detector becomes overwhelmed by the gamma ray signal.

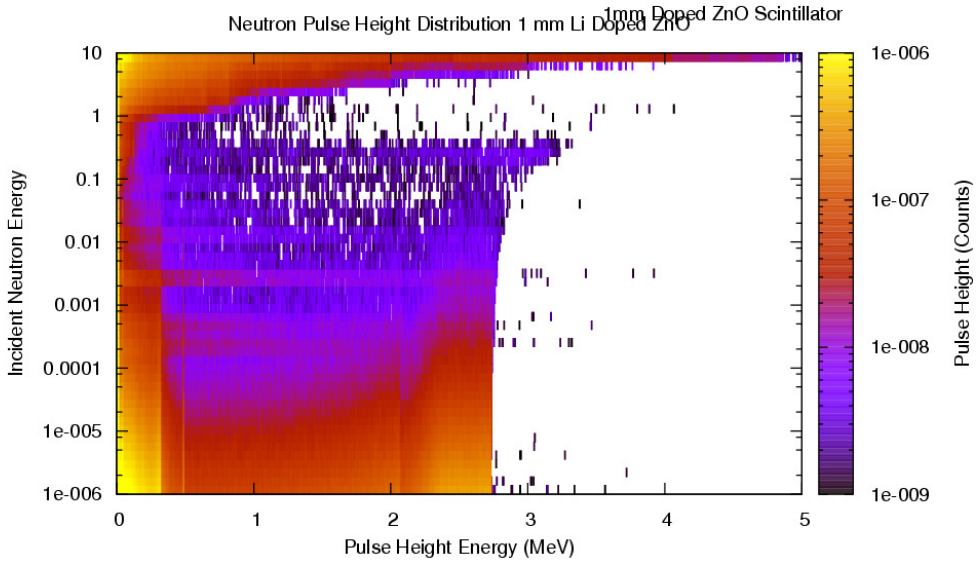

Figure 96 Pulse height distribution simulation resulting from neutrons incident on a 1 mm lithium doped ZnO with a 5 µm ^{6}LiF conformal coating.

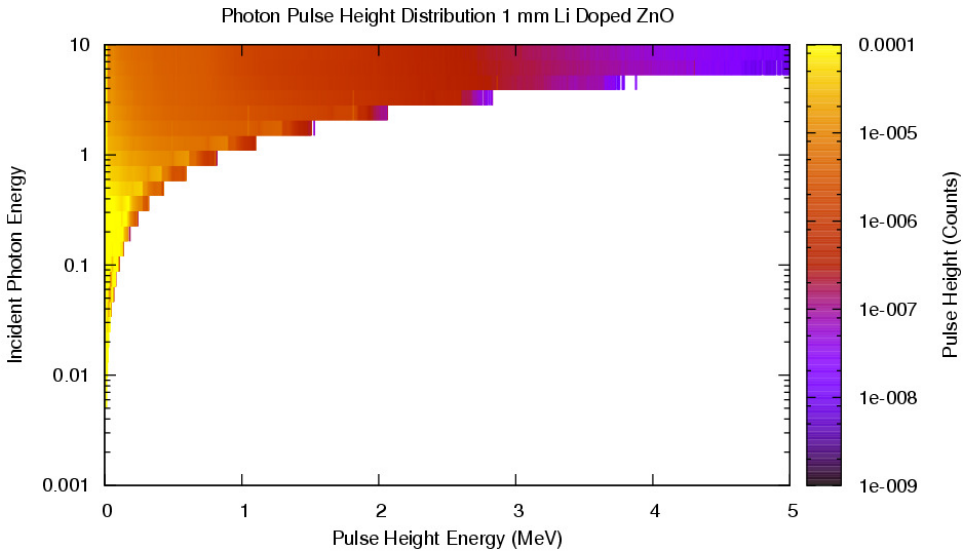

Figure 97 Pulse height distribution resulting from various photon energies in a 1 mm thick ZnO doped scintillator.

To adequately test the neutron detectors, several reference neutron detectors were needed. Four different reference detectors were used. The first is a standard ^{3}He tube from LND Inc. The tube has a 0.635 cm diameter and a 10.16 cm length. Pressurized at 2 ATM, the detector is a standard representation of a ^{3}He tube. The second reference detector is a ^{10}B lined gas filled detector. At 30.48 cm in length and 2.54 cm diameter, this is a good example of a lined detector. The third detector used is a $^{10}BF_3$ detector. This gas filled detector is 30.48 cm in length and 2.54 cm diameter and is a good example of a $^{10}BF_3$ detector. Lastly, a lithiated glass scintillator was used. This lithiated glass scintillator is 1.27 cm in thickness and 5.08 cm in diameter and is in the form of a right circular cylinder. These four detectors were selected because of their prevalence in commerce.

The two neutron sources were used for these tests. First, the ^{241}AmBe driven steady state graphite pile spectra will be presented. Later, the GSDS will be presented. The steady state graphite pile provides an excellent, simple testing ground for the thermal neutron detectors. The GSDS provides a means to select out energy responses.

For the lithiated glass scintillator, the characteristic in the pulse height spectra of note is the large (n,α) peak. In Figure 98, this peak centers around channel 215. To obtain neutron counts, one integrates under the peak and subtracts the integral of the background continuum. This can be done in the Maestro[2] software (107), or outside in a secondary data processing program.

For ^{10}B lined gas filled tubes, there is no discernable (n,α) peak. This is due to one of the particles routinely being emitted into the wall of the detector since the reaction is isotropic in the center of mass. Unless the incident neutron causing the reaction has a high energy, one particle will be emitted into the wall. The particle emitted into the wall does not produce useful ionization events. An example pulse height spectra can be seen in Figure 99.

---

[2] Maestro version 6.05 available from E.G.&G Ortec was used.

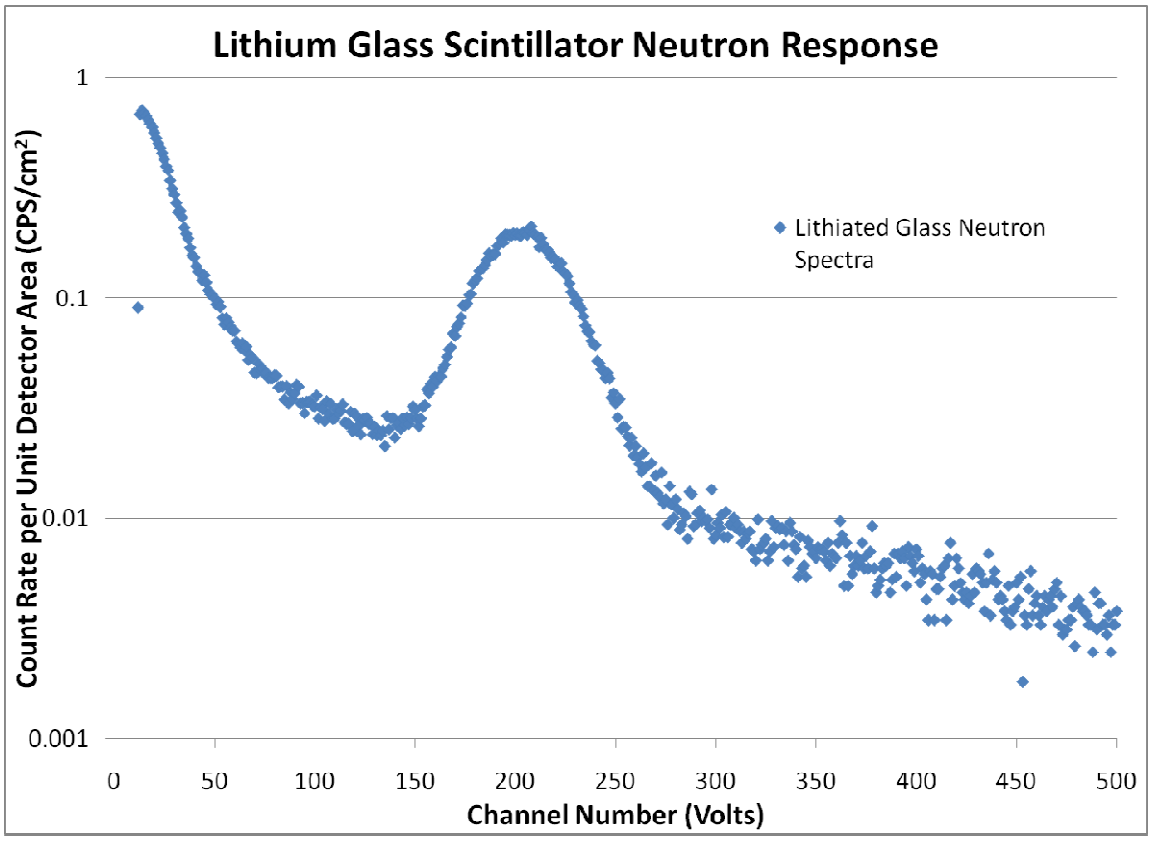

Figure 98 Reference ^{6}Li glass scintillator n,α pulse height distribution for thermal neutrons. The feature of note is the (n,α) peak centered at channel 215.

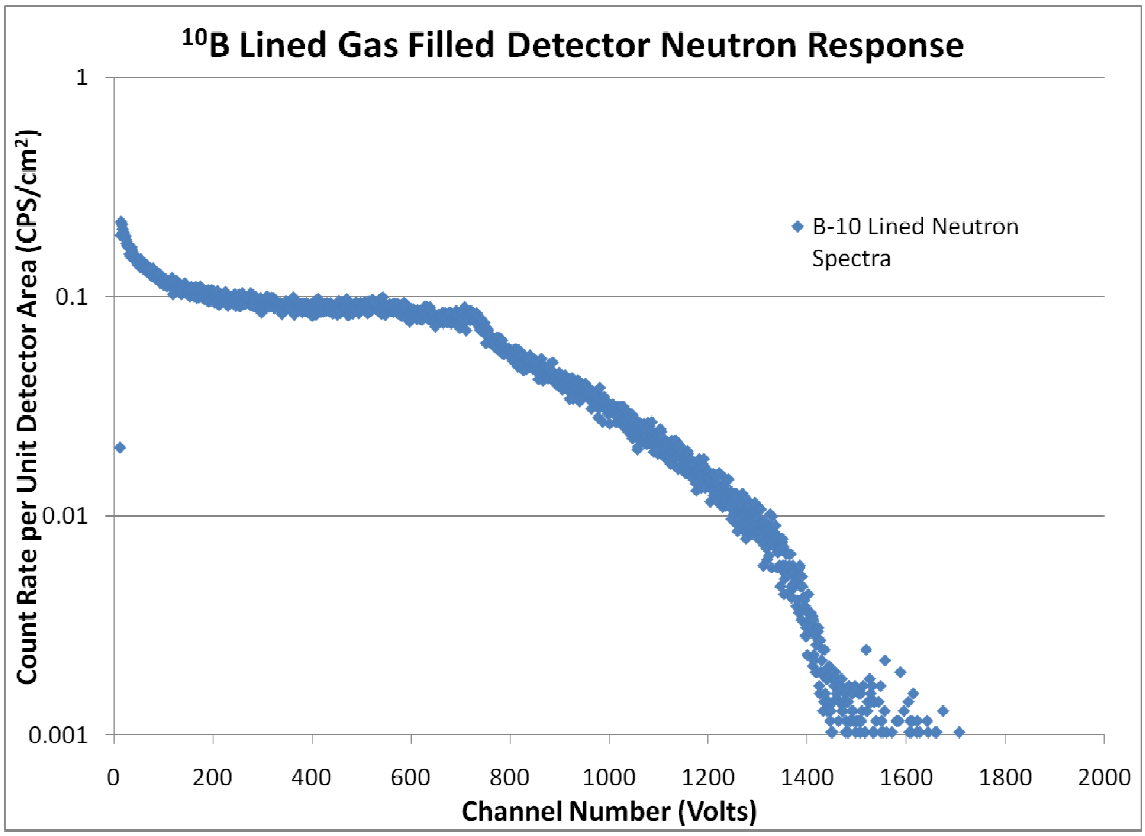

Figure 99. ^{10}B lined tube pulse height spectra.

Moving towards the next boron containing gas filled tube, one logically progresses to the $^{10}BF_3$ tube. The $^{10}BF_3$ tube has three unique characteristics to its pulse height spectra. The unique characteristics form the stair stepped spectra shown in Figure 100. Due to the low gas pressure in these tubes, it is a frequent occurrence that one particle will strike the wall and will impart a very small portion of its energy to the fill gas. The first step in the spectra is the recoiling ^{7}Li nuclei. The alpha particle in this step of the pulse height distribution strikes the wall. The second step is the alpha particle gets collected and the ^{7}Li nuclei strikes the wall. Lastly, the third distinct feature is the full energy collection peak which is the furthest to the right. This signifies a reaction which occurs near the center of the detector and both particles have deposited their energy in the fill gas. The wall effect can be clearly seen in Figure 100. Usually, there is a small second peak at a higher energy corresponding to the reaction branching to the ground

state of ^{7}Li. This is visible, but faintly due to the blurring of the spectra due to the tube's old age. This small peak can be seen around channel 900 of the spectra.

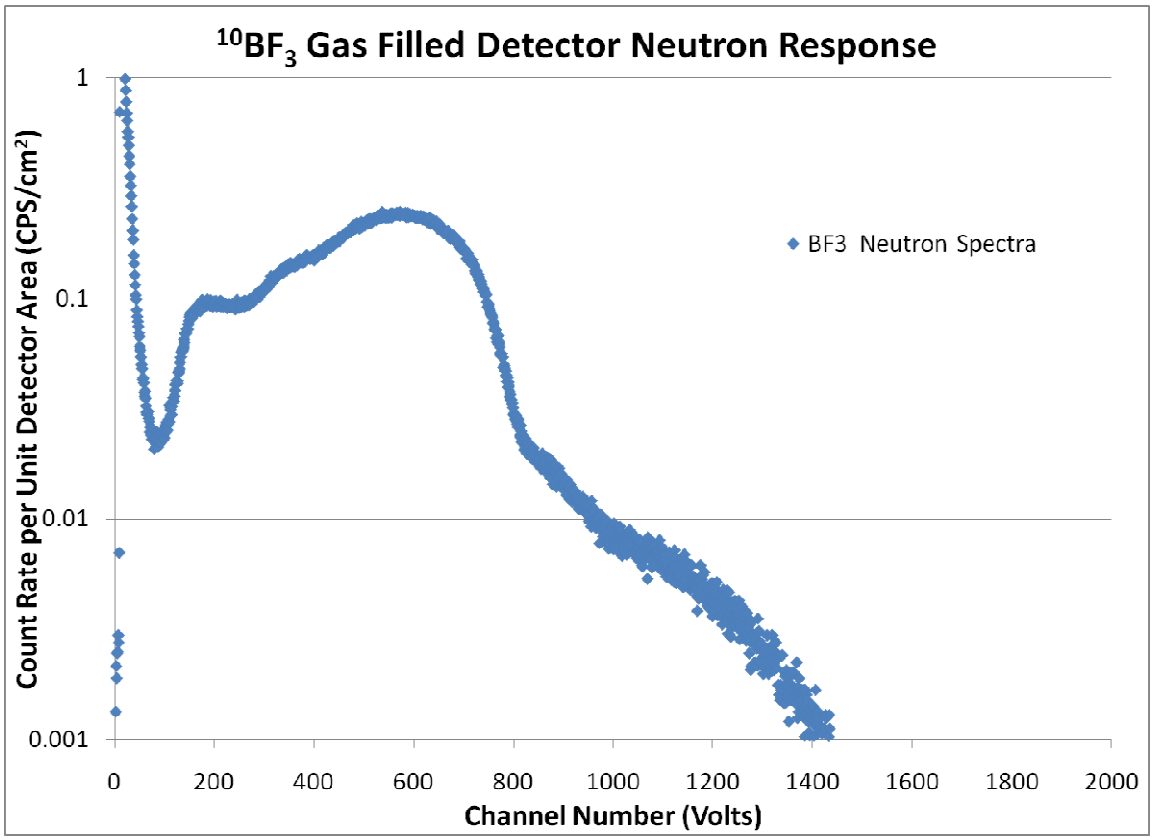

Figure 100 $^{10}BF_3$ tube pulse height distribution.

Lastly, a ^{3}He tube pulse height distribution for thermal neutrons is presented. The ^{3}He tube shows three unique features as well. The first is the continuum of the two charged particles produced in the reaction. This is between channels 300 and 900. Above that is the main full energy peak. ^{3}He tubes exhibit the wall effect similar to that of the $^{10}BF_3$ detector tubes do. The wall effect however is less stair stepped because both particles produced in the reaction have similar charges. The excellent neutron versus gamma discrimination is given rise from the fact the gamma pulse height distribution ends at channel 100 for the pulse height spectrum shown in Figure 101.

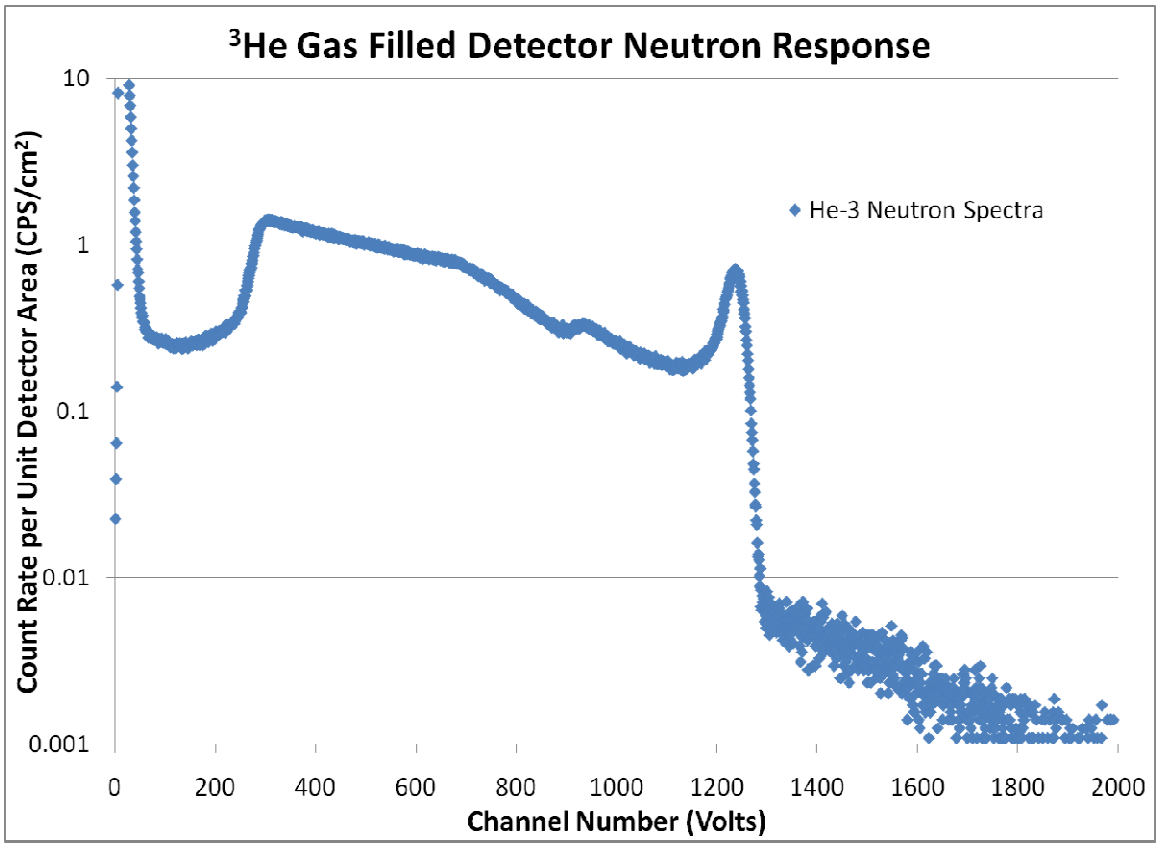

Figure 101 ^{3}He tube pulse height spectra.

The first novel neutron detector to be compared is boron doped ZnO. Boron was incorporated into the matrix during growth. The sample grown was via the MOCVD method. The sample was 6 µm thick and coated conformally with ^{6}LiF at 10 µm. The recipe that was used was a pulsed growth recipe which resulted in the most optically clear sample. This pulsed growth recipe of 20 sccm flow rate of TMB at a pulsed rate of 42:1. The sample exhibits a large peak which is discernable from the gamma radiation response. The detector's response can be seen in Figure 102 and Figure 103. The (n,α) peak is a combination of B and Li based reactions. Due to the thin size, the detector has good neutron versus gamma discrimination.

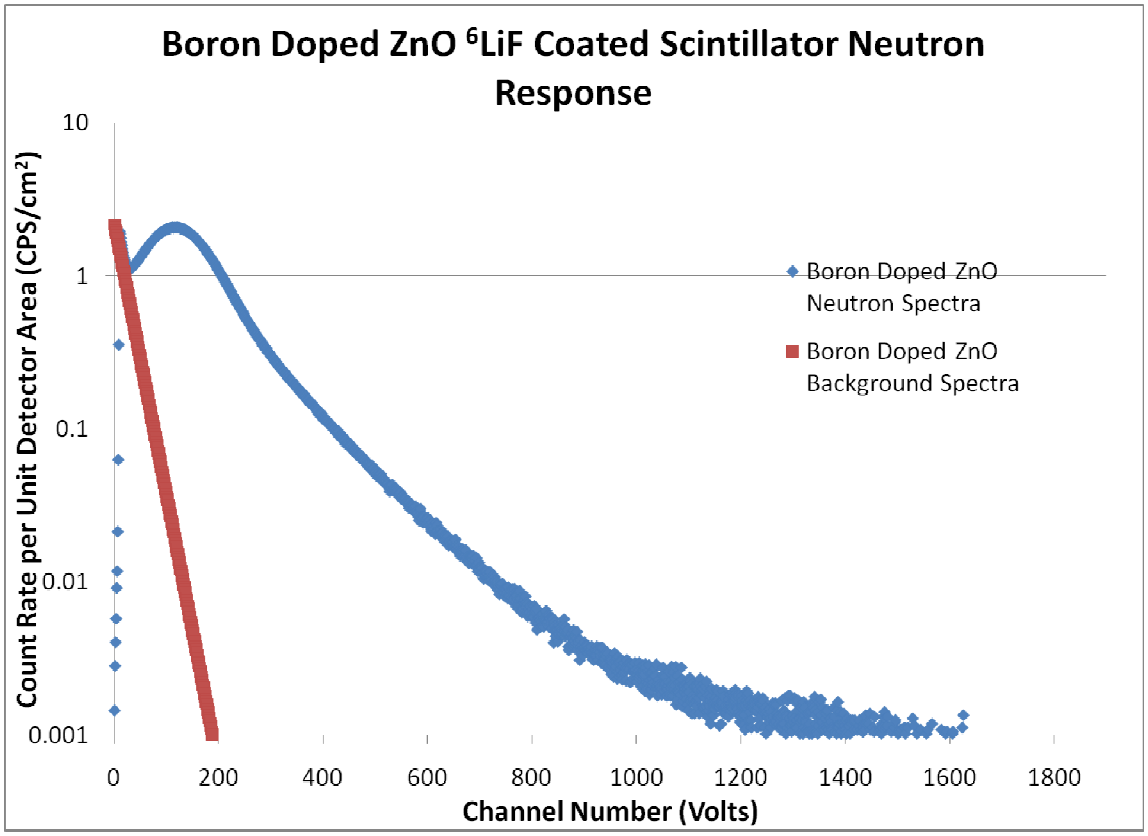

Figure 102 (n,α) spectra from ^{6}LiF coated B doped ZnO. The n,alpha peak is clearly visible. The vertical axis is logarithmic.

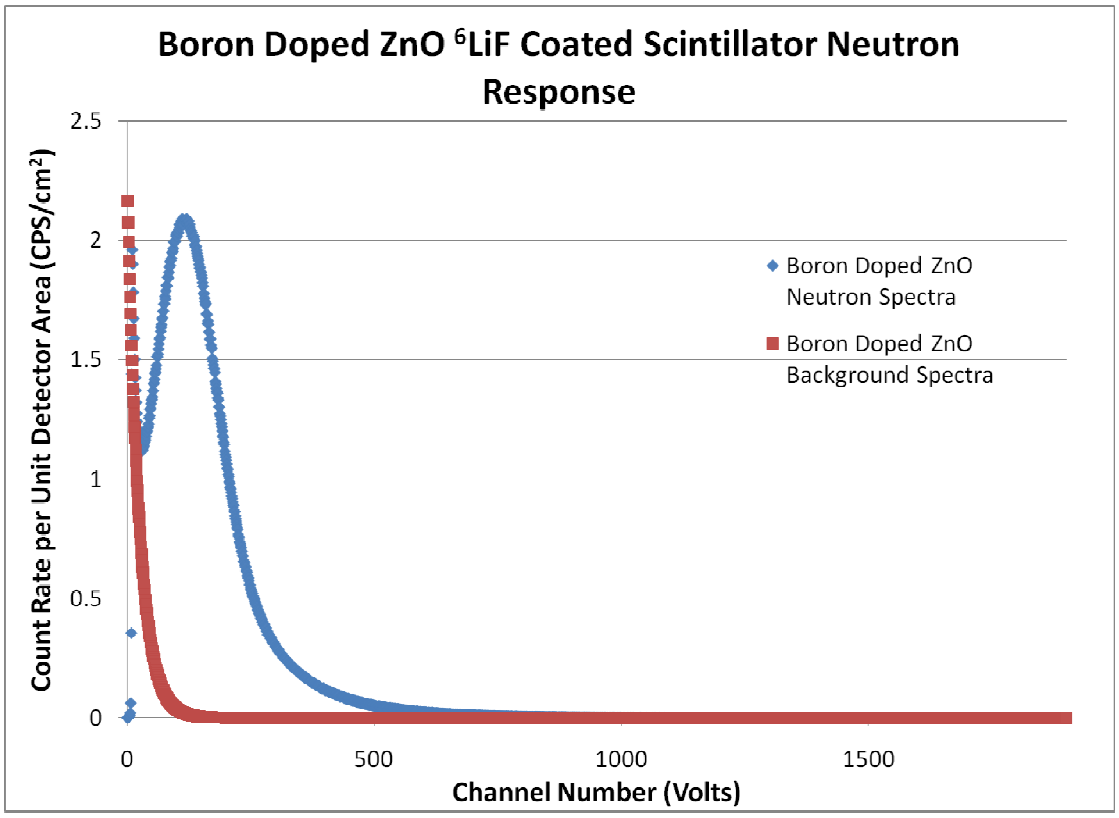

Figure 103 (n,α) spectra from ^{6}LiF coated B doped ZnO. The n,alpha peak is clearly visible. The vertical axis is linear.

Similar to the boron, lithium doped ZnO exhibits the characteristic (n,α) peak that boron and lithiated glass exhibit. The lithiated sample that was used in this test was an MOCVD grown sample with a thickness of 6.2 µm. A conformal coating of ^{6}LiF was applied over the surface with a 10µm thickness. The recipe that was used was a pulsed growth recipe which resulted in the most optically clear sample. This continuous growth recipe of 100 sccm flow rate of lithium cyclopentamadine. The sample exhibits a large peak which is discernable from the gamma radiation response. The detector's response can be seen in Figure 104and Figure 105. The (n,α) peak ^{6}Li based reactions. Due to the thin size, the detector has good neutron versus gamma discrimination.

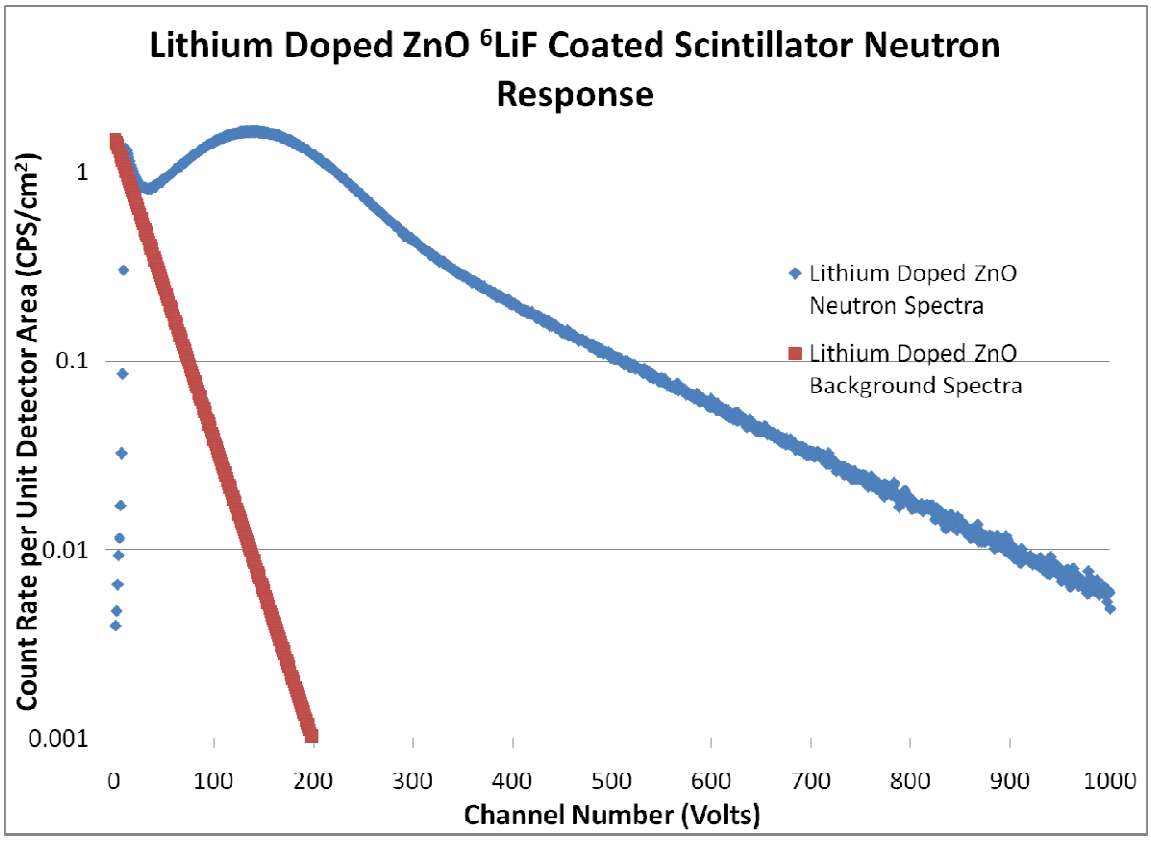

Figure 104 (n,α) spectra from ^{6}LiF coated Li doped ZnO. The n,alpha peak is clearly visible. The vertical axis is logarithmic.

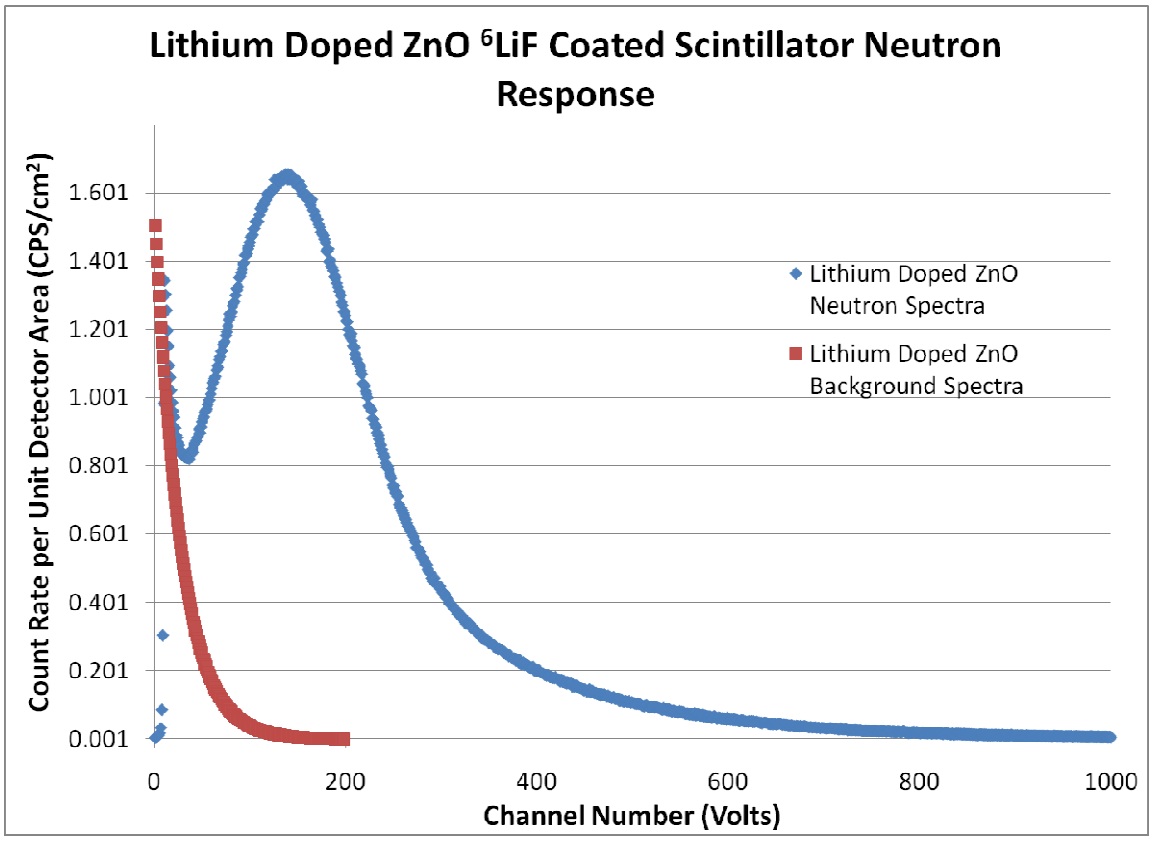

Figure 105 (n,α) spectra from ^{6}LiF coated Li doped ZnO. The n,alpha peak is clearly visible. The vertical axis is linear.

Out of the detectors grown, lithium and boron are the only two detector types which have neutron target nuclei directly in the crystalline matrix. This allows for most of the energy of both particles to be collected. A bulk growth sample was also tested. The result can be seen in Figure 106. A comparison between the two MOCVD grown samples can be seen in Figure 107. Lithium which is a clearer sample, had a lower dopant loading than the boron containing sample, mostly due to the volatility of the boron sample. Due to the growth of only ~6µm worth of ZnO, the material does not fully collect all of the energy of both particles. The count rate is significantly higher due to more reactions in a thicker sample as well as more of the energy being imparted to the material.

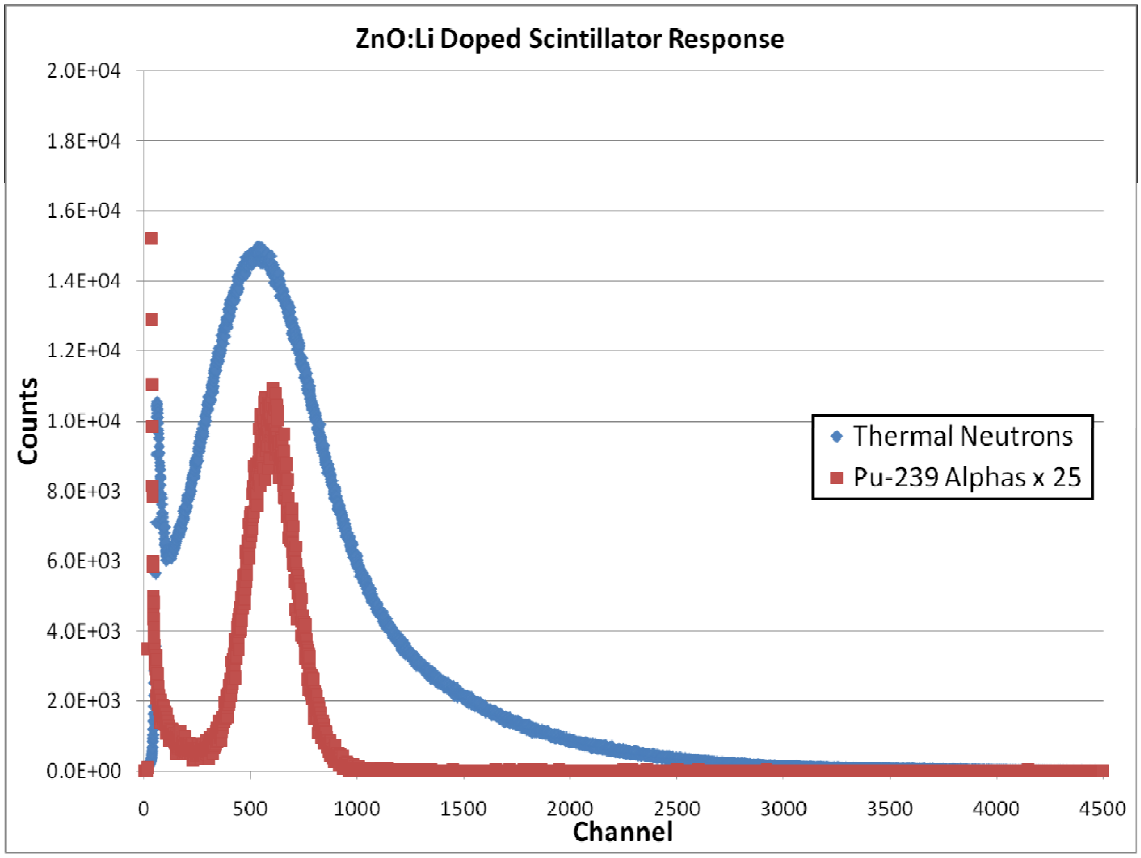

Figure 106 (n,α) spectra from Li doped bulk ZnO. The n,alpha peak is clearly visible. The vertical axis is linear.

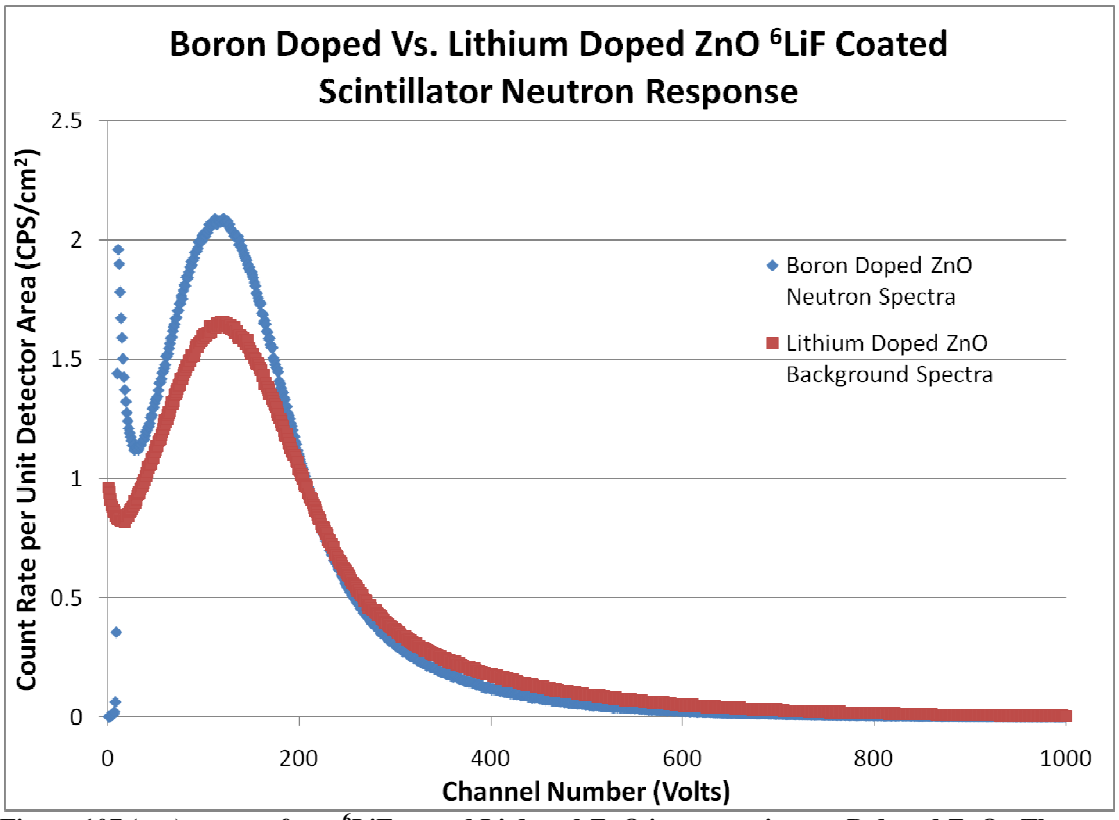

Figure 107 (n,α) spectra from ^{6}LiF coated Li doped ZnO in comparison to B doped ZnO. The n,alpha peak is clearly visible.

The remainder of the doped ZnO and undoped samples do not have neutron target nuclei in them, but they are still well suited for detecting neutrons. These samples were conformally coated with 10 µm worth of ^{6}LiF through an evaporative coating process. These samples can only collect one of the charged particles produced in the ^{6}Li (n,α) reaction due to the isotropic nature of this reaction in the center of mass. The remainder of the samples all resemble the ^{10}B lined tube pulse height distribution since it can only collect one of the charged particles.

First up is the aluminum doped ZnO sample. The AZO sample was 10 µm thick with a 10 µm thick conformal coating of ^{6}LiF. The AZO exhibits a lower pulse height distribution for the two particles which is expected due to its lower scintillation light output. The AZO pulse height distribution can be seen in Figure 108.

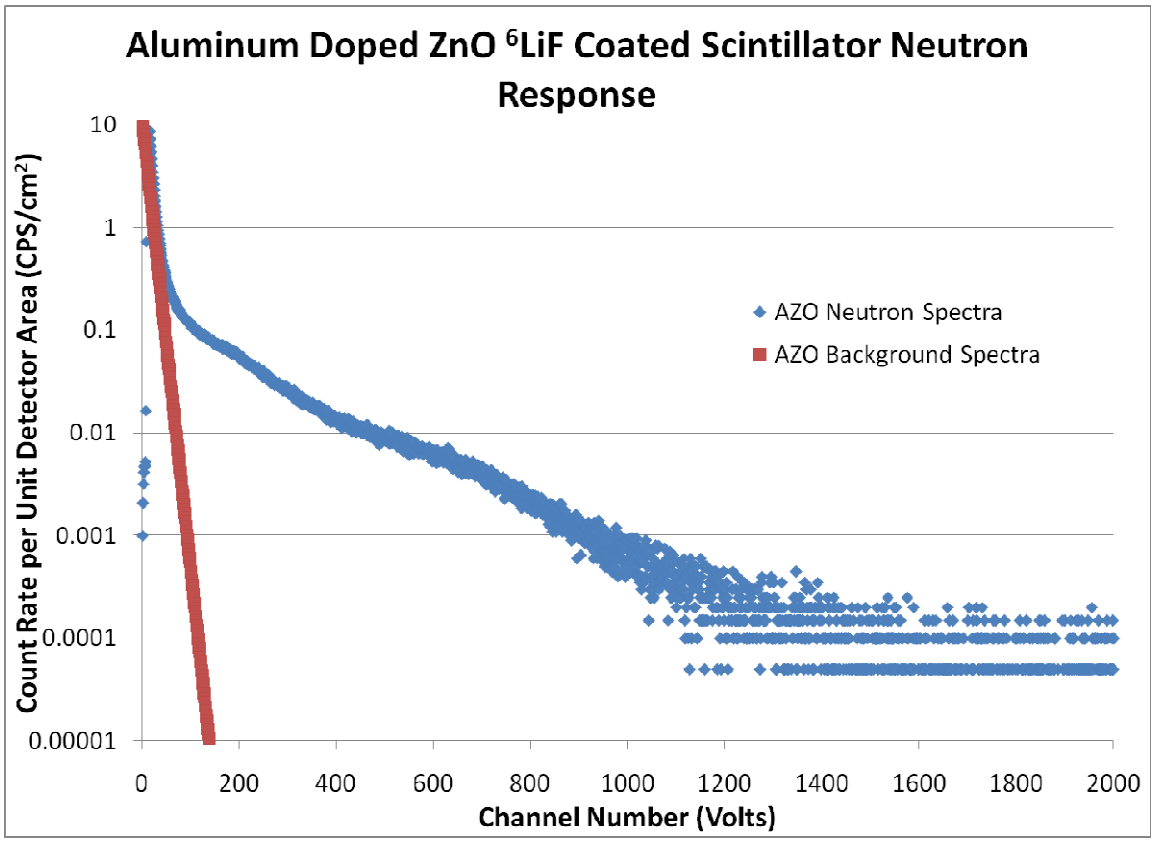

Figure 108 n,alpha spectra for simple coated ^{6}LiF structured AZO and the corresponding 100 mR/hr gamma ray field. Neutron versus gamma discrimination is still acceptable, however the alpha spectra has turned into a continuum which resembles a ^{10}B lined tube.

Gallium doped ZnO performed well with decent neutron versus gamma discrimination. The sample used was 8.1 µm thick with a 10 µm conformal coating of ^{6}LiF. The background 100 mR/hr gamma ray field is easily discerned from the neutron component of the spectra.

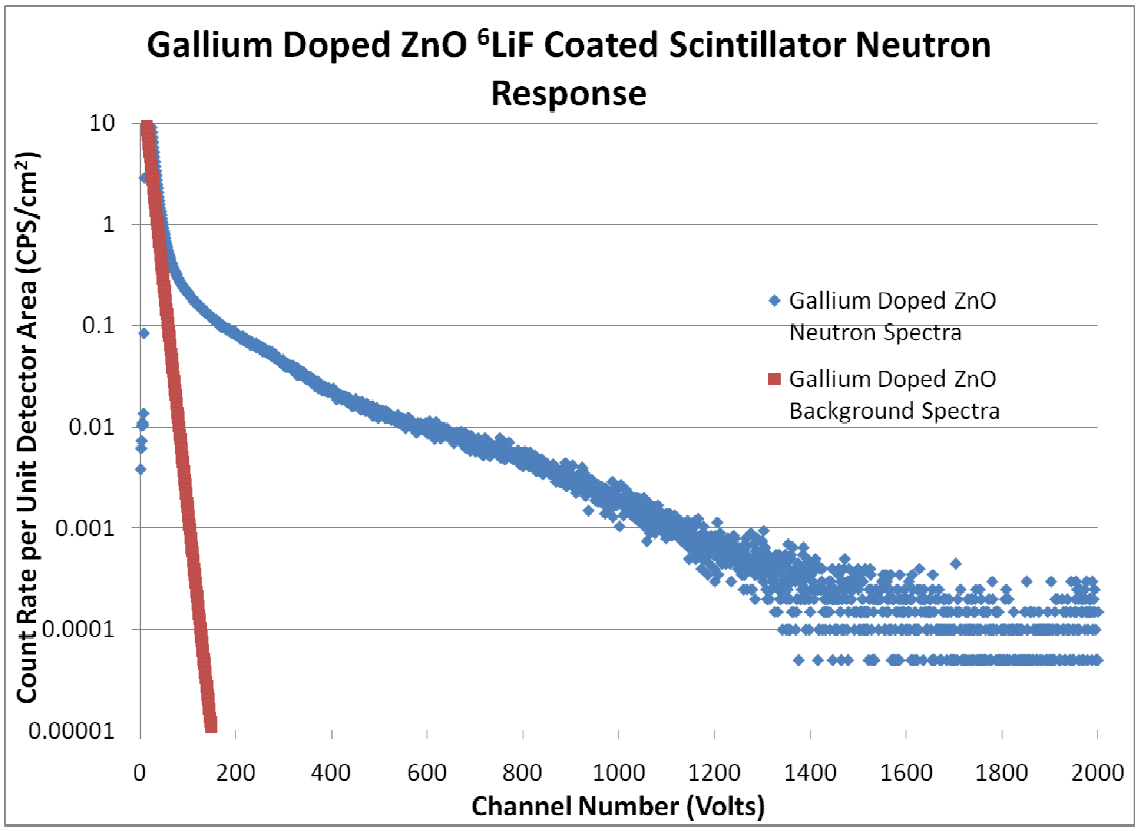

Figure 109 n,alpha spectra for simple coated ^{6}LiF structured gallium doped ZnO and the corresponding 100 mR/hr gamma ray field. Neutron versus gamma discrimination is still acceptable, however the alpha spectra has turned into a continuum which resembles a ^{10}B lined tube.

Nitrogen doped ZnO performed acceptably with decent neutron versus gamma discrimination. The sample used was 9.3 µm thick with a 10 µm conformal coating of ^{6}LiF. The sample was annealed for 5 minutes under an oxygen overpressure to remove some of the trapped hydrogen. The background 100 mR/hr gamma ray field is easily discerned from the neutron component of the spectra. The overall edge of the neutron alpha and triton reactions happen at a lower energy due to the significantly lower light yield from the hydrogen passivation. While the sample was clear, the lower light yield is not desirable in scintillator performance.

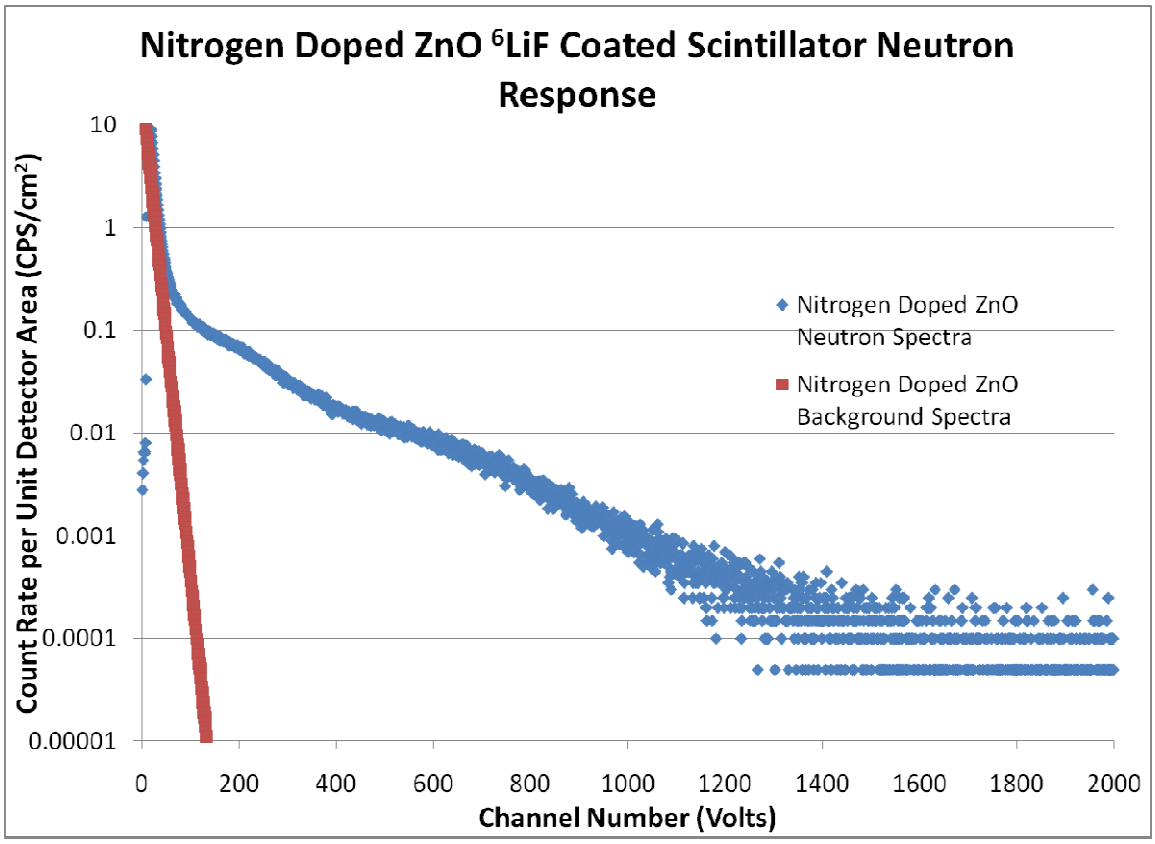

Figure 110 n,alpha spectra for simple coated ^{6}LiF structured nitrogen doped ZnO and the corresponding 100 mR/hr gamma ray field. Neutron versus gamma discrimination is still acceptable, however the alpha spectra has turned into a continuum which resembles a ^{10}B lined tube.

Undoped ZnO performed well with decent neutron versus gamma discrimination. The sample used was 6.4 µm thick with a 10 µm conformal coating of ^{6}LiF. Without doping, the ZnO crystal can be difficult to maintain optical clarity at thicknesses larger than 6 µm. The background 100 mR/hr gamma ray field is easily discerned from the neutron component of the spectra.

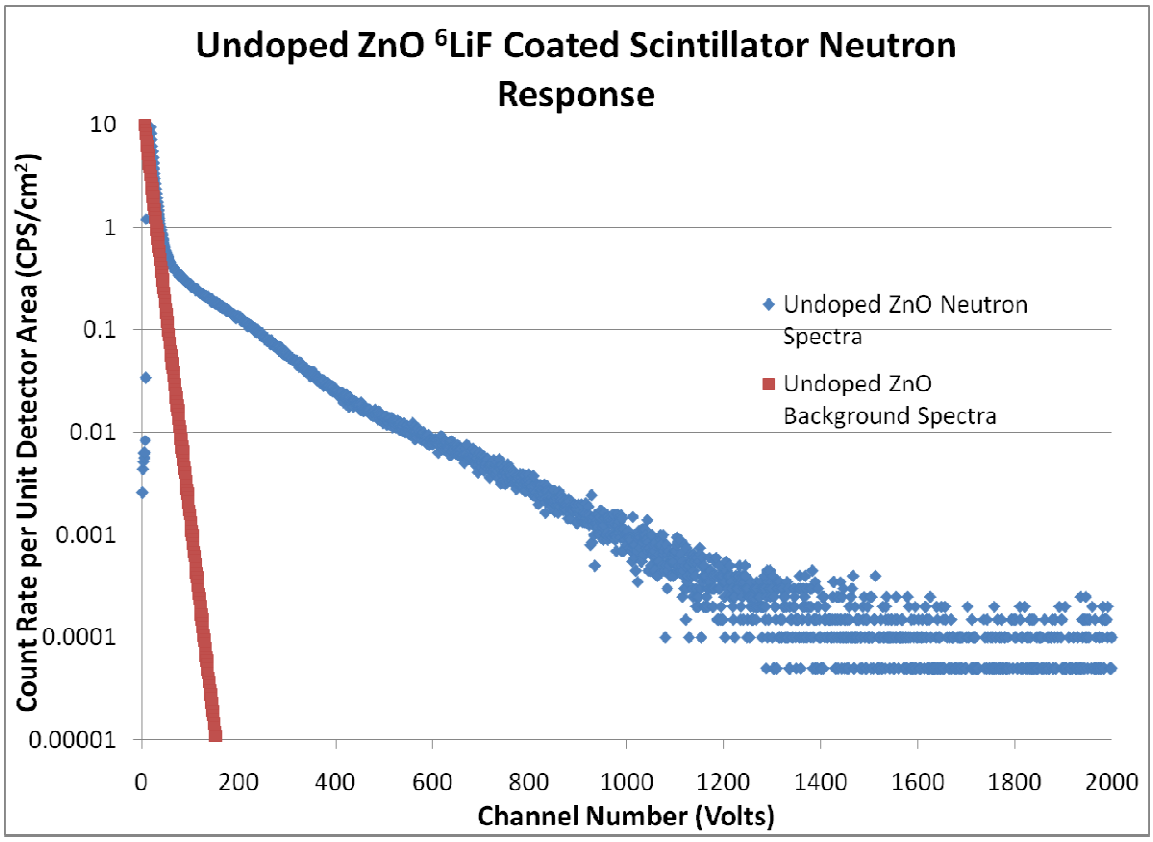

Figure 111 n,alpha spectra for simple coated ^{6}LiF structured undoped ZnO and the corresponding 100 mR/hr gamma ray field. Neutron versus gamma discrimination is still acceptable, however the alpha spectra has turned into a continuum which resembles a ^{10}B lined tube.

Gadolinium doped ZnO was also tested. Gadolinium samples were MOCVD grown. The gadolinium samples performed significantly worse than the other lithium doped samples, and exhibited poor neutron versus gamma discrimination. The sample used was 5.9 µm thick. The background 100 mR/hr gamma ray field is no longer easily discerned from the neutron component of the spectra.

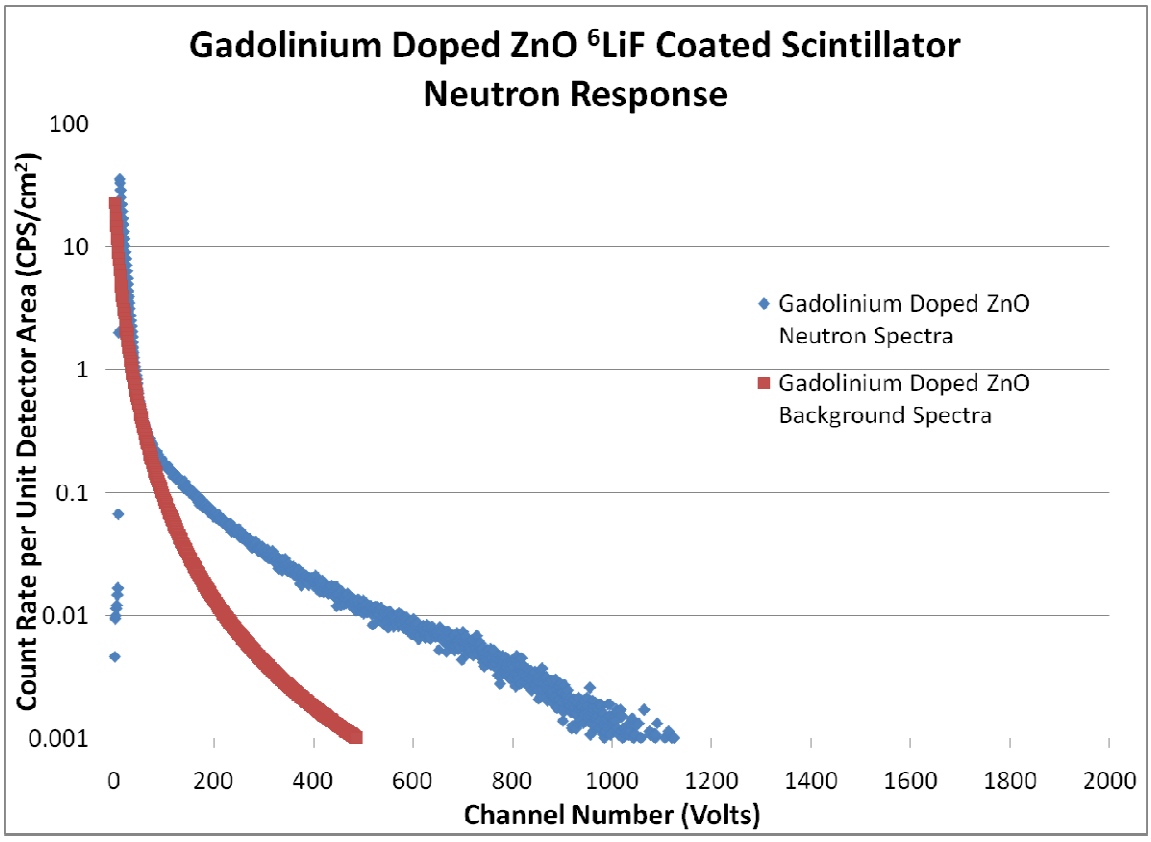

Figure 112 n,gamma-> conversion electron spectra for uniformly doped gadolinium ZnO and the corresponding 100 mR/hr gamma ray field. Neutron versus gamma discrimination is becoming unacceptable, however the conversion electron spectra is a continuum which resembles the gamma ray response with a slight peak where the curve rounds off around channel 800.

A comparison of the GSDS data shows the sensitivity to each detector type to various neutron energies. An example of the GSDS data can be seen in Figure 113. From this data one can calculate the energy dependent neutron detection efficiency relative to a known detector such as ^{3}He. Only boron doped ZnO and AZO are compared here. Appendix C contains the remainder of the GSDS data and subsequent analysis.

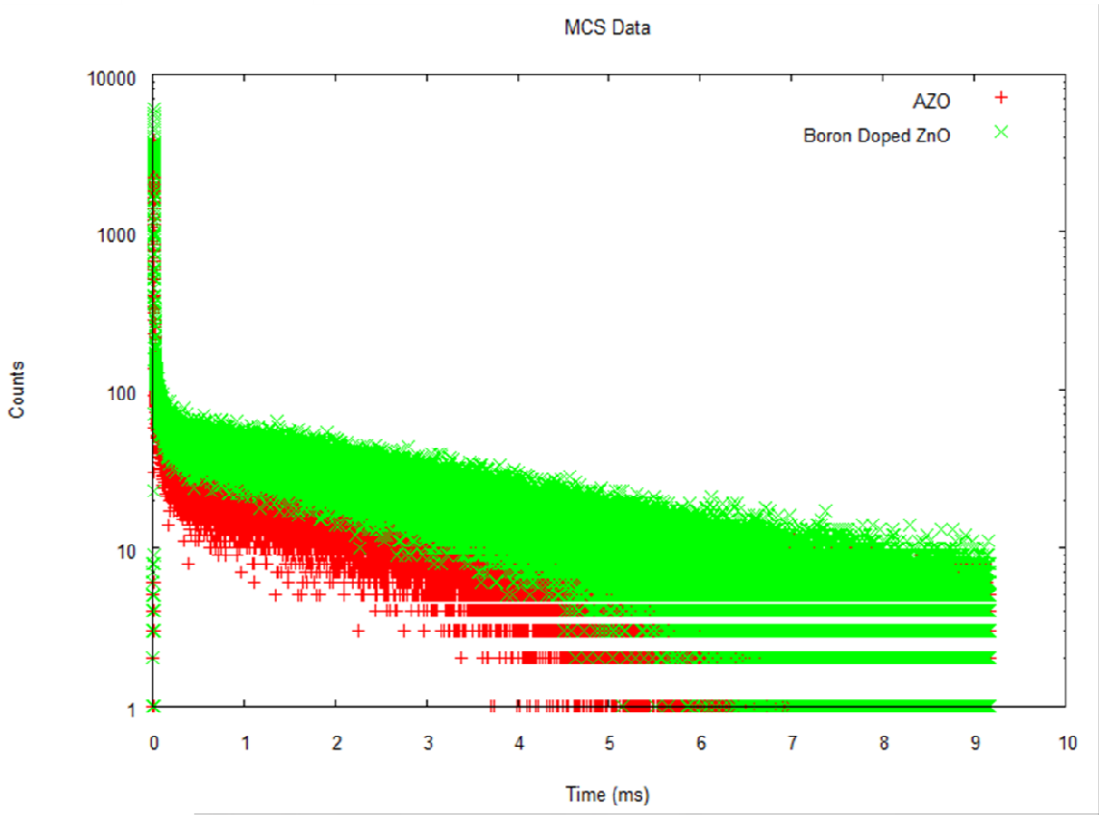

Figure 113 Time dependent neutron count rate from the GSDS for AZO and Boron doped ZnO.

To quantitatively compare the results of the neutron detection system, the detectors response to the steady state neutron thermal neutron flux, the detector count rates as a function of detector area have been computed. Summing the response over all channels above the gamma ray cutoff, the efficiency of each of the scintillators is compared in Figure 114. The count rates for all of the detectors were summed above the zero value gamma ray cutoff. This was defined by where the 100 mR/hr gamma ray field became zero in the pulse height distribution. This method ensures all of the responses are compared with the same neutron versus gamma discrimination as that achieved by ^{3}He.

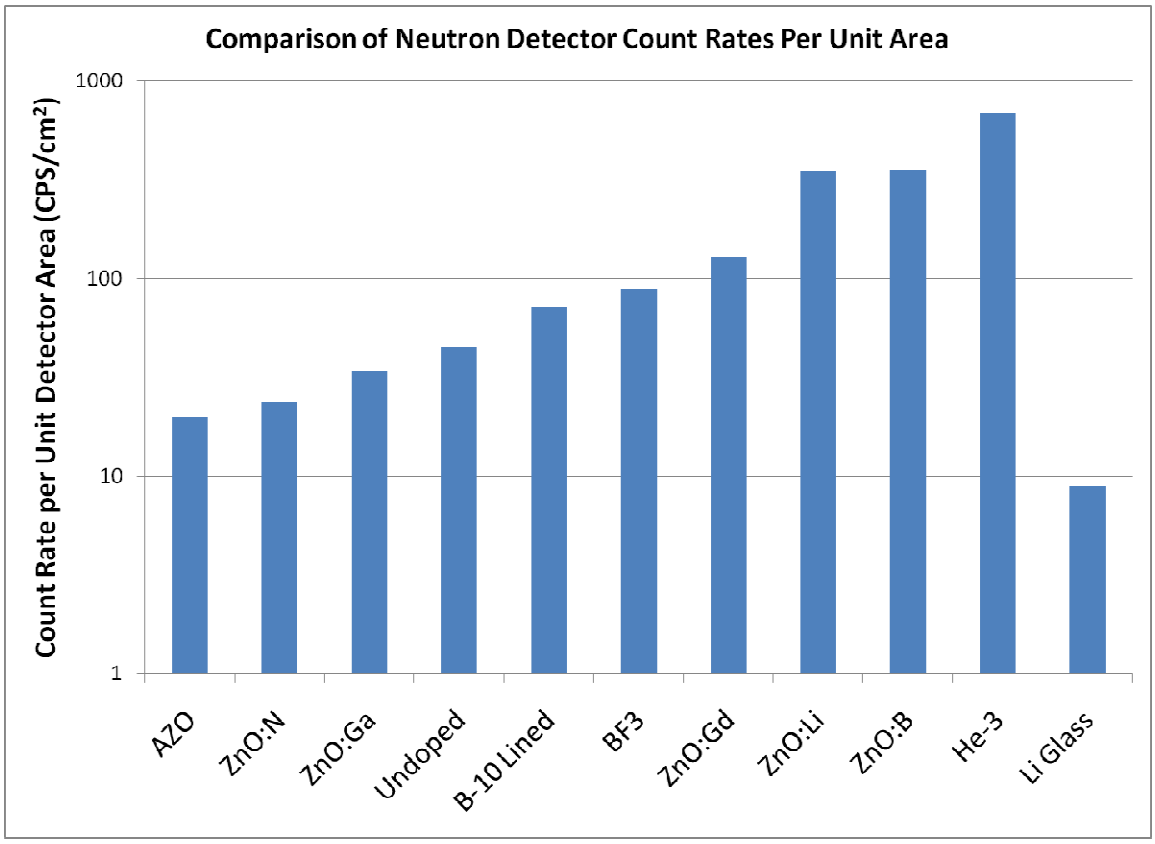

Figure 114 Comparison of count rates per unit area for neutron detectors tested. The count rate was summed above the zero value gamma ray cutoff.

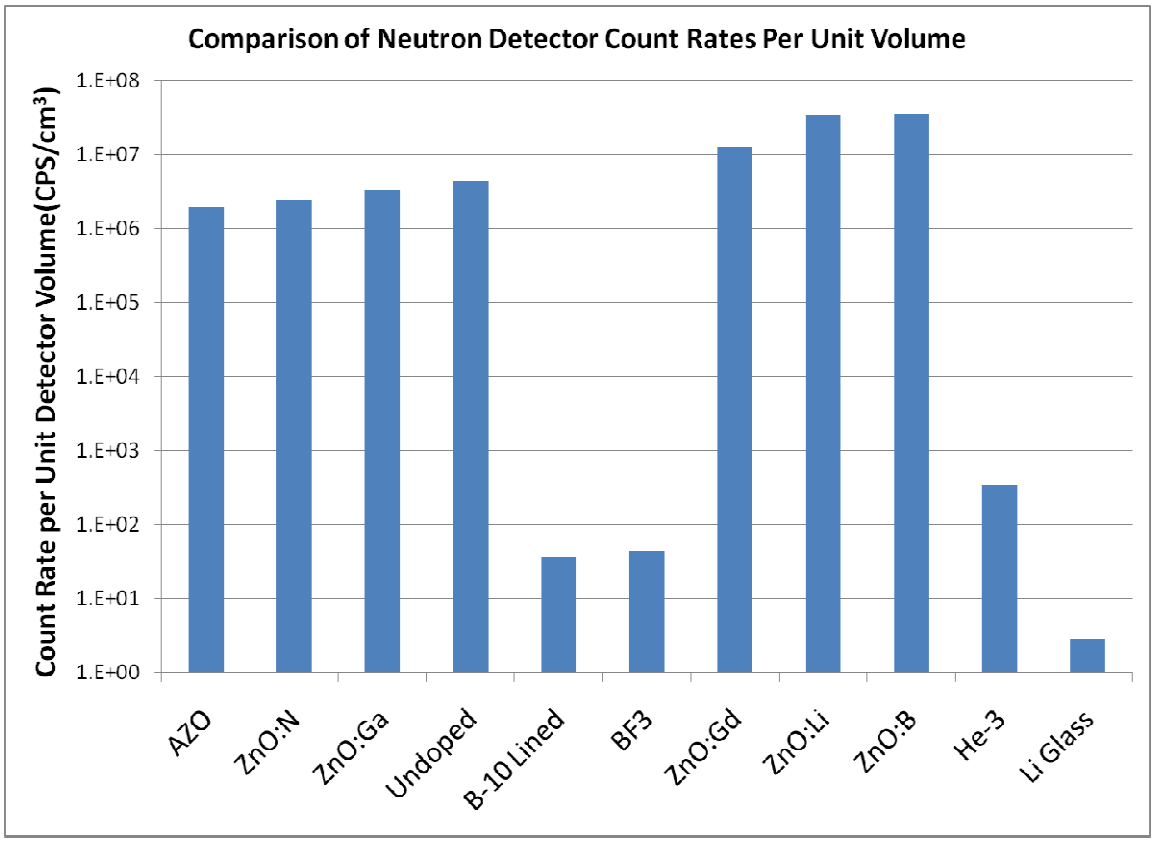

Figure 115 Comparison of count rates per unit volume for neutron detectors tested. The count rate was summed above the zero value gamma ray cutoff.

CHAPTER IX

CONCLUSIONS

The zinc oxide scintillator has been found to be a good neutron radiation detector. Zinc oxide can be grown in a number of different ways including bulk melt growth and MOCVD growth. Thin films can be grown which exhibit neutron versus gamma discrimination capabilities equivalent ^{3}He and superior to conventional neutron detectors using boron and lithium, particularly lined ^{10}B tubes. High thermal neutron cross sections have been seen which produce highly efficient neutron detectors. It has been shown that it is not necessary to observe a (n,α) peak to create a neutron detector with good neutron versus gamma discrimination. While this should be the ultimate goal of the road to the realization of a neutron spectrometer based on the Q value of the reaction, this is not necessary if one just wants a good neutron detector with good neutron versus gamma discrimination.

Novel ZnO neutron detectors have been modeled in MCNP5. Using these modeled detectors, growth studies were undertaken to optimize the scintillator structures. Growth was successfully carried out using MOCVD as well as bulk melt growth processes. The samples which do not possess lithium or boron interstitially mixed into the matrix currently resemble the response of a boron lined gas filled tube. This is due to the inability to collect both particles because of the coating thickness. Two sided scintillators can be grown over conformal ^{6}LiF coatings. The full energy peak for both the triton and alpha particle in the ^{6}Li (n,α) reaction can be collected in doped scintillators. This Q value plus the incident neutron's kinetic energy could be used for neutron spectroscopy.

It has been shown that doped ZnO scintillators exhibit superior characteristics than undoped ZnO in optical clarity, light yield and neutron detection. However, when

doping the scintillator, there is an optimal point of dopant concentration. Unlike bandgap engineering semiconductors where the bandgap can be tuned by varying the proportion between two components (108) of a compound semiconductor, the scintillator dopants being added do not produce more semiconductor materials. Past the optimal value the material becomes either conducting or insulating, opaque and looses performance. This is in part because there are not many oxide based semiconductors other than MnO and MgO. Determining these peak values was the key to this work. After the peak improvement, the increased dopant, even though in theory it should raise detection efficiencies, actually impedes performance.

The thermal neutron reaction was found to be dominated by mostly surface reactions. Comparing count rates versus surface area, the detectors at 1 layer thick perform well in comparison to conventional neutron detectors. When comparing the count rate per unit volume of the detector, the thin film ZnO scintillators are the superior neutron detector compared to other conventional neutron detectors. The conformal coating thickness was initially selected to be 10 μm based on ease of growth. However, this thickness was not optimized for neutron detection or as it came to be found out in the course of this work, for fabrication either. A switch from thermal evaporation to electron beam evaporation should yield in higher efficiency coatings of thinner thicknesses. 10-50 nm layers of ^{6}LiF repeated over layers of doped ZnO would yield higher efficiencies and be easier to fabricate. Currently under the 10 μm thickness the probability even for a 2 sided device is low that both particles will enter the scintillator. By minimizing this thickness to 10-50 nm and increasing the number of layers, an improved scintillator is possible.

The MCNPX models of the neutron detectors show that the optimal neutron versus gamma discrimination capabilities of the ZnO scintillator are realized when the scintillator thickness is kept as thin as possible. Making stacks of one or two sided scintillators offset with sapphire substrates (or other non scintillating / non Cherenkov

radiation emitting materials) is beneficial for increasing the neutron detection efficiency but effectively separates the responses of each scintillator keeping the gamma response minimized. Neutron versus gamma discrimination can be achieved at larger thicknesses, but at a noticeable cost in efficiency if one uses the zero crossing value of the photon response for the low energy cutoff.

By examining the models produced in MCNP5 and MCNPX, and extrapolating from current data, stacks of 3 or 4 of these scintillators can have efficiencies equal to or greater than ^{3}He tubes. The detectors are already equivalent in neutron versus gamma discrimination. The speed of the ^{3}He tube versus the ZnO scintillator, the ZnO scintillator is a superior choice. The ZnO scintillator can be grown in large surface area devices producing very efficient neutron detectors, with efficiencies superior to ^{3}He tubes. These novel devices are superior to lithiated glass, $^{10}BF_3$ tubes and ^{10}B-lined tubes for overall efficiencies and speed. The fabrication cost of these scintillators is relatively low in comparison to that of ^{3}He or other structures. In addition, there exists a direct road to commercialization of these devices through local companies such as Cermet Inc.

In regards to the commercialization of this device for homeland security, this doped ZnO structure shows promise at filling the need for a near term ^{3}He tube replacement. Either bulk melt grown materials or MOCVD grown materials are suitable for this endeavor. Bulk melt grown materials have the promise of large throughput and very thick samples. However, bulk melt growth does parasitically consume a lot of material in the fabrication process and would not be a good use of limited enriched ^{6}Li compounds. Current bulk melt growth materials result in a small fraction of usable material from a single casting boule. While this material could be reused and recast, the material that is cut and polished away becomes contaminated and is not suitable for recasting.

Detectors that utilize the conformal coatings of neutron detector materials are the most economical road to commercialization with bulk melt growth materials. MOCVD

grown materials grown with a larger, scaled up version of the reactor do show promise as well into commercialization. Here, rapid layer changes and enriched lithium can be used to its advantage to make thin multi-layered stacks of materials. These materials grown through this method could approach the 100% intrinsic efficiency devices that are needed. With single stacks that were grown herein, 43% intrinsic efficiencies were achieved for thermal neutrons. For science based experiments, the MOCVD grown detector method provides the most promise. With precise control, the MOCVD method can allow for specific detector designs to be produced easily focusing on specific neutron energies. With higher control of the fabrication process and the photonic crystal structures increasing and localizing light yields, the MOCVD method is a superior choice for nuclear physics measurements.

A photonic crystal scintillator was produced which improves the performance of the light collection in the ZnO scintillator. This is the first realization of a photonic crystal scintillator, where the scintillator structure itself is a photonic crystal. This initial design based on silicon rods and ZnO conformally grown over the surface is a fabrication challenge. The end result however is quite positive and shows promise for future iterations.

Overall, this work has shown that regardless of the growth method, doped ZnO and ^{6}LiF coated ZnO with or without dopants can produce a highly efficient neutron scintillator. Dopant studies were conducted for three types of dopants, ones for wavelength shifting, crystal transparency improvement and neutron detector nuclei. In the crystal transparency regime, aluminum improves the optical clarity of the sample but UV shifts the scintillation spectrum. In the wavelength shifting dopants, gallium and boron exhibit a good blue wavelength shift however they produce optically cloudy materials due to the oxide form of each of these materials being a white, opaque material. Lithium and boron can be doped as neutron detector nuclei with lithium producing a more optically clear material. Lithium does blue shift the scintillation spectrum slightly

but is difficult to grow by MOCVD due to lack of a good precursor. Lithium acetatonate shows the most promise for growth of MOCVD lithium doped ZnO. It was found that a tradeoff between dopant materials and scintillation luminosity are inversely proportional. While the dopant materials add beneficial characteristics to the scintillator, at high dopant levels, it quenches the scintillation capabilities. A fine balance must be struck between dopant characteristics and scintillation luminosities.

CHAPTER X

FUTURE WORK

In future work, 1D stacks of repeating dielectric materials should be investigated to improve the photonic crystal scintillator. These stacks can introduce a Distributed Bragg Reflector which can provide nearly specular reflectance for the scintillation wavelength. The photonic crystal structure does produce guided mode scintillation and prohibit the lateral flow of light. It however does not have any selection on which way the light propagates in the vertical direction. To improve this, a DBR stack can be grown over the ^{6}LiF coating to produce a selected direction of scintillation. It was observed that the PMT glass window contributes to the gamma ray background. The MOCVD growth reactor, with a major overhaul or upgrade to current designs could drastically improve crystalline quality and crystalline growth rates.

The lithium sources used in this work were less than optimal. In the future, work should be done to investigate new lithium precursor sources. With the mind on available sources of enriched ^{6}Li, this work should focus on lithium carbonate, lithium metal or lithium fluoride. These are the only current commercial forms of enriched lithium. Flash evaporators can be used, and significant work lately has been undertaken by many commercial entities on this field, which can bring the lithium precursor problem to a close. This would entail redesign of the chamber configuration to support one of these evaporators. The MOCVD growth reactor used in this project while highly functional and useful in a proof of concept, but is not suitable for further work without a complete overhaul. The early design of this reactor predates the commercial counterparts currently deployed for III-V and GaN growth. These matured MOCVD growth technologies have progressed substantially since the design of the reactor used in this project. New features include a laminar flow chimney which guides the reactant gasses to the platter allowing

for higher utilization of the metal organic precursors. The chamber used herein was a custom built reactor which did not have any of these new features. The flow rate was limited due to pump limitations which grew more difficult as the project continued. Without a functional exhaust throttling valve, manual control was made using a hand controlled butterfly valve. This provided coarse adjustment of chamber pressures, but did not have a significant improvement in crystal growth.

The bulk melt growth process shows the nearest road to commercialization with capabilities already in place to facilitate rapid deployment. Work must be conducted at incorporation of enriched ^{6}Li based materials to the growth process to ascertain the intrinsic efficiency improvement of these materials. Also, a rapid cutting/polishing process which limits the amount of material that is destroyed in the process is needed. The largest cost in the raw materials to fabricate these detectors is the ^{6}Li precursor. To economize the growth process, this material must not be wasted.

To continue the research on the photonic crystal structure, more selective etching recipes are needed to improve the scintillator performance. The more selective the etching process, the deeper the structure can be cut. A low cost method for fabrication of the photonic crystal structures should be investigated. One such method investigated was the use of an Anodized Aluminum Oxide (AAO) self ordering template (109). The AAO template can be used as opposed to a photoresist mask. Etching can occur directly through the structure. AAO can be produced in large quantities using a selective etching and wet chemistry process. Lastly, investigation into hybrid photonic crystals such as annular photonic crystal structures which require a significantly more challenging growth method should be investigated.

APPENDIX A

GRAPHITE SLOWING DOWN SPECTROMETER STUDY

A study of the optimal location to utilize for the graphite slowing down spectrometer was undertaken. Due to the modular nature of the graphite pile, several different locations could have been used by restacking the pile in a different geometric configuration. Below are presented several different time dependent neutron spectra as a function of position. While the position used (Position 7) is not optimal, for the scope of this thesis it was adequate. Presented in Figure 117 through Figure 137 are the time dependent neutron flux profiles as a function of position. Shown in Figure 138 through Figure 157 are the lethargy flux profiles as a function of time at the previous positions in the GSDS.

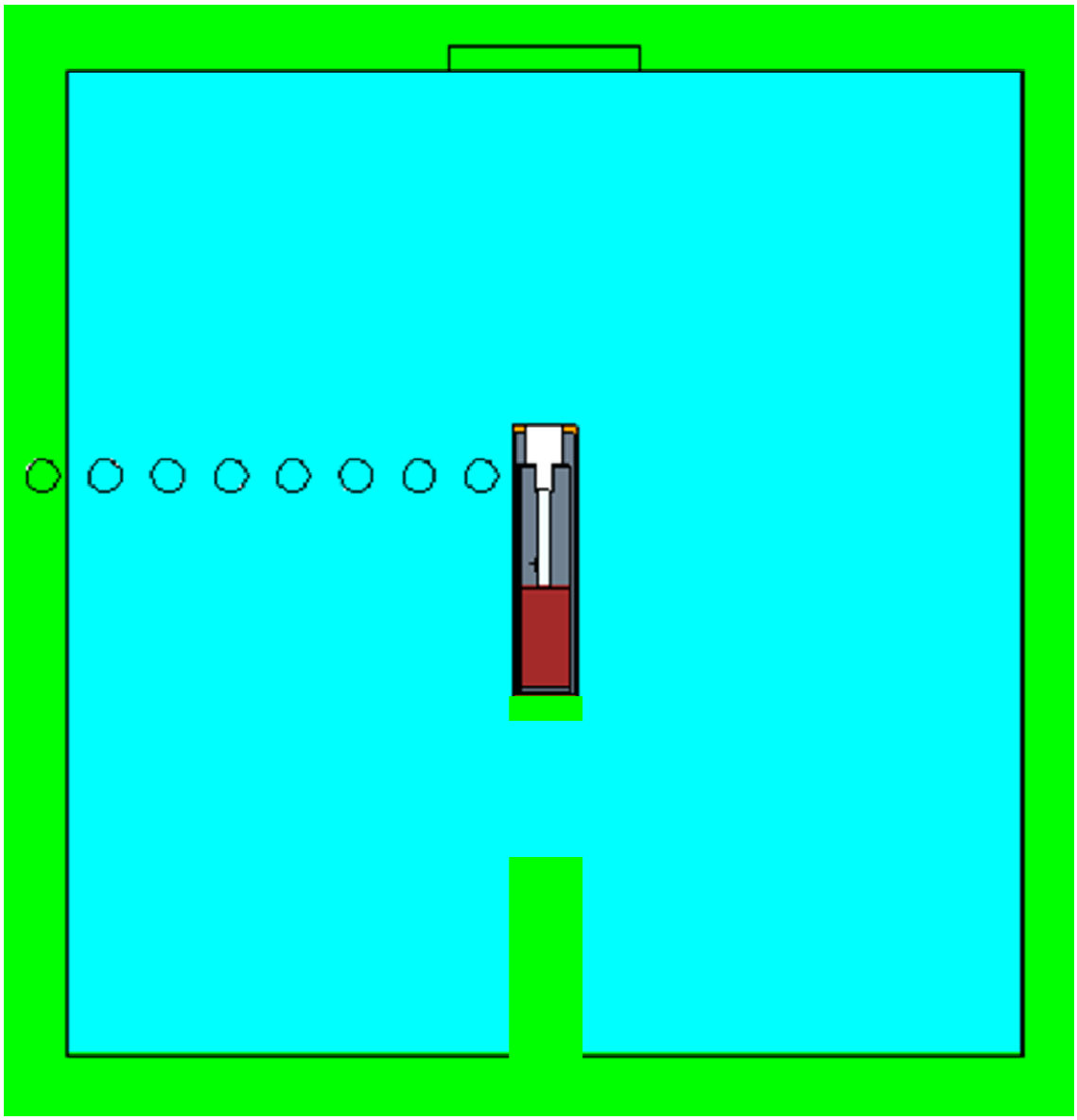

Figure 116 MCNP5 model of the GSDS and neutron generator. The spheres are tally spheres for the proposed positions of the measurement.

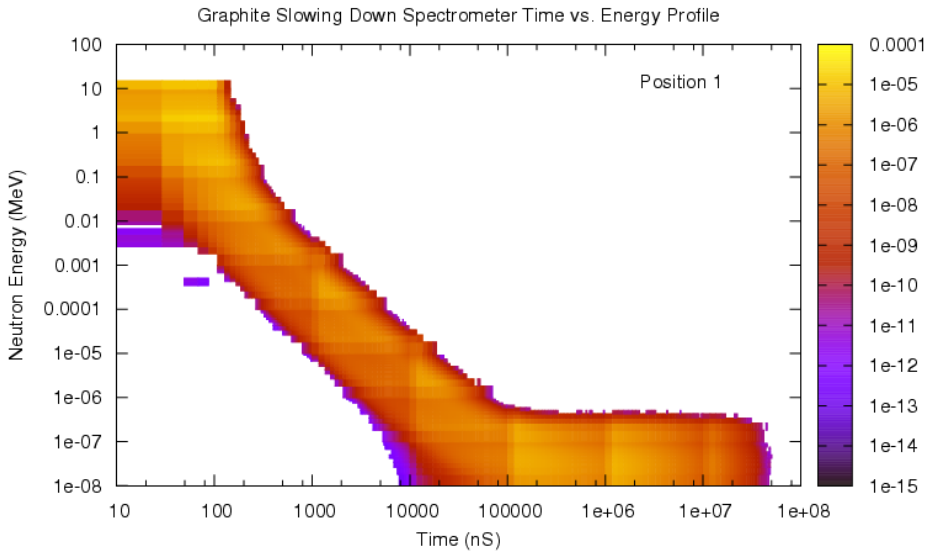

Figure 117 Position 1 of the GSDS.

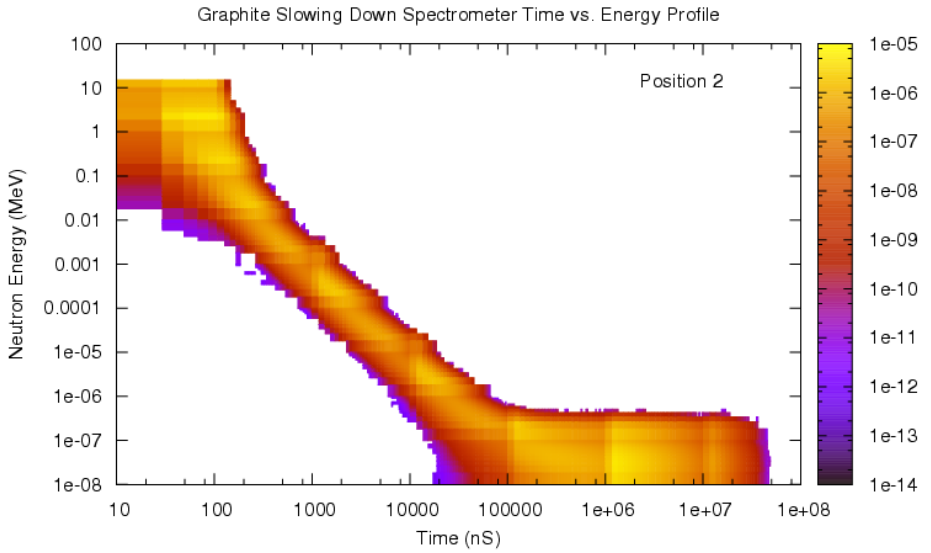

Figure 118 Position 2 of the GSDS.

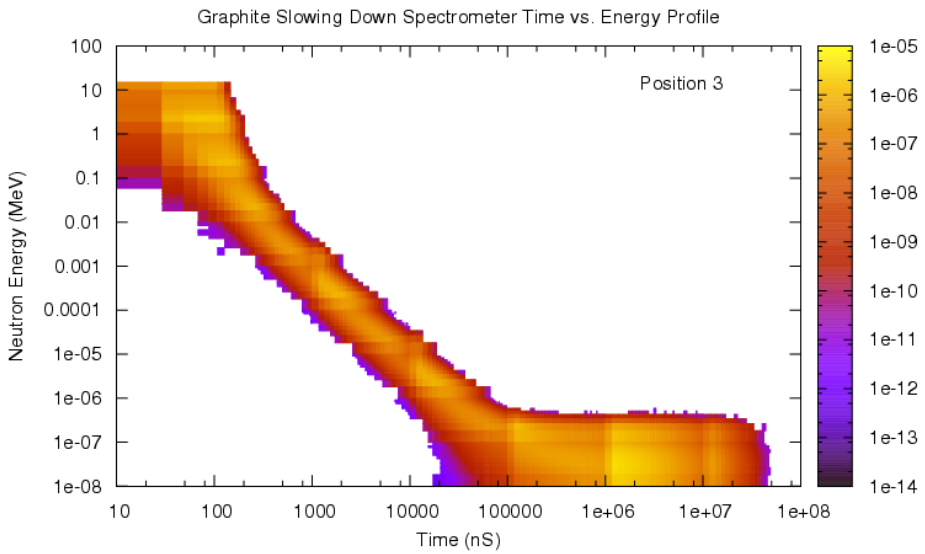

Figure 119 Position 3 of GSDS.

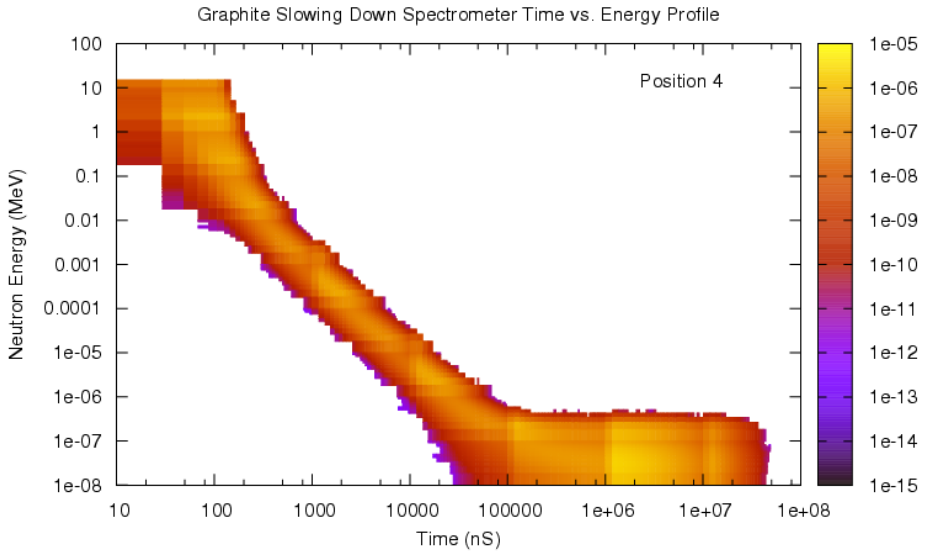

Figure 120 Position 4 of the GSDS

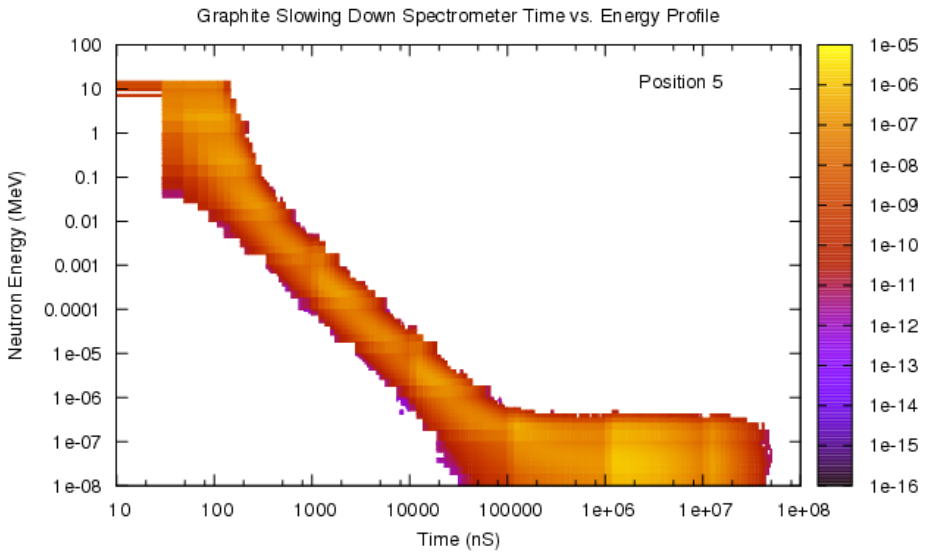

Figure 121 Position 5 of the GSDS

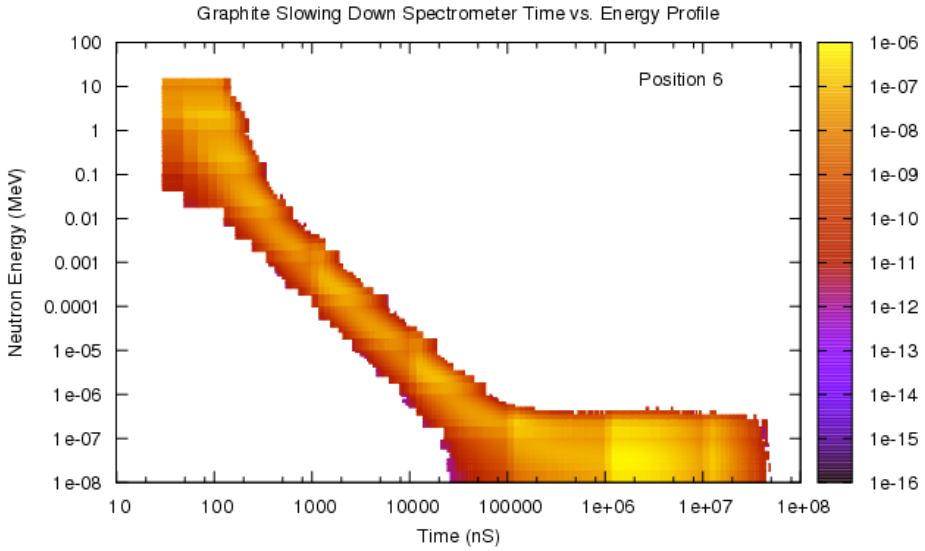

Figure 122 Position 6 of the GSDS.

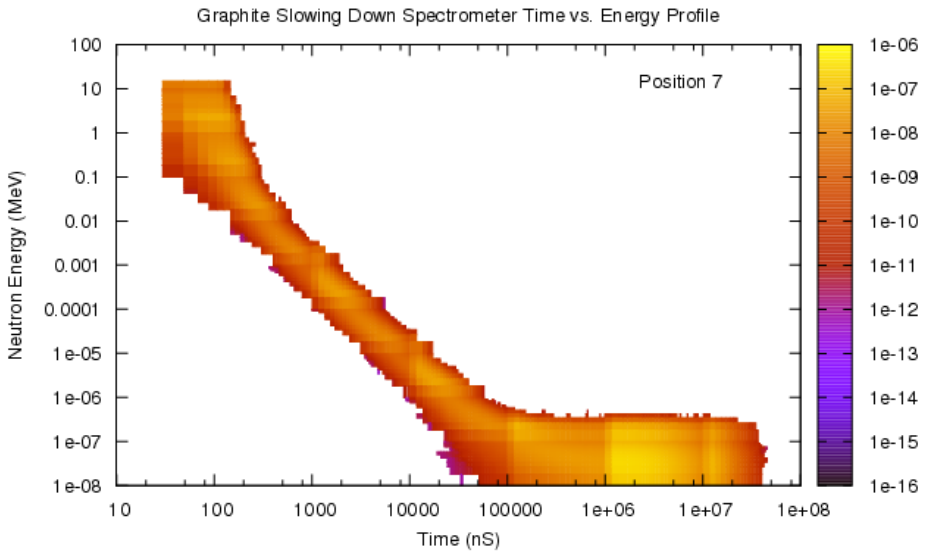

Figure 123 Position 7 of the GSDS.

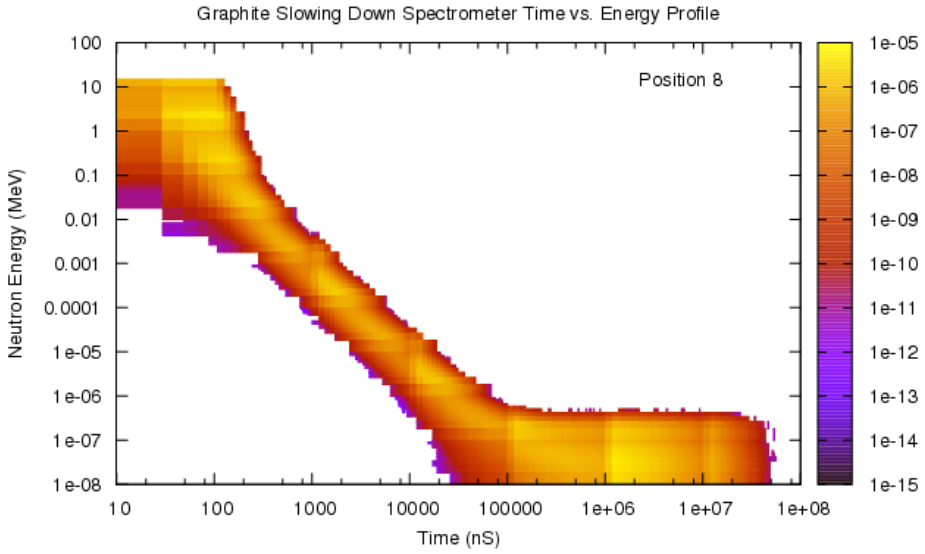

Figure 124 Position 8 of the GSDS.

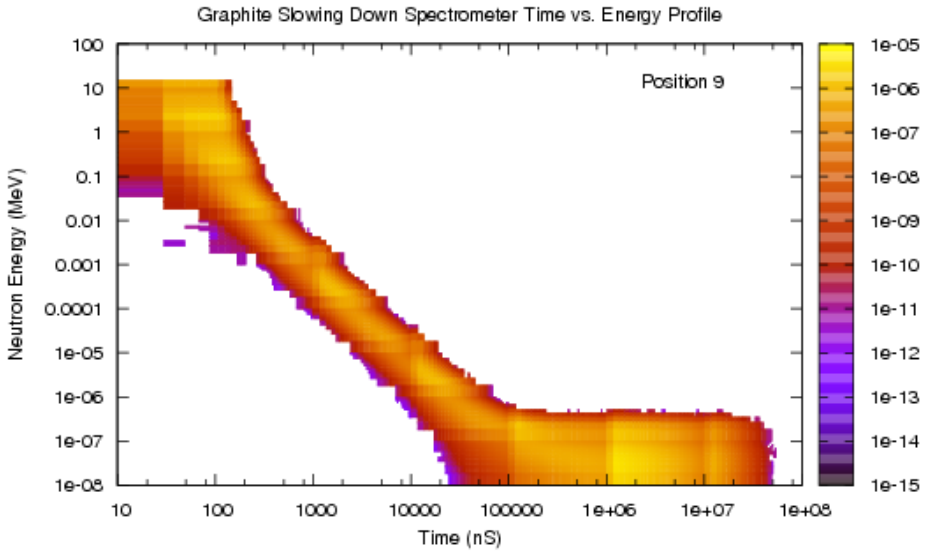

Figure 125 Position 9 of the GSDS.

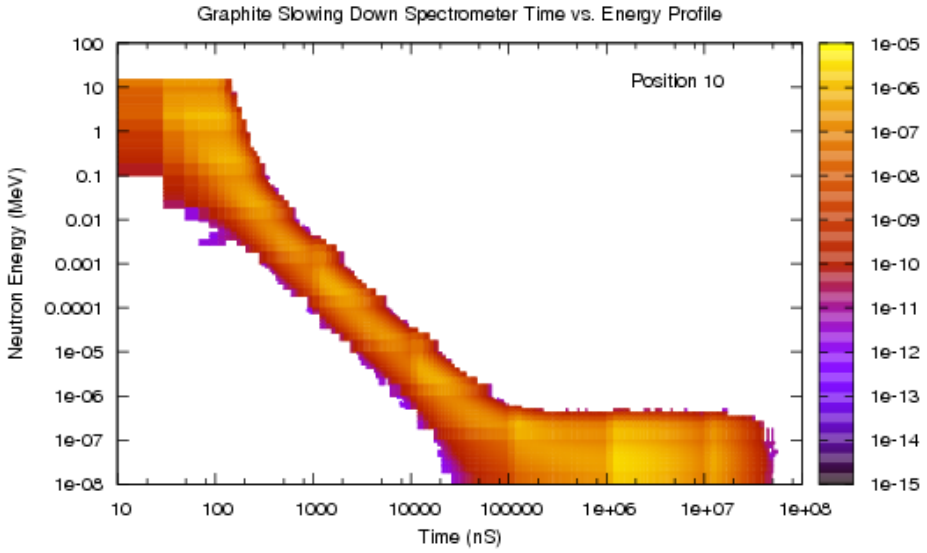

Figure 126 Position 10 of the GSDS.

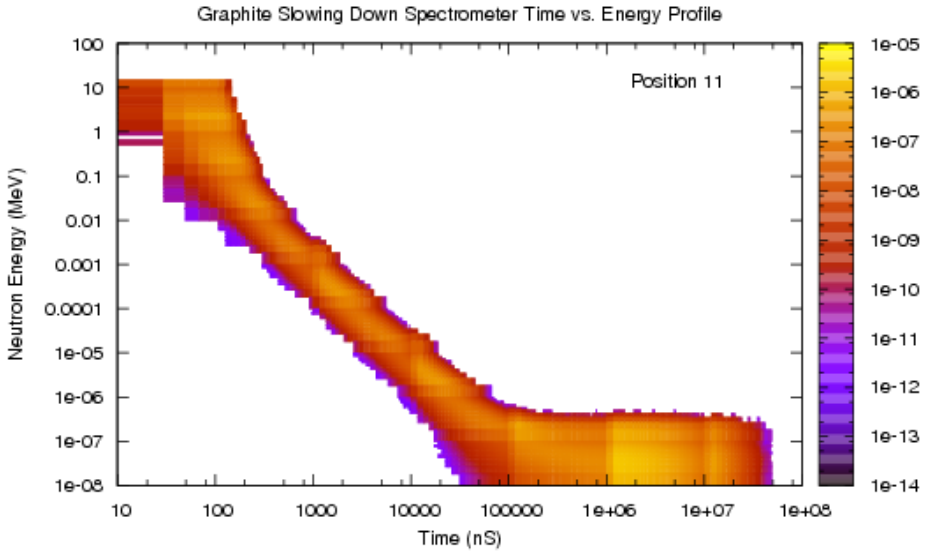

Figure 127 Position 11 of the GSDS.

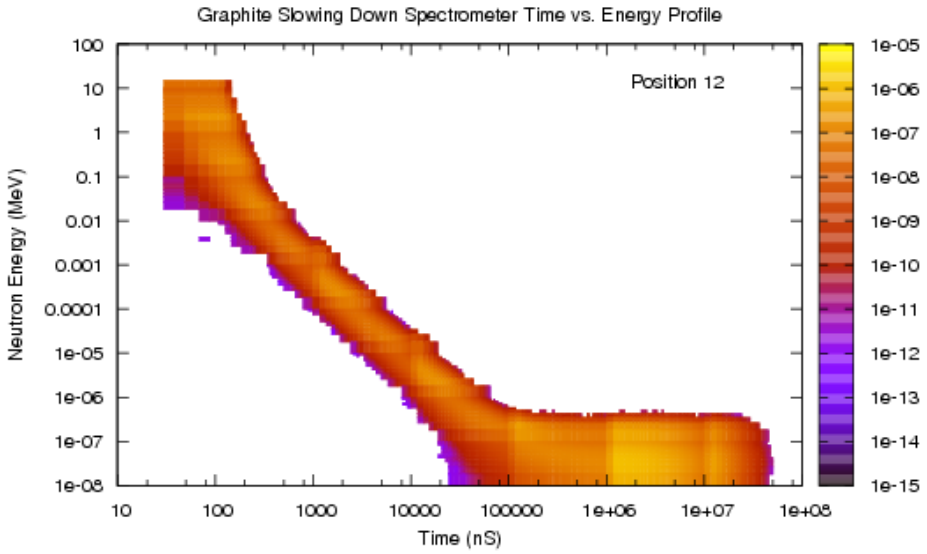

Figure 128 Position 12 of the GSDS.

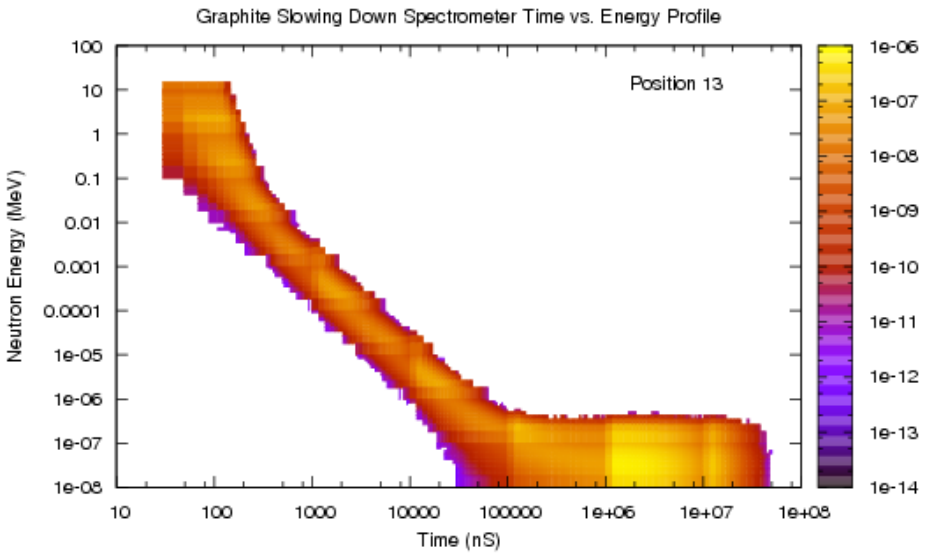

Figure 129 Position 13 of the GSDS.

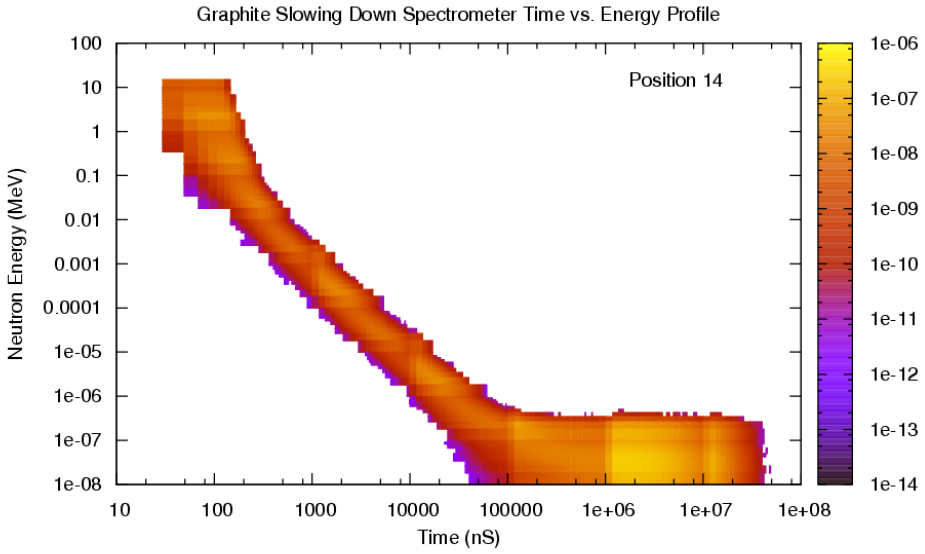

Figure 130 Position 14 of the GSDS.

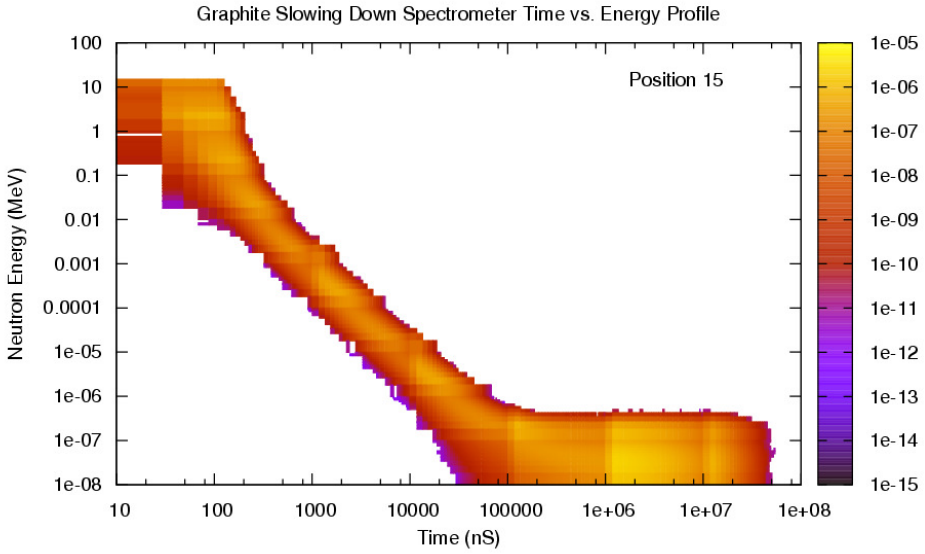

Figure 131 Position 15 of the GSDS.

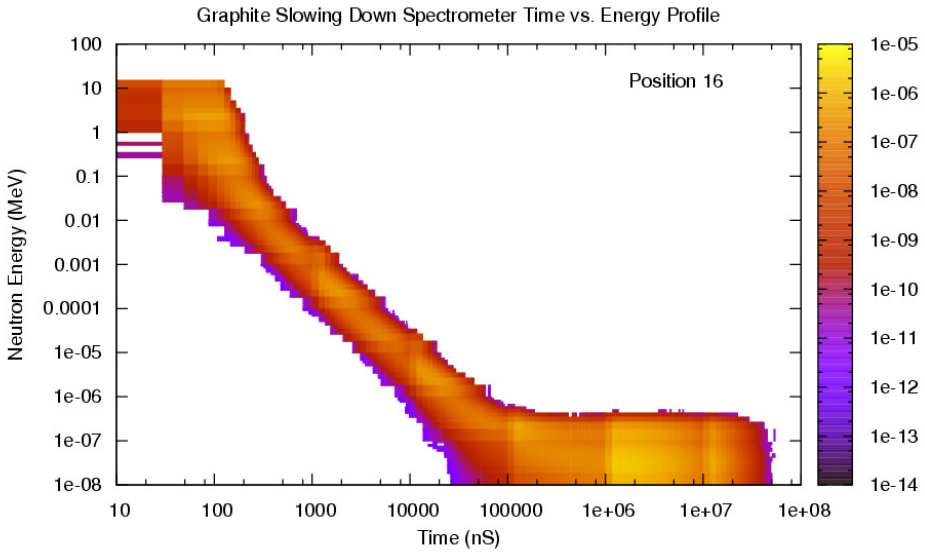

Figure 132 Position 16 of the GSDS.

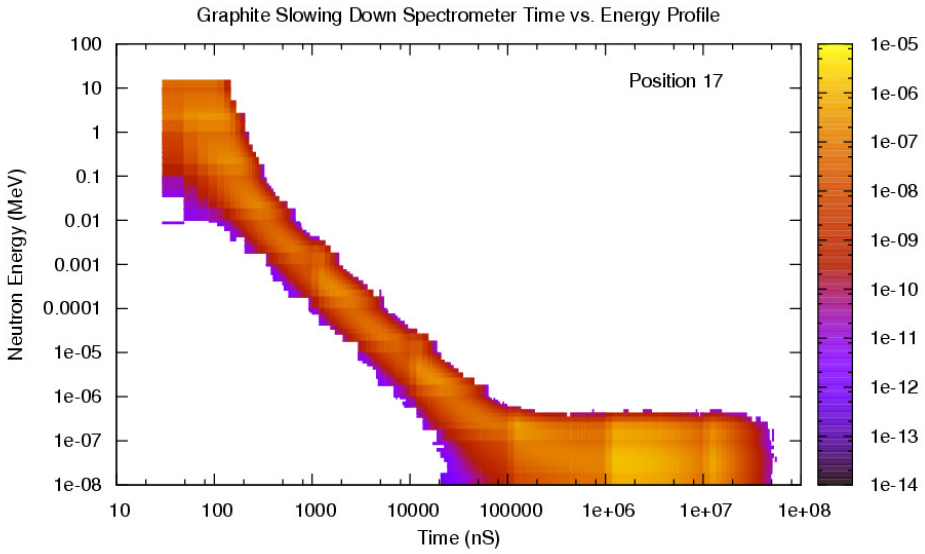

Figure 133 Position 17 of the GSDS.

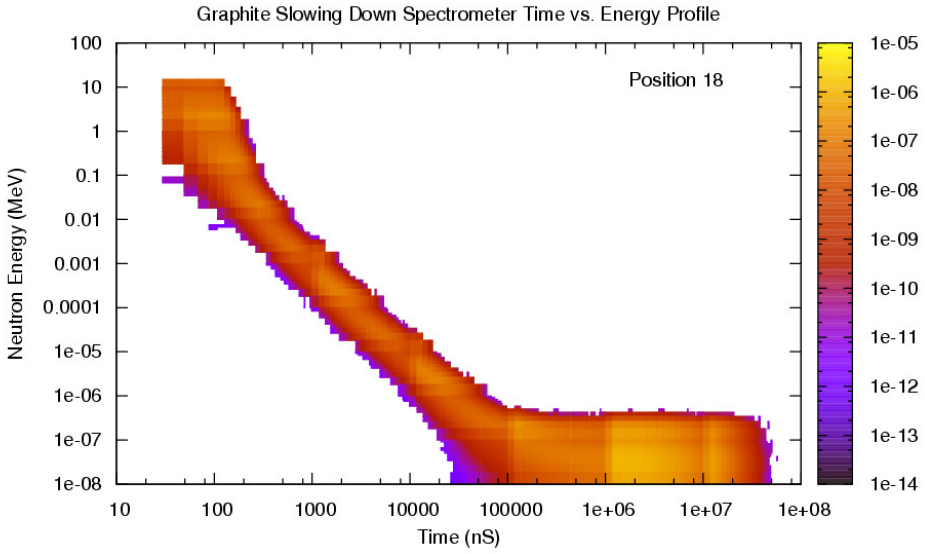

Figure 134 Position 18 of the GSDS.

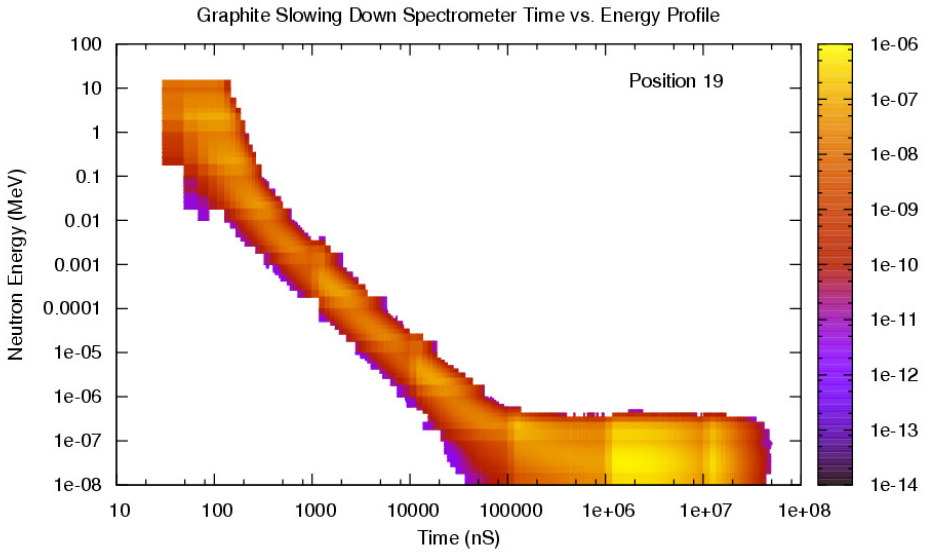

Figure 135 Position 19 of the GSDS.

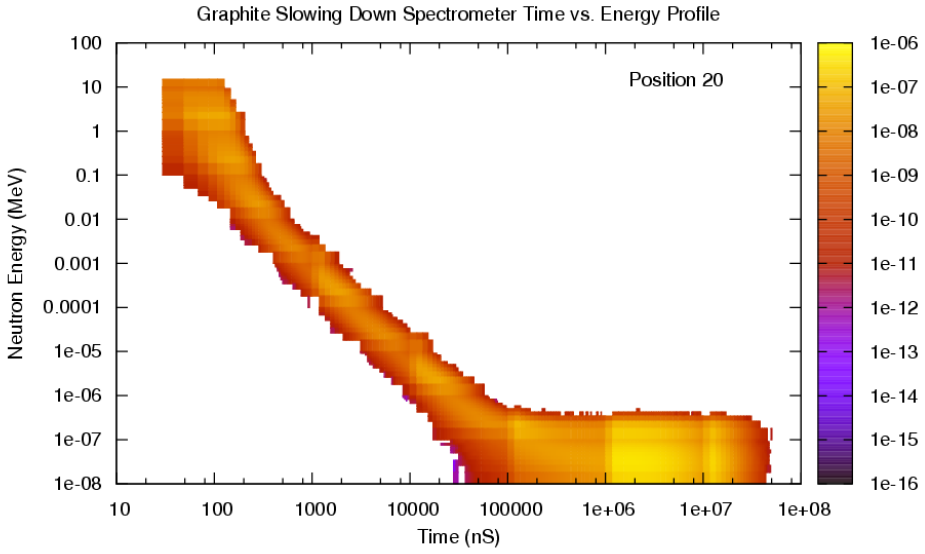

Figure 136 Position 20 of the GSDS.

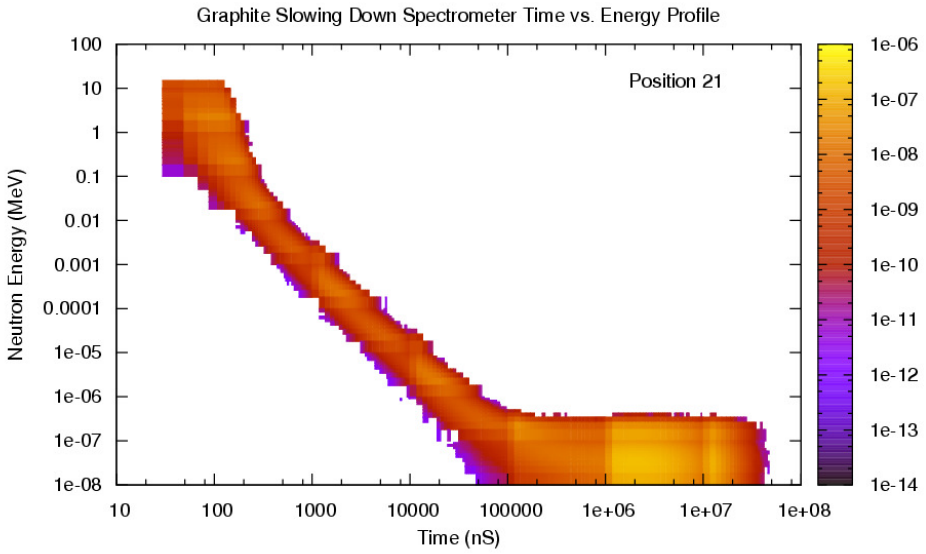

Figure 137 Position 21 of the GSDS.

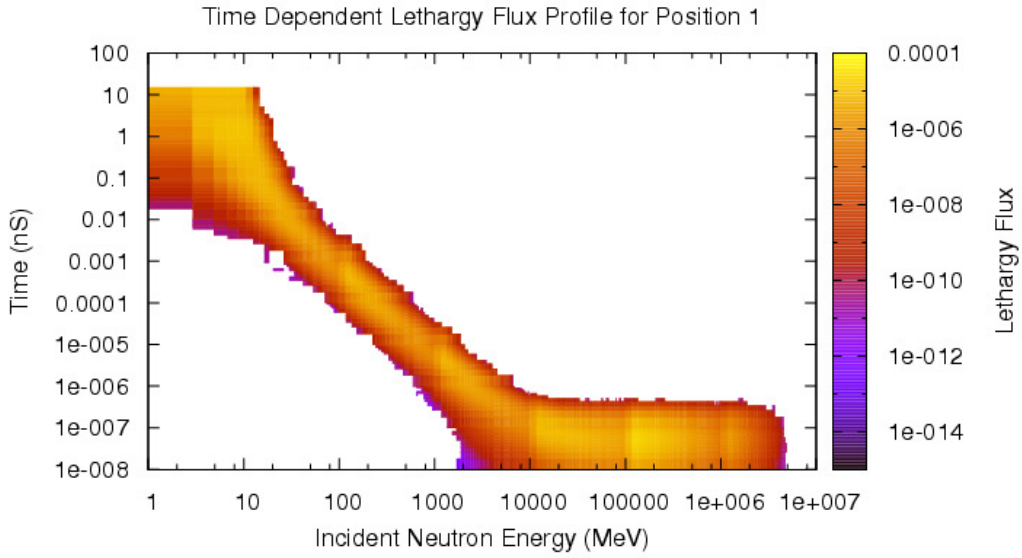

Figure 138 Lethargy flux profile for the GSDS position 1.

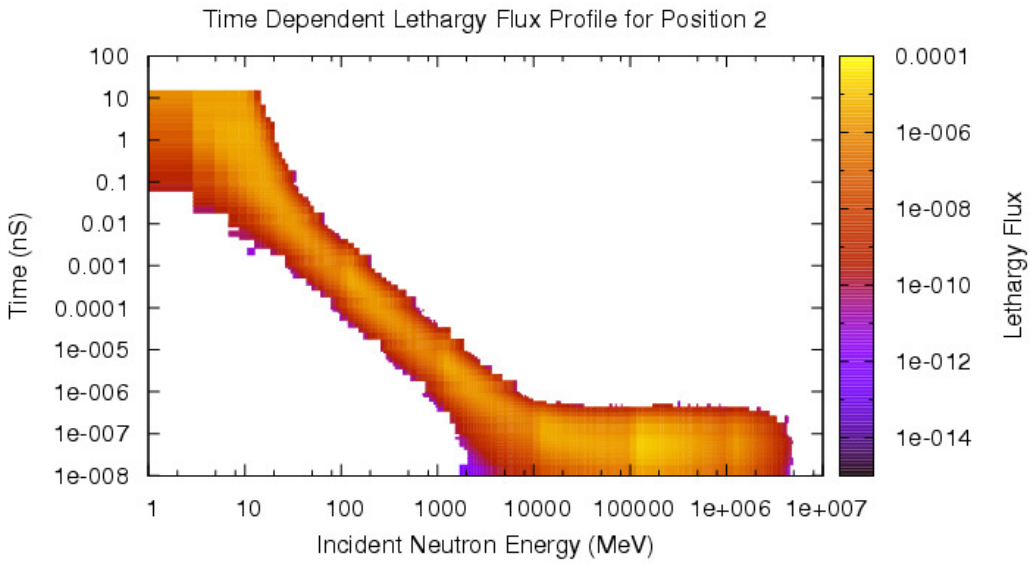

Figure 139 Lethargy flux profile for the GSDS position 2.

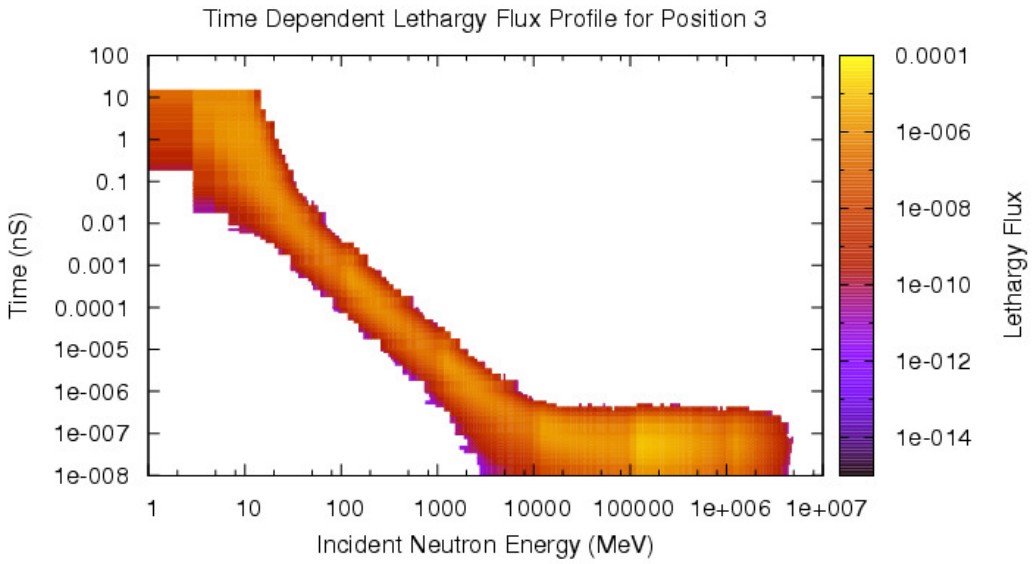

Figure 140 Lethargy flux profile for the GSDS position 3.

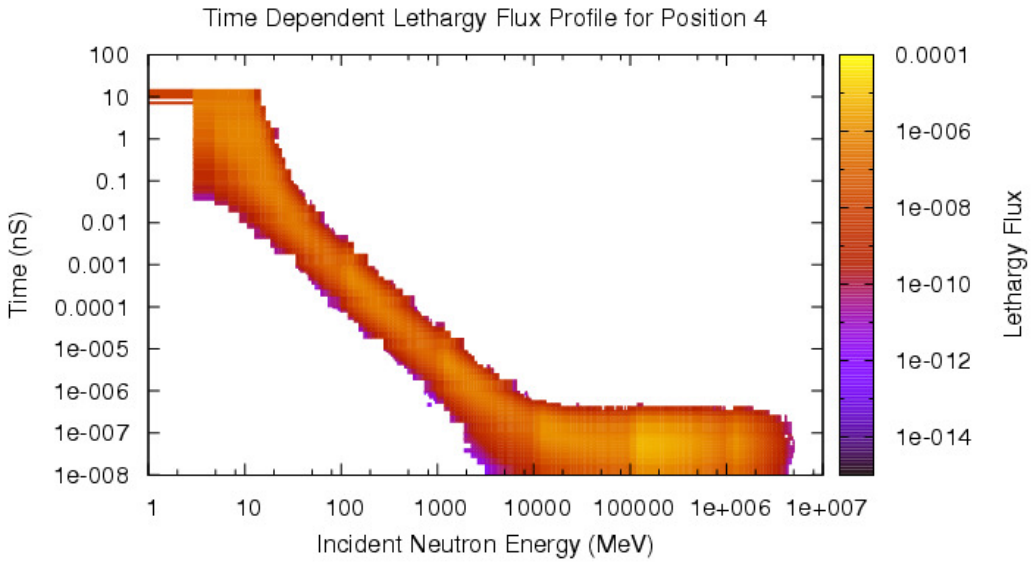

Figure 141 Lethargy flux profile for the GSDS position 4.

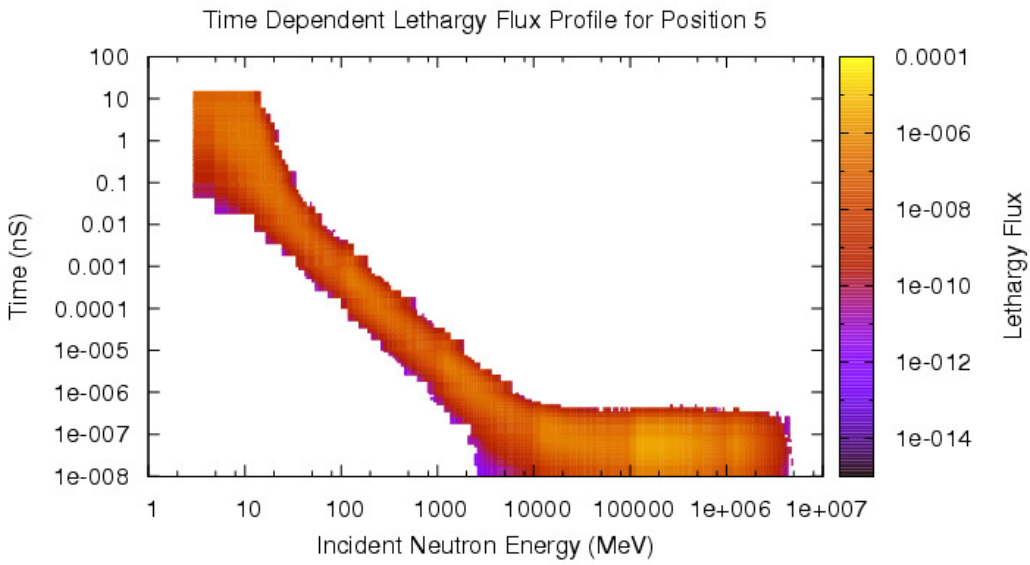

Figure 142 Lethargy flux profile for the GSDS position 5.

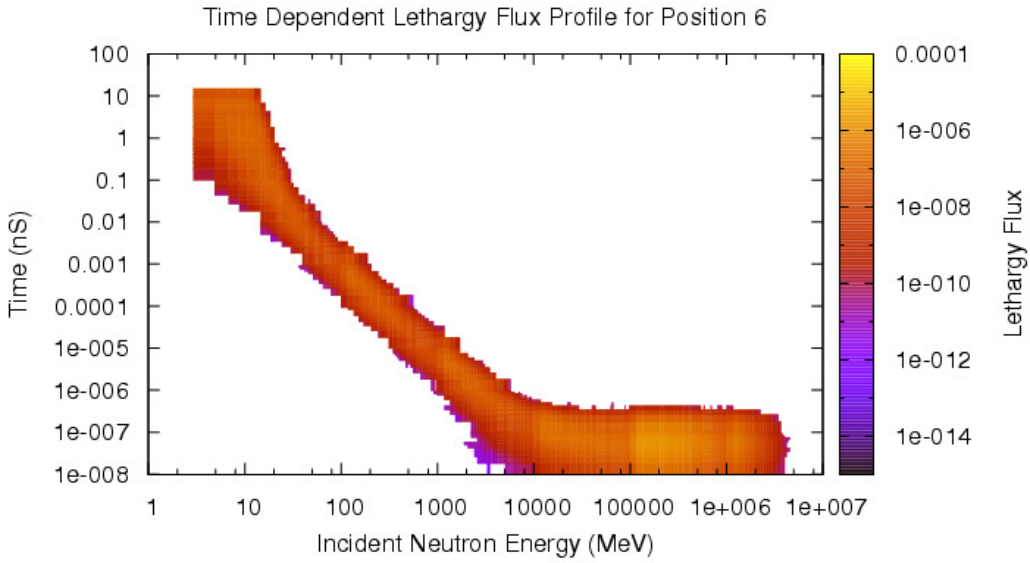

Figure 143 Lethargy flux profile for the GSDS position 6.

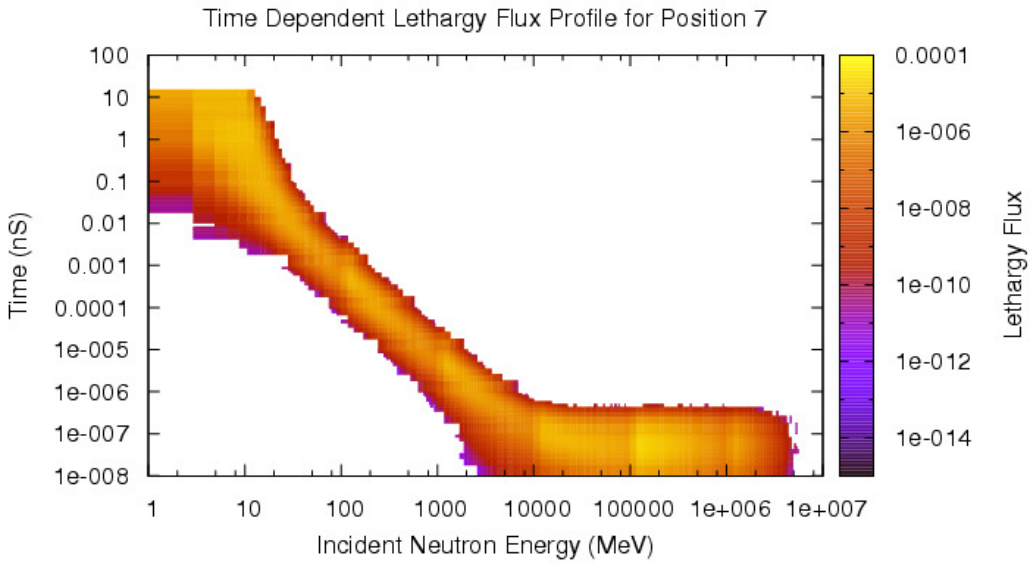

Figure 144 Lethargy flux profile for the GSDS position 7.

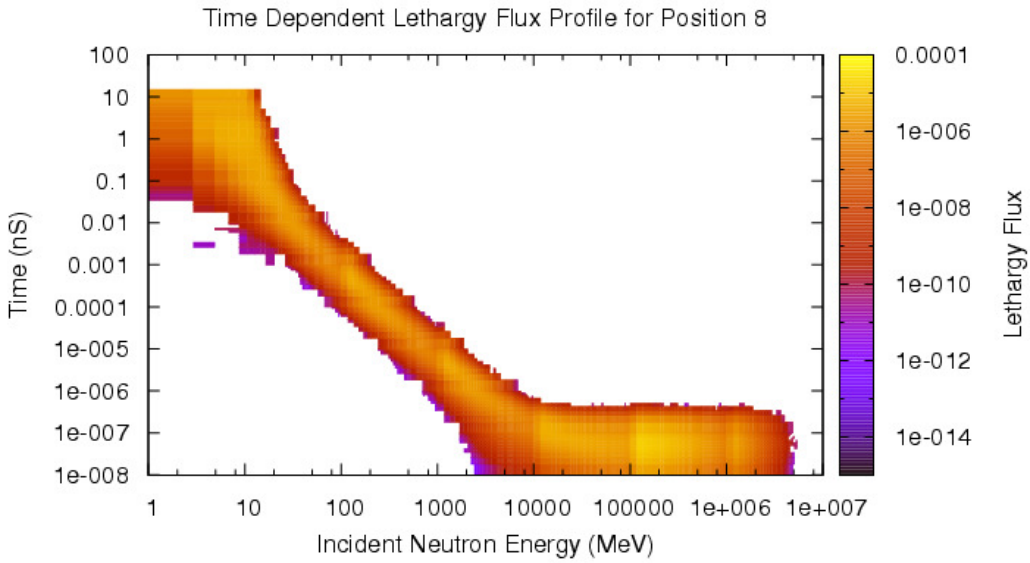

Figure 145 Lethargy flux profile for the GSDS position 8.

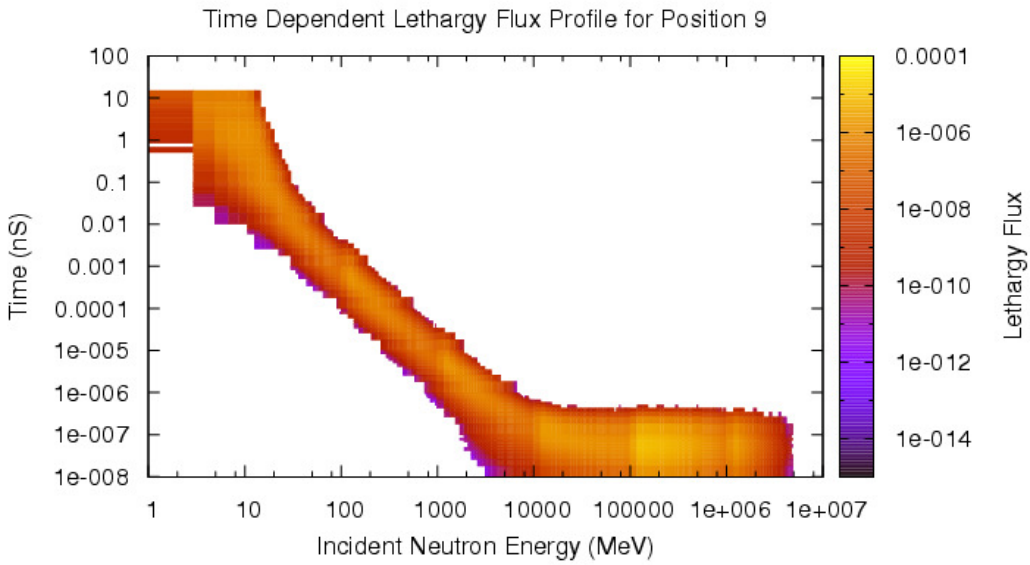

Figure 146 Lethargy flux profile for the GSDS position 9.

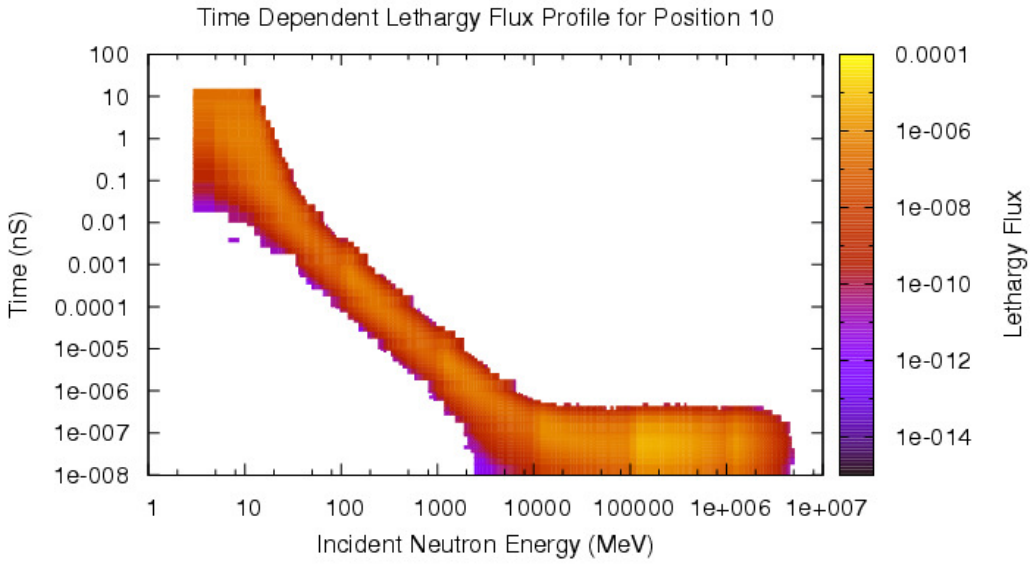

Figure 147 Lethargy flux profile for the GSDS position 10.

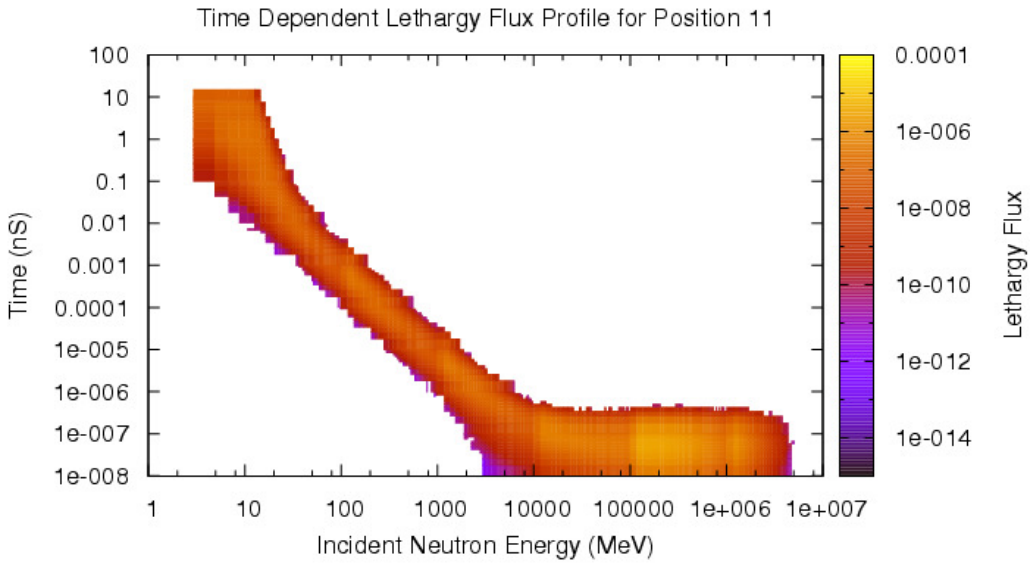

Figure 148 Lethargy flux profile for the GSDS position 11.

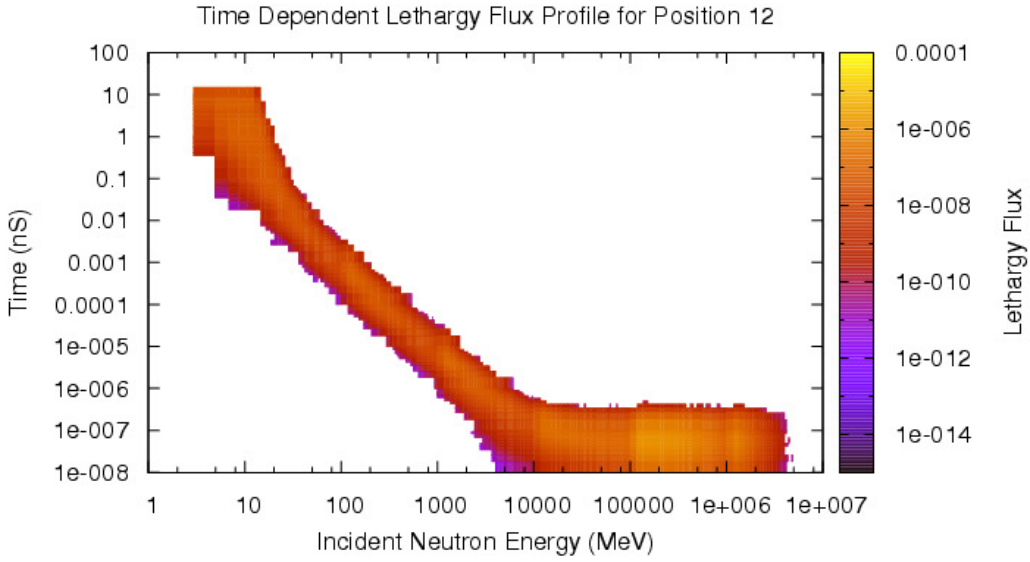

Figure 149 Lethargy flux profile for the GSDS position 12.

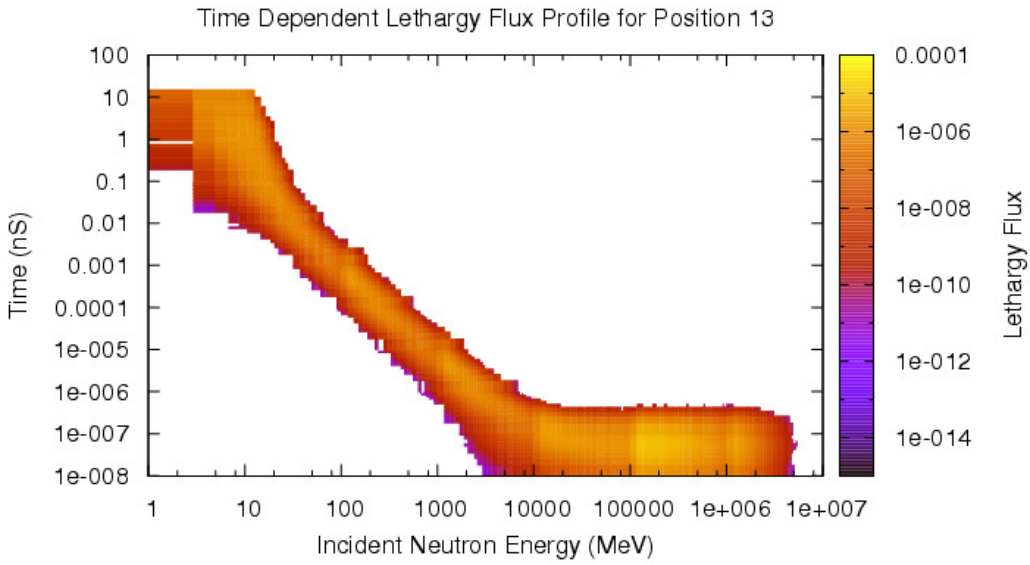

Figure 150 Lethargy flux profile for the GSDS position 13.

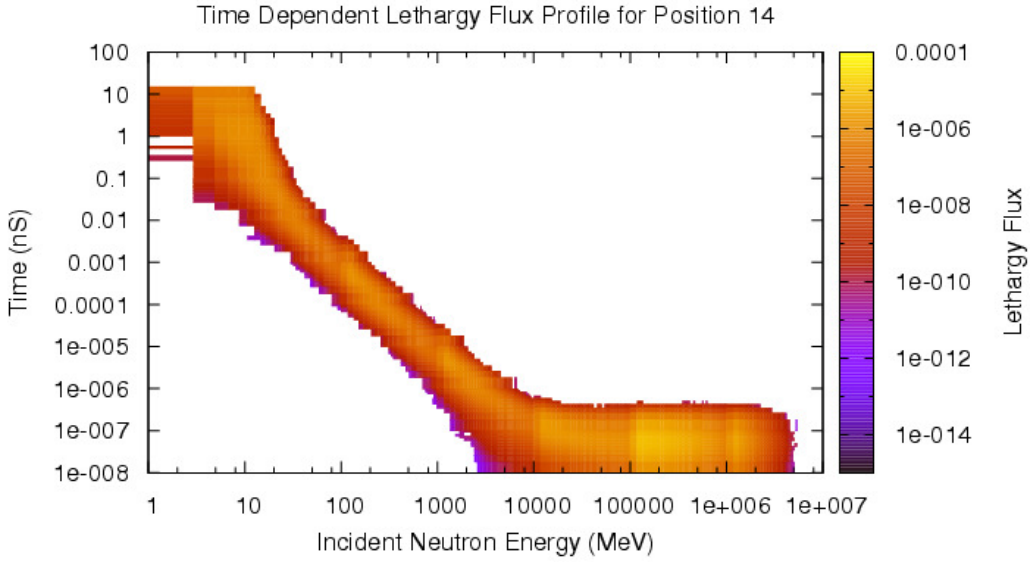

Figure 151 Lethargy flux profile for the GSDS position 14

.

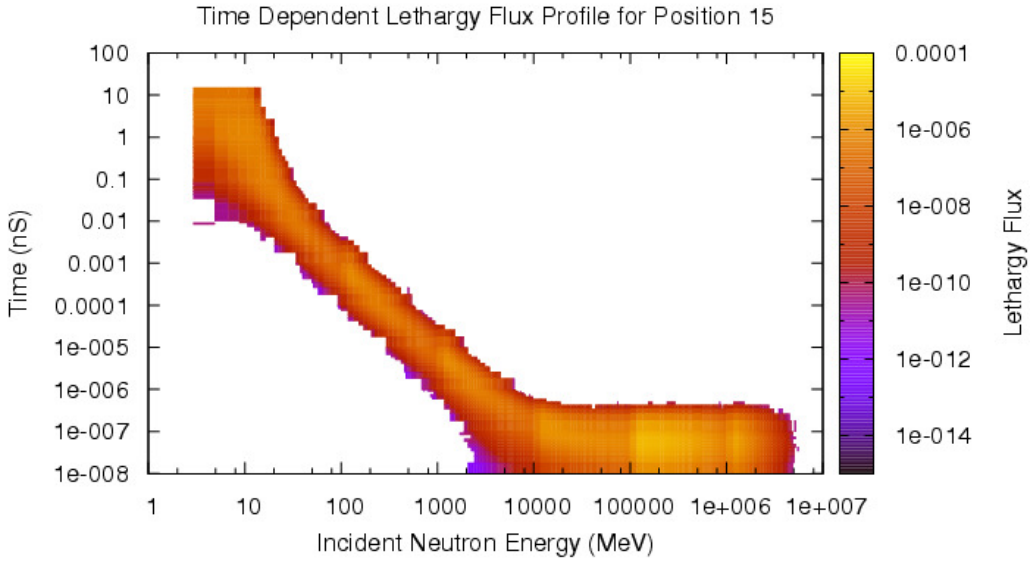

Figure 152 Lethargy flux profile for the GSDS position 15.

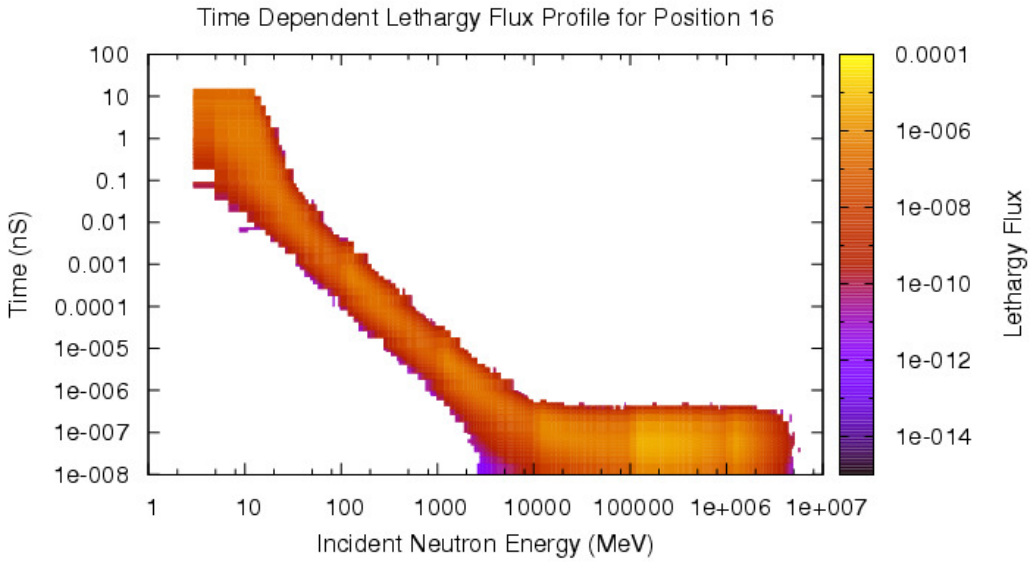

Figure 153 Lethargy flux profile for the GSDS position 16.

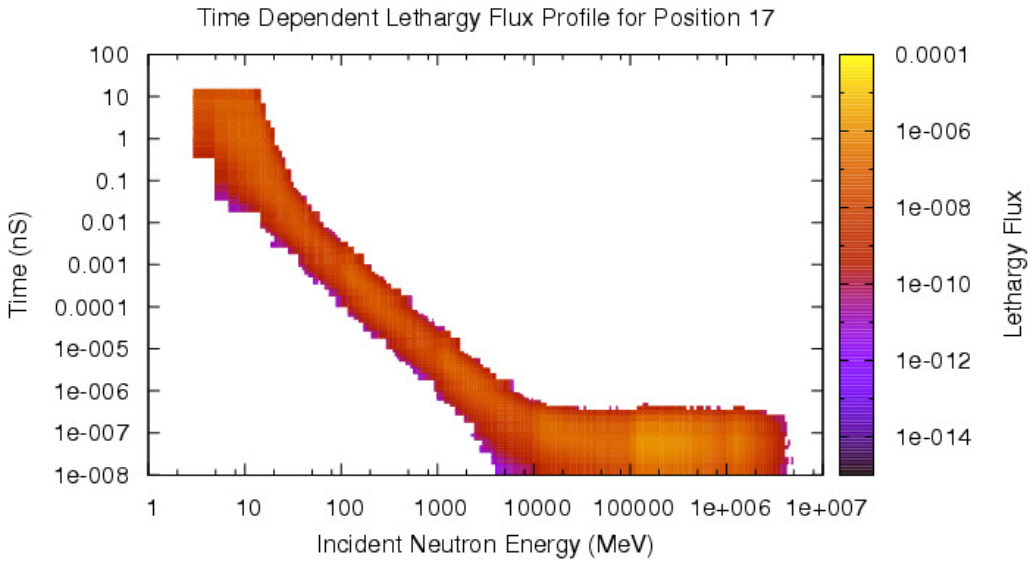

Figure 154 Lethargy flux profile for the GSDS position 17.

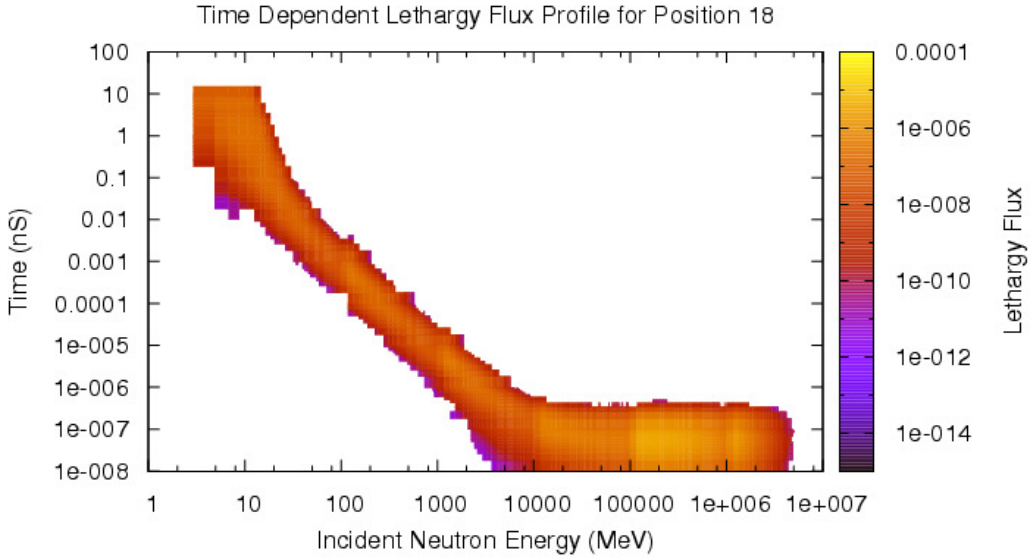

Figure 155 Lethargy flux profile for the GSDS position 18.

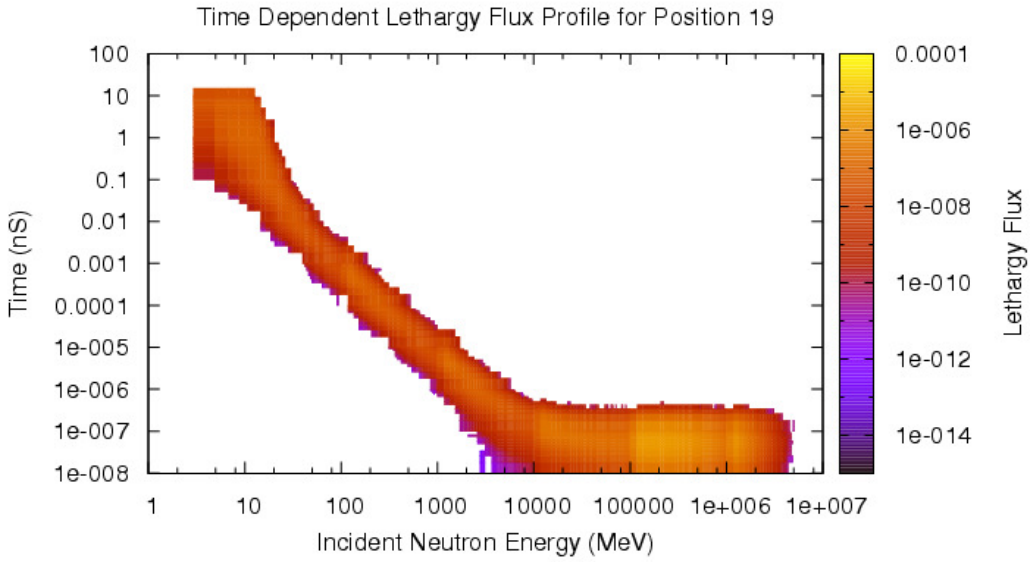

Figure 156 Lethargy flux profile for the GSDS position 19.

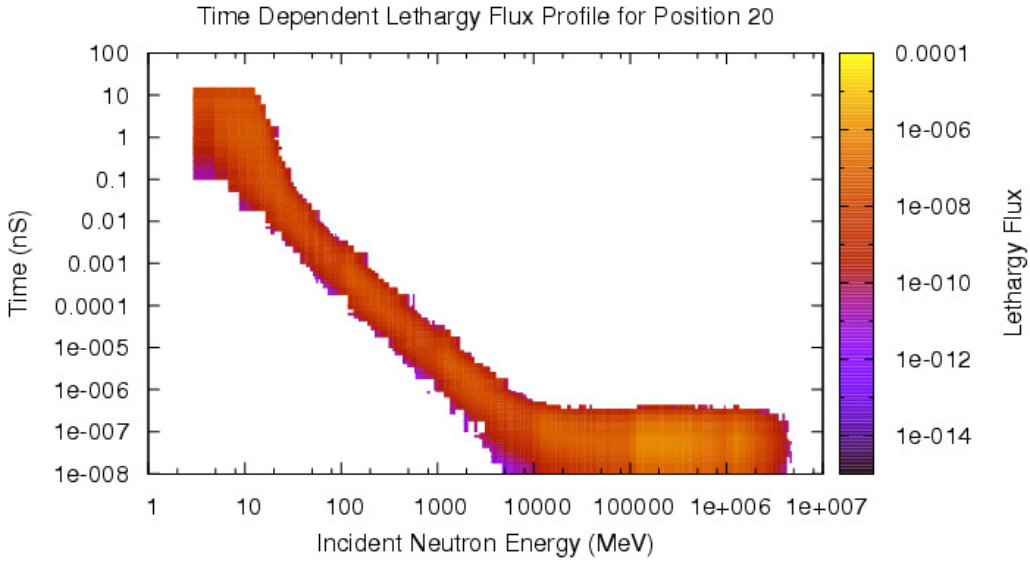

Figure 157 Lethargy flux profile for the GSDS position 20.

APPENDIX B

NEUTRON DETECTOR SIMULATION STUIDES

Many neutron detector configurations were studied over the course of this thesis. Several perturbations on the layered and stacked configurations were studied to define an optimal configuration that maximizes the neutron response and minimizes the gamma ray response. Shown below are pulse height distributions resulting from a one sided scintillator. The three components are shown in Figure 158 which are the components from gamma rays, alpha particles and tritons. These three components are plotted as a function of neutron energy in a series of two dimensional color maps shown in Figure 159 to Figure 317. A one sided scintillator conformally coated with 15 μm of ^{6}LiF are shown. Stacks of 1 mm, 0.5 mm, and 15 μm scintillators for two to 15 one sided scintillators are shown. The 1mm scintillator does not exhibit neutron versus gamma discrimination while the 15 μm scintillator does.

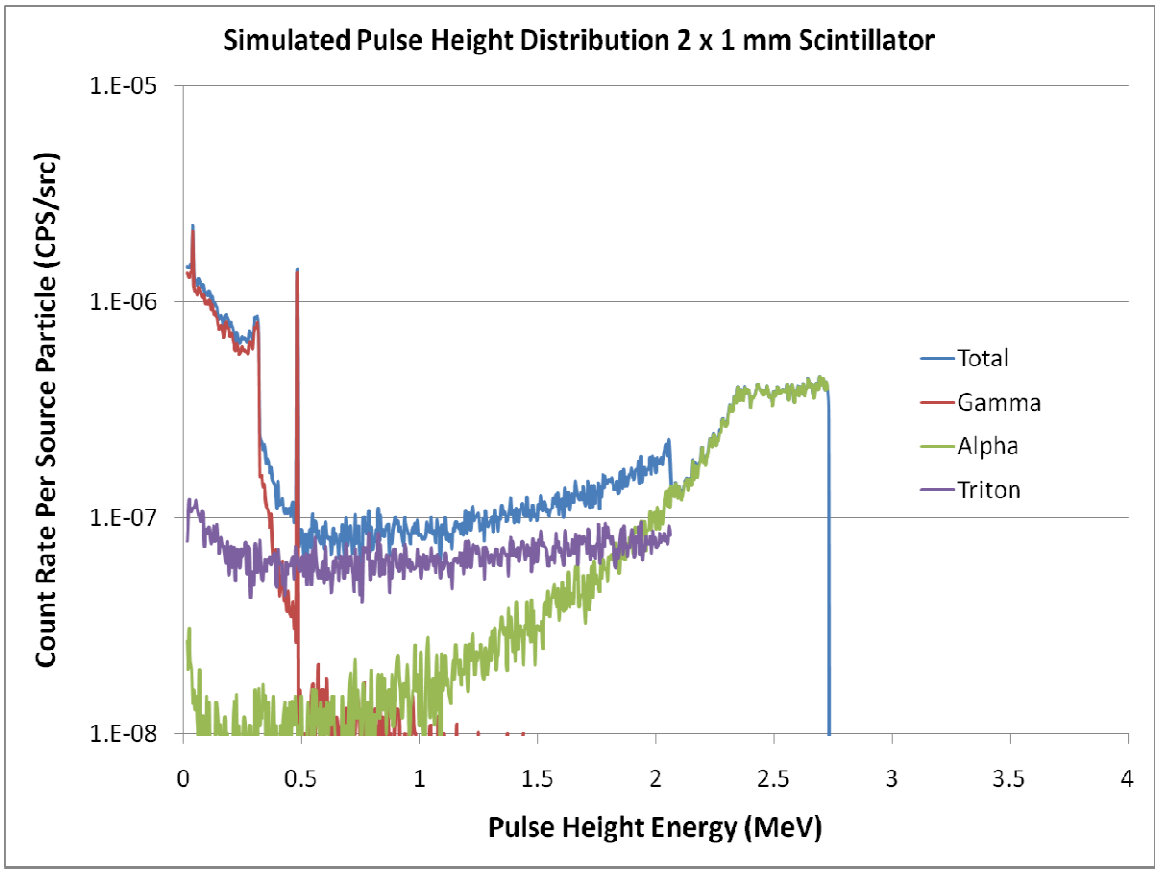

Figure 158 Three components to the scintillator pulse height distribution for two layers of a 1 mm scintillator.

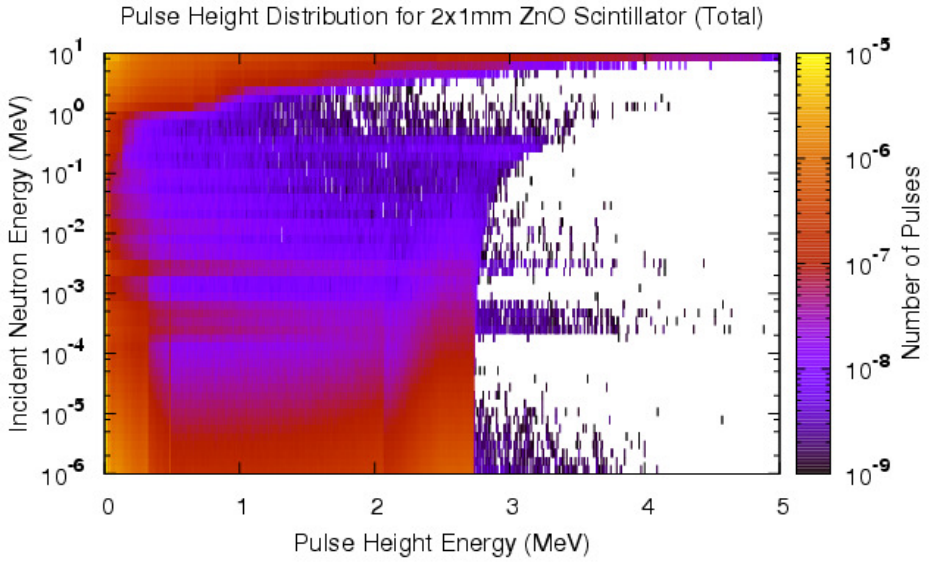

Figure 159 Pulse height distribution for all particles in a 2x1mm scintillator stack.

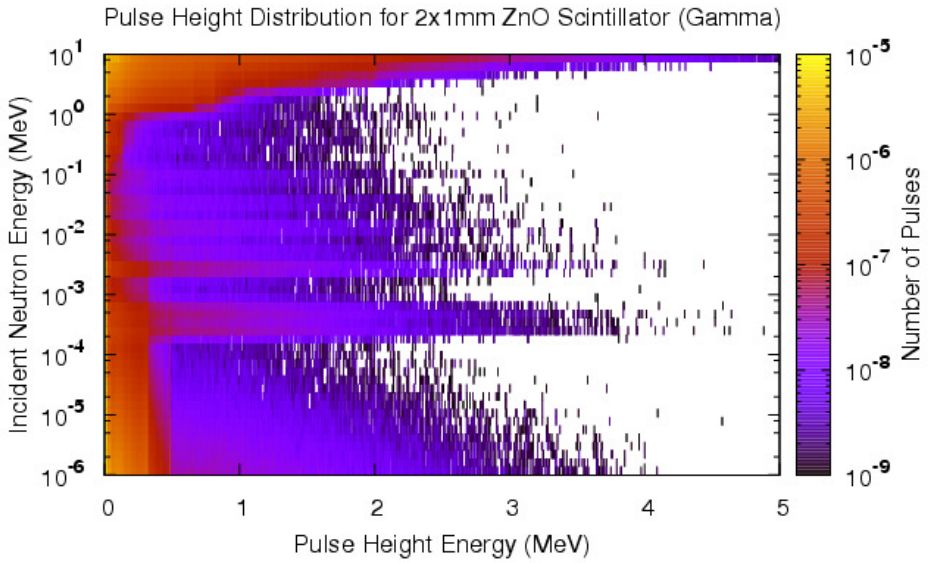

Figure 160 Pulse height distribution for gamma rays in a 2x1mm scintillator stack.

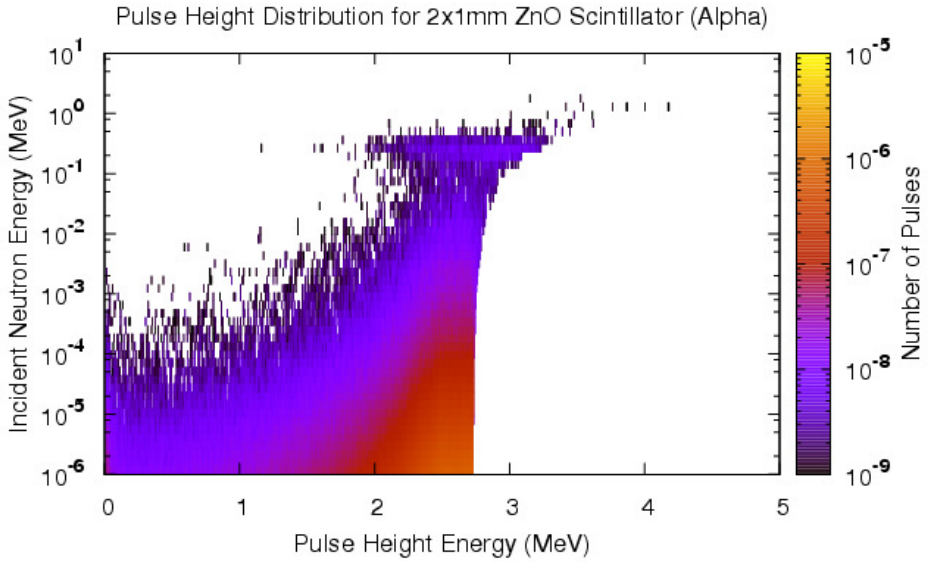

Figure 161 Pulse height distribution for alpha particles in a 2x1mm scintillator stack.

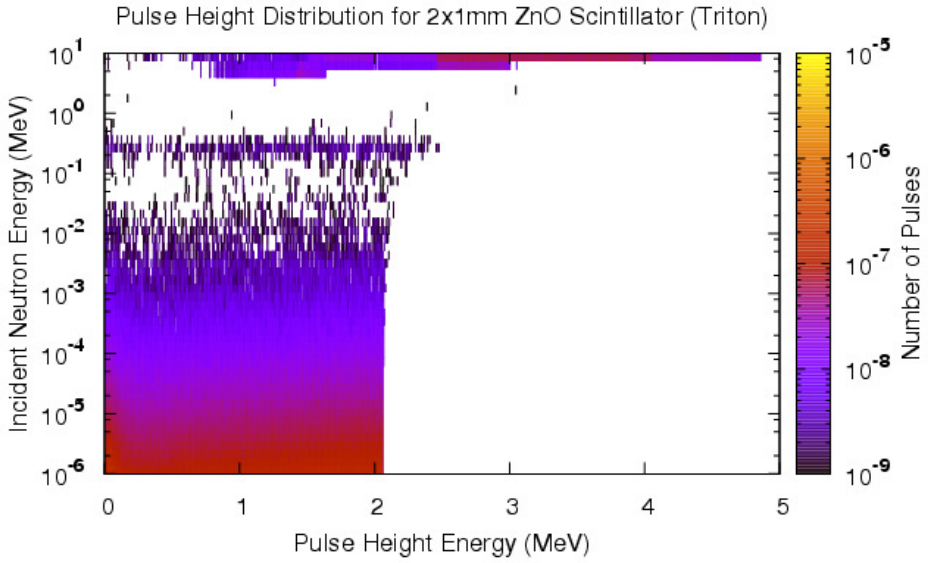

Figure 162 Pulse height distribution for trition particles in a 2x1mm scintillator stack.

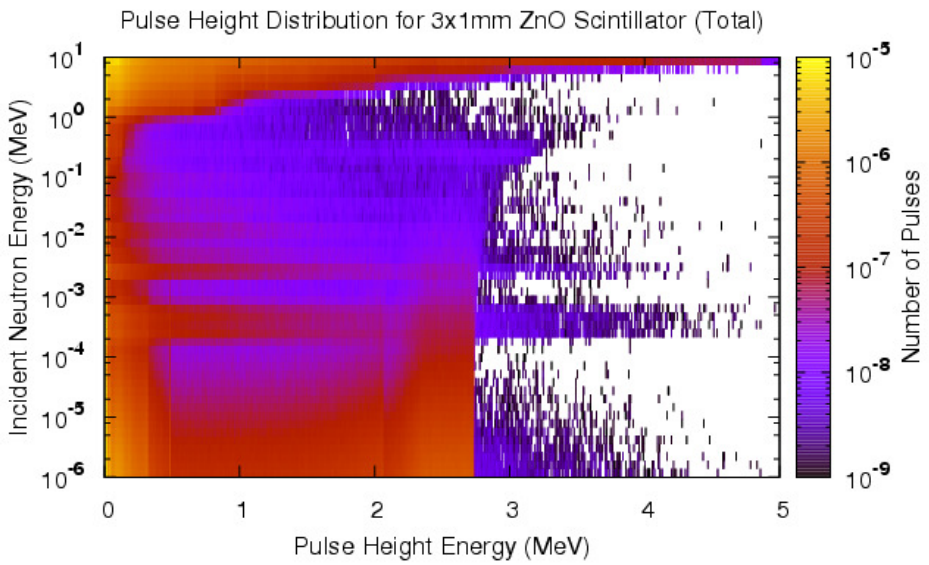

Figure 163 Pulse height distribution for all particles in a 3x1mm scintillator stack.

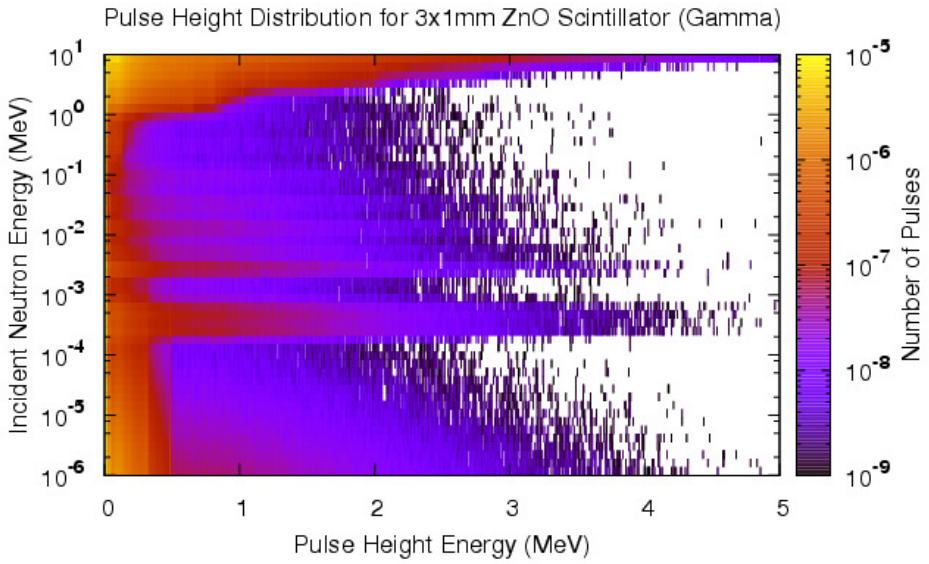

Figure 164 Pulse height distribution for gamma rays in a 3x1mm scintillator stack.

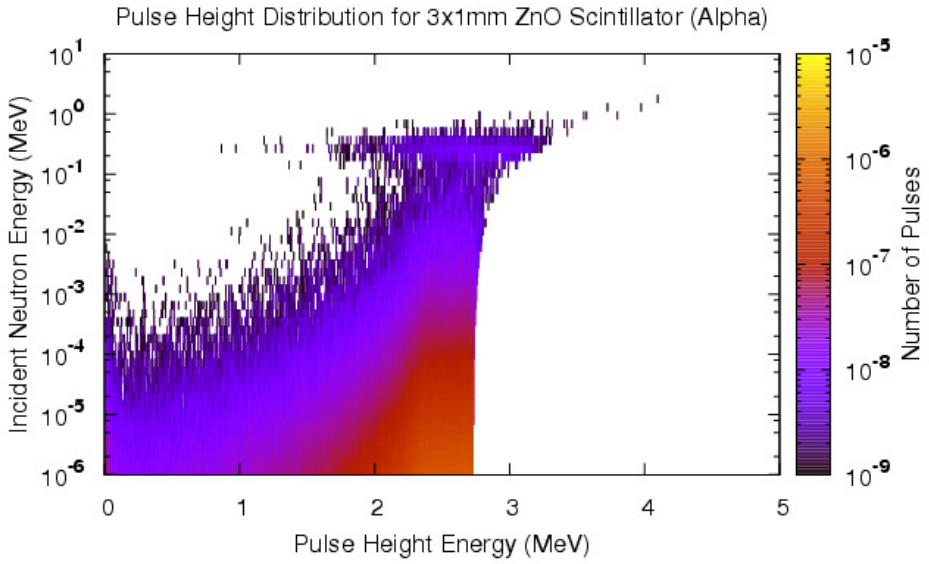

Figure 165 Pulse height distribution for alpha particles in a 3x1mm scintillator stack.

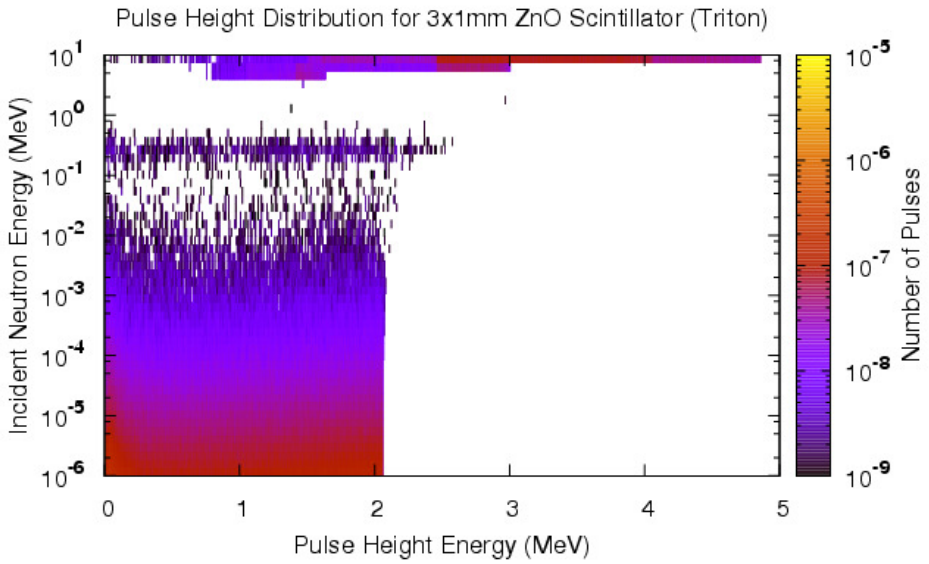

Figure 166 Pulse height distribution for triton particles in a 3x1mm scintillator stack.

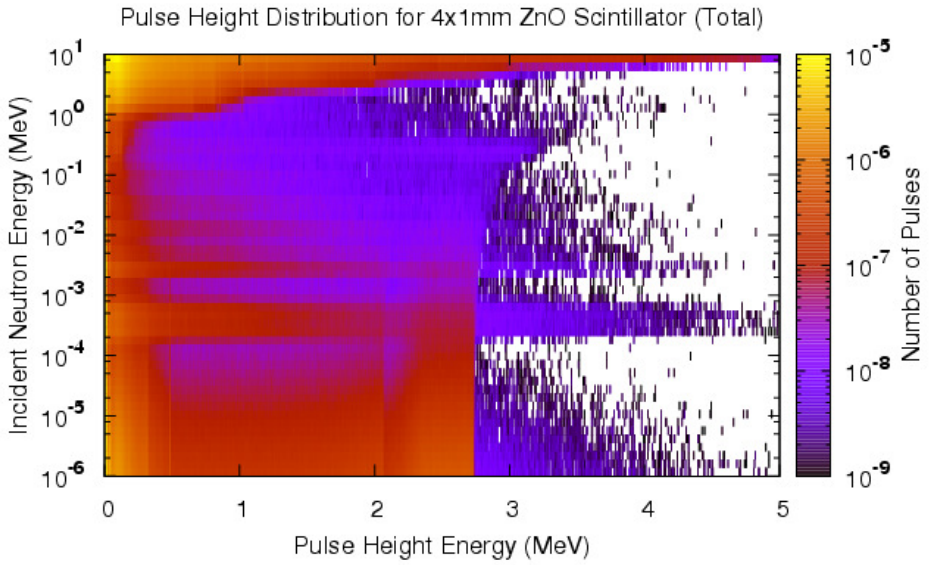

Figure 167 Pulse height distribution for all particles in a 4x1mm scintillator stack.

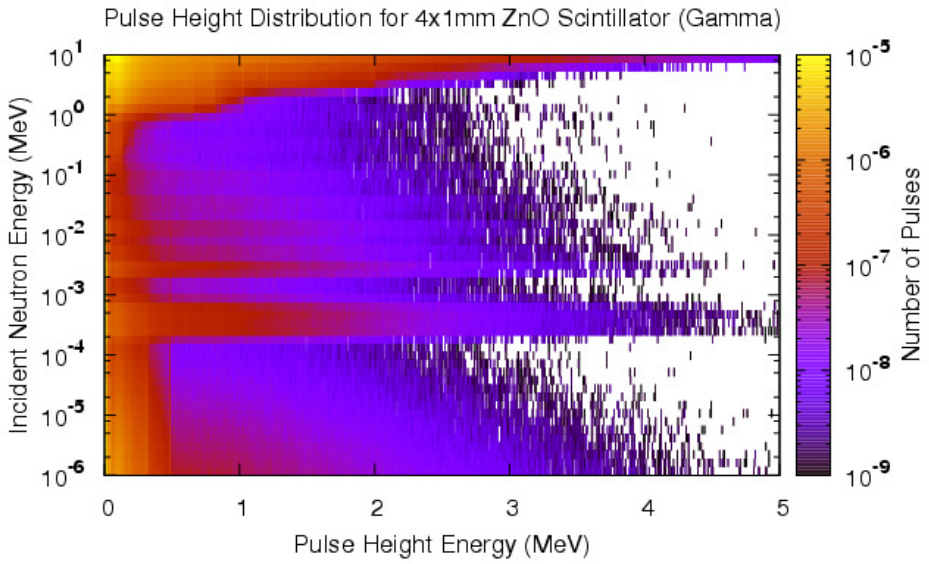

Figure 168 Pulse height distribution for gamma rays in a 4x1mm scintillator stack.

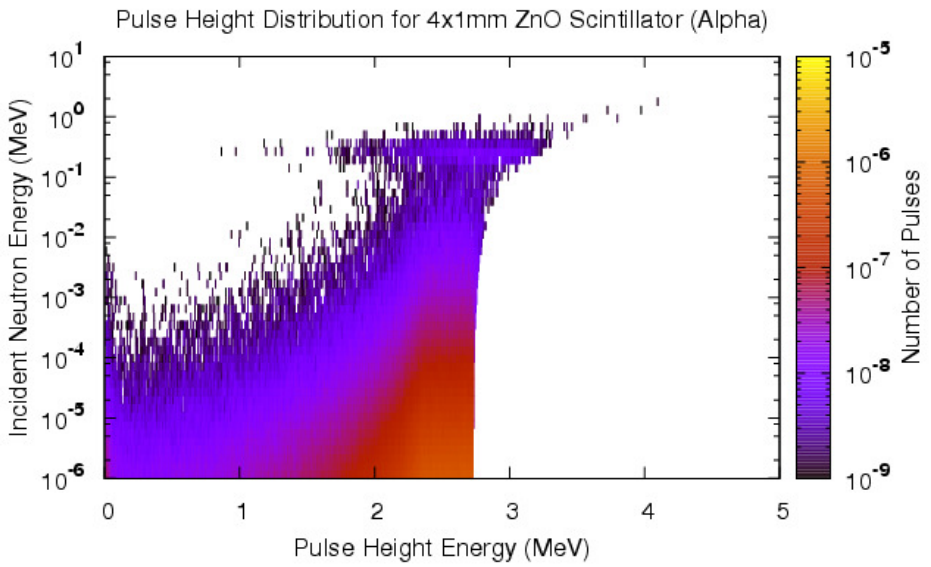

Figure 169 Pulse height distribution for alpha particles in a 4x1mm scintillator stack.

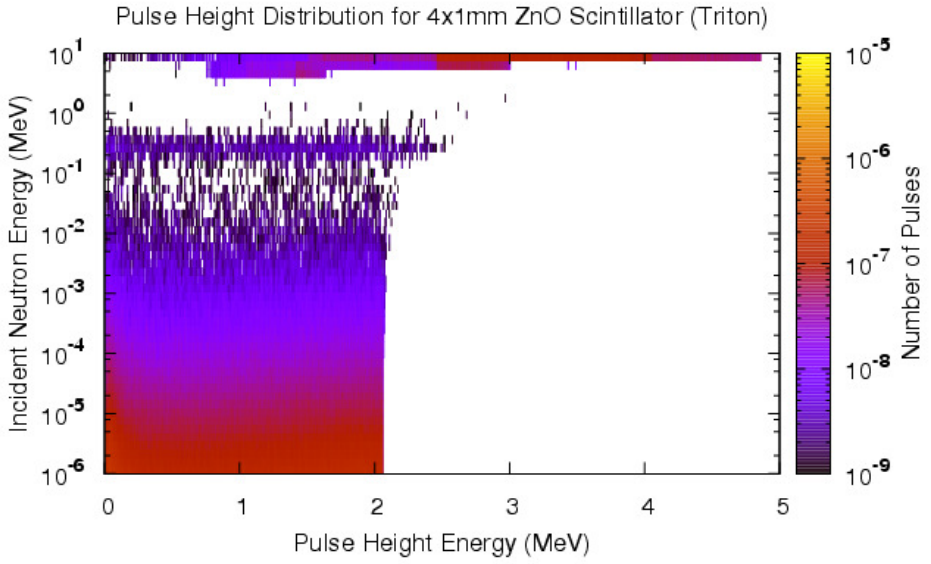

Figure 170 Pulse height distribution for triton particles in a 4x1mm scintillator stack.

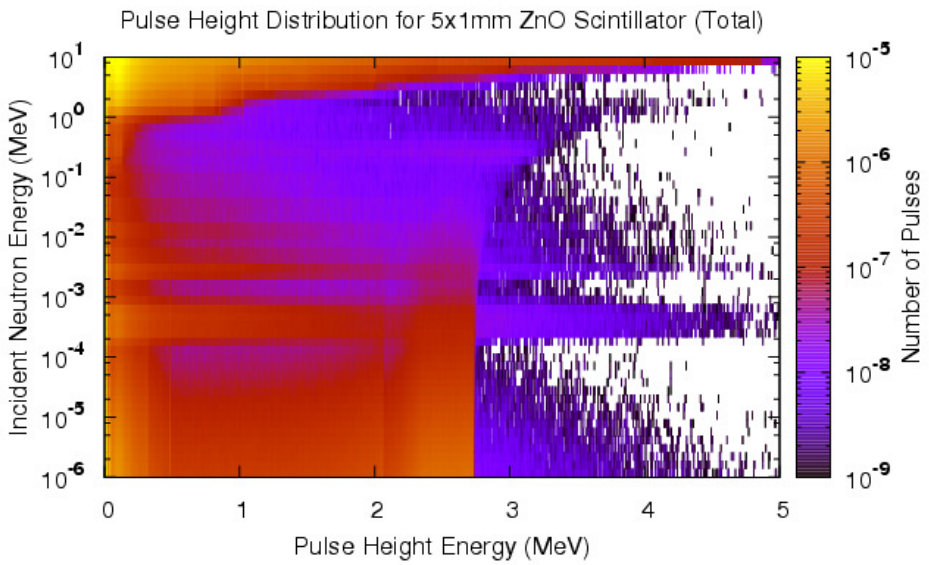

Figure 171 Pulse height distribution for all particles in a 5x1mm scintillator stack.

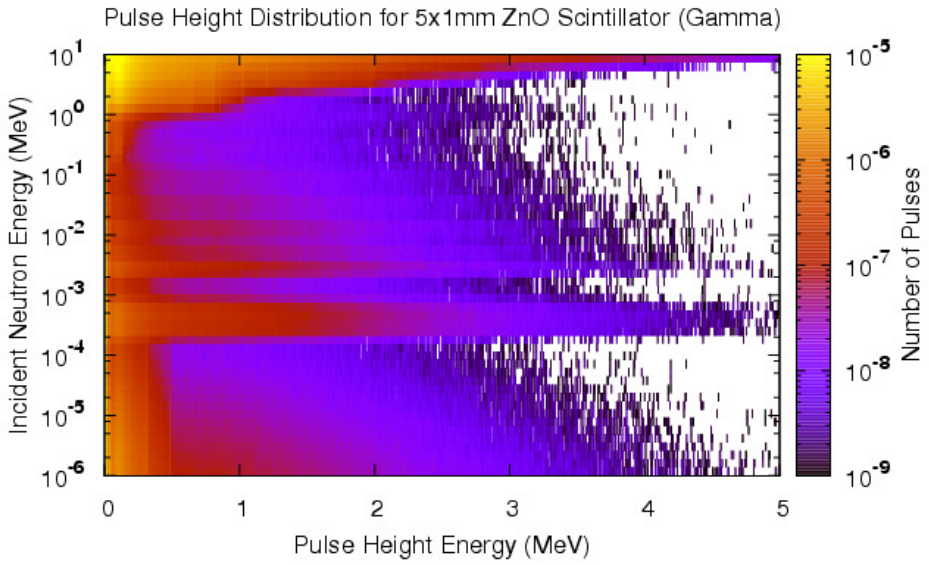

Figure 172 Pulse height distribution for gamma rays in a 5x1mm scintillator stack.

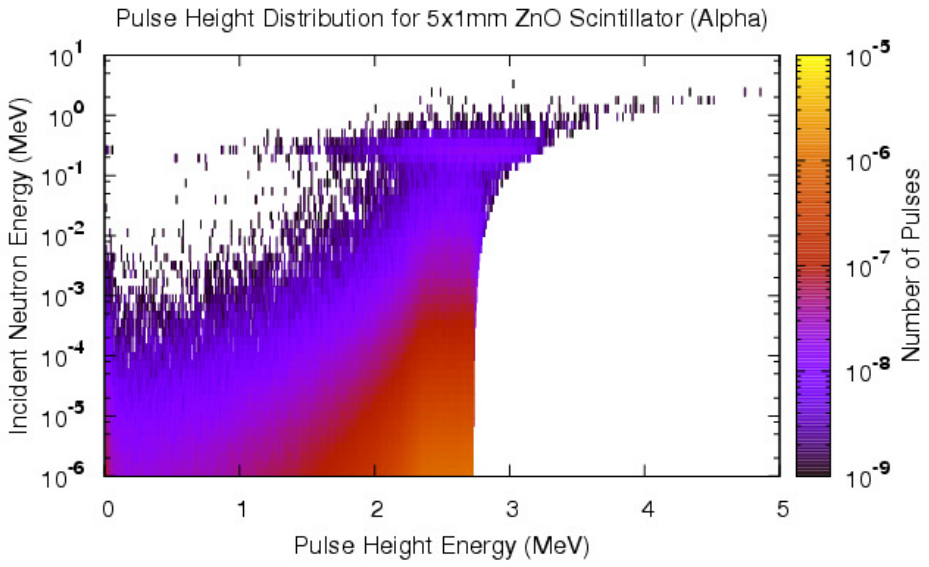

Figure 173 Pulse height distribution for alpha particles in a 5x1mm scintillator stack.

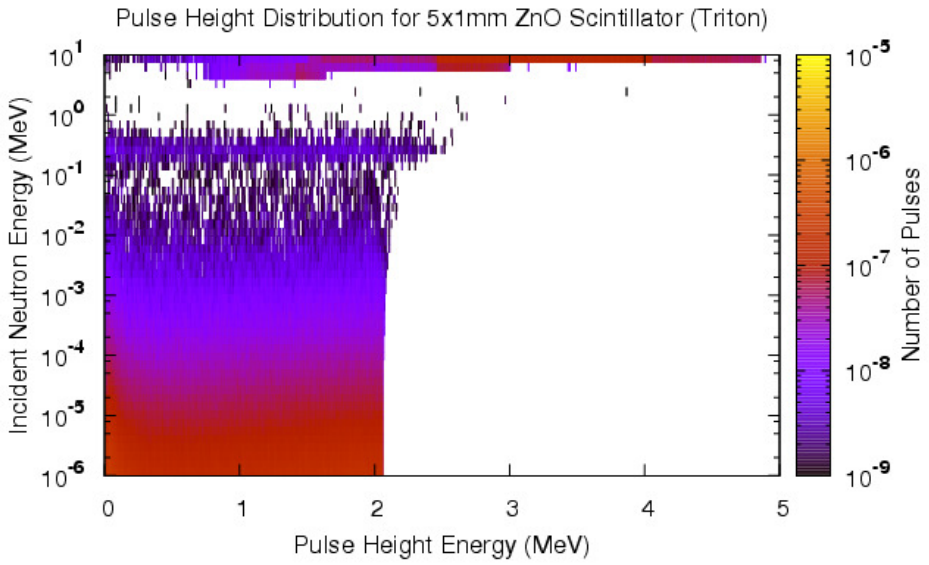

Figure 174 Pulse height distribution for triton particles in a 5x1mm scintillator stack.

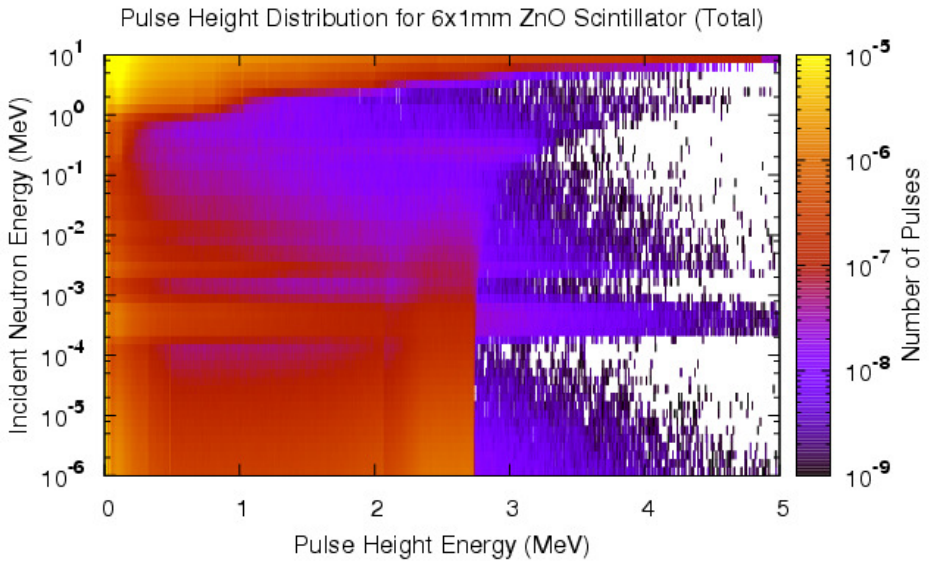

Figure 175 Pulse height distribution for all particles in a 6x1mm scintillator stack.

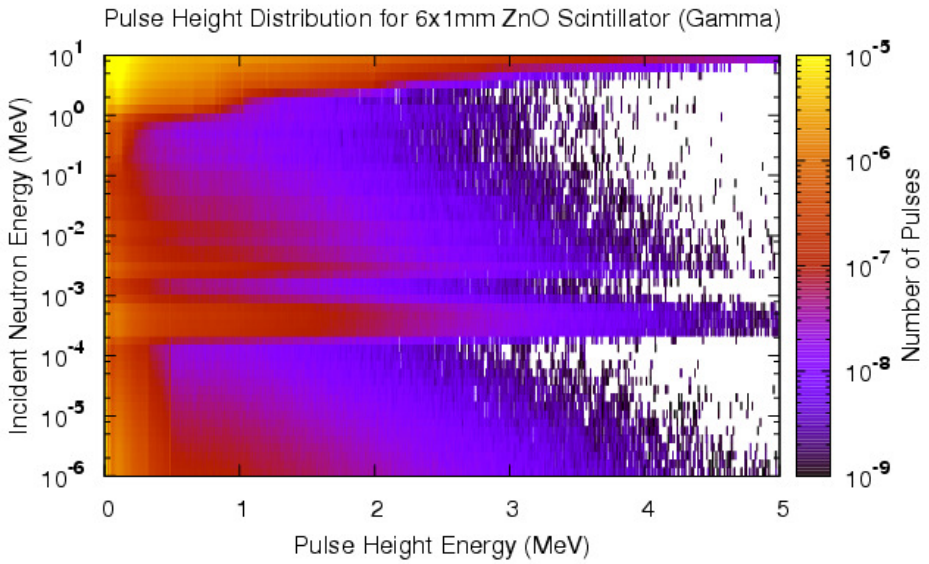

Figure 176 Pulse height distribution for gamma rays in a 6x1mm scintillator stack.

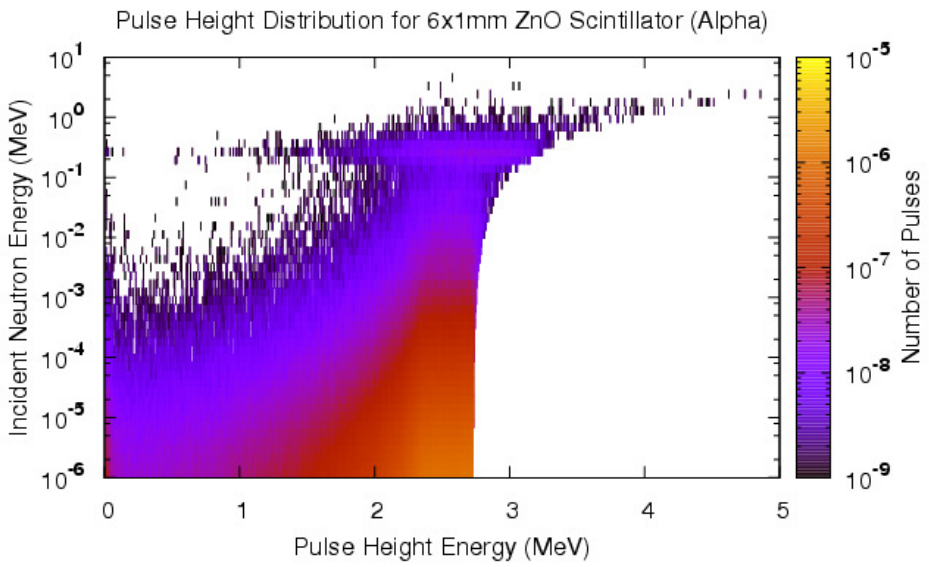

Figure 177 Pulse height distribution for alpha particles in a 6x1mm scintillator stack.

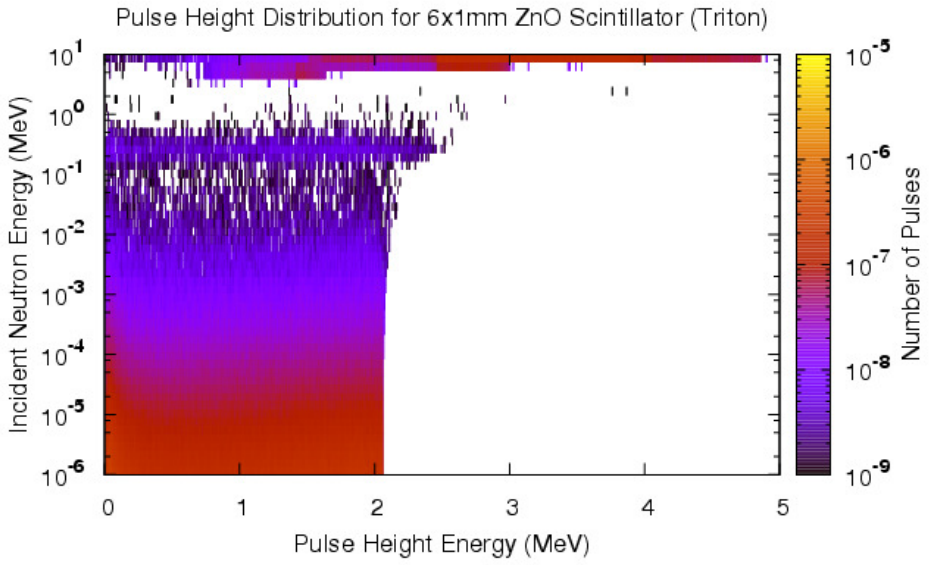

Figure 178 Pulse height distribution for triton particles in a 6x1mm scintillator stack.

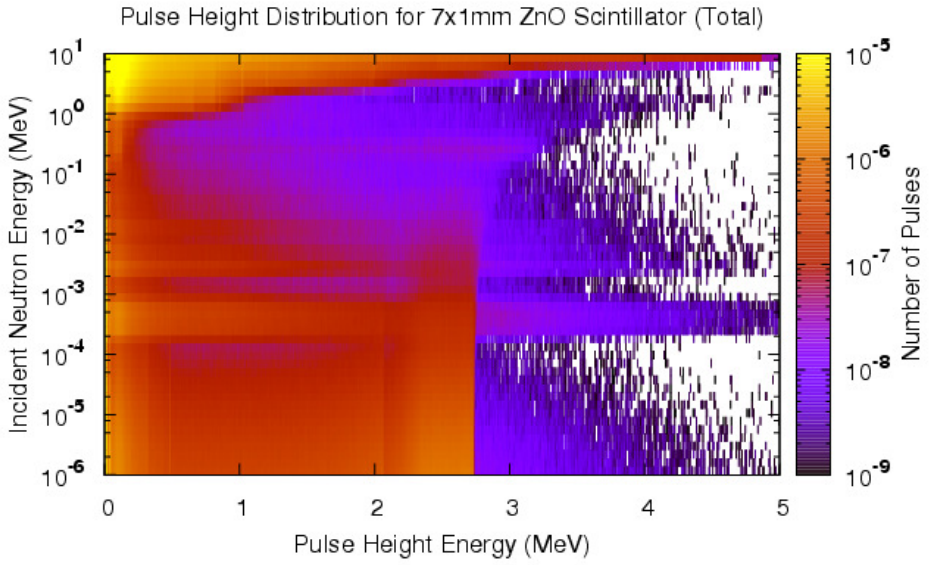

Figure 179 Pulse height distribution for all particles in a 7x1mm scintillator stack.

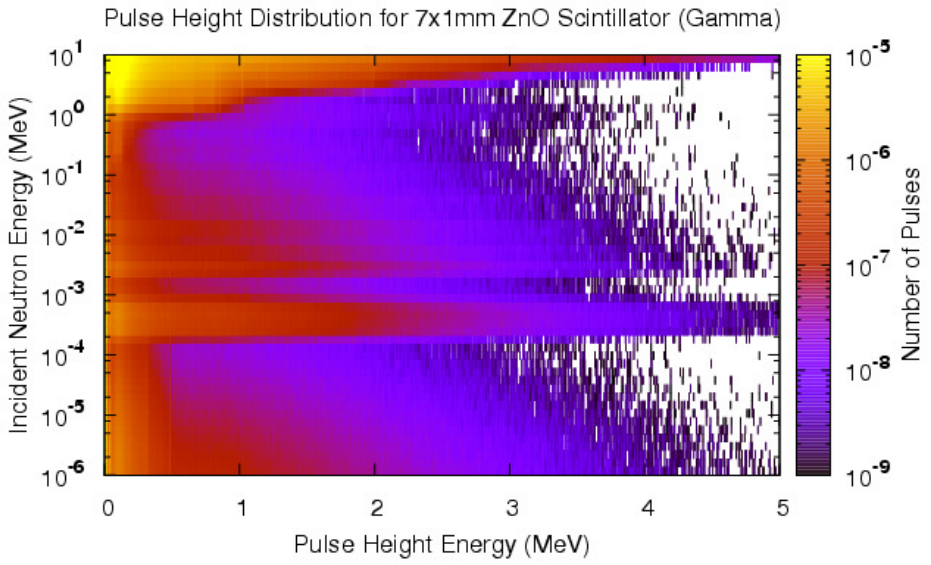

Figure 180 Pulse height distribution for gamma rays in a 7x1mm scintillator stack.

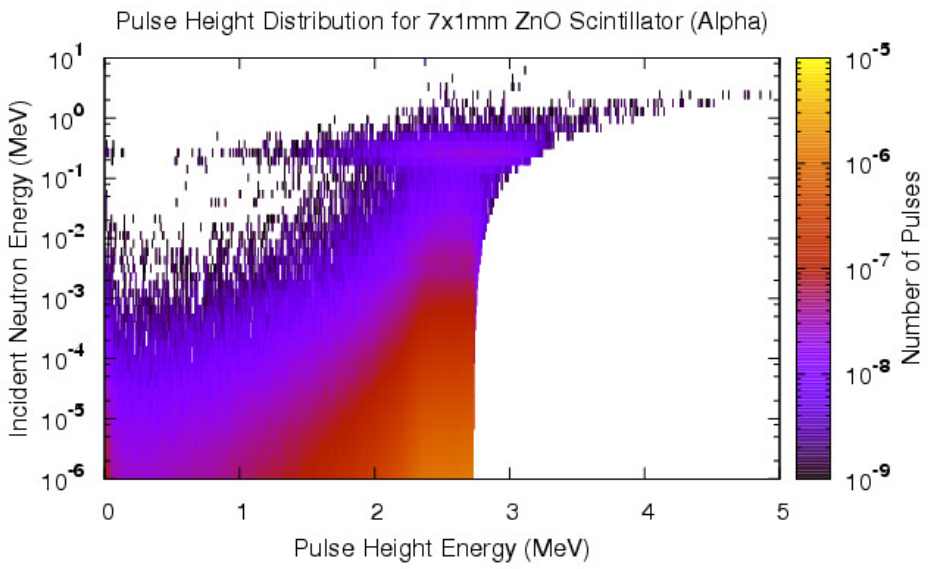

Figure 181 Pulse height distribution for alpha particles in a 7x1mm scintillator stack.

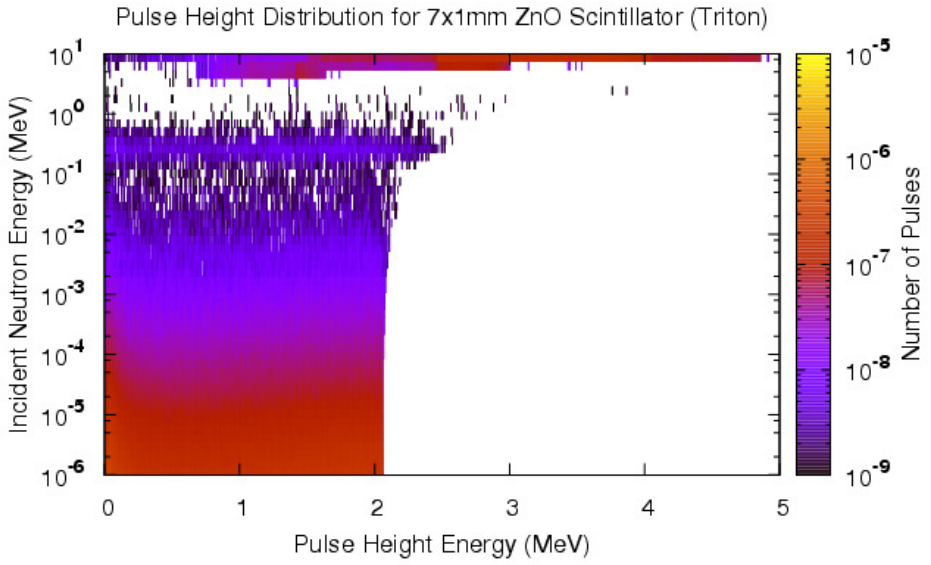

Figure 182 Pulse height distribution for triton particles in a 7x1mm scintillator stack.

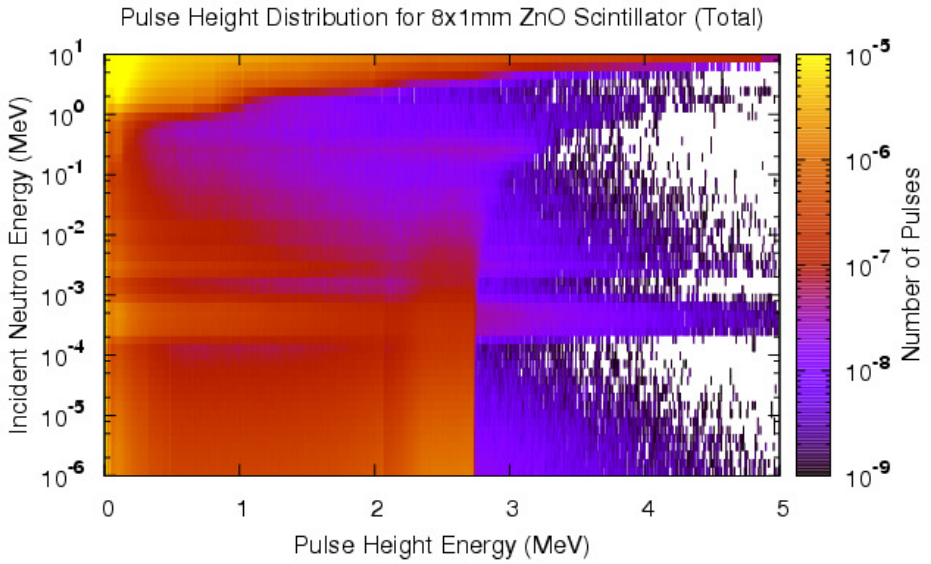

Figure 183 Pulse height distribution for all particles in a 8x1mm scintillator stack.

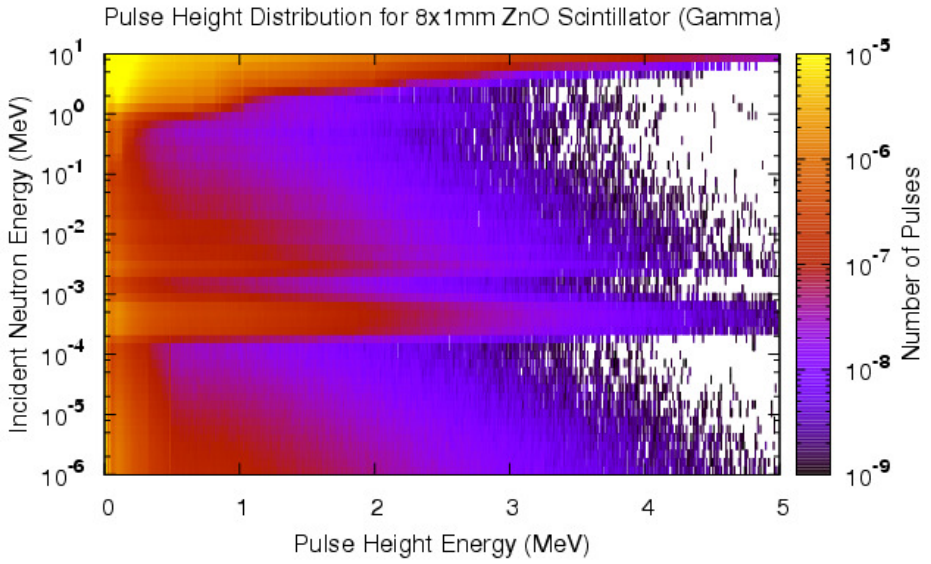

Figure 184 Pulse height distribution for gamma rays in a 8x1mm scintillator stack.

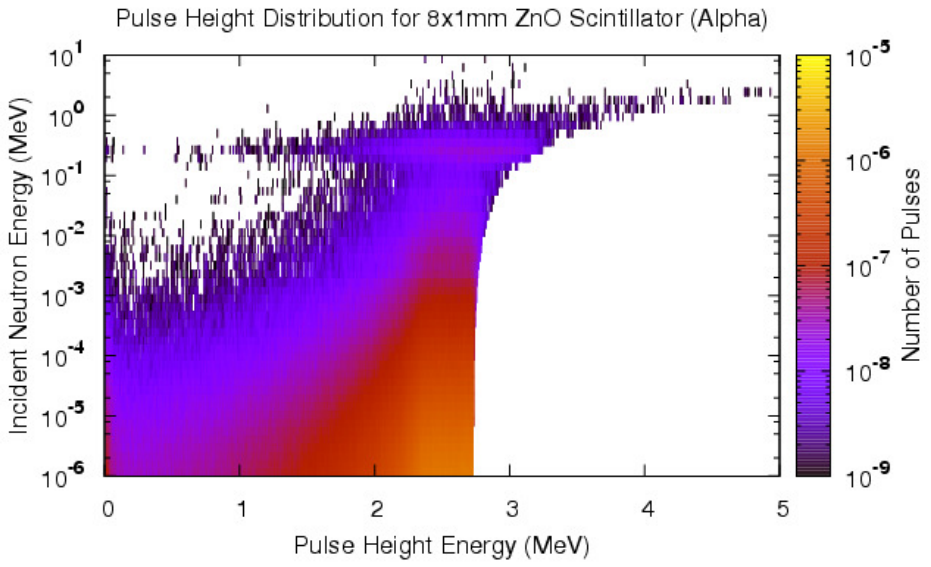

Figure 185 Pulse height distribution for alpha particles in a 8x1mm scintillator stack.

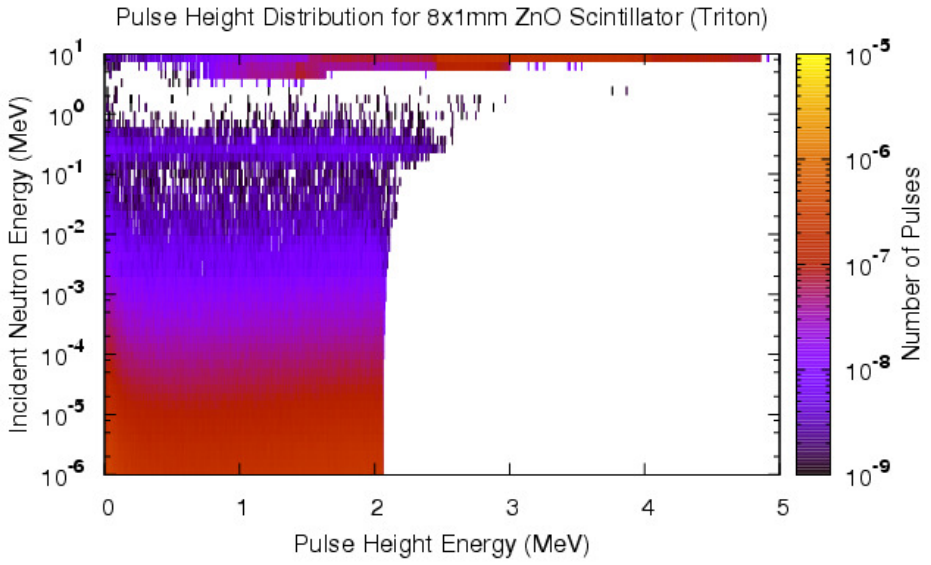

Figure 186 Pulse height distribution for triton particles in a 8x1mm scintillator stack.

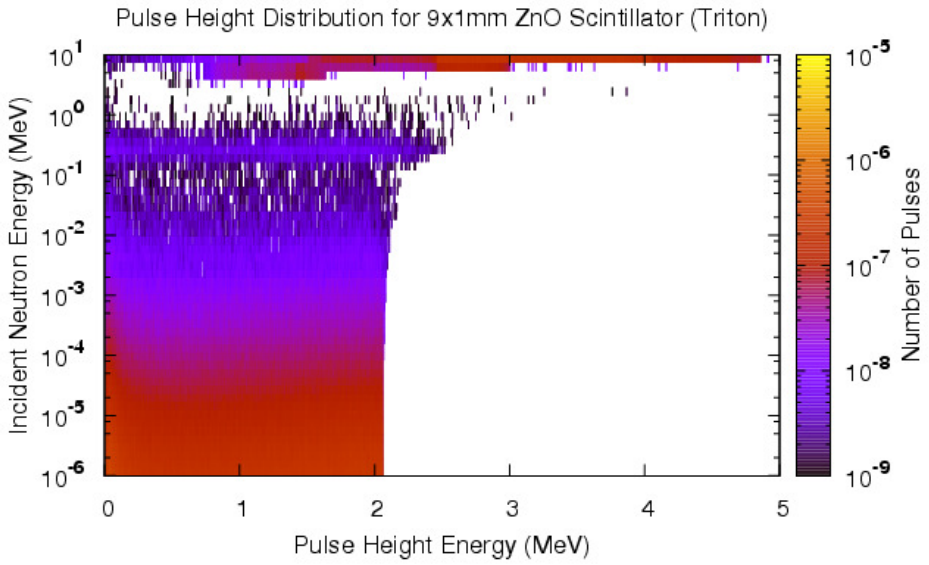

Figure 187 Pulse height distribution for triton particles in a 9x1mm scintillator stack.

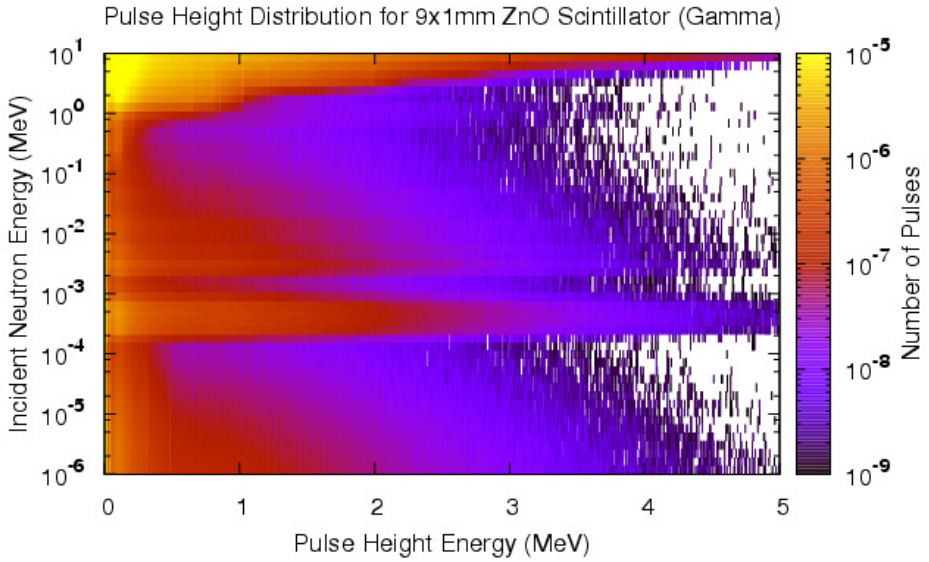

Figure 188 Pulse height distribution for gamma rays in a 9x1mm scintillator stack.

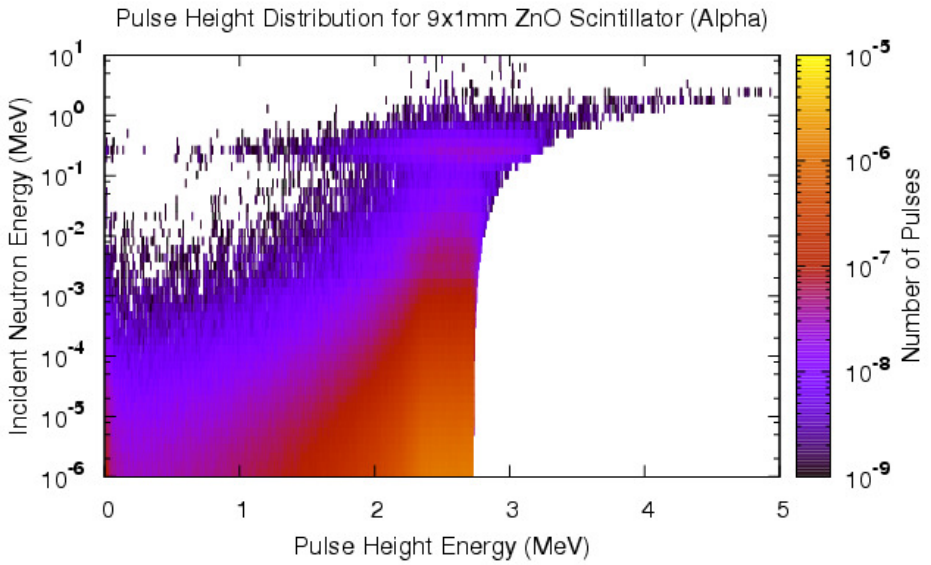

Figure 189 Pulse height distribution for alpha particles in a 9x1mm scintillator stack.

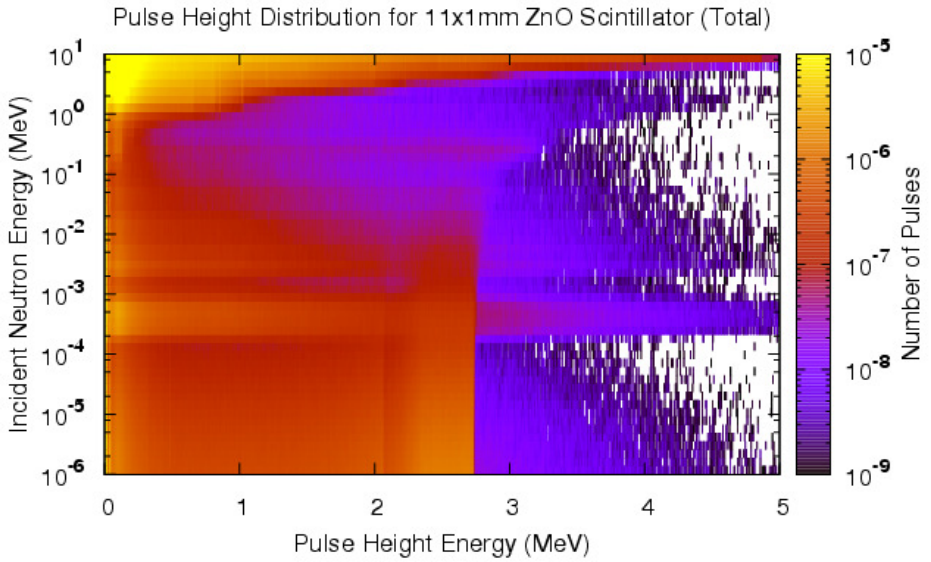

Figure 190 Pulse height distribution for all particles in a 11x1mm scintillator stack.

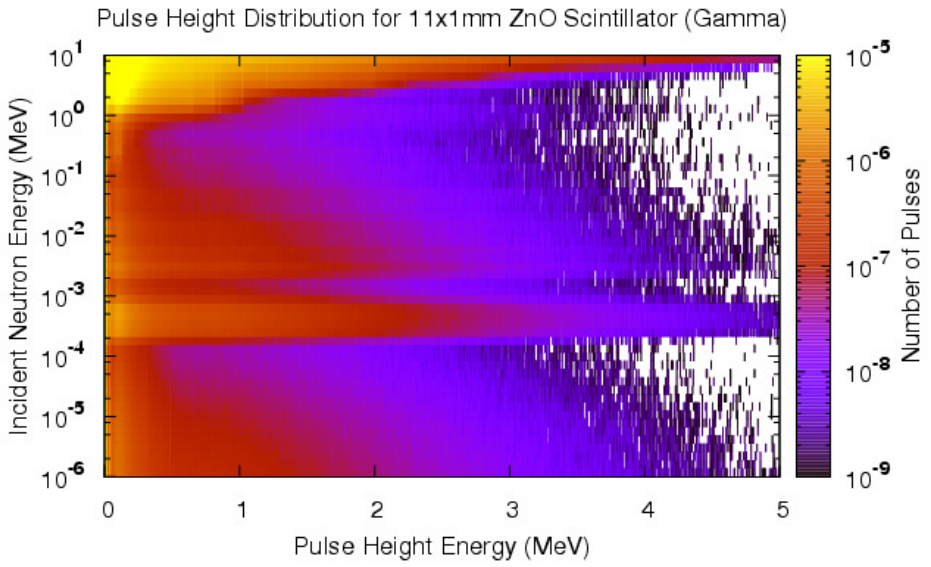

Figure 191 Pulse height distribution for gamma rays in a 11x1mm scintillator stack.

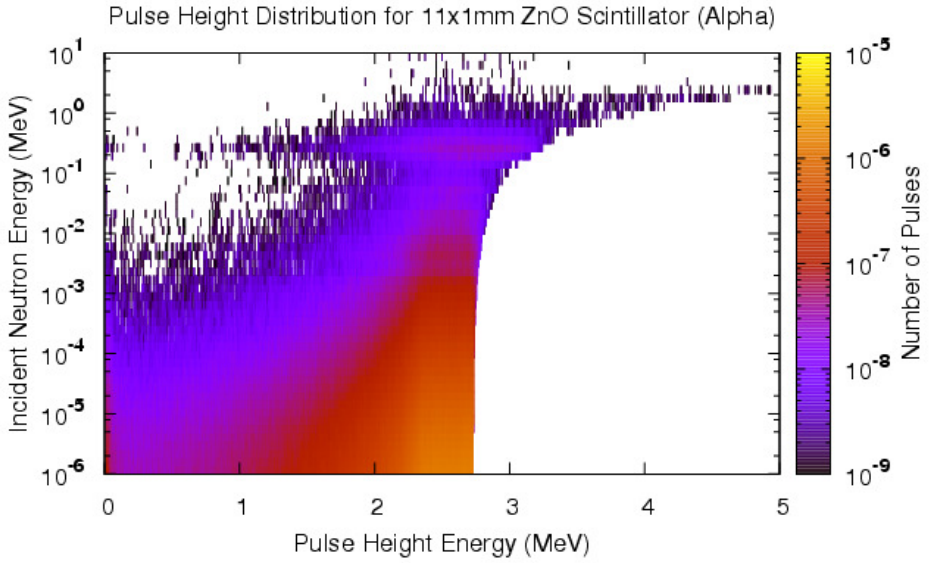

Figure 192 Pulse height distribution for alpha particles in a 11x1mm scintillator stack.

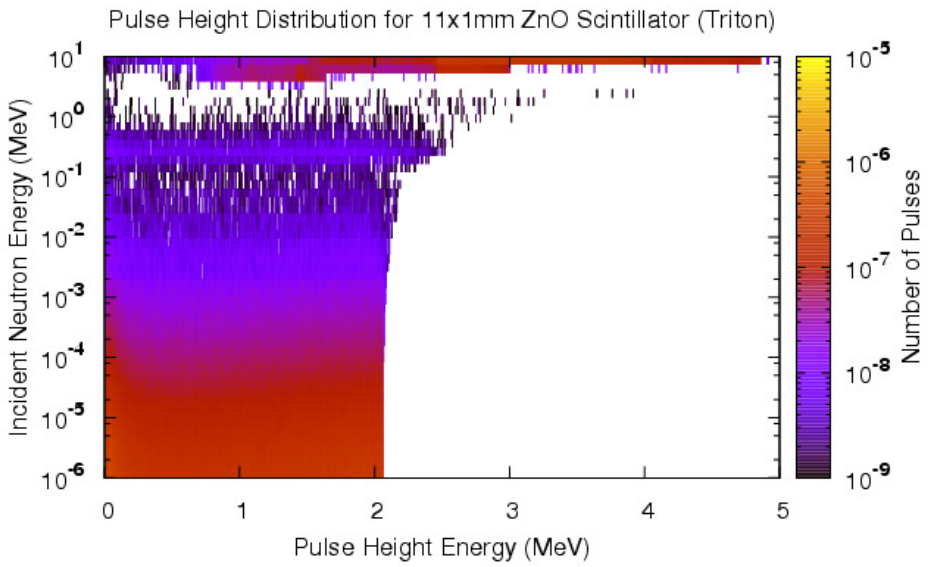

Figure 193 Pulse height distribution for triton particles in a 11x1mm scintillator stack.

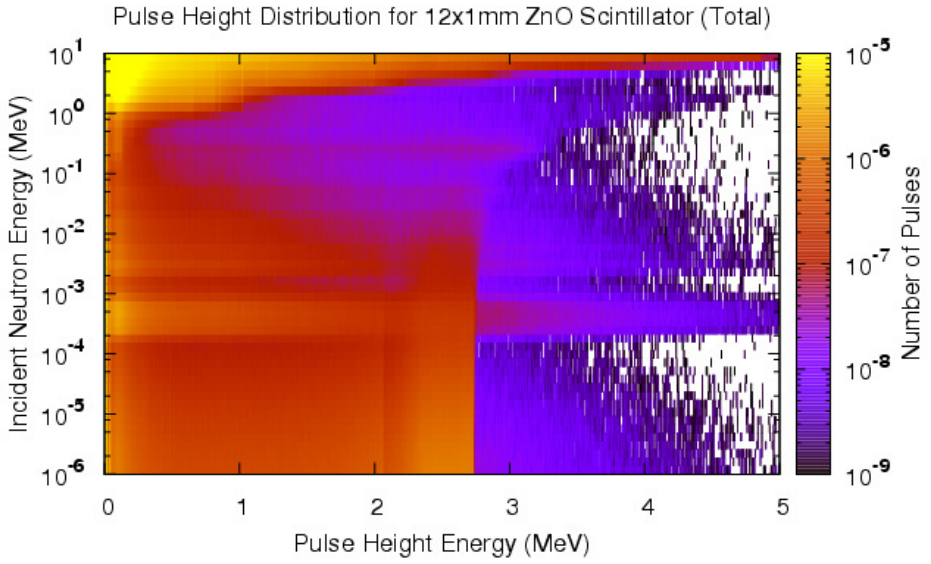

Figure 194 Pulse height distribution for all particles in a 12x1mm scintillator stack.

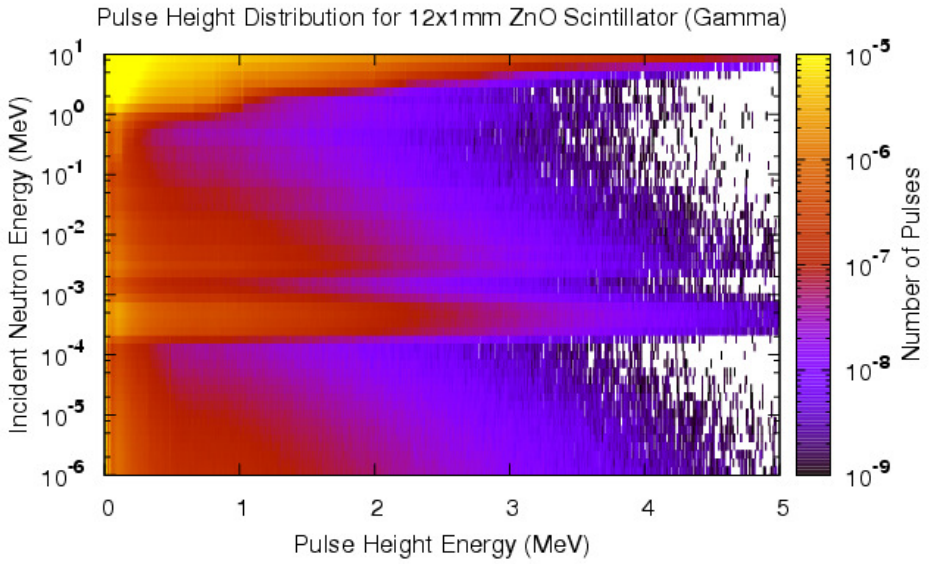

Figure 195 Pulse height distribution for gamma rays in a 12x1mm scintillator stack.

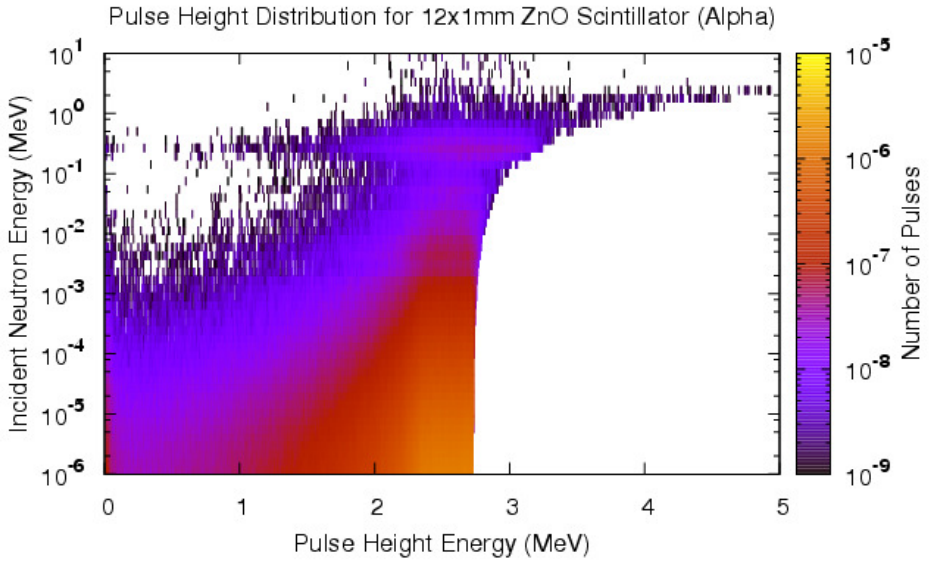

Figure 196 Pulse height distribution for alpha particles in a 12x1mm scintillator stack.

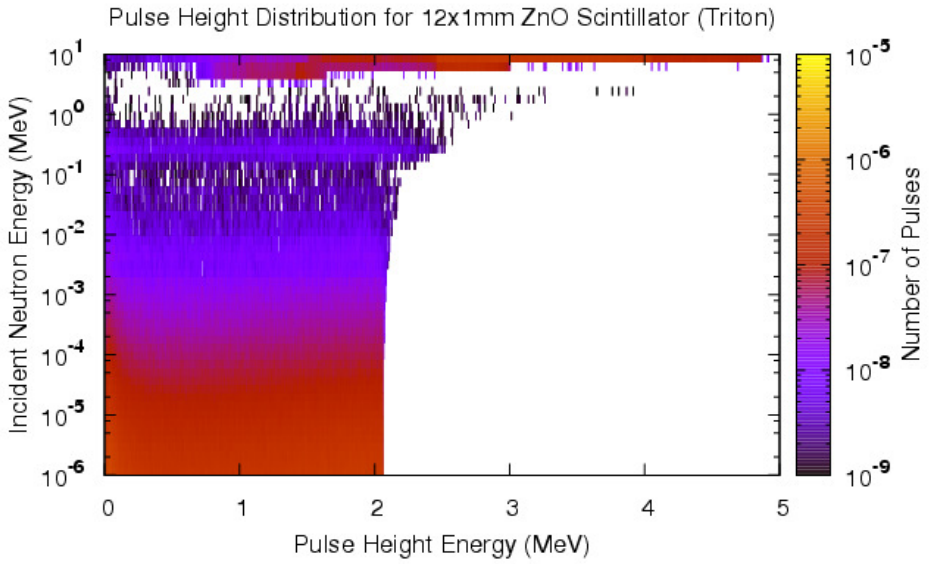

Figure 197 Pulse height distribution for triton particles in a 12x1mm scintillator stack.

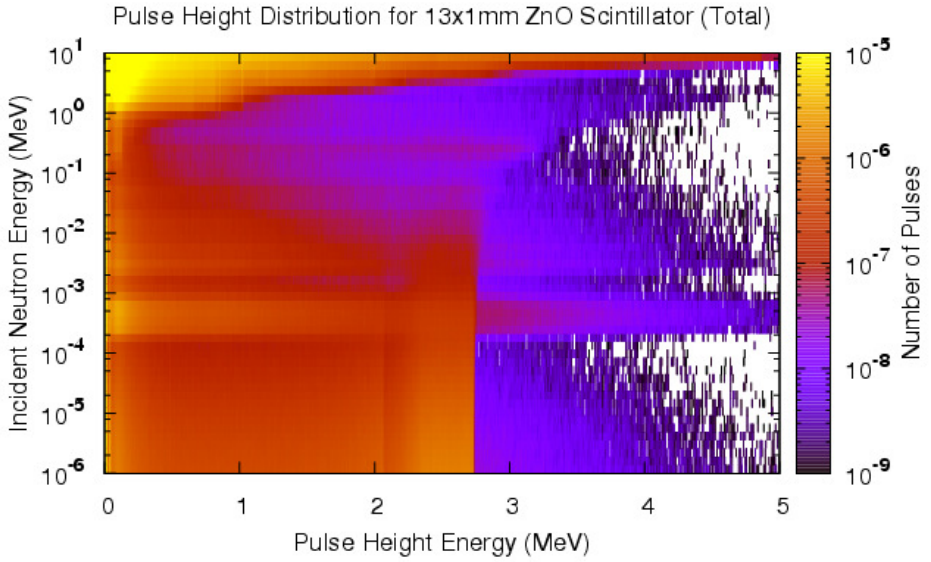

Figure 198 Pulse height distribution for all particles in a 13x1mm scintillator stack.

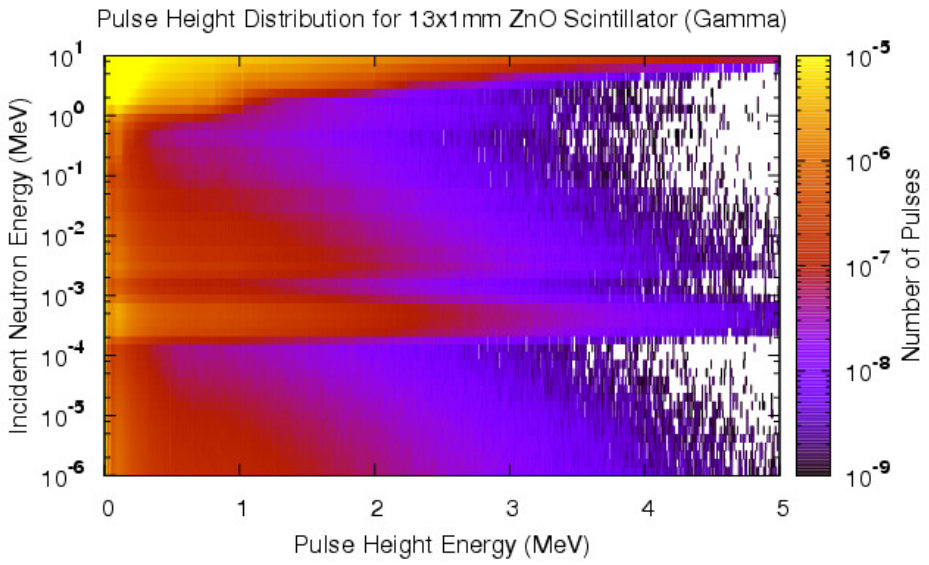

Figure 199 Pulse height distribution for gamma rays in a 13x1mm scintillator stack.

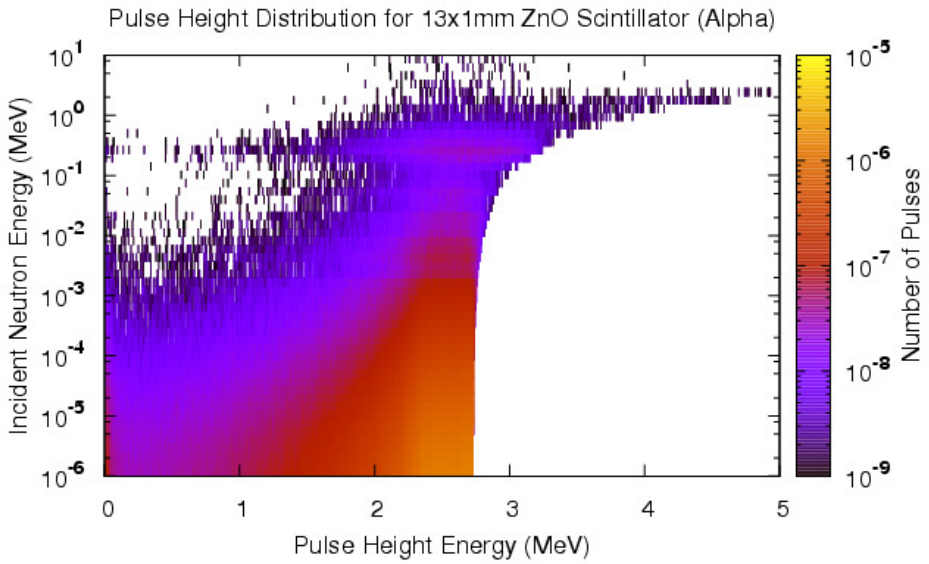

Figure 200 Pulse height distribution for alpha particles in a 13x1mm scintillator stack.

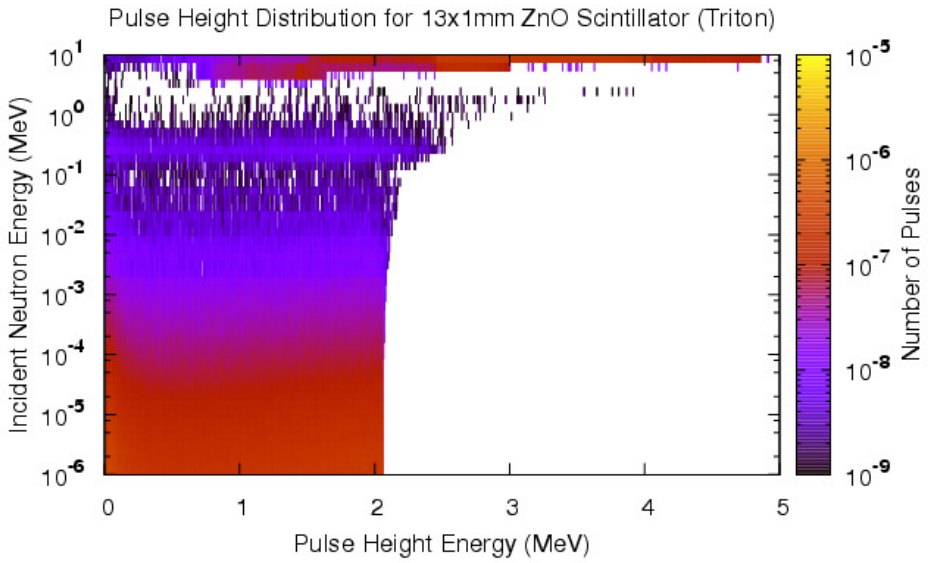

Figure 201 Pulse height distribution for triton particles in a 13x1mm scintillator stack.

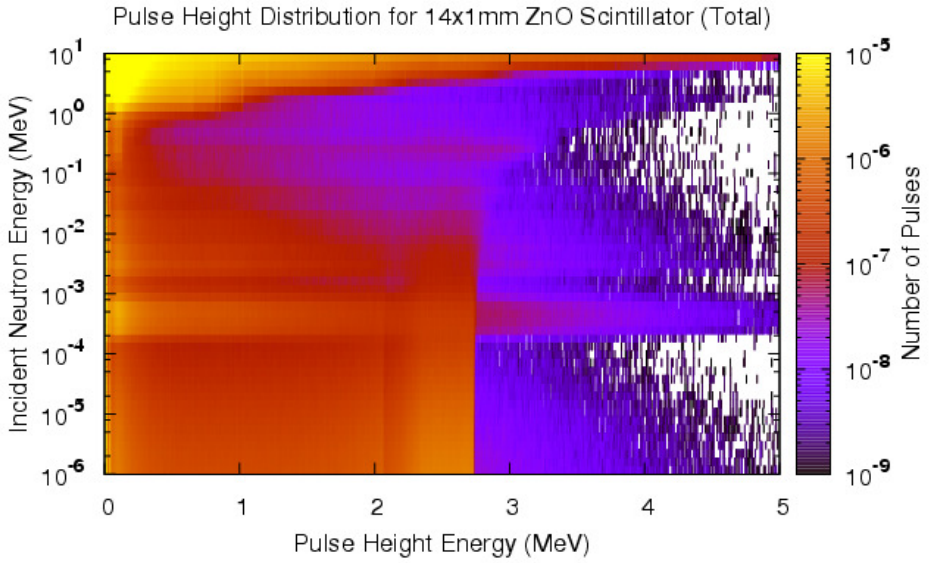

Figure 202 Pulse height distribution for all particles in a 14x1mm scintillator stack.

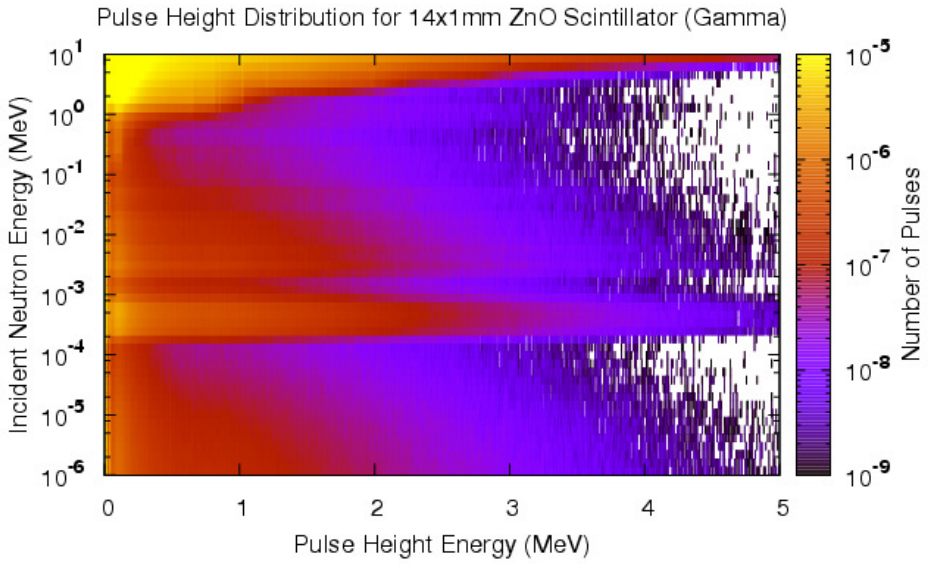

Figure 203 Pulse height distribution for gamma rays in a 14x1mm scintillator stack.

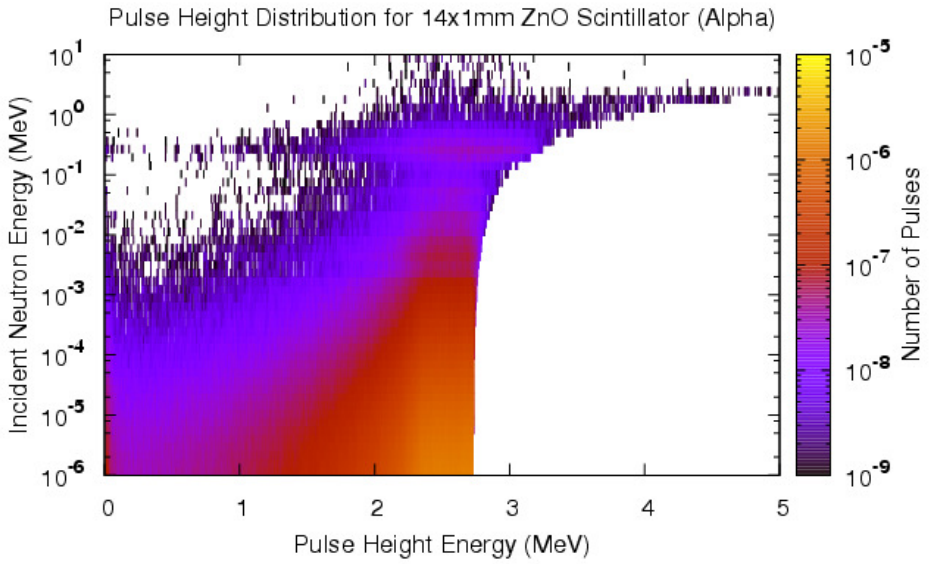

Figure 204 Pulse height distribution for alpha particles in a 14x1mm scintillator stack.

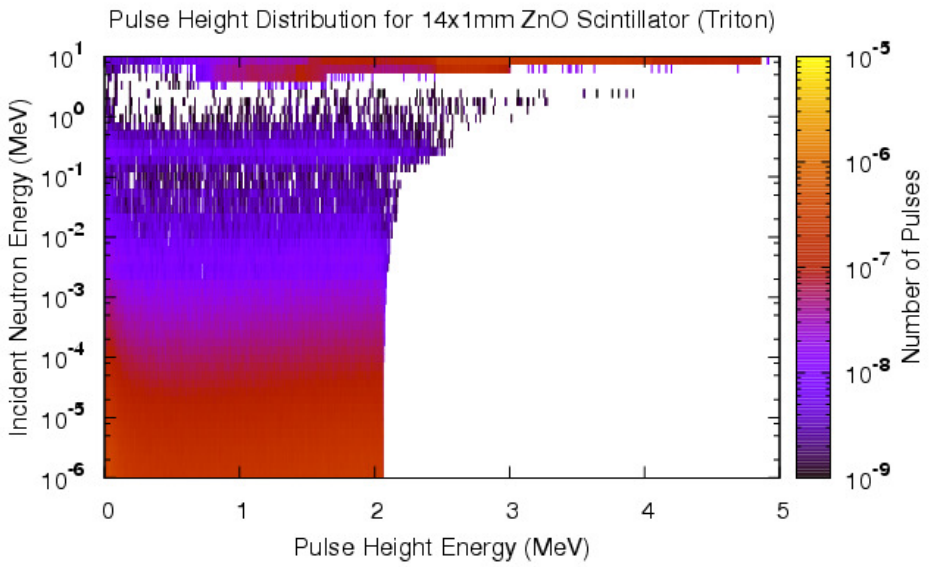

Figure 205 Pulse height distribution for triton particles in a 14x1mm scintillator stack.

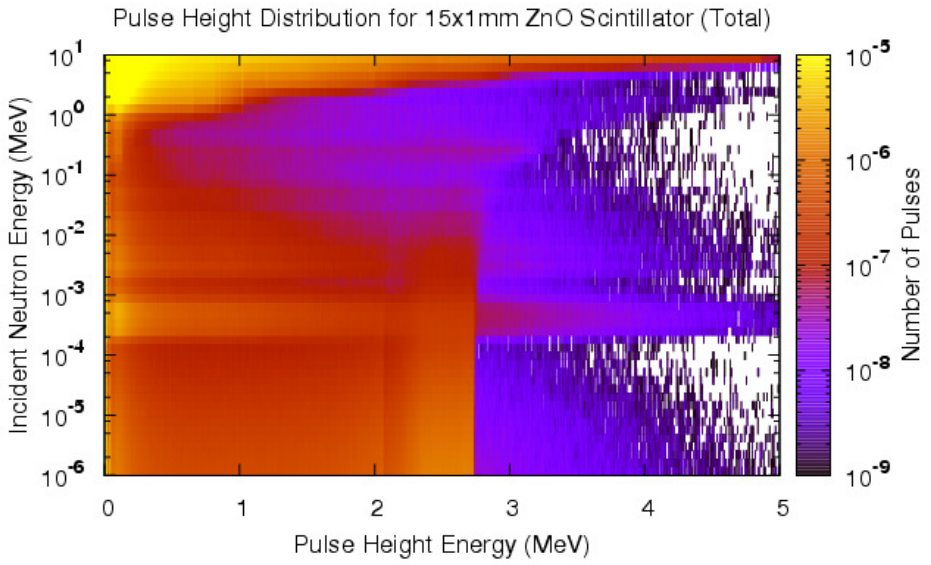

Figure 206 Pulse height distribution for all particles in a 15x1mm scintillator stack.

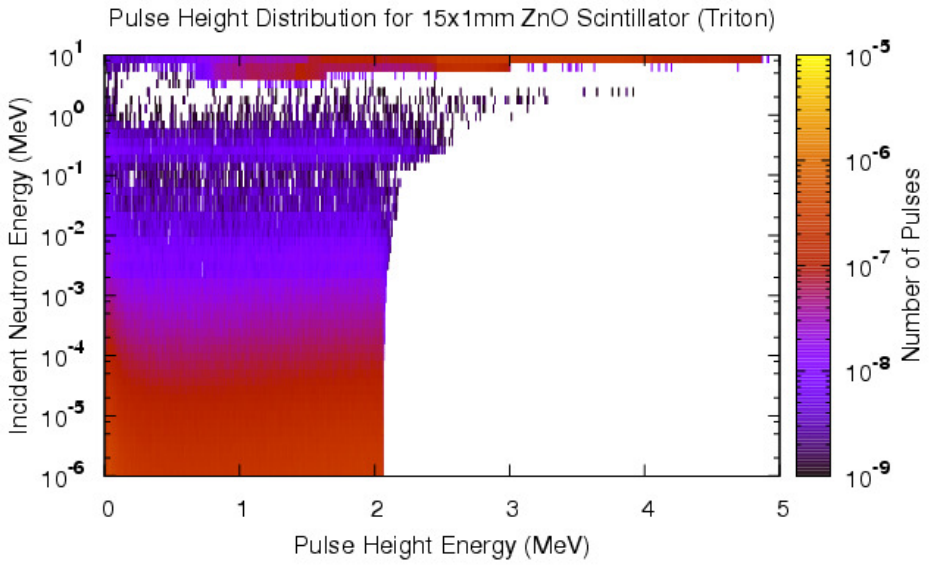

Figure 207 Pulse height distribution for tritons in a 15x1mm scintillator stack.

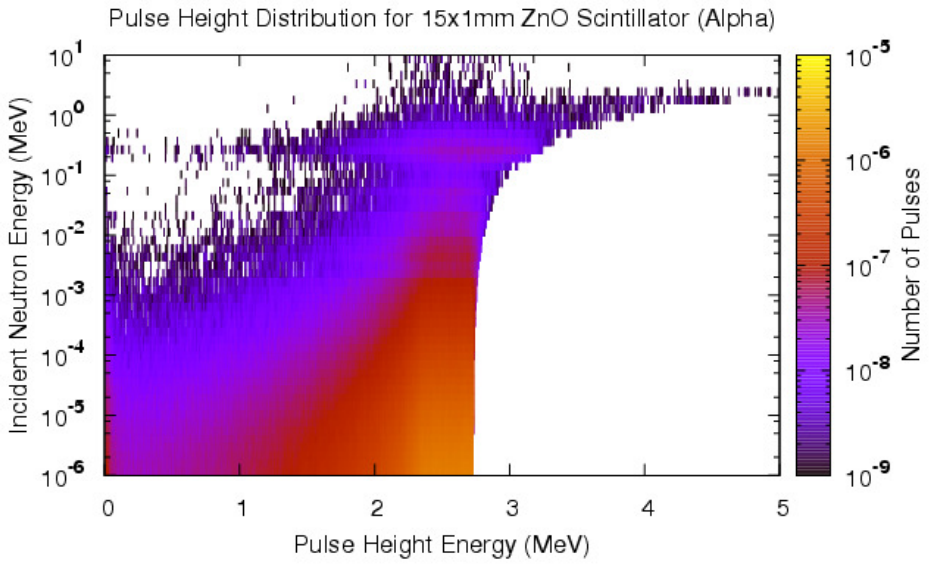

Figure 208 Pulse height distribution for alpha particles in a 15x1mm scintillator stack.

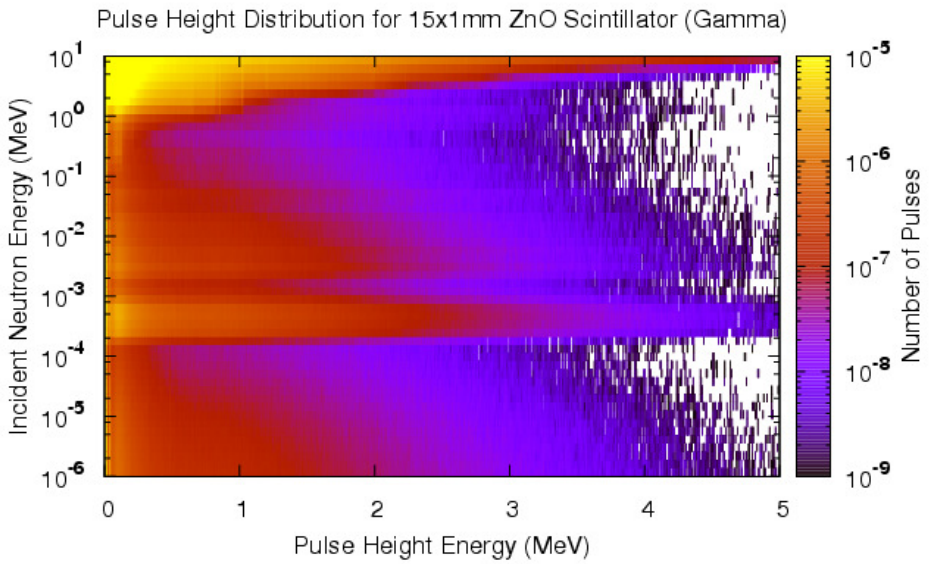

Figure 209 Pulse height distribution for gamma ray particles in a 6x1mm scintillator stack.

0.5 MM SAMPLES

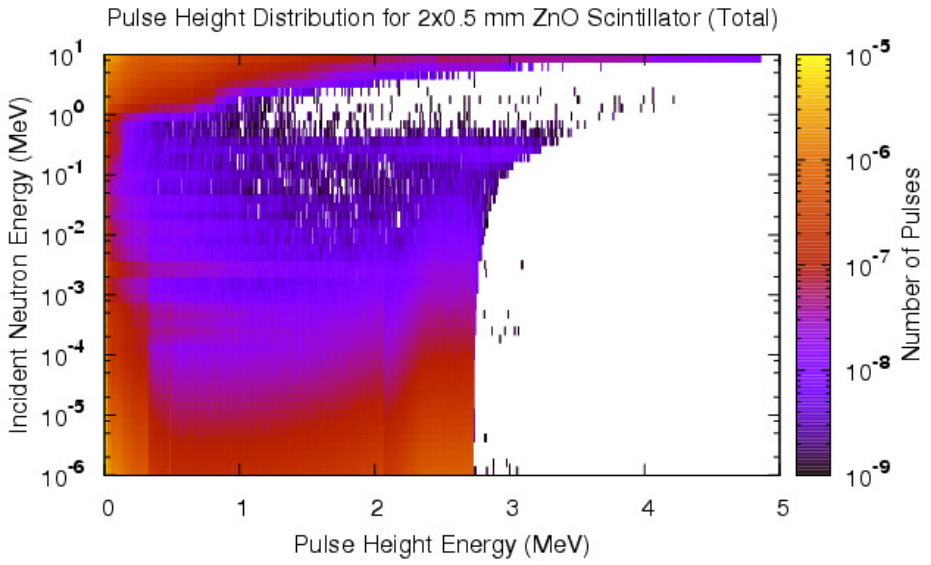

Figure 210 Pulse height distribution for all particles in a 2x0.5mm scintillator stack.

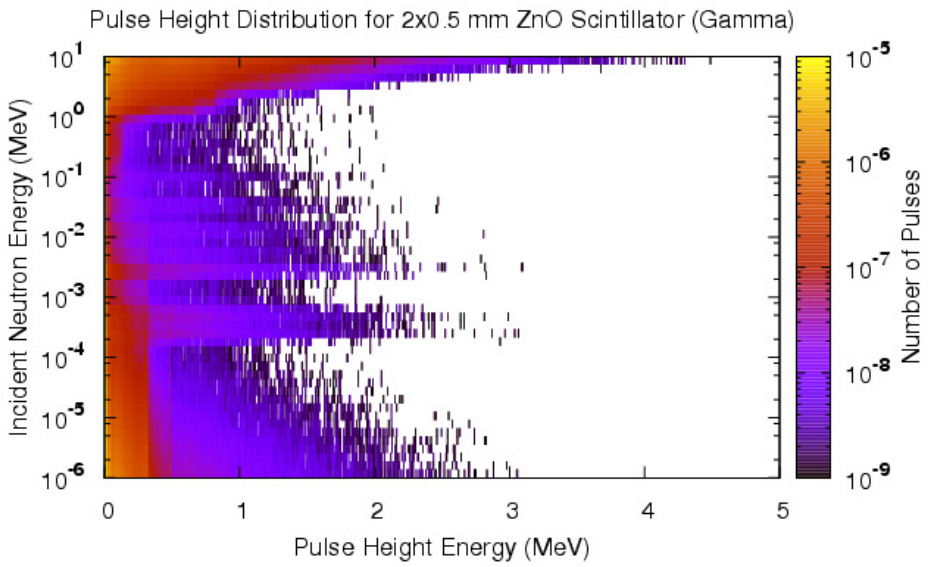

Figure 211 Pulse height distribution for gamma rays in a 2x0.5mm scintillator stack.

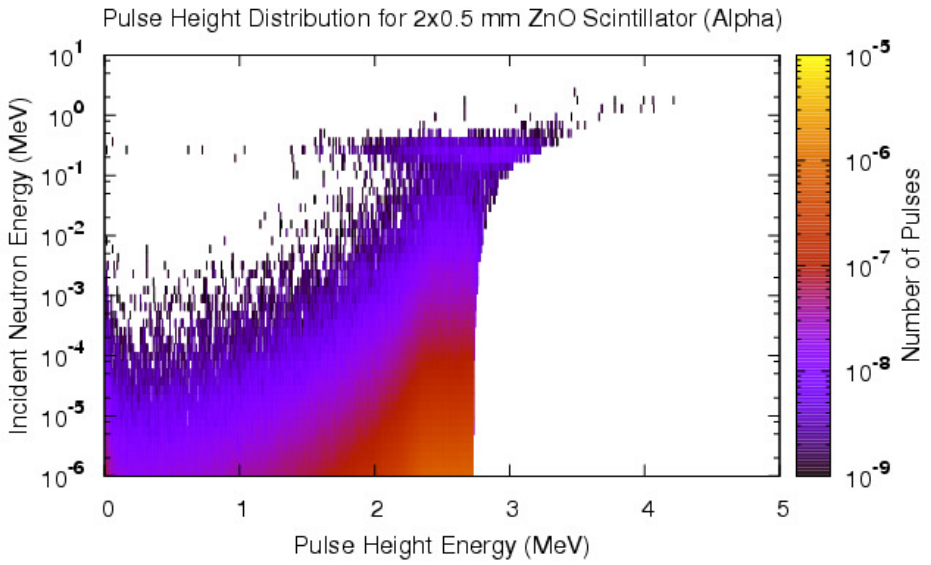

Figure 212 Pulse height distribution for alpha particles in a 2x0.5mm scintillator stack.

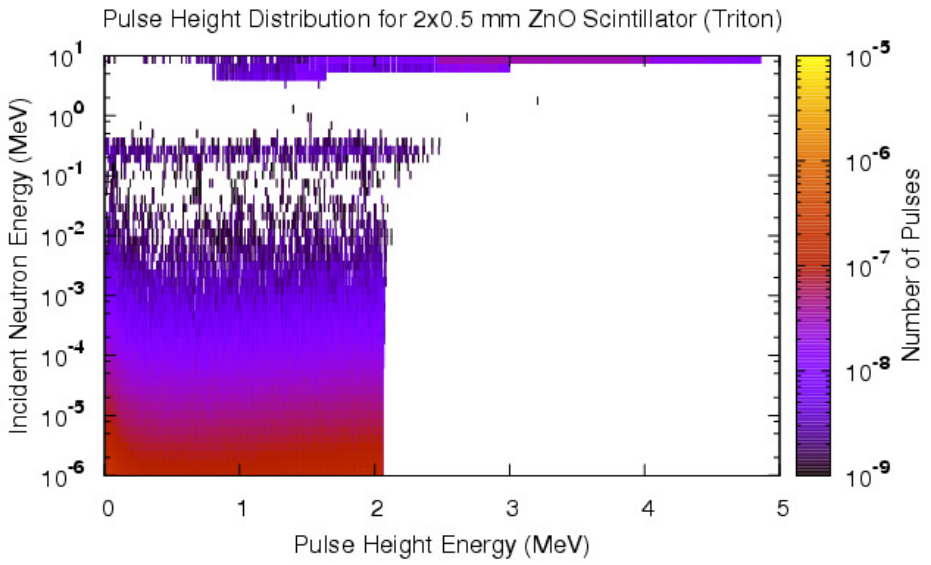

Figure 213 Pulse height distribution for triton particles in a 2x0.5mm scintillator stack.

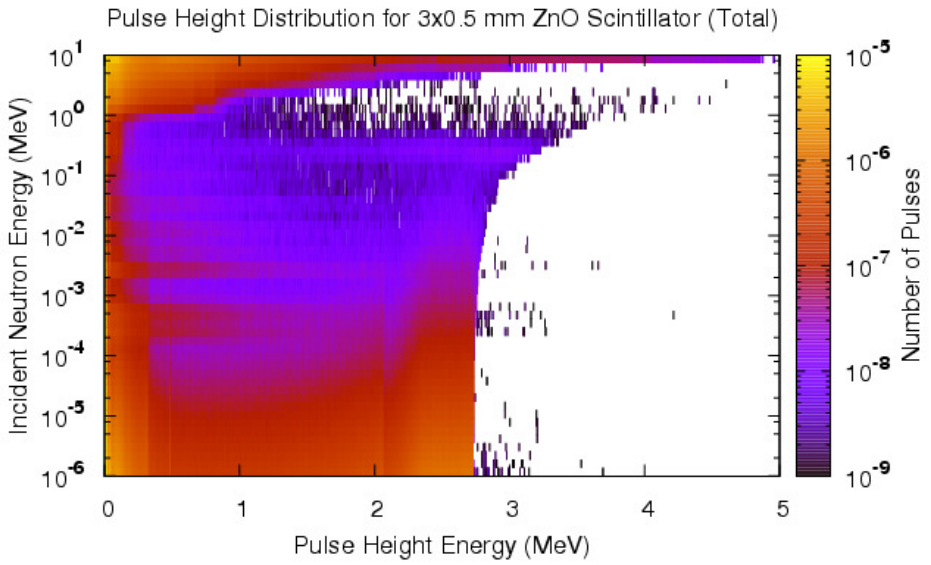

Figure 214 Pulse height distribution for all particles in a 3x0.5mm scintillator stack.

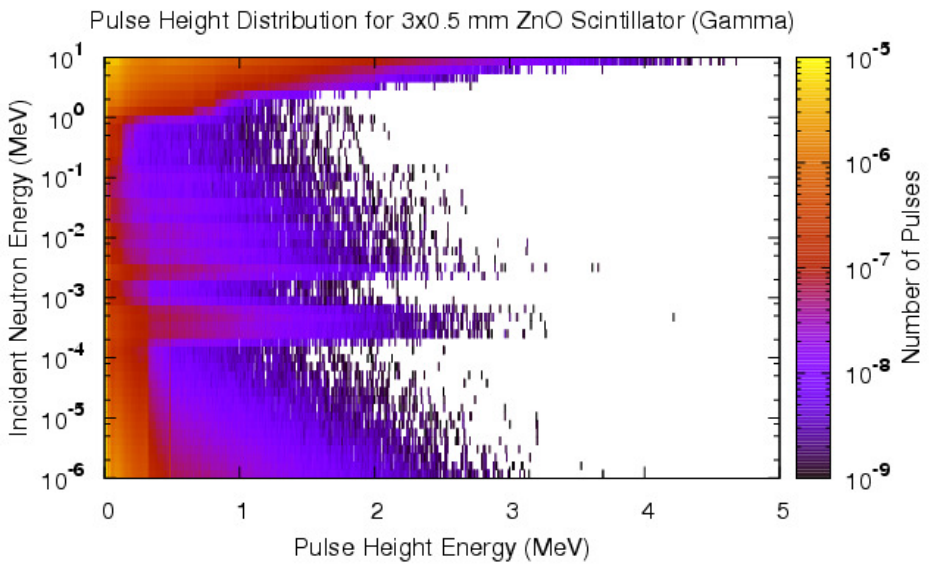

Figure 215 Pulse height distribution for gamma rays in a 3x0.5mm scintillator stack.

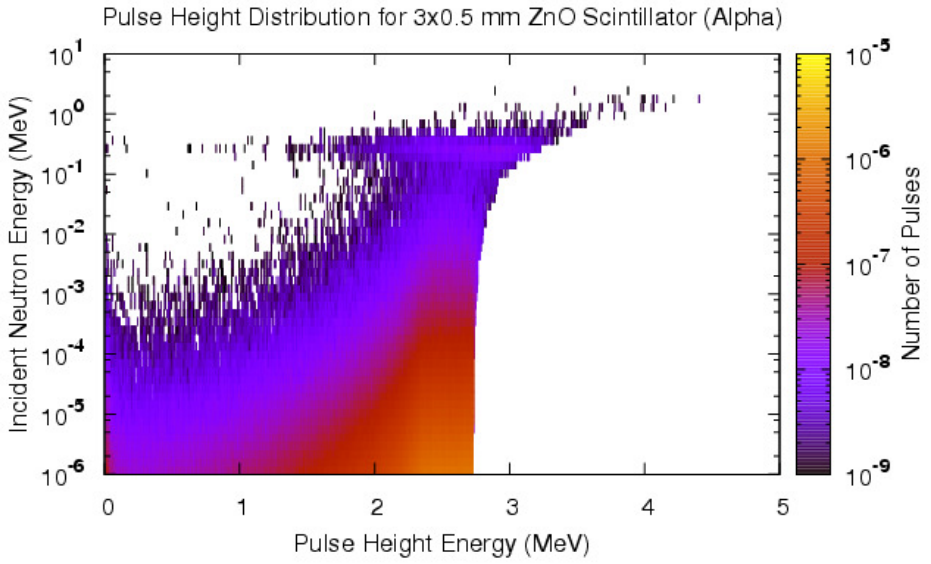

Figure 216 Pulse height distribution for alpha particles in a 3x0.5mm scintillator stack.

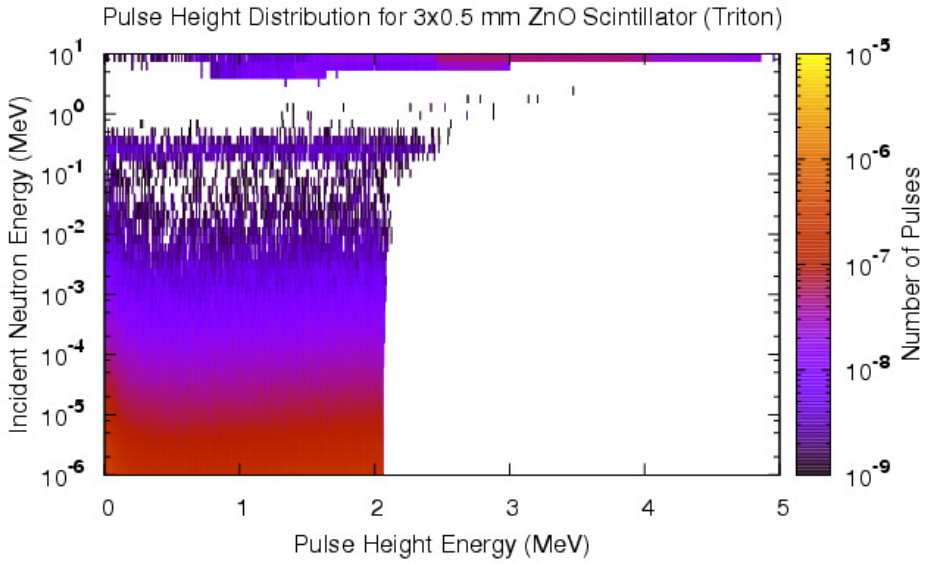

Figure 217 Pulse height distribution for triton particles in a 3x0.5mm scintillator stack.

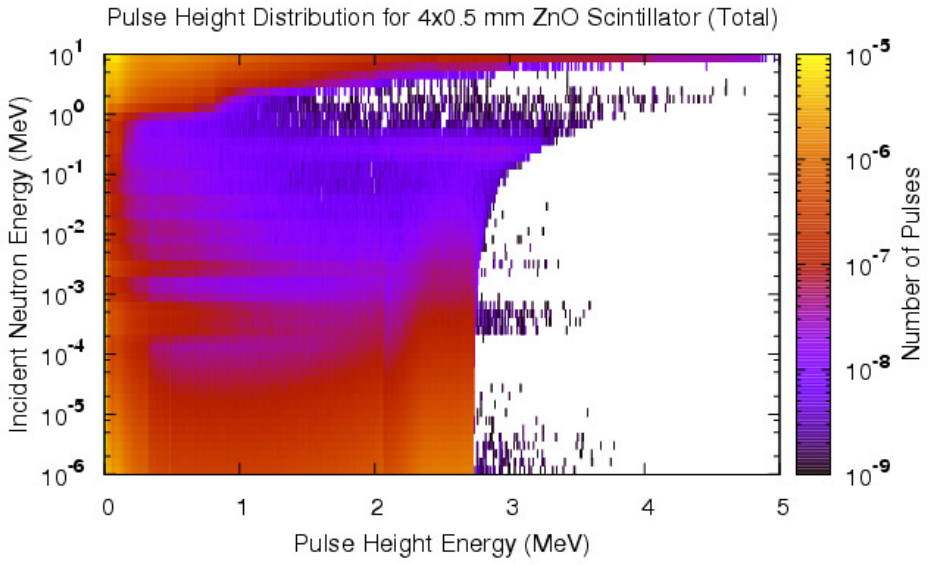

Figure 218 Pulse height distribution for all particles in a 4x0.5mm scintillator stack.

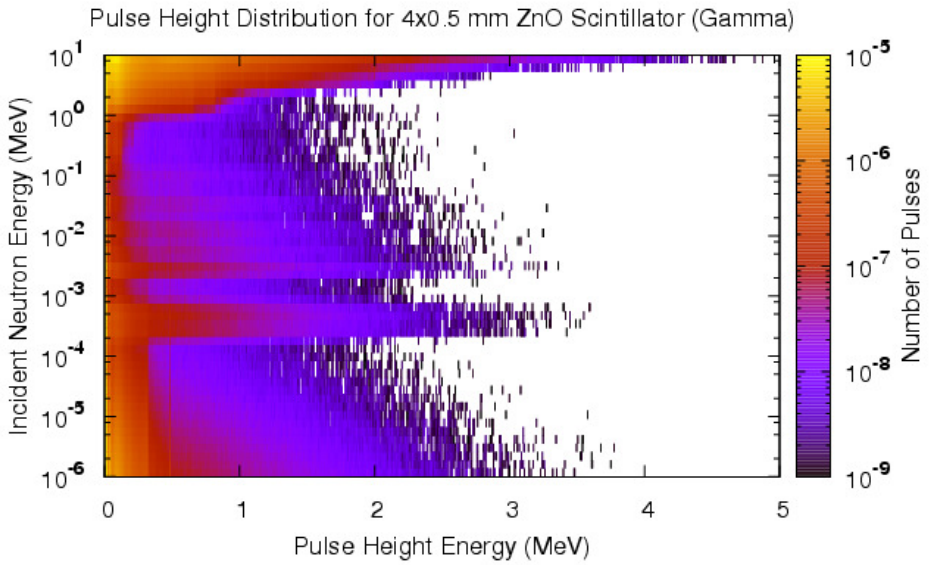

Figure 219 Pulse height distribution for gamma rays in a 4x0.5mm scintillator stack.

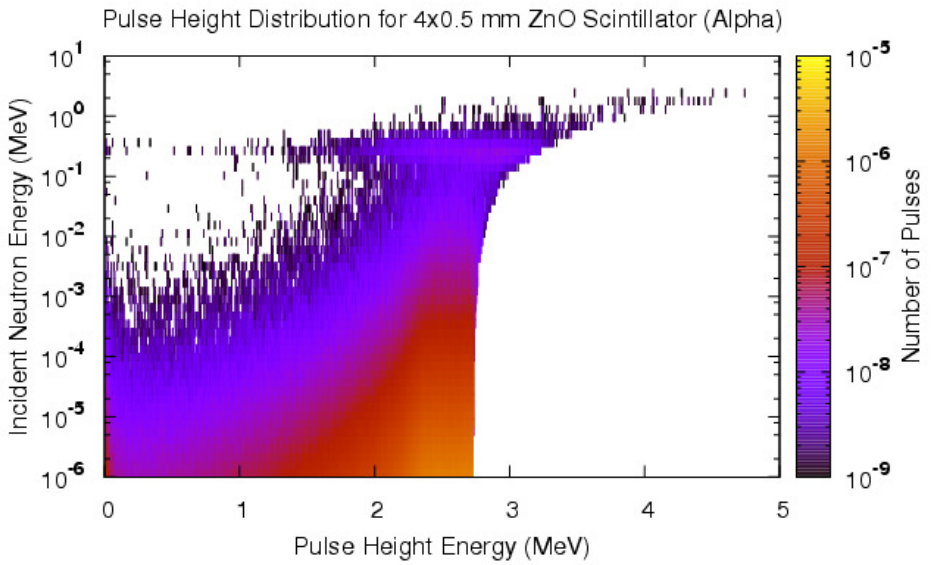

Figure 220 Pulse height distribution for alpha particles in a 4x0.5mm scintillator stack.

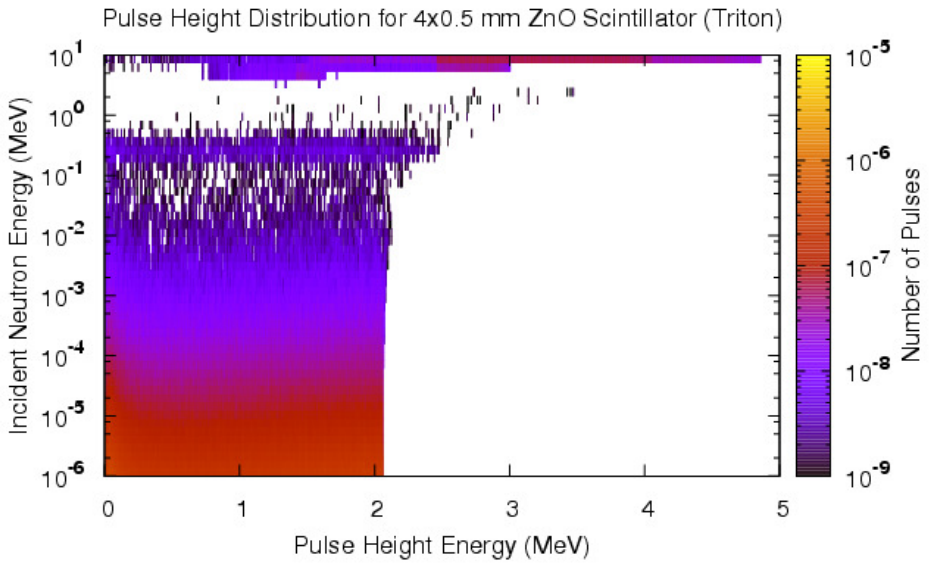

Figure 221 Pulse height distribution for triton particles in a 4x0.5mm scintillator stack.

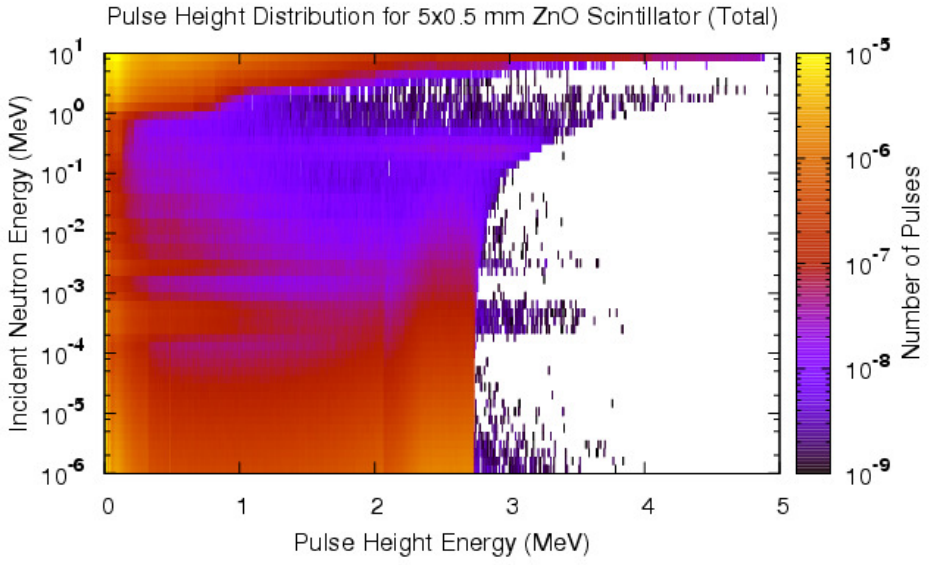

Figure 222 Pulse height distribution for all particles in a 5x0.5mm scintillator stack.

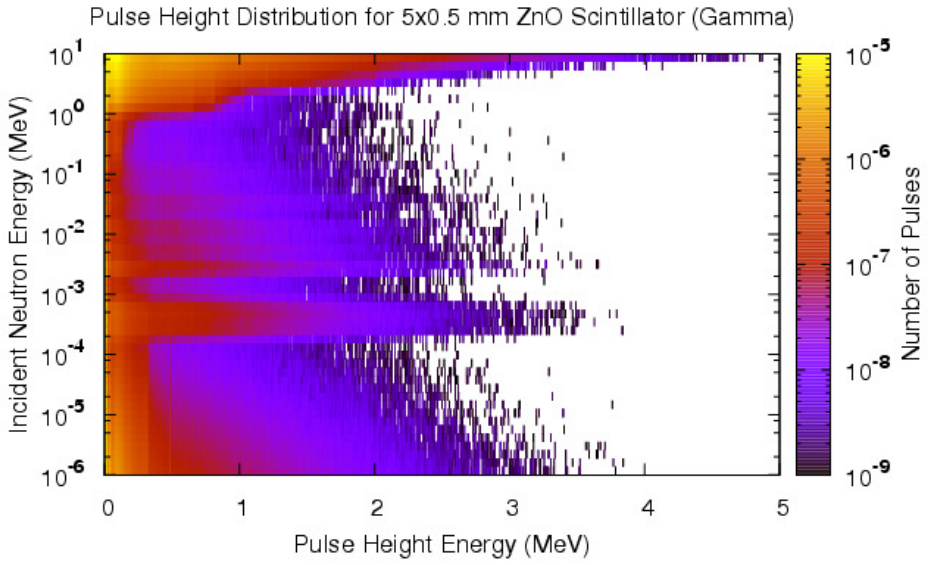

Figure 223 Pulse height distribution for gamma rays in a 5x0.5mm scintillator stack.

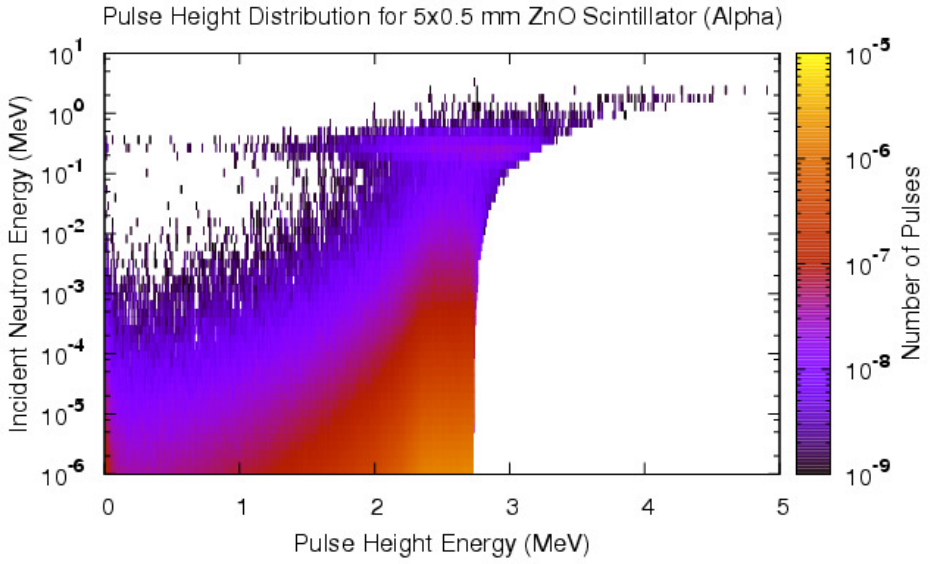

Figure 224 Pulse height distribution for alpha particles in a 5x0.5mm scintillator stack.

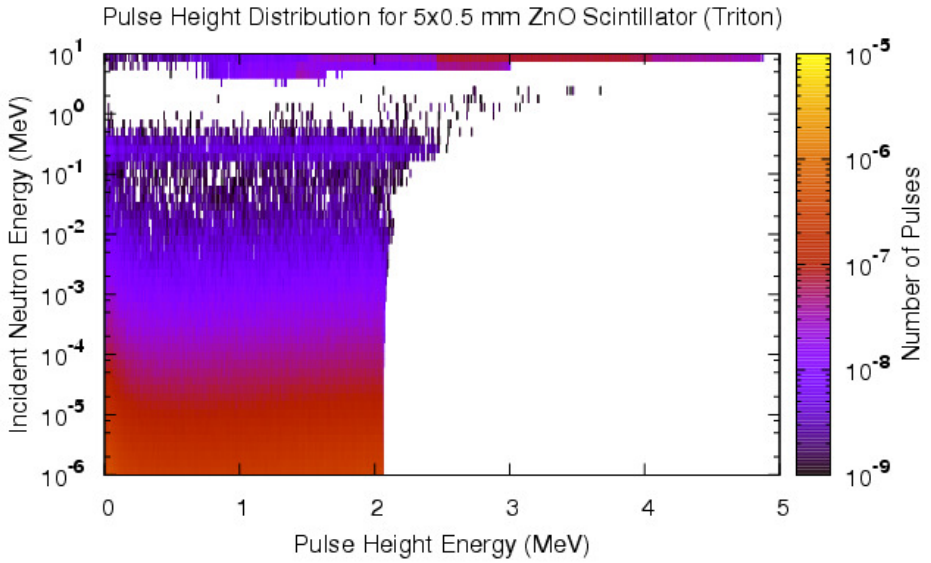

Figure 225 Pulse height distribution for triton particles in a 5x0.5mm scintillator stack.

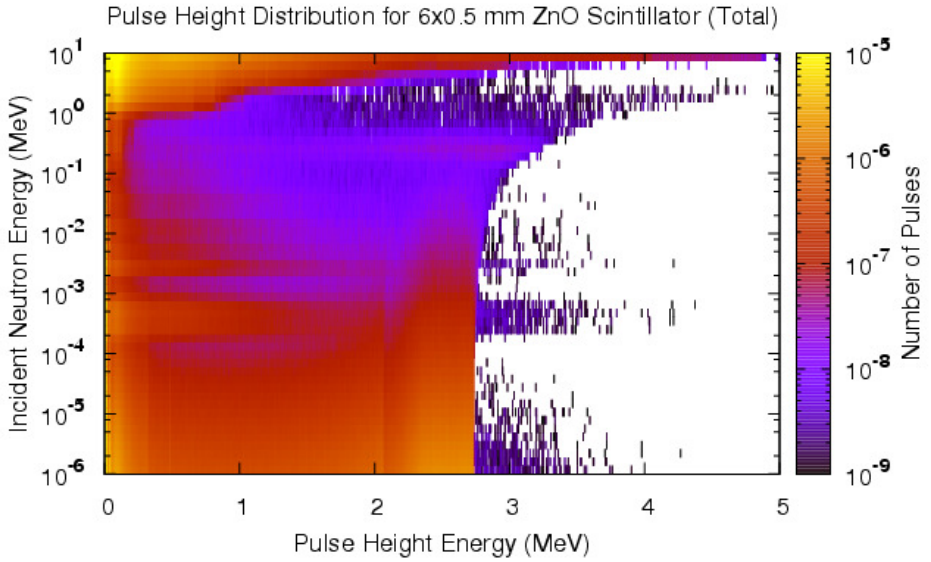

Figure 226 Pulse height distribution for all particles in a 6x0.5mm scintillator stack.

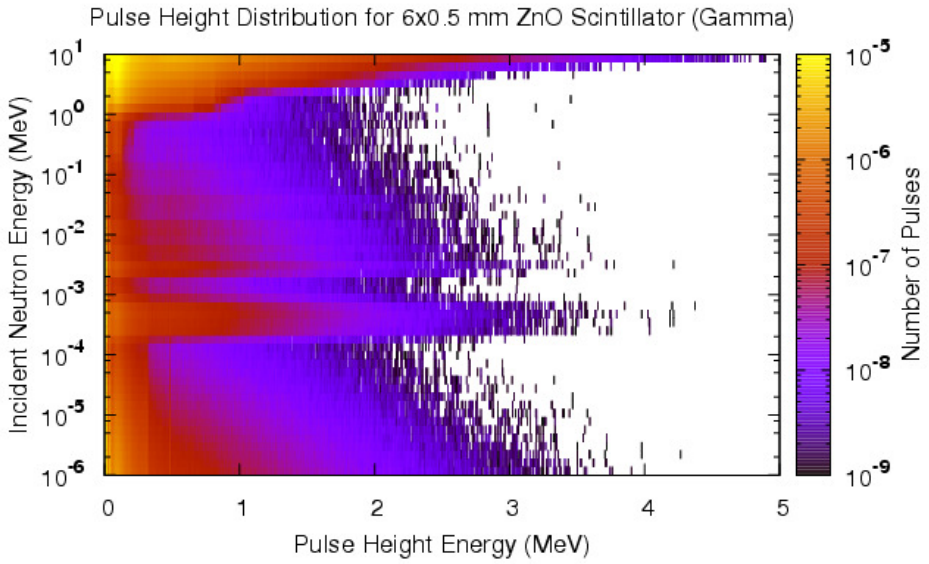

Figure 227 Pulse height distribution for gamma rays in a 6x0.5mm scintillator stack.

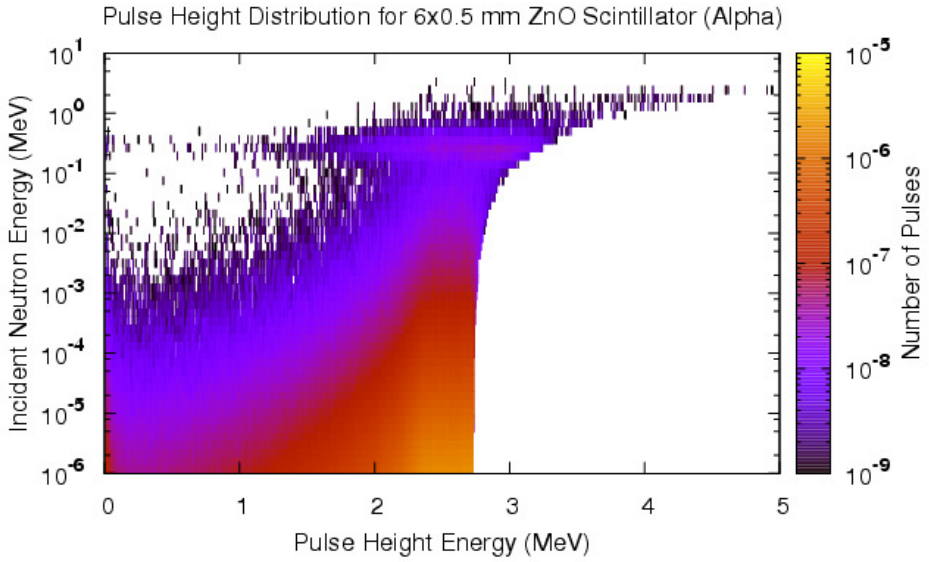

Figure 228 Pulse height distribution for alpha particles in a 6x0.5mm scintillator stack.

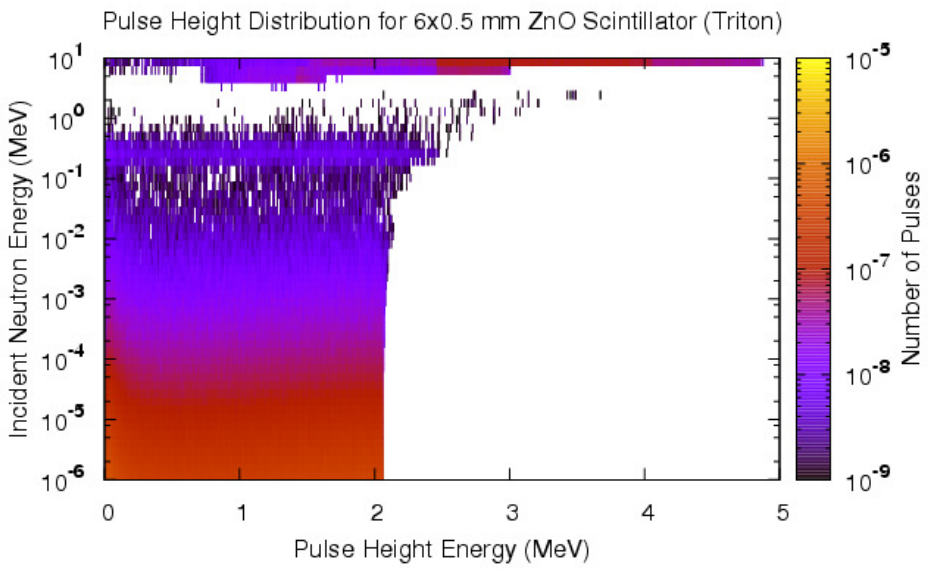

Figure 229 Pulse height distribution for triton particles in a 6x0.5mm scintillator stack.

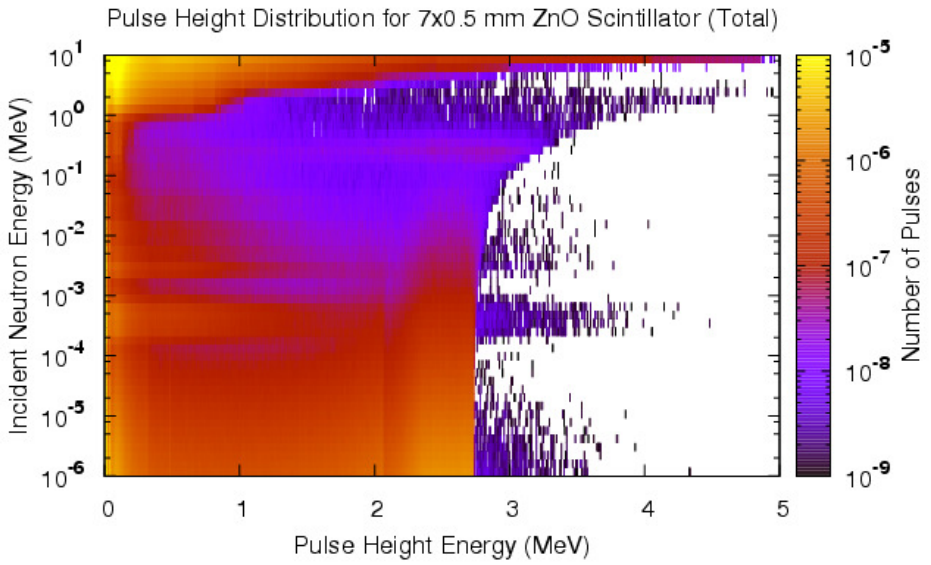

Figure 230 Pulse height distribution for all particles in a 7x0.5mm scintillator stack.

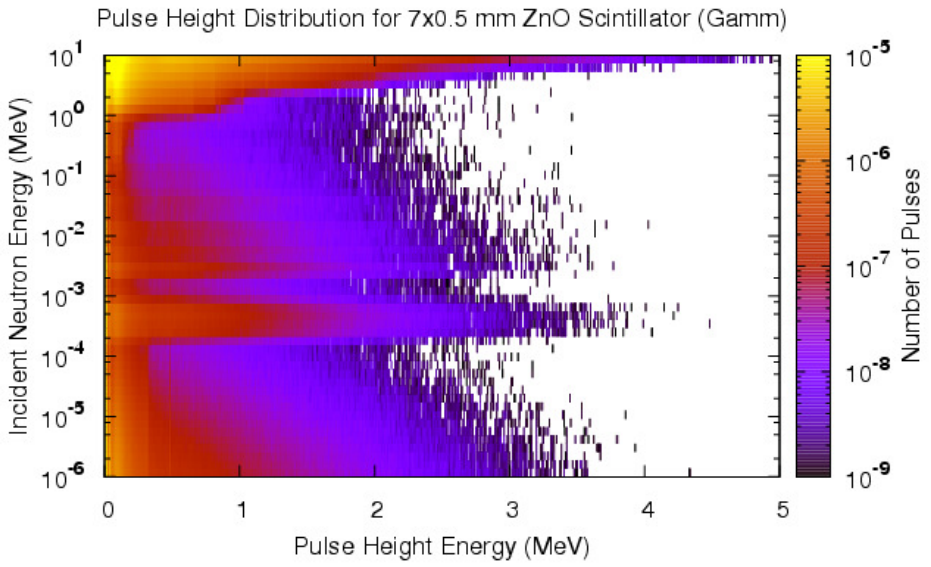

Figure 231 Pulse height distribution for gamma rays in a 7x0.5mm scintillator stack.

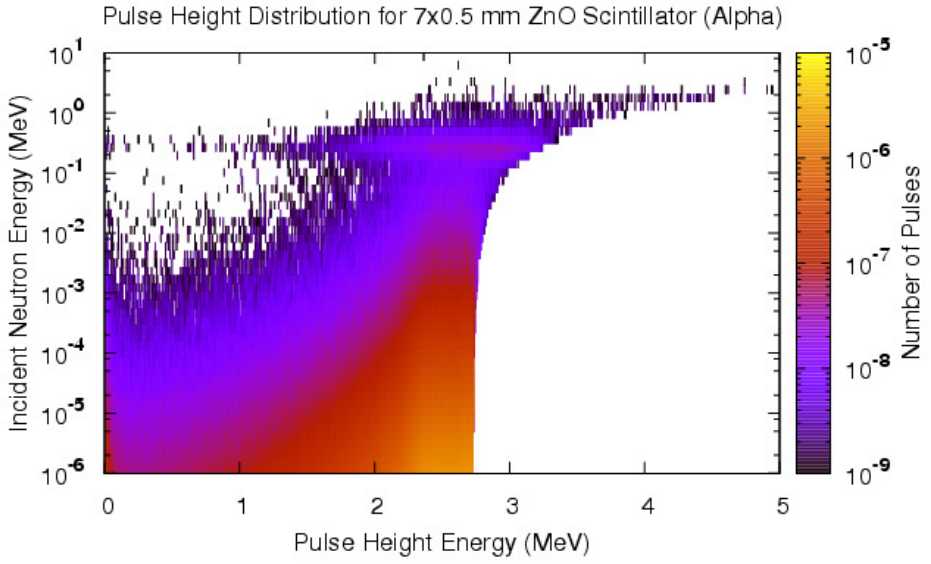

Figure 232 Pulse height distribution for alpha particles in a 7x0.5mm scintillator stack.

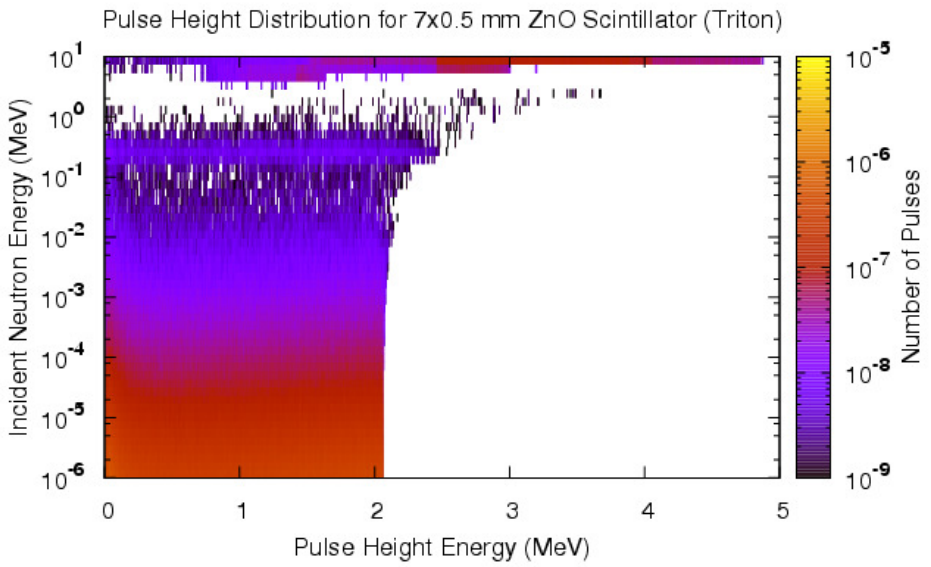

Figure 233 Pulse height distribution for triton particles in a 7x0.5mm scintillator stack.

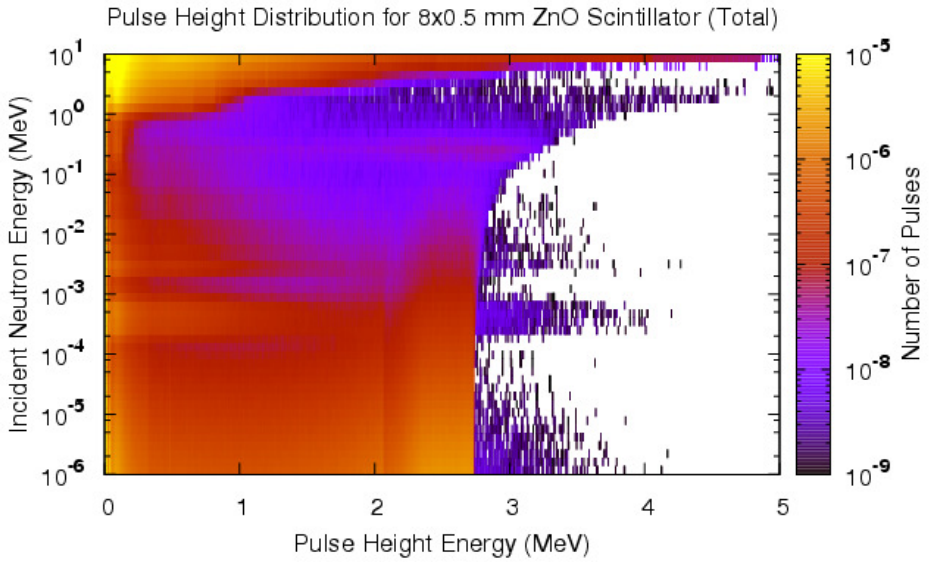

Figure 234 Pulse height distribution for all particles in a 8x0.5mm scintillator stack.

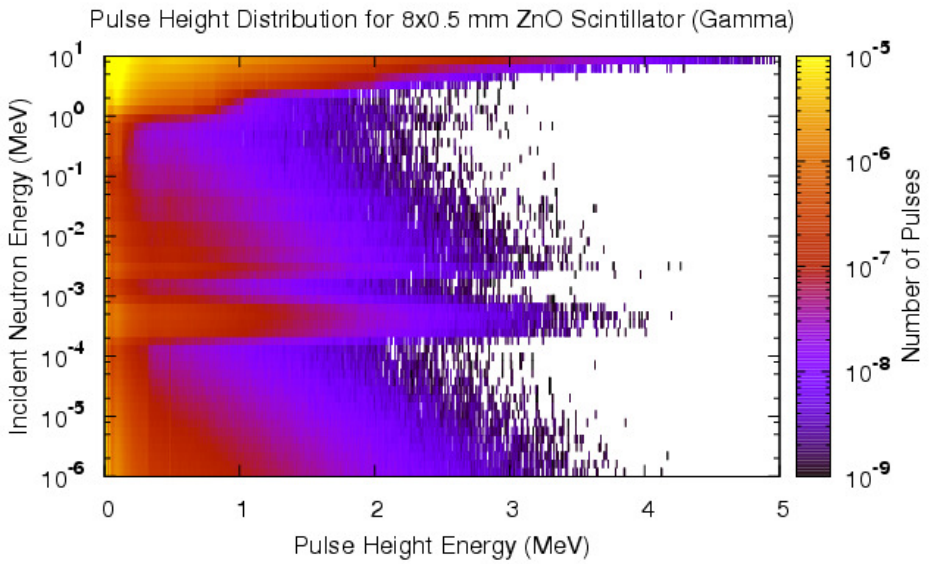

Figure 235 Pulse height distribution for gamma rays in a 8x0.5mm scintillator stack.

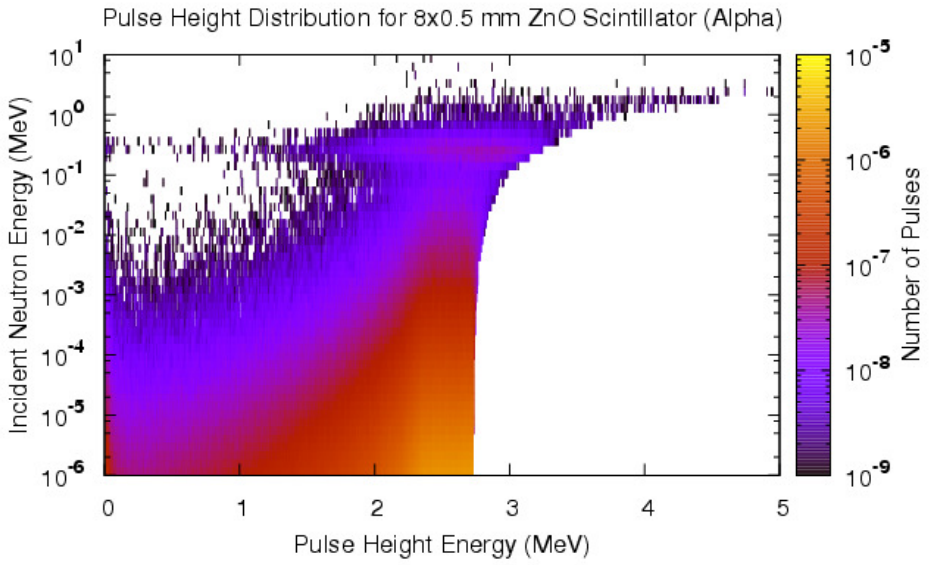

Figure 236 Pulse height distribution for alpha particles in a 8x0.5mm scintillator stack.

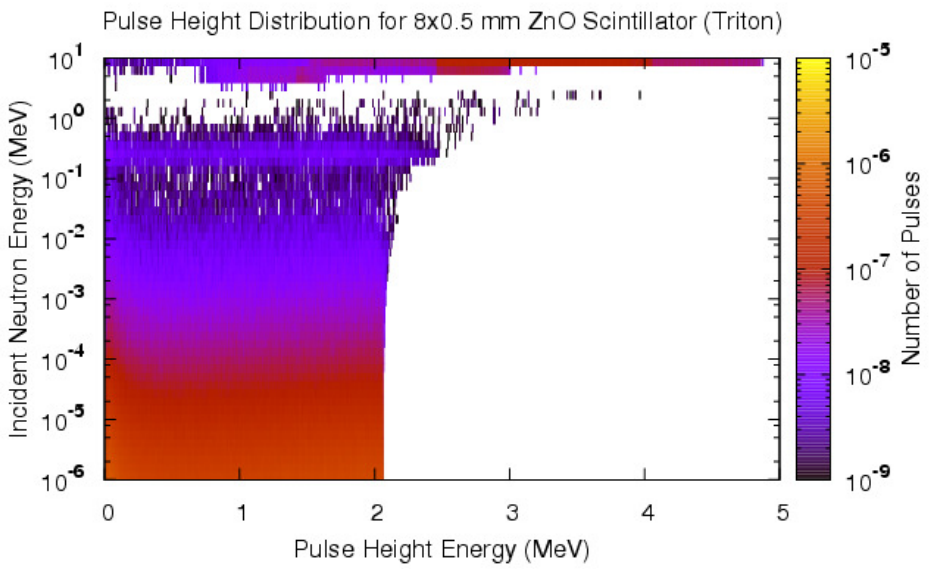

Figure 237 Pulse height distribution for triton particles in a 8x0.5mm scintillator stack.

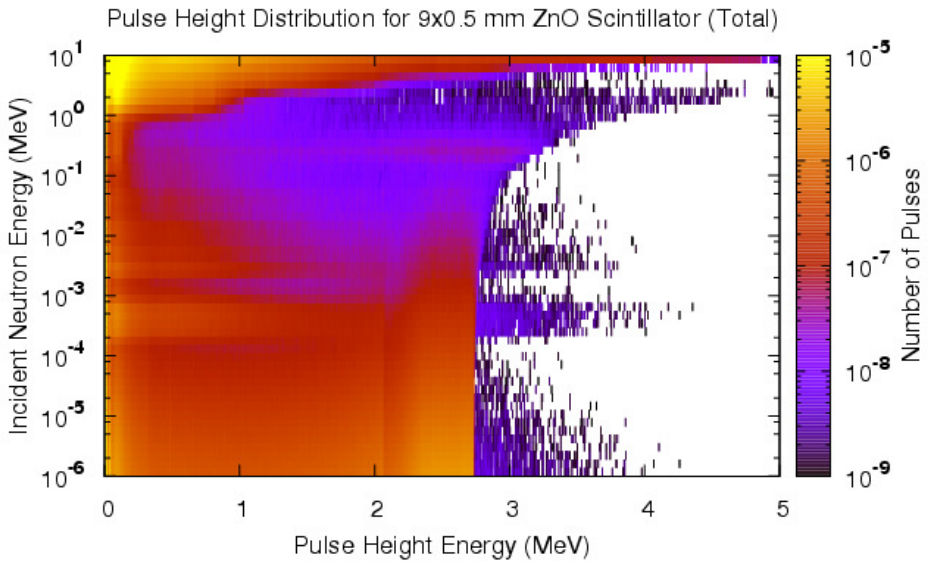

Figure 238 Pulse height distribution for all particles in a 9x0.5mm scintillator stack.

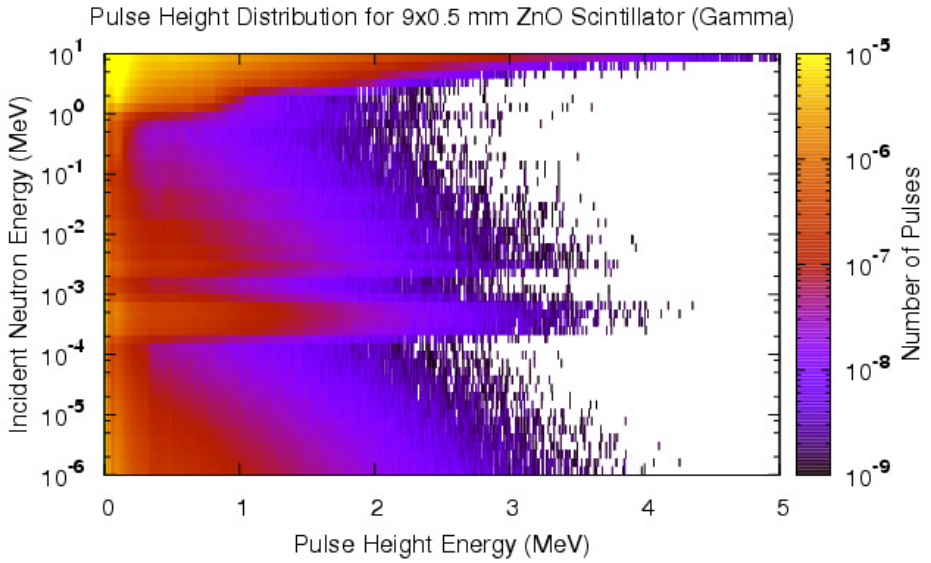

Figure 239 Pulse height distribution for gamma rays in a 9x0.5mm scintillator stack.

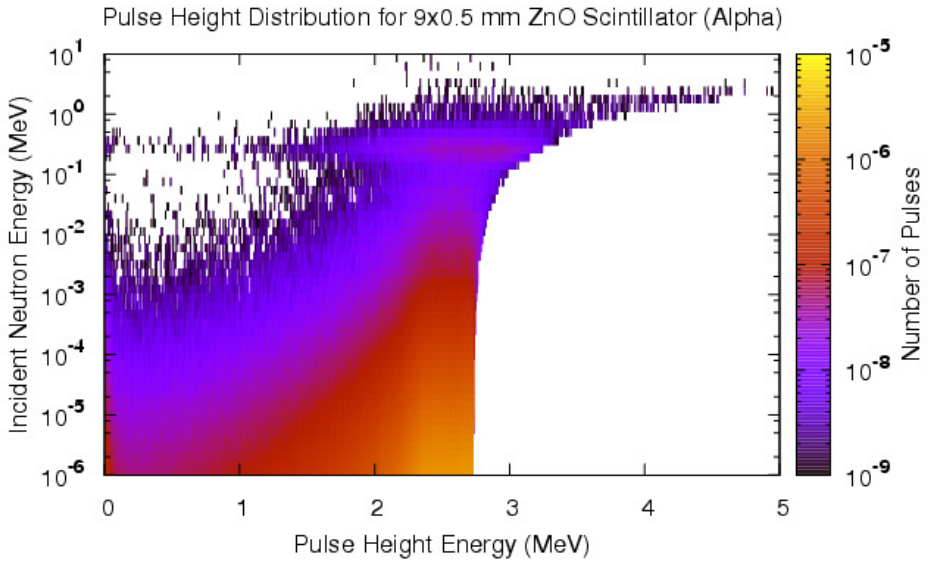

Figure 240 Pulse height distribution for alpha particles in a 9x0.5mm scintillator stack.

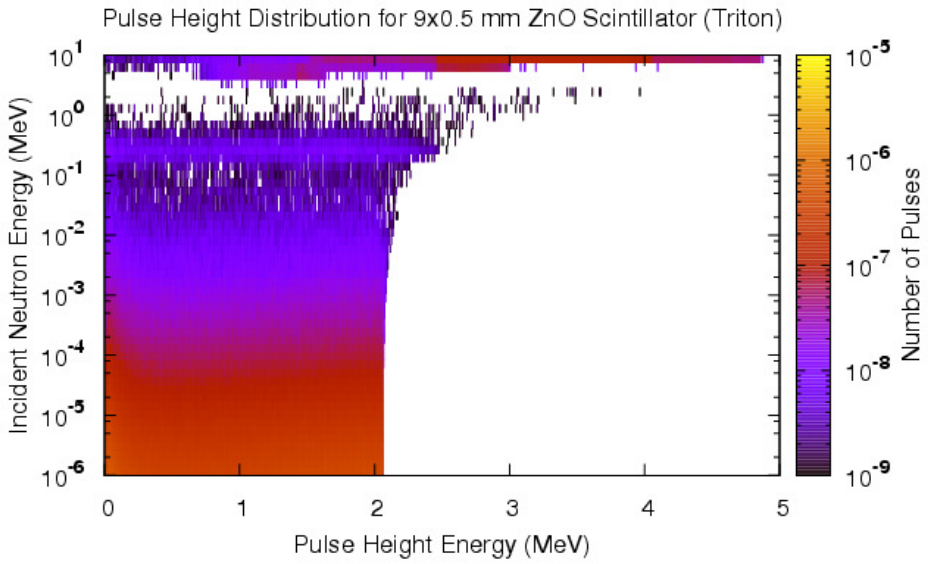

Figure 241 Pulse height distribution for triton particles in a 9x0.5mm scintillator stack.

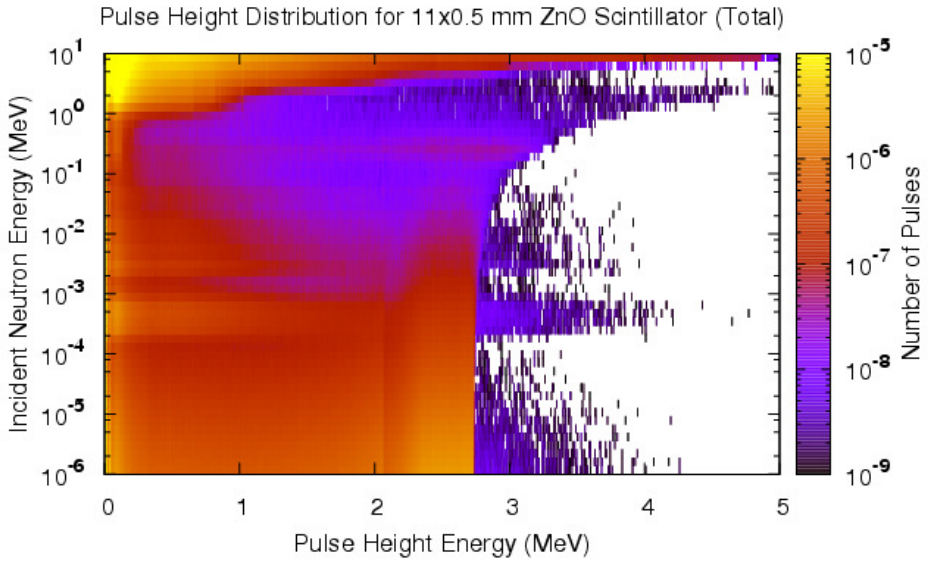

Figure 242 Pulse height distribution for all particles in a 11x0.5mm scintillator stack.

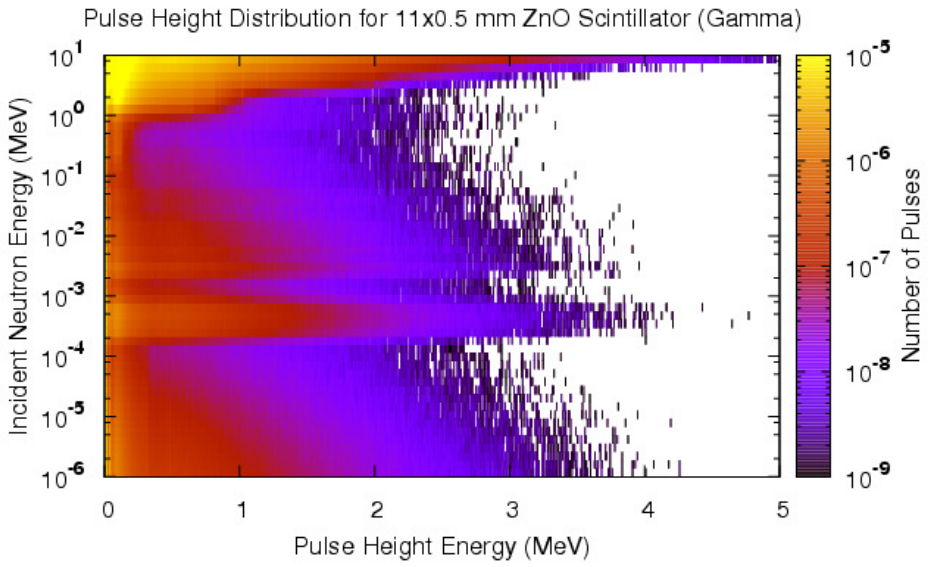

Figure 243 Pulse height distribution for gamma rays in a 11x0.5mm scintillator stack.

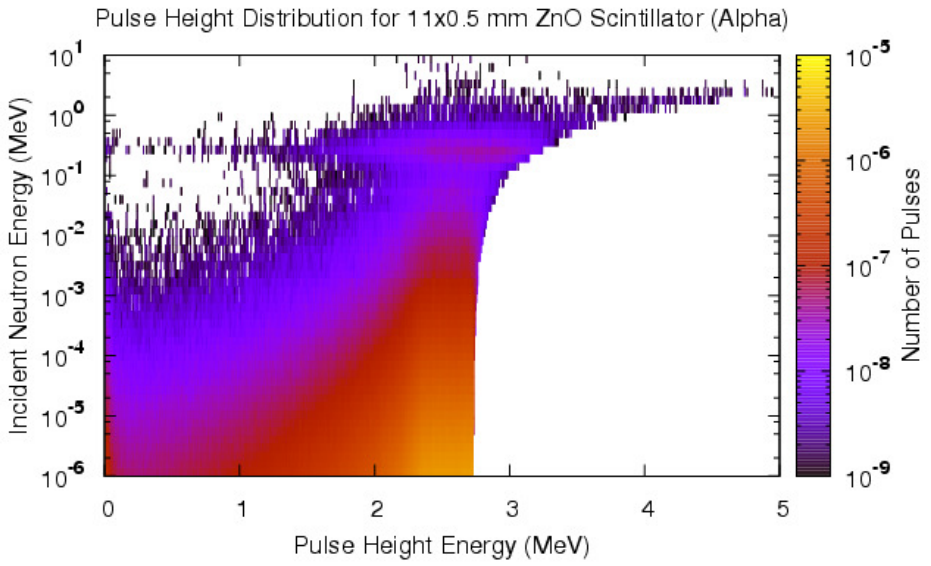

Figure 244 Pulse height distribution for alpha particles in a 11x0.5mm scintillator stack.

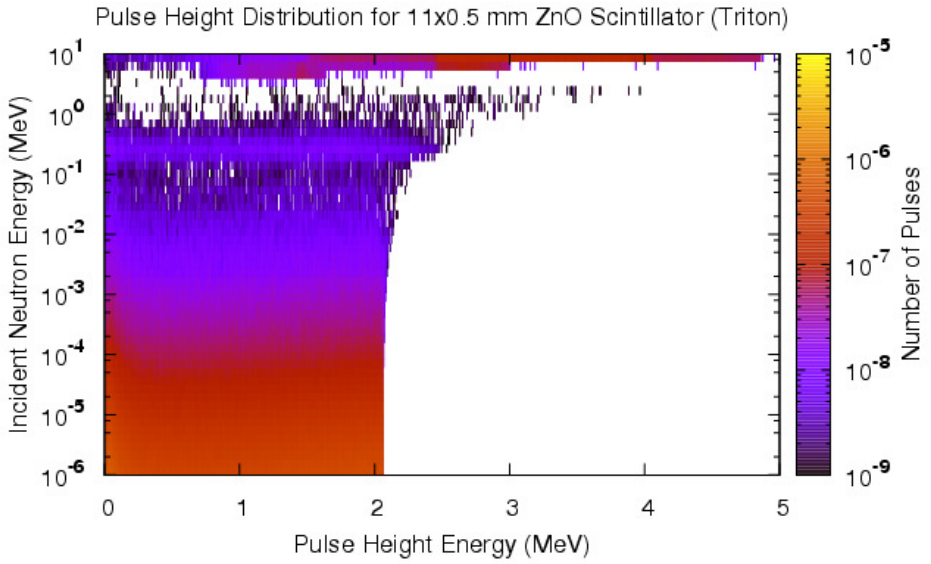

Figure 245 Pulse height distribution for triton particles in a 11x0.5mm scintillator stack.

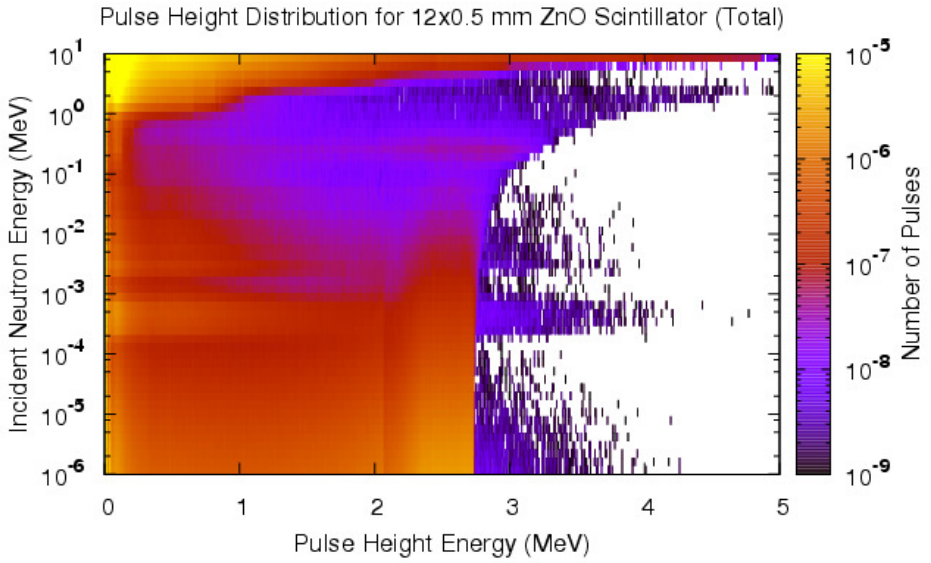

Figure 246 Pulse height distribution for all particles in a 12x0.5mm scintillator stack.

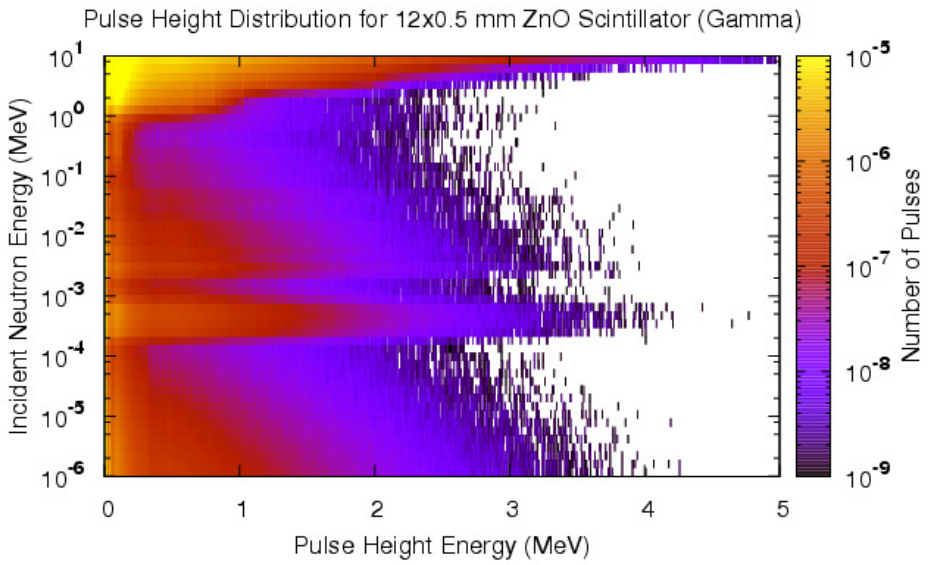

Figure 247 Pulse height distribution for gamma rays in a 12x0.5mm scintillator stack.

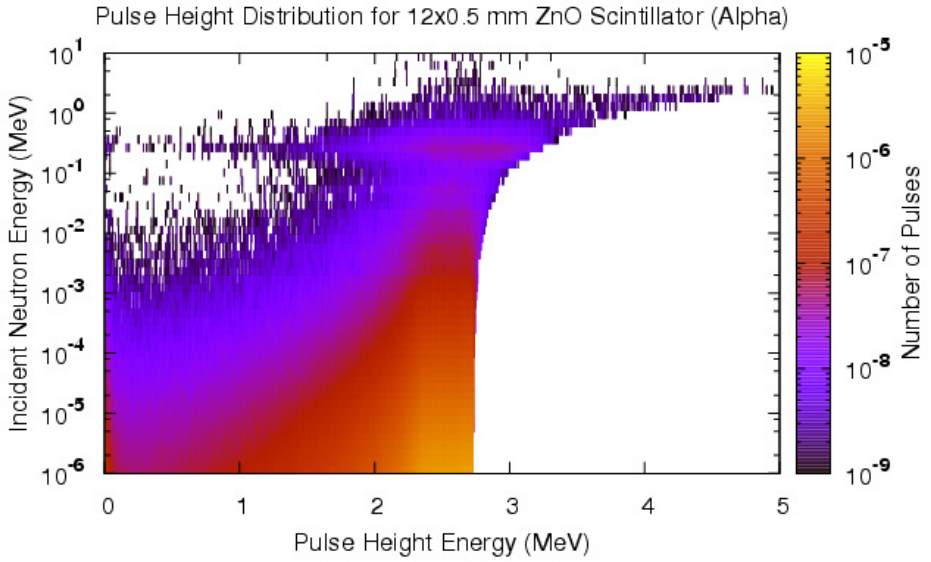

Figure 248 Pulse height distribution for alpha particles in a 12x0.5mm scintillator stack.

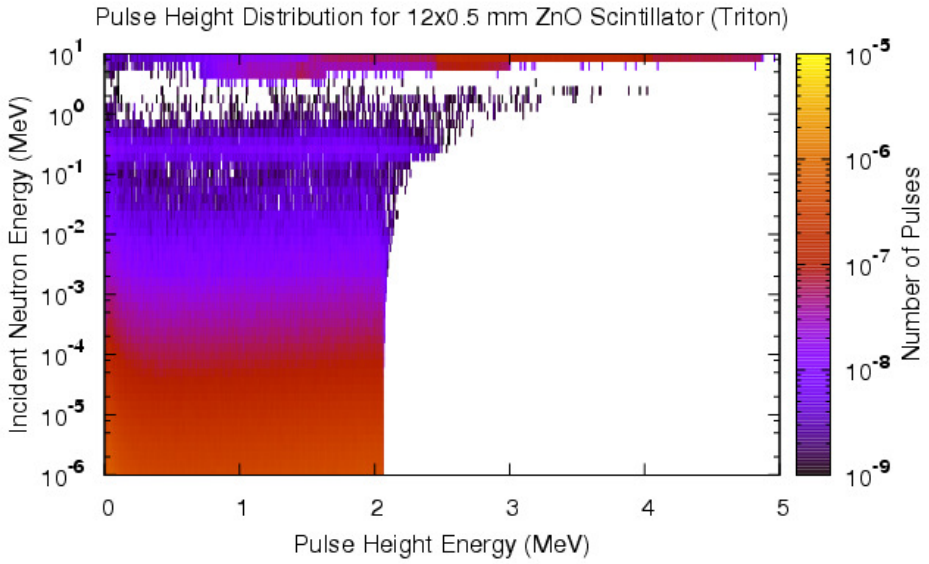

Figure 249 Pulse height distribution for triton particles in a 12x0.5mm scintillator stack.

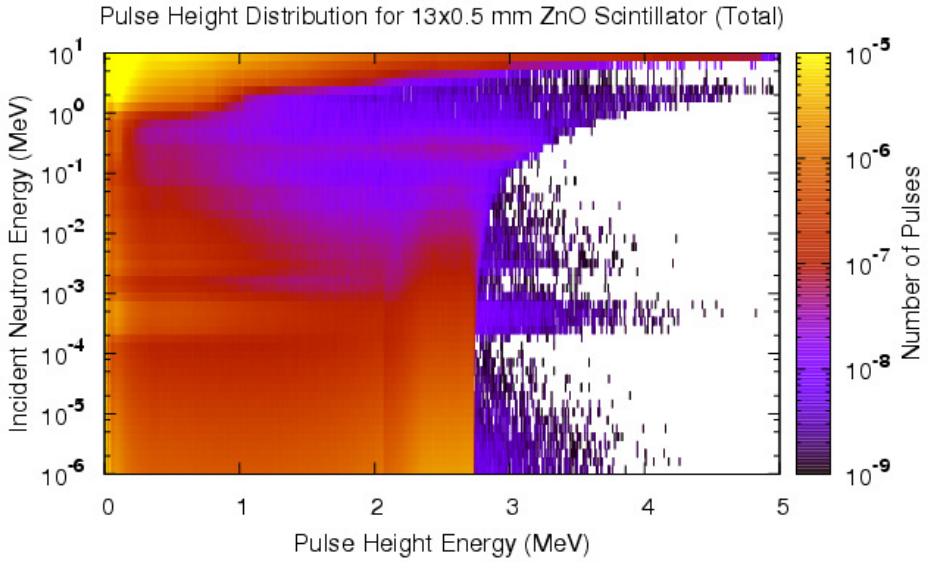

Figure 250 Pulse height distribution for all particles in a 13x0.5mm scintillator stack.

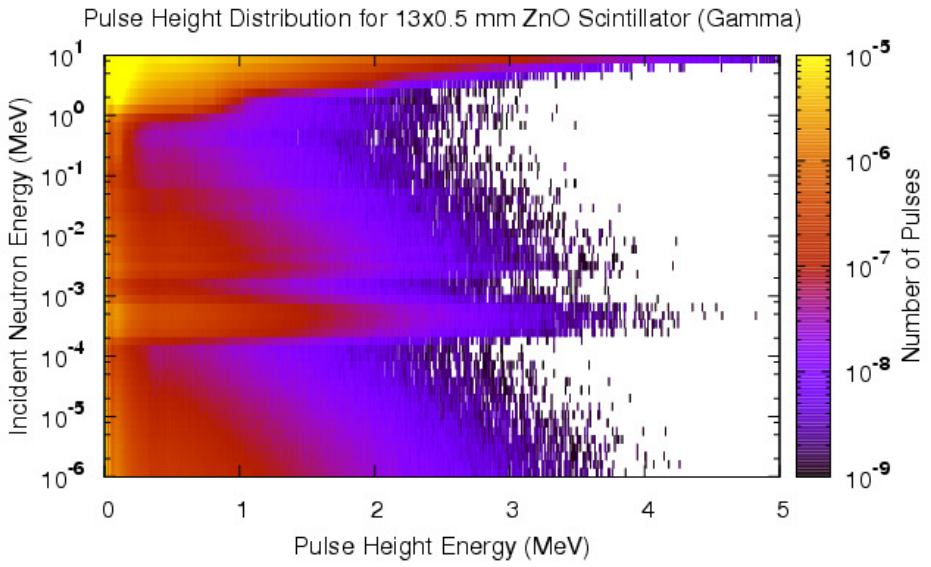

Figure 251 Pulse height distribution for gamma rays in a 13x0.5mm scintillator stack.

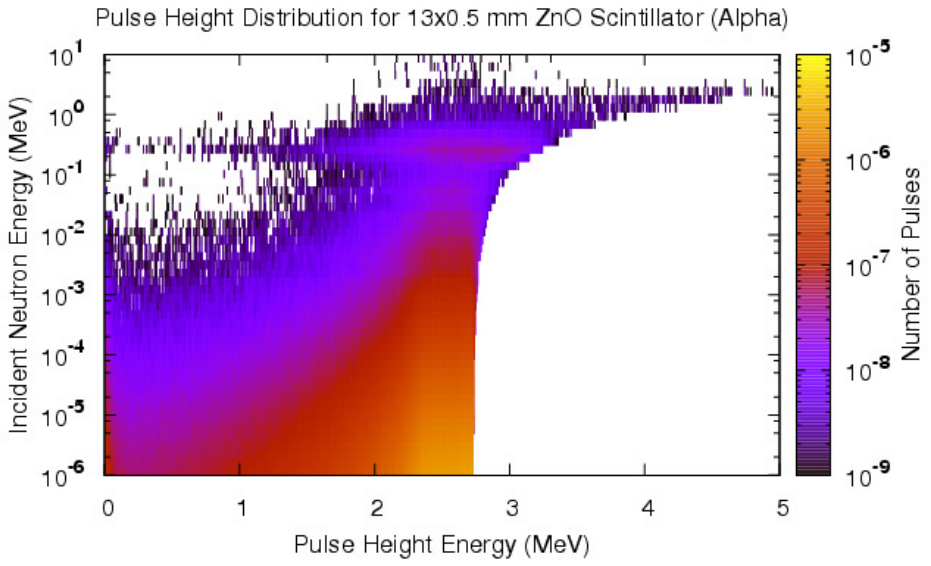

Figure 252 Pulse height distribution for alpha particles in a 13x0.5mm scintillator stack.

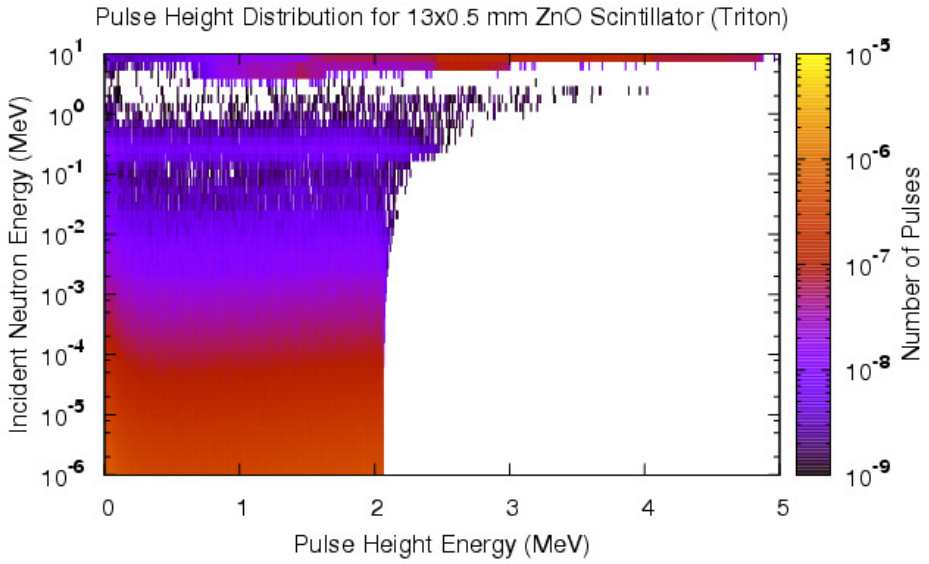

Figure 253 Pulse height distribution for triton particles in a 13x0.5mm scintillator stack.

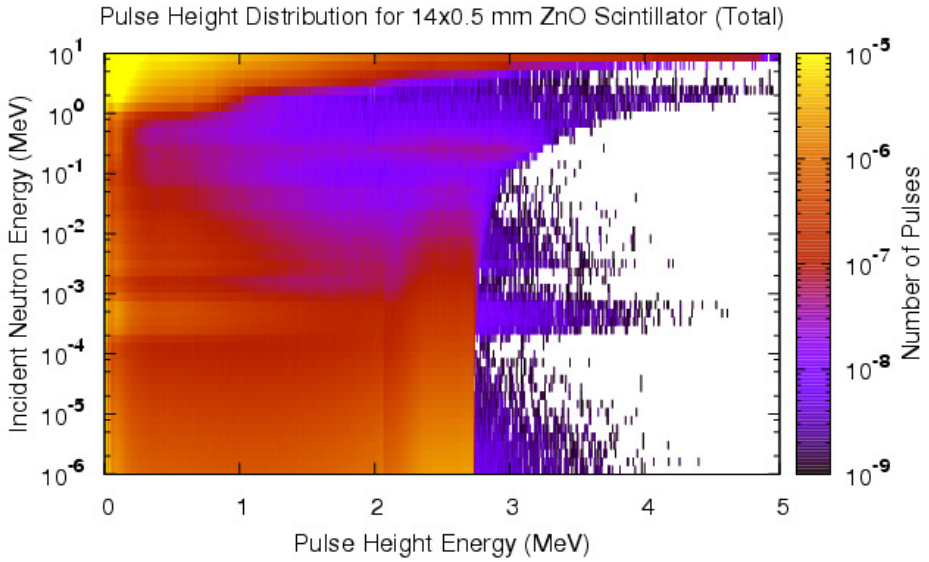

Figure 254 Pulse height distribution for all particles in a 14x0.5mm scintillator stack.

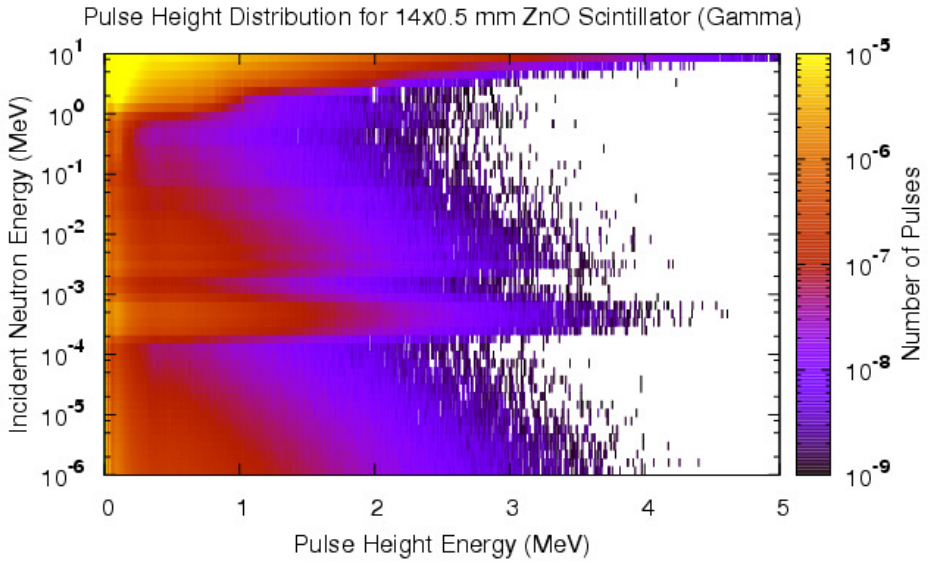

Figure 255 Pulse height distribution for gamma rays in a 14x0.5mm scintillator stack.

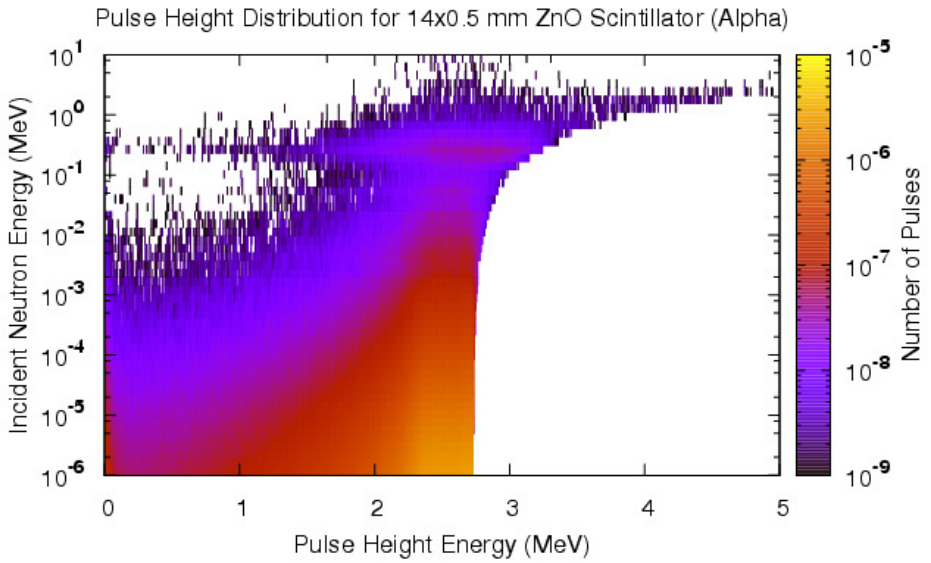

Figure 256 Pulse height distribution for alpha particles in a 14x0.5mm scintillator stack.

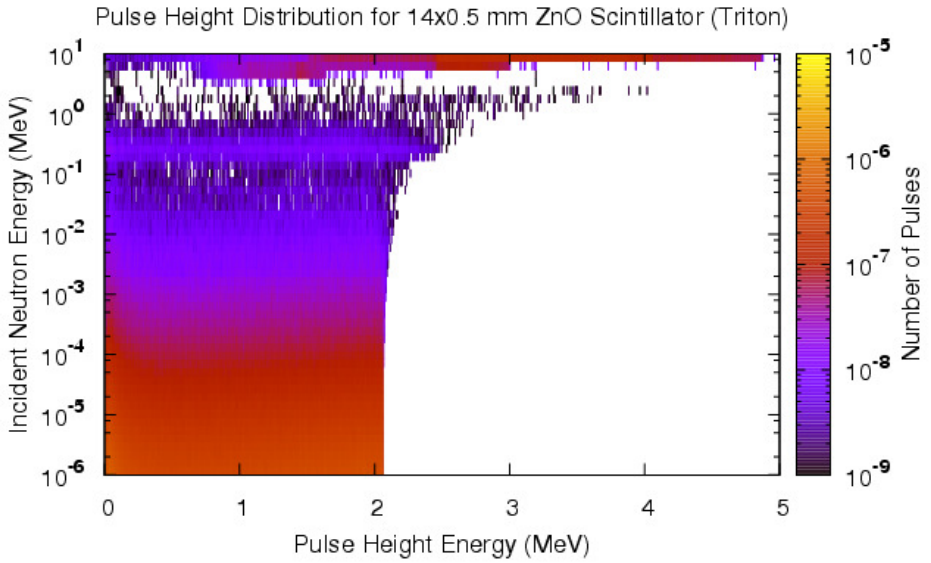

Figure 257 Pulse height distribution for triton particles in a 14x0.5mm scintillator stack.

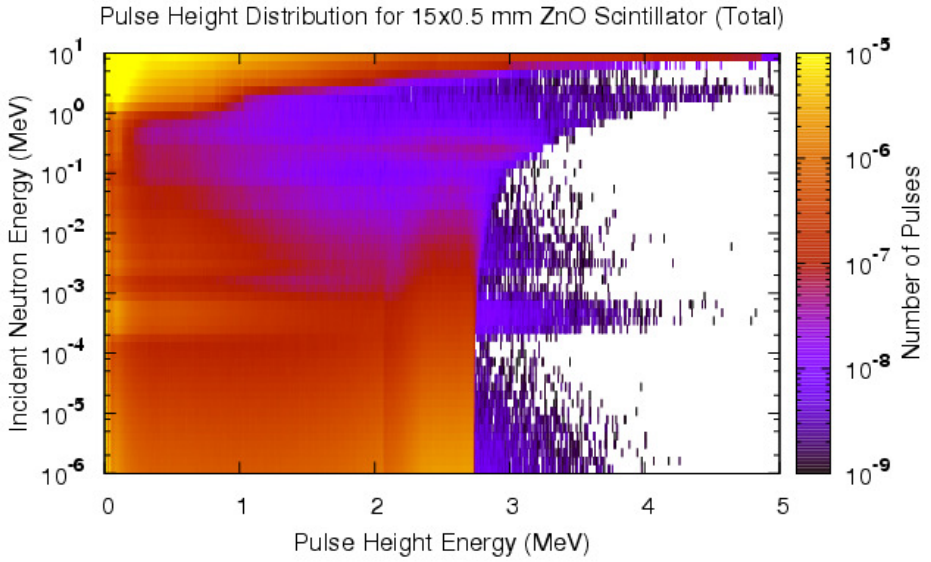

Figure 258 Pulse height distribution for all particles in a 15x0.5mm scintillator stack.

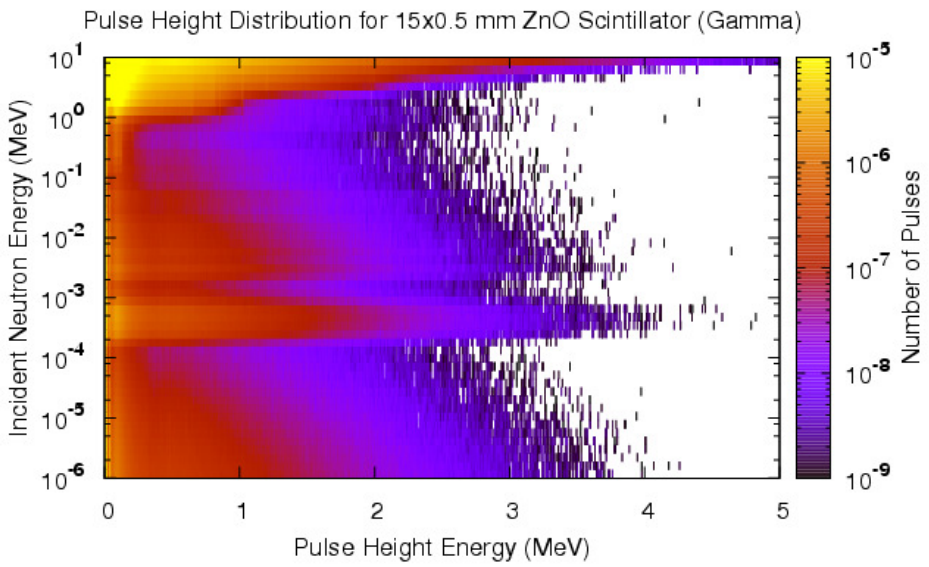

Figure 259 Pulse height distribution for gamma rays in a 15x0.5mm scintillator stack.

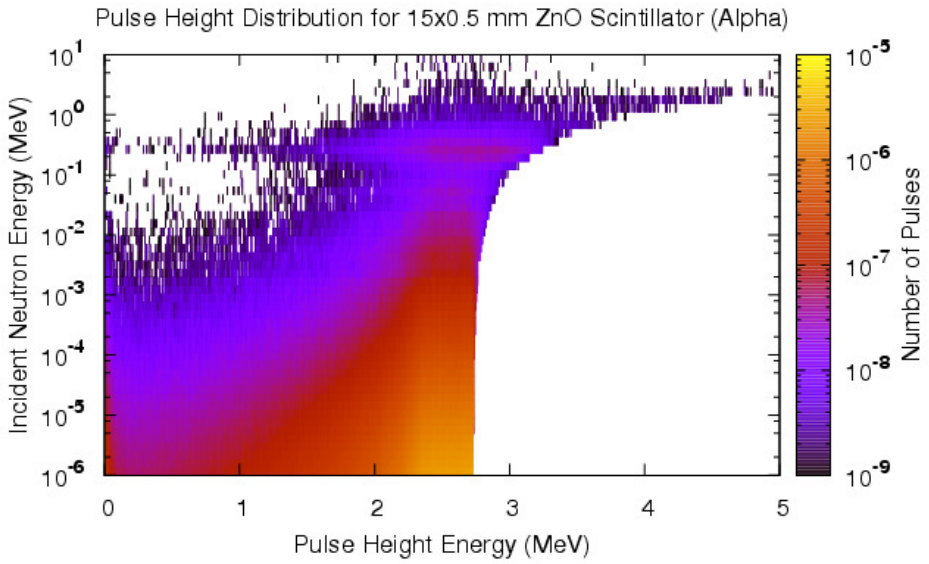

Figure 260 Pulse height distribution for alpha particles in a 15x0.5mm scintillator stack.

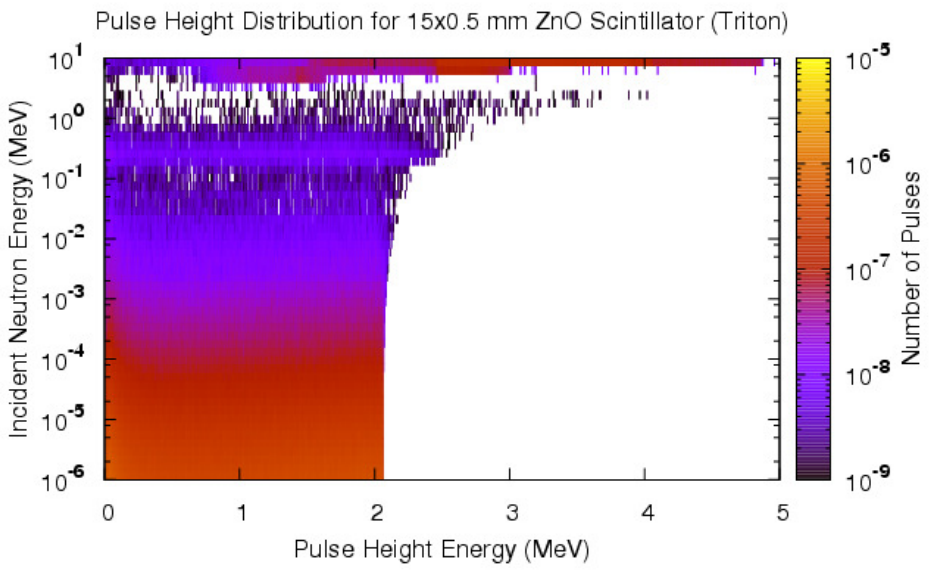

Figure 261 Pulse height distribution for triton particles in a 15x0.5mm scintillator stack.

15 µM DETECTORS

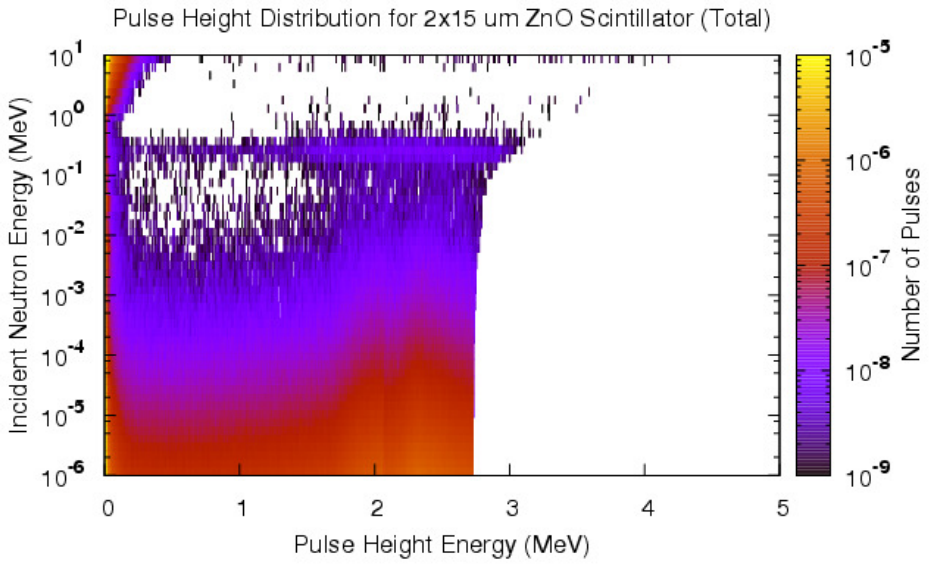

Figure 262 Pulse height distribution for all particles in a 2x15µm scintillator stack.

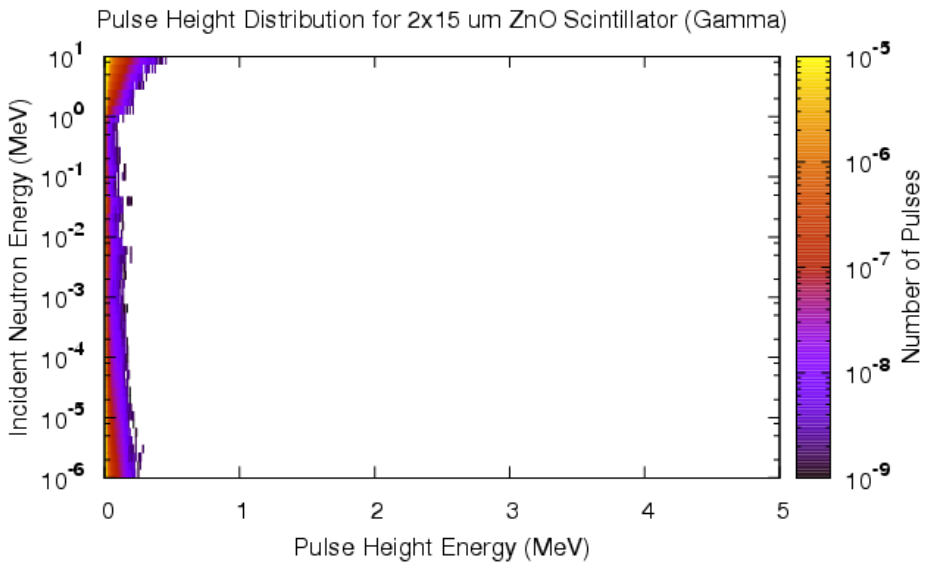

Figure 263 Pulse height distribution for gamma rays in a 2x15µm scintillator stack.

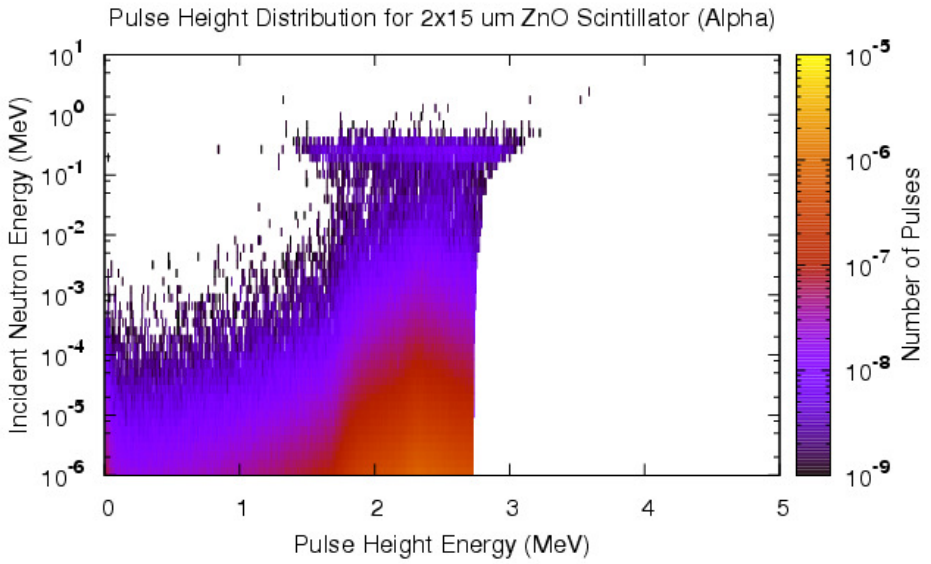

Figure 264 Pulse height distribution for alpha particles in a 2x15µm scintillator stack.

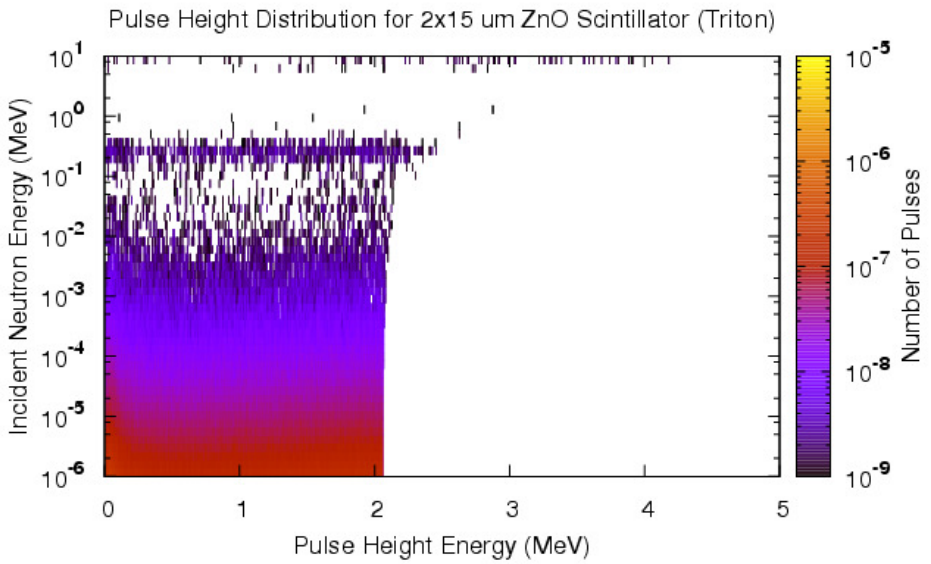

Figure 265 Pulse height distribution for triton particles in a 2x15µm scintillator stack.

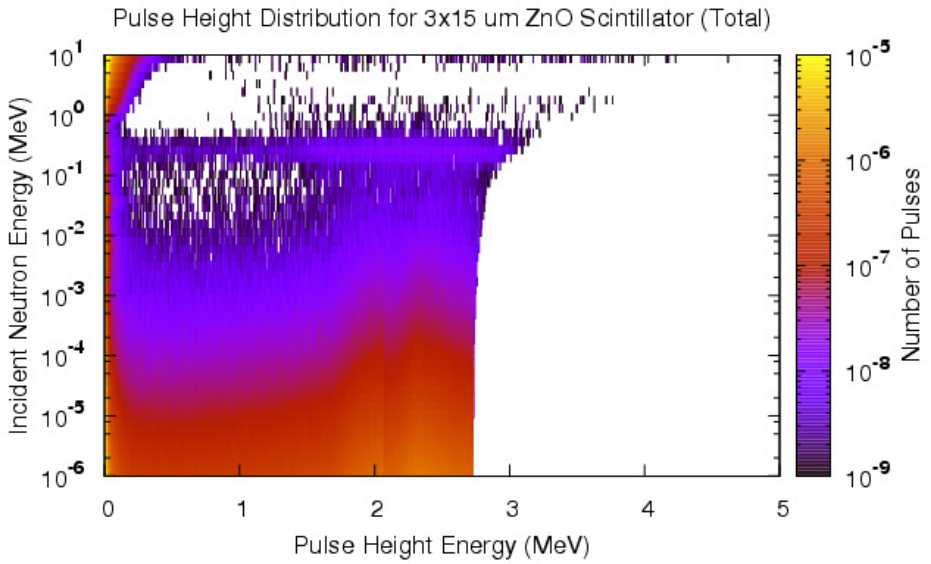

Figure 266 Pulse height distribution for all particles in a 3x15µm scintillator stack.

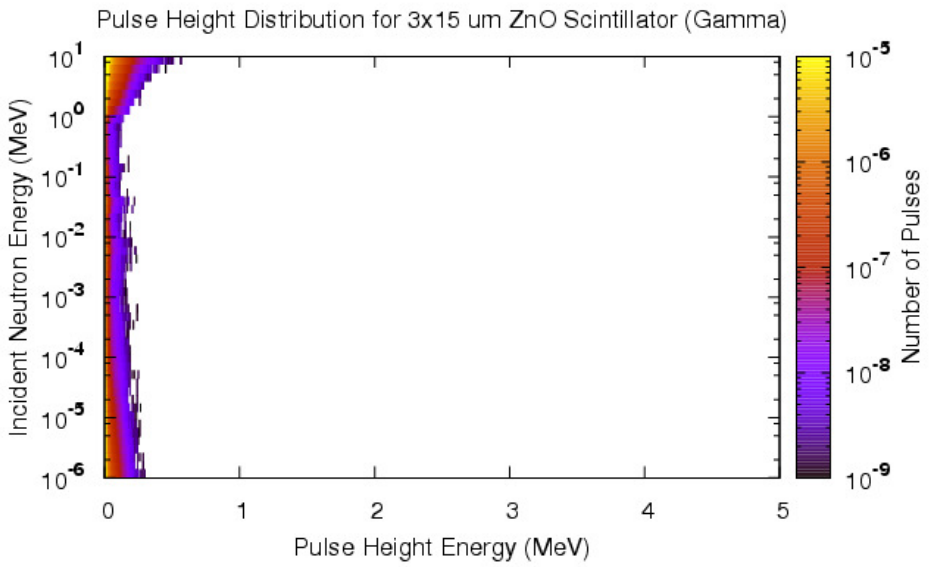

Figure 267 Pulse height distribution for gamma rays in a 3x15µm scintillator stack.

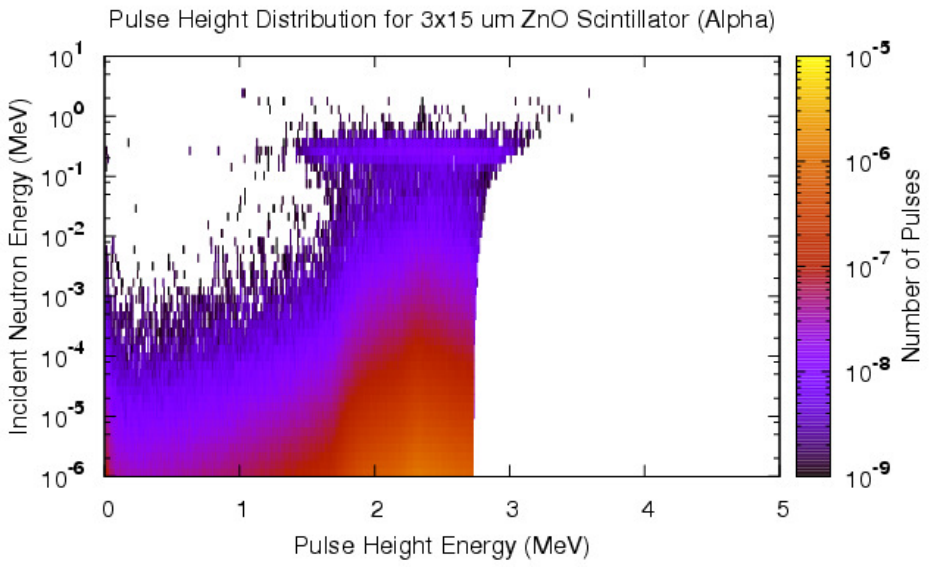

Figure 268 Pulse height distribution for alpha particles in a 3x15µm scintillator stack.

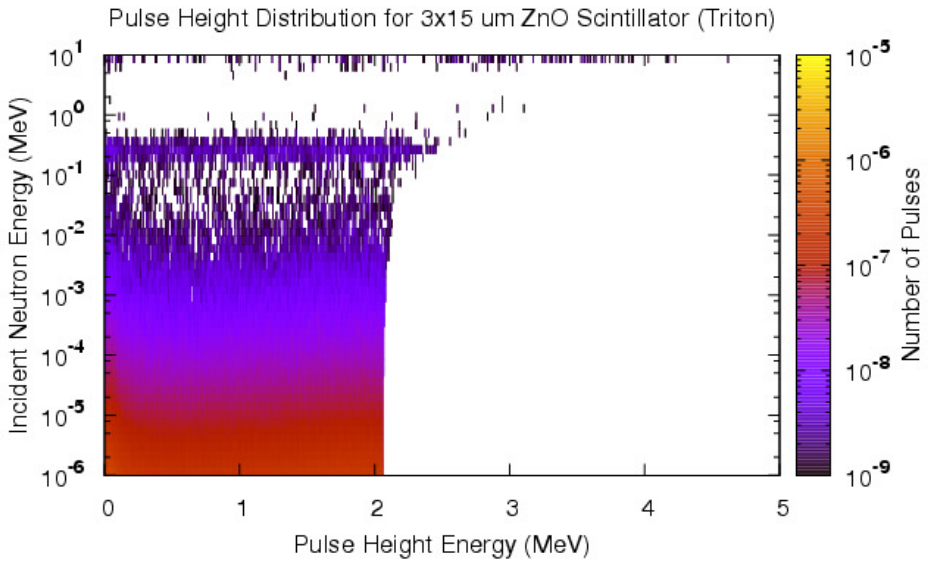

Figure 269 Pulse height distribution for triton particles in a 3x15µm scintillator stack.

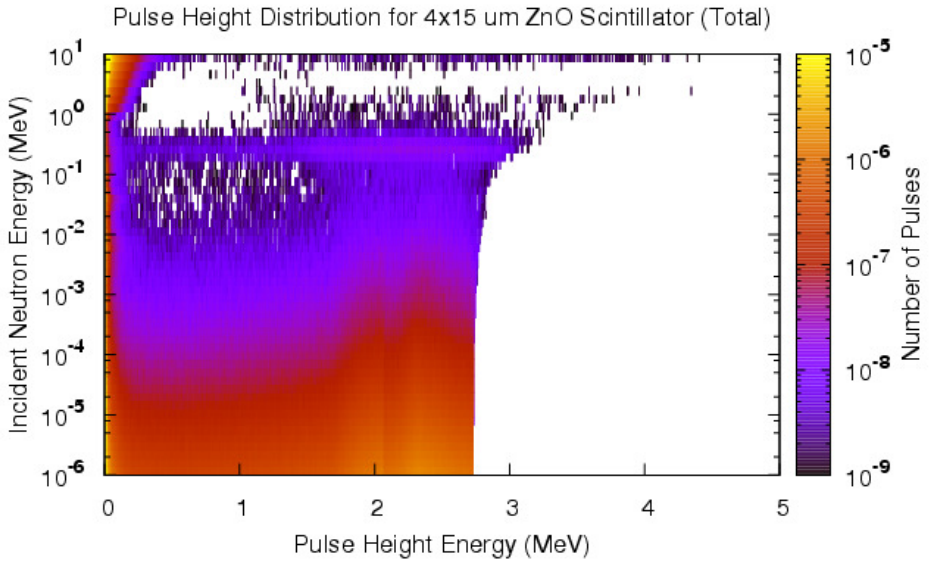

Figure 270 Pulse height distribution for all particles in a 4x15µm scintillator stack.

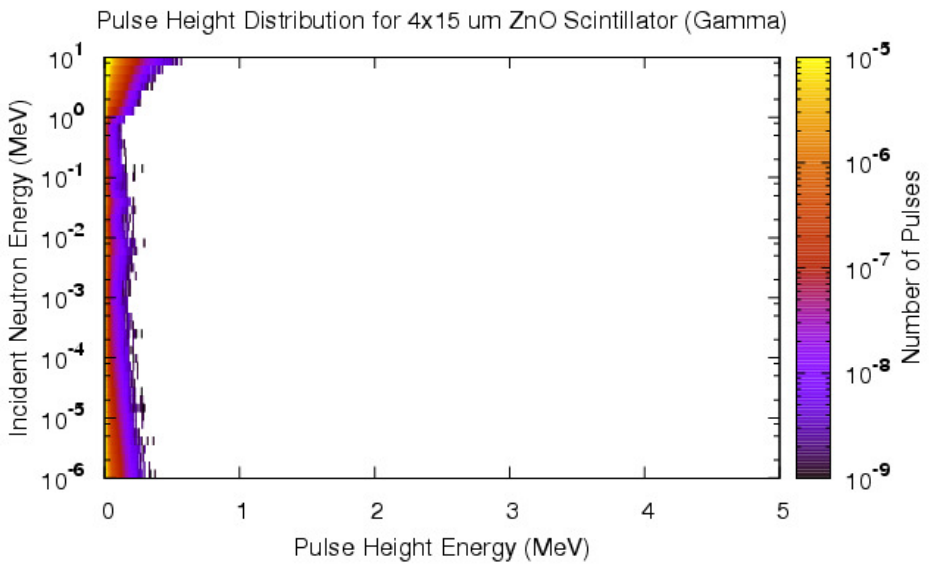

Figure 271 Pulse height distribution for gamma rays in a 4x15µm scintillator stack.

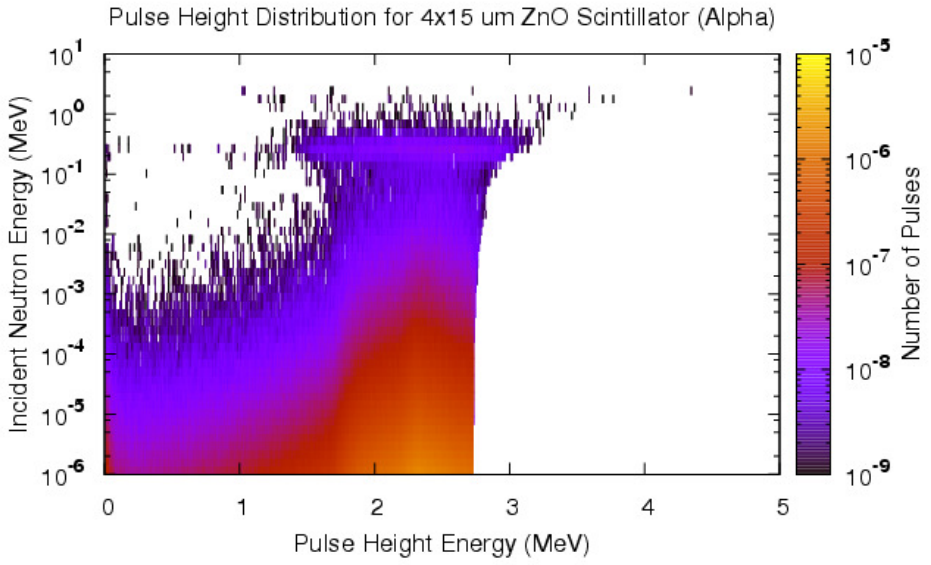

Figure 272 Pulse height distribution for alpha particles in a 4x15µm scintillator stack.

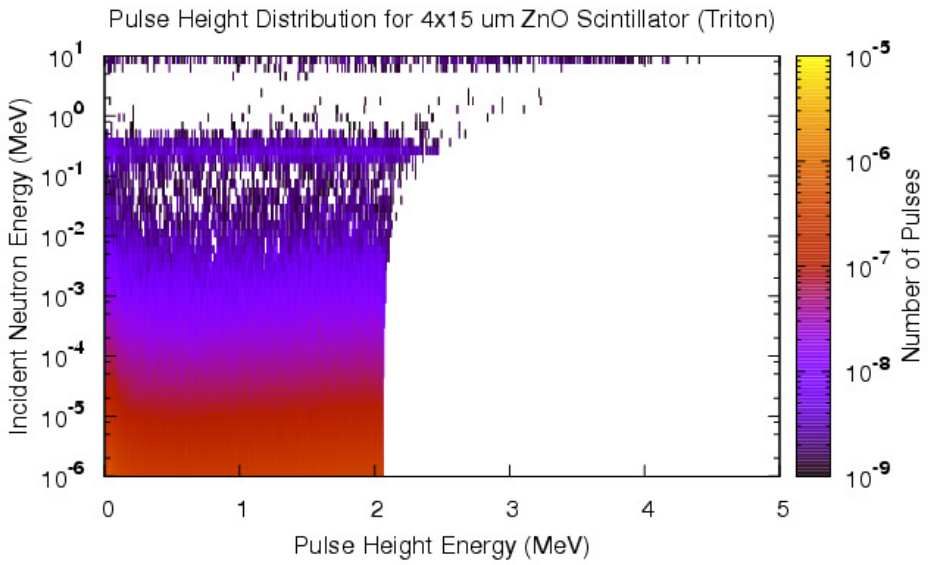

Figure 273 Pulse height distribution for triton particles in a 4x15µm scintillator stack.

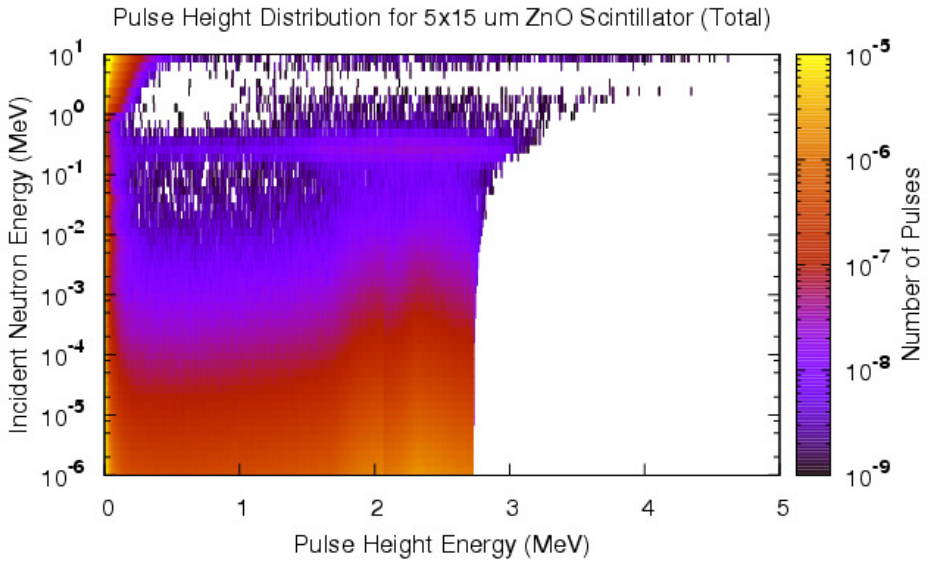

Figure 274 Pulse height distribution for all particles in a 5x15µm scintillator stack.

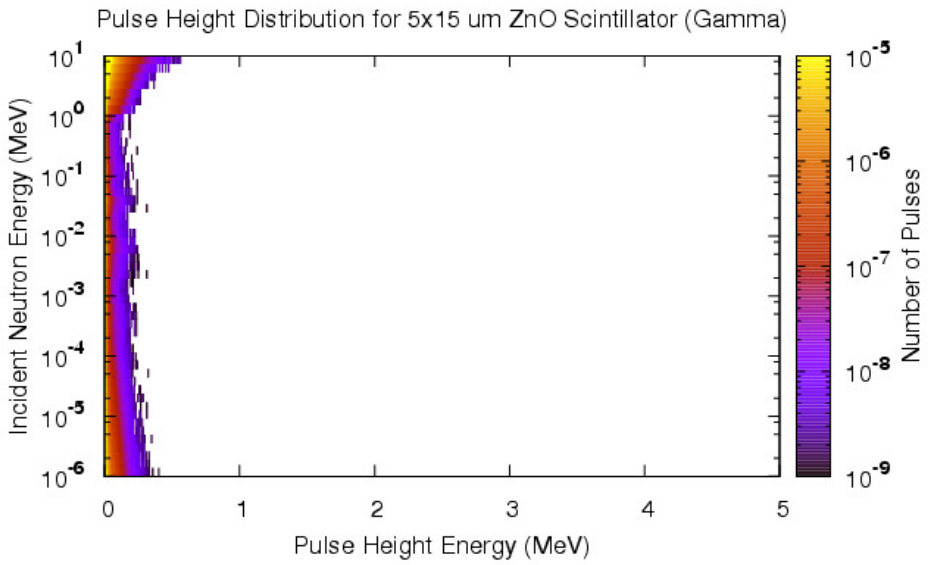

Figure 275 Pulse height distribution for gamma rays in a 5x15µm scintillator stack.

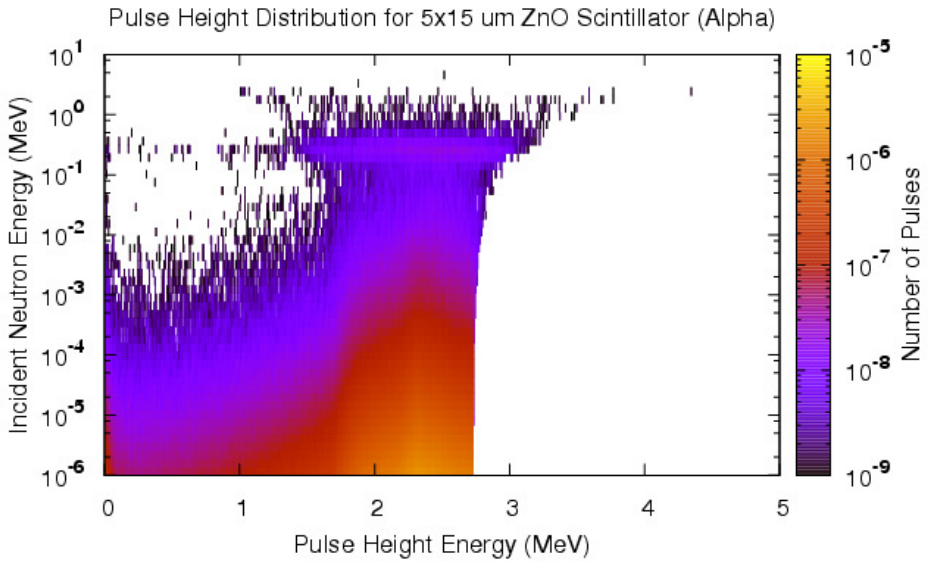

Figure 276 Pulse height distribution for alpha particles in a 5x15µm scintillator stack.

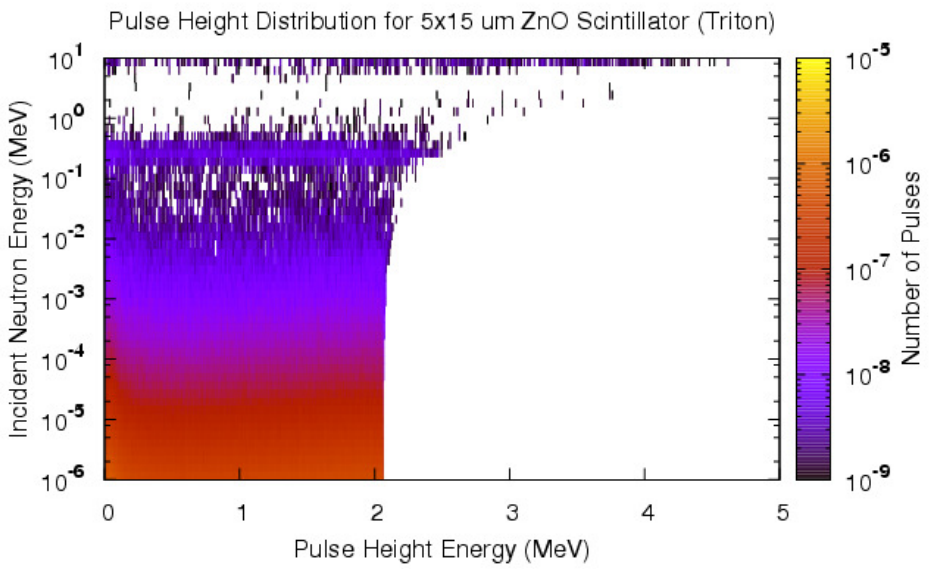

Figure 277 Pulse height distribution for triton particles in a 5x15µm scintillator stack.

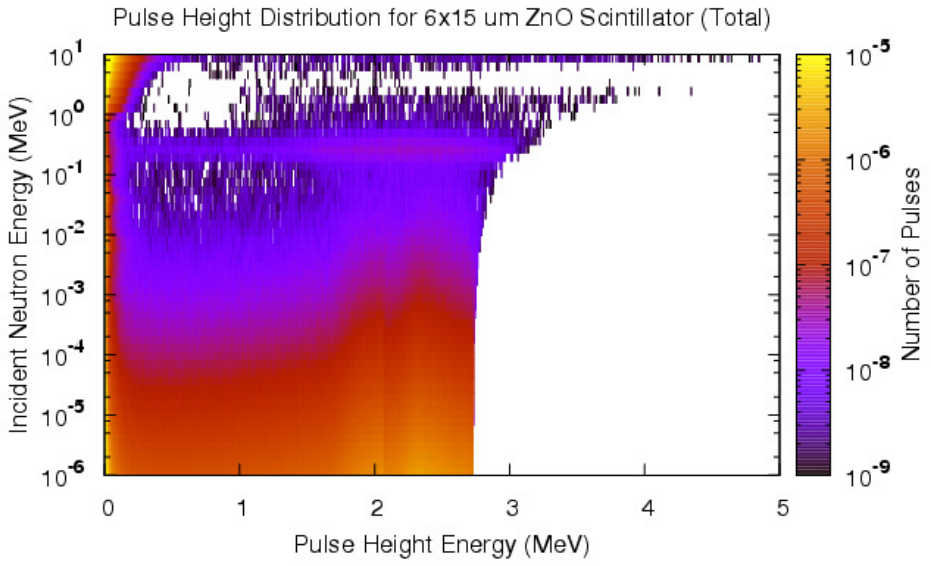

Figure 278 Pulse height distribution for all particles in a 6x15µm scintillator stack.

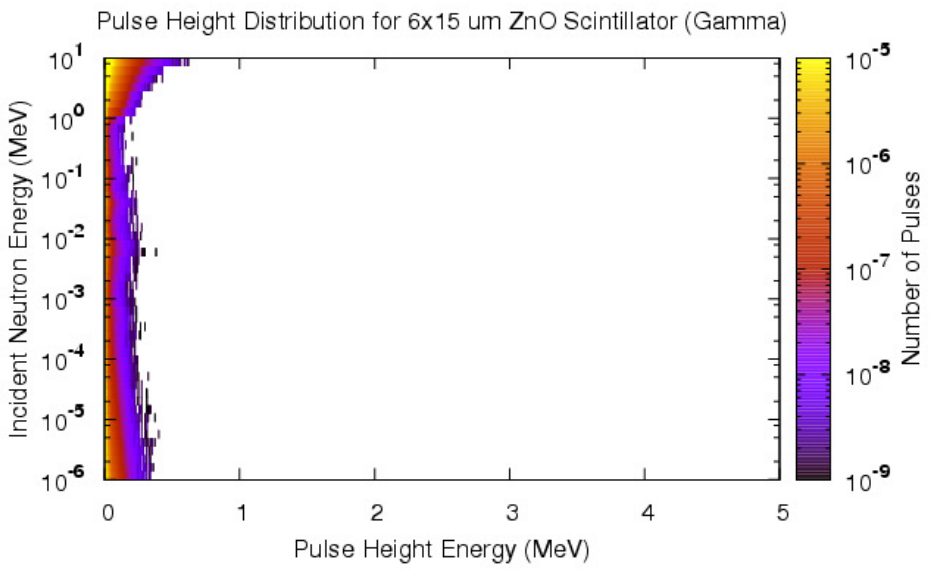

Figure 279 Pulse height distribution for gamma rays in a 6x15µm scintillator stack.

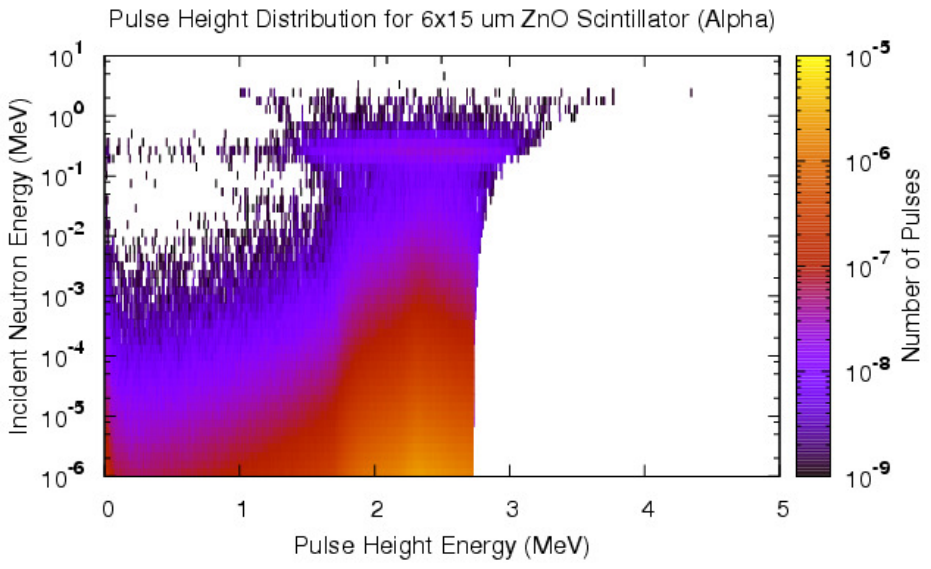

Figure 280 Pulse height distribution for alpha particles in a 6x15µm scintillator stack.

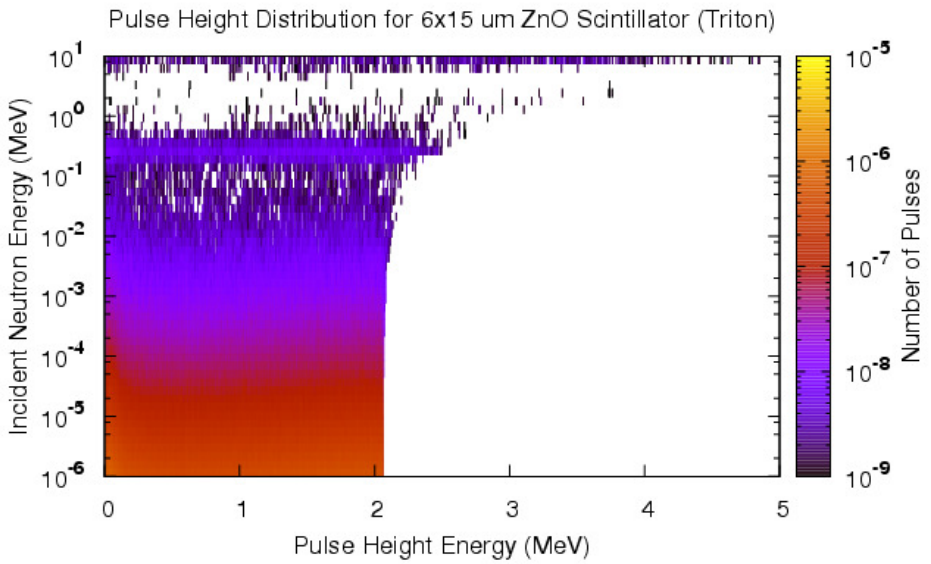

Figure 281 Pulse height distribution for triton particles in a 7x15µm scintillator stack.

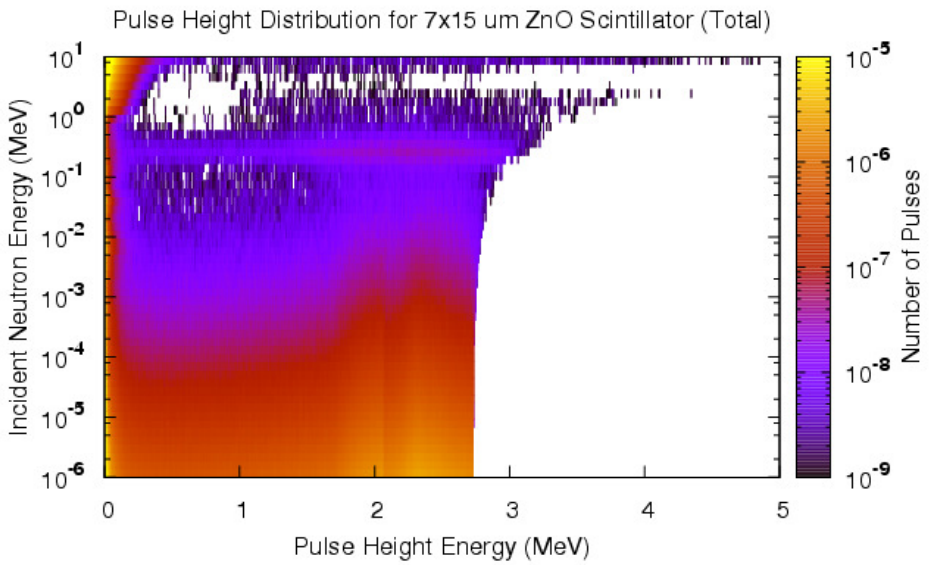

Figure 282 Pulse height distribution for all particles in a 7x15µm scintillator stack.

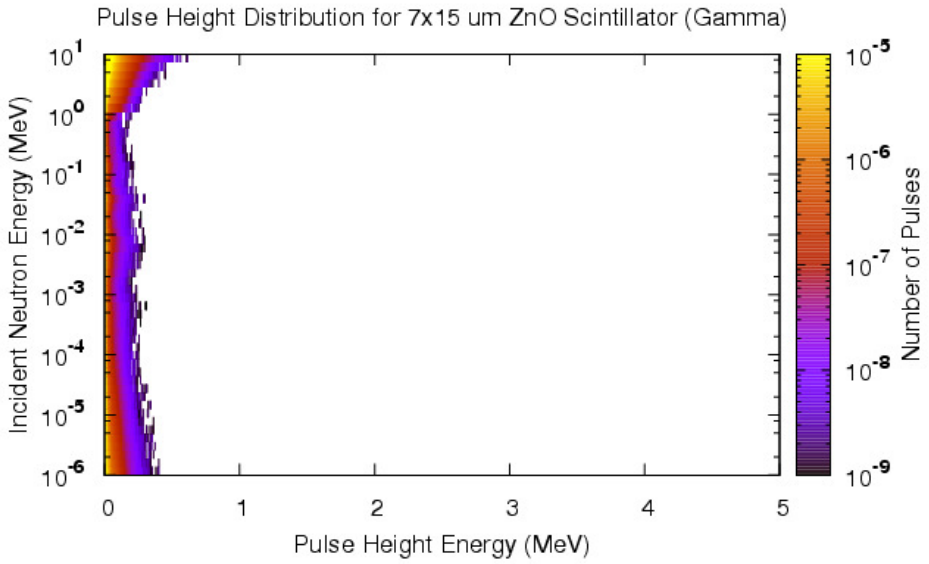

Figure 283 Pulse height distribution for gamma rays in a 7x15µm scintillator stack.

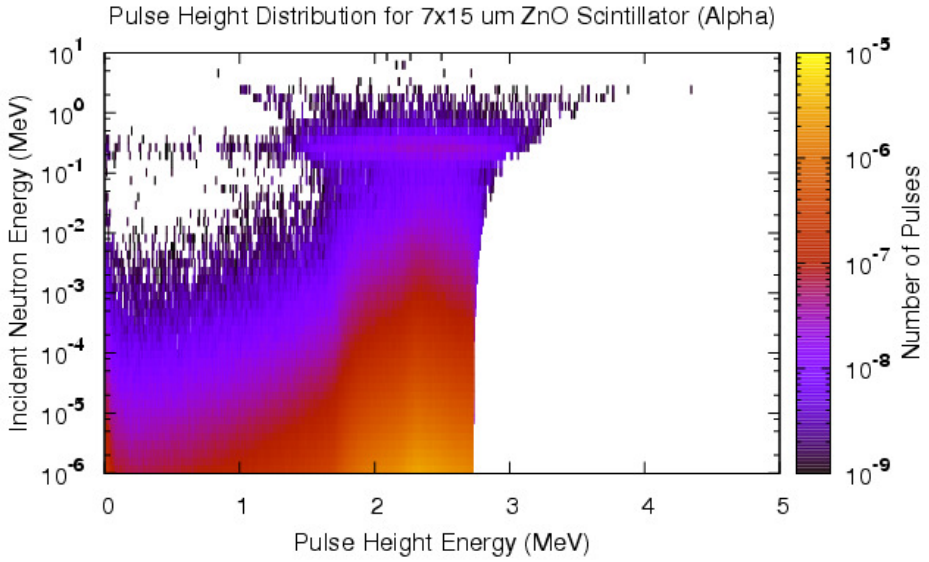

Figure 284 Pulse height distribution for alpha particles in a 7x15µm scintillator stack.

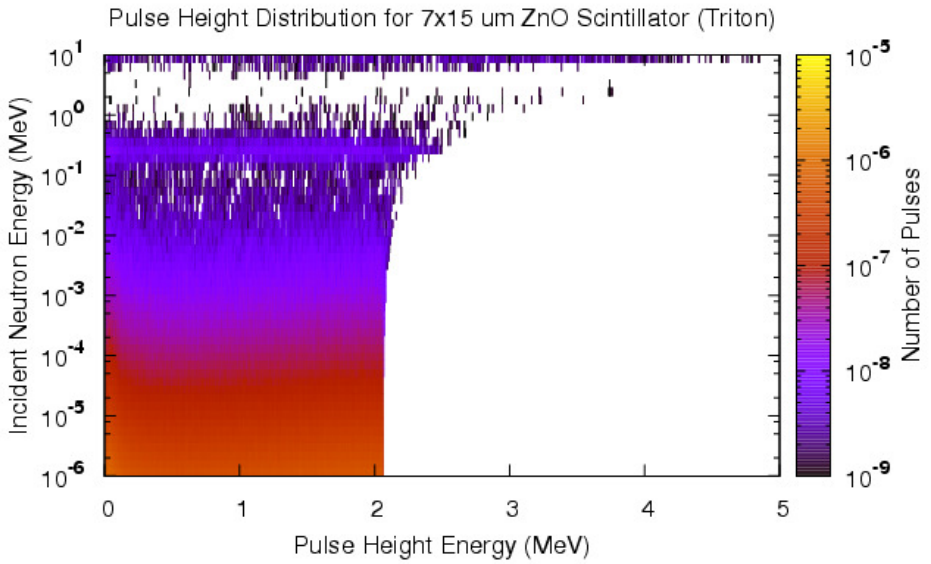

Figure 285 Pulse height distribution for triton particles in a 8x15µm scintillator stack.

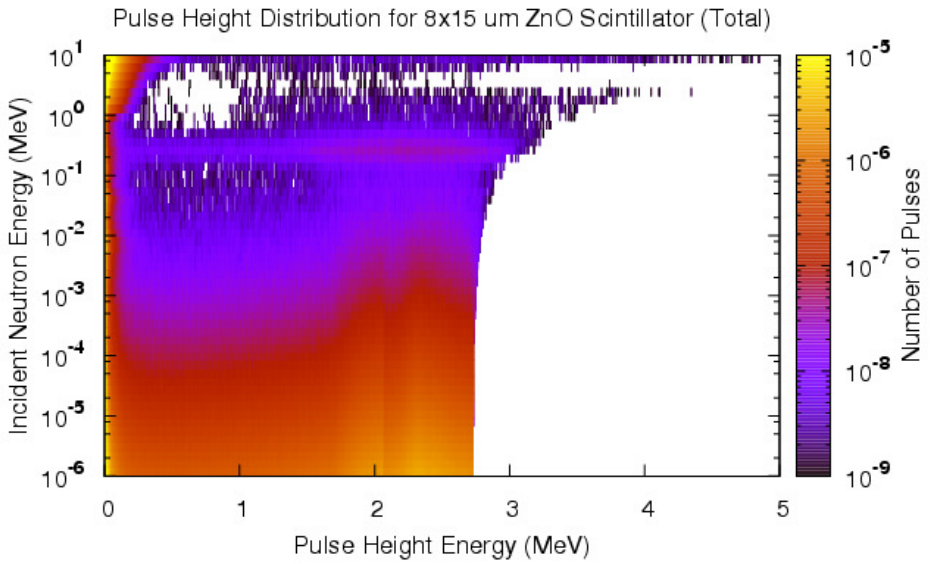

Figure 286 Pulse height distribution for all particles in a 8x15µm scintillator stack.

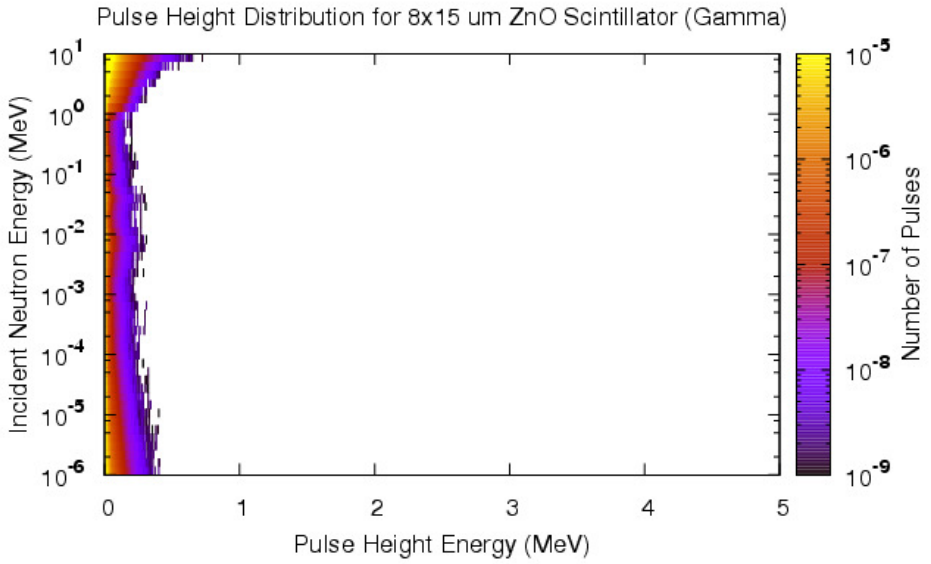

Figure 287 Pulse height distribution for gamma rays in a 8x15µm scintillator stack.

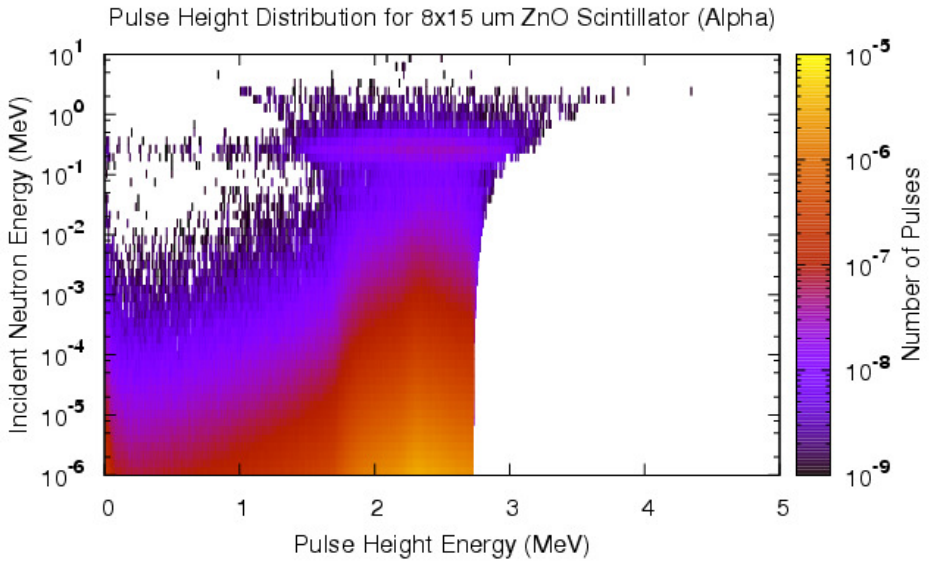

Figure 288 Pulse height distribution for alpha particles in a 8x15µm scintillator stack.

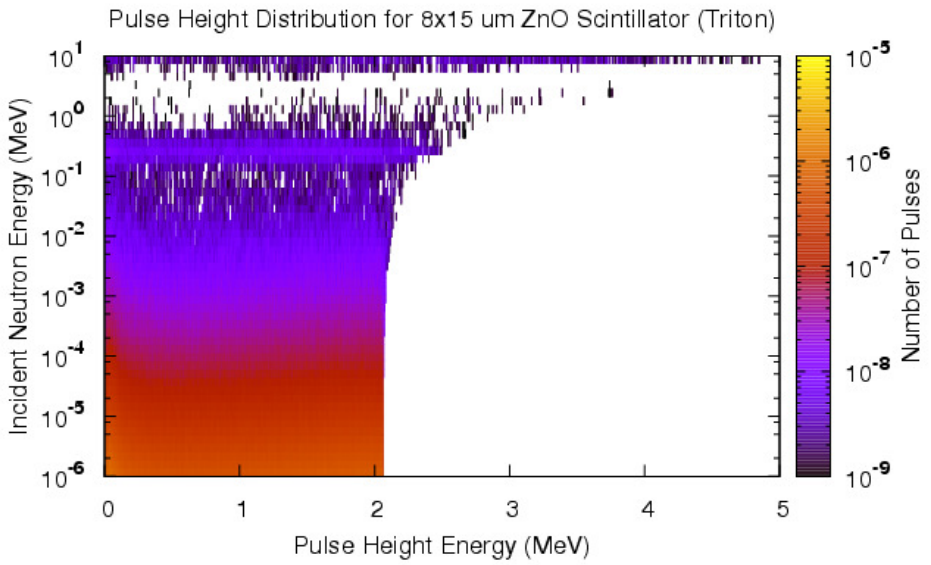

Figure 289 Pulse height distribution for triton particles in a 8x15µm scintillator stack.

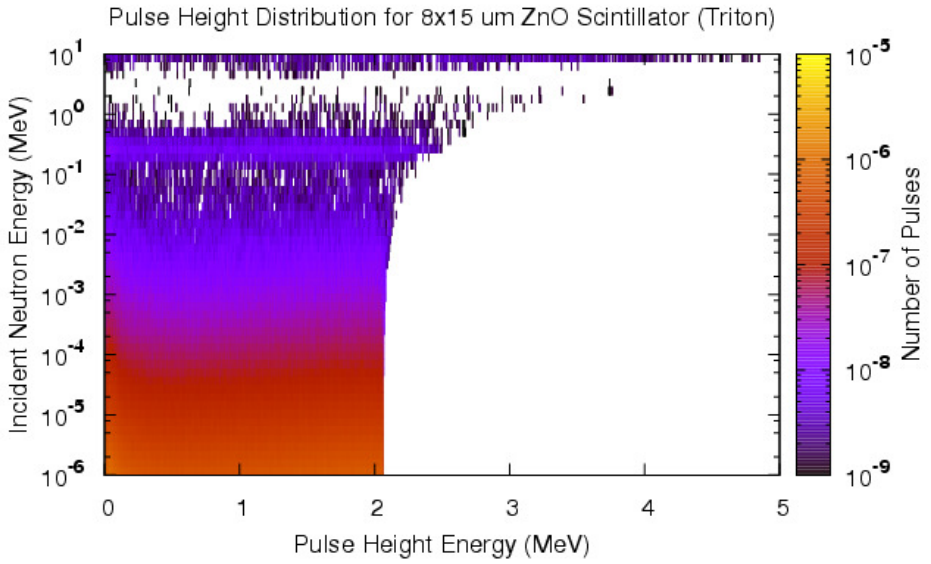

Figure 290

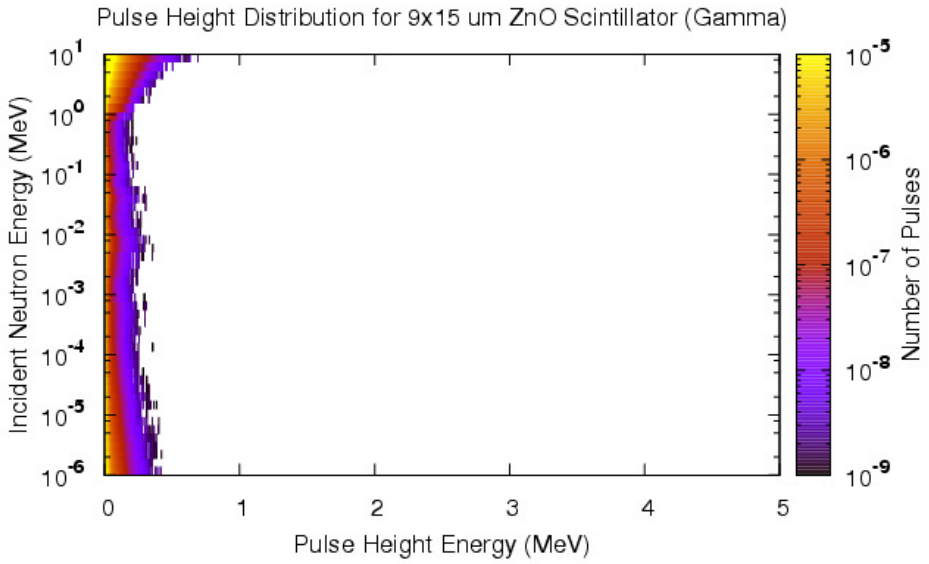

Figure 291 Pulse height distribution for gamma rays in a 9x15µm scintillator stack.

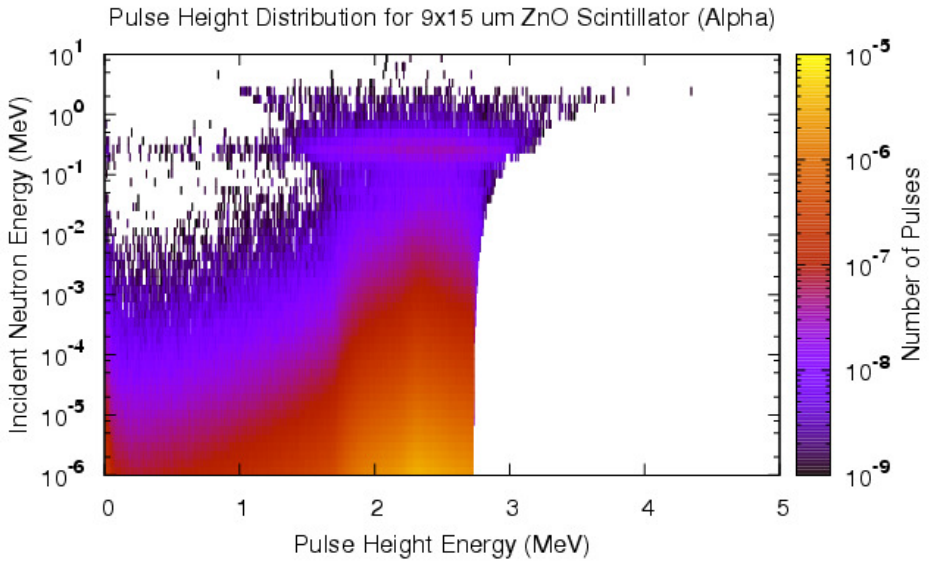

Figure 292 Pulse height distribution for alpha particles in a 9x15µm scintillator stack.

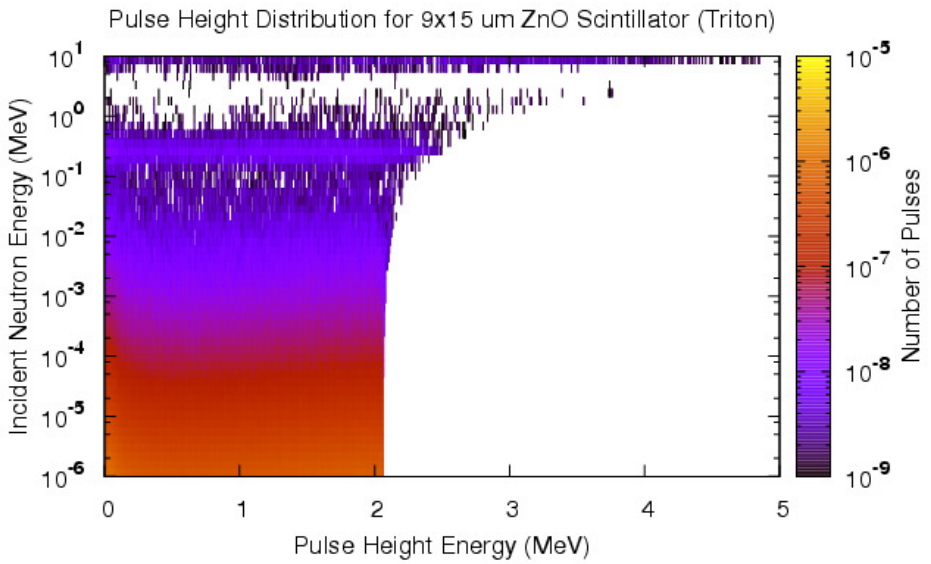

Figure 293 Pulse height distribution for triton particles in a 9x15µm scintillator stack.

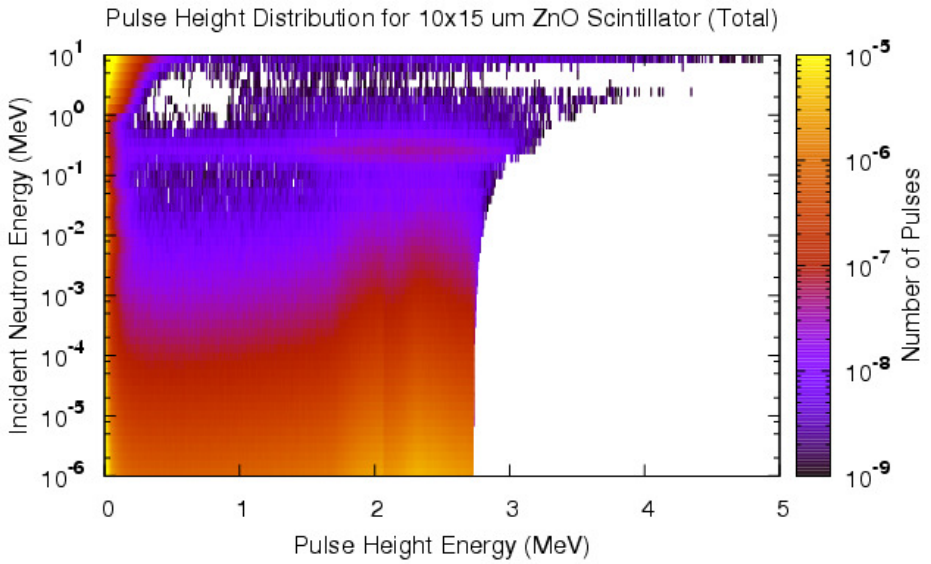

Figure 294 Pulse height distribution for all particles in a 10x15µm scintillator stack.

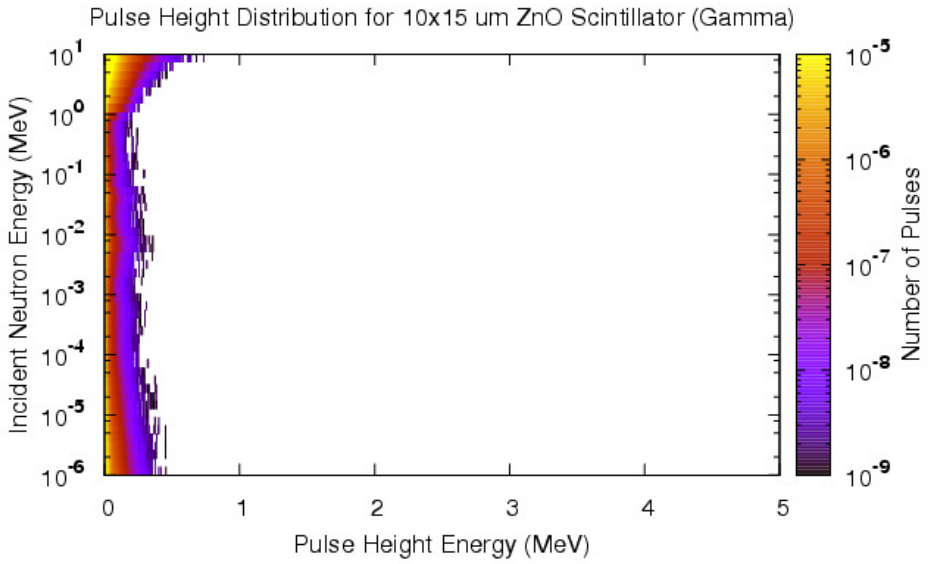

Figure 295 Pulse height distribution for gamma rays in a 10x15µm scintillator stack.

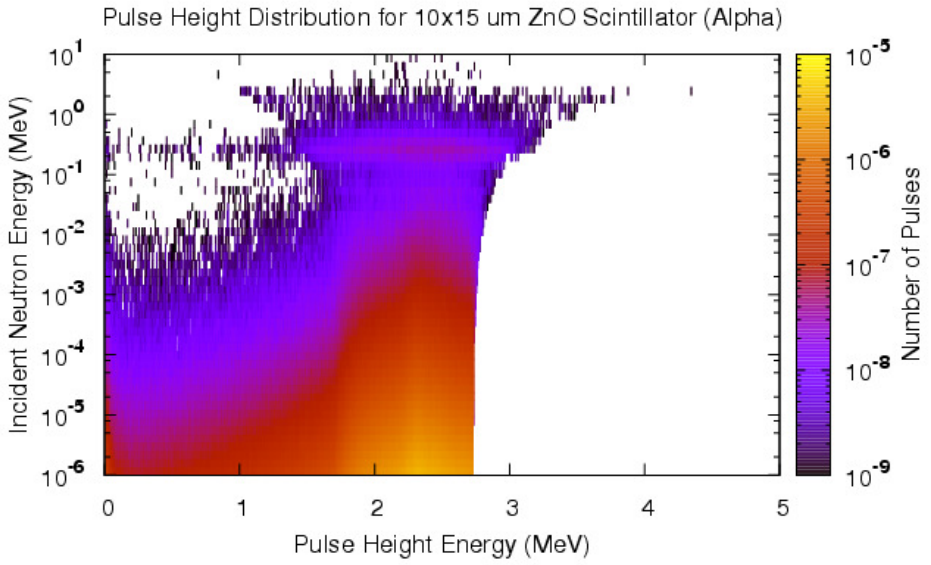

Figure 296 Pulse height distribution for alpha particles in a 10x15µm scintillator stack.

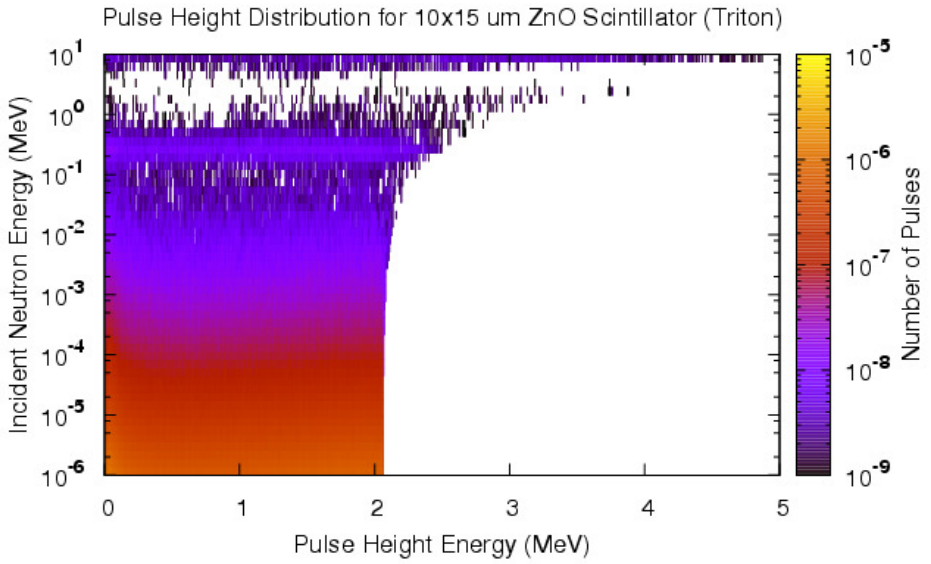

Figure 297 Pulse height distribution for triton particles in a 10x15µm scintillator stack.

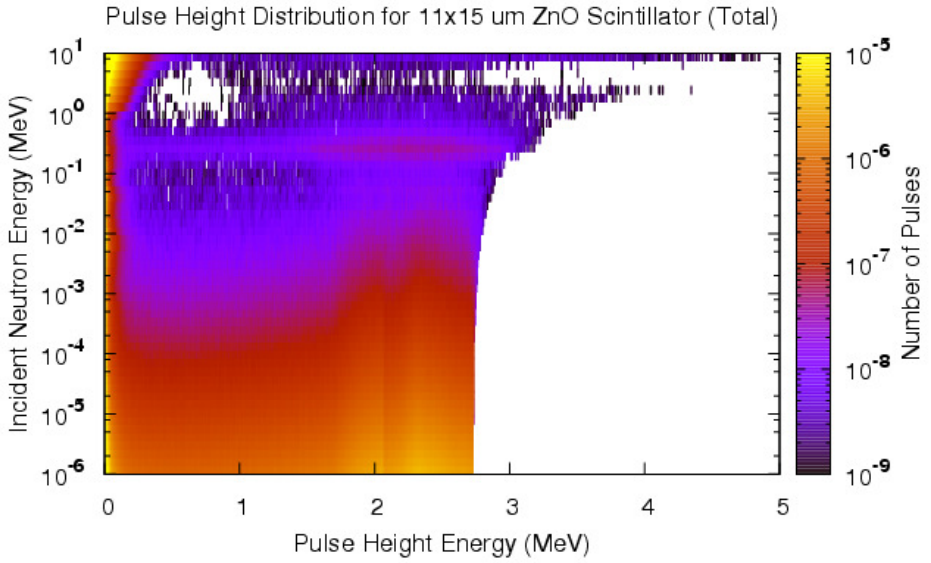

Figure 298 Pulse height distribution for all particles in a 11x15µm scintillator stack.

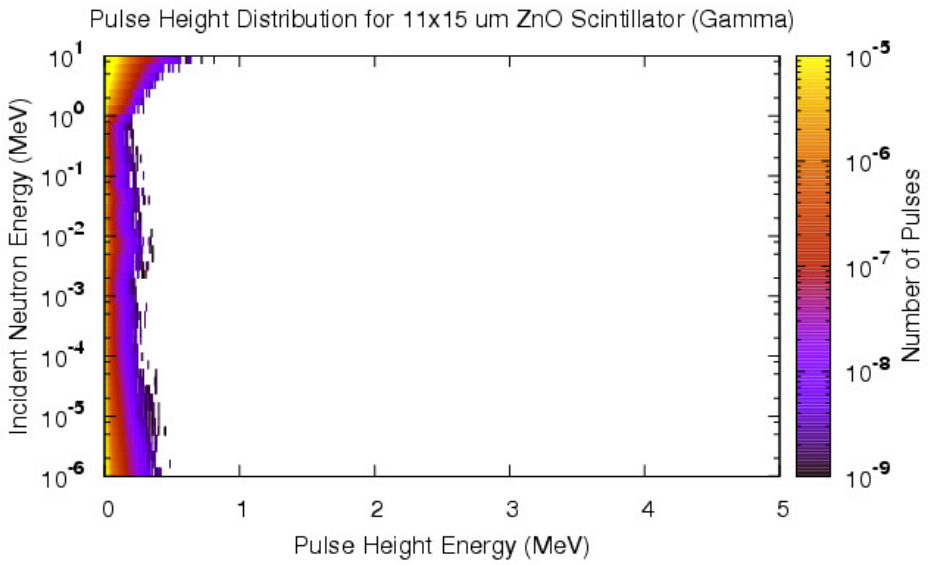

Figure 299 Pulse height distribution for gamma rays in a 11x15µm scintillator stack.

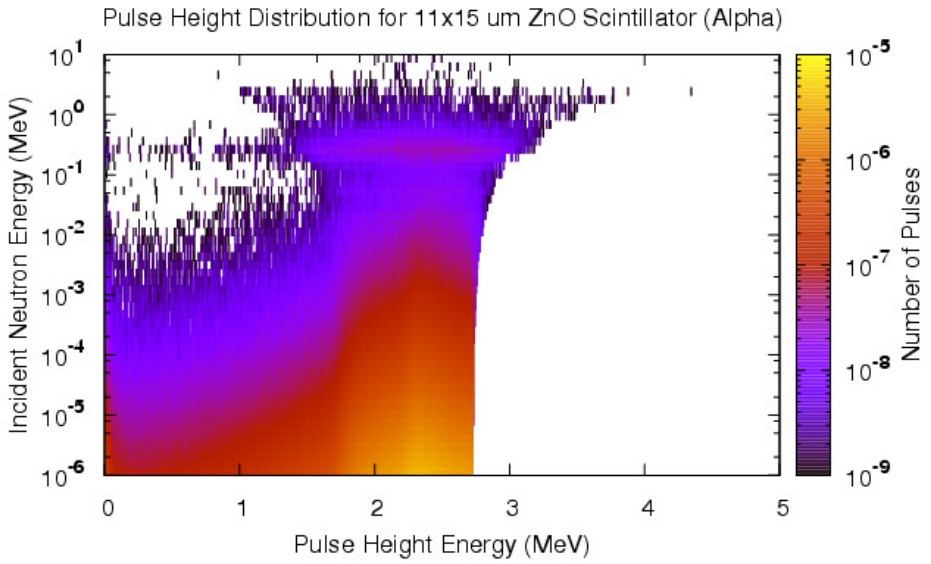

Figure 300 Pulse height distribution for alpha particles in a 11x15µm scintillator stack.

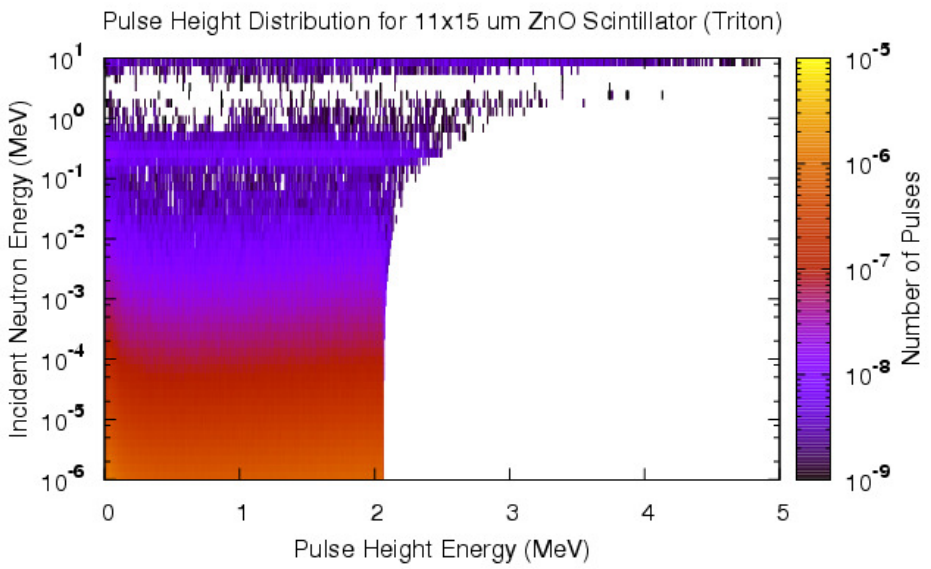

Figure 301 Pulse height distribution for triton particles in a 11x15µm scintillator stack.

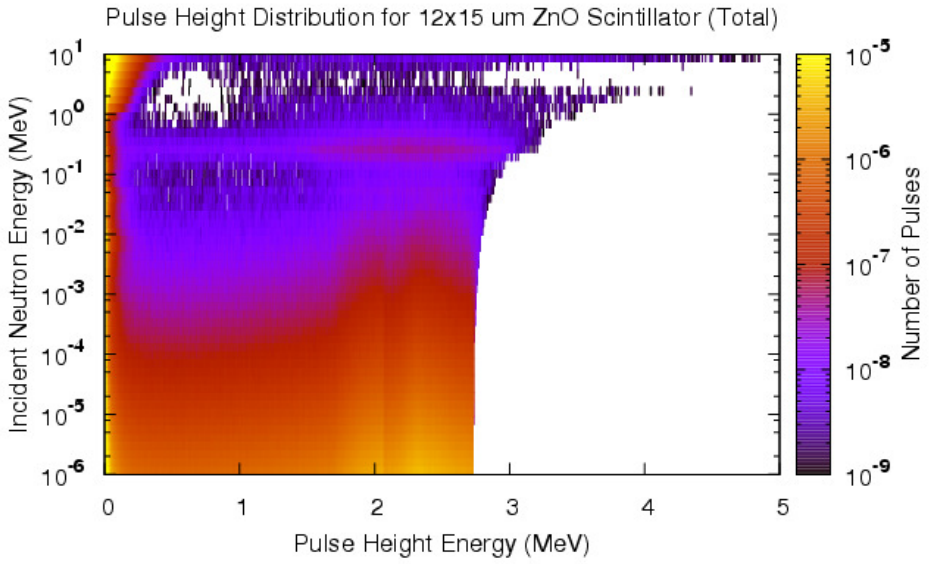

Figure 302 Pulse height distribution for all particles in a 12x15µm scintillator stack.

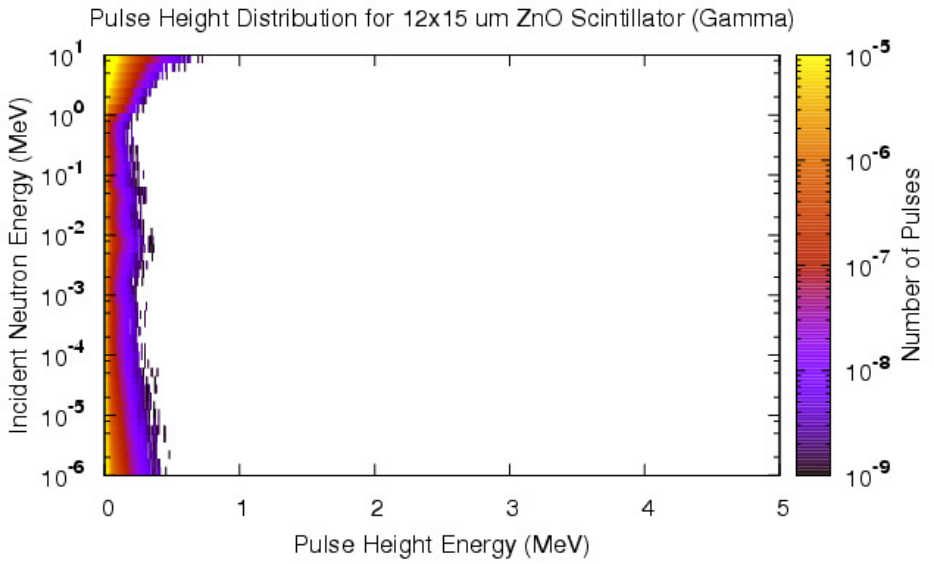

Figure 303 Pulse height distribution for gamma rays in a 12x15µm scintillator stack.

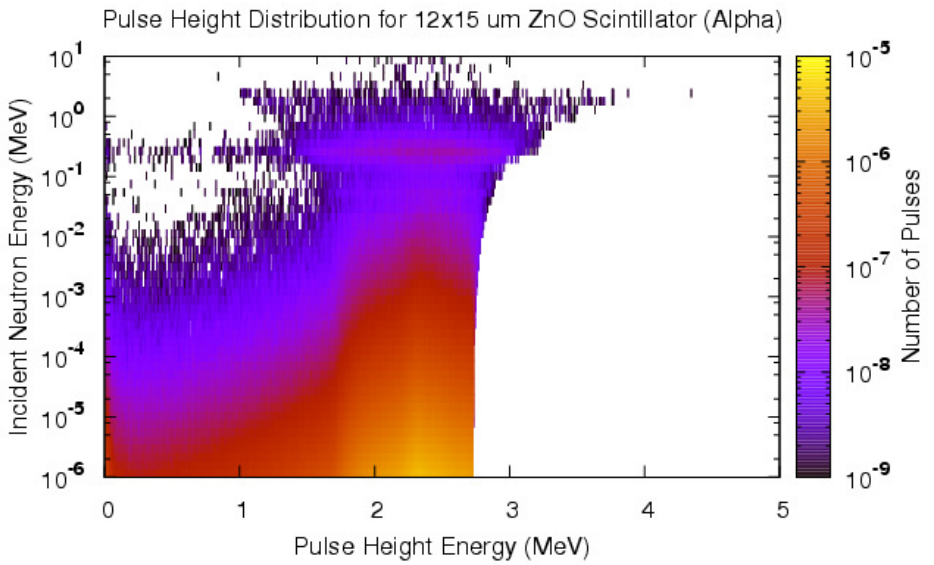

Figure 304 Pulse height distribution for alpha particles in a 12x15µm scintillator stack.

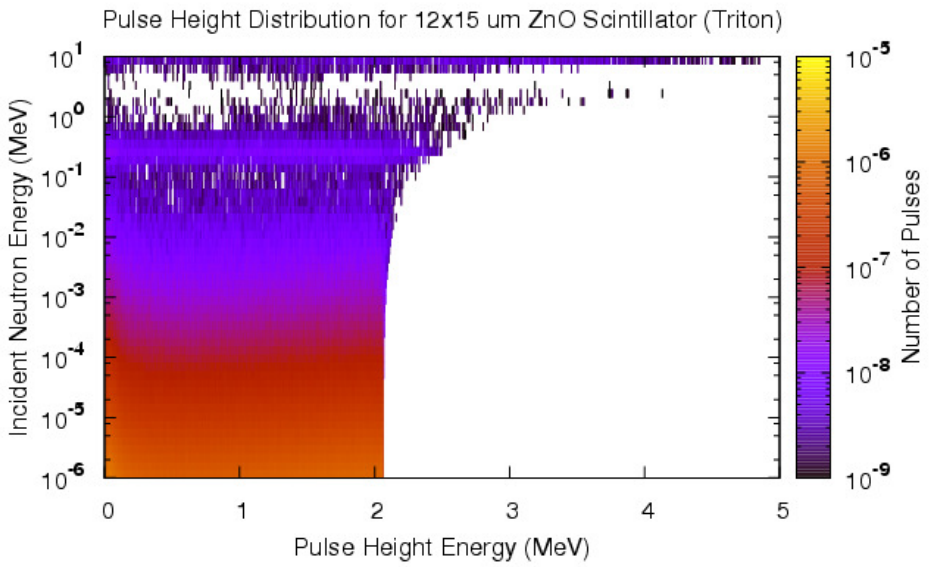

Figure 305 Pulse height distribution for triton particles in a 12x15µm scintillator stack.

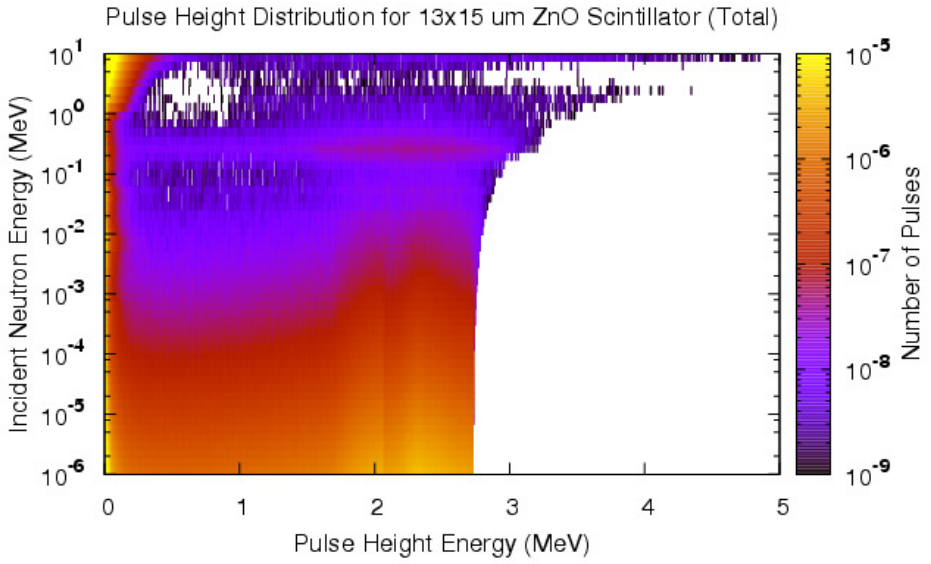

Figure 306 Pulse height distribution for all particles in a 13x15µm scintillator stack.

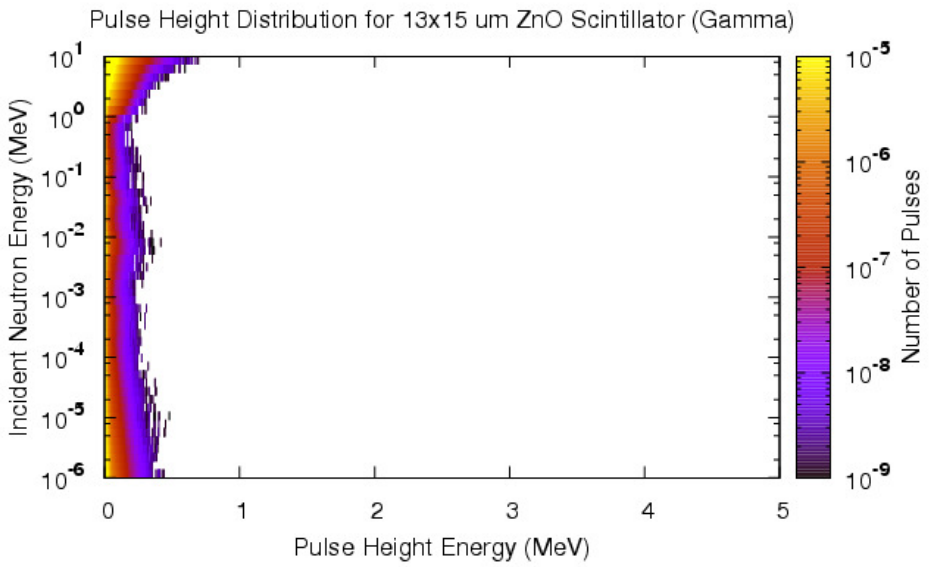

Figure 307 Pulse height distribution for gamma rays in a 13x15µm scintillator stack.

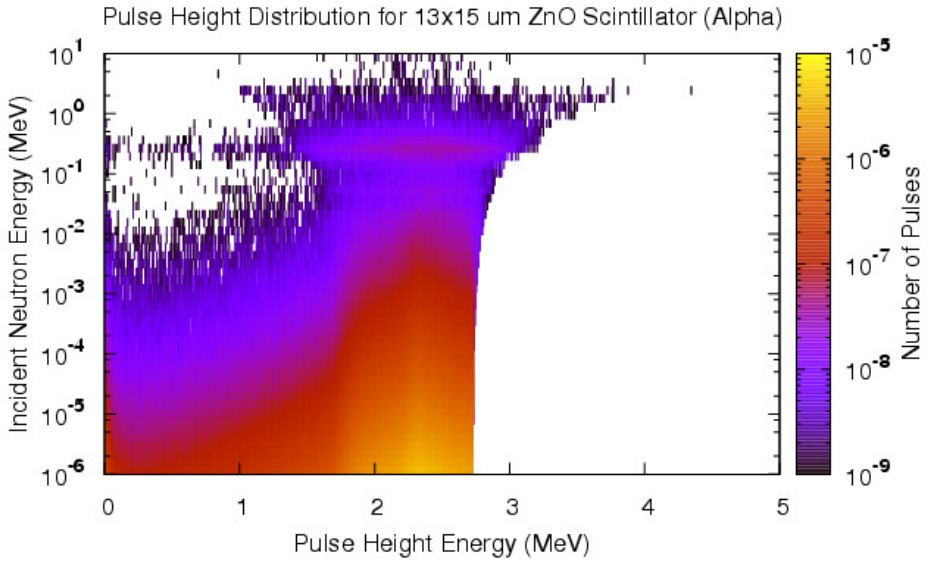

Figure 308 Pulse height distribution for alpha particles in a 13x15µm scintillator stack.

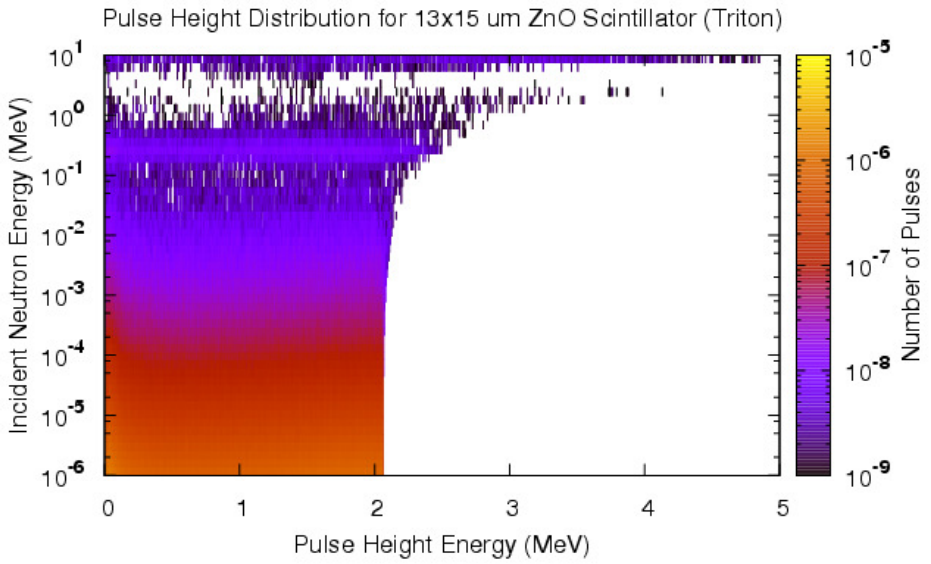

Figure 309 Pulse height distribution for triton particles in a 13x15µm scintillator stack.

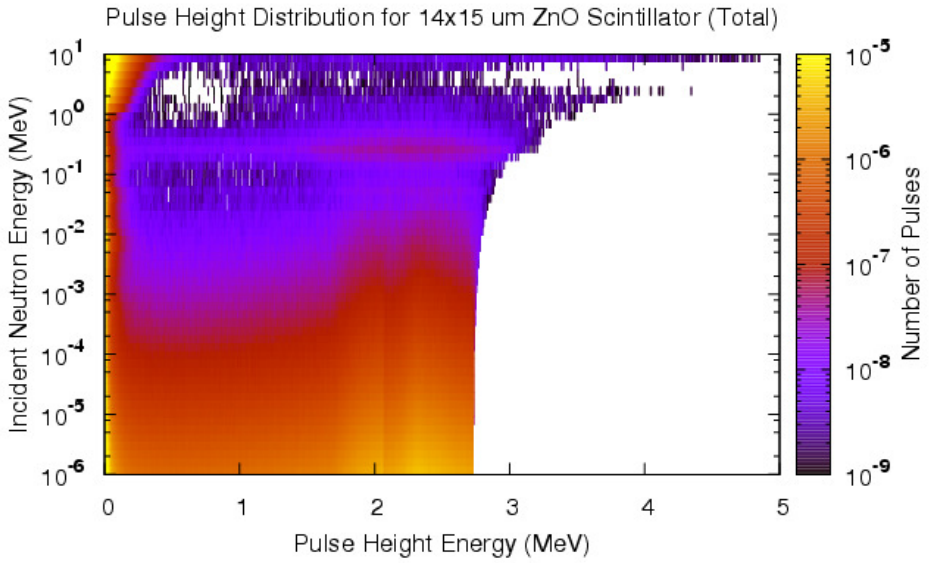

Figure 310 Pulse height distribution for all particles in a 14x15µm scintillator stack.

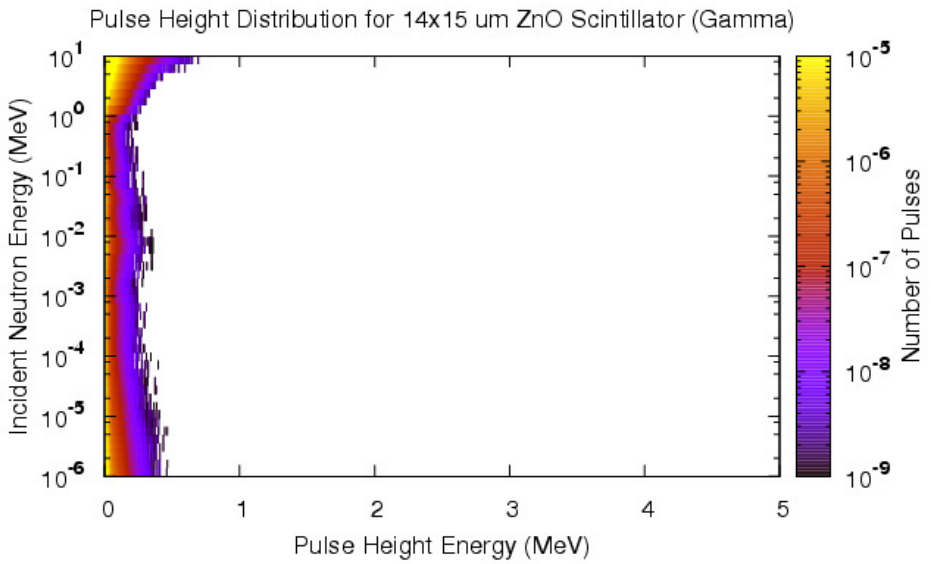

Figure 311 Pulse height distribution for gamma rays in a 14x15µm scintillator stack.

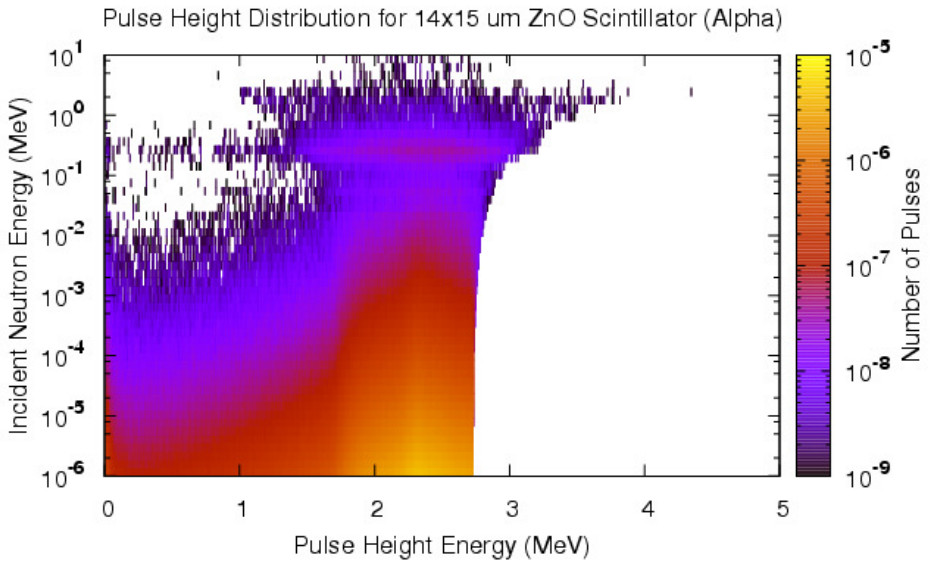

Figure 312 Pulse height distribution for alpha particles in a 14x15µm scintillator stack.

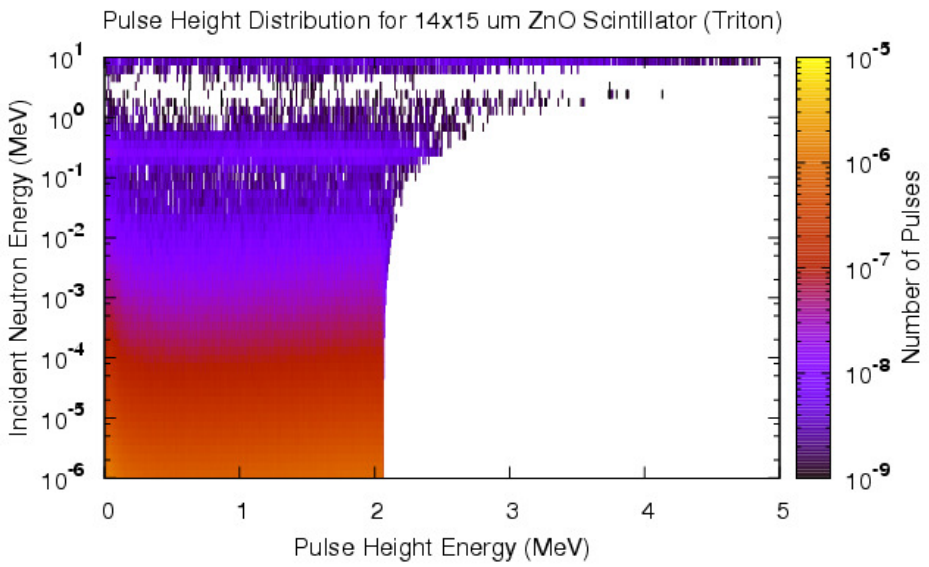

Figure 313 Pulse height distribution for triton particles in a 14x15µm scintillator stack.

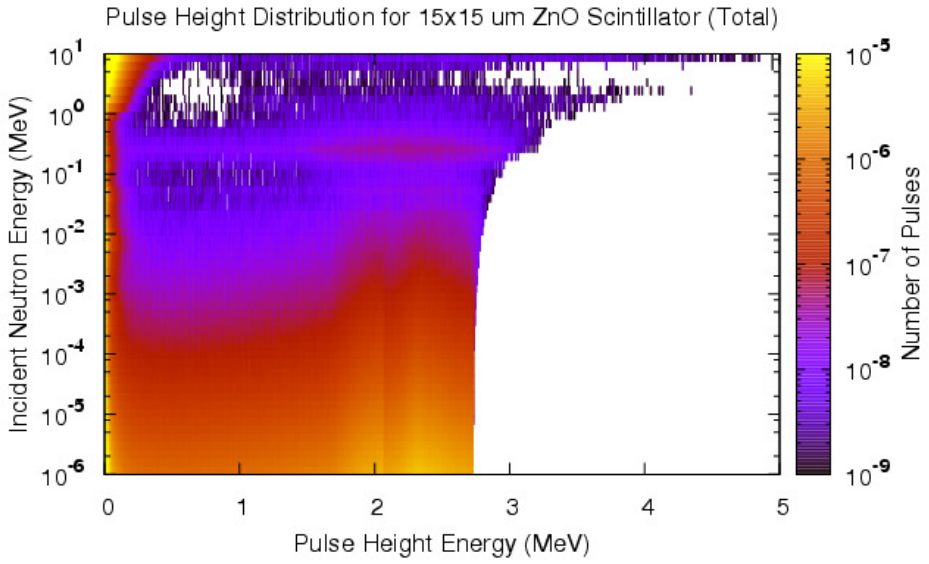

Figure 314 Pulse height distribution for all particles in a 15x15µm scintillator stack.

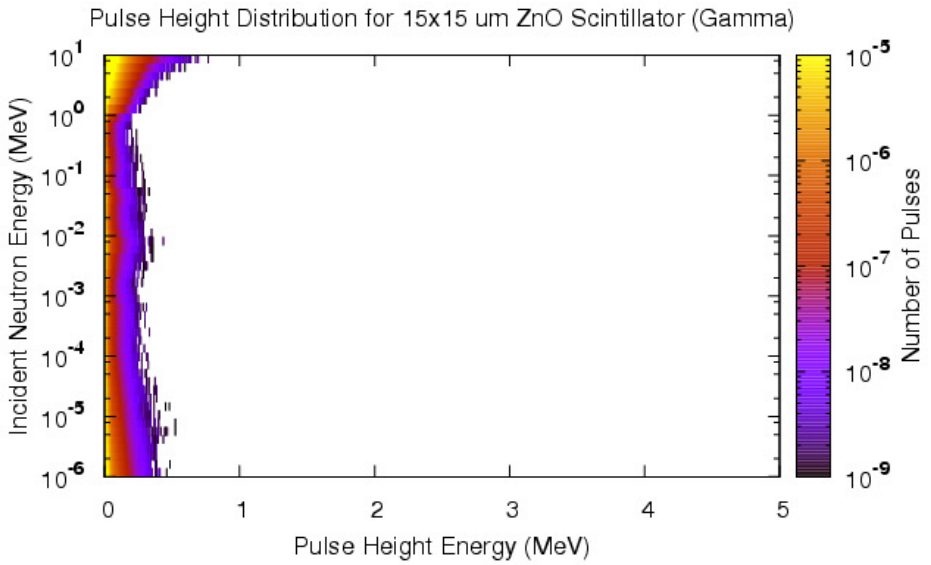

Figure 315 Pulse height distribution for gamma rays in a 15x15µm scintillator stack.

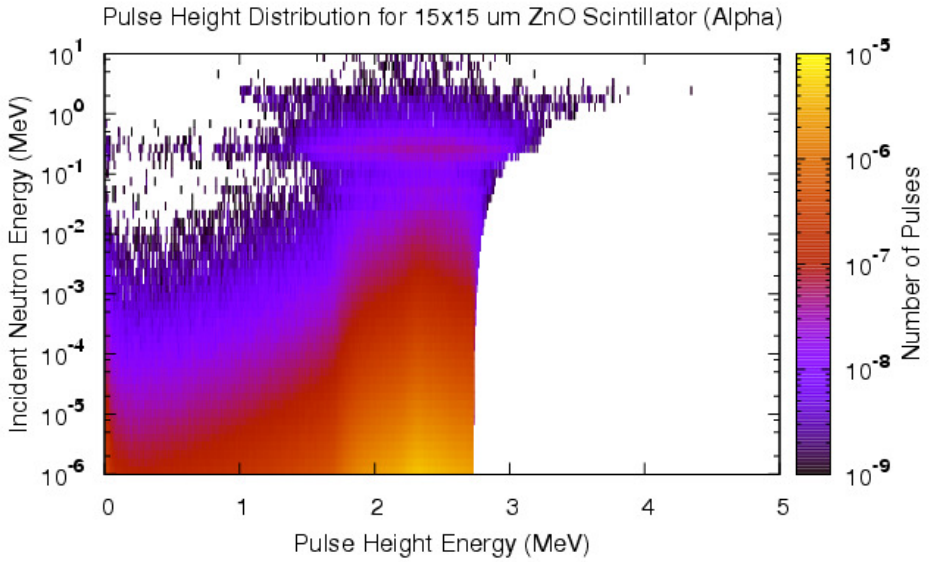

Figure 316 Pulse height distribution for alpha particles in a 15x15µm scintillator stack.

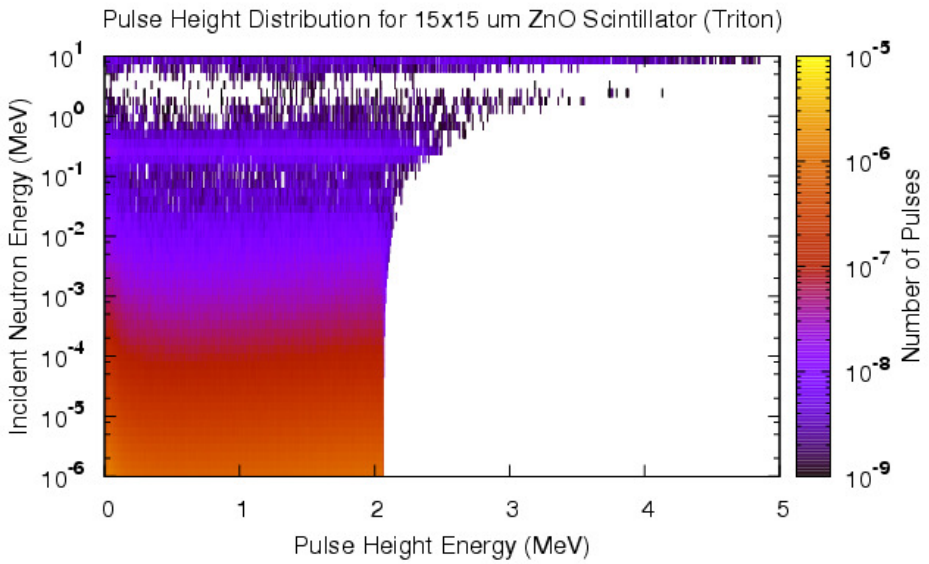

Figure 317 Pulse height distribution for triton particles in a 15x15µm scintillator stack.

APPENDIX C

GRAPHITE SLOWING DOWN SPECTROMETER DATA

Using position 7 of the GSDS, count rates relative to the ^{3}He tube have been calculated. These are shown below. The energies were calculated using Equation 16. Since each of the samples was coated with ^{6}LiF, they exhibit a small peak in efficiency around 200 keV, the peak in the ^{6}Li(n,α) reaction. AZO can be seen in Figure 318. Boron doped ZnO can be found in Figure 319. Lithium doped ZnO can be found in Figure 320. Undoped ZnO can be found in Figure 321. Gallium doped ZnO can be found in Figure 322. Nitrogen doped ZnO can be found in Figure 323. Due to the long decay time of the thermal neutron pulse, and it's non-proportion with respect to time, only neutron energies down to ~50 eV can effectively be measured using this system.

$$E = 16.878 * t^{-2.093}$$

Equation 16 Equation relating the time after the D-T pulse to the neutron energy for the GSDS at position 7.

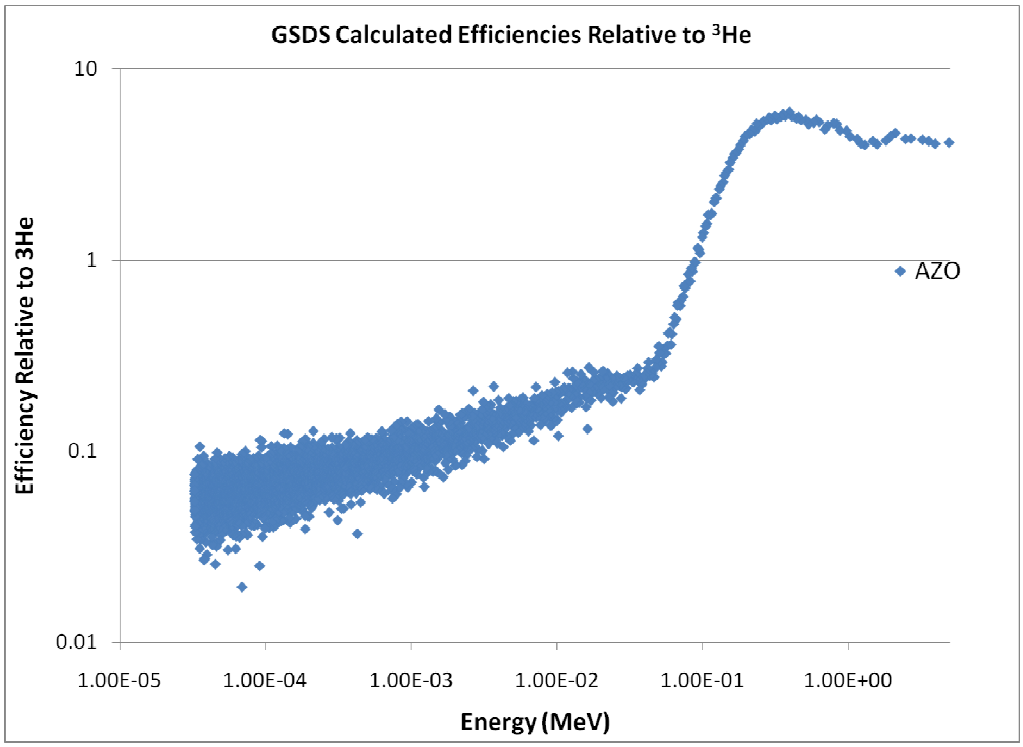

Figure 318 AZO relative count rate to ^{3}He.

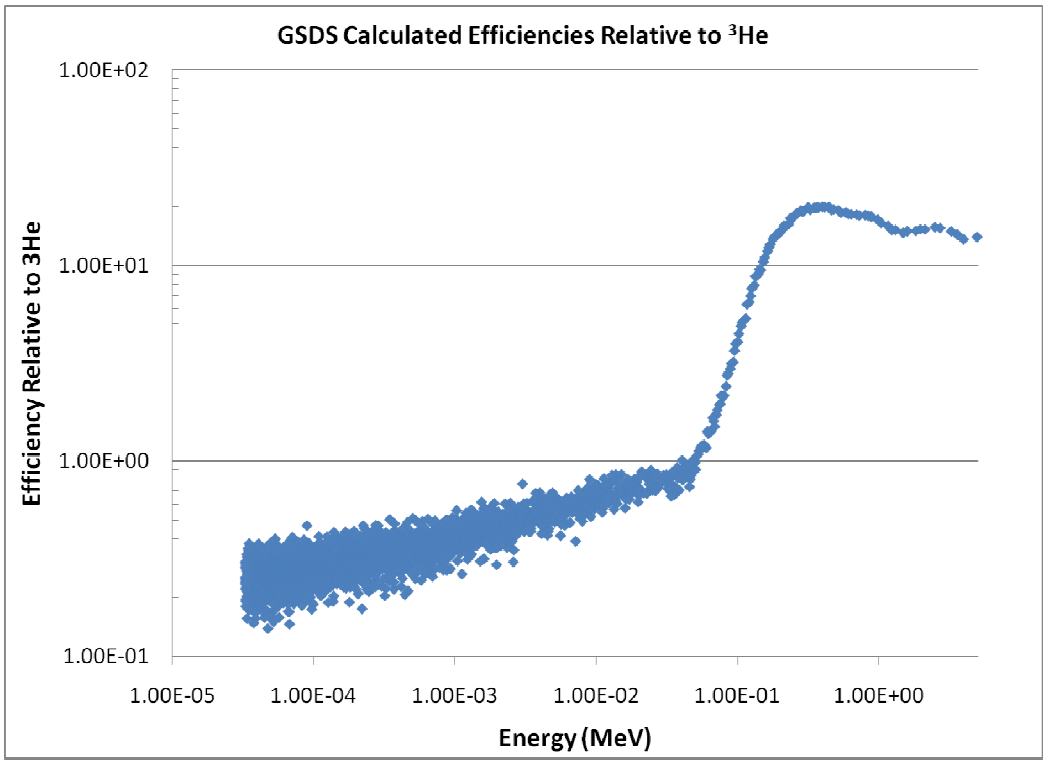

Figure 319 B:ZnO relative count rate to ^{3}He.

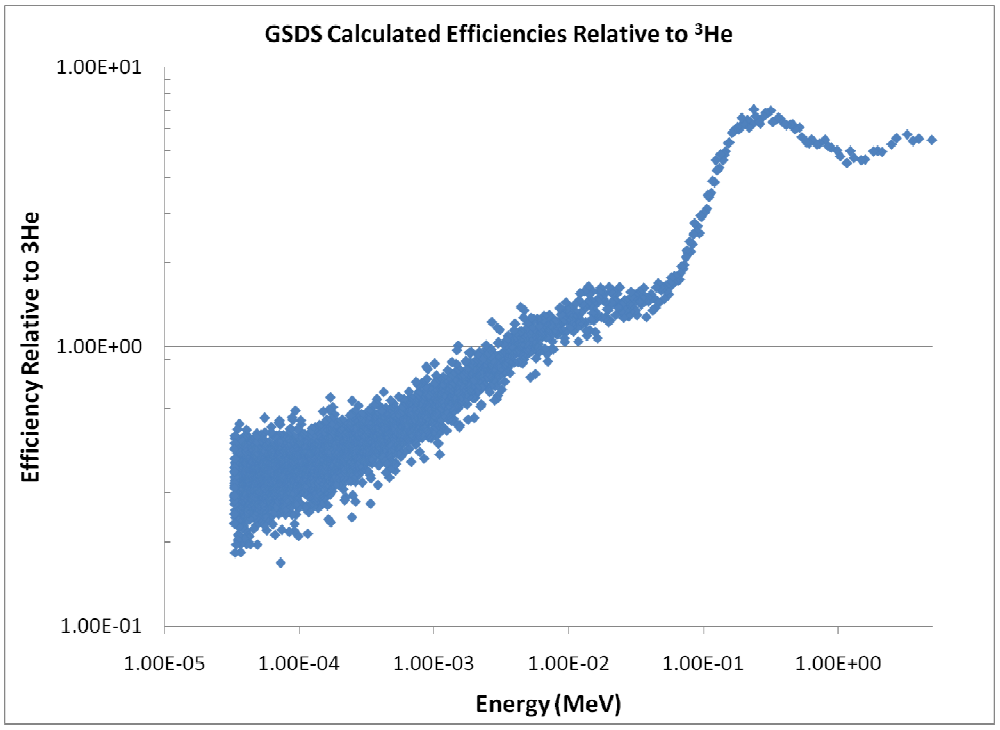

Figure 320 Li:ZnO relative count rate to^{3}He.

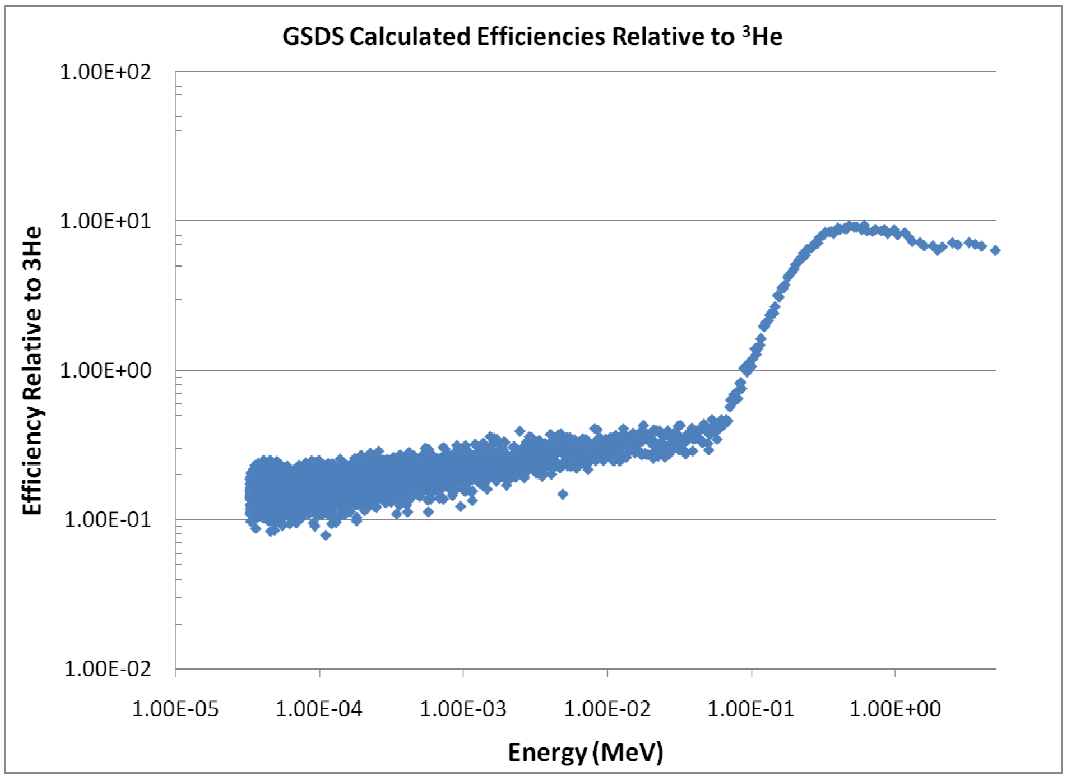

Figure 321 Undoped ZnO relative count rate to^{3}He.

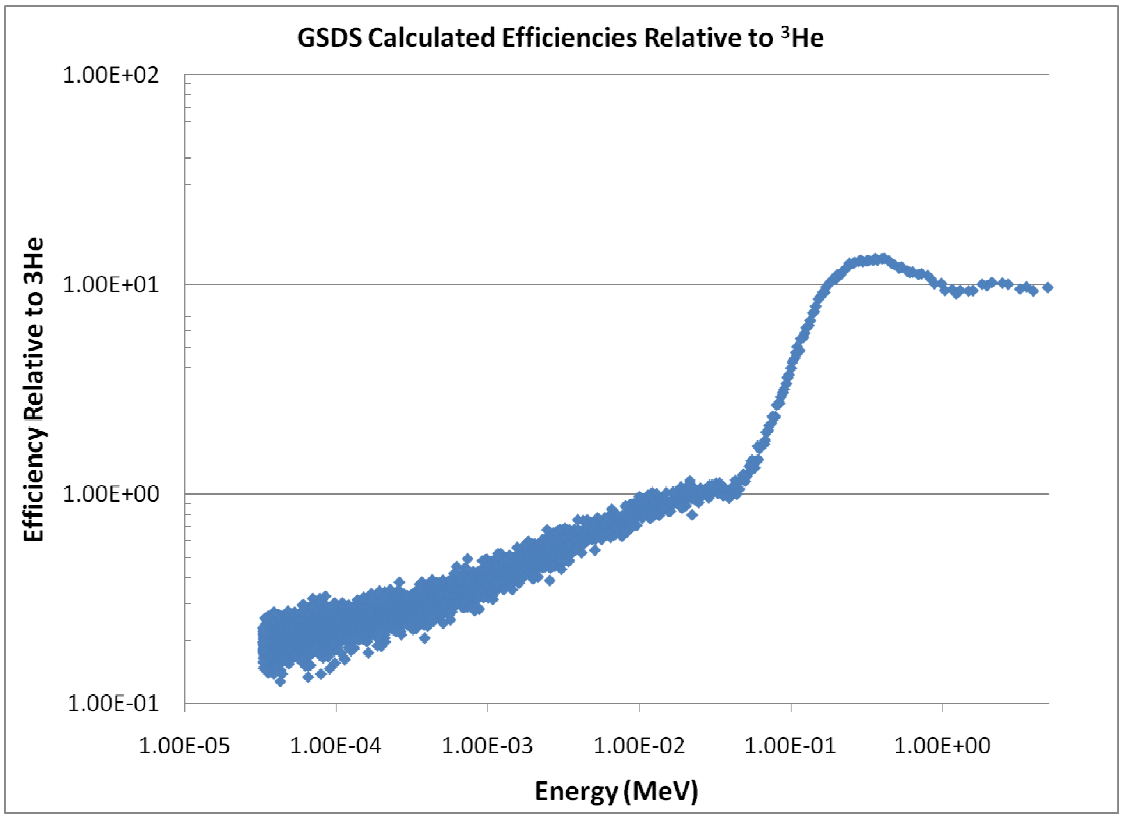

Figure 322 Ga:ZnO relative count rate to^{3}He.

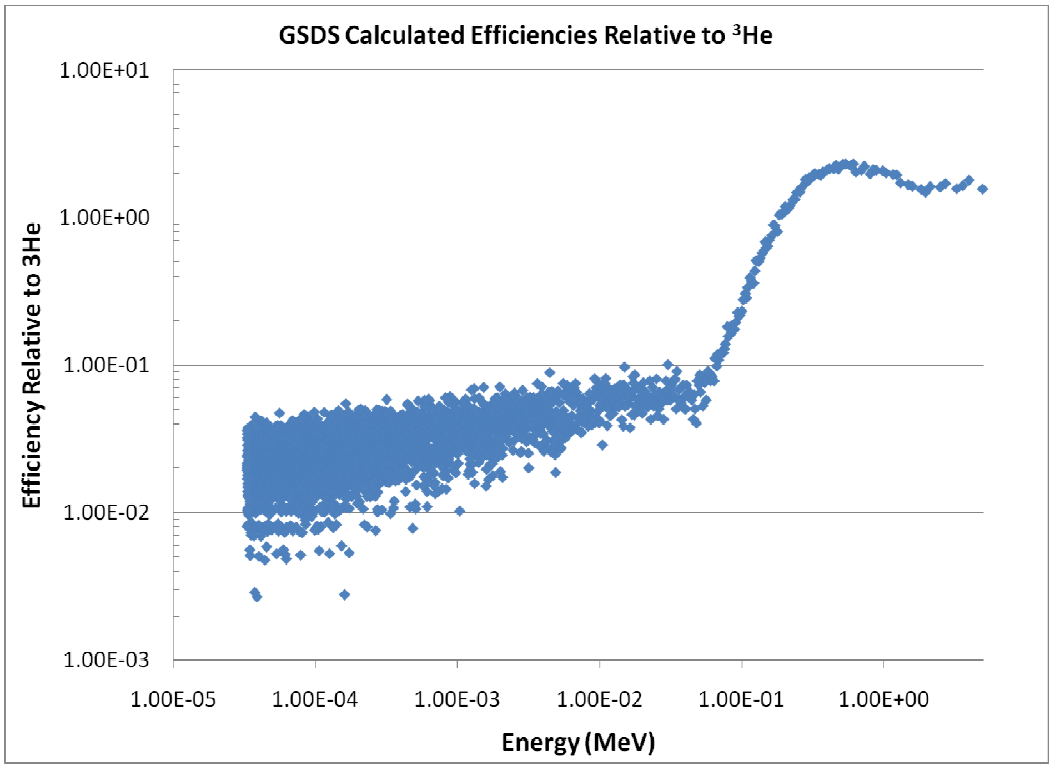

Figure 323 N:ZnO relative count rate to^{3}He.

APPENDIX D

PULSE HEIGHT RISE AND FALL TIMES

Several different pulses were digitized for each of the scintillators using the alpha source. These can be seen below in Figures 324- Figure 328. The pulses show a very fast rise and fall time which is limited mostly to the speed of the PMT. In future work a faster PMT and digital oscilloscope are needed to measure these parameters adequately.

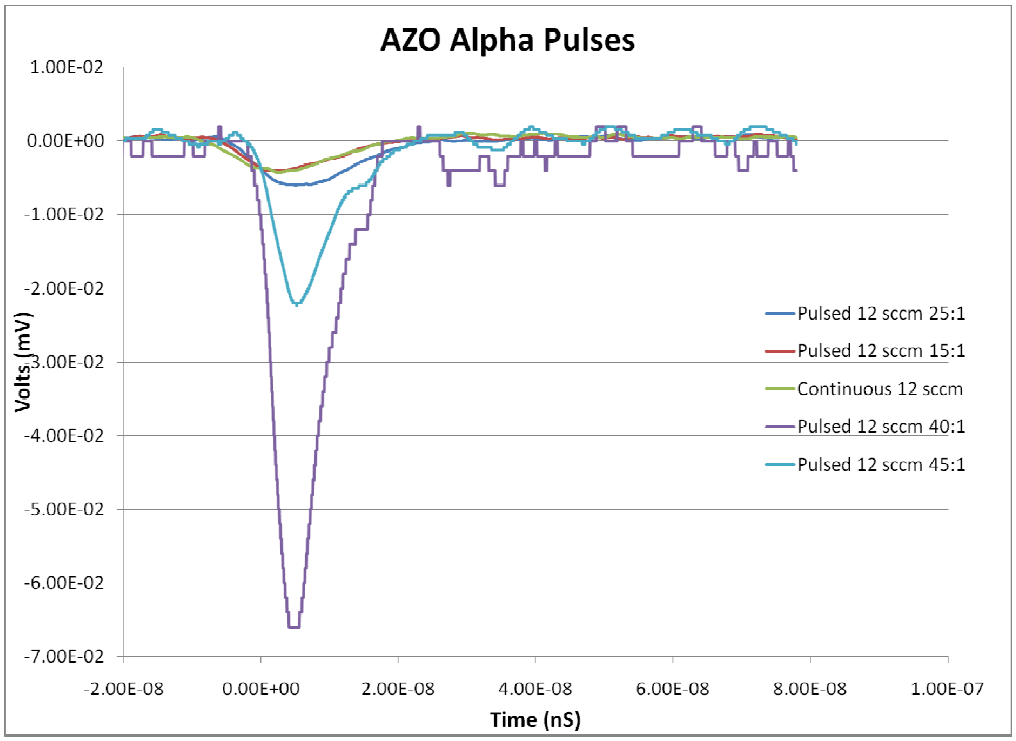

Figure 324 Pulse digitization of AZO.

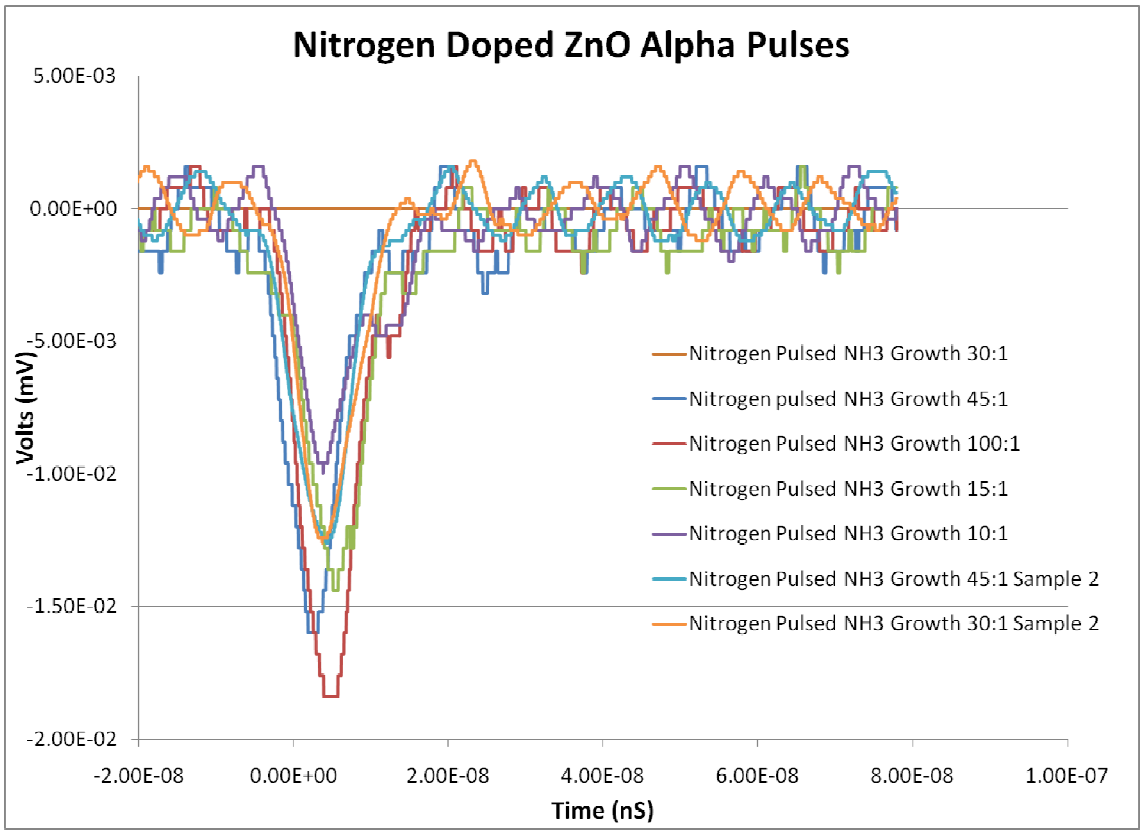

Figure 325 Pulse digitization of N:ZnO.

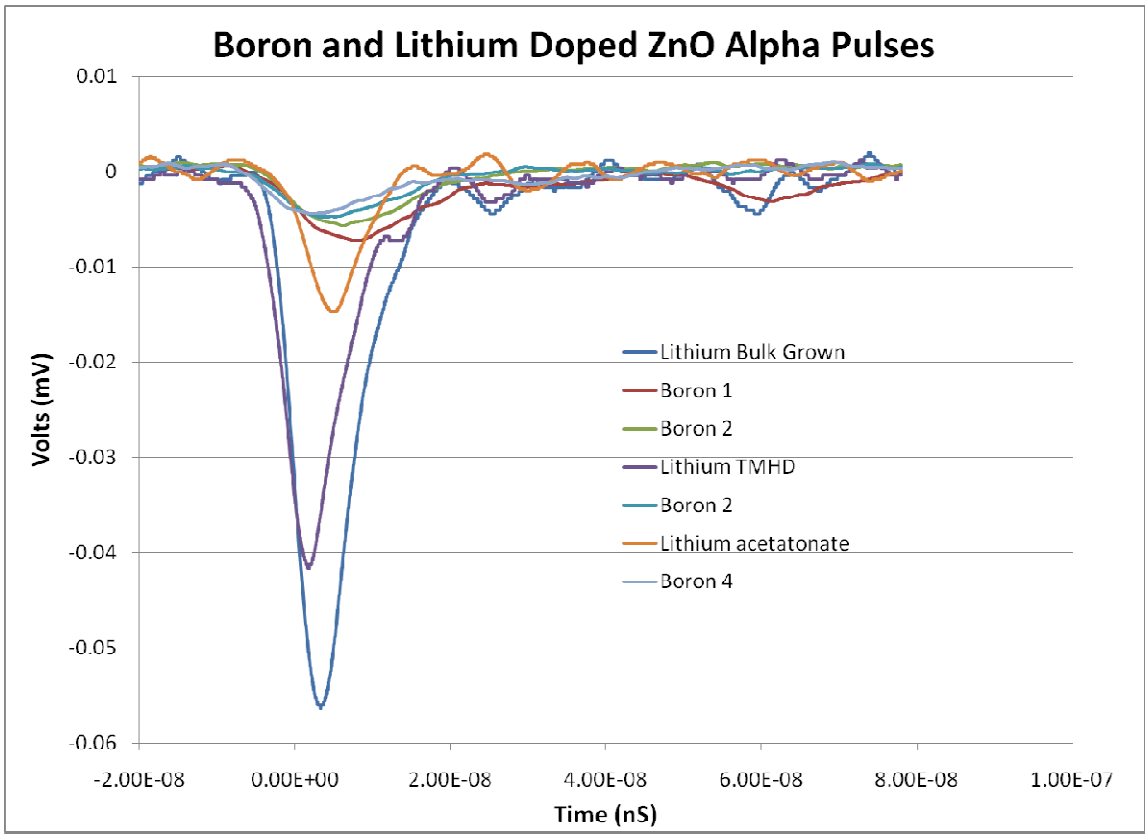

Figure 326 Pulse digitization of B:ZnO and Li:ZnO.

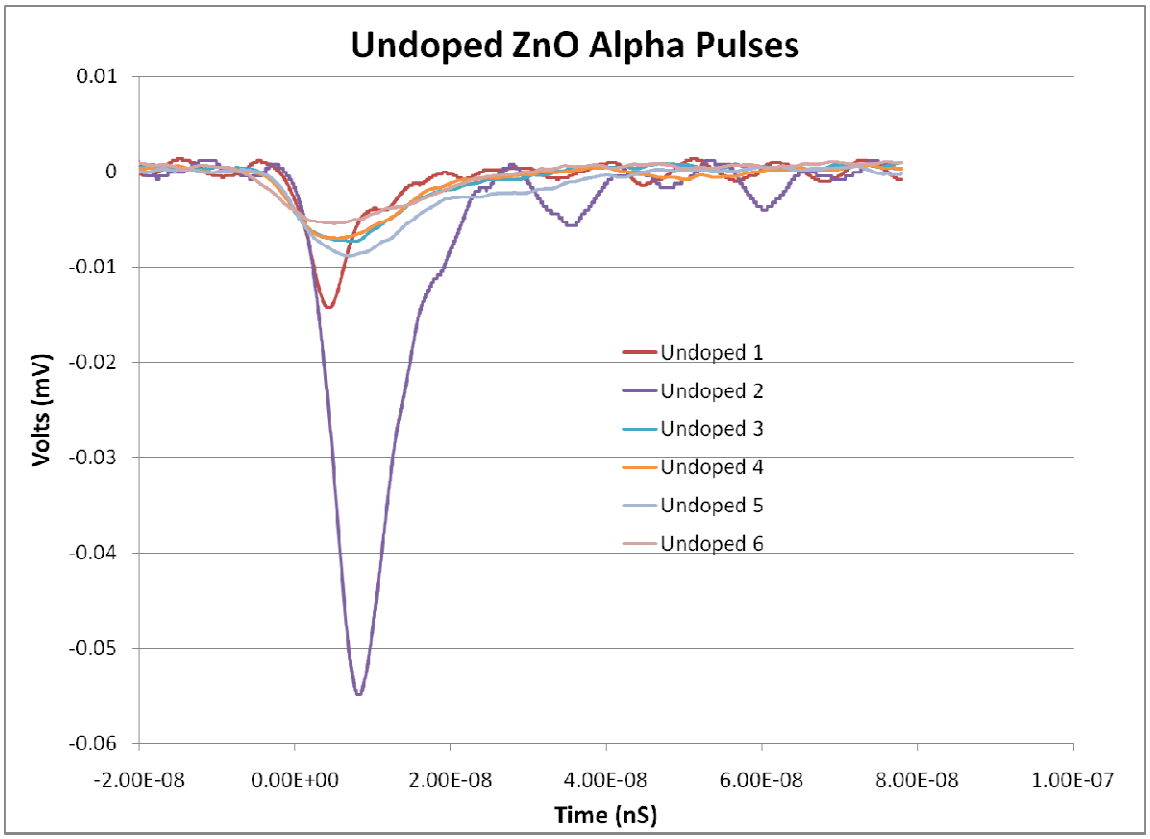

Figure 327 Pulse digitization of undoped ZnO

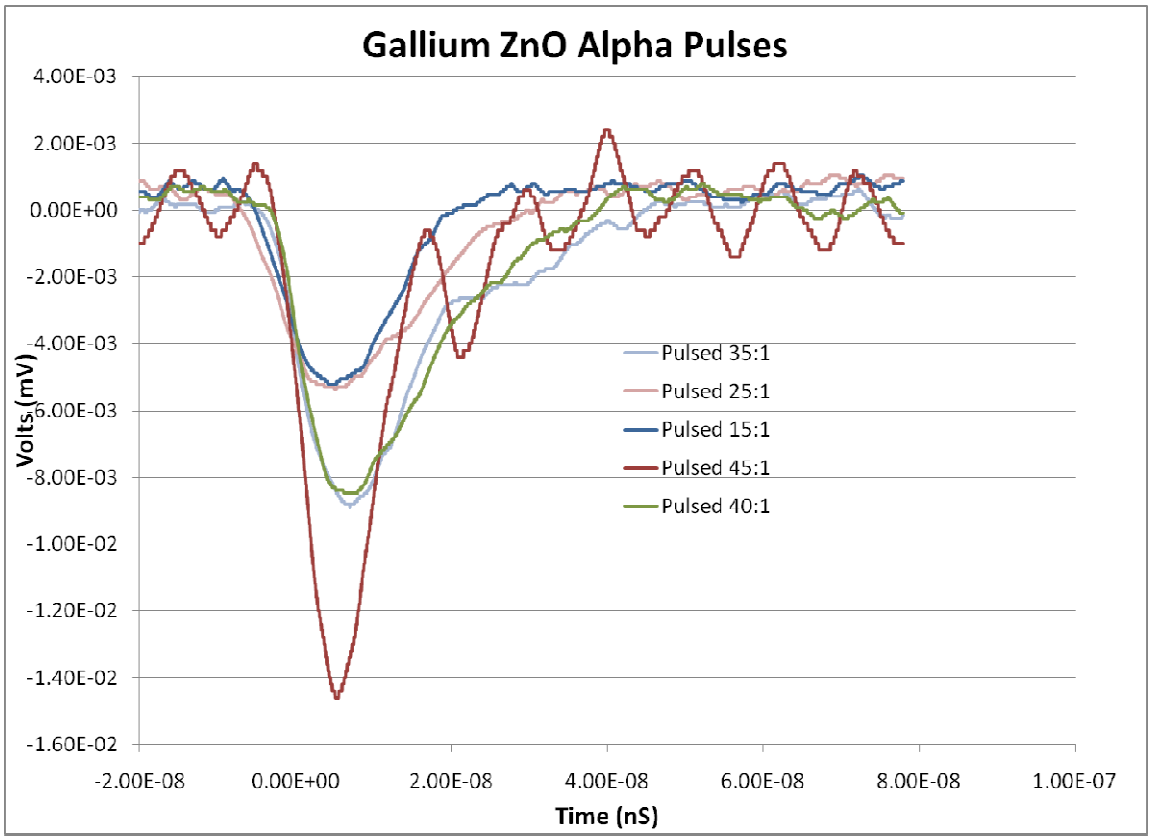

Figure 328 Pulse digitization of Ga:ZnO.

CHAPTER XI

Bibliography

1. **Cooper, Ron, et.al.** *A PROGRAM FOR NEUTRON DETECTOR RESEARCH AND DEVELOPMENT.* ORNL : Oak Ridge National Laboratory, 2003.
2. **Kouzes,** *The 3He Supply Shortage.* Pacific Northwest National Laboratory, 2009, PNNL-18388.
3. **Hanson, T.,** *Methods in Science and Engineering.* AIP, 2005, Vol. 803.
4. **National Academic Press,** *The Impact of Selling the Federal Helium Researve.* Washington D.C. : National Academy Press, 2004.
5. **Aliberti, G. Et. Al.** Nuclear Data Sensitivity, Uncertinty and Target Accuracy Assesment for Future Nuclear Systems. *Annuls of Nuclear Energy.* 2006, Vol. I, 33.
6. **Slaughter, D. et. al.,** *Detection of Special Nuclear Material in Cargo Containers using Neutron Interrogation.*, Lawrence Livermore National Laboratory, 2003, Vols. UCRL-ID-155315.
7. **Mihalczo, J., Mattingly, J., Neal, J., Mullens J.** *Nuclear Instruments and Methods B.* 1-4, Elsevier, 2004, Vol. 213.
8. **Nieto, M.,** *Resource Note on Photofission of Nuclei, for U-235 and Pu-239 Detection,*Los Alamos National Laboratory, 2003, Vols. LA-UR-03-2056.
9. **Lavietes, A. D.,** *Preliminary Uranium Enrichment Analysis Results Using Cadmium Zinc Telluride Detectors.* Grenoble, France Lawrence Livermore National Laboratory, 1995.
10. **Congress, United States of America.** *Security and Accountability for Every Port Act.* 2006. H.R.4954.
11. **Moss, C.E.,** *Nuclear Instruments and Methods B.* 1-4, Elsevier , 2005, Vol. 241.

12. **Jones, J. et. al.,** *Photofission-based Material Detection: Technology Demonstrations.*: Idaho National Enginering Enviromental Laboratory, 2003, Vols. INEEL/EXT-02-01406.

13. **R. Norman, J. Jones et. al.,** *PITAS Generation III System Design Report: The Developmental Prototype.* Idaho National Laboratory, 2008, Vols. INL/EXT-08-13798.

14. **Tuli, K. Jangdish.** *Nuclear Wallet Cards.* Brookhaven : National Nuclear Data Center, April 2005.

15. **Kopp, M. Valentine, K., Chrisophorou, L. Carter, J.,** *Nuclear Instruments and Methods in Physics Research.* 2-3, Elsevier, 1982, Vol. 201.

16. **Thomas, D., Alevra, A.,** *Nuclear Instruments and Methods A,.* 1-2, 476

17. **Burgett, Eric.** *A Broad Spectrum Neutron Spectrometer.* Atlanta : Georgia Institute of Technology, 2008.

18. **Wiegel, Burkhard et. al.** *Neutron Multisphere and More, NEMUS.*

19. **Seabury, E., Chichester, D.,***A Study of 3He Detectors for Active Interrogation.* Idaho National Laboratory, 2009, Vols. INL/CON-09-15931.

20. **Dighe, P., Prasad, K., Kataria, S.** *Nuclear Instruments and Methods A.* 1-2, Elsevier, 2004, Vol. 523.

21. *Physica.* **Boyd, H., Hamilton, J., Sattler, A., Goudsmit, P.** 1, Elsevier, 1964, Vol. 30.

22. **Rhodes, R.,** *Makding of the atomic bomb,* Simon and Schuster, 1986.

23. . **Wender, S. et. al.,** *Nuclear Instruments and Methods, A*1-2, Elsevier, 1993, Vol. 336.

24. **Welty, R.J., C.L. Cheung, C.E. Reinhardt,T.F. Wang.** *Roadmap for High Efficiency Solid-State Neutron Detectors".* Boston : SPIE Optics, 2005.

25. **Welty, R.J., C.L. Cheung, C.E. Reinhardt, T.F. Wang.** *Solid State Pillar Structred Thermal Neutron Detector.* Peutro Rico : IEEE Nuclear Science Symposium, 2005.

26. **S.L. Belinger, W.J. McNeil, T.C. Unruh, D.S. McGregor,** *Angular response of Perforated Silicon Diode High Efficiency Neutron Detectors.* Waikiki : IEEE Nuclear Science Symposium, 2007.

27. **Birks, J.** *The Theory and Practice of Scintillation Counting.* New York : Pergamon Press, 1964.

28. **Moszynski, M. et. al.,** *Nuclear Instruments and Methods A.* 1-2, Elsevier, 1994, Vol. 350.

29. . **Rochman, D. et. al.** *Nuclear Instruments and Methods A.*1-2,. : Elsevier, 2004, Vol. 523.

30. **Batchelor, R., Gilboy, W., Parker, J., Towele, J.,** *Nuclear Instruments and Methods.* 1, Elsevier, 1961, Vol. 13.

31. —. **Roush, M., Wilson, M., Hornyak, W.** 1, s.l. : Elsevier, 1964, Vol. 31.

32. **Czirr, J., et al.,** *Nuclear Instruments and Methods A.* 1-2, Elsevier, 2002, Vol. 476.

33. **Flaska, M., Pozzi, S.** *Nuclear Instruments and Methods A.* 2-3, Elsevier, 2009, Vol. 599.

34. **Technologies, ELJEN,** *EJ-301 MSDS Data Sheet.***.** 2005.

35. **Mihalczo, J., Mullens, J. Mattingly, J., Valentine, T.,** *Nuclear Instruments and Methods A.* 2-3, Elsevier, 2000, Vol. 450.

36. **Turner, J.** *Atoms, Radiation, and Radiation Protection,*Wiley-VCH, 2009.

37. **Choong, W.,** *Performance of a Facility for Measuring Scintillator Non-Proportionality.***.** Lawrence Berkeley National Laboratory, 2008, Vols. LBNL-784E.

38. **Gardiner, R., et. al.,** *Applied Radiation and Isotopes.* 4-5, s.l. : Elsevier, 2000, Vol. 53.

39. **Leinweberm, G., et. al.,** *Nuclear Science and Engineering,*Elsevier, 2006, Vol. 154.

40. **Berger, M., Seltzer, S.,** *Tables of Energy-Loss and Ranges of Electrons and Positrons.* 1964.

41. **Vavilov, P.V.,** *Soviet Physics JETP.* 1957, Vol. 5.

42. **Ziegler, J., Biersack, J., Ziegler, M.,** *SRIM: The Stopping and Range of Ions in Matter.* Morrisville : Lulu Press Company, 2008.

43. **McKinney, G. et. al.,** *MCNPX 2.7.X - New Features Being Developed ,*Los Alamos National Laboratory, 2010, Vols. LA-UR-09-6788.

44. **Krane, K.** *Introductory Nuclear Physics,*Wiley, 1987.

45. **Knoll, Glen.** *Radiation Detection and Measurements.* 2004.

46. **Rooney, B., Valentine, J.,** *IEEE Transactions of Nuclear Science.***.** 3, 1997, Vol. 44.

47. **Lunby** *Physics Review.***,**AIP, 1950, Vol. 80.

48. **Nikl, M.,** *Physica Status Solidi (a).* 2, s.l. : Wiley VCH, 2000, Vol. 178.

49. **Birks, J., Firk, F.,** *Physics Today.* 8, s.l. : Elsevier, 1962, Vol. 18.

50. **Photonics, Hammamatsu,** *Photomultiplier Tube Properties.* 2008.

51. **Curran, S.,** *Luminescence and the Scintillation Counter.* London : Buttersworth Scientific Publications, 1953.

52. **James, K. Masterson, M.,** *Nuclear Instruments and Methods A.* 1-2, s.l. : Elsevier, 1992, Vol. 313.

53. **Curran, S.C., Baker, W.R.,***U.S. Atomic Energy Commission Report M.D.D.C-1926.***.** 1944.

54. **Lehmann W.,** *Sol. Stat. Elec.* 1966, Vol. 9.

55. **Pan, M. et. al.,** *Journal of Electronic Materials.* 4, s.l. : Springer, 2007, Vol. 36.

56. **Hull, E., et. al.,** *Nuclear Instruments and Methods.* 1-4, s.l. : Elsevier, 1995, Vol. 364.

57. **Kligshirm.,** *Phys. Status Solidi B.* 1975, Vol. 71.

58. **Morkoc, H., Ozgur, U.** *Zinc Oxide,*Wiley-VCH, 2009.

59. **Matsumoto, F., et. al.,** *Japanese Journal of Applied Physics.* 1, s.l. : JJAP, 1999, Vol. 38.

60. **Chichibu, et. al.,** *Journal of Applied Physics.* **S.** 1996, Vol. 79.

61. **Zhang, Y., et. al.,** *Chinese Physics Review Letters.* 4, s.l. : CPL, 2009, Vol. 26.

62. **Simpson P.J., et. al.** *Nuclear Instruments and Methods A.***.** 2003, Vol. 505.

63. **Simpson P.J., et. al.** *Nuclear Instruments and Methods A.***.** 2003, Vol. 505.

64. **Nickel, N., Terukov, E.** *Zinc Oxide - A Material for Micro- and Optoelectronic Applications.* St. Petersburg : Springer, 2004.

65. **Rossler, U., ed.,** *New Series, Group III.* 22, Heidelberg : Springer, 1999, Vol. 178.

66. **Kucheyev, S. et. al.,** *Applied Physics Letters.* 6, s.l. : AIP, 2002, Vol. 80.

67. **Onodera, A., et. al.,** *Japanese Journal of Applied Physics.* 1, s.l. : JJAP, 1996, Vol. 35.

68. **Postava, K., et. al.,** *Journal of Applied Physics.* 11, s.l. : Elsevier, 2000, Vol. 87.

69. **Bass, M., et. al.** *Handbook of Optics, Third Edition, Volume II, Design Fabrication and Testing,*McGraw Hill Professional, 2009.

70. **Nunes, P. et. al.,** *Vacuum.* 3-4, s.l. : Elsevier, 2002, Vol. 64.

71. **Reynolds, D., et. al.,** *Physical Review B.* 4, s.l. : APS, 1999, Vol. 60.

72. **Haupt, M. et. al.,** *Jourlan of Applied Physics.* 10, s.l. : AIP, 2003, Vol. 93.

73. **Kato, H., Sano, M., Miyamoto, K., You, T.,** *Japanese Journal of Applied Physics.* 1, s.l. : JJAP, 2003, Vol. 42.

74. **Wang, S.** *Method and Aparatus for Zinc Oxide Single Crystal Boule Growth. 7279040B1* United States of America, October 9, 2007.

75. **Ohshima, E., et. al.,** *Journal of Crystal Growth.* 1-2, s.l. : Elsevier, 2004, Vol. 260.

76. —. **Croxall, D. Ward, R., Wallace, C. Kell, R.** 2, s.l. : Elsevier, 1974, Vol. 22.

77. **Suscavage, M., et. al.,** *Journal of Nitride Semiconductor Research.* 1, 2004, Vol. 4.

78. **Razeghi, M.** *The MOCVD Challenge.* Bristol : Institute of Physics Publishing, 1995.

79. **Jansen, A., Orazem, M., Fox, B., Jesser, W.,** *Journal of Crystal Growth.* 2-3, s.l. : Elsevier, 1991, Vol. 112.

80. **Gurary, A., et. al.** *Induction Heated Chemical Vapor Deposition Reactor. 6368404B1* United States of America, April 9, 2002.

81. **Jensen, K. Fotiadas, D., Mountziaris, T.,** *Journal of Crystal Growth.* 1, s.l. : Elsevier, 1991, Vol. 107.

82. **Liu, Y. et. al.,** *Journal of Electronic Materials.* 1, Boston : Springer, 2007, Vol. 29.

83. **Xu, W., Ye, Z., Zhou, T., Zhu, L., Huang, J.,** *Journal of Crystal Growth.* 1-2, s.l. : elsevier, 2004, Vol. 265.

84. **Olson, J., Kibbler, A.** *Nuclear Instruments and Methods A. 1-3*, s.l. : Elsevier, 1986, Vol. 77.

85. **Nakamura, S.,** *Japanese Journal of Applied Physics.* 1, s.l. : JJAP, 1991, Vol. 30.

86. **Moffat, H., Jensen, K.,** *Journal of Crystal Growth.* 1-3, s.l. : Elsevier, 1986, Vol. 77.

87. **Ohtomo, A., et. al.,** *Applied Physics Letters.* 1, s.l. : Elsevier, 1999, Vol. 75.

88. **Lim, S., Kwon, S., Kim, H.,** *Thin Solid Films.* 7, s.l. : Elsevier, 2008, Vol. 516.

89. **Booth, T., Brown, F., Bull, J.,** *MCNP5 1.50 Release Notes,*Los Alamos National Laboratory, 2008, Vols. LA-UR-08-2300.

90. **Petrie, L., Fox, P., Lucius, K.,** *Standard Composition Library.* Section M8, s.l. : Oak Ridge National Laboratory, 2000, Vols. ORNL/NUREG/CSD-2/V3/R6.

91. **Bramblett, R., Ewing, R., Bonner, T.,** *Nuclear Instruments and Methods.* 1, s.l. : Elsevier, 1960, Vol. 9.

92. **Howell, R., et. al.,** *Radiation Protection Dosimetry,*In Press.

93. **Burgett, E., Hertel, N., Howel, R.,** *IEEE Transactions on Nuclear Science.* 3, s.l. : IEEE, 2008, Vol. 56.

94. **Burgett, E.** *A Broad Spectrum Neutron Spectrometer for High Energy Neutron Detection.* M.S. Thesis : Georgia Institute of Technology, 2008.

95. **Sweezy, J., Hertel, N., Veinot, K.,** *Nuclear Instruments and Methods A.* 1-2, s.l. : Elsevier, 2002, Vol. 476.

96. **Hertel, N., Davidson, W.,** *Nuclear Instruments and Methods A.* 2-3, s.l. : Elsevier, 1985, Vol. 238.

97. **Hawari, A. Werhing, B., Radulescu, H., Abdurrahman, N.** *Nuclear Instruments and Methods A.*1-4, s.l. : Elsevier, 1999, Vol. 442.

98. **Rochman, D., et. al.,** *Nuclear Instruments and Methods A.*1-2, s.l. : Elsevier, 2005, Vol. 550.

99. **Kinoshita, Katsuhisa Kudo and Tamiyoshi,** *Fusion Engineering and Design.* 1989, 2004, Vol. 10.

100. **Schuhmacher, H.,** *Radiation Protection Dosimetry.* 110, 2004, Vols. 1-4.

101. **Nolte, R.,** *Nuclear Instruments and Methods A.*110, s.l. : Oxford, 2004, Vols. 1-4.

102. *Science.* **Vukusic, P. Hooper, I.** 5751, s.l. : AAAS, 2005, Vol. 310.

103. **Joannopolous, J., Johnson, S., Winn, J., Meade, R.,** *Photonic Crystals: Modeling the Flow of Light.* Princeton : Princeton University Press, 2008.

104. **Yablonovitch, E.,** *Journal of the Optics Society of America, B.* 2, s.l. : Optics Society of America, 1993, Vol. 10.

105. **Bloembergen, N.** *Nonlinear Optics, 4th Edition,*World Scientific Publishing Company, 2005.

106. **Williams, T. Kelly, C.,** *Gnuplot, An Interactive Plotting Program.* 2010.

107. **Vo, D.,** *Evaluation of the Commercial Spectrometer Systems for Safegaurds Applications Using the Germanium Detectors,*Los Alamos National Laboratory, 1998, Vols. LA-UR-98-2939.

108. **Choi, Y., et. al.,** *IEEE Transactions on Electron Devices.* 1, s.l. : IEEE, 2010, Vol. 57.

109. **Lee, W., Nielsch, K. Gosele, U.,** *Nanotechnology..* 47, s.l. : Elseiver, 2007, Vol. 18.

110. **Wilks, J.** *The Properties of Liquid and Solid Helium.* Oxford : Camden Press, 1967.

111. **Voytchev, M., Iniguez, M. Mendez, R., Mananaes, A., Rodriguez, L. Barquero, R.,** *Neutron Detection with a Silicon PIN Photodiode and 6LiF Converter.* 2003, Nucl. Instr. Meth. A, pp. 546-552.

112. **Reynolds.,** *"High Quality, Melt-Grown ZnO Single Crystals".* 2009, Journal of Applied Physics, p. 4809.

113. **Neal,** *ZnO Scintillators.***.** 2008, IEEE Transactions on Nuclear Science, Vol. 55, p. 1397.

114. **Burgett, E. Hertel, N.,** *"Collimated Thermal Neutron Beam Line at the Georgia Tech Graphite Pile Facility"***.** Washington DC : ANS, 2008. Transactions of the American Nuclear Society.

115. **Chichibu S., et.al.,** *J. Appl. Phys.* 1996, Vol. 79.

116. **Strellis, D., Gozani, T.,** *Applied radiation and Isotopes.* 5-6, s.l. : Elsevier , 2005, Vol. 63.

117. **Filss, P.,** *Nuclear Engineering and Design.* 2, s.l. : Elsevier, 1991, Vol. 131.

118. **Cho, A,** *Science***.** 5954, s.l. : AAAS, 2009, Vol. 326.

119. **Cochran, T., Paine, C.,** *Nuclear Weapons Databook,*National Nuclear Data Center, 1995.